Transactions of the ASME®

Technical Editor, LEWIS T. WHEELER (1997)

Department of Mechanical Engineering,
University of Houston,
Houston, TX 77204-4792

APPLIED MECHANICS DIVISION

Chairman, L. B. FREUND
Secretary, C. T. HERAKOVICH
Associate Technical Editors,
R. ABEYARATNE (1994)
T. R. AKYLAS (1994)
D. M. BARNETT (1996)
S. A. BERGER (1994)
I. M. DANIEL (1996)
G. J. DVORAK (1995)
E. J. HAUG, JR. (1996)
S. LICHTER (1995)
W. K. LIU (1996)
X. MARKENSCOFF (1994)
D. M. PARKS (1995)
J. N. REDDY (1995)
J. W. RUDNICKI (1994)
W. N. SHARPE, JR. (1996)
S. W. SHAW (1997)
C. F. SHIH (1995)
P. D. SPANOS (1994)
M. TAYA (1996)
F. Y. M. WAN (1994)

BOARD ON COMMUNICATIONS

Chairman and Vice-President
R. D. ROCKE

Members-at-Large
T. BARLOW, T. DEAR, L. M. KEER, J. KITTO,
W. MORGAN, E. M. PATTON, S. PATULSKI,
R. E. REDER, R. SHAH, A. VAN DER SLUYS,
F. M. WHITE, J. WHITEHEAD

OFFICERS OF THE ASME
President, J. H. FERNANDES
Exec. Director
D. L. BELDEN
Treasurer
R. A. BENNETT

PUBLISHING STAFF
Mng. Dir., Publ.,
CHARLES W. BEARDSLEY
Managing Editor,
CORNELIA MONAHAN
Production Editor,
JUDITH SIERANT
Production Assistant,
MARISOL ANDINO

Transactions of the ASME, Journal of Applied Mechanics (ISSN 0021-8936) is published quarterly (Mar., June, Sept., Dec.) for $165.00 per year by The American Society of Mechanical Engineers, 345 East 47th Street, New York, NY 10017. Second class postage paid at New York, NY and additional mailing office. POSTMASTER: Send address changes to Transactions of the ASME, Journal of Applied Mechanics, c/o THE AMERICAN SOCIETY OF MECHANICAL ENGINEERS, 22 Law Drive, Box 2300, Fairfield, NJ 07007-2300.

CHANGES OF ADDRESS must be received at Society headquarters seven weeks before they are to be effective. Please send old label and new address.

PRICES: To members, $40.00, annually: to nonmembers, $165.00. Add $24.00 for postage to countries outside the United States and Canada.

STATEMENT from By-Laws. The Society shall not be responsible for statements or opinions advanced in papers or . . . printed in its publications (B7.1, Par. 3).

COPYRIGHT © 1994 by The American Society of Mechanical Engineers. Authorization to photocopy material for internal or personal use under circumstances not falling within the fair use provisions of the Copyright Act is granted by ASME to libraries and other users registered with the Copyright Clearance Center (CCC) Transactional Reporting Service provided that the base fee of $3.00 per article is paid directly to CCC, 27 Congress St., Salem, MA 01970. Request for special permission or bulk copying should be addressed to Reprints/Permission Department.

INDEXED by Applied Mechanics Reviews and Engineering Information, Inc. Canadian Goods & Services Tax Registration #126148048

Journal of Applied Mechanics

Published Quarterly by The American Society of Mechanical Engineers

VOLUME 61 • NUMBER 1 • MARCH 1994

TECHNICAL PAPERS

1 The Effect of Wire Rope Mechanics on the Material Properties of Cord Composites: An Elasticity Approach (93-WA/APM-23)
C. K. Shield and G. A. Costello

9 The Effect of Wire Rope Mechanics on the Material Properties of Cord Composite Laminates—An Energy Approach (93-WA/APM-24)
C. K. Shield and G. A. Costello

16 Steady Motion of a Thread Over a Rotating Roller
R.-J. Yang

23 Antiplane Shear Deformations for Homogeneous and Inhomogeneous Anisotropic Linearly Elastic Solids
C. O. Horgan and K. L. Miller

30 The End Problem of Incompressible Elastic Cylinders (93-WA/APM-21)
Y. Ling, P. A. Engel, and J. A. Geer

38 Analysis of Kinked Interfacial Crack Under Out-of-Plane Shear
S. R. Choi, K. S. Lee, and Y. Y. Earmme

45 A Progressive Damage Modeling Based on the Continuum Damage Mechanics and its Finite Element Analysis
S. J. Kim and W. D. Kim

54 Three-Dimensional Unilateral Frictionless Contact Problem for Finite Bodies (93-WA/APM-20)
V. L. Rabinovich, S. R. Sipcic, and V. K. Sarin

60 The Contact Behavior Between Laminated Composite Plates and Rigid Spheres
E. Wu and C. S. Yen

67 Mechanical and Thermal Wrinkling of Polymer Membranes (93-WA/APM-25)
H. C. Chiu, R. C. Benson, M. D. Fiscella, and S. J. Burns

71 A Second-Law Analysis of Thermoelastic Damping
V. R. Kinra and K. B. Milligan

77 Characteristics of Modal Coupling in Nonclassically Damped Systems Under Harmonic Excitation
I. W. Park, J. S. Kim, and F. Ma

84 Distributed Transfer Function Analysis of Complex Distributed Parameter Systems
B. Yang

93 On Statistics of First-Passage Failure
G. Q. Cai and Y. K. Lin

100 Component Modal Synthesis Methods Based on Hybrid Models, Part I: Theory of Hybrid Models and Modal Truncation Methods
L. Jezequel and H. D. Setio

109 Component Modal Synthesis Methods Based on Hybrid Models, Part II: Numerical Tests and Experimental Identification of Hybrid Models
L. Jezequel and H. D. Setio

117 Angular Momentum of a Torque-Free Deforming Axisymmetric Gyro
F. P. J. Rimrott and F. Janabi-Sharifi

124 Theoretical Simulation of an Anomalous Response in a Torsional Oscillator (93-WA/APM-22)
M. Negahban

131 Mode-Locking and Chaos in a Jeffcott Rotor With Bearing Clearances
S.-K. Choi and S. T. Noah

139 A Rotation Rate Sensor Based Upon a Rayleigh Resonator
N. S. Clarke and J. S. Burdess

144 Domains of Attraction of a Forced Beam by Interpolated Mapping
W. K. Lee and M. R. Ghang

152 Dynamic Response of a Spinning Timoshenko Beam With General Boundary Conditions and Subjected to a Moving Load (93-WA/APM-26)
J. W.-Z. Zu and R. P. S. Han

161 Boundary Layer Transient Hygroscopic Stresses in Orthotropic Thick Shells Under External Pressure
G. A. Kardomateas and C. B. Chung

169 Thermo-Elastoviscoplastic Buckling Behavior of Plates
G. J. Simitses and Y. Song

176 The Mechanics of Ideal Forming (93-WA/APM-19)
K. Chung and O. Richmond

182 The Internal Stresses in Wound Rolls With the Presence of a Nip Roller
J. K. Good, Z. Wu, and M. W. R. Fikes

186 Analysis of High-Speed Rotating Disks With Variable Thickness and Inhomogeneity
K.-Y. Yeh and R. P. S. Han

192 Thermal Stresses in a Bimaterial Joint: An Experimental Analysis
D. Post, J. D. Wood, B. Han, V. J. Parks, and F. B. Gerstle, Jr.

(Contents continued on Outside Back Cover)

Downloaded 04 May 2010 to 171.66.16.52. Redistribution subject to ASME license or copyright; see http://www.asme.org/terms/Terms_Use.cfm

CONTENTS (CONTINUED)

BRIEF NOTES

199 On the Permanent Rotation of a Torque-Free Two-Body System With a Flexible Connection
Y. Z. Liu and F. P. J. Rimrott

202 The Study of Mechanical Parameters of Finite Deformation of Membranes
Gao Yongxiang and Luo Jisheng

204 A Numerical Solution of Two-Dimensional Torsional Waves in an Elastic/Viscoplastic Cylinder
Kaishin Liu and Takashi Yokoyama

206 On a Class of Planar Motions of Flexible Rods
H. Cohen and M. Epstein

208 A Note on Oscillatory Couette Flow in a Rotating System
R. Ganapathy

209 Closed-Form Analysis of the Free Edge Effect in Angle-Ply Laminates
W. Becker

211 Stochastic Response of Hysteretic System to Narrow-Band Excitation
W. Q. Zhu, C. D. Huang, and T. T. Soong

213 Stresses Around a Circular Hole in a Uniform Bar in Torsion
J. A. Greenwood

214 A Note on Axisymmetric *J*-Integrals
H. F. Nied

217 Potential Functions of an Edge Dislocation Associated With a Circular Inclusion
Ru-Min Chao

219 Green Functions for Cylindrical Elastic Waves in Aluminum: Comparison Between Theory and Experiments
A. Mourad, B. Castagnede, and E. Mottay

221 Criteria of Dynamic Crack Initiation
Masaaki Watanabe

DISCUSSIONS

224 **Random Vibrations of Externally Damped Viscoelastic Timoshenko Beams With General Boundary Conditions, by M. P. Singh and A. S. Abdelnaser—Discussion by I. Elishakoff**

225 **Buckling of Thick Orthotropic Cylindrical Shells Under External Pressure** and **Stability Loss in Thick Transversely Isotropic Cylindrical Shells Under Axial Compression, by G. Kardomateas—Discussion by S. B. Dong with Author's Closure**

BOOK REVIEWS

226 ***Fundamentals of Friction: Macroscopic and Microscopic Processes*, edited by I. L. Singer and H. M. Pollack . . .** Reviewed by **O. Vingsbo**

226 ***The General Problem of the Stability of Motion*, by A. M. Lyapuunov . . .** Reviewed by **J. A. Walker**

ERRATUM

66 **Steady-State Transonic Motion of a Line Load Over an Elastic Half-Space: The Corrected Cole/Huth Solution, by H. G. Georgiadis and J. R. Barber and published in the Sept. 1993 issue of the *Journal of Applied Mechanics***

ANNOUNCEMENTS AND SPECIAL NOTES

22 Thermal Stresses '95—Announcement

53 Change of Address Form

83 Europe-U.S. Workshop on Fracture of Quasibrittle Materials—Announcement

130 Eighth International Conference on Pressure Vessel Technology—Announcement

160 19th International Congress of Theoretical and Applied Mechanics—Announcement

227 Books Received by the Office of the Technical Editor

228 Worldwide Mechanics Meetings List

230 Information for Authors

Downloaded 04 May 2010 to 171.66.16.52. Redistribution subject to ASME license or copyright; see http://www.asme.org/terms/Terms_Use.cfm

The Effect of Wire Rope Mechanics on the Material Properties of Cord Composites: An Elasticity Approach

C. K. Shield
Assistant Professor,
Department of Civil and Mineral Engineering,
University of Minnesota,
Minneapolis, MN 55455
Mem. ASME

G. A. Costello
Professor,
Department of Theoretical and Applied Mechanics,
University of Illinois at Urbana-Champaign,
Urbana, IL 61801

An analytical model is presented for the behavior of cord reinforced rubber composite plates taking into account the extension-twisting coupling of the cord based on an equilibrium formulation. The effect of the cord mechanics on the unidirectional lamina properties is investigated for various modulus ratios and geometries. The equations of equilibrium are derived for the unidirectional plate. Solutions are found for the following plate problems, uniaxial tension along the cord direction, uniaxial tension perpendicular to the cord direction, and pure shear. These solutions are used to obtain average material properties and to investigate the influence of cord mechanics on the plate response. For very flexible synthetic rubbers, the behavior of the unidirectional lamina exhibits a good deal of extension twisting coupling, whereas for stiffer vulcanized rubbers, the rubber acts to restrain the cords from unwinding.

Introduction

The use of wire-rope-reinforced composites has become commonplace in today's society. The most common form of wire rope composites is wire-rope-reinforced rubber laminates (hereafter called cord-rubber laminates). These types of composites are used in pneumatic tires, conveyer belts, and various military components, such as sonar domes. This combination of materials is especially effective when the composite material needs to be strong in extension in the cord direction, but also needs to be flexible in the plane perpendicular to the cords. This property is desirable in conveyer belts, so that they will not fatigue quickly as they change direction over rollers, but will be strong enough not to pull apart from the tensile forces driving them. This property is also desirable in car tires. They need the strength in the cord direction to hold the air pressure, but need to be flexible in order to provide a comfortable ride and cut down on fatigue from bumpy roads.

A good review of the work done in cord-rubber composites is presented by Walter (1978). Currently the main methods for analyzing cord-rubber composites are experimental methods, classical lamination theory methods, and finite element methods. Kumar and Bert (1982) performed a series of tension tests to determine the in-plane stress-strain response of a single-ply unidirectional cord-rubber composite at various cord angles. Hsieh (1985) presented a finite element model for cord-reinforced laminates. Analytical methods for predicting composite behavior are superior to experimental methods, because of the large number of design variables available in composite design. Analytical solutions can cut down on the number of design cycles and can be used to optimize designs.

Before the mechanical response of an assemblage of cord-rubber layers can be understood, the mechanics of a single unidirectional lamina must be understood. The mechanics of this lamina should be based on the mechanics of its constituents, cord, and matrix. Investigators have steered away from analytical models for cord composites because of the difficulty in analyzing the cord mechanics. Many investigators who have tried to predict the behavior of cord composites analytically have typically ignored the mechanics of the cord, and treated the cord-rubber lamina as an orthotropic material. Gough (1967) and Tangorra (1969) developed expressions for the elastic constants of a single unidirectional ply based on the methods of analyzing plywood. They neglected the flexural stiffness of the cords and treated them as unidirectional load carrying members, with no transverse properties. They ignored the tension-twisting coupling of the cord. Akasaka and Hirano (1972) further simplified the Gough-Tangorra relations by utilizing the large difference in moduli, and the fact that for most applications, the cord volume fraction is small. Once the elastic constants are known for a single ply, the constants for a ply, or series of plies at arbitrary orientations, can be determined using classical lamination theory (Jones, 1975) if lamination

Contributed by the Applied Mechanics Division of THE AMERICAN SOCIETY OF MECHANICAL ENGINEERS for presentation at the ASME Winter Annual Meeting, New Orleans, LA, Nov. 28–Dec. 3, 1993.

Discussion on this paper should be addressed to the Technical Editor, Professor Lewis T. Wheeler, Department of Mechanical Engineering, University of Houston, Houston, TX 77204-4792, and will be accepted until four months after final publication of the paper itself in the ASME JOURNAL OF APPLIED MECHANICS.

Manuscript received by the ASME Applied Mechanics Division, Sept. 9, 1992; final revision, Feb. 10, 1993. Associate Technical Editor: J. N. Reddy.

Paper No. 93-WA/APM-23.

Copyright © 1994 by ASME
Downloaded 03 May 2010 to 171.66.16.20. Redistribution subject to ASME license or copyright; see http://www.asme.org/terms/Terms_Use.cfm

theory is appropriate. Shield and Costello (1993) have investigated the appropriateness of lamination theory for cord composites when the cord-matrix modulus ratios are very large.

By modeling the cord composite as orthotropic a part of the mechanical response of the cord is neglected. If the cord is treated as a single body it exhibits extension-twisting coupling; when a cord is pulled on, it also rotates. Costello (1990) has developed both a general theory and a linear theory for the response of a cord that exhibits this behavior. This coupling between extension and rotation will also be apparent in the general lamina response. Therefore, it may not be appropriate to classify the lamina as orthotropic. To include these effects a more general theory will be developed.

Classical lamination theory is based on some approximations that are not necessary when considering cord composites. In classical lamination theory, the exact distribution of the cord in the ply is not taken into account. With typical fiber composites this is a benefit, because the exact location of the reinforcement is not known. However, in cord composites the cords are purposefully placed carefully in the matrix, and their location is known. Typically, the cords are all evenly spaced at specific heights through the thickness of the plate. The cord is also much larger than a typical fiber in a fiber composite. Fibers are usually several orders of magnitude smaller than the thickness of the ply while the cords are on the order of the thickness of the ply.

The models developed in this work will be based on the cord equations of Costello (1990). An equilibrium formualation will be presented. For this theory the action of the cords will be smeared out over the layer containing the cords, but acting at the exact height that they are placed in the ply. Three specific problems will be solved using this method: (1) the solution to the axial tension problem along the cord axis, (2) the solution of the axial tension problem perpendicular to the cord axis, and (3) the solution to the pure shear problem, thus the effective moduli in the 1 and 2-directions can be predicted as well as the amount of extension-twisting coupling. The fourier series solution to the general loading case of a simply supported plate is given in Kittredge (1991). The bending response of unidirectional lamina is treated in a separate paper (Shield and Costello, 1992).

Steel cord-rubber composites have a characteristic large stiffness ratio mismatch. The stiffness ratio, $E_{\text{cord}}/E_{\text{matrix}}$, can range from 58 for vulcanized rubber to between 3000-50,000 for synthetic rubbers. With this large mismatch between the moduli, the shear in the plate cannot be ignored for most loading situations. However, the Kirchhoff theory is a reasonable approximation in cases where the ends of the plate are constrained to remain normal and plane, or if the cords are close to the middle surface. Hence the Kirchhoff theory is a reasonable approximation for problems involving uniaxial tension with the cords along the neutral surface. The matrix material will be considered to be linear elastic. This approximation is valid, because the rubber typically sees small strains due to the presence of the much stiffer cords. No viscoelastic properties will be taken into account. The cords will be treated as unimodular, having the same response in tension as in compression. The bimodular property of the cords has been dealt with elsewhere in the literature (Prakash et al. 1991). The current results will be compared with the results of Gough and Tangorra, as well as Akasaka and Hirano, to evaluate the suitability of these theories.

Formulation

Equilibrium Equations for a Plate Element. The formulation will be based upon the equilibrium of a small element of the plate. The in-plane and out-of-plane plate equations for an infinitesimal element of lengths dx and dy and height h can be derived by summing forces and moments on the element in the x, y, and z directions. If the changes in force and moment resultants across the element are represented by a first-order Taylor series, the usual plate equilibrium equations arise:

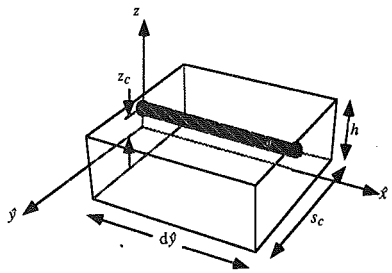


Fig. 1 Cord element

$$\frac{\partial N_x}{\partial x}+\frac{\partial N_{yx}}{\partial y}+p_x=0, \tag{1}$$

$$\frac{\partial N_{xy}}{\partial x}+\frac{\partial N_y}{\partial y}+p_y=0, \tag{2}$$

$$Nxy=Nyx, \tag{3}$$

$$\frac{\partial Q_x}{\partial x}+\frac{\partial Q_y}{\partial y}+p_z=0, \tag{4}$$

$$\frac{\partial M_x}{\partial x}+\frac{\partial M_{yx}}{\partial y}-Q_x=0, \tag{5}$$

and

$$\frac{\partial M_{xy}}{\partial x}+\frac{\partial M_y}{\partial y}-Q_y=0. \tag{6}$$

Equations (4)–(6) can be combined to yield the plate equation

$$\frac{\partial^2 M_x}{\partial x^2}+\frac{\partial^2}{\partial x\partial y}\,(M_{xy}+M_{yx})+\frac{\partial^2 M_y}{\partial y^2}+p_z=0. \tag{7}$$

While these equations were derived for an infinitesimal plate element, one approximation is to extend their use to an element that has finite length in one dimension. Consider the cord composite plate element shown in Fig. 1. The x-direction lines up with the cord direction and the element has finite length, s_c, in the y-direction, where s_c is the perpendicular spacing between the cords. The thickness of the element is h. The cord is a simple strand and is on the middle surface. As an approximate solution, one can enforce the plate Eqs. (1)–(3) and (7) derived above on this element. However, some of the assumptions made when deriving those equations may be violated. For example, because of the finite length, a first-order Taylor series approximation may not be accurate enough. Also, because of the finite length, it may be possible for the element in Fig. 1 to have a moment resultant in the z-direction, due to the variation of σ_x with y over the length s_c. This model with the above approximations is identical with that for an infinitesimal element with the contributions of the cord smeared out along the plane containing the cord. In an element of width dy, there would be dy/s_c cords distributed across the element, and hence the contribution of the cords to the resultants acting on this element would be found by multiplying the resultants of a single cord by dy/s_c.

Kinematics. The present theory uses the Kirchhoff theory approximations. The displacements along the x and y-directions are assumed to be linear functions of the thickness coordinate z; the transverse displacement is assumed to be constant through the thickness of the plate; hence

Downloaded 03 May 2010 to 171.66.16.20. Redistribution subject to ASME license or copyright; see http://www.asme.org/terms/Terms_Use.cfm

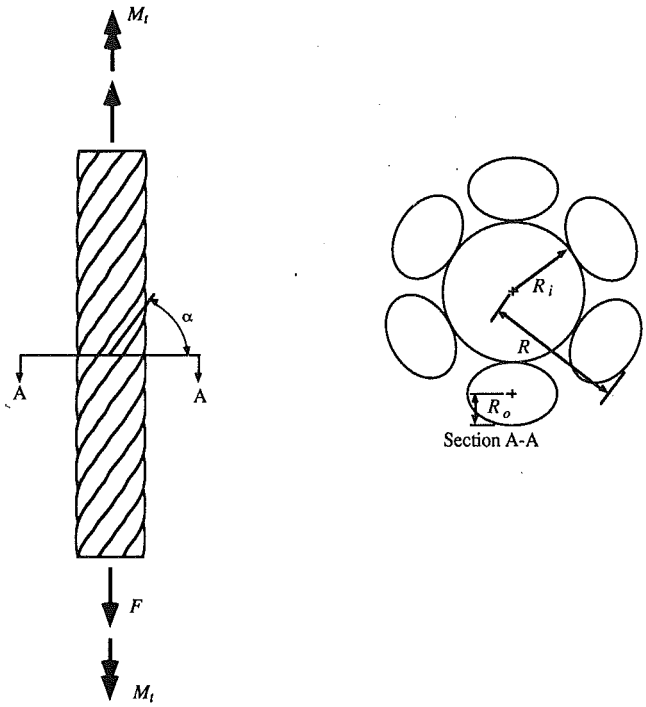


Fig. 2 Loading and geometry of a simple strand

$$u(x, y, z) = U(x, y) - z\frac{\partial W}{\partial x}$$

$$v(x, y, z) = V(x, y) - z\frac{\partial W}{\partial y} \tag{8}$$

and

$$w(x, y, z) = W(x, y),$$

where U, V, and W are the displacements of a point (x, y) on the middle surface.

Constitutive Equations for the Cords. The constitutive equations for a simple cord have been derived by Costello (1990) by considering the equilibrium of each wire in the cord. Figure 2 shows the geometry and loading of a simple cord. By investigating the axial response of a cord, Costello found that the axial force in the cord (F), and the twisting moment in the cord (M_t) can be represented as linear functions of the axial strain (ϵ) and the rotational strain (β),

$$\frac{F}{A_c E_c} = c_1\epsilon + c_2\beta \tag{9}$$

and

$$\frac{M_t}{E_c R^3} = c_3\epsilon + c_4\beta, \tag{10}$$

where E_c is the modulus of the cord material, R is the radius of the cord, $A_c = \Sigma_i \pi R_i^2$ is the metallic cross-section of the cord, and c_1, c_2, c_3, and c_4 are the cord constants that depend on the cord helix angle(α), the Poisson's ratio for the cord (ν_c), and the ratio of the outer to inner wire radii of the cord. The rotational strain β is defined as $\beta = R\tau_s$, where τ_s is the twist per unit length of the cord.

By investigating the bending response of a cord, Costello found that the bending moment in the cord (M_b) is a linear function of the curvature of the cord,

$$\frac{M_b}{E_c R^3} = c_5 R\kappa, \tag{11}$$

where κ is the curvature of the cord, and $c_5 = \frac{\pi}{4}\left[\frac{2m_2 \sin\alpha}{2+\nu_c\cos^2\alpha}\left(\frac{R_o}{R}\right)^4 + \left(\frac{R_i}{R}\right)^4\right]$, where m_2 is the number of outer wires in the cord, R_o is the radius of an outer wire, and R_i is the radius of the center wire.

The strains and curvature of the cord can be related to the plate displacements as follows: the axial strain displacement relation is given by

$$\epsilon = \frac{\partial u}{\partial x} = \left[\frac{\partial U}{\partial x} - z_c\frac{\partial W}{\partial x}\right]_{y=y_o}, \tag{12}$$

the twist per unit length is given by

$$\tau_s = -\frac{\partial^2 v}{\partial x \partial z} = \left[\frac{\partial^2 W}{\partial x \partial y}\right]_{y=y_o}, \tag{13}$$

and the bending curvature is given by

$$\kappa = \left[-\frac{\partial^2 W}{\partial x^2}\right]_{y=y_o}, \tag{14}$$

where $y = y_0$ is the equation of location of the chord and z_c is the height the cord is off the neutral surface, in this analysis $z_c = 0$.

Constitutive Equations of the Plate Element. For this element, the results can be thought of as consisting of a contribution from the matrix plus a contribution from the cord. The matrix resultant contributions can be found by considering an equivalent element made entirely of the matrix material. The loss in stiffness of the matrix due to the loss of volume of the matrix (the volume occupied by the cords) will be neglected. The components of the resultants due to the matrix are given by

$$M_{x_m} = \int_{-h/2}^{h/2}\sigma_x z\, dz = -D_m\left(\frac{\partial^2 W}{\partial x^2} + \nu_m\frac{\partial^2 W}{\partial y^2}\right),$$

$$M_{ym} = \int_{-h/2}^{h/2}\sigma_y z\, dz = -D_m\left(\frac{\partial^2 W}{\partial y^2} + \nu_m\frac{\partial^2 W}{\partial x^2}\right)$$

$$M_{xy_m} = M_{yx_m} = \int_{-h/2}^{h/2}\tau_{xy} z\, dz = -(1-\nu_m)\, D_m\frac{\partial^2 W}{\partial x \partial y}$$

$$N_{x_m} = \int_{-h/2}^{h/2}\sigma_x dz = C_m\left(\frac{\partial U}{\partial x} + \nu_m\frac{\partial V}{\partial y}\right)\Bigg]$$

$$N_{y_m} = \int_{-h/2}^{h/2}\sigma_y dz = C_m\left(\frac{\partial V}{\partial y} + \nu_m\frac{\partial U}{\partial x}\right), \tag{15}$$

and

$$N_{xy_m} = \int_{-h/2}^{h/2}\tau_{xy} dz = \frac{1-\nu_m}{2}\, C_m\left(\frac{\partial U}{\partial y} + \frac{\partial V}{\partial x}\right),$$

where $C_m = \frac{E_m h}{1-\nu_m^2}$, $D_m = \frac{E_m h^3}{12(1-\nu_m^2)}$, E_m is the modulus of elasticity of the matrix material and ν_m is the Poisson's ratio for the matrix material.

The resultant contributions due to the cord are based on the cord assumptions. The cord is assumed to be able to transmit only a force in the x-direction, a twisting moment in the y-z plane, and a bending moment in the $x-z$ plane. Hence

$$M_{y_c} = M_{yx_c} = N_{y_c} = N_{xy_c} = 0. \tag{16}$$

The only nonzero resultant contributions are due to the bending moment M_b, the twisting moment M_t, and the axial force F.

$$M_{x_c} = \frac{M_b}{s_c} = \frac{-E_c R^4 c_5}{s_c}\frac{\partial^2 W}{\partial x^2},$$

$$M_{xy_c} = \frac{-M_t}{s_c} = \frac{-E_c R^3}{s_c}\left[c_3\frac{\partial U}{\partial x} + c_4 R\frac{\partial^2 W}{\partial x \partial y}\right]$$

$$N_{x_c} = \frac{F}{s_c} = \frac{A_c E_c}{s_c}\left[c_1\frac{\partial U}{\partial x} + c_2 R\frac{\partial^2 W}{\partial x \partial y}\right] \tag{17}$$

Downloaded 03 May 2010 to 171.66.16.20. Redistribution subject to ASME license or copyright; see http://www.asme.org/terms/Terms_Use.cfm

Note that the second of Eqs. (17) adds in-plane coupling to Eq. (7).

The complete resultants are expressed by

$$M_x = M_{x_m} + M_{x_c},$$
$$M_y = M_{y_m},$$
$$M_{xy} = M_{xy_m} + M_{xy_c}$$
$$M_{yx} = M_{yx_m},$$
$$N_x = N_{x_m} + N_{x_c},$$
$$N_y = N_{y_m}, \tag{18}$$

and

$$N_{xy} = N_{xy_m}.$$

It is evident from Eqs. (18) that $M_{xy} \neq M_{yx}$, which is a usual assumption in plate and lamination theory (Jones, 1975).

Equations of Equilibrium for the Composite Plate Element. Equations (15)–(18) can be substituted into Eqs. (1), (2), and (7), resulting in the equations of equilibrium in terms of the displacement;

$$\left(C_m + \frac{c_1 A_c E_c}{s_c}\right) \frac{\partial^2 U}{\partial x^2} + C_m \frac{1-\nu_m}{2} \frac{\partial^2 U}{\partial y^2} + C_m \frac{1+\nu_m}{2} \frac{^2V}{\partial x \partial y} + \frac{c_2 A_c E_c R}{s_c} \frac{\partial^3 W}{\partial x^2 \partial y} + p_x = 0 \tag{19}$$

$$C_m \frac{(1-\nu_m)}{2} \frac{\partial^2 V}{\partial x^2} + C_m \frac{\partial^2 V}{\partial y^2} + C_m \frac{(1+\nu_m)}{2} \frac{\partial^2 U}{\partial x \partial y} + p_y = 0, \tag{20}$$

and

$$\left(D_m + \frac{c_5 E_c R^4}{s_c}\right) \frac{\partial^4 W}{\partial x^4} - \left(2D_m + \frac{c_4 E_c R^4}{s_c}\right) \frac{\partial^4 W}{\partial x^2 \partial y^2} - D_m \frac{\partial^4 W}{\partial y^4} - \frac{c_3 E_c R^3}{s_c} \frac{\partial^3 U}{\partial x^2 \partial y} + p_z = 0. \tag{21}$$

Again, it is evident from Eqs. (19) and (21) that coupling exists between extension and twisting through the $\partial^3 W/\partial x^2 \partial y$ term in the first equation and the $\partial^3 U/\partial x^2 \partial y$ term in the last equation.

Results

Although the equations of equilibrium, Eqs. (19)–(21), represent a complex coupled system of partial differential equations for some specific loading and boundary conditions, it is possible to find an exact solution.

A Solution to the Uniaxial Tension Problem. Consider the problem of uniaxial tension, with the cords on the middle surface, running along the axis of tension. For this problem, $N_x = N$ everywhere, and all other stress and moment resultants should be zero. Hence the equations to be solved consist of

$$N_x = \left(C_m + \frac{c_1 E_c A_c}{S_c}\right) \frac{\partial U}{\partial x} + C_m \nu_m \frac{\partial V}{\partial y} + \frac{c_2 E_c A_c R}{s_c} \frac{\partial^2 W}{\partial x \partial y} = N, \tag{22}$$

$$N_y \propto \frac{\partial V}{\partial y} + \nu_m \frac{\partial U}{\partial x} = 0, \tag{23}$$

$$N_{xy} \propto \frac{\partial U}{\partial y} + \frac{\partial V}{\partial x} = 0, \tag{24}$$

$$M_x = -\left(D_m + \frac{c_5 E_c R^4}{s_c}\right) \frac{\partial^2 W}{\partial x^2} - D_m \nu_m \frac{\partial^2 W}{\partial y^2} = 0, \tag{25}$$

$$M_y \propto \frac{\partial^2 W}{\partial y^2} + \nu_m \frac{\partial^2 W}{\partial x^2} = 0 \tag{26}$$

$$M_{xy} = -\left(D_m(1-\nu_m) + \frac{c_4 E_c R^4}{s_c}\right) \frac{\partial^2 W}{\partial x \partial y} - \frac{c_3 E_c R^3}{s_c} \frac{\partial U}{\partial x} = 0, \tag{27}$$

and

$$M_{yx} = -D_m (1-\nu_m) \frac{\partial^2 W}{\partial x \partial y}. \tag{28}$$

This set of equations does not have a solution. Satisfying Eq. (28) requires that $\partial^2 W/\partial x \partial y = 0$, which when substituted into Eq. (27) yields $\partial U/\partial x = 0$. Substituting this result into Eq. (23) yields $\partial V/\partial y = 0$. If these three derivatives are zero, then it is not possible to satisfy Eq. (22). However, if the last two boundary conditions are combined, requiring that

$$M_{xy} + M_{yx} = -\left(2D_m(1-\nu_m) + \frac{c_4 E_c R^4}{s_c}\right) \frac{\partial^2 W}{\partial x \partial y} - \frac{c_3 E_c R^3}{s_c} \frac{\partial U}{\partial x} = 0, \tag{29}$$

then the remaining six equations can be satisfied by the following:

$$U(x, y) = \frac{N\left(\frac{E_c R^4 c_4}{s_c} + 2D_m(1-\nu_m)\right)x}{\frac{A_c E_c^2 R^4}{s_c^2} C + 2D_m(1-\nu_m)\frac{A_c E_c c_1}{s_c} + \frac{E_c R^4 c_4}{s_c} C_m(1-\nu_m^2) + 2D_m(1-\nu_m)C_m(1-\nu_m^2)}$$

$$V(x, y) = \frac{-N\nu_m\left(\frac{E_c R^4 C_4}{S_c} + 2D_m(1-\nu_m)\right)y}{\frac{A_c E_c^2 R^4}{s_c^2} C + 2D_m(1-\nu_m)\frac{A_c E_c c_1}{S_c} + \frac{E_c R^4 c_4}{S_c} C_m(1-\nu_m^2) + 2D_m(1-\nu_m)C_m(1-\nu_m^2)}$$

$$W(x, y) = \frac{-N\frac{E_c R^3 c_3}{s_c}xy}{\frac{A_c E_c^2 R^4}{s_c^2} C + 2D_m(1-\nu_m)\frac{A_c E_c c_1}{s_c} + \frac{E_c R^4 c_4}{s_c} C_m(1-\nu_m^2) + 2D_m(1-\nu_m)C_m(1-\nu_m^2)} \tag{30}$$

where $C = c_1 c_4 - c_2 c_3$.

This solution can then be used to derive some of the material properties of the composite lamina. The effective moduli can be calculated using these results. In this case, the modulus of elasticity in the cord direction is given by

Downloaded 03 May 2010 to 171.66.16.20. Redistribution subject to ASME license or copyright; see http://www.asme.org/terms/Terms_Use.cfm

$$E_1 = \frac{\sigma_x}{\epsilon_x}, \tag{31}$$

where

$$\sigma_x = N/h, \tag{32}$$

and

$$\epsilon_x = \frac{\partial U}{\partial x}, \tag{33}$$

where $U(x, y)$ is defined by the first of Eqs. (30). Hence,

$$E_1 = E_m + c_1 E_c v_c \left[1 - \frac{6c_2 c_3 v_c (1+\nu_m)}{c_1 (\overline{A}\overline{h}^2 \overline{E} + 6c_4 v_c (1+\nu_m)} \right], \tag{34}$$

where $v_c = \dfrac{A_c}{s_c h}$ is the cord volume fraction, $\overline{A} = A_c/R^2$, $\overline{h} = h/R$, and $\overline{E} = E_m/E_c$. The nondimensionalized area, $\overline{A}$, must take on a value between 0 and π. The nondimensionalized thickness $\overline{h}$ cannot assume a value lower than 4, but would typically be between 5 and 10. When the modulus ratio is moderate ($\overline{E} = 1/58$) the term in the brackets is approximately 1, and hence can be approximated by

$$E_1 \approx E_m + c_1 E_c v_c. \tag{35}$$

However, for composites with a larger modulus mismatch ($\overline{E} = 1/5000$ to $\overline{E} = 1/50000$), the expression can be approximated by

$$E_1 = E_m + c_1 E_c v_c \left[1 - \frac{c_2 c_3}{c_1 c_4} \right], \tag{36}$$

where the term in brackets represents the decrease in cord stiffness due to the nonzero cord rotation.

The Poisson's ratio is defined by

$$\nu_{12} = \frac{-\epsilon_y}{\epsilon_x}, \tag{37}$$

where

$$\epsilon_y = \frac{\partial V}{\partial y}, \tag{38}$$

in which $V(x, y)$ is defined by the second of Eq. (30). Hence

$$\nu_{12} = \nu_m = 0.5. \tag{39}$$

Also the twist per unit length of the plate is

$$\tau_s^* = \frac{\partial^2 W(l, 0)}{\partial x \partial y}, \tag{40}$$

where $W(x, y)$ is given by the last of Eqs. (30). Hence

$$\frac{\tau_s^*}{\dfrac{-c_3 N}{CRE_c v_c h}} = \frac{Cv_c^2}{Cv_c^2 + c_4 v_c \overline{E} + \overline{A}\overline{h}^2 \overline{E} \dfrac{1}{6(1+\nu_m)} (c_1 v_c + \overline{E})}, \tag{41}$$

where the denominator of the left-hand side is the twist per unit length of a single cord loaded by a force equivalent to the total force of the distributed load divided by the number of cords as given by Eqs. (9) and (10). This ratio illustrates the reduction in twist caused by the matrix.

These values can be compared with the work of Gough and Tangorra and Akasaka and Hirano. Both of these works treat the unidirectional lamina as an orthotropic material, with five independent material properties. The Gough-Tangorra relationships are given by

$$\begin{aligned} E_1 &= c_1 E_c v_c + E_m (1 - v_c) = E_m + (c_1 E_c - E_m) v_c, \\ E_2 &= \frac{4E_m (1 - v_c)[c_1 E_c v_c + E_m (1 - v_s)]}{3c_1 E_c v_c + 4E_m (1 - v_c)}, \\ G_{12} &= G_m (1 - v_c), \\ \nu_{12} &= 0.5, \end{aligned} \tag{42}$$

and

$$\nu_{21} = \nu_{12} E_2 / E_1,$$

where the subscript 1 denotes material properties along the cords and the subscript 2 denotes material properties perpendicular to the cords. These equations are quite similar to the Halpin-Tsai equations, as usually used in composite plate theory; however, both theories treat the matrix as being incompressible and ignore the transverse properties of the cords, avoiding the difficult problem of determining the Poisson's ratio of a cord..

The Akasaka-Hirano equations are given by

$$\begin{aligned} E_1 &= c_1 E_c v_c, \\ E_2 &= \frac{4}{3} E_m, \\ G_{12} &= G_m, \\ \nu_{12} &= 0.5, \end{aligned} \tag{43}$$

and

$$\nu_{21} = 0.$$

These equations are further simplifications of the Gough-Tangorra equations, taking advantage of the large difference in moduli between rubber and steel; essentially all the strength in the cord direction is attributed to the cords and the strength perpendicular to the cord direction to the matrix. In addition, the cord volume fraction is considered small compared with unity.

For the purposes of comparison, a typical tire cord is selected as the reinforcement. The material and geometric properties are given by

Young's modulus (E_c)	200 GPa
Poisson's ratio (ν_c)	0.25
Helix angle	81.4 deg
Center wire radius (R_i)	0.15 mm
6 outer wires with radii (R_0)	0.14 mm
Cord radius ($R = R_i + 2R_o$)	0.43 mm
c_1	0.967
c_2	0.0828
c_3	0.187
c_4	0.0723.

The effective modulus of elasticity in the 1-direction (E_1), normalized by the modulus of elasticity of the cord material (E_c), is plotted against the cord volume fraction in Figs. 3(*a*), 3(*b*), and 3(*c*) for cord to matrix modulus ratios of $E_c/E_m = 58$, $E_c/E_m = 5000$, and $E_c/E_m = 50{,}000$, as well as for two thickness to cord radius ratios ($h/R = 5$, and $h/R = 10$). As can be seen by the symbolic representation above, the current value of E_1 and the value given by Gough and Tangorra are essentially the same when the modulus ratio is 58, whereas the Akasaka-Hirano value is less stiff for this modulus ratio. For the two larger modulus ratios the Gough-Tangorra and Akasaka-Hirano curves are indistinguishable, and so only the Akasaka-Hirano curve is shown. The significant loss in stiffness of the cord due to the free rotation boundary condition predicted by the current theory is displayed in the plots for the two larger moduli ratios. The h/R term contributes the most for moderate moduli ratios.

All three models yield a Poisson's ratio in the 1-2 direction of one half. However, only the current model predicts any extension-twisting coupling in the unidirectional case. Figure 4 is a plot of the normalized twist per unit length (τ_s^*/τ_s) versus cord volume fraction (v_c) for a typical tire lamina with a cord helix angle of 81.4 deg. The twist is plotted for modulus ratios $E_c/E_m = 58$, $E_c/E_m = 5000$, and $E_c/E_m = 50000$, as well as for two plate thickness to cord radius ratios $h/R = 5$, and $h/R = 10$. The twist per unit length is normalized by the twist that a single cord would undergo if it were loaded by a force equivalent to the total force of the distributed load divided by the number

Downloaded 03 May 2010 to 171.66.16.20. Redistribution subject to ASME license or copyright; see http://www.asme.org/terms/Terms_Use.cfm

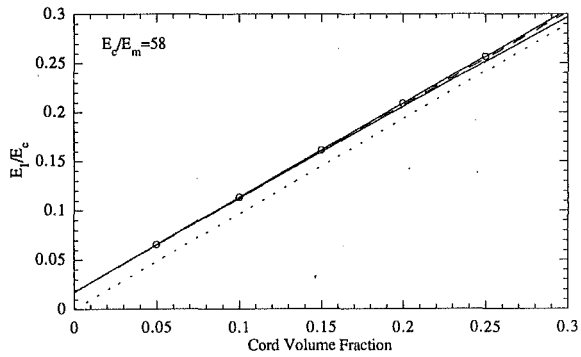


Fig. 3 (*a*)

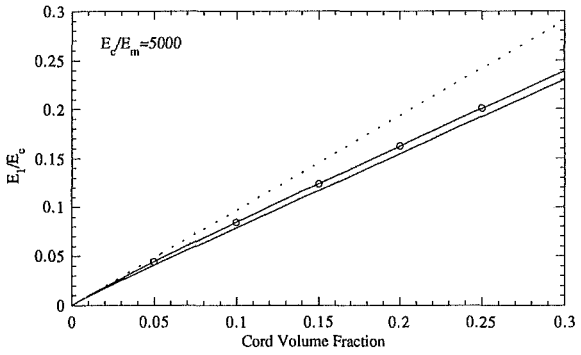


Fig. 3 (*b*)

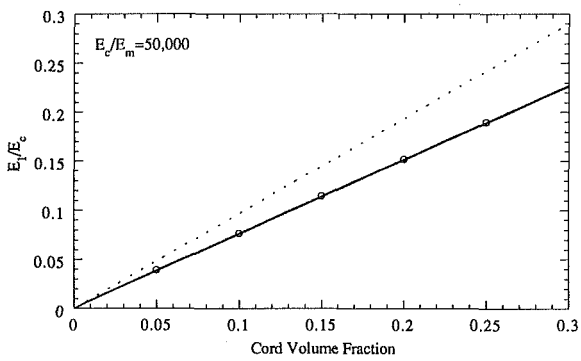


Fig. 3 (*c*)

Fig. 3 Extensional stiffness E_l/E_m versus cord volume fraction v_c for (*a*) $E_c/E_m = 58$, (*b*) $E_c/E_m = 5000$, and (*c*) $E_c/E_m = 50{,}000$. The plain solid line represents the current theory, with $\bar{h}=5$, the solid line with circles represents the current theory with $\bar{h}=5$, the solid line with circles represents the current theory with $\bar{h}=10$, the long dashed line represents the Gough-Tangorra theory, and the short dashed line represents the Akasaka-Hirano theory.

of cords ($F=Ns_c$, $M_t=0$) as given by Eqs. (9) and (10). This ratio illustrates the reduction in twist caused by the matrix. As is expected, the twist decreases as the plate thickness is increased, and hence the polar moment of inertia is increased.

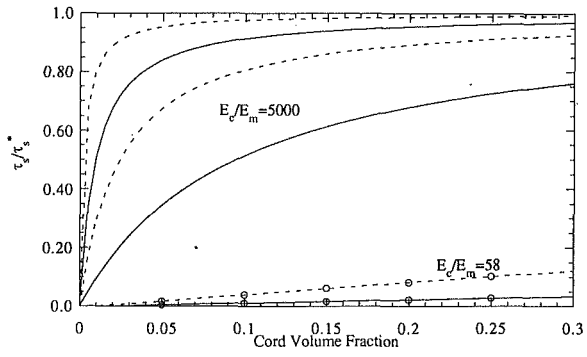


Fig. 4 Twist per unit length τ_s^*/τ_s versus cord volume faction v_c for two plate thicknesses and three modulus ratios. The dashed lines are for $\bar{h}=5$ values, and the solid lines are for the $\bar{h}=10$ values. The lines with the circles are for the smallest modulus ratio, $E_c/E_m=58$.

Neither the Gough-Tangorra nor Akasaka-Hirano relations allow for any twisting in the uniaxial tension case. This extension-twisting coupling for the unidirectional case illustrates the fact that this material is not orthotropic. For the smallest modulus ratio the twisting of the plate is not that large and is a small percentage of that for a mesh made entirely of wire rope (less than five percent for the typical cord volume fraction $v_c=0.1$); however, for the larger modulus ratios, the matrix does very little to restrict the rotation of the cords. For applications when the modulus mismatch is small, or when the rotation is prohibited by the boundary conditions, it is probably reasonable to use the orthotropic results.

A Solution to the Uniaxial Tension Problem Perpendicular to the Cords. Consider the problem of uniaxial tension with the cords on the middle surface running perpendicular to the axis of tension. For this problem, $N_y=N$ everywhere, and all other stress and moment resultants should be zero. Hence the equations to be solved consist of

$$N_x=\left(C_m+\frac{c_1E_cA_c}{s_c}\right)\frac{\partial U}{\partial x}+C_m\nu_m\frac{\partial V}{\partial y}+\frac{c_2E_cA_cR}{s_c}\frac{\partial^2 W}{\partial x\partial y}=0,$$

$$N_y=C_m\left(\frac{\partial V}{\partial y}+\nu_m\frac{\partial U}{\partial x}\right)=N,$$

$$N_{x_y}\propto\frac{\partial U}{\partial y}+\frac{\partial V}{\partial x}=0,$$

$$M_x=-\left(D_m+\frac{c_5E_cR^4}{s_c}\right)\frac{\partial^2 W}{\partial x^2}-D_m\nu_m\frac{\partial^2 W}{\partial y^2}=0,$$

$$M_y\propto\frac{\partial^2 W}{\partial y^2}+\nu_m\frac{\partial^2 W}{\partial x^2}=0,$$

$$M_{xy}=-\left(D_m\,(1-\nu_m)+\frac{c_4E_cR^4}{s_c}\right)\frac{\partial^2 W}{\partial x\partial y}-\frac{c_3E_cR^3}{s_c}\frac{\partial U}{\partial x}=0, \quad (44)$$

and

$$M_{yx}=-D_m\,(1-\nu_m)\frac{\partial^2 W}{\partial x\partial y}=0.$$

Again this set of equations does not have a solution, but the last two conditions can again be combined. The solution to this set of equations is given by

$$U(x,\,y)=\frac{-N\nu_m\left(\dfrac{c_4E_cR^4}{s_c}+2D_m(1-\nu_m)\right)x}{\dfrac{A_cE_c^2R^4C}{s_c^2}+2D_m(1-\nu_m)\dfrac{A_cc_1E_c}{s_c}+C_m(1-\nu_m^2)\dfrac{c_4E_cR^4}{s_c}+2C_mD_m(1-\nu_m)(1-\nu_m^2)}$$

Downloaded 03 May 2010 to 171.66.16.20. Redistribution subject to ASME license or copyright; see http://www.asme.org/terms/Terms_Use.cfm

$$V(x,y)=\frac{N\left(\frac{A_cR^4E_c^2C}{S_c^2}+2D_m(1-\nu_m)\frac{A_cc_1E_c}{s_c}+C_m\frac{c_4E_cR^4}{s_c}+2C_mD_m(1-\nu_m)\right)y}{C_m\frac{A_cE_c^2R^4C}{s_c^2}+2D_m(1-\nu_m)\frac{A_cc_1E_c}{S_c}+C_m(1-\nu_m^2)\frac{c_4E_cR^4}{s_c}+2C_mD_m\,(1-\nu_m)(1-\nu_m^2)\Big)}$$

$$W(x,y)=\frac{N\frac{c_3E_cR^3\nu_m}{s_c}xy}{\frac{A_cE_c^2R^4C}{s_c^2}+2D_m(1-\nu_m)\frac{A_cc_1E_c}{s_c}+C_m(1-\nu_m^2)\frac{c_4E_cR^4}{s_c}+2C_mD_m(1-\nu_m)(1-\nu_m^2)} \tag{45}$$

where $C=c_1c_4-c_2c_3$.

The material properties in the direction perpendicular to the cords (the 2-direction) can be extracted from the preceding results. The modulus of elasticity in the 2-direction is given by

$$E_2=\frac{\sigma_y}{\epsilon_y}, \tag{46}$$

where

$$\sigma_y=\frac{N}{h} \tag{47}$$

and

$$\epsilon_y=\frac{\partial V}{\partial y}, \tag{48}$$

where $V(x, y)$ is given above. Hence,

$$E_2=\frac{4E_m[c_1E_cv_c+E_m]+\frac{24(1+\nu_m)v_cE_c}{\bar{A}\bar{h}^2}(c_4E_m+CE_cv_c)}{[4E_m+4(1-\nu_m^2)v_cc_1E_c]+\frac{24(1+\nu_m)v_c}{\bar{A}\bar{h}^2\bar{E}}(c_4E_m+CE_cv_c(1-\nu_m^2))}, \tag{49}$$

where $\bar{A}=A_c/R^2$, $\bar{h}=h/R$, and $\bar{E}=E_m/E_c$. This expression can be approximated by

$$E_2\approx\frac{4E_m[c_1E_cv_c+E_m]}{[4E_m+4(1-\nu_m^2)v_cc_1E_c]}\approx\frac{4E_m[c_1E_cv+E_m]}{[4E_m+3v_cc_1E_c]} \tag{50}$$

for $\nu_m=0.5$. For very small cord volume fractions this approximation matches the Gough-Tangorra expression for E_2 whereas for larger cord volume fractions, this expression approaches the Akasaka-Hirano expression for E_2. Figure 5 is a plot of the transverse modulus of elasticity (E_2/E_m) versus cord volume fraction (v_c) for the current theory, and for the Gough-Tangorra theory, for three modulus ratios. The Akasaka-Hirano theory predicts E_2/E_m to be 4/3, and is not shown on the figure. This stiffness in the 2-direction shows almost no variation with $\bar{h}$, and hence only one value of $\bar{h}$ is used in the figure. This figure shows that the three methods represent E_2 quite differently. The results of the current method agree most closely with the Gough-Tangorra equation for small cord volume fractions and small modulus ratio, but the Gough-Tangorra equation diverges for cord volume fractions larger than 0.05. The Akasaka-Hirano equation agrees well with the current methods for larger values of cord volume fraction and larger modulus ratios.

The Poisson's ratio in the 2-1 direction is given by

$$\nu_{21}=\frac{-\epsilon_x}{\epsilon_y}=\nu_m\frac{E_2}{E_1}. \tag{51}$$

Figure 6 shows a plot of the transverse Poisson's ratio (ν_{21}) versus cord volume fraction. The Akasaka-Hirano equation ($\nu_{21}=0.0$) is not shown. The Gough-Tangorra value agrees well with the current study for all three modulus ratios, and in the case of the two larger moduli ratios the two values are indistinguishable on the figure. However, the Akasaka-Hirano values do not agree well with the current study in the case of the smaller modulus ratio.

A Solution to the Pure Shear Problem. Consider the problem of pure shear, with the cords on the middle surface. For this problem, $N_{xy}=N$ everywhere, and all other stress and moment resultants should be zero. Hence the equations to be solved consist of

$$N_x=\left(C_m+\frac{c_1E_cA_c}{s_c}\right)\frac{\partial U}{\partial x}+C_m\nu_m\frac{\partial V}{\partial y}+\frac{c_2E_cA_cR}{s_c}\frac{\partial^2W}{\partial x\partial y}=0,$$

$$N_y\propto\left(\frac{\partial V}{\partial y}+\nu_m\frac{\partial U}{\partial x}\right)=0,$$

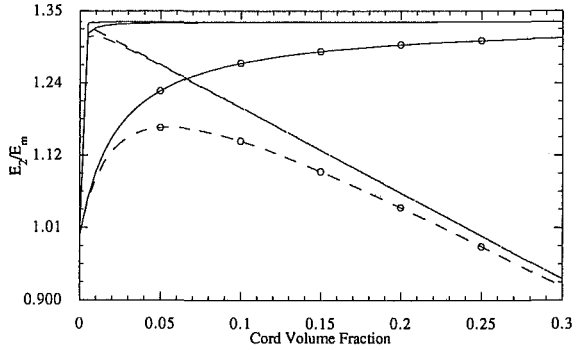


Fig. 5 Extensional stiffness E_2/E_m versus cord volume fraction v_c for three modulus ratios. The dashed lines represent the Gough-Tangorra theory, and the solid lines represent the current theory. The smallest modulus ratio is indicated by the lines with circles.

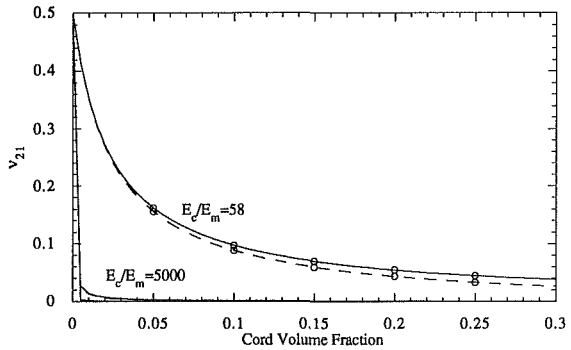


Fig. 6 Poisson's ratio ν_{21} versus cord volume fraction v_c for three modulus ratios. The dashed lines represent the Gough-Tangorra theory and the solid lines represent the current theory. The smallest modulus ratio is indicated by the lines with circles.

Downloaded 03 May 2010 to 171.66.16.20. Redistribution subject to ASME license or copyright; see http://www.asme.org/terms/Terms_Use.cfm

$$N_{xy} = C_m \left(\frac{1-\nu_m}{2}\right) \left(\frac{\partial U}{\partial y} + \frac{\partial V}{\partial x}\right) = N$$

$$M_x = -\left(D_m + \frac{c_5 E_c R^4}{s_c}\right) \frac{\partial^2 W}{\partial x^2} - D_m \nu_m \frac{\partial^2 W}{\partial y^2} = 0,$$

$$M_y \propto \frac{\partial^2 W}{\partial y^2} + \nu_m \frac{\partial^2 W}{\partial x^2} = 0,$$

$$M_{xy} = -\left(D_m(1-\nu_m) + \frac{c_4 E_c R^4}{s_c}\right) \frac{\partial^2 W}{\partial x \partial y} - \frac{c_3 E_c R^3}{s_c} \frac{\partial U}{\partial x} = 0, \quad (52)$$

and

$$M_{xy} = -D_m (1-\nu_m) \frac{\partial^2 W}{\partial x \partial y} = 0.$$

The solution to this set of equations is given by

$$U(x, y) = a_1 y,$$

$$V(x, y) = a_2 x,$$

and

$$W(x, y) = 0,$$

such that

$$(1-\nu_m) C_m (a_1 + a_2) = N.$$

The in-plane shear modulus is easily calculated from the above results. The shear modulus in the 1-2 direction is given by

$$G_{12} = \frac{\tau_{xy}}{\gamma_{xy}},$$

where

$$\tau_{xy} = \frac{N}{h}$$

and

$$\gamma_{xy} = \frac{\partial U}{\partial y} + \frac{\partial V}{\partial x} = \frac{2N}{(1-\nu_m) C_m},$$

where $U(x, y)$ and $V(x, y)$ are given above. Hence

$$G_{12} = G_m.$$

This result is identical to the Akasaka-Hirano value and is a good approximation of the Gough-Tangorra approximation for small values of ν_c.

References

Akasaka, T., and Hirano, M., 1972, "Approximate Elastic Constants of Fiber Reinforced Rubber Sheet and Its Composite Laminate," *Fukugo Zairyo* (*Composite Materials & Structures*), Vol. 1, pp. 70–76.

Costello, G. A., 1990, *Theory of Wire Rope*, Springer-Verlag, New York.

Gough, V. E., 1968, "Stiffness of Cord and Rubber Constructions," *Rubber Chemistry and Technology*, Vol. 41, pp. 988–1021.

Hsieh, K. T., 1985, "Modeling of Cord-Reinforced Rubber Laminates," Ph.D. Thesis, University of Texas.

Jones, R. M., 1975, *Mechanics of Composite Materials*, McGraw-Hill, New York.

Kittredge, C. A., 1991, "Static Response of Cord Composite Plates," Ph.D. Thesis, University of Illinois at Urbana-Champaign.

Kumar, M., and Bert, C. W., 1982, "Experimental Characterization of Mechanical Behavior of Cord-Rubber Composites," *Tire Science and Technology*, Vol. 10, Nos. 1–4, pp. 37–54.

Prakash, A., Conway, T., and Costello, G. A., 1992, "Compression of a Cord," ASME JOURNAL OF APPLIED MECHANICS, Vol 59, pp. S213–S216.

Shield, C. K., and Costello, G. A, 1992, "The Bending of Cord Composite Plates," to be published.

Shield, C. K., and Costello, G. A., 1993, "The Effect of Wire Rope Mechanics on the Mechanical Response of Cord Composite Laminates—An Energy Approach," ASME JOURNAL OF APPLIED MECHANICS, Vol. 60.

Tangorra, G. 1969, "Fiber-Reinforced, Oriented Rubber Sheets," *Proceedings of International Rubber Conference*, Moscow, pp. 459–466.

Walter, J. D., 1978, "Cord-Rubber Tire Composites: Theory and Applications," *Rubber Chemistry and Technology*, Vol. 51, No. 3, pp. 524–576.

Walter, J. D., and Patel, H. P., 1979, "Approximate Expressions for the Elastic Constants of Cord-Rubber Laminates," *Rubber Chemistry and Technology*, Vol. 52, No. 4, pp. 710–724.

Downloaded 03 May 2010 to 171.66.16.20. Redistribution subject to ASME license or copyright; see http://www.asme.org/terms/Terms_Use.cfm

The Effect of Wire Rope Mechanics on the Mechanical Response of Cord Composite Laminates: An Energy Approach

C. K. Shield
Assistant Professor,
Department of Civil and Mineral Engineering,
University of Minnesota,
Minneapolis, MN 55455
Mem. ASME

G. A. Costello
Professor,
Department of Theoretical and Applied Mechanics,
University of Illinois at Urbana-Champaign,
Urbana, IL 61801
Fellow ASME

The behavior of one-ply and two-ply laminated cord-rubber composite plates in uniaxial tension is presented. The plate mechanical properties are presented as functions of cord angle for various cord-modulus to matrix-modulus ratios. The model developed takes account of the extension-twisting coupling of the cord, as well as the exact location of the cord within the composite plate. An energy method formulation is used, and the model is solved using the Ritz method. The current results are compared to classical lamination theory results to show the limits of usefulness for classical lamination theory for this class of composites.

Introduction

The use of wire-rope-reinforced composites has become commonplace in today's society. The most common form of wire rope composites is wire-rope-reinforced rubber laminates (hereafter called cord-rubber laminates). These types of composites are used in pneumatic tires, conveyer belts, and various military components, such as sonar domes. This combination of materials is especially effective when the composite material needs to be strong in extension in the cord direction, but also needs to be flexible in the plane perpendicular to the cords. This property is desirable in conveyer belts, so that they will not fatigue quickly as they change direction over rollers but will be strong enough not to pull apart from the tensile forces driving them. This property is also desirable in car tires. They need the strength in the cord direction to hold the air pressure, but need to be flexible in order to provide a comfortable ride, and cut down on fatigue from bumpy roads.

A good review of the work done in cord-rubber composites is presented by Walter (1978). Currently the main two methods for analyzing cord-rubber composites are experimental and finite element. Kumar and Bert (1982) performed a series of tension tests to determine the in-plane stress-strain response of a single-ply unidirectional cord-rubber composite at various cord angles. Hsieh (1985) presented a finite element model for cord-reinforced laminates. Analytical methods for predicting composite behavior are superior to experimental methods because of the large number of design variables available in composite design. Analytical solutions can cut down on the number of design cycles and can be used to optimize designs.

Investigators have steered away from analytical models for cord composites because of the difficulty in analyzing the cord mechanics. Many investigators, who have tried to predict the behavior of cord composites analytically, have typically ignored the mechanics of the cord and treated the cord-rubber lamina as an orthotropic material. Gough (1968) and Tangorra (1969) developed expressions for the elastic constants of a single unidirectional ply based on the methods of analyzing plywood. They neglected the flexural stiffness of the cords, and treated them as unidirectional load carrying members, with no transverse properties. They ignored the tension-twisting coupling of the cord. Akasaka and Hirano (1972) further simplified the Gough-Tangorra relations by utilizing the large difference in moduli, and the fact that for most applications, the cord volume fraction is small. This author has developed analytical expressions for the unidirectional ply material properties while taking into account the mechanics of the cord (Shield, 1992).

By modeling the cord composite as orthotropic, a part of the mechanical response of the cord is neglected. If the cord is treated as a single body it exhibits extension-twisting coupling when a cord is pulled on, it also rotates. Costello (1990) has developed both a general theory and a linear theory for the response of a cord that exhibits this behavior. This coupling between extension and rotation will also be apparent in the general lamina response. Therefore, it may not be advisable to classify the lamina as orthotropic. To include these effects a more general theory will be developed.

Classical lamination theory (CLT) is based on some approximations that are not necessary when considering cord composites. In CLT the exact distribution of the cord in the ply is not taken into account. With typical fiber composites

Contributed by the Applied Mechanics Division of THE AMERICAN SOCIETY OF MECHANICAL ENGINEERS for presentation at the ASME Winter Annual Meeting, New Orleans, LA, Nov. 28–Dec. 3, 1993.

Discussion on this paper should be addressed to the Technical Editor, Professor Lewis T. Wheeler, Department of Mechanical Engineering, University of Houston, Houston, TX 77204-4792, and will be accepted until four months after final publication of the paper itself in the ASME JOURNAL OF APPLIED MECHANICS.

Manuscript received by the ASME Applied Mechanics Division, Sept. 21, 1992; final revision, Apr. 6, 1993. Associate Technical Editor: J. N. Reddy.

Paper No. 93-WA/APM-24.

Copyright © 1994 by ASME
Downloaded 03 May 2010 to 171.66.16.20. Redistribution subject to ASME license or copyright; see http://www.asme.org/terms/Terms_Use.cfm

this is a benefit, because the exact location of the cords is not known. However, in cord composites, the cords are purposefully placed carefully in the matrix, and their location is known. Typically the cords are all evenly spaced at specific heights through the thickness of the plate. The cord is also much larger than a typical fiber in a fiber composite. Fiber diameters are usually several orders of magnitude smaller than the thickness of the ply, while the cord diameters are on the order of the thickness of the ply.

An energy method approach will be taken to describe the behavior of cord-composite plates. The models developed in this work will be based on the cord equations of Costello (1990). A strain energy density for the cords will be formulated based on Costello's cord equations. The strain energy of the plate will be calculated, and then the total energy of the system will be minimized using the Ritz method. In this method, the exact location of each cord will be used in finding the strain energy in the plate. This method will be used to look at the effect of the cord angle on the material properties for single-ply and two-ply antisymmetric plates.

Formulation

One way to calculate the deformation of a cord-composite plate is by minimizing the energy of the system. The energy in the system can be divided into three distinct parts: the strain energy in the matrix (U_m), the strain energy in the cords (U_c), and the potential energy of the external load (Ω). In order to derive expressions for each of the three energy components, some assumptions must be made. The deformations of the plate are limited to those allowed by the Kirchhoff plate theory. In the case of uniaxial tension, the Kirchhoff theory yields a reasonable answer because there will not be any bending of the plate, hence normals will remain straight and normal.

The matrix material will be considered to be linear elastic. No viscoelastic properties will be taken into account. The cords will be treated as unimodular, having the same response in tension as in compression. Geometrically, the cords will be treated as one-dimensional line elements. They will be allowed to carry only an axial load F, a twisting moment M_t, and a bending moment M_b. The main application of this work is toward steel cord-rubber composites, and hence some of the assumptions made will take advantage of the properties of these two materials, as used in such standard applications as tires and conveyer belts. Typically the cord volume fraction is small. The stiffness ratio, $E_{\text{cord}}/E_{\text{matrix}}$, can range from 58 for highly vulcanized rubber to between 3000-50,000 for synthetic rubbers. The loss of strain energy in the matrix, due to the volume occupied by the cords, will be neglected. This is a reasonable approximation because of the large modulus ratio and the small cord volume fraction.

Strain Energy in the Matrix. Consider a plate of length l, width b, and thickness h. For simplicity in later formulations, let the origin of the axis system be at the middle plane of the plate at the center of the left end. For the plate, the strain energy in the matrix is given by

$$U_m=\frac{1}{2}\int_0^l\int_{-b/2}^{b/2}\int_{-h/2}^{h/2}(\sigma_x\epsilon_x+\sigma_y\epsilon_y+\tau_{xy}\gamma_{xy})dzdydx. \tag{1}$$

Here the assumption is made that the decrease in the strain energy of the matrix, due to the volume occupied by the cords, is negligible. Hooke's law for plane stress is used as the constitutive relationship between stress and strain. The deformation fields are given by the Kirchhoff theory approximations. The lateral displacement of the plate does not vary through the plate thickness; hence

$$w(x, y, z)=W(x, y), \tag{2}$$

where $W(x, y)$ is the lateral displacement of the middle surface ($z=0$). The in-plane displacements vary over the plate thickness linearly,

$$u(x, y, z)=U(x, y)-z\frac{\partial W(x, y)}{\partial x},$$

$$v(x, y, z)=V(x, y)-z\frac{\partial W(x, y)}{\partial y}, \tag{3}$$

where $U(x, y)$ and $V(x, y)$ are the in-plane displacements of the middle surface..

The stresses and strains corresponding to the displacement functions (Eqs. (2)–(3)) may be substituted into Eq. (1), yielding an integrand with explicit dependence on z. The z-integration can be peformed, leaving the integrand as a function of x and y only. Hence the strain energy of the matrix is given by

$$U_m=\frac{1}{2}\int_0^l\int_{-b/2}^{b/2}\left\{C_m\left(\frac{\partial U}{\partial x}+\nu_m\frac{\partial V}{\partial y}\right)\frac{\partial U}{\partial x}\right.$$
$$+C_m\left(\frac{\partial V}{\partial y}+\nu_m\frac{\partial U}{\partial x}\right)\frac{\partial V}{\partial y}+D_m\left(\frac{\partial^2 W}{\partial x^2}+\nu_m\frac{\partial^2 W}{\partial y^2}\right)\frac{\partial^2 W}{\partial x^2}$$
$$+D_m\left(\frac{\partial^2 W}{\partial y^2}+\nu_m\frac{\partial^2 W}{\partial x^2}\right)\frac{\partial^2 W}{\partial y^2}+C_m\frac{1-\nu_m}{2}\left(\frac{\partial U}{\partial y}+\frac{\partial V}{\partial x}\right)^2$$
$$\left.+2D_m(1-\nu_m)\left(\frac{\partial^2 W}{\partial x\partial y}\right)^2\right\}dydx, \tag{4}$$

where $C_m=\dfrac{E_m h}{1-\nu_m^2}$, $D_m=\dfrac{E_m h^3}{12(1-\nu_m^2)}$, E_m is the modulus of elasticity of the matrix material, and ν_m is the Poisson's ratio of the matrix material.

Strain Energy in a Cord. As was stated above, the cord will be treated as one-dimensional. Its constitutive behavior, as described by Costello, is given by the following:

$$\frac{F}{A_c E_c}=c_1\epsilon+c_2 R\tau_s,$$

$$\frac{M_t}{E_c R^3}=c_3\epsilon+c_4 R\tau_s$$

$$\frac{M_b}{E_c R^3}=c_5\frac{R}{\rho}, \tag{5}$$

where $A_c=\Sigma_j \pi R_j^2$ is the metallic cross-sectional area; R_j is the radius of an individual wire; R is the outside radius of the cord; E_c is the modulus of elasticity of the material; ϵ is the axial strain; τ_s is the twist per unit length of the cord; ρ is the radius of curvature and c_1, c_2, c_3, c_4 and c_5 are constants that depend on the helix angle of the cord (α), the ratio of inner wire diameter to outer wire diameter (R_i/R_o); and Poisson's ratio for the material (ν_c) and can be determined analytically.

Consider a cord located at $z=z_c$ in the matrix. Let the cord be of length l_c, in the $\hat{x}$ direction. Let the $\hat{z}$ and z-directions coincide, and the $\hat{y}$-direction be defined by the right-hand rule. The equation of the cord location is given by $\hat{y}=\hat{y}_o$, $z=z_c$. The strain energy in the cord will consist of the integration along the length of the cord of the strain energy densities associated with tension, twisting, and bending,

$$U_c=\frac{1}{2}\int_0^{l_c}\left[F\epsilon+M_t\tau_s+M_b\frac{1}{\rho}\right]d\hat{x} \tag{6}$$

where the integration is along the length of the cord. The axial strain-displacement relation is given by

$$\epsilon=\frac{\partial\hat{u}}{\partial\hat{x}}=\left[\frac{\partial\hat{U}}{\partial\hat{x}}-z_c\frac{\partial W}{\partial\hat{x}}\right]_{\hat{y}=\hat{y}_o}. \tag{7}$$

The twist per unit length is given by

Downloaded 03 May 2010 to 171.66.16.20. Redistribution subject to ASME license or copyright; see http://www.asme.org/terms/Terms_Use.cfm

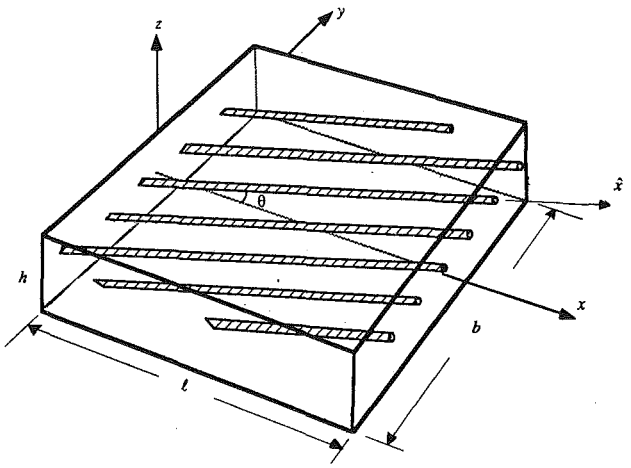


Fig. 1 Cord and plate geometry for an angle-ply lamina

$$\tau_s = \frac{-\partial^2 \hat{v}}{\partial \hat{x} \partial z} = \left[\frac{\partial^2 W}{\partial \hat{x} \partial \hat{y}} \right]_{\hat{y}=\hat{y}_o} \tag{8}$$

The bending curvature is given by

$$\frac{1}{\rho} = \left[\frac{-\partial^2 W}{\partial \hat{x}^2} \right]_{\hat{y}=\hat{y}_o} \tag{9}$$

where $\hat{U}(\hat{x}, \hat{y})$ is the in-plane displacement in the $\hat{x}$-direction of the middle surface ($z=0$) and $W(\hat{x}, \hat{y})$ is the out-of-plane displacement of the middle surface.

The expression for the strain energy in the cord as a function of middle surface displacements arises from the substitution of Eqs. (5) and (7)–(9) into Eq. (6), resulting in

$$U_c = \frac{1}{2} \int_0^{l_c} E_c \left[A_c c_1 \left(\frac{\partial \hat{U}}{\partial \hat{x}} \right)^2 + R(A_c c_2 + R^2 c_3) \frac{\partial \hat{U}}{\partial \hat{x}} \frac{\partial^2 W}{\partial \hat{x} \partial \hat{y}} - 2A_c z_c c_1 \frac{\partial \hat{U}}{\partial \hat{x}} \frac{\partial^2 W}{\partial \hat{x}^2} + R^4 c_4 \left(\frac{\partial^2 W}{\partial \hat{x} \partial \hat{y}} \right)^2 + (R^4 c_5 + A_c c_1 z_c^2) \left(\frac{\partial^2 W}{\partial \hat{x}^2} \right)^2 - R z_c (A_c c_2 + R^2 c_3) \frac{\partial^2 W}{\partial \hat{x} \partial \hat{y}} \frac{\partial^2 W}{\partial \hat{x}^2} \right] d\hat{x}. \tag{10}$$

Strain Energy in the Composite Plate. As was stated before, the strain energy in the composite plate (U_p) can be broken into the strain energy in the matrix plus the strain energy in the cords. Hence the total strain energy has the form

$$U_p = U_m + \sum_{\text{cords}} U_c,$$

where the appropriate coordinate system is used for each layer of cords. This investigation is limited to the cases of one layer of parallel cords at the middle surface ($z=0$) and the case of two layers of parallel cords with the bottom layer at $z=-z_c$ running at an angle of θ to the x-axis, and the top layer at $z=+z_c$ running at an angle of $-\theta$ to the x-axis. The first configuration is shown in Fig. 1.The second configuration is commonly known as an antisymmetric angle-ply laminate. In the first case, the total energy of the system has the functional form

$$E = \int_0^l \int_{-b/2}^{b/2} F \left[\frac{\partial U}{\partial x}, \frac{\partial U}{\partial y}, \frac{\partial V}{\partial x}, \frac{\partial V}{\partial y}, \frac{\partial^2 W}{\partial x^2}, \frac{\partial^2 W}{\partial x \partial y}, \frac{\partial^2 W}{\partial y^2} \right] dy dx + \sum_{\text{cords}} \int_0^{l_c} G \left[\frac{\partial \hat{U}}{\partial \hat{x}}, \frac{\partial^2 W}{\partial \hat{x}^2}, \frac{\partial^2 W}{\partial \hat{x} \partial \hat{y}} \right]_{\hat{y}=\hat{y}_{\text{cord}},\ z=0} d\hat{x} + \Omega$$

where Ω is the potential energy of the external load. Minimizing this expression for the energy by means of the calculus of variations would involve solving the partial differential equations derived from the first variation of F, subject to boundary conditions along each cord as determined by the first variation of G, as well as whatever boundary conditions are global to the plate, including the loading requirements. Hence the field equations (the isotropic plate equations in the case of classical theory) would need to be solved in each area of the matrix and pieced together across the cords using the boundary conditions that arise from the first variations of G. If there were a large number of cords this would quickly become an insurmountable task. It should also be noted here that, because the cords are treated as one-dimensional, the derivatives of the displacements across the cords would not have to be continuous. The displacements on both sides of the cords would have to match, but there could be discontinuities in the slopes and other derivatives of the displacements due to the cords, further complicating this solution procedure.

However, once the form of the energy is known, approximate methods may be used to minimize it. For this study, the method of Ritz was chosen. The displacements are approximated by a sum of admissible functions with the magnitude of each function becoming a generalized coordinate:

$$U(x, y) = \sum_i \sum_j a_{ij} U_{ij}(x, y),$$
$$V(x, y) = \sum_i \sum_j c_{ij} V_{ij}(x, y),$$
$$W(x, y) = \sum_i \sum_j d_{ij} W_{ij}(x, y), \tag{11}$$

where $U_{ij}(x, y)$, $V_{ij}(x, y)$, $W_{ij}(x, y)$, are admissible functions (i.e., they must satisfy the geometric boundary conditions but not necessarily the natural boundary conditions), and the unknown magnitudes, a_{ij}, c_{ij}, and d_{ij} are the generalized coordinates. The Ritz method yields an exact solution when the set of admissible functions forms a complete set over the interval of space occupied by the plate. It has been noted that truncating this series tends to give reasonable solutions, when the admissible functions are chosen carefully. However, convergence to the correct solution is not guaranteed in the case of a truncated set of functions. The convergence of the Ritz method to this problem was investigated by Kittredge (1991). It is also worth noting that the truncated Ritz method is better at describing the global deformations of the plate. The local features may not be picked up. These solutions also tend to describe the deformations much better than the stresses and other parameters produced from differentiation of the displacements (Langhaar, 1962).

Results

Material Constants of Unidirectional Lamina. The results for unidirectional lamina properties determined by the energy method agree exactly with the previous results of this author (Shield, 1992) derived using an equilbrium formulation. These expressions are presented here for comparison purposes with the results of Gough and Tangorra and Akasaka and Hirano. The latter two theories treat the unidirectional lamina as an orthotropic material with five material properties. This approach differs from that of the current work, where the unidirectional lamina is treated as being monocyclic. The material constants corresponding to those used in the orthotropic representation found by this author using an equilibrium method are given by

$$E_1 = E_m + c_1 E_c v_c \left[1 - \frac{6c_2 c_3 v_c (1+\nu_m)}{c_1 (\overline{Ah^2 E} + 6c_4 v_c (1+\nu_m)} \right],$$

Downloaded 03 May 2010 to 171.66.16.20. Redistribution subject to ASME license or copyright; see http://www.asme.org/terms/Terms_Use.cfm

$$E_2=\frac{4E_m[c_1E_c\upsilon_c+E_m]+\dfrac{24(1+\nu_m)\upsilon_cE_c}{\overline{A}\overline{h}^2}(c_4E_m+CE_c\upsilon_c)}{[4E_m+4(1-\nu_m^2)\upsilon_cc_1E_c]+\dfrac{24(1+\nu_m)\upsilon_c}{\overline{A}\overline{h}^2\overline{E}}(c_4E_m+CE_c\upsilon_c(1-\nu_m^2))},$$

$$\nu_{12}=\nu_m,$$

$$\nu_{21}=\nu_m\frac{E_2}{E_1}, \tag{12}$$

and the normalized twist of a unidirectional lamina is given by

$$\frac{\tau_s^*}{\tau_s}=\frac{C\upsilon_c^2}{C\upsilon_c^2+c_4\upsilon_c\overline{E}+\overline{A}\overline{h}^2\overline{E}\dfrac{1}{6(1+\nu_m^2)}(c_1\vartheta_c+\overline{E})},$$

where $\overline{A}=A_c/R^2$, $\overline{h}=h/R$, $\overline{E}=E_m/E_c$, $\tau_s=(-c_3N/CRE_c\vartheta_ch)$ is the twist per unit length of a single cord under a proportional amount of axial load, υ_c is the cord volume fraction and $c = c_1c_4 - c_2c_3$. The Gough-Tangorra relationships are given by

$$E_1=c_1E_c\upsilon_c+E_m(1-\upsilon_c),$$

$$E_2=\frac{4E_m(1-\upsilon_c)[c_1E_c\upsilon_c+E_m(1-\upsilon_c)]}{3c_1E_c\upsilon_c+4E_m(1-\vartheta_c)},$$

$$G_{12}=G_m(1-\upsilon_c),$$

$$\nu_{12}=0.5,$$

$$\nu_{21}=\nu_{12}\,E_2/E_1,$$

$$\tau_s^*=0. \tag{13}$$

These equations are quite similar to the Halpin-Tsai equations, as usually used in composite plate theory; however, both theories threat the matrix as being incompressible, and ignore the transverse properties of the cords, avoiding the difficult problem of determining the Poisson's ratio of a cord.

The Akasaka-Hirano equations are given by

$$E_1=c_1E_c\vartheta_c,$$

$$E_2=4E_m/3,$$

$$G_{12}=G_m,$$

$$\nu_{12}=0.5,$$

$$\nu_{21}=0,$$

$$\tau_s^*=0. \tag{14}$$

These equations are further simplifications of the Gough-Tangorra equations, taking advantage of the large difference in moduli between rubber and steel; essentially the strength in the cord direction is attributed to the cords and the strength perpendicular to the cord direction to the matrix. In addition, the cord volume fraction is considered small compared with unity.

Material Properties for Angle-Ply Lamina, and Antisymmetric Angle-Ply Laminates. The general expressions for the strain, twist per unit length, and curvature along the cord were derived above. These Eqs. (7)–(9) are written in terms of the coordinate system aligned with the cord ($\hat{x}-\hat{y}-\hat{z}$ system). To be of use, these expressions must be transformed to the global coordinate system (x-y-z system). Consider an angle-ply lamina where the cords run at an angle θ to the x-axis, and hence the $\hat{x}-\hat{y}$ coordinate system is rotated by an angle θ with respect to the $x-y$ coordinate system. A transformation of variables can be used to write the expressions for the hatted variables in terms of the unhatted system. Hence the expression for the strain energy in each cord can be expressed in terms of the unhatted coordinate system and deformation field.

The material constants for arbitrary cord angle lamina can be found by investigating the response of the lamina to uniaxial tension. The displacement functions assumed for the middle surface displacements were as follows:

$$U(x, y)=a_{10}x+a_{11}xy,$$

$$V(x, y)=c_{10}x+c_{01}y+c_{11}xy,$$

$$W(x, y)=d_{11}x\,y. \tag{15}$$

These assumed displacement functions satisfy the geometric boundary conditions

$$U(0, y)=0,$$

$$W(0, y)=0.$$

The strain energy density in the matrix can easily be integrated along x and y to determine the strain energy in the matrix. The potential energy of the load is given by

$$\Omega=\int_{-b/2}^{b/2}U(l, y)N dy. \tag{16}$$

The strain energy in the cords must be evaluated by integrating along the length of each cord. The length of each cord is dependent, not only on the length of the plate, but also on the width of the plate and the angle of orientation of the cords. The calculations for the strain energy in the system were carried out using *Mathematica*.

Now that the energy in the system is found as a function of the generalized coordinates, the energy can be minimized by setting the derivatives of the energy with respect to each generalized coordinate equal to zero. This will generate a set of six linear equations in the six unknowns.

The plate moduli can be extracted from the displacements as follows. The effective modulus of elasticity in the x-direction is given by

$$E_x=\frac{N/h}{\dfrac{1}{bl}\displaystyle\int_{-b/2}^{b/2}U(l, y)dy},$$

where the denominator is the average axial strain (ϵ_x) of the plate. The effective Poisson's ratio in the x-y direction is given by

$$\nu_{xy}=\frac{-\epsilon_y}{\epsilon_x}=\frac{-\displaystyle\int_0^l[V(x, b/2)-V(x, -b/2)]dx}{\displaystyle\int_{-b/2}^{b/2}U(l, y)dy}$$

where ϵ_y is the average transverse strain of the plate. The twist per unit length in the x-direction is

$$\tau_s^*=\frac{\partial^2W(l, 0)}{\partial x\partial y}. \tag{17}$$

The theories of Gough-Tangorra and Akasaka-Hirano both treat the unidirectional cord composite as an orthotropic material. The material properties for a single-ply lamina of arbitrary cord orientation can be found by using a transformation of variables, as described in Jones (1975), resulting in the following properties. The effective modulus of elasticity in the x-direction is given by

$$\frac{1}{E_x}=\frac{1}{E_1}\cos^4\theta+\left(\frac{1}{G_{12}}-\frac{2\nu_{12}}{E_1}\right)\sin^2\theta\cos^2\theta+\frac{1}{E_2}\sin^4\theta. \tag{18}$$

The effective Poisson's ratio in the x-y direction can be found by

$$\nu_{xy}=E_x\left(\frac{\nu_{12}}{E_1}-\frac{1}{4}\left(\frac{1+\nu_{12}}{E_1}+\frac{1+\nu_{21}}{E_2}-\frac{1}{G_{12}}\right)\sin^2 2\theta\right). \tag{19}$$

This theory does not predict any twisting of the lamina, when loaded by an axial force; hence

$$\tau_s^*=0.$$

Downloaded 03 May 2010 to 171.66.16.20. Redistribution subject to ASME license or copyright; see http://www.asme.org/terms/Terms_Use.cfm

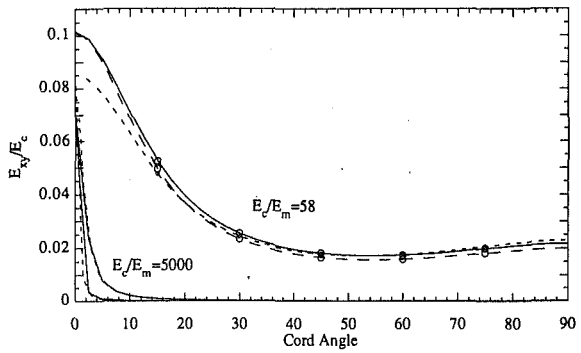


Fig. 2 Extensional stiffness E_x/E_c versus cord angle θ for an angle-ply lamina for three modulus ratios, $E_c/E_m = 58$, $E_c/E_m = 5000$, and $E_c/E_m = 50{,}000$. The solid curves represent the current work, the short dashed curves represent the Akasaka-Hirano theory, and the long dashed curve represents the Gough-Tangorra theory. The curves marked with circles represent the lowest modulus ratio.

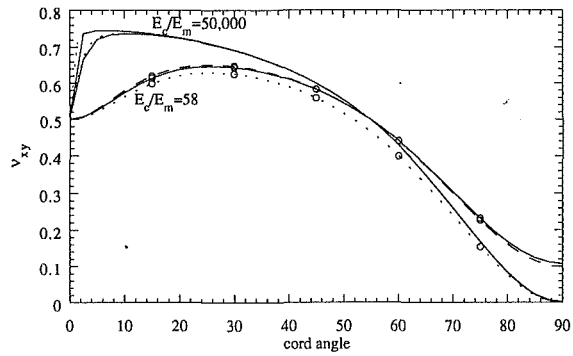


Fig. 3 Poisson's ratio ν_{xy} versus cord angle θ for an angle-ply lamina for three modulus ratios, $E_c/E_m = 58$, $E_c/E_m = 5000$, and $E_c/E_m = 50{,}000$. The solid curves represent the current work, the short dashed curves represent the Akasaka-Hirano theory, and the long dashed curve represents the Gough-Tangorra theory. The curves marked with circles represent the lowest modulus ratio.

For the purposes of comparison a typical tire cord is selected as the reinforcement. The material and geometric properties are given by

Young's modulus (E_c)	200 GPa
Poisson's ratio (ν_c)	0.25
Helix angle (α)	81.4 deg
Center wire radius (R_i)	0.15 mm
6 outer wires with radii (R_o)	0.14 mm
Cord radius ($R = R_i + 2R_o$)	0.43 mm
c_1	0.967
c_2	0.0828
c_3	0.187
c_4	0.0723.

The matrix and plate properties are given by

Poisson's ratio (ν_m)	0.50
Cord volume fraction (v_c)	0.088
$\frac{\bar{h}}{A}$	5.02
	2.38.

Figure 2 is a plot of the normalized modulus of elasticity in the x-direction (E_x/E_c) versus cord angle (θ) for three values of the modulus ratio $E_c/E_m = 58$, $E_c/E_m = 5{,}000$ and $E_c/E_m = 50{,}000$. The Akasaka-Hirano and Gough-Tangorra representations are indistinguishable at the larger two ratio values; hence only the Akasaka-Hirano and current method values are plotted for these two ratios. For the smaller modulus ratio, when the cord angle is less than 20 deg, the Gough-Tangorra theory and the energy method agree very well. When the cord angle is greater than 20 deg, the Akasaka-Hirano theory agrees more closely with the energy method results, but all three theories agree well. All three theories agree well for the larger two moduli ratios. Notice that the minimum value of the modulus occurs at a cord angle of about 55 deg for all three theories. This may not be intuitive, one would expect that for cord angles from approximately 55 to 90 deg, the modulus of elasticity would be equal to the modulus of elasticity of the matrix ($E_x/E_m = 1$). However, for angles greater than 55 deg the cords are under compression, so the stiffness of the cords acts to keep the width of the plate from shrinking, but because the matrix material was assumed to be incompressible, the total volume of matrix material must remain constant. The plate theory assumptions that the transverse shearing strain (ϵ_z) is zero keep the thickness of the matrix material from decreasing; therefore, the only way for the plate to elongate under these assumptions is if it shrinks in width. For these large cord angles, two of the assumptions are questionable: the first, that the transverse strain (ϵ_z) is zero, and secondly, the assumption that the cords have the same modulus in tension as in compression, when in fact the cords should be treated as bimodular, being much weaker in compression than in tension (Prakash et al., 1992). However, this stiffening reaction, even with these poor assumptions, does not have much effect, even at 90 deg where the cords have the largest compressive load. Here $E_x/E_m = 1.2$ for all three modulus ratios.

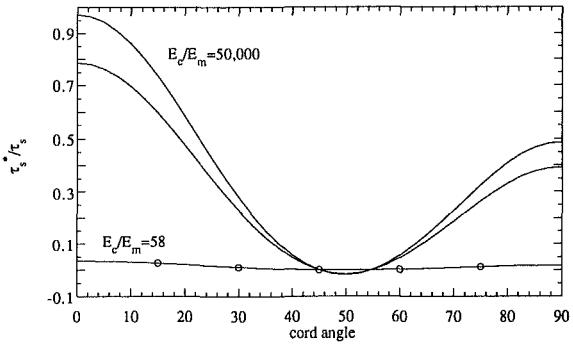


Fig. 4 Twist per unit length versus cord angle θ for an angle-ply lamina. The solid curves represent the current work. The curve marked with circles represents the lowest modulus ratio.

The effective Poisson's ratio in the x-y direction (ν_{xy}) versus cord angle for the three modulus ratios previously listed is shown in Fig. 3. As already indicated, the Gough-Tangorra and Akasaka-Hirano representations are indistinguishable at the larger two modulus ratios; hence the Gough-Tangorra representation is not shown. For the smallest modulus ratio, $E_c/E_m = 58$, the Gough-Tangorra theory and the energy method agree very well throughout the entire range of cord angles, whereas the Akasaka-Hirano curve lies somewhat below the preceding two curves. This is mainly due to the Akasaka-Hirano assumption that $\nu_{21} = 0$. The maximum value of ν_{xy}, for the smallest modulus ratio, occurs at a cord angle of about 25 deg, at a value of 0.65. The maximum for the two larger modulus ratio occurs closer to 0 deg. There is very little difference in the representation of the Poisson's ratios for the two larger moduli ratios.

Figure 4 is a plot of the normalized twist per unit length (τ_s^*/τ_s) versus cord angle for the three representative modulus ratios. The twist per unit length is normalized by the twist that a plate made entirely of cords at a cord angle of 0 deg would have. This normalization points out the damping effect of the matrix material on the twist of the plate. Neither the Gough-Tangorra nor the Akasaka-Hirano theory predicts any twist of the plate under this loading condition. The twist per unit length is zero when the cord angle is 45 deg. This corresponds to the configuration when all of the load is taken by the matrix, and the cords are unloaded. The only cord angle for which

Downloaded 03 May 2010 to 171.66.16.20. Redistribution subject to ASME license or copyright; see http://www.asme.org/terms/Terms_Use.cfm

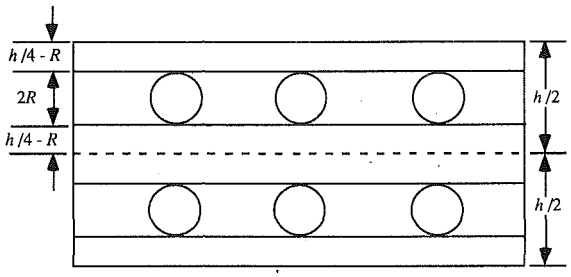


Fig. 5 Five-layer lamination model

the plate rotates opposite to that of the cord rotation in tension is 50 deg. All three modulus ratios show the same type of behavior of twist with respect to cord orientation. However, this effect is amplified by the larger modulus ratios.

The current method can be applied directly to find the material properties for a two-ply antisymmetric laminate. The material properties for a laminate made of orthotropic lamina can be related to the unidirectional lamina constants using CLT as described as Jones (1975). The results of Gough and Tangorra, as well as Akasaka and Hirano have been used in conjunction with CLT to predict the material properties of these laminates. These results will only be presented graphically for comparisons to the current results. In the case of two-ply antisymmetric angle-ply laminates an extensional-twisting coupling is predicted by CLT even when the lamina are assumed to be orthotropic, hence in these cases all three theories will predict twist when the plate is loaded uniaxially in tension.

There are two possible CLT representations for a two-ply cord laminate. The first is to consider the laminate as made up of two layers of thickness $h/2$, with a row of cords centered in each layer. The other representation is to consider the laminate as made up of five layers (see Fig. 5). Here two layers of cord-matrix material $2R$ thick are surrounded by three layers of matrix material. This representation, although harder to implement, only smears the cord contribution out over a layer the thickness of the cords; and hence will likely lead to better results. The current results are compared with the five-layer CLT model, except where noted.

A plot of the normalized modulus of elasticity in the x-direction (E_x/E_c) versus cord angle (θ) is shown in Fig. 6. The Gough-Tangorra curves are not shown for the larger two modulus ratios because they are indistinguishable from the Akasaka-Hirano curves. These cures are very similar to the corresponding curves for the single-layer case. As before, the Gough-Tangorra results match the energy method results extemely well for cord angles between 0 deg and 20 deg for the smallest modulus ratio. For this modulus ratio, for cord angles between 20 and 90 deg, the Akasaka-Hirano results match the energy method results more closely. Again, the modulus has its minimum around 55, where $E_x/E_m \approx 1$. For cord angles larger than 50 deg, it increases slightly, as was explained previously for the single layer case. This effect diminishes for the larger moduli ratios. There is good agreement between CLT and the current theory for the larger two moduli ratios.

The Poisson's ratio in the $x-y$ direction (ν_{xy}) versus cord angle (θ) is shown in Fig. 7(a) for $E_c/E_m = 58$ and in Fig. 7(b) for the larger two modulus ratios, $E_c/E_m = 5000$ and $E_c/E_m = 50{,}000$. For clarity of the plot, the Gough-Tangorra results are not shown for the larger two modulus ratios. For this two-ply laminate, the Akasaka-Hirano results agree very well with the energy method over the entire range of cord angles for the smaller modulus ratio. The Gough-Tangorra solution has the same general shape but is slightly larger than the two other methods. The maximum value of ν_{xy} occurs around 25 deg for the energy method, but both the Gough-Tangorra and Akasaka-Hirano solutions have the maximum occurring at slightly larger cord angles, around 35 deg, for the smallest

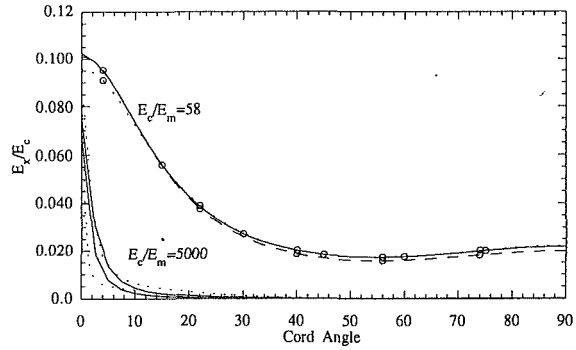


Fig. 6 Extensional stiffness E_x/E_c versus cord angle θ for a two-layer antisymmetric angle-ply laminate. The solid curves represent the current work, the short dashed curves represent the Akasaka-Hirano theory, and the long dashed curve represents the Gough-Tangorra theory. The curves marked with circles represent the lowest modulus ratio.

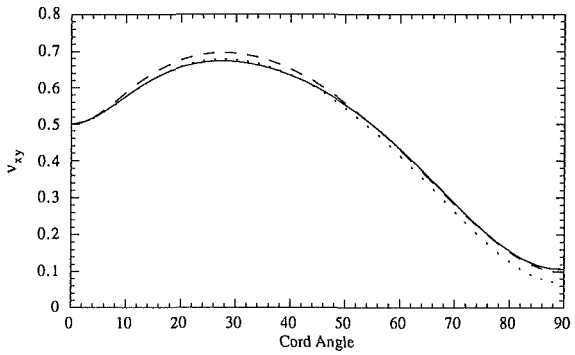


Fig. 7 (a)

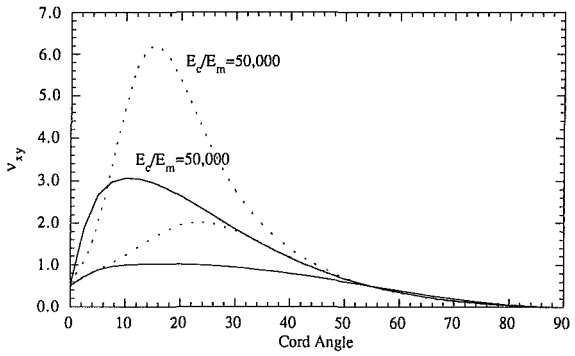


Fig. 7 (b)

Fig. 7 Poisson's ratio ν_{xy} versus cord angle θ for a two-layer antisymmetric angle-ply laminate with modulus ratios of (a) $E_c/E_m = 58$; (b) $E_c/E_m = 5000$ and $E_c/E_m = 50{,}000$. The solid curves represent the current work, the short dashed curves represent the Akasaka-Hirano theory and the long dashed curve represents the Gough-Tangorra theory.

modulus ratio. For the larger two modulus ratio, CLT predicts a much larger value of Poisson's ratio than the current method. Cembrola and Dudek (1985) remarked on a similar significant difference between CLT and experimental results. The shapes of the curves are also dissimilar for the larger modulus ratios.

Figures 8(a), 8(b), and 8(c) are plots of the normalized twist per unit length (τ_s^*/τ_s) versus cord angle (θ) for the three modulus ratios. In each of these three plots, the results for both two-layer and five-layer CLT are shown. Only the Akasaka-Hirano results are shown for the larger two modulus ratios. In the case of antisymmetric angle-ply laminates, CLT does predict a tension-twisting coupling for composites composed of orthotropic lamina, as is evident by the solid and dashed lines. At a cord angle of 0 deg, neither the Gough-Tangorra

Downloaded 03 May 2010 to 171.66.16.20. Redistribution subject to ASME license or copyright; see http://www.asme.org/terms/Terms_Use.cfm

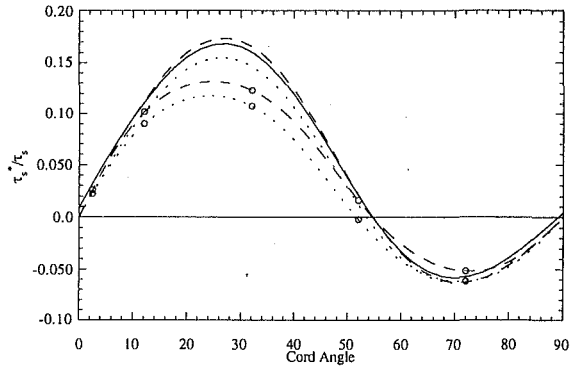


Fig. 8 (*a*)

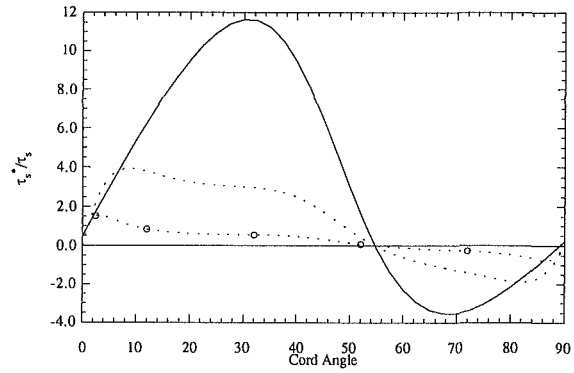


Fig. 8 (*b*)

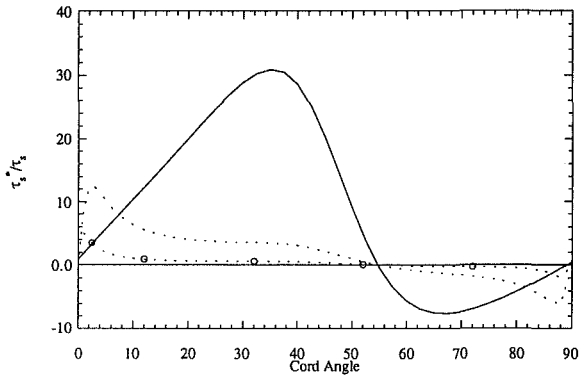


Fig. 8 (*c*)

Fig. 8 Twist per unit length versus cord angle θ for a two-layer antisymmetric angle-ply laminate with modulus ratios of (*a*) $E_c/E_m = 58$, (*b*) $E_c/E_m = 5000$, and (*c*) $E_c/E_m = 50{,}000$. The solid curves represent the current work, the short dashed curves represent two-layer and five-layer CLT used with the Akasaka-Hirano approximations, and the long dashed curves represent two-layer and five-layer CLT used with the Gough-Tangorra approximations. The curves marked with circles represent two-layer CLT.

nor the Akasaka-Hirano theory shows any twist, whereas the current theory does show twist. Although the general shapes of the curves are similar for the smallest modulus ratio, all three predict significantly different values of twist. The current theory predicts the level of twist somewhere between the five-layer CLT using the Akasaka-Hirano constants and the five-layer CLT using the Gough-Tangorra constants. For the larger two modulus ratios, the current method predicts much more twist than CLT, and the shapes of the curves are no longer similar. In every case, the five-layer CLT predicts more twist than the two-layer CLT. For the middle modulus ratio, $E_c/E_m = 5000$, the three curves agree well for cord angles between 0 and 5 deg. Both the energy method and the Akasaka-Hirano curves have a zero-crossing around 55 deg for any value of modulus ratio.

It is clear that the amount of twist of the composite will be affected by the positioning of the cords with respect to the middle suface. In CLT it is assumed that each lamina is made of a homogeneous material. This would imply that the cords would need to be uniformly distributed through the entire thickness of the layer. For fiber composites, where the fiber diameters are very small compared with the thickness of the layer, this is probably a reasonable approximation; however, in cord composites, the diameter of the cord may be as much as one-half of the thickness of the layer. The cords are also found at discrete heights, not distributed uniformly through the thickness. Even when the laminate is considered to be five layers, two cord-matrix layers sandwiched between five pure matrix layers, the cords are not uniformly distributed through the thickness of their respective layers. In this case the diameter of the cord is exactly that of the layer, and hence the cord area is concentrated near the middle of the layer.

References

Akasaka, T., and Hirano, M., 1972, "Approximate Elastic Constants of Fiber Reinforced Rubber Sheet and Its Composite Laminate," *Fukugo Zairyo* (*Composite Materials & Structures*), Vol. 1, pp. 70–76.

Cembrola, R. J., and Dudek, T. J., 1985, "Cord/Rubber Material Properties," *Rubber Chemistry and Technology*, Vol. 58, pp. 830–856.

Costello, G. A., 1990, *Theory of Wire Rope*, Springer-Verlag, New York.

Gough, V. E., 1968, "Stiffness of Cord and Rubber Constructions," *Rubber Chemistry and Technology*, Vol. 41, pp. 988–1021.

Hsieh, K. T.,1985, "Modeling of Cord-Reinforced Rubber Laminates," Ph.D. Thesis, University of Texas.

Jones, R. M., *Mechanics of Composite Materials*, McGraw-Hill, New York.

Kittredge, C. A., 1991, "Static Response of Cord Composite Plates,"Ph.D. Thesis, University of Illinois at Urbana-Champaign.

Kumar, M., and Bert, C. W., 1982, "Experimental Characterization of Mechanical Behavior of Cord-Rubber Composites, *Tire Science and Technology*, Vol. 10, Nos. 1-4, pp. 37-54.

Langhaar, H., 1962, *Energy Methods in Applied Mechanics*, Robert E. Krieger, Malabar, FL.

Prakash, A., Conway, T., and Costello, G. A., 1992, "Compression of a Cord," ASME Journal of Applied Mechanics, Vol. 59, pp. S213–S216.

Shield, C. A., and Costello, G. A., 1993, "The Effect of Wire Rope Mechanics on the Material Properties of Cord Composites—An Elasticity Approach," ASME Journal of Applied Mechanics, Vol. 60.

Tangorra, G., 1969, "Fiber-Reinforced, Oriented Rubber Sheets," *Proceedings of International Rubber Conference*, Moscow, pp. 459–466.

Walter, J. D., 1978, "Cord-Rubber Tire Composites: Theory and Applications," *Rubber Chemistry and Technology*, Vol. 51, No. 3, pp. 524–576.

Downloaded 03 May 2010 to 171.66.16.20. Redistribution subject to ASME license or copyright; see http://www.asme.org/terms/Terms_Use.cfm

Steady Motion of a Thread Over a Rotating Roller

R.-J. Yang
Department of Engineering Science,
National Cheng-Kung University,
Tainan, Taiwan

Dynamic equations of steady motion governing the behavior of threads over rotating arbitrary-axisymmetric rollers are derived. Various types of boundary conditions resulting in initial value or boundary value problems are discussed. Analytical solutions for the case of a circular cylinder are found. Two of the integrals obtained are exact. The third one, being a perturbation result, is thus approximate. Comparisons of results for a circular cylinder with those for tapered and parabolic rollers are made.

1 Introduction

Moving threads (strings or tapes) over rotating rollers can be found in many engineering applications, such as textile and magnetic tape recording technologies. In textile plants, threads move at speeds over 50 m/sec from spinning to winding up. Furthermore, a thread may pass over several rollers which change the direction of the thread, the thread enters and leaves a roller tangentially with some inclination. Similarly, in the magnetic tape recording process, a moving tape always executes small lateral motion along a guided roller. In general, the portion of the thread (or tape) in contact with the roller surface does not lie in a plane. Thus, the equation predicting the tension distribution in a planar thread cannot be applied. A more sophisticated model is required for the prediction of dynamic behavior of the thread over a rotating roller.

Dynamic equations governing the behavior of the thread over a rotating circular cylinder were independently derived by Moustafa (1975) and Ono (1979). The following assumptions were made in the Moustafa's derivation: (a) the motion is steady (i.e., the speed of the thread and the angular speed of the roller are constant); (b) the thread is inextensible and perfectly flexible; (c) there is Coulomb friction between the thread and roller surface with a homogeneous friction coefficient; and (d) the thread is in contact with the roller surface and the roller has a constant radius. His derivation ended up with a set of nonlinear ordinary differential equations. The equations were then integrated numerically for cases when the ratio of the thread speed to the tangential component of the roller surface is very close to unity. In the Ono's formulation, he used inhomogeneous friction coefficient in the derivation and ended up with a set of partial differential equations. However, he had to assume the thread tension distribution according to a planar behavior in order to obtain analytical solutions.

It is worthwhile to extend further the formulation developed in Moustafa (1975) because it is not necessary that the roller be a circular cylinder. Equations governing the behavior of the thread over a rotating roller with varying diameter will be derived here. Of course, it is expected that these equations all reduce to Moustafa's derivation when the radius of the roller is constant. Moreover, the boundary conditions were not stated clearly nor all possible realistic boundary conditions were treated in Moustafa (1975). A detailed description of all possible initial value and boundary value problems will also be given in this paper.

For the case when the roller is a circular cylinder, the analytical solutions developed herein will be used in place of the numerical solutions (Moustafa, 1975). In this circumstance, a new independent variable is introduced, and the original two differential equations of motion are transformed to three first-order ordinary differential equations. Two of the three equations hold exact closed-form integrals, while the remaining one is to be solved by a perturbation method assuming the ratio of the thread speed (V) to the absolute value of the tangential component of the roller surface velocity ($|v|$) is $1+\epsilon$ with $\epsilon \ll 1$ as the perturbation parameter. The solution of the perturbation result possesses an accuracy up to the order ϵ^3. The integrals together with the perturbation solution are then used to solve and discuss various initial value and boundary value problems. The solution obtained from the perturbation method will become less accurate when ϵ can no longer be regarded as small. Therefore, the range of the perturbation parameter, ϵ, required to assure a good solution should be established. This range will be determined by comparing perturbation results with ones obtained by numerical integration of the exact differential equations of motion.

For the case of noncircular cylindrical rollers, it appears that the chances of obtained closed-form analytical solutions are extremely small. Numerical integration techniques will be employed to study the system motion. Several different shapes of rollers will be studied and compared with the results for the circular cylindrical roller.

Contributed by the Applied Mechanics Division of THE AMERICAN SOCIETY OF MECHANICAL ENGINEERS for publication in the ASME JOURNAL OF APPLIED MECHANICS.

Discussion on this paper should be addressed to the Technical Editor, Professor Lewis T. Wheeler, Department of Mechanical Engineering, University of Houston, Houston, TX 77204-4792, and will be accepted until four months after final publication of the paper itself in the ASME JOURNAL OF APPLIED MECHANICS.

Manuscript received by the ASME Applied Mechanics Division, May 4, 1992; final revision, Nov. 18, 1992. Associate Technical Editor: D. J. Inman.

Copyright © 1994 by ASME
Downloaded 03 May 2010 to 171.66.16.20. Redistribution subject to ASME license or copyright; see http://www.asme.org/terms/Terms_Use.cfm

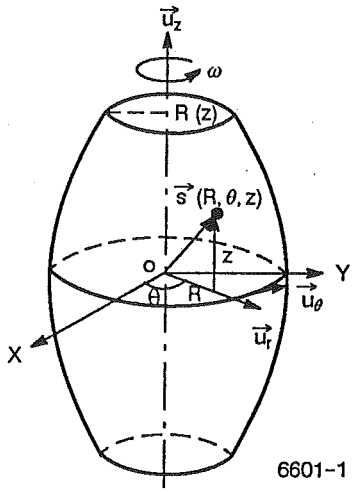


Fig. 1 Coordinate system

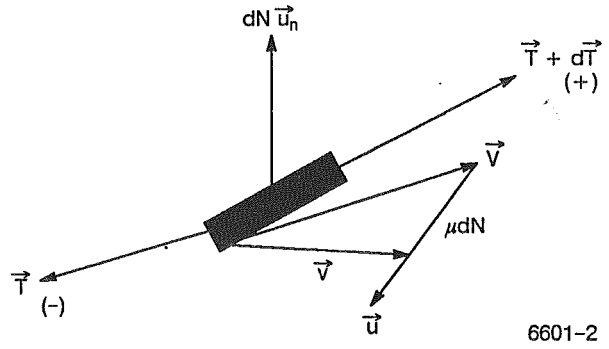


Fig. 2 Forces acting on a thread element

2 Formulation

The radius of a roller is given by $R = R(z)$ and the position vector of a thread particle over the roller in cylindrical coordinates is $\mathbf{S} = R\mathbf{u}_r + z\mathbf{u}_z$ (see Fig. 1). Note that the thread particle is kept in contact with the roller surface. Thus the velocity of a thread particle over the roller is

$$\mathbf{V} = \left(\dot{z}\,\frac{dR}{dz}\,\mathbf{u}_r + R\mathbf{u}_\theta + \dot{z}\mathbf{u}_z\right) VP \tag{1}$$

where

$$P = \left(R^2 + \dot{z}^2 + \left(\dot{z}\,\frac{dR}{dz}\right)^2\right)^{-1/2}.$$

The dot denotes differentiation with respect to θ and V is the speed of a thread particle over the roller. It can be shown that the acceleration of a thread particle over the roller is

$$\mathbf{a} = A_r\mathbf{u}_r + A_\theta\mathbf{u}_\theta + A_z\mathbf{u}_z + \frac{dV}{dt}\left(\dot{z}\,\frac{dR}{dz}\,\mathbf{u}_r + R\mathbf{u}_\theta + \dot{z}\mathbf{u}_z\right)P \tag{2}$$

where

$$A_r = V^2P^4\left(\dot{z}^2(R^2+\dot{z}^2)\,\frac{d^2R}{dz^2} + \left(R^2\ddot{z} - 2R\dot{z}^2\,\frac{d^2R}{dz^2}\right)\frac{dR}{dz} - R^3 - R\dot{z}^2\right) \tag{3}$$

$$A_\theta = V^2P^4\left(-R\dot{z}^3\,\frac{dR}{dz}\,\frac{d^2R}{dz^2} + \dot{z}\left(R^2 - R\ddot{z}\,\frac{dR}{dz} + 2\dot{z}^2 + 2\left(\dot{z}\,\frac{dR}{dz}\right)^2\right)\frac{dR}{dz} - R\dot{z}\ddot{z}\right) \tag{4}$$

$$A_z = V^2P^4\left(-\dot{z}^4\,\frac{dR}{dz}\,\frac{d^2R}{dz^2} - R\dot{z}^2\,\frac{dR}{dz} + R^2\ddot{z}\right). \tag{5}$$

Three assumptions were used so far. They are (a) the thread particle is in contact with the roller surface, (b) the roller is axisymmetric, and (c) the thread is inextensible. Equations (1) and (2) are valid even in unsteady motion. In steady motion, the thread speed, V, is constant and dV/dt vanishes.

Consider an inextensible thread element with length dl and density per unit length ρ, where $dl = d\theta/P$, $d\theta > 0$. The thread is subjected to tensions at both end $\mathbf{T}$ and $\mathbf{T} + d\mathbf{T}$, the normal force $d\mathbf{N}$, and the Coulomb friction force μdN (in the direction of $\mathbf{u}$), where μ is the dynamic coefficient of friction and the unit vector $\mathbf{u}$ lies in the opposite direction of the relative velocity of the thread element to the roller surface beneath; it is assumed that the thread element is always in contact with the roller surface. The thread element must be in contact with roller surface if the magnitude of normal force, dN, is greater than zero. From the geometry (see Fig. 2) $\mathbf{u}$ can be expressed as

$$\mathbf{u} = \frac{1}{\alpha}\left(\left(\frac{\nu}{PR} - V\right)\mathbf{u}_\theta - \frac{V\dot{z}}{R}\,\frac{dR}{dz}\,\mathbf{u}_r - \frac{V\dot{z}}{R}\,\mathbf{u}_z\right) \tag{6}$$

where

$$\alpha = \left(\left(\frac{\nu}{PR} - V\right)^2 + \left(\frac{V\dot{z}}{R}\,\frac{dR}{dz}\right)^2 + \left(\frac{V\dot{z}}{R}\right)^2\right)^{1/2}.$$

ν is the component of the circumferential velocity, $\omega \times R\mathbf{u}_r$, of the roller surface under the thread element; ω is the angular speed of the roller, a constant in steady motion.

The tension $\mathbf{T}$ in the thread is parallel to its velocity $\mathbf{V}$ (see Fig. 2, Eq. (1), and note the sign convention). Thus the tension $\mathbf{T}$ can be expressed as

$$\mathbf{T} = T_1\mathbf{u}_r + T_2\mathbf{u}_\theta + T_3\mathbf{u}_z$$

where

$$T_1 = PT\dot{z}\,\frac{dR}{dz}, \quad T_2 = PTR, \quad T_3 = PT\dot{z}.$$

Express $d\mathbf{T}$ as

$$d\mathbf{T} = dT_r\mathbf{u}_r + dT_\theta\mathbf{u}_\theta + dT_z\mathbf{u}_z$$

where

$$dT_r = \left(\left(\dot{T}\dot{z}\,\frac{dR}{dz} + T\ddot{z}\,\frac{dR}{dz} + T\dot{z}^2\,\frac{d^2R}{dz^2} - TR\right)P - \lambda T\dot{z}\,\frac{dR}{dz}\right)d\theta \tag{7}$$

$$dT_\theta = \left(\left(\dot{T}R + 2T\dot{z}\,\frac{dR}{dz}\right)P - \lambda TR\right)d\theta \tag{8}$$

$$dT_z = \left(\left(\dot{T}\dot{z} + T\ddot{z}\right)P - \lambda T\dot{z}\right)d\theta \tag{9}$$

$$\lambda = \left(\dot{z}\,\frac{dR}{dz}\left(\ddot{z}\,\frac{dR}{dz} + \dot{z}^2\,\frac{d^2R}{dz^2} + R\right) + \dot{z}\ddot{z}\right)P^3.$$

The normal force, $d\mathbf{N}$, acting on the thread element is along the direction of the unit normal vector ($\mathbf{u}_n$) of the roller surface. $\mathbf{u}_n = (\mathbf{u}_r - dR/dz\mathbf{u}_z)Q$, $Q = (1 + (dR/dz)^2)^{-1/2}$. Express $d\mathbf{N}$ as $d\mathbf{N} = dN_r\mathbf{u} + dN_z\mathbf{u}_z$, where

$$dN_r = dNQ \tag{10}$$

$$dN_z = -dN\left(\frac{dR}{dz}\right)Q. \tag{11}$$

Since the cylindrical coordinate system (r,θ,z) is inertial, the equations of motion for a thread element are, according the Newton's law,

(a) along the $\mathbf{u}_r$ direction

$$dT_r + dN_r - \frac{\mu dNV\dot{z}}{\alpha R}\,\frac{dR}{dz} = \rho dlA_r, \tag{12}$$

Downloaded 03 May 2010 to 171.66.16.20. Redistribution subject to ASME license or copyright; see http://www.asme.org/terms/Terms_Use.cfm

(b) along the $\mathbf{u}_\theta$ direction

$$dT_\theta + \frac{\mu dN}{\alpha}\left(\frac{\nu}{PR} - V\right) = \rho dl A_\theta, \tag{13}$$

(c) along the $\mathbf{u}_z$ direction

$$dT_z + dN_z - \frac{\mu dN V \dot{z}}{\alpha R} = \rho dl A_z. \tag{14}$$

Expressions for A_r, A_θ, A_z, dT_r, dT_θ, dT_z, dN_r, and dN_z are given, respectively, by Eqs. (3), (4), (5), (7), (8), (9), (10), and (11). Note that $dV/dt = 0$ in steady motion. After substitution of expression for dT_r, dN_r, and A_r into Eq. (12), we obtain

$$n = \alpha\left(\left(\frac{T}{\rho V^2} - 1\right)\left(\gamma - R^2\ddot{z}\frac{dR}{dz}\right)P^3 - \frac{\dot{T}\dot{z}P}{\rho V^2}\frac{dR}{dz}\right)G > 0 \tag{15}$$

where

$$G = \left(\alpha Q - \frac{\mu \dot{z} V}{R}\frac{dR}{dz}\right)^{-1}$$

$n = (1/\rho V^2)(dN/d\theta)$ is the nondimensional normal force per radian acting on the thread element and $\gamma = (R^2 + \dot{z}^2)(R - \dot{z}^2(d^2R/dz^2)) + 2R\dot{z}^2(dR/dz)^2$. Substituting expressions of dT_θ, A_θ, dT_z, dN_z, A_z, and Eq. (15) into Eqs. (13) and (14), and eliminating terms of $T/\rho V^2$ and $\dot{T}/\rho V^2$, one may show that

$$\ddot{z} = \beta\left((\alpha_1\dot{z} + \alpha_2 R)\left(R - \dot{z}^2\frac{d^2R}{dz^2}\right) + 2\dot{z}^2\frac{dR}{dz}\left(1 + \alpha_2\frac{dR}{dz}\right)\right) \tag{16}$$

where

$$\beta = \frac{1}{R}\left(1 + \alpha_2\frac{dR}{dz}\right)^{-1}, \quad \alpha_1 = \mu\left(\frac{\nu}{PR} - V\right)G,$$

$$\alpha_2 = \left(\alpha\frac{dR}{dz}Q + \frac{\mu\dot{z}V}{R}\right)G.$$

Expressions for dT_z, dN_z, A_z, Eqs. (15) and (16) may be substituted into Eq. (14) with the result

$$\frac{\dot{T}}{\rho V^2} = \frac{1}{\alpha_3}\left(\frac{T}{\rho V^2} - 1\right)\left(\alpha_1 R + \dot{z}\frac{dR}{dz} - \alpha_2\dot{z}\right)\left(\dot{z}^2\frac{d^2R}{dz^2} - R\right), \tag{17}$$

where

$$\alpha_3 = \frac{1}{P^2}\left(1 + \alpha_2\frac{dR}{dz}\right).$$

Note that the Greek symbols α, β, γ, α_1, α_2, and α_3 defined above are all functions of z and $\dot{z}$. Also, n in Eq. (15) should be greater than zero to keep a thread element in contact with the roller surface. Obviously, Eq. (15) is a constraint to the solutions of Eqs. (16) and (17). For a given roller surface $R = R(z)$ and supplementary conditions on z and T, Eqs. (16) and (17) can be solved (at least numerically). Once z and T are found, n should be checked from Eq. (15) to satisfy the constraint.

3 Initial and Boundary Value Problems

An initial value problem, in the present problem, is defined as one for which all the associated supplementary conditions are given at one specified value of θ only. If the conditions for a problem are specified at two different θ values, it is called a boundary value problem. The system of Eqs. (16) and (17) is third order, thus for cases when a unique solution may exist, three supplementary conditions will be required. There are 20 possible combinations of supplementary conditions on T, z, and $\dot{z}$ at θ_i and θ_f, where θ_i and θ_f can be, for example, the θ coordinate of the point of entry and the point of departure of the thread on the surface of the roller, respectively. As will be seen later, two of the twenty are initial value problems; while the remaining eighteen are boundary value problems.

Initial Value Problems. Denote $T_i = T(\theta_i)$, $T_f = T(\theta_f)$, $z_i = z(\theta_i)$, $z_f = z(\theta_f)$, $\dot{z}_i = \dot{z}(\theta_i)$, and $\dot{z}_f = \dot{z}(\theta_f)$. Two types of initial value problems may occur. They are (a) when the supplementary conditions are specified at the entry station θ_i, i.e., T_i, z_i, and $\dot{z}_i$ are given; (b) when the conditions are specified at the departure station θ_f, i.e., T_f, z_f, and $\dot{z}_f$ are given. Solutions for initial value problems are easy to obtain and they are expected to be unique. This is in contrast to the boundary value problems whose solutions may be nonunique and even nonexistent.

Boundary Value Problems. Theoretically speaking, there are a total of 18 possible combinations of supplementary conditions which give rise to boundary value problems for a fully coupled third-order system of differential equations. The 18 sets are

(1) $z_i, \dot{z}_i, T_f$, (2) $z_f, \dot{z}_f, T_i$, (3) $z_i, \dot{z}_f, T_i$,
(4) $z_i, \dot{z}_f, T_f$, (5) $\dot{z}_i, z_f, T_i$, (6) $\dot{z}_i, z_f, T_f$,
(7) z_i, z_f, T_i, (8) z_i, z_f, T_f, (9) z_i, T_i, T_f,
(10) z_i, T_i, T_f, (11) $\dot{z}_i, \dot{z}_f, T_i$, (12) $\dot{z}_i, \dot{z}_f, T_f$,
(13) $\dot{z}_i, T_i, T_f$, (14) $\dot{z}_f, T_i, T_f$, (15) $z_i, z_f, \dot{z}_f$,
(16) $\dot{z}_i, z_f, \dot{z}_f$, (17) $z_i, \dot{z}_i, z_f$, (18) $z_i, \dot{z}_i, \dot{z}_f$.

As Eq. (16) for z is second order and decoupled from Eq. (17) for T, it is clear that the first two sets degenerate into initial value problems, solving first for z and then for T. Once z is determined, an initial value problem for T ensues. The z and T equations are fully coupled by the conditions given in sets (9) and (10). It will be shown later that solutions associated with these two sets are nonunique when the roller is a circular cylinder. For the remaining sets from (11) to (18), the solutions for z and T are either nonexistent or nonunique. This again will become clear later after studying solutions for a circular cylindrical roller.

4 Solutions for the Case of Cylindrical Roller

When the roller is a circular cylinder, it is easily verified that for $R = R_0 = \text{constant}$, $dR/dz = d^2R/dz^2 = 0$, Eqs. (16) and (17) reduce to

$$\ddot{z} = \frac{\mu\nu\dot{z}(R^2 + \dot{z}^2)^{1/2}}{((\nu(R_0^2 + \dot{z}^2)^{1/2} - R_0V)^2 + (V\dot{z})^2)^{1/2}}, \tag{18}$$

$$\frac{\dot{T}}{\rho V^2} = \frac{\mu(T/\rho V^2 - 1)(V - R_0\nu/(R_0^2 + \dot{z}^2)^{1/2})R_0}{((\nu(R_0^2 + \dot{z}^2)^{1/2} - R_0V)^2 + (V\dot{z})^2)^{1/2}}. \tag{19}$$

This is in agreement with Moustafa (1979). Similarly, Eq. (15) reduces to

$$n = R_0(T/\rho V^2 - 1)/(R_0^2 + \dot{z}^2)^{1/2} > 0. \tag{20}$$

Thus, in this case, the constraint becomes $T > \rho V^2$. That is, the speed of the thread should not exceed the speed of transverse wave propagation in the thread with tension T and linear density ρ, if the thread in steady motion is to remain in contact with the roller surface.

Defining $z' = dz/(R_0 d\theta)$ and $y = (1 + z'^2)^{1/2}$, Eqs. (18), (19), and (20) are transformed into, respectively,

$$\frac{dy}{d\theta} = \frac{\mu\nu(y^2 - 1)}{((V^2 + \nu^2)y^2 - 2V\nu y)^{1/2}}, \tag{21}$$

Downloaded 03 May 2010 to 171.66.16.20. Redistribution subject to ASME license or copyright; see http://www.asme.org/terms/Terms_Use.cfm

$$\frac{1}{\rho V^2}\frac{dT}{d\theta}=\frac{\mu(T/\rho V^2-1)(Vy-\nu)}{y((V^2+\nu^2)y^2-2V\nu y)^{1/2}}, \tag{22}$$

$$n=(T/\rho V^2-1)/y. \tag{23}$$

Some results from the numerical investigations of the above system of equations were presented in Moustafa (1979). In what follows, we will present analytical solutions instead of numerical solutions.

Choosing y as the independent variable, one can show that for $y>1$

$$\frac{d(T/\rho V^2)}{dy}=\frac{(T/\rho V^2-1)(yV/\nu-1)}{y(y^2-1)}, \tag{24}$$

$$\mu\frac{d\theta}{dy}=(\text{sgn }\nu)\frac{((V^2/\nu^2+1)y^2-2yV/\nu)^{1/2}}{y^2-1}, \tag{25}$$

$$\frac{\mu}{R_0}\frac{dz}{dy}=\pm(\text{sgn }\nu)\left(\frac{(V^2/\nu^2+1)y^2-2yV/\nu}{y^2-1}\right)^{1/2}, \tag{26}$$

where sgn ν is "+1" if ν is positive, it is "−1" if ν is negative. In Eq. (26) the upper plus sign should be used if z increases with respect to θ or time; the lower minus sign should be used if z decreases with respect to θ or time. It is evident from Eq. (24) that the minimum tension in the thread, when $\nu>0$, occurs at $y=\nu/V$ since the second derivative of Eq. (24) at this point is positive. No such extreme point will occur when $V>\nu$. Exact integrals of Eqs. (24) and (25), and an approximate integral of Eq. (26) can be found. They are

(a) tension in the thread

$$\frac{T}{\rho V^2}-1=C_1 y(y-1)^{(1/2)((V/\nu)-1)}(y+1)^{-(1/2)((V/\nu)+1)}, \tag{27}$$

(b) angular position of the thread, $\mu\neq 0$

$$\mu\theta=C_2+(\text{sgn }\nu)\frac{1}{2}\sqrt{\left(\frac{V}{\nu}\right)^2+1}\left\{2\ln|2\sqrt{y^2-2Ay}+2y-2A|\right.$$
$$-\sqrt{1-2A}\ln\left|\frac{2((1-2A)\sqrt{y^2-2Ay}+2(y-Ay-A))}{y-1}\right|$$
$$\left.+\sqrt{1+2A}\ln\left|\frac{2((1-2A)\sqrt{y^2-2Ay}-2(y+Ay-A))}{y+1}\right|\right\} \tag{28}$$

where $A=(V/\nu)/((V/\nu)^2+1)$.

(c) axial location of the thread in the limit ϵ tends to zero and $\mu\neq 0$.

$$\frac{\mu z}{R_0}=C_3\pm(\text{sgn }\nu)\left\{\sqrt{2(1+\epsilon)}[\sqrt{y(y+\text{sgn }\nu)}\right.$$
$$-(\text{sgn }\nu)\ln(\sqrt{y}+\sqrt{y+\text{sgn }\nu})]$$
$$+\frac{\sqrt{2}\epsilon^2}{4\sqrt{1+\epsilon}}\left[\sqrt{y(y+\text{sgn }\nu)}+(\text{sgn }\nu)\ln(\sqrt{y}+\sqrt{y+\text{sgn }\nu})\right.$$
$$\left.\left.+\frac{\sqrt{2}}{2}\ln\left(\frac{\sqrt{2y}-(\text{sgn }\nu)\sqrt{y+\text{sgn }\nu}}{\sqrt{2y}+(\text{sgn }\nu)\sqrt{y+\text{sgn }\nu}}\right)\right]\right\}+O(\epsilon^4). \tag{29}$$

Note that $\epsilon=V/|\nu|-1$.

(d) normal force per radian acting on the thread

$$n=C_1(y-1)^{(1/2)((V/\nu)-1)}(y+1)^{-(1/2)((V/\nu)+1)} \tag{30}$$

where C_1, C_2, and C_3 are constants of integration to be determined from supplementary conditions. Note that Eqs. (27)–(30) are dimensionless. Thus, for a rotating circular cylinder the dependent variables $T/\rho V^2$, $\mu\theta$, $\mu z/R$, and n are functions of y with ϵ as the only parameter. The quantities $(T/\rho V^2-1)/C_1$, $\mu\theta-C_2$, $\pm(\mu z/R_0-C_3)$, and n/C_1 can be plotted against y with ϵ as the parameter.

Two exceptional cases are considered as follows.

Case I: The Planar Thread. When y is identically equal to unity, Eqs. (24)–(26) are invalid. In this case, Eqs. (21)–(23) have to be used by setting $y=1$. It is easy to show that the solutions are $z=$ constant, $T/\rho V^2=1+C\exp[\text{sgn}(V-\nu)\mu\theta]$ and $n=C\exp[\text{sgn}(V-\nu)\mu\theta]$. Thus the thread lies in a plane $z=$ constant and the tension in the thread varies exponentially with θ, which is in agreement with Phelan (1970).

Case II: The Frictionless Roller. In the limit of a frictionless roller or thread, μ is equal to zero. Eqs. (21)–(23) and the definition of z' lead to $z=R_0z_0'\theta+z_0$, $T=T_0$ and $n=(T_0/\rho V^2-1)/(1+z_0'^2)^{1/2}$, where z_0, z_0', and T_0 are constants. Thus, if the frictional effect is negligible, then the thread behaves in a helical form on the roller surface and its tension as well as normal force per radian are constant.

Examples of Initial and Boundary Value Problems. As illustrations, an initial value problem with the supplementary conditions at $\theta_i=0$, $z_i=0$, $z_i'=\tan 4$ deg, and $T_i/\rho V^2=1.5092$ is given. y is determined as $y=(1+z_i'^2)^{1/2}$. Thus, the three constants of integration can be determined in Eqs. (27), (28), and (29). Numerical results for three values of ϵ are shown in Figs. 3 to 5. In the range of ϵ considered, i.e., $|\epsilon|\leq 0.002$, no significant variations of the thread shape are observed. As mentioned before, the solution to the initial value problem is unique. The case of the planar thread with the same initial conditions ($z_i=0$, $T_i/\rho V^2=1.5092$), is also presented in Figs. 3 to 5. It is clear from Fig. 4 that the tension increases (de-

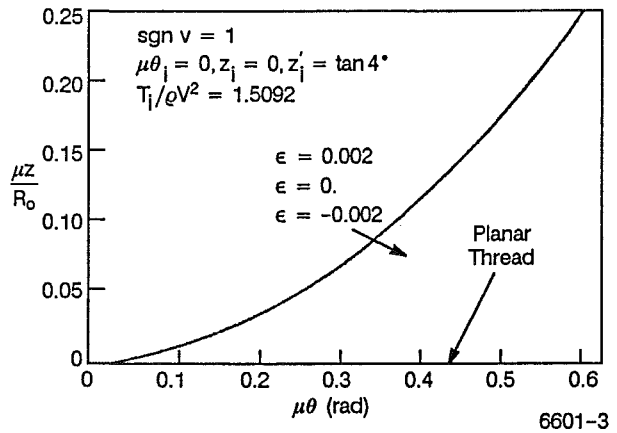


Fig. 3 Axial location of thread

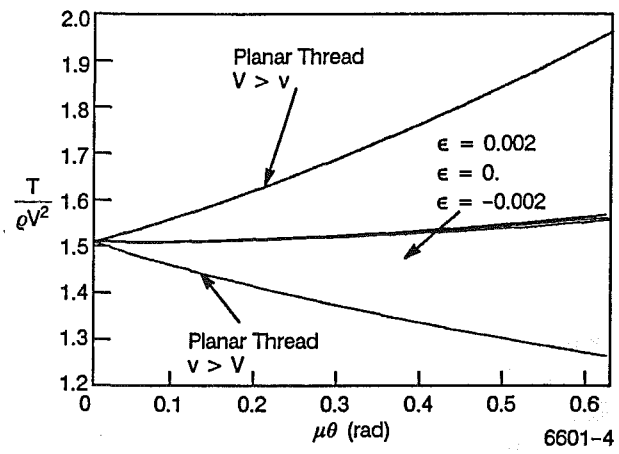


Fig. 4 Tension distribution in thread

Downloaded 03 May 2010 to 171.66.16.20. Redistribution subject to ASME license or copyright; see http://www.asme.org/terms/Terms_Use.cfm

creases) exponentially with respect to $\mu\theta$ when $V>v$ ($v>V$) if the thread remains in the plane $z=0$. It is interesting to note that the tension increases with respect to $\mu\theta$ when $|\epsilon|$ is small. The variation of normal force per radian acting on the thread as a function of $\mu\theta$ is shown in Fig. 5. The decrease of n with respect to $\mu\theta$ for the nonplanar thread is in contrast to the increase of $T/\rho V^2$ in Fig. 4. This may be attributed to the increase in y with respect to $\mu\theta$.

Boundary conditions listed in the previous section can be grouped into six categories, namely (1)-(6), (7)-(8), (9)-(10), (11)-(12), (13)-(14), and (15)-(18), respectively. The solution procedures for all cases in the same category are similar. Note that z does not appear explicitly in Eqs. (18)-(20). Thus, the value of z can be shifted by a constant value without affecting the solution. Three examples are given below.

The first example is illustrated for case (1). The supplementary conditions are at $\theta=\theta_i$, $z=z_i$, $z'=z_i'$, and at $\theta=\theta_f$, $T=T_f$. The conditions on θ_i and z_i fix the constants C_2 and C_3, respectively. Thus, let $\theta=\theta_f$ in the θ integral, and y_f can be solved. With y_f determined, then the condition of T_f fixes the constant C_1. Note that from Eq. (21) it is easily seen that θ varies monotonically with respect to y for $y>1$ since $dy/d\theta\neq 0$. That is, the relation between y and θ is a one-to-one function. Thus, if a solution exists, it is unique.

The second example is illustrated for case (9) when the supplementary conditions are at $\theta=\theta_i$, $z=z_i$ and $T=T_i$; at $\theta=\theta_f$, $T=T_f$. Thus, Eq. (27) gives two relations with C_1, y_i and y_f to be determined. Similarly, from Eq. (28), θ_i and θ_f lead to two relations with C_2, y_i, and y_f to be determined. Thus, four equations and four unknowns result. Solution to this problem can be nonunique as seen by the numerical example below. Sample runs are made with the following data: $\rho=0.2$ g/m, $\mu=0.2$, $R_0=2$ cm, $V=50$ m/sec, $\theta_i=0$, $\theta_f=\pi$, $z_i=0$, $T_i=38.5$ g, and $T_f=40$ g with $v=49.9$, 50, and 50.1 m/sec, respectively. For each v value there can be found two solutions satisfying the supplementary conditions. Initial and final angles of inclination of the thread, initial, and final force per radian acting on the thread, and the final axial location of the thread are tabulated, respectively, for the two solutions A and B.

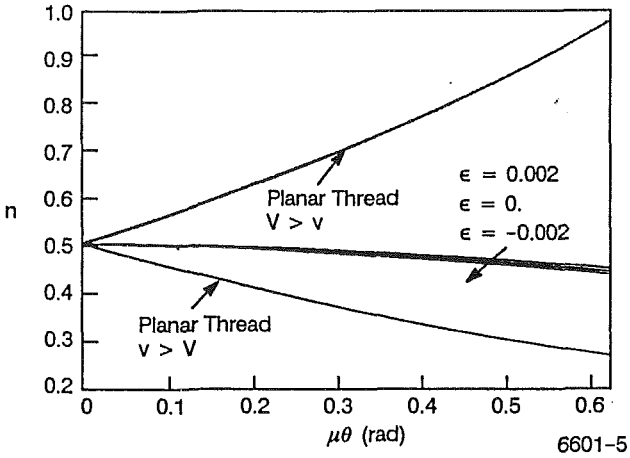


Fig. 5 Normal force per radian acting on thread

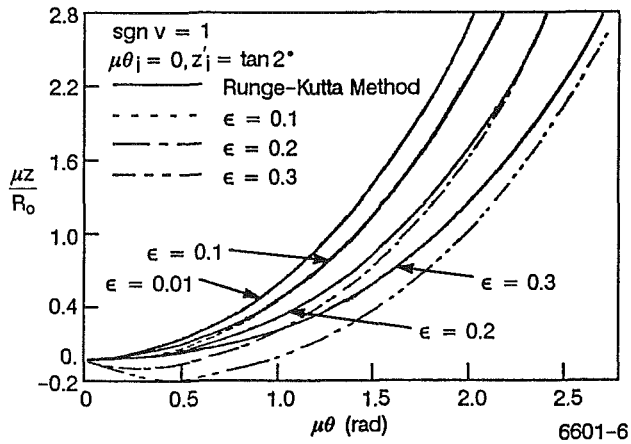


Fig. 6 Axial location of thread. Comparison between perturbation integral and Runge-Kutta method

		$v=49.9$ m/se	$v=50$ m/sec	$v=50.1$ m/se
Initial inclined angle of the thread on the roller surface (degree)	A	4.84	5.93	6.88
	B	68.30	68.24	68.18
Final inclined angle of the thread on the roller surface (degree)	A	37.14	37.99	38.72
	B	76.80	76.77	76.74
Final axial location of the thread on the roller surface (cm)	A	2.58	2.72	2.83
	B	20.89	20.84	20.78
Initial normal force per radian acting on the thread (g)	A	12.94	12.92	12.90
	B	4.80	4.82	4.83
Final normal force per radian acting on the thread (g)	A	11.51	11.42	11.31
	B	3.31	3.32	3.33

The nonuniqueness arises from the multiple roots for y_i and y_f. This may be attributed to different solution branches associated with stable or unstable equilibria. Discussions on the stability of the thread motion is beyond the scope of the present paper. In the sample runs, solution A was obtained from the initial guess of $y_i=1.01$, $y_f=1.3$; while solution B was obtained from the initial guess of $y_i=1.5$, $y_f=3.0$.

In the third one, case (11) is illustrated. Supplementary conditions are at $\theta=\theta_i$, $z'=z_i'$, and $T=T_i$, and at $\theta=\theta_f$, $z'=z_f'$. Substituting either (θ_i,y_i) or (θ_f,y_f) into Eq. (28), one may determine a value for C_2. Generally speaking, the values of C_2 obtained from (θ_i,y_i) and (θ_f,y_f) are not consistent. Thus, the solution does not exist as a rule. If the values of C_2 are consistent, the solution in this rare case will be nonunique. This is because C_2 remains arbitrary. However, this nonuniqueness is superficial since a constant shift of z as mentioned earlier does not affect the physical phenomenon.

Remarks on the Range of Validity of the Perturbation Integral. The perturbation integral for z, Eq. (29), is accurate up to the other ϵ^3. In the limit $\epsilon=0$, Eq. (29) gives the exact result. It is the purpose here to discuss the smallness of ϵ for which the integral for z remains valid by comparing results given by Eq. (29) to the numerical fourth-order Runge-Kutta results of the exact differential equation for a range of ϵ values. Comparisons of results obtained, respectively, from the perturbation method and the Range-Kutta method are shown in Fig. 6. No significant differences occur between the perturbed results and the exact results when $\epsilon=0.01$. Errors in the perturbed results are less than 0.2 percent. It appears that when $\epsilon<0.1$, the perturbation integral gives a quite good result. For values of ϵ somewhat beyond 0.1, the perturbation integral (Eq. (29) with the upper sign and sgn $v=1$) becomes inconsistent since the initial slope $dz/d\theta$ is negative. However, the

Downloaded 03 May 2010 to 171.66.16.20. Redistribution subject to ASME license or copyright; see http://www.asme.org/terms/Terms_Use.cfm

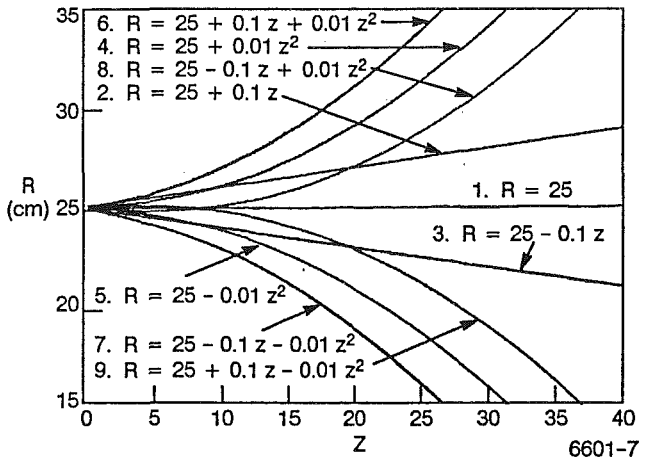


Fig. 7 Shape of roller surface

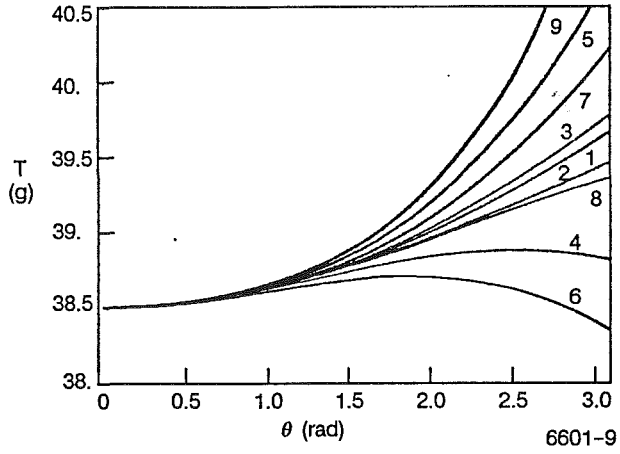


Fig. 9 Tension distribution in thread

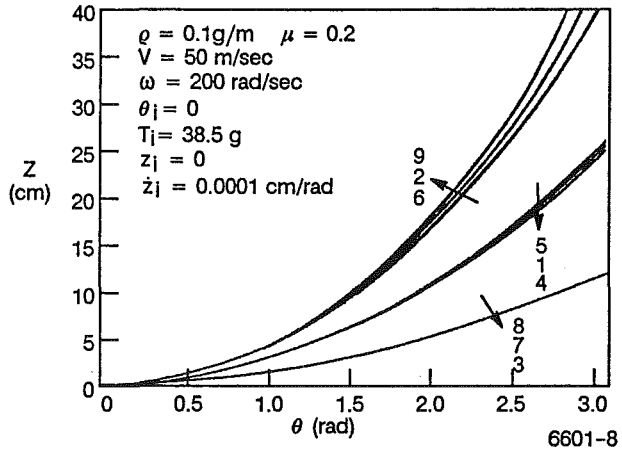


Fig. 8 Axial location of thread

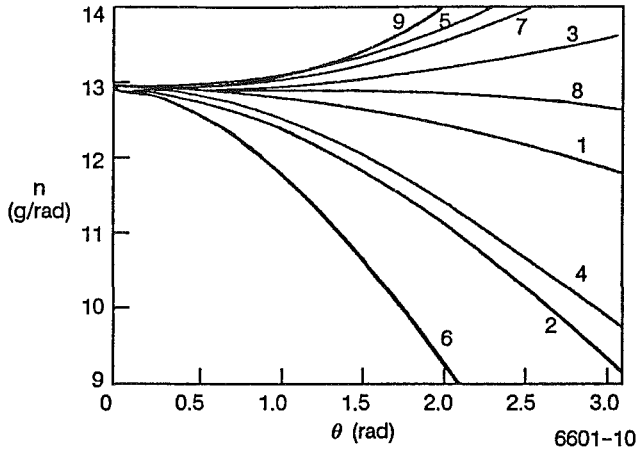


Fig. 10 Normal force per radian acting on thread

exact results indicate that the initial slope remains positive. This is a clear indication of the breakdown of the perturbation integral. Note that the above statements are only concerned with the sample run. A general conclusion for the range of ϵ values required to assure an accurate solution from the perturbation cannot be drawn because the validity of the integral depends on ϵ and y simultaneously.

5 Solutions for the Case of Tapered and Parabolic Rollers

In the practical applications, the roller may have a tapered shape, a polynomial shape, an exponential shape, etc. In this section, numerical integration (fourth-order Runge-Kutta method) will be applied to solve equations of motion because the chances of obtaining closed-form solutions of Eqs. (16) and (17) appear to be extremely small. Comparisons of these results with those for the circular cylinder will be shown.

Initial value problems of threads over rotating tapered and parabolic rollers are illustrated to show the behavior of the threads. The shapes of rollers investigated are shown in Fig. 7. Results of numerical integration are shown in Figs. 8 to 10. The effects of the slope of roller surface can now be seen. It is noted from Fig. 8 that the axial location of the thread on a tapered-upward roller (curve 2 in Fig. 7) increases faster than that for the thread on a tapered-downward roller (curve 3 in Fig. 7); on the contrary, in Fig. 9, the tension in thread on a tapered-downward roller increases faster than that for the thread on a tapered-upward roller. This is because the thread is "pulled" ($v<V$) when $R<R_0$, and it is "pushed" ($V<v$) when $R>R_0$. Also, the results for normal force (from Fig. 10) indicates that this force in the thread on a tapered-downward roller increases with respect to θ, whereas it decreases with respect to θ when the thread is on a tapered-upward roller. Effects of the curvature of the roller surface are shown by curve 4 and curve 5. It is seen that the curvature of the roller surface has less of an effect on the axial location, z, of the thread than does the slope of the roller surface. Furthermore, a negative curvature of the roller surface (curve 5 in Fig. 7) results in a faster increase in tension with θ than a positive curvature (curve 4 in Fig. 7) does. Also, n increases with θ in the case of negative curvature of roller surface and it decreases with θ for positive curvature of roller surface. The combined effects of slope and curvature of the roller surface are also shown by curves 6, 7, 8, and 9. It shows that the slope of the roller surface has a significant effect on z, while the curvature of the roller surface plays a major role in T and n.

6 Concluding Remarks

1 Equations for the steady motion of a thread over a rotating roller with varying radius are derived. The equations agree with the ones given in Moustafa (1975) when the roller has a constant radius.

2 Exact integrals of tension and angular position as a function of y are obtained for the steady motion of the thread over a rotating cylindrical roller. In addition, a perturbation integral for the axial location of the thread is obtained for small values of ϵ.

3 Discussions of initial as well as boundary value problems are carried out for the case of a cylindrical roller. Solutions

Downloaded 03 May 2010 to 171.66.16.20. Redistribution subject to ASME license or copyright; see http://www.asme.org/terms/Terms_Use.cfm

for initial value problems are unique, whereas the solutions for boundary value problems may be nonunique and even nonexistent.

4 The effects of slope and curvature of the roller surface are investigated by numerical integration for the case of rollers with varying radius. The slope and curvature of roller investigated play major roles in affecting the axial location and tension distribution of the thread, respectively.

Acknowledgments

The author is indebted to Prof. D. N. Fan at Howard University for his encouragement and guidance during the course of this work. The support of Prof. M. Holt at the University of California, Berkeley is also acknowledged.

References

Moustafa, M., 1975, "The Behavior of Threads over Rotating Rolls," *Journal of Engineering Science*, College of Engineering, University of Riyadh, Vol. 1, No. 2.

Ono, K., 1979, "Lateral Motion of an Axially Moving String on a Cylindrical Guide Surface," ASME JOURNAL OF APPLIED MECHANICS, Vol. 46, pp. 905–912.

Phelan, P. M., 1970, *Fundamentals of Mechanical Design*, McGraw-Hill, New York.

Downloaded 03 May 2010 to 171.66.16.20. Redistribution subject to ASME license or copyright; see http://www.asme.org/terms/Terms_Use.cfm

Antiplane Shear Deformations for Homogeneous and Inhomogeneous Anisotropic Linearly Elastic Solids

C. O. Horgan
Professor,
Fellow ASME.

K. L. Miller
Graduate Student.

Department of Applied Mathematics,
School of Engineering and Applied Science,
University of Virginia,
Charlottesville, VA 22903

Antiplane shear deformations of a cylindrical body, with a single displacement field parallel to the generators of the cylinder and independent of the axial coordinate, are one of the simplest classes of deformations that solids can undergo. They may be viewed as complementary to the more familiar plane deformations. Antiplane (or longitudinal) shear deformations have been the subject of the considerable recent interest in nonlinear *elasticity theory for homogeneous isotropic solids. In contrast, for the* linear *theory of* isotropic *elasticity, such deformations are usually not extensively discussed. The purpose of the present paper is to demonstrate that for* inhomogeneous anisotropic linearly elastic solids *the antiplane shear problem* does *provide a particularly tractable and illuminating setting within which effects of anisotropy and inhomogeneity may be examined. We consider infinitesimal antiplane shear deformations of an inhomogeneous anisotropic linearly elastic cylinder subject to prescribed surface tractions on its lateral boundary whose only nonzero component is axial and which does not vary in the axial direction. In the absence of body forces,* not all arbitrary anisotropic cylinders *will sustain an antiplane shear deformation under such tractions. Necessary and sufficient conditions on the elastic moduli are obtained which* do allow *an antiplane shear. The resulting boundary value problems governing the axial displacement are formulated. The most general elastic symmetry consistent with an antiplane shear is described. There are at most 15 independent elastic coefficients associated with such a material. In general, there is a* normal *axial stress present, which can be written as a linear combination of the two dominant shear stresses. For a material with the cylindrical cross-section a plane of elastic symmetry (monoclinic, with 13 moduli), the normal stress is no longer present. For* homogeneous *materials, it is shown how the governing boundary value problem can be transformed to an equivalent isotropic problem for a transformed cross-sectional domain. Applications to the issue of assessing the influence of anisotropy and inhomogeneity on the decay of Saint-Venant end effects are described.*

1 Introduction

Antiplane shear deformations are one of the simplest classes of deformations that solids can undergo. In antiplane shear of a cylindrical body, the displacement is parallel to the generators of the cylinder and is independent of the axial coordinate. Thus antiplane shear, with just a single axial displacement field, may be viewed as complementary to the more complicated (yet perhaps more familiar) plane strain deformation, with its two in-plane displacements. In recent years, considerable attention has been paid to the analysis of antiplane shear deformations within the context of *nonlinear* elasticity theory, for both incompressible and compressible homogeneous *isotropic* solids. In the nonlinear context, such studies were largely motivated by the promise of relative analytic simplicity compared with plane problems. In contrast, for the *linear theory of isotropic* elasticity, antiplane shear deformations are rarely discussed since the plane problems are tractable in this case. However, even in this elementary context, the antiplane shear problem (governed by a Neumann problem for Laplace's equation) plays a useful role as a pilot problem, within which various aspects of elasticity solutions may be examined in a simple setting, e.g., mode III crack problems.

While antiplane (or longitudinal) shear deformations were considered by the earlier workers in *nonlinear* elasticity, recent impetus was supplied by papers of Knowles (1976, 1977a) on incompressible and compressible isotropic materials. As pointed out in these papers, while in the *linear* (or *linearized*) theory of homogeneous *isotropic* elastic solids, nontrivial equilibrium states of antiplane shear *are always possible* in the absence of body forces for *any* material, such is not the case in the finite theory. (Here and henceforth, "nontrivial" means

Contributed by the Applied Mechanics Division of THE AMERICAN SOCIETY OF MECHANICAL ENGINEERS for publication in the ASME JOURNAL OF APPLIED MECHANICS.

Discussion on this paper should be addressed to the Technical Editor, Professor Lewis T. Wheeler, Department of Mechanical Engineering, University of Houston, Houston, TX 77204-4792, and will be accepted until four months after final publication of the paper itself in the ASME JOURNAL OF APPLIED MECHANICS.

Manuscript received by the ASME Applied Mechanics Division, July 1, 1992; final revision, Nov. 23, 1992. Associate Technical Editor: R. M. Bowen.

Copyright © 1994 by ASME
Downloaded 03 May 2010 to 171.66.16.20. Redistribution subject to ASME license or copyright; see http://www.asme.org/terms/Terms_Use.cfm

that the displacement gradient is nonconstant. Simple shear deformations, for which the displacement gradient *is* constant, are always sustainable both in the linear and nonlinear theory.) Necessary and sufficient conditions on the strain energies for homogeneous isotropic nonlinearly elastic materials which do allow antiplane shear were obtained in Knowles (1976, 1977a); see also Jiang and Knowles (1991) for further contributions in the compressible case. Applications to mode III fracture are described in Knowles (1977b) while stress concentration problems have been investigated by Abeyaratne and Horgan (1983), Jafari et al. (1984), and Horgan and Silling (1987). Axisymmetric finite antiplane shear deformations for compressible materials have been examined recently by Polignone and Horgan (1992) where further references to the literature may be found.

In the present paper, we confine attention to *linear* (or *linearized*) elasticity and consider infinitesimal antiplane shear deformations of an *inhomogeneous*, *anisotropic* cylinder. The cylinder is subjected to prescribed surface tractions on its lateral boundary whose only nonzero component is axial and which does not vary in the axial direction. In the absence of body forces, we show that *not all arbitrary anisotropic bodies* will sustain an antiplane shear deformation under such tractions (Section 2). The governing equilibrium equations are shown to reduce to a system of three differential equations for the single unknown axial displacement and thus the system is overdetermined. (This is quite analogous to what happens in the finite theory for *isotropic* materials.) Necessary and sufficient conditions on the elastic constants (or on the elastic coefficients in the inhomogeneous case) are obtained in Section 2 which *do* allow an antiplane shear under the traction boundary conditions specified above. In Section 3, the basic boundary value problems governing the axial displacement are described. These are standard oblique-derivative boundary value problems for a single second-order partial differential equation. The stresses are given as linear combinations of first derivatives of the displacement. In Section 4, the results are specialized to materials with particular elastic symmetries. First, we consider the homogeneous *isotropic* case and recover the well-known result that, in this case, *antiplane shear is always possible for any isotropic material and that the governing problem is simply the Neumann problem for Laplace's equation*. Comparable results hold for the inhomogeneous isotropic case. The most general anisotropic symmetry consistent with antiplane shear is then described. This is conveniently done using the two-suffix elasticity tensor c_{ij}, with explicit matrix form given in Eq. (47); there are at most 15 independent elastic moduli in $\mathbf{c}$. The two shearing stresses depend on just three of these elastic moduli and so the governing boundary value problem depends only on these three moduli. There is an interesting *normal stress effect* in that an axial normal stress is generally present which also depends on two additional elastic moduli, which are different from those already mentioned. This axial stress may be written as linear combinations of the main shearing stresses (see (48)). If the material symmetry is further specialized to the monoclinic system (with 13 moduli), corresponding to the cylinder having its cross-sectional plane a plane of elastic symmetry, there is no longer an associated axial normal stress. Further specialization leads to the orthotropic material; in this case the governing problem can be reduced, by a rescaling, to the isotropic problem. In Section 5, we confine attention to *homogeneous materials* and show how the governing problem can be transformed to an equivalent isotropic problem for a transformed cross-sectional domain. An analogy with the *torsion problem* for a homogeneous anisotropic cylinder is briefly discussed. In Section 6, we describe two immediate applications of the theory developed in the earlier sections. Both of these concern Saint-Venant end effects in antiplane shear. The cross-section of the cylinder is now taken to be a semi-infinite strip, subject to self-equilibrated end loads. In the *homogeneous* case, a formula for the rate of *exponential decay* of stresses with distance from the loaded end is obtained (see (67)), which is *explicit* in the anisotropy parameters. For a highly anisotropic material (modeling a fiber-reinforced composite) an asymptotic estimate for the decay rate is found which predicts *slow* decay away from the end of the strip, so that the corresponding characteristic *decay length is large* relative to the strip width. Such results, which have been previously obtained for the plane and axisymmetric problems (see, e.g., Horgan, 1982; Horgan, 1989), are found here in a comparatively easy way. The second application described in Section 6 is concerned with the influence of *inhomogeneity* on the decay of end effects. Recent results of Horgan and Payne (1993) are discussed in the present context showing that *exponential* decay like $\exp(-kx_1)$, $\exp(-kx_1^{1/2})$ or $\exp(-kx_1^2)$ (where x_1 is the axial coordinate in the strip) or *polynomial* decay at differing rates can occur depending on the degree of inhomogeneity of the material.

Elasticity models involving variable elastic coefficients are widely used in soil mechanics and geophysics. *Antiplane shear* models with variable coefficients have also been used in fracture mechanics to model damage and local crack-tip process zones (see, e.g., Schovanec, 1989, and the references cited therein).

2 Antiplane Shear Deformations of an Anisotropic Linearly Elastic Solid

We consider the elastostatic problem associated with the equilibrium of an inhomogeneous anisotropic linearly elastic cylindrical body, with simply connected cross-section, whose generators are parallel to the x_3-axis of a rectangular cartesian coordinate system. The cylinder is subjected to prescribed surface tractions $\mathbf{t}^*$ on its lateral boundary whose only nonzero component is axial and which does not vary in the axial direction. Thus

$$t_1^*=0,\ t_2^*=0,\ t_3^*=t_3^*(x_1, x_2), \tag{1}$$

on the lateral surface. The cylinder is assumed to be sufficiently long so that end effects in the axial direction are negligible. The surface tractions (1) would be expected to give rise to a deformation whose displacement components are of the form

$$u_1=0,\ u_2=0,\ u_3=u_3(x_1, x_2). \tag{2}$$

Such a deformation is called an *antiplane shear*. This displacement field may be regarded as a natural complement to that of *plane strain* where $u_\alpha = u_\alpha(x_1, x_2)$, $u_3 = 0$.

The generalized Hooke's law for an arbitrary inhomogeneous anisotropic linearly elastic solid in three dimensions is given by

$$T_{ij}=C_{ijkl}E_{kl}, \tag{3}$$

where T_{ij} denotes the stress tensor, $E_{ij} = (u_{i,j} + u_{j,i})/2$ the infinitesimal strain tensor, and $C_{ijkl} = C_{ijkl}(\mathbf{x})$ are the elastic coefficients satisfying the usual symmetry conditions

$$C_{ijkl}=C_{jikl},\ C_{ijkl}=C_{ijlk},\ C_{ijkl}=C_{klij}, \tag{4}$$

so that the number of independent components of $\mathbf{C}$ is 21. On using the second of (4) and the strain-displacement relations we write (3) as

$$T_{ij}=C_{ijkl}u_{k,l}, \tag{5}$$

which, in view of (2), reduces to

$$T_{ij}=C_{ij3\alpha}u_{3,\alpha}, \tag{6}$$

where the Greek subscripts range over the values 1, 2. The equilibrium equations, in the absence of body forces, are

$$T_{ij,j}=0. \tag{7}$$

We first consider the case of a *homogeneous* solid so that

Downloaded 03 May 2010 to 171.66.16.20. Redistribution subject to ASME license or copyright; see http://www.asme.org/terms/Terms_Use.cfm

the components of $\mathbf{C}$ are constants. By virtue of (6) and (2) we see that $T_{ij} = T_{ij}(x_1, x_2)$ so that (7) reduce to

$$T_{i\beta,\beta} = 0. \tag{8}$$

On substitution from (6) in (8), we find that the axial displacement u_3 must satisfy

$$C_{i\beta 3\alpha} u_{3,\alpha\beta} = 0 \text{ on } D, \tag{9}$$

where D denotes the plane cross-section of the cylinder. The system (9) consists of *three differential equations for the single unknown u_3 and thus is overdetermined* in general. Hence an *arbitrary* homogeneous anisotropic solid will *not*, in general, sustain an antiplane shear deformation.

We turn now to the boundary conditions (1). On employing the relation $t_i = T_{ij} n_j$, where $\mathbf{n}$ denotes the unit outward normal on the lateral boundary, we find that (1) holds provided

$$C_{\alpha\beta 3\gamma} u_{3,\gamma} n_\beta = 0 \text{ on } \partial D, \tag{10}$$

$$C_{3\beta 3\gamma} u_{3,\gamma} n_\beta = t_3^* \text{ on } \partial D, \tag{11}$$

where ∂D denotes the boundary of D.

A necessary and sufficient condition for a nontrivial (i.e., grad $u \neq$ *constant*) *state of antiplane shear to be possible subject to the boundary conditions* (1) now follows from (9), (10), and (11). Thus if $\mathbf{C}$ is such that

$$C_{\alpha\beta 3\gamma} \equiv 0 \ (\alpha, \beta, \gamma = 1, 2), \tag{12}$$

the first two differential equations in (9) are satisfied identically as well as the two boundary conditions (10). The axial displacement u_3, henceforth denoted by u, must then satisfy the third of (9) and the boundary condition (11), so that

$$C_{3\beta 3\alpha} u_{,\alpha\beta} = 0 \text{ on } D, \tag{13}$$

$$C_{3\beta 3\alpha} u_{,\alpha} n_\beta = t_3^* \text{ on } \partial D, \tag{14}$$

where $t_3^* = t_3^*(x_1, x_2)$ is a prescribed function on ∂D. The boundary value problem (13), (14) for u is one of oblique derivative type for a second-order linear partial differential equation with constant coefficients. On employing the divergence theorem and (13), it is readily shown that the prescribed traction t_3^* must be such that

$$\int_{\partial D} t_3^* ds = 0 \tag{15}$$

for a solution of (13), (14) to exist. Of course, (15) would also follow from the restriction on the data (1) necessary for overall force equilibrium. Thus we have shown that the condition (12) is *sufficient* to ensure that every solution $u_3 \equiv u$ of (13), (14) (with grad $u \neq$ constant on D) automatically satisfies (9), (10), and (11). Conversely, suppose that u_3 is a solution of (9), (10), (11) such that grad $u \neq$ constant on D. At each point on ∂D, the boundary conditions (10) may be viewed as a system of two linear equations for the two quantities $u_{3,1}$ and $u_{3,2}$. The determinant C of the coefficients in these equations is

$$C = (C_{1131}C_{2132} - C_{2131}C_{1132})n_1^2 + (C_{1231}C_{2232} - C_{2231}C_{1232})n_2^2 + (C_{1131}C_{2232} - C_{2231}C_{1132})n_1 n_2$$

where n_1, n_2 are the components of the unit outward normal on ∂D. Excluding the very special case where all three coefficients of n_1^2, n_2^2 and $n_1 n_2$ vanish and excluding special geometries, C will, in general, be nonzero *unless* condition (12) is satisfied. This implies that $u_{3,1}$ and $u_{3,2}$ are then identically zero on ∂D, which in turn shows that the boundary condition (11), with $t_3^* \neq 0$, cannot be satisfied. Thus the condition (12) is also *necessary* for a nontrivial state of antiplane shear to be possible subject to the boundary conditions (1).

We turn now to consider how the above arguments are modified if the material is *inhomogeneous* so that $\mathbf{C} = \mathbf{C}(\mathbf{x})$. In this case, on using (6) in (7), we find that

$$(C_{ij3\alpha} u_{3,\alpha})_{,j} = 0, \tag{16}$$

which we write as

$$C_{ij3\alpha} u_{3,\alpha j} + C_{ij3\alpha,j} u_{3,\alpha} = 0. \tag{17}$$

The boundary conditions are still given by(10), (11) where it is now understood that $\mathbf{C} = \mathbf{C}(\mathbf{x})$. Since (10), (11) are to hold for all x_3, it is clear that $\mathbf{C}$ must be independent of the axial coordinate x_3 so that

$$\mathbf{C} = \mathbf{C}(x_1, x_2), \tag{18}$$

and (17) may now be written as

$$(C_{i\beta 3\alpha} u_{3,\alpha})_{,\beta} = 0 \text{ on } D. \tag{19}$$

This is the counterpart of (9) for the inhomogeneous case. The system (19) is again an overdetermined system of three differential equations for the single unknown u_3, subject to the boundary conditions (10), (11). Thus, using similar arguments to those used in the homogeneous case, we deduce that *necessary and sufficient conditions for a nontrivial state of antiplane shear deformation to be possible for the inhomogeneous material subject to the boundary conditions (1) are that (18) hold, together with*

$$C_{\alpha\beta 3\gamma}(x_1, x_2) \equiv 0 \ (\alpha, \beta, \gamma = 1, 2). \tag{20}$$

The axial displacement $u_3 = u$ must then satisfy

$$(C_{3\beta 3\alpha} u_{,\alpha})_{,\beta} = 0 \text{ on } D, \tag{21}$$

$$C_{3\beta 3\alpha} u_{,\alpha} n_\beta = t_3^* \text{ on } \partial D. \tag{22}$$

The boundary value problem (21), (22) (the inhomogeneous analog of (13), (14)) now involves a second-order partial differential equation with *variable coefficients*. It is still required that the prescribed traction t_3^* be such that (15) holds.

We observe that in establishing *necessity* in the foregoing, for both homogeneous and inhomogeneous materials, we have made use of the boundary conditions (1). Thus our results are both problem dependent and material dependent. Since the system of differential Eqs. (9) (or (19)) is overdetermined, it would be desirable to obtain necessary and sufficient conditions on the elasticity tensor for (9) (or (19)) to sustain nontrivial states of antiplane shear *regardless of boundary conditions* (cf. Knowles 1976, 1977a for the nonlinear problem). While the conditions (12) (or (18), (20)) are clearly *sufficient*, it remains to be seen whether they are also *necessary* in these circumstances.

3 Basic Boundary Value Problems; Stresses

To facilitate further discussion of the basic boundary value problems (13), (14) and (21), (22), it is convenient to use the notation

$$a_{\alpha\beta} \equiv C_{3\beta 3\alpha}, \tag{23}$$

where by virtue of the third symmetry in (4) we have

$$a_{\alpha\beta} = a_{\beta\alpha}. \tag{24}$$

Then (13), (14) may be written as

$$a_{\alpha\beta} u_{,\alpha\beta} = 0 \text{ on } D, \tag{25}$$

$$a_{\alpha\beta} u_{,\alpha} n_\beta = t_3^* \text{ on } \partial D, \tag{26}$$

while (21), (22) become

$$(a_{\alpha\beta} u_{,\alpha})_{,\beta} = 0 \text{ on } D, \tag{27}$$

$$a_{\alpha\beta} u_{,\alpha} n_\beta = t_3^* \text{ on } \partial D. \tag{28}$$

These are the standard oblique-derivative boundary value problems for second-order partial differential equations. We will assume that the differential Eqs. (25) and (27) are *elliptic*, as expected in modeling equilibrium problems. To ensure this, it is sufficient to assume that

$$a_{11} > 0, \ a_{11}a_{22} - a_{12}^2 \equiv A^2 > 0, \tag{29}$$

where, in the variable coefficient case, (29) is understood to hold at all (x_1, x_2) in D. With the hypotheses (29), standard

Downloaded 03 May 2010 to 171.66.16.20. Redistribution subject to ASME license or copyright; see http://www.asme.org/terms/Terms_Use.cfm

arguments show that solutions to the above boundary value problems are unique to within a constant (corresponding to a rigid-body translation). The assumptions (29) may be written directly in terms of components of **C**, on using (23), but we shall not make use of this version of (29) in this paper.

The stresses arising due to an antiplane shear may be found from (6), (18), (20). Thus we find that

$$T_{\alpha\beta}=0,\ T_{3\alpha}=C_{3\alpha 3\beta}u_{,\beta}\equiv a_{\alpha\beta}u_{,\beta}, \tag{30}$$

$$T_{33}=C_{333\alpha}u_{,\alpha}, \tag{31}$$

for the inhomogeneous case. For the homogeneous material, the stresses are also given by (30), (31) with the **C** (and thus $a_{\alpha\beta}$) being constant. The appearance of a *normal axial stress component* T_{33} in (31) is noteworthy. Such a normal stress also arises in the *nonlinear* theory for *isotropic* materials (see, e.g., the references cited in the second paragraph of the Introduction). As we shall discuss in the next section the normal stress arising here is strictly an *anisotropic* effect.

4 Isotropic Materials; Symmetry Classes

It is of interest to consider the simplifications that occur in the preceding when specific elastic symmetries are assumed. In particular, we begin with the reduction to isotropy. When the material is *isotropic*, we have

$$C_{ijkl}(\mathbf{x})=\lambda(\mathbf{x})\delta_{ij}\delta_{kl}+\mu(\mathbf{x})(\delta_{ik}\delta_{jl}+\delta_{il}\delta_{kj}), \tag{32}$$

where $\lambda(\mathbf{x})$, $\mu(\mathbf{x})$ are the Lame coefficients and δ_{ij} is the Kronecker delta. First we consider the homogeneous isotropic material where λ and μ are constants. When **C** is given by (32), it is readily verified that (12) is satisfied so that antiplane shear *is always possible* for *any homogeneous isotropic material*. The boundary value problem (13), (14) in this case reduces to

$$\mu u_{,\alpha\alpha}=0 \text{ on } D, \tag{33}$$

$$\mu\partial u/\partial n=t_3^* \text{ on } \partial D, \tag{34}$$

where $\partial u/\partial n$ denotes the normal derivative of u. Thus, for $\mu \neq 0$, (33), (34) is simply the Neumann problem for Laplace's equation. Of course, these results for the isotropic material are well known. In this case, the stresses given by (30), (31) reduce to

$$T_{\alpha\beta}=0,\ T_{3\alpha}=\mu u_{,\alpha},\ T_{33}=0. \tag{35}$$

Thus there is no axial normal stress in the isotropic case. For the *inhomogeneous* isotropic material, (32) and (18) imply that

$$\lambda(\mathbf{x})=\lambda(x_1, x_2),\ \mu(\mathbf{x})=\mu(x_1, x_2). \tag{36}$$

The condition (20) is seen to be satisfied so that again antiplane shear is *always possible* and u is to satisfy

$$\left.\begin{aligned}[\mu(x_1, x_2)u_{,\alpha}]_{,\alpha}=0 \text{ on } D,\\ \mu(x_1, x_2)\partial u/\partial n=t_3^*(x_1, x_2) \text{ on } \partial D.\end{aligned}\right\} \tag{37}$$

This is a Neumann problem for the second-order partial differential Eq. $(37)_1$. The stresses are still given by (35) with $\mu = \mu(x_1, x_2)$.

To facilitate the investigation of other elastic symmetries, it is convenient now to adopt the usual notation of linear anisotropic elasticity with single index notation for stress and strain:

$$\left.\begin{aligned}T_{11}=T_1,\ T_{22}=T_2,\ T_{33}=T_3,\ T_{23}=T_4,\ T_{31}=T_5,\ T_{12}=T_6,\\ E_{11}=E_1,\ E_{22}=E_2,\ E_{33}=E_3,\ 2E_{23}=E_4,\ 2E_{31}=E_5,\ 2E_{12}=E_6.\end{aligned}\right\} \tag{38}$$

Thus (3) can be written as

$$T_p=c_{pq}E_q(p, q=1, 2, \cdots 6), \tag{39}$$

where the 6×6 matrix with components c_{pq} represent the components of C_{ijkl}. By virtue of the third symmetry in (4), the matrix **c** is symmetric so that

$$c_{pq}=c_{qp}, \tag{40}$$

and there are at most 21 independent components of **c**.

We begin with the homogeneous case where c_{pq} are constants. The necessary and sufficient condition (12) for antiplane shear to be possible in the general anisotropic solid can be written in terms of the c_{pq} as

$$c_{14}=0,\ c_{15}=0,\ c_{24}=0,\ c_{25}=0,\ c_{46}=0,\ c_{56}=0, \tag{41}$$

so that there are at most 15 independent constants in **c**. The resulting boundary value problem (13), (14) can now be written as

$$c_{55}u_{,11}+2c_{45}u_{,12}+c_{44}u_{,22}=0 \text{ on } D, \tag{42}$$

$$c_{55}u_{,1}n_1+c_{45}(u_{,1}n_2+u_{,2}n_1)+c_{44}u_{,2}n_2=t_3^* \text{ on } \partial D. \tag{43}$$

Of course (42), (43) is merely (25), (26) again, now rewritten in the usual elasticity notation. In terms of the c_{pq}, the conditions (29) ensuring ellipticity of (42) are

$$c_{55}>0,\ c_{55}c_{44}-c_{45}^2\equiv A^2>0. \tag{44}$$

The corresponding stresses follow from (30), (31) as

$$\left.\begin{aligned}T_{\alpha\beta}=0,\ T_{32}\equiv T_4=c_{45}u_{,1}+c_{44}u_{,2},\\ T_{31}\equiv T_5=c_{55}u_{,1}+c_{45}u_{,2}\end{aligned}\right\} \tag{45}$$

and

$$T_{33}\equiv T_3=c_{35}u_{,1}+c_{34}u_{,2}, \tag{46}$$

respectively. It is of interest to note that the *shear stresses* $T_{3\alpha}$ ($\alpha = 1, 2$) depend only on the three constants c_{44}, c_{45}, and c_{55} (and thus the differential Eq. (42) and boundary condition(43) involve only these three constants) while the *axial normal stress* T_{33} also depends on two additional different constants, namely c_{34} and c_{35}. Thus, of the 15 constants present in **c**, only 5 of these play a role in the antiplane shear problem.

It is convenient now to express **c**, with (41) taken into account, in matrix form as

$$\mathbf{c}=\begin{pmatrix} c_{11} & c_{12} & c_{13} & 0 & 0 & c_{16}\\ c_{21} & c_{22} & c_{23} & 0 & 0 & c_{26}\\ c_{31} & c_{32} & c_{33} & c_{34} & c_{35} & c_{36}\\ 0 & 0 & c_{43} & c_{44} & c_{45} & 0\\ 0 & 0 & c_{53} & c_{54} & c_{55} & 0\\ c_{61} & c_{62} & c_{63} & 0 & 0 & c_{66}\end{pmatrix}. \tag{47}$$

The 3 constants arising in (42),(43), (45) appear in the 2×2 submatrix indicated by the dashed rectangle in (47), while the other two constants arising in the normal stress (46) appear in ovals in (47). The normal stress T_{33} arising here is clearly due to *anisotropy*, in contrast to the situation in *finite antiplane shear* for an isotropic material where such a stress arises due to *nonlinearity*. Alternatively, one could interpret the T_{33} as playing a role somewhat analogous to that of the axial normal stress arising in *plane strain* for linear *isotropic* materials. Thus, from (45), (46), T_{33} may be expressed directly in terms of the shear stresses as

$$T_{33}=A^{-2}[(c_{35}c_{44}-c_{34}c_{45})T_{31}+(c_{34}c_{55}-c_{35}c_{45})T_{32}], \tag{48}$$

where $A > 0$ is defined in (44).

Returning to (47), *representing the most general anisotropic symmetry for which antiplane shear is possible, subject to the boundary conditions* (*1*) it can be verified that **c** does not describe a particular elastic symmetry class among the standard ten distinct elastic symmetries (see, e.g., Cowin and Mehrabadi (1987) and Cowin (1989) for a clear discussion of the latter). However, several of these classes are subclasses of the **c** in (47). For example, a material with the x_1, x_2 plane a plane of elastic symmetry (monoclinic system, 13 constants) is described by (47) if

Downloaded 03 May 2010 to 171.66.16.20. Redistribution subject to ASME license or copyright; see http://www.asme.org/terms/Terms_Use.cfm

$$c_{34}=0,\ c_{35}=0. \tag{49}$$

These are precisely the two constants appearing explicitly in the normal stress (46). Thus, *antiplane shear* (*with zero normal stress* T_{33}) is *always possible* for the cylinder with x_1, x_2 plane a plane of elastic symmetry. The boundary value problem for the out-of-plane displacement u is given by (42), (43) and the resulting stresses by (45).

While this paper is concerned solely with the antiplane shear deformation (2), we digress briefly here to make some remarks on the complementary *plane strain* deformation $u_\alpha = u_\alpha(x_1, x_2)$, $u_3 = 0$ arising due to nonzero tractions $t^*_\alpha(x_1, x_2)$ on the lateral boundary of the cylinder. It is well known (see, e.g., Lekhnitskii (1981)) that an *arbitrary anisotropic* elastic cylinder, subjected to such surface tractions, will not sustain a state of pure plane strain. The deformation, with $u_i = u_i(x_1, x_2)$ $(i = 1, 2, 3)$, is called a generalized plane deformation (Lekhnitskii (1981)) and the inplane displacements u_1, u_2 are *coupled* with the out-of-plane displacement u_3. Such deformations have been investigated by Lekhnitskii (1981) and independently by Eshelby et al. (1953) and Stroh (1958). The Stroh formulation has been the subject of much recent attention (see, e.g., Ting and Chou (1981), Hwu and Ting (1989), Suo (1990) and the references cited therein). It is observed in most of the above references and elsewhere that, for the cylinder with the x_1, x_2 plane a plane of elastic symmetry, *pure plane strain* is possible and that the inplane displacements u_α are *uncoupled* from the out-of-plane displacement u_3. *It is worth observing, however, that this is also the case when* $\mathbf{c}$ *has the more general form* (47). (For the pure plane strain deformation, the nonzero constants c_{34}, c_{35} in (47) do *not appear explicitly* since $E_q \equiv 0$ $(q = 3, 4, 5)$.)

Returning to (47), (49) we see that further specialization of (47), (49) leads to other standard symmetries for which antiplane shear (with $T_{33} = 0$) is always possible. Thus if, in addition to (49), we set

$$c_{16}=0,\ c_{26}=0,\ c_{36}=0,\ c_{45}=0 \tag{50}$$

in (47), we obtain an *orthotropic* material (with nine independent elastic constants). In this case, a major simplification occurs since the mixed derivative term in (42) vanishes and (42), (43) read

$$c_{55}u_{,11}+c_{44}u_{,22}=0 \text{ on } D, \tag{51}$$

$$c_{55}u_{,1}n_1+c_{44}u_{,2}n_2=t^*_3 \text{ on } \partial D. \tag{52}$$

A simple rescaling can be used to reduce (51), (52) to a Neumann problem for Laplace's equation (on a scaled domain) as found in the isotropic case. For the orthotropic material, the stresses (45) simplify to

$$T_{32}=c_{44}u_{,2},\ T_{31}=c_{55}u_{,1}. \tag{53}$$

Thus, for the orthotropic material,only *two* elastic constants play a role in the antiplane shear problem.

When the material is *inhomogeneous*, so that $\mathbf{c} = \mathbf{c}(x_1, x_2)$ (c.f. (18)), the considerations just carried out for constant $\mathbf{c}$ carry over with obvious modification. The differential Eq. (27) now reads

$$[c_{55}u_{,1}+c_{45}u_{,2}]_{,1}+[c_{45}u_{,1}+c_{44}u_{,2}]_{,2}=0 \text{ on } D, \tag{54}$$

while the boundary condition is still given by (43) with $\mathbf{c} = \mathbf{c}(x_1, x_2)$. The stresses are still given by (45), (46) with $\mathbf{c} = \mathbf{c}(x_1, x_2)$.

5 Transformation to an Equivalent Isotropic Problem

In this section, we confine attention to *homogeneous* materials so that $\mathbf{c}$ is constant and the governing differential equation is given by (42). It turns out that (42) also arises in a completely different context in linear anisotropic elasticity, namely, that of *torsion* of a cylinder (with cross-section D) due to end moments only (see, e.g., Sokolnikoff (1956), Section 51 or Lekhnitskii (1981), Section 51). In this context, u is proportional to the *warping function*. In the torsion problem, the stresses of interest are still T_{31}, T_{32} and are given in terms of the warping function by relations of the form (45) which, however,contain *additive* terms linear in x_1 and x_2. As a consequence,the *traction-free* boundary conditions in the torsion problem, while containing terms of the form of those on the left in (43), are of a different character from (43) since they also involve the coordinates x_1 and x_2 explicitly. Nevertheless, it is possible to make use of some techniques developed for the torsion problem to investigate the antiplane shear problem (42), (43). In particular, a variety of coordinate transformations have been used, in the context of torsion, to convert the differential Eq. (42) to Laplace's equation on a transformed domain $\mathfrak{D}$ (see, e.g., the texts cited above).

In what follows, we describe one such transformation which converts the problem (42), (43) to a Neumann problem for Laplace's equation on $\mathfrak{D}$. We define new coordinates x, y through the transformation

$$x=\frac{x_1}{c_{55}},\ y=\frac{1}{A}\left(x_2-\frac{c_{45}}{c_{55}}x_1\right), \tag{55}$$

where the positive constant A, defined in (44), is

$$A=\sqrt{c_{44}c_{55}-c_{45}^2}. \tag{56}$$

Writing

$$u(x_1, x_2)=u(x, y), \tag{57}$$

it is readily verified that the differential Eq. (42) is transformed to

$$\nabla^2 u \equiv u_{,xx}+u_{,yy}=0 \text{ on } \mathfrak{D}, \tag{58}$$

where $\mathfrak{D}$ denotes the transformation of the domain D under (55). It should be remarked that (55) is not the only transformation which converts (42) to Laplace's equation. Clearly any multiple of the right-hand sides of (55) by the same constant will also be admissible; the primary change of variable can also be carried out by x rather than by y as in (55). Turning now to the boundary conditions, we assume that the boundary ∂D of D can be expressed as $\phi(x_1,x_2) = 0$ so that the unit outward normal $\mathbf{n}$ on ∂D has components

$$n_\alpha=\phi_{,\alpha}/|\nabla\phi| \text{ on } \partial D. \tag{59}$$

Then, if the boundary of $\partial\mathfrak{D}$ is written as $\Phi(x, y) = 0$ so that the unit outward normal $\mathbf{N}$ on $\partial\mathfrak{D}$ has components

$$N_x=\Phi_{,x}/|\nabla\Phi|,\ N_y=\Phi_{,y}/|\nabla\Phi|, \tag{60}$$

it can be verified that the boundary condition (43) transforms to

$$\frac{\partial u}{\partial N}=t^*_3(x,y)F(x, y) \text{ on } \partial\mathfrak{D}, \tag{61}$$

where

$$F^2(x, y)=\left[\Phi_{,x}^2-\frac{2c_{45}}{A}\Phi_{,x}\Phi_{,y}+\frac{(c_{45}^2+c_{55}^2)}{A^2}\Phi_{,y}^2\right]/(\Phi_{,x}^2+\Phi_{,y}^2). \tag{62}$$

The boundary value problem (58), (61) constitutes a Neumann problem for Laplace's equation on $\mathfrak{D}$. Thus the variety of solution techniques available for the Neumann problem can be applied to (58), (61). We observe that the elastic constants now appear only on the right in the boundary condition (61), by virtue of (62), as well as in the transformation (55). This should facilitate the analysis of the dependence of solution of the antiplane shear problem on the material parameters. As pointed out in Sokolnikoff (1956), (55) transforms elliptical domains to elliptical domains and rectangles into parallelograms. We shall not pursue this further here; however, in the next section, we describe the use of a transformation of the form (55) for entirely different purposes.

Downloaded 03 May 2010 to 171.66.16.20. Redistribution subject to ASME license or copyright; see http://www.asme.org/terms/Terms_Use.cfm

6 Influence of Anisotropy and Inhomogeneity on the Decay of Saint-Venant End Effects

Considerable progress has been made in recent years in understanding the effects of anisotropy on the decay of stresses with distance from boundaries subjected to self-equilibrating loads as arises in analysis of Saint-Venant's principle (see, e.g., Horgan and Knowles (1983) and Horgan (1989) for recent reviews; see also Horgan and Simmonds (1991), Crafter et al. (1993), and Wang et al. (1993)). In particular, for highly anisotropic materials (or fiber-reinforced composites), it is now well known that very *slow* decay rates can occur with end effects being transmitted considerable distances from the loaded ends (see, e.g., Horgan (1982) and Horgan and Simmonds (1994) for a thorough discussion of such extended end effects). Most of the work described in the above references concerns the plane or axisymmetric problems, for homogeneous (or piecewise homogeneous) materials. In this section, we describe briefly how corresponding results for the antiplane shear problem may be obtained in a much simpler way. We also discuss results on the influence of *inhomogeneity* which have, as yet, no known counterparts for the plane or axisymmetric problems.

We begin with the *homogeneous* material and return to the basic boundary value problem (25), (26). The cross-sectional domain D is now taken to be the interior of the semi-infinite strip

$$D=\{(x_1, x_2)/x_1>0, 0<x_2<h\}, \tag{63}$$

and the prescribed traction t_3^* is taken to be zero everywhere on the boundary except on the end $x_1 = 0$ where it is necessarily self-equilibrated. The usual *energy method* (see, e.g., Horgan and Knowles (1983) and Horgan (1989)) for deriving a Saint-Venant type decay estimate for finite energy solutions of (25) involves a function $E(z)$ defined by

$$E(z)=\int_z^\infty \int_0^h a_{\alpha\beta}u_{,\alpha}u_{,\beta}dA,\ z\geq x_1>0. \tag{64}$$

This function can be shown to satisfy a first-order differential inequality whose solution furnishes an explicit decay estimate for $E(z)$, showing in particular for *constant* $a_{\alpha\beta}$ that $E(z)$ must decay *exponentially*. However, in contrast to the situation for Laplace's equation, for example, a direct application of this method (as given by Mieth (1975)) does *not* yield the *optimal* decay rate. The latter may be readily obtained by a separation of variables technique. In a recent paper (Horgan and Payne, 1993) it has been shown that a preliminary change of variables of the form

$$\xi=A^{-1}[a_{22}x_1-a_{12}x_2],\ \eta=x_2, \tag{65}$$

(which is a variation of the transformation (55)) *does* allow one to use the energy method to obtain the optimal energy decay rate so that one finds that solutions of (25), (26) decay in energy norm at least as fast as $\exp(-2kx_1)$, as $x_1 \to \infty$, with estimated decay rate k given by

$$k=\pi a_{22}/h(a_{11}a_{22}-a_{12}^2)^{1/2}. \tag{66}$$

The decay rate (66) is *optimal* in the sense that the exact solution decays as $\exp(-kx_1)$ with k given by (66). The stresses, given by (30), (31), also decay as $\exp(-kx_1)$. Converting (66) to the elasticity notation introduced in Section 4, we have

$$k=\frac{\pi c_{44}}{h(c_{44}c_{55}-c_{45}^2)^{1/2}}, \tag{67}$$

which is the estimated (and exact) decay rate for the most general material (described by (47)) allowing antiplane shear. When $c_{45} = 0$ (such as for an orthotropic material), (67) simplifies to

$$k=\frac{\pi}{h}\left(\frac{c_{44}}{c_{55}}\right)^{1/2}, \tag{68}$$

while the isotropic case can be found on letting $c_{44} = c_{55} (=\mu)$ in (68) so that

$$k=\frac{\pi}{h}, \tag{69}$$

which is the well-known exact decay rate for harmonic functions on the semi-infinite strip D.

Suppose now that the material described by (47) is *highly anisotropic* so that

$$c_{44}\ll c_{55}. \tag{70}$$

This may be viewed as modeling the case of a fiber-reinforced material with fibers parallel to the x_1-axis. Introducing the dimensionless quantity ϵ by

$$\epsilon=\frac{c_{44}}{c_{55}},\ (\epsilon\ll 1), \tag{71}$$

and expanding the right-hand side of (67) in a Taylor expansion (for small ϵ), we find that

$$k\sim\frac{\pi}{h}\epsilon^{1/2}\ \text{as}\ \epsilon\to 0, \tag{72}$$

thus predicting a *very slow* decay rate in this limit. The characteristic *decay length* (the distance over which the stress (at fixed height x_2) decays to one percent of its value at $x_1 = 0$) is then given by

$$\lambda=\frac{(\ln 100)}{k}=\frac{4.6}{k}\sim\frac{4.6}{\pi}h\epsilon^{-1/2}\ \text{as}\ \epsilon\to 0, \tag{73}$$

which is *large* compared with the strip width. The asymptotic estimates (72), (73), which are obtained directly here from the explicit result (67), have counterparts in the plane strain case. Their derivations in this case (see, e.g., Choi and Horgan (1977), Horgan (1982)) are much more complicated than the relatively simple arguments outlined here.

We turn now to the *inhomogeneous* material, with governing boundary value problem given by (27), (28), again take D to be the semi-infinite strip (63) and summarize briefly some recent results obtained by Horgan and Payne (1993) on the influence of *inhomogeneity* on the decay of Saint-Venant end effects. Very little is known about this issue outside the present context. Using a generalization of the transformation (65), Horgan and Payne (1993) established an energy decay estimate for solutions of (27), (28) (or equivalently (54), (43)) which yields a characterization for the *estimated decay rate* (a lower bound for the exact decay rate) in terms of the coefficients $a_{\alpha\beta}$ (x_1, x_2). A variety of examples were provided by Horgan and Payne (1993) illustrating various aspects of their main result. Some of these will now be described.

To begin with, suppose that the $a_{\alpha\beta}$ (suitably nondimensionalized) are given by

$$a_{11}\equiv c_{55}=1+\frac{x_1}{h},\ a_{12}\equiv c_{45}=1/2,\ a_{22}\equiv c_{44}=1+\frac{x_2^2}{h^2}. \tag{74}$$

Then solutions of (27), (28) (or equivalently (54), (43)) decay in energy norm at least as fast as

$$\exp\left(\frac{-k_1x_1^{1/2}}{h^{1/2}}\right),\ k_1=8\sqrt{2}, \tag{75}$$

as $x_1 \to \infty$. We observe that the power of x_1 in the decaying exponential is ½ instead of 1, as in the homogeneous case. A second example is a modification of (74) where a_{11} has quadratic growth in x_1 so that

$$a_{11}\equiv c_{55}=1+\frac{x_1^2}{h^2},\ a_{12}\equiv c_{45}=1/2,\ a_{22}\equiv c_{44}=1+\frac{x_2^2}{h^2}. \tag{76}$$

Then, it is shown by Horgan and Payne (1993) that solutions now decay in energy norm at least *polynomially* as

Downloaded 03 May 2010 to 171.66.16.20. Redistribution subject to ASME license or copyright; see http://www.asme.org/terms/Terms_Use.cfm

$$\left(\frac{x_1}{h}\right)^{-k_1/2} \quad \text{as } x_1 \to \infty, \tag{77}$$

where k_1 is given by (75).

In the next example, a_{12} and a_{22} are taken to be constant and $a_{11} = a_{11}(x_1)$ has polynomial growth. Thus let

$$a_{11} \equiv c_{55} = 2 + \left(\frac{x_1}{h}\right)^{\alpha}, \; a_{12} \equiv c_{45} = -1, \; a_{22} \equiv c_{44} = 1, \tag{78}$$

where α is a positive constant. It is shown by Horgan and Payne (1993) that if $\alpha > 2$ there may not be any solution of (27), (28) which decays to zero in energy norm as $x_1 \to \infty$, for $\alpha < 2$ all decaying solutions decay at least *exponentially* in energy norm at least as fast as

$$\exp\left\{-2\pi\left(\frac{x_1}{h}\right)^{(1-\alpha/2)}/(1-\alpha/2)\right\} \text{ as } x_1 \to \infty, \tag{79}$$

while if $\alpha = 2$ all decaying solutions decay at least *polynomially* in energy norm at least as fast as

$$\left[\frac{\left(1+\frac{x_1^2}{h^2}\right)^{1/2}+\frac{x_1}{h}}{1+\sqrt{2}}\right]^{-2\pi} \quad \text{as } x_1 \to \infty. \tag{80}$$

This result for $\alpha = 2$ is consistent with that for (76) where the x_1-dependence of a_{11} was also quadratic.

Finally, we describe an example for which the decay in energy norm is *faster* than $\exp(-\gamma x_1)$ for any positive γ. Thus let

$$a_{11} \equiv c_{55} = 1, \; a_{12} \equiv c_{45} = \left(1+\frac{x_1}{h}\right)/2, \; a_{22} \equiv c_{44} = \left(1+\frac{x_1}{h}\right)^2. \tag{81}$$

Then, it is shown by Horgan and Payne (1993) that the energy decay as $x_1 \to \infty$ is at least as fast as

$$\exp\left(-\beta\frac{x_1^2}{h^2}\right), \; \beta = 2\sqrt{3}\,\pi/3. \tag{82}$$

It is clear from the foregoing examples that the precise form of material inhomogeneity has a significant influence on the decay character of Saint-Venant end effects in antiplane shear. The results also suggest the interesting possibility of "tailoring" the material to produce a desired decay character. It remains to be seen whether comparable results can be obtained in the plane problem.

Acknowledgments

This research was supported by the U.S. National Science Foundation under Grant No. MSS-91-02155 and by the U.S. Army Research Office under Grant DAAL03-91-G-0022. The research of K. L. Miller was also supported by a National Defense Science and Engineering Graduate Fellowship (NDSEGF) sponsored by the U.S. Air Force, an Amelia Earhart Fellowship sponsored by the Zonta International Foundation and a Virginia Space Grant Consortium Graduate Fellowship. We are grateful to the reviewers for their constructive comments on an earlier version of the manuscript.

References

Abeyaratne, R., and Horgan, C. O., 1983, "Bounds on Stress Concentration Factors in Finite Antiplane Shear," *J. Elasticity*, Vol. 13, pp. 49–61.

Choi, I., and Horgan, C. O., 1977, "Saint-Venant's Principle and End Effects in Anisotropic Elasticity," ASME JOURNAL OF APPLIED MECHANICS, Vol. 44, pp. 424–430.

Cowin, S. C., 1989, "Properties of the Anisotropic Elasticity Tensor," *Quart. J. Mech. Appl. Math.*, Vol. 42, pp. 249–266.

Cowin, S. C., and Mehrabadi, M. M., 1987, "On the Identification of Material Symmetry for Anisotropic Elastic Materials," *Quart. J. Mech. Appl. Math.*, Vol. 40, pp. 451–476.

Crafter, E. C., Heise, R. M., Horgan, C. O., and Simmonds, J. G., 1993, "The Eigenvalues for a Self-equilibrated, Semi-infinite, Anisotropic Elastic Strip," ASME JOURNAL OF APPLIED MECHANICS, Vol. 60, pp. 276–281.

Eshelby, J. D., Read, W. T., and Shockley, W., 1953, "Anisotropic Elasticity with Applications to Dislocation Theory," *Acta Mat.*, Vol. 1, pp. 251–259.

Horgan, C. O., 1982, "Saint-Venant End Effects in Composites," *J. Composite Materials*, Vol. 16, pp. 411–422.

Horgan, C. O., 1989, "Recent Developments Concerning Saint-Venant's Principle: An Update," ASME *Applied Mechanics Reviews*, Vol. 42, pp. 295–303.

Horgan, C. O., and Knowles, J. K., 1983, "Recent Developments Concerning Saint-Venant's Principle," *Advances in Applied Mechanics*, ed, J. W. Hutchinson, Academic Press, New York, Vol. 23, pp. 179–269.

Horgan, C. O., and Payne, L. E., 1993, "On the Asymptotic Behavior of Solutions of Linear Second-Order Boundary-Value Problems on a Semi-Infinite Strip," *Arch. Rational Mech. Anal.*, Vol. 124, pp. 277–303.

Horgan, C. O., and Silling, S. A., 1987, "Stress Concentration Factors in Finite Anti-Plane Shear: Numerical Calculations and Analytical Estimates," *J. Elasticity*, Vol. 18, pp. 83–91.

Horgan, C. O., and Simmonds, J. G., 1991, "Asymptotic Analysis of an End Loaded, Transversely Isotropic, Elastic, Semi-infinite Strip Weak in Shear," *Int. J. Solids Structures*, Vol. 27, pp. 1895–1914.

Horgan, C. O., and Simmonds, J. G., 1994, "Saint-Venant End Effects in Composite Structures," *Composities Engineering*, Vol. 3 (in press).

Hwu, C., and Ting, T. C. T., 1989, "Two-dimensional Problems of the Anisotropic Elastic Solid with an Elliptic Inclusion," *Quart. J. Mech. Appl. Math.*, Vol. 42, pp. 553–572.

Hwu, C., and Ting, T. C. T., 1989, "Two-dimensional Problems of the Anisotropic Elastic Solid with an Elliptic Inclusion," *Quart. J. Mech. Appl. Math.*, Vol. 42, pp. 553–572.

Jafari, A. H., Horgan, C. O., and Abeyaratne, R., 1984, "Finite Anti-plane Shear of an Infinite Slab with a Traction-free Elliptical Cavity: Bounds on the Stress Concentration Factor," *Int. J. Nonlinear Mechanics*, Vol. 19, pp. 431–443.

Jiang, Q., and Knowles, J. K., 1991, "A Class of Compressible Elastic Materials Capable of Sustaining Finite Anti-plane Shear," *J. Elasticity*, Vol. 25, pp. 193–201.

Knowles, J. K., 1976, "On Finite Anti-plane Shear for Incompressible Elastic Materials," *J. Austral. Math. Soc.*, Vol. 19 (Series B), pp. 400–415.

Knowles, J. K., 1977a, "A Note on Anti-plane Shear for Compressible Materials in Finite Elastostatics," *J. Austral. Math. Soc.*, Vol. 20 (Series B), pp. 1–7.

Knowles, J. K., 1977b, "The Finite Anti-plane Shear Field Near the Tip of a Crack for a Class of Incompressible Elastic Solids," *Int. J. of Fracture*, Vol. 13, pp. 611–639.

Lekhnitskii, S. G., 1981, *Theory of Elasticity of an Anisotropic Body*, Mir Publishers, Moscow.

Mieth, H.-J., 1975, "Uber Abklingende Losungen Elliptischer Randwertprobleme (Prinzip von Saint-Venant)," Dissertation, Technische Hochschule Darmstadt.

Polignone, D. A., and Horgan, C. O., 1992, "Axisymmetric Finite Anti-plane Shear of Compressible Nonlinearly Elastic Circular Tubes," *Quart. Appl. Math.*, Vol. 50, pp. 323–341.

Schovanec, L., 1989, "An Antiplane Shear Crack in a Nonhomogeneous Elastic Material," *Engineering Fracture Mechanics*, Vol. 32, pp. 21–28.

Sokolnikoff, I. S., 1956, *Mathematical Theory of Elasticity*, McGraw-Hill, New York.

Stroh, A. N., 1958, "Dislocations and Cracks in Anisotropic Elasticity," *Phil. Mag.*, Vol. 3, pp. 625–646.

Suo, Z., 1990, "Singularities, Interfaces and Cracks in Dissimilar Anisotropic Media," *Proc. R. Soc. Lond.*, Vol. A427, pp. 331–358.

Ting, T. C. T., and Chou, S. C., 1981, "Edge Singularities in Anisotropic Composites," *Int. J. Solids Structures*, Vol. 17, pp. 1057–1068.

Wang, M. Z., Ting, T. C. T., and Yan, G., 1993, "The Anisotropic Elastic Semi-infinite Strip," *Quart. Appl. Math.*, Vol. 51, pp. 283–297.

Downloaded 03 May 2010 to 171.66.16.20. Redistribution subject to ASME license or copyright; see http://www.asme.org/terms/Terms_Use.cfm

Yun Ling
Development Engineer,
Contact Physics Research,
Harrisburg, PA 17105-3608
Mem. ASME

P. A. Engel
Professor,
Department of Mechanical and
Industrial Engineering,
Fellow ASME.

J. A. Geer
Professor,
Department of System Science.

State University of New York
at Binghamton,
Binghamton, NY 13902-6000

The End Problem of Incompressible Elastic Cylinders

The end problem of incompressible elastic cylinders is formulated and is solved by an eigenfunction expansion method. Various methods for the determination of the unknown coefficients of the expansion are studied and a variational approach which minimizes the total potential energy is suggested. A transformation is introduced for a better calculation of the stiffness of a cylinder. The Benthem and Minderhoud (1972) expansion is used to describe the interfacial stress distributions. The difficulties of using this expansion for thin cylinders are overcome by utilizing the Cesaro sum (Powell and Shah, 1972). Numerical results for the compression of bonded rubber cylinders are presented and discussed.

1 Introduction

The end problem of an elastic cylinder has been studied by numerous authors (e.g., Little and Childs, 1967; Benthem and Minderhould, 1972; Robert and Keer, 1987; Kim and Steele, 1992). Some authors (e.g., Horvay and Mirabal, 1958) have realized that the results derived for a compressible material can be applied to an incompressible one by letting the Poisson's ratio $\nu \to 0.5$. But no one has so far formulated the problem for an incompressible material separately. Since interested only in the incompressible case, we shall formulate the problem separately in Section 2, in which the operation involving the denominator $1-2\nu$ is avoided.

The problem is then solved by an eigenexpansion method in Section 3, leaving the unknown coefficients, called participating factors, to be determined by the prescribed end conditions. Little and Childs (1967) have constructed a biorthogonal relation for the determination of the participating factors. The biorthogonal relationship led to an infinite set of linear algebraic equations. Gerhardt and Cheng (1981) have shown that these equations are generally ill conditioned, and thus developed the diagonally dominant method so that the linear system of equations would converge numerically. However, both the biorthogonal method and the diagonally dominant method are derived based on mathematical manipulations and lack physical interpretations. In practice, a series solution has to be truncated somewhere. For a given number of eigenvalues, it is more meaningful to determine the participating factors such that the end conditions be satisfied "as well as possible." Thus, in Section 4 we develop a variational method in which the participating factors are chosen such that the total potential energy is a minimum. The least-square method is also suggested and a comparison among the various methods is given.

It is well known that for a displacement problem, in which end displacements are prescribed, there is usually a singularity at the corner of a cylinder. This singularity causes the expansions of the displacements and stresses at the plane ends to converge slowly. The problem involving singularities has been studied by Benthem and Minderhoud (1972), Robert and Keer (1987), and Kim and Steele (1992), based on the eigenexpansion approach. Their basic idea is to extract the singularity such that the remaining series converges faster. An alternative approach, the singularity integral equation method, has been suggested by Gupta (1974). But it appeared to involve substantial numerical work, as pointed out by Kim and Steele (1992). A novel method was developed by Gregory and Wan (1984) to deal with the singularity. Its applications are, however, limited to the case where the St. Venant's principle or the reciprocity theorem applies. In Section 5, we first introduce a simple transformation, basically an integral operation, to improve the calculation of the compression stiffness of a cylinder, this idea is inspired by Spence's work (1983) on the problem of an infinite strip. We then use the Benthem and Minderhoud (1972) expansion, together with the Cesaro sum (Powell and Shah, 1972) (if necessary), to describe the interfacial stresses.

This study is motivated by the calculation of the stiffness and stress distributions of axially compressed bonded rubber

Contributed by the Applied Mechanics Division of THE AMERICAN SOCIETY OF MECHANICAL ENGINEERS for presentation at the ASME Winter Annual Meeting, New Orleans, LA, Nov. 28–Dec. 3, 1993.

Discussion on this paper should be addressed to the Technical Editor, Professor Lewis T. Wheeler, Department of Mechanical Engineering, University of Houston, Houston, TX 77204-4792, and will be accepted until four months after final publication of the paper itself in the ASME JOURNAL OF APPLIED MECHANICS.

Manuscript received by the ASME Applied Mechanics Division, Aug. 3, 1992; final revision, Mar. 4, 1993. Associate Technical Editor: F. Y. M. Wan.

Paper No. 93-WA/APM-21.

Copyright © 1994 by ASME
Downloaded 03 May 2010 to 171.66.16.20. Redistribution subject to ASME license or copyright; see http://www.asme.org/terms/Terms_Use.cfm

cylinders, which have a wide application as springs in anti-vibration mountings (Lindley, 1966). Although many approximate analyses and experimental studies on the compression of bonded rubber cylinders existed in the literature (e.g., Gent et al., 1959, 1974; Beatty, 1977; Ling et al., 1992), a rigorous solution has never been given. Thus in Section 6, numerical results on the compression of bonded rubber cylinders are presented.

2 Mathematical Formulation

Using the cylindrical coordinated system (r', θ', z'), consider a cylinder occupying the region $0 \le r' \le R'$ and $-L' \le z' \le +L'$, where R' is the radius and $2L'$ is the height of the cylinder. The problem is restricted to the axisymmetrical case without torsion. Let σ_r', σ_θ', σ_z' be the normal stresses, $\tau' = \tau_{rz}'$ the nonzero shear stress, and u' and w' the displacements in the radial and z'-directions, respectively. Nondimensional quantities will be used, defined as

$$r = \frac{r'}{R'}, \quad z = \frac{z'}{R'}, \quad u = \frac{u'}{R'}, \quad w = \frac{w'}{R'},$$

$$L = \frac{L'}{R'}, \quad \sigma_r = \frac{\sigma_r'}{2G}, \quad \tau = \frac{\tau'}{2G}, \text{ etc.} \tag{1}$$

where G' is the shear modulus and L is the height-to-diameter ratio.

We consider a finite cylinder under a deformation symmetrical about the $z = 0$ plane, with prescribed end displacements. Thus the boundary conditions can be written as

$$z = L, \ 0 \le r \le 1: \ u = u_b, \quad w = w_b, \tag{2}$$

$$z = 0, \ \ 0 \le r \le 1: \ \tau = w = 0, \tag{3}$$

where the subscript b denotes a given function. The curved surface of the cylinder is considered free of stresses:

$$r = 1, \ \ -L \le z \le +L: \ \ \sigma_r = \tau = 0. \tag{4}$$

The nonzero strain components are

$$\epsilon_{rr} = \frac{\partial u}{\partial r}, \quad \epsilon_{\theta\theta} = \frac{u}{r}, \quad \epsilon_{zz} = \frac{\partial w}{\partial z}, \quad \epsilon_{rz} = \frac{\partial w}{\partial r} + \frac{\partial u}{\partial z}, \tag{5}$$

and the nonzero stress components for an incompressible material are (Green and Zerna, 1968)

$$\sigma_r = p + \frac{\partial u}{\partial r}, \quad \sigma_\theta = p + \frac{u}{r}, \quad \sigma_z = p + \frac{\partial w}{\partial z}, \quad \tau = \frac{1}{2}\left(\frac{\partial w}{\partial r} + \frac{\partial u}{\partial z}\right), \tag{6}$$

where p is the hydrostatic pressure. The equilibrium equations in the absence of body forces can be expressed as

$$L_u = \frac{\partial p}{\partial r} + \frac{\partial^2 u}{\partial r^2} + \frac{1}{2}\frac{\partial}{\partial z}\left(\frac{\partial w}{\partial r} + \frac{\partial u}{\partial z}\right) + \frac{1}{r}\left(\frac{\partial u}{\partial r} - \frac{u}{r}\right) = 0,$$

$$L_w = \frac{\partial p}{\partial z} + \frac{\partial^2 w}{\partial z^2} + \frac{1}{2}\frac{\partial}{\partial r}\left(\frac{\partial w}{\partial r} + \frac{\partial u}{\partial z}\right) + \frac{1}{2r}\left(\frac{\partial w}{\partial r} + \frac{\partial u}{\partial z}\right) = 0. \tag{7}$$

The displacements u and w are subject to the constraint

$$\epsilon_{rr} + \epsilon_{\theta\theta} + \epsilon_{zz} = \frac{\partial u}{\partial r} + \frac{u}{r} + \frac{\partial w}{\partial z} \equiv 0. \tag{8}$$

3 General Solution

Assume a solution of the form

$$u = U(r)\exp(-\gamma z), \quad w = W(r)\exp(-\gamma z),$$

$$p = P(r)\exp(-\gamma z). \tag{9}$$

Substituting Eq. (9) into Eq. (8) yields

$$W(r) = \frac{1}{\gamma}\left(\frac{dU}{dr} + \frac{U}{r}\right). \tag{10}$$

Eliminating p and w by using Eqs. (7), (9), and (10), we obtain an ordinary differential equation for U:

$$\left[\frac{d^2}{d\rho^2} + \frac{1}{\rho}\frac{d}{d\rho} + \left(1 - \frac{1}{\rho^2}\right)\right]^2 U = 0, \tag{11}$$

where $\rho = \gamma r$. The solution of Eq. (11) bounded at $r = 0$ is

$$U = C_1 J_1(\gamma r) + C_2 r J_0(\gamma r), \tag{12}$$

where C_1 and C_2 are constants, dependent on γ, and J_0 and J_1 are Bessel functions of order 0 and 1, respectively.

With $U(r)$ known, all other quantities can be found, for example,

$$\sigma_r = \left[\gamma J_0(\gamma) - \frac{J_1(\gamma r)}{r}\right] C_1 - \gamma J_1(\gamma r) r C_2,$$

$$\tau = -\gamma J_1(\gamma r) C_1 - [J_1(\gamma r) + \gamma J_0(\gamma r)] C_2. \tag{13}$$

Satisfying the boundary conditions (4), two homogeneous linear equations for C_1 and C_2 are obtained and the condition that the problem has a nontrivial solution requires that γ is a root of the transcendental equation

$$\gamma\left[J_0^2(\gamma) + \left(1 - \frac{1}{\gamma}\right) J_1^2(\gamma)\right] = 0. \tag{14}$$

The root $\gamma = 0$ corresponds to a homogeneous deformation, with stresses and displacements being

$$\sigma_r^h = \sigma_\theta^h = \tau^h = 0, \quad \sigma_z^h = -\frac{3}{2}\sigma_0; \quad u^h = \frac{1}{2}\sigma_0 r, \quad w^h = -\sigma_0 z, \tag{15}$$

where σ_0 is chosen as

$$\sigma_0 = -\frac{4}{3}\int_0^1 \sigma_z r dr. \tag{16}$$

The nonzero roots of Eq. (14) are denoted as γ_j ($j = 1, 2, \cdots$) in an increasing order of the absolute values. It is known that if γ is a root, then $-\gamma$, γ^*, and $-\gamma^*$ are also roots (where the superscript "*" denotes the complex conjugate). We now define

$$\sigma_z^e = \sigma_z - \sigma_z^h, \quad \tau^e = \tau - \tau^h, \quad u^e = u - u^h, \quad w^e = w - w^h. \tag{17}$$

Then the nonhomogeneous part of stresses and displacements are found to be

$$\begin{Bmatrix} \sigma_z^e \\ \tau^e \\ u^e \\ w^e \end{Bmatrix} = \sum_{\mathrm{Re}(\gamma_j) \ne 0} a_j \exp(-\gamma_j z) \begin{Bmatrix} \phi_j^{(1)}(r) \\ \phi_j^{(2)}(r) \\ \phi_j^{(3)}(r) \\ \phi_j^{(4)}(r) \end{Bmatrix}, \tag{18}$$

where a_j are unknown coefficients, called participating factors, to be determined by the end conditions, and the eigenfunctions $\phi_j^{(i)}$ ($i = 1, 2, 3, 4$) are defined in Appendix A. The hydrostatic pressure p follows:

$$p = \sum_{\mathrm{Re}(\gamma_j) \ne 0} a_j \{\gamma_j^2 J_1(\gamma_j) J_0(\gamma_j r)\} \exp(-\gamma_j z) - \sigma_0/2. \tag{19}$$

Comparing the equations derived above with the corresponding equations for a compressible material given by Swan (1968) and many other authors (e.g., Little and Childs, 1967), we find that the results for an incompressible material are just the limiting cases for a compressible material as the Poisson's ratio $\nu \to 0.5$, as expected.

4 Determination of Participating Factors

We first consider a semi-infinite cylinder with the plane end at $z = 0$ and prescribed end stresses:

$$\sigma_b = 1 - 2r^2, \quad \tau_b = 2.4r - 2.6r^3 + 0.2r^5, \tag{20}$$

since this problem has been computed by both Little and Childs (1967) and Gerhardt and Cheng (1981). The stresses σ_z and τ for a semi-infinite cylinder can be expressed by

Downloaded 03 May 2010 to 171.66.16.20. Redistribution subject to ASME license or copyright; see http://www.asme.org/terms/Terms_Use.cfm

$$\sigma_z \sum_{\mathrm{Re}(\gamma_j)>0} a_j \phi_j^{(1)}(r)\exp(-\gamma_j z),$$
$$\tau = \sum_{\mathrm{Re}(\gamma_j)>0} a_j \phi_j^{(2)}(r)\exp(-\gamma_j z). \tag{21}$$

There are many ways to make the end conditions be satisfied "as well as possible." The simplest one is the least-square method (LSM). Defining an "error" as

$$E=\int_0^1 \left\{ \left[\sum_{\mathrm{Re}(\gamma_j)>0} a_j \phi_j^{(1)}(r) - \sigma_b \right]^2 + \left[\sum_{\mathrm{Re}(\gamma_j)>0} a_j \phi_j^{(2)}(r) - \tau_b \right]^2 \right\} rdr \tag{22}$$

and requiring that E be a minimum, we obtain

$$\sum_k S_{jk} a_k = F_j, \tag{23}$$

where

$$F_j=\int_0^1 [\sigma_b \phi_j^{(1)} + \tau_b \phi_j^{(2)}] rdr, \quad S_{jk}=\int_0^1 [\phi_j^{(1)}\phi_k^{(1)} + \phi_j^{(2)}\phi_k^{(2)}] rdr. \tag{24}$$

We may also determine a_j by a variational approach, requiring that the total potential energy be a minimum for the given number of eigenvalues. The variation of the total potential energy can be found as

$$\delta U=\int_0^I \int_0^1 (\sigma_z \delta\epsilon_{zz} + \sigma_r \delta\epsilon_{rr} + \sigma_\theta \sigma\epsilon_{\theta\theta} + \tau\delta\epsilon_{rz}) rdrdz - \int_0^1 [\sigma_b \delta w + \tau_b \delta u]_{z=0} rdr. \tag{25}$$

Using Eqs. (5) and (6), integrating Eq. (25) by parts, and letting $\delta U=0$, we obtain

$$\int_0^L \int_0^1 (L_u \delta u + L_w \delta w) rdrdz - \int_0^L [\sigma_r \delta u + \tau \delta w]_{r=1} dz - \int_0^1 [(\sigma_z - \sigma_b)\delta w + (\tau - \tau_b)\delta u]_{z=0} rdr = 0. \tag{26}$$

Noting Eq. (7), and the boundary conditions (4), we have

$$\int_0^1 \{[(\sigma_z)_{z=0} - \sigma_b](\delta w)_{z=0} + [(\tau)_{z=0} - \tau_b](\delta u)_{z=0}\} rdr = 0, \tag{27}$$

which results in a system of linear Eqs. (23) with the coefficients defined as

$$F_j=\int_0^1 [\sigma_b \phi_j^{(4)} + \tau_b \phi_j^{(3)}] rdr, \quad S_{jk}=\int_0^1 [\phi_k^{(1)}\phi_j^{(4)} + \phi_k^{(2)}\phi_j^{(3)}] rdr. \tag{28}$$

We may refer to this variational method as the "virtual displacement method" (VDM).

By using the eigenvalues γ_j given by Little and Childs (1967), the participating factors can be computed. The comparison between the calculated end stresses and the prescribed ones are shown in Tables 1 and 2. We find that both the least-square method and the virtual displacement method give a more accurate result than the diagonally dominant method (DDM) (Gerhardt and Cheng, 1981; Robert and Keer, 1987) for a given number of eigenvalues, especially when only a few eigenvalues are used. When more eigenvalues are used, the solution calculated by all the methods were found to approach the prescribed values, and each participating factor eventually settles down to a constant (exact) value as N (the number of pairs of eigenvalues used) increases. The biorthogonal method is not presented here for comparison, since Gerhardt and Cheng (1981) have shown that it is inferior to the diagonally dominant method.

Table 1 Normal stress σ_z at $z=0$
(N=pairs of eigenvalues used)

r	σ_b	N=5 (DDM)	N=5 (LSM)	N=5 (VDM)	N=15 (DDM)	N=15 (LSM)	N=15 (VDM)
0.00	1.0000	0.8328	1.0010	0.9992	0.9854	0.9977	0.9984
0.20	0.9200	0.9896	0.9191	0.9194	0.9227	0.9204	0.9204
0.40	0.6800	0.6216	0.6767	0.6764	0.6768	0.6801	0.6801
0.60	0.2800	0.3240	0.2892	0.2907	0.2851	0.2793	0.2794
0.80	-0.2800	-0.2949	-0.2891	-0.2898	-0.2879	-0.2800	-0.2803
1.00	-1.0000	-1.0544	-0.9840	-0.9963	-1.0134	-1.0062	-1.0090

Table 2 Shear stress τ at $z=0$

r	τ_b	N=5 (DDM)	N=5 (LSM)	N=5 (VDM)	N=15 (DDM)	N=15 (LSM)	N=15 (VDM)
0.00	0.0000	0.0000	0.0000	0.0000	0.0000	0.0000	0.0000
0.20	0.4593	0.4438	0.4611	0.4624	0.4557	0.4594	0.4593
0.40	0.7956	0.7821	0.7969	0.7963	0.7993	0.7952	0.7953
0.60	0.8940	0.9328	0.8961	0.8968	0.8902	0.8939	0.8938
0.80	0.6543	0.5968	0.6411	0.6374	0.6567	0.6556	0.6555
1.00	0.0000	0.0000	0.0000	0.0000	0.0000	0.0000	0.0000

We now consider a finite cylinder under compression. The plane ends of the cylinder are assumed to be bonded to two rigid plates such that no lateral displacement is allowed on the bonded surfaces. The cylinder is axially compressed by a compressible load F' and its plane ends remain horizontal during the compression. Then the prescribed displacements are: $u_b=0$, $(dw/dr)_b=0$ or $w_b=-w_0=$ an unknown constant. The relation between σ_0 and F' is $\sigma_0=F'/E'A'$, where E' is the elastic modulus and A' is the cross-sectional area of the cylinder.

The stresses and displacements for a finite cylinder under a deformation symmetrical about the $z=0$ plane can be expressed as

$$\sigma_z = \sum_{\mathrm{Re}(\gamma_k)>0} a_k \exp(-\gamma_k L)\cosh(\gamma_k z)\phi_k^{(1)} - \frac{3\sigma_0}{2},$$
$$\tau = -\sum_{\mathrm{Re}(\gamma_k)>0} a_k \exp(-\gamma_k L)\sinh(\gamma_k z)\phi_k^{(2)},$$
$$u = \sum_{\mathrm{Re}(\gamma_k L)>0} a_k \exp(-\gamma_k L)\cosh(\gamma_k z)\phi_k^{(3)} + \frac{\sigma_0 r}{2},$$
$$w = -\sum_{\mathrm{Re}(\gamma_k L)>0} a_k \exp(-\gamma_k L)\sinh(\gamma_k z)\phi_k^{(4)} - \sigma_0 z. \tag{29}$$

The variational method can also be used for a displacement problem. It is easy to prove that to minimize the total potential energy, the condition

$$\int_0^1 [(u-u_b)(\delta\tau) + (w-w_b)(\delta\sigma_z)]_{z=L} rdr = 0 \tag{30}$$

must hold. Equation (30) leads to a set of linear algebraic equations

$$\sum_k S_{jk} a_k = \sigma_0 F_j, \tag{31}$$

where

$$F_j=-\frac{s_j}{2}\int_0^1 \phi_j^{(2)} r^2 dr, \quad S_{jk}=\int_0^1 [c_k s_j \phi_k^{(3)}\phi_j^{(2)} + s_k c_j \phi_k^{(4)}\phi_j^{(1)}] rdr, \tag{32}$$

with c_k and s_k being defined as

Downloaded 03 May 2010 to 171.66.16.20. Redistribution subject to ASME license or copyright; see http://www.asme.org/terms/Terms_Use.cfm

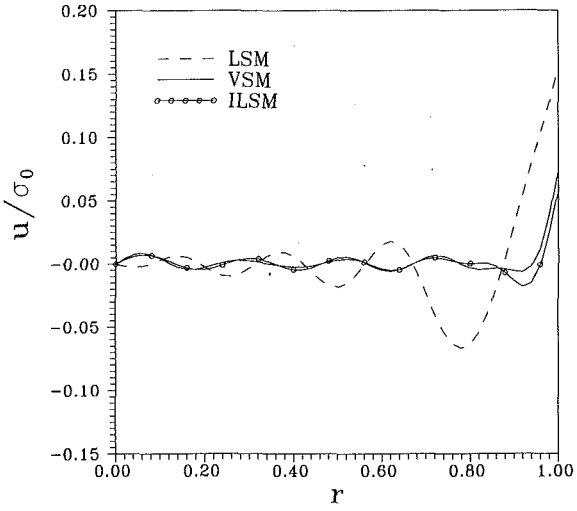


Fig. 1(*a*)

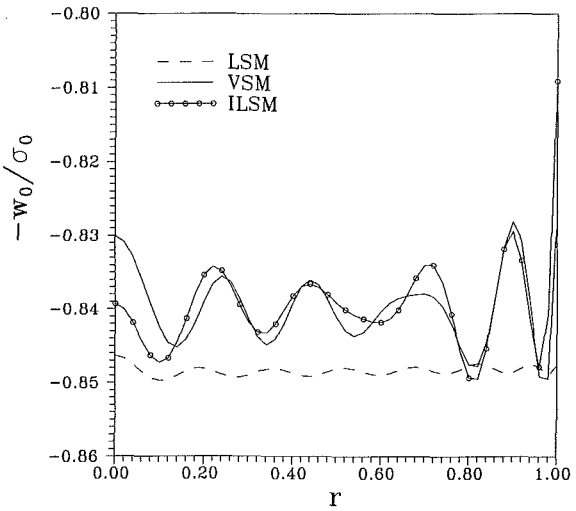


Fig. 1(*b*)

Fig. 1 Comparison of displacements at $z = L = 1.0$ calculated by various methods, using ten pairs of eigenvalues. The final value of w/σ_0 is about -0.8374. (*a*) radial displacement, $u_b = 0$; (*b*) axial displacement.

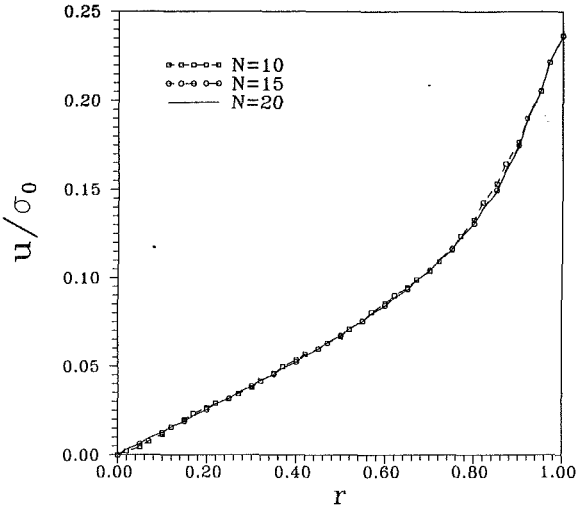


Fig. 2(*a*)

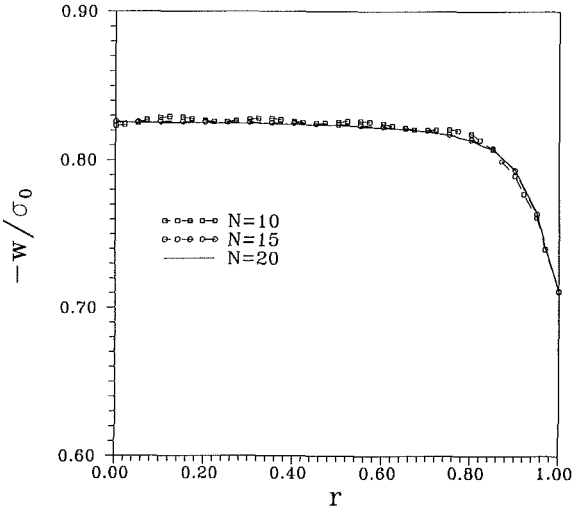


Fig. 2(*b*)

Fig. 2 Displacements at $z = 0.9L = 0.9*1.0 = 0.9$ calculated by VSM for various numbers of eigenvalues. (*a*) radial displacement; (*b*) axial displacement.

$$c_k = [\exp(-2\gamma_k L) + 1]/2, \quad s_k = [\exp(-2\gamma_k L) - 1]/2. \tag{33}$$

We may refer to this variational method as the "virtual stress method" (VSM). Comparing the virtual stress method with the diagonally dominant method (Robert and Keer, 1987), we find that they are essentially the same.

For the least-square method, we may define

$$E = \int_0^1 \left[(u^e + u^h)^2 + \left(\frac{dw}{dr}\right)^2 \right]_{z=L} rdr. \tag{34}$$

Requiring that E be a minimum, we can have a set of algebraic equations for a_j. However, numerical calculations suggest that the least-square solutions based on Eq. (34) converge poorly in comparison with the virtual stress method or the diagonally dominant method, as shown in Fig. 1. The reason for this is due to the stress singularity at the corners of the cylinder.

Through a local analysis, Benthem and Minderhoud (1972) have shown that at the bonded surface $z = L$

$$\sigma_z, \tau \to (1-r)^{-\lambda}, \quad u, w \to (1-r)^{1-\lambda}, \tag{35}$$

as $r \to 1$, where λ is a constant with $\mathrm{Re}(\lambda) \le 1$, determined by

$$\cos^2\left(\frac{\pi\lambda}{2}\right) + (1-\lambda)^2 - 1 = 0. \tag{36}$$

The "gravest" root of Eq. (36) is found to be

$$\lambda = 0.40538836. \tag{37}$$

Thus the use of dw/dr, which has a singularity as $r \to 1$ in Eq. (34), may explain the poor behavior of the least-square method. On the other hand, the effect of the singularity in Eq. (30) is weakened by the product of $u\delta\tau$ and $w\delta\sigma$, since they tend to cancel the singularities. Therefore, the advantage of the virtual stress method over the least-square method based on Eq. (34) is not surprising. However, the least-square solution can be improved by requiring that

$$E = \int_0^1 \left\{ \left[\sum_j a_j c_j \phi_j^{(3)}(r) + \frac{\sigma_0 r}{2} \right]^2 + \left[\sum_j a_j s_j (\phi_j^{(4)}(r) - \phi_j^{(4)}(0)) \right]^2 \right\} rdr \tag{38}$$

be a minimum, since the effect of singularity here is not as adverse as in Eq. (34). The solutions based on Eq. (38) are also plotted in Fig. 1. We can see that they are much better than those predicted by minimizing Eq. (34). We may refer to the least-square method based on Eq. (38) as the "improved least-square method" (ILSM).

Downloaded 03 May 2010 to 171.66.16.20. Redistribution subject to ASME license or copyright; see http://www.asme.org/terms/Terms_Use.cfm

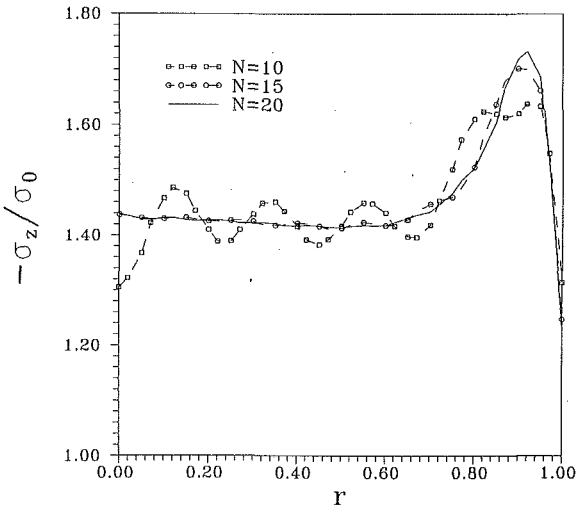


Fig. 3(*a*)

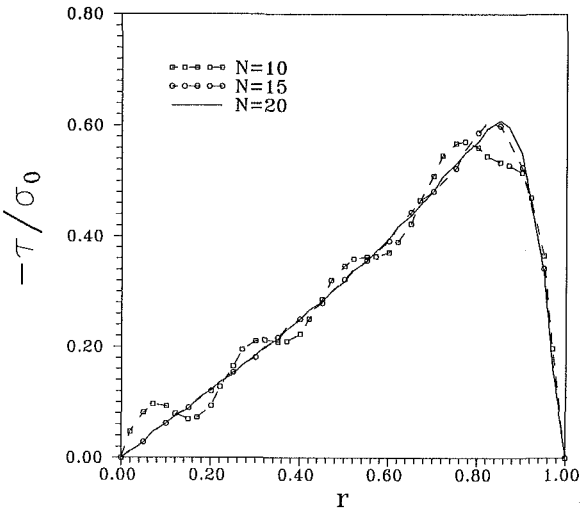


Fig. 3(*b*)

Fig. 3 Stresses at $z=0.9L=0.9*1.0=0.9$ calculated by VSM for various numbers of eigenvalues. (*a*) axial stress; (*b*) shear stress.

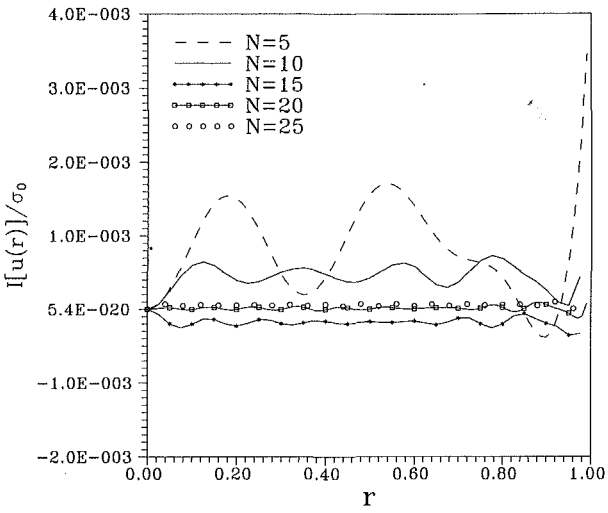


Fig. 4(*a*)

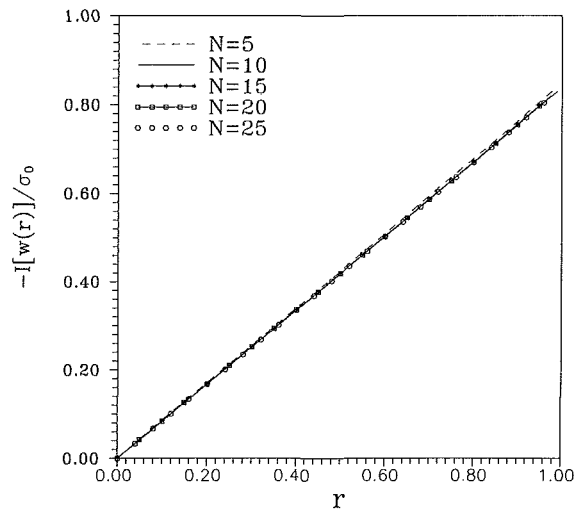


Fig. 4(*b*)

Fig. 4 Transformed displacements at $z=L=1.0$ calculated for various numbers of eigenvalues, showing a faster rate of convergence. (*a*) radial displacement; (*b*) axial displacement.

The calculated displacements at $z=L$ were found to converge to the prescribed ones in a slow oscillating way. However, away from the bonded surface $z=L$, say at $z=0.9L$, the solutions converge much faster, as shown in Figs. 2 and 3.

5 Calculation of Interfacial Displacements and Stresses

From Fig. 1(*b*), we note that the vertical displacement w at the interface oscillates about some true value and an averaging operation over the radius of the cylinder may give a better estimation of the true value. Thus, we introduce a transformation

$$I[f(r)]=\int_0^r f(t)\,dt, \tag{39}$$

where $f(t)$ is a function whose integral over $0\le r\le 1$ exists. Then the displacements at the interface can be transformed as

$$\begin{aligned} I[u(r)]&=\sum_j a_j c_j I[\phi_j^{(3)}(r)]+\frac{\sigma_0}{4}r^2\sim 0,\\ I[w(r)]&=\sum_j a_j s_j I[\phi_j^{(4)}(r)]-\sigma_0 Lr\sim -w_0 r. \end{aligned} \tag{40}$$

The significance of this transformation is more than just averaging; it makes the effect of the singularity less significant through the integration. For example, the term $1/(1-r)^{\lambda}$ becomes $(1-r)^{1-\lambda}$ as a result of the transformation. Thus, the new series (40) are expected to converge faster than those before the transformation. This is confirmed by Fig. 4 in comparison with Fig. 1. Note that a plot in Fig. 4(*b*) is almost a perfect straight line, and the downward deflection w_0 is simply its slope. Thus the transformation provides a more accurate way to obtain w_0, and hence the stiffness of the cylinder.

To describe the interfacial stress distribution, we use Benthem and Minderhoud's expansion (1972):

$$\begin{aligned} \sigma_z^e&=-\alpha[(1-r)^{-\lambda}+\lambda(1-r)]+\frac{3}{2}\sigma_0+\sum_{m=1}^{NT} b_m J_0(\mu_m r),\\ \tau&=-C_\alpha\alpha[(1-r)^{-\lambda}-g(r)]+\sum_{m=1}^{NT} d_m J_1(k_m r), \end{aligned} \tag{41}$$

where μ_m and k_m are the mth root of $J_0(\mu)=0$ and $J_1(k)=0$, respectively; α is a constant called the strength of singularity; b_m and d_m are the unknown coefficients; $C_\alpha=(\lambda/(1-\lambda))\tan(\lambda\pi/2)$ and $g(r)=(1-r)+\lambda(1+\lambda)(r^2-r)/2$. Using the biorthogonal relation (Little and Childs, 1967)

Downloaded 03 May 2010 to 171.66.16.20. Redistribution subject to ASME license or copyright; see http://www.asme.org/terms/Terms_Use.cfm

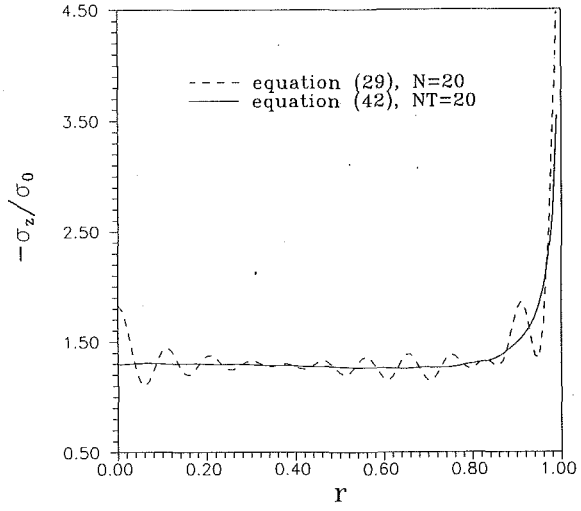


Fig. 5(*a*)

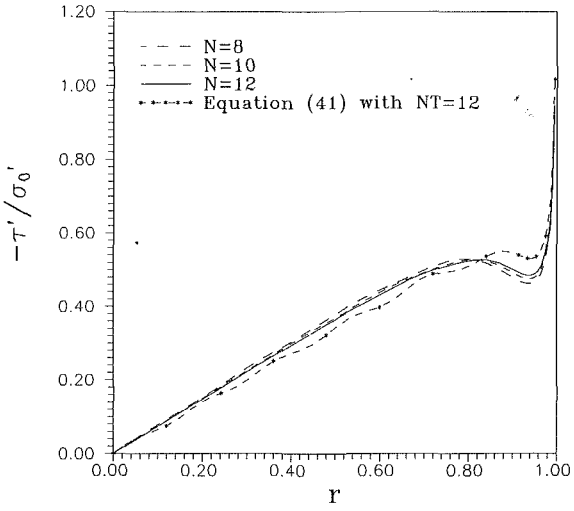


Fig. 6(*a*)

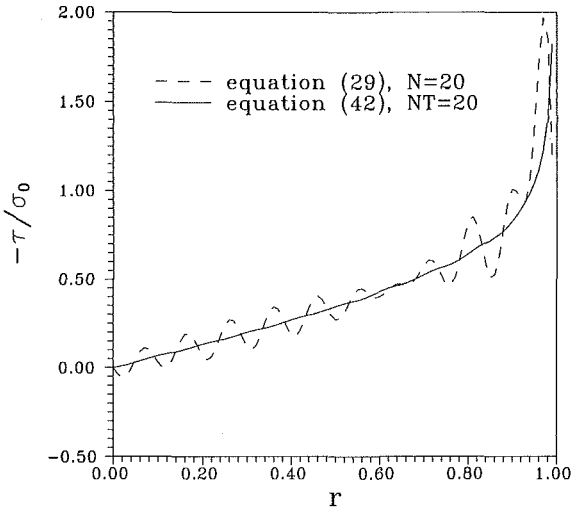


Fig. 5(*b*)

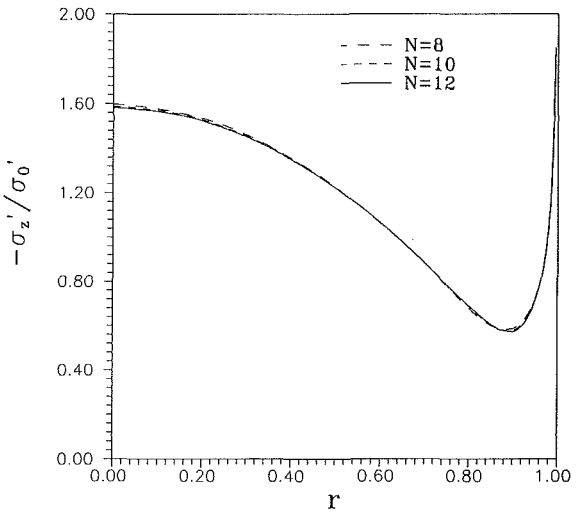


Fig. 6(*b*)

Fig. 5 Interfacial stresses calculated by Eq. (41), using unknowns. The strength of singularity is found to be about $\alpha = 0.551$. The oscillating curves are obtained by Eq. (29), without extracting the singularity. (*a*) normal stress; (*b*) shear stress.

Fig. 6 The effect of the Cesaro sum for a cylinder of $L = 0.25$. The curves showing local oscillations are calculated from Eqs. (41) with $NT = 12$, without using the Cesaro sum. $\sigma_0' = F'/A'$ is the average normal stress. (*a*) shear stress; (*b*) normal stress.

$$\int_0^1 [\phi_k^{(1)} W_j^{(1)} + \phi_k^{(3)} W_j^{(3)}] r dr = \delta_{kj} N_j/2,$$

$$\int_0^1 [\phi^{(2)} W_j^{(2)} + \phi_k^{(4)} W_j^{(4)}] r dr = \delta_{kj} N_j/2, \quad (42)$$

where the biorthogonal functions $\{W_j^{(i)}\}$ are given in Appendix A, δ_{kj} is the Kronecher delta, and

$$N_j = -2\gamma_j J_0^2(\gamma_j) - \gamma_j J_1^2(\gamma_j) + J_0(\gamma_j) J_1(\gamma_j). \quad (43)$$

We find

$$c_j \int_0^1 (\tau^e)_{z=L} W_j^{(2)} r dr - s_j \int_0^1 [(\sigma_z^e)_{z=L} W_j^{(1)} + (u^e)_{z=L} W_j^{(3)}] r dr = 0. \quad (44)$$

One more equation can be obtained by noting that σ_z^e is self-equilibrating, i.e.,

$$\int_0^1 \sigma_z^e r dr = 0. \quad (45)$$

The stresses predicted by Eqs. (41) are plotted in Fig. 5; the results based on Eq. (29) are also plotted there. The convergence is obvious. Benthem and Minderhoud (1972) and Robert and Keer (1987) reported that only a small number of unknowns, say $NT \leq 6$, could be included to obtain accurate results since Eqs. (41) are over completed. However, in our calculation of a cylinder of $L = 1$, we used up to 41 unknowns ($NT = 20$) and yet no convergence problem was found. The reason for this may be that we used double precision calculations.

A problem arises when the Benthem and Minderhoud method is applied to thin cylinders: the solutions exhibit local oscillations, and are no longer smooth. The reason for the oscillations may be that for a thin cylinder the other roots of Eqs. (36) may also play important roles while the expansion (41) considers only the gravest one.

Joseph and Sturges (1978) has shown that the Cesaro sum (Powell and Shah, 1972) may be used to improve the convergence of a biorthogonal series, which exhibits an oscillatory character of convergence. To use the Cesaro sum to suppress the local oscillations we rewrite Eqs. (41) as

Downloaded 03 May 2010 to 171.66.16.20. Redistribution subject to ASME license or copyright; see http://www.asme.org/terms/Terms_Use.cfm

$$\sigma_{z,n} = -\alpha_{,n}[(1-r)^{-\lambda} - \lambda(1-r)] + \sum_{m=1}^{n} b_{m,n} J_0(\mu_m r),$$
$$\tau_{,n} = -C_\alpha \alpha_{,n}[(1-r)^{-\lambda} - g(r)] + \sum_{m=1}^{n} d_{m,n} J_1(k_m r), \quad (46)$$

where $\sigma_{z,n}$ and $\tau_{,n}$ are the stresses computed with $NT = n$ and $\alpha_{,n}$ $b_{m,n}$, and $d_{m,n}$ are the corresponding constants. The Cesaro sum for the normal stress σ_z is defined as

$$\sigma_z^{(N)} = \frac{1}{N}\sum_{n=1}^{N} \sigma_{z,n} = -\left(\frac{1}{N}\sum_{n=1}^{N} \alpha_{,n}\right)[(1-r)^{-\lambda} + \lambda(1-r)] + \sum_{m=1}^{N}\left(\frac{1}{N}\sum_{n=1}^{N-m+1} b_{m,n}\right) J_0(\mu_m r). \quad (47)$$

The effect of the Cesaro sum is illustrated in Fig. 6. We can seen that smooth curves have been obtained.

It is realized that the Cesaro sum may also be directly used to improve the rate of convergence of the eigenfunction expansion (29), as Joseph and Sturges (1978) did for a similar problem of Stokes flow. However, using the Benthem and Minderhoud expansion and the Cesaro sum together makes the convergence much faster.

6 Numerical Results for Bonded Rubber Cylinders Under Compression

Rubber is widely used as springs. The stiffness of a spring is its most important characteristics. The nondimensional stiffness is defined as

$$k = \frac{F'/(2w_0')}{E'A'/(2L')} = \frac{L}{w_0/\sigma_0}, \quad (48)$$

where $2w_0'$ is the total axial deflection. The nondimensional stiffness obtained by the series solution is shown in Table 3, in which the shape factor S, defined as the ratio of one loaded area to the force-free area (i.e., $S = R'/4L' = 1/4L$), is a commonly used parameter in rubber spring design. It has been noted that the use of the transformed relation (40) to calculate the stiffness for thin cylinders is important because the original series (29) converges very slowly for thin cylinders.

The friction coefficient μ of rubber-to-steel under a dry contact condition ranges from 1.6 to 10 (Neale, 1973). Figure 7 gives the ratio of τ to σ_z for cylinders for $S = 1$ and 4. The ratio of τ to σ_z along the interfaces is found to be much smaller than μ, except for extremely thin cylinders, in which slip may occur in some region near $r = 1$. However, under a no lubricant condition, slip can never occur at the corner, since at $r = 1$ the ratio of τ to σ_z is equal to $C_\alpha = 0.504$, much smaller than μ. Thus we conclude that in the absence of lubricants, the friction on the interfaces will usually prevent slipping.

Therefore, the "elastic modulus" E_m measured by compressing a rubber cylinder between two steel plates without lubricating the interfaces is overestimated. Table 3 shows that even when the height-to-diameter ratio is 3:1, the measured elastic modulus E_m is still 5.7 percent higher than the actual value. The measured elastic modulus can be corrected by using Table 3:

$$E' = E_m/k. \quad (49)$$

The interfacial stress distributions are shown in Fig. 8. We can see that (1) for a thin cylinder, the normal stress distribution is very close to a parabola, and the shear stress distribution is close to a straight line, except near the corner; this result agrees well with the experimental observations by Gent et al. (1974); (2) the strength of singularity decreases as the cylinder becomes thinner; and (3) for a thin cylinder, the effect of the singularity is confined to a very small region in the neighborhood of the corner; this explains why Gent et al. failed to detect the singularity in their experiments.

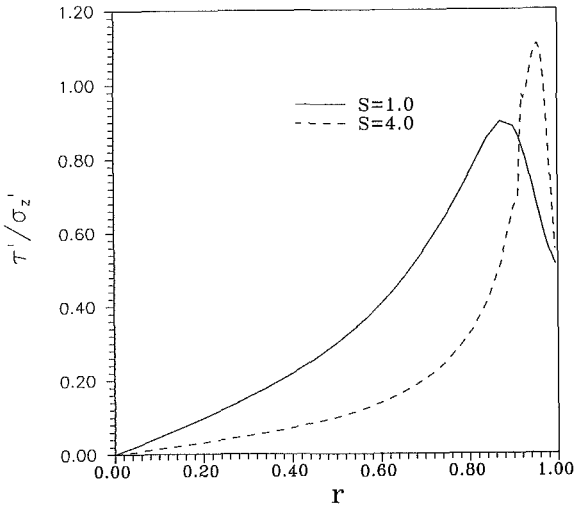


Fig. 7 The ratio of τ-to-σ_z at interface

7 Conclusions

The end problem of an incompressible cylinder was formulated. A variational method and a least-square method were proposed for the determination of the participating factors. Among the various methods, the variational method is deemed favorably because it has a very clear physical meaning: it minimizes the total potential energy. Moreover, for mixed end-condition problems, the variational method can be shown to lead to the biorthogonal solution in which the participating factors can be directly obtained without solving a set of equations (see Little and Childs, 1967). It is, however, noted that all the discussed methods can be classified as the "weight function" approach.

A transformation was introduced for the better estimation of the stiffness of a cylinder. The transformed displacements converge much faster since the effect of the singularity becomes less significant after the transformation. The singular behavior of the interfacial stresses was described by Benthem and Minderhoud's expansion. The difficulty of using this expansion for thin cylinders was overcome by the Cesaro sum.

Numerical results for bonded rubber cylinders in compres-

Table 3 Nondimensional stiffness k

(L=Height-to-diameter ratio, S=shape factor)

L	25	5	4	3	2	1	0.5
S	1/100	1/20	1/16	1/12	1/8	1/4	1/2
k	1.006	1.034	1.042	1.057	1.088	1.194	1.538
L	0.25	0.125	0.0625	1/40	1/60	1/80	
S	1	2	4	10	15	20	
k	2.931	8.741	31.25	196.3	440.5	780.0	

Downloaded 03 May 2010 to 171.66.16.20. Redistribution subject to ASME license or copyright; see http://www.asme.org/terms/Terms_Use.cfm

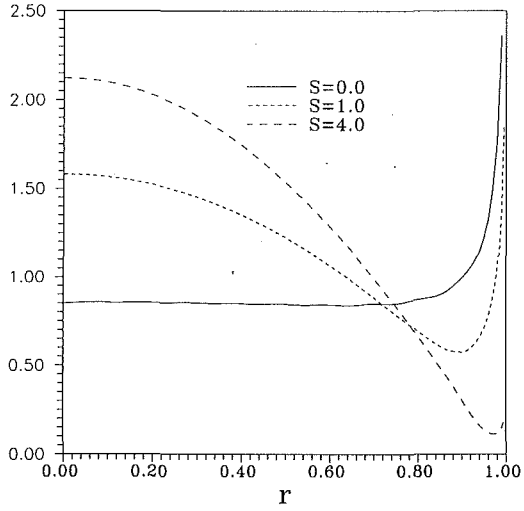


Fig. 8(*a*)

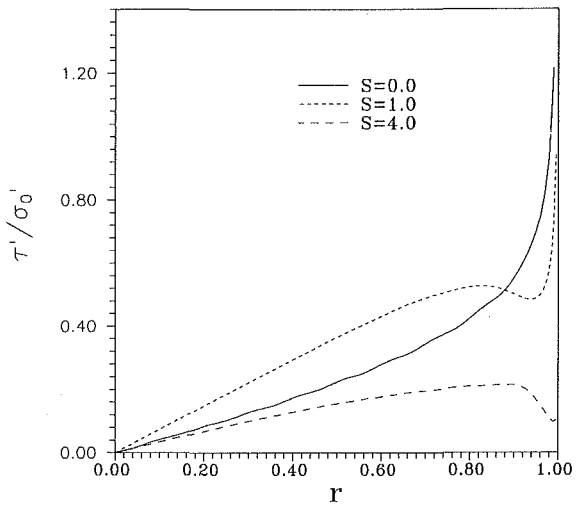


Fig. 8(*b*)

Fig. 8 Interfacial stress distributions for various shape factors. $\sigma_0' = F'/A'$ is the average normal stress. (*a*) normal stress; (*b*) shear stress.

sion were presented. The compression stiffness was tabulated, which can be used for design. It was also shown that in the absence of lubricants, friction on the interfaces usually prevents slipping. The resulting stress distributions were compared with existing experimental studies. A better understanding of the problem of the compression of bonded rubber cylinders under small deformation has been achieved.

References

Beatty, M. F., 1977, "Elastic Stability of Rubber Bodies in Compression," *Finite Elasticity*, R. S. Rivlin, ed.

Benthem, J. P., and Minderhoud, P., 1972, "The Problem of the Solid Cylinder Compressed Between Rough Rigid Stamps," *Int. J. of Solids and Structures*, Vol. 8, pp. 1027–1042.

Gent, A. N., and Lindley, P. B., 1959, "The Compression of Bonded Rubber Blocks," *Proc. Instn. Mech. Engrs., London*, Vol. 173, pp. 111–117.

Gent, A. N., et al., 1974, "Interfacial Stresses for Bonded Rubber Blocks in Compression and Shear," ASME JOURNAL OF APPLIED MECHANICS, Vol. 41, pp. 885–859.

Gerhardt, T. D., and Cheng, S., 1981, "A Diagonally Dominant Solution for the Cylinder End Problem," ASME JOURNAL OF APPLIED MECHANICS, Vol. 48, pp. 876–880.

Green, A. E., and Zerna, W., 1968, *Theoretical Elasticity*, Oxford University Press, Oxford, U.K.

Gregory, R. D., and Wan, F. Y. M., 1984, "Decaying States of Plane Strain in a Semi-Infinite Strip and Boundary Conditions for Plate Theory," *J. of Elasticity*, Vol. 14, pp. 27–64.

Gupta, G. D., 1974, "The Analysis of the Semi-Infinite Cylinder Problem," *Int. J. Solids Structures*, Vol. 10, pp. 137–148.

Horvay, G., and Mirable, J. A., 1958, "The End Problem of Cylinders," ASME JOURNAL OF APPLIED MECHANICS, Vol. 25, pp. 561–571.

Joseph, D. D., and Sturges, L., 1978, "The Convergence of Biorthogonal Series for Biharmonic and Stokes Flow Edge Problems: Part II," *SIAM Journal on Applied Mathematics*, Vol. 34, pp. 7–26.

Kim, Y. Y., and Steele, C. R., 1992, "Static Axisymmetrical End Problems in Semi-Infinite and Finite Solid Cylinders," ASME JOURNAL OF APPLIED MECHANICS, Vo. 59, pp. 69–76.

Lindley, P. B., 1966, *Engineering Design with Natural Rubber*, Natural Rubber Producers' Research Association, London.

Ling, Y., Engel, P. A., and Brodsky, Wm. L., 1992, "Nonlinear Load-Deflection Relations of Bonded Elastomeric Circular Disks and Strips," *Rubber Chemistry and Technology*, Vol. 65, pp. 917–931.

Little, R. W., and Childs, S. B., 1967, "Elastostatic Boundary Region Problem in Solid Cylinders," *Q. Appl. Math.*, Vol. 25, pp. 261–274.

Neale, M. J., 1973, *Tribology Handbook*, Newnes-Butterworths, London.

Powell, R. E., and Shah, S. M., 1972, *Summability Theory and Applications*, Van Nostrand Reinhold, London.

Robert, M., and Keer, L. M., 1987, "An Elastic Circular Cylinder with Displacement Prescribed at the End-Axially Symmetrical Case," *Q. Jl Mech. Appl. Math.*, Vol. 40, pp. 339–363.

Spence, D. A., 1983, "A Class of Biharmonic End-Strip Problems Arising in Elasticity and Stokes Flow," *IMA J. Appl. Math.*, Vol. 30, pp. 107–139.

Swan, G. N., 1968, "The Semi-Infinity Cylinders with Prescribed End Displacements," *SIAM J. of Appl. Math.*, Vol. 16, pp. 860–881.

APPENDIX A

The eigenfunctions are defined as

$$\begin{aligned}
\phi_j^{(1)}(r) &= [2\gamma_j^2 J_1(\gamma_j) - \gamma_j^3 J_0(\gamma_j)] J_0(\gamma_j r) - \gamma_j^3 J_1(\gamma_j) r J_1(\gamma_j r) \\
\phi_j^{(2)}(r) &= -\gamma_j^3 J_0(\gamma_j) J_1(\gamma_j r) + \gamma_j^3 J_1(\gamma_j) r J_0(\gamma_j r) \\
\phi_j^{(3)}(r) &= [\gamma_j J_1(\gamma_j) + \gamma_j^2 J_0(\gamma_j)] J_1(\gamma_j r) - \gamma_j^2(\gamma_j) r J_0(\gamma_j r) \\
\phi_j^{(4)}(r) &= [\gamma_j^2 J_0(\gamma_j) - \gamma_j J_1(\gamma_j)] J_0(\gamma_j r) + \gamma_j^2 J_1(\gamma_j) r J_1(\gamma_j r).
\end{aligned} \tag{A1}$$

The biorthogonal functions are

$$W_j^{(1)} = \phi_j^{(4)}/K_j, \quad W_j^{(2)} = -\phi_j^{(3)}/K_j, \quad W_j^{(3)} = -\phi_j^{(2)}/K_j, \quad W_j^{(4)} = \phi_j^{(1)}/K_j, \tag{A2}$$

where $K_j = 2\gamma^2 J_1^2(\gamma)$.

Downloaded 03 May 2010 to 171.66.16.20. Redistribution subject to ASME license or copyright; see http://www.asme.org/terms/Terms_Use.cfm

S. R. Choi
Department of Mechanical Engineering,
Yeungnam University,
Gyongsan, Korea

K. S. Lee
Department of Mechanical Engineering,
University of Ulsan,
Ulsan, Korea

Y. Y. Earmme[1]
Department of Mechanical Engineering,
Korea Advanced Institute of Science
and Technology,
373-1 Kusong-Dong, Yusung-Gu,
Taejon, 305-701, Korea

Analysis of a Kinked Interfacial Crack Under Out-of-Plane Shear

A kinked interfacial crack under out-of-plane shear is analyzed where a straight interfacial crack is kinked into material 1 out of the interface. Employing the Wiener-Hopf technique, the solution is obtained in a closed form. Discontinuity in the stress intensity factor as the kink angle ω approaches zero is found, while the energy release rate is shown to be continuous at $\omega=0$. The limit case of the kinked length b *approaching zero is also investigated. The result shows that the stress field has $1/\sqrt{r}$ singularity and the energy release rate at $b=0^+$ is enhanced at some ω if the crack kinks into the more compliant material.*

1 Introduction

Problem of interfacial crack has been an interesting subject since the work by Williams (1959), and a number of works related to this topic have been recently published. (See, for instance, the work by Rice (1988).) Rice (1988) has justified the use of the fracture mechanics concept based on the stress intensity factors, even though the stress field very close to the crack tip shows the oscillatory behavior together with the physically unacceptable interpenetration of the crack surfaces. Kinking of a crack, on the other hand, has drawn much attention due to its importance in connection with the initiation of a crack under mixed-mode loading and the results of the kinked crack under in-plane loading in homogeneous materials are well documented by Karihaloo (1982). The kinked crack out of an interface poses an interesting problem since it is important to predict whether an interfacial crack will propagate in the interface or it will kink out of the interface. The analysis of the kinked interfacial crack under in-plane loading has been performed by Hayashi and Nemat-Nasser (1981), He and Hutchinson (1989), and Mukai et al. (1990). Due to the complexity of the problem, the solution is obtained numerically solving singular integral equations.

Recently, Choi and Earmme (1990) analyzed the kinked crack in homogeneous materials under antiplane loading using the Wiener-Hopf technique. Since the out-of-plane problem is much easier to deal with, a closed-form solution was obtained and it is found that as the kinked length b goes to zero, the stress at the tip has the $r^{-1/2}$ singularity, contrary to the result given by Theocaris and Makrakis (1987). The purpose of this study is to analyze the kinked interfacial crack under antiplane loading. The problem is formulated in terms of the Mellin transform, which is solved by the Wiener-Hopf technique. Special attention is given to the case of the kinked length $b\to 0$, and the stress intensity factor and the energy release rate as a function of the kinked length b, the kink angle ω, and the elastic moduli of the bimaterial are obtained. The limiting case of $\omega\to 0$ is also investigated in regard to the discontinuity of the stress intensity factor.

2 Mathematical Formulation

As shown in Fig. 1, a semi-infinite (main) interfacial crack lies along the negative x-axis with a kink of length b and angle ω. The positive x-axis is the boundary of the material 1 (occupying the upper half) and 2 (occupying the lower half). Each material is assumed to be linear elastic, with shear moduli μ_1 and μ_2, respectively. A pair of out-of-plane loads, each of magnitude Q, are applied at the crack surface of $x=-l$. In terms of the polar coordinates, the displacement $W(r, \theta)$ in the z direction satisfies

$$\nabla^2 W(r,\theta)=\left(\frac{\partial^2}{\partial r^2}+\frac{1}{r}\frac{\partial}{\partial r}+\frac{1}{r^2}\frac{\partial^2}{\partial\theta^2}\right)W(r,\theta)=0. \qquad (1)$$

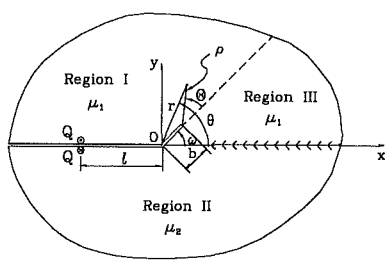


Fig. 1 Semi-infinite kinked interfacial crack. A pair of out-of-plane loads, each of magnitude Q are applied at $r=l$, $\theta=\pm\pi$, respectively.

[1]To whom all correspondence should be addressed.

Contributed by the Applied Mechanics Division of THE AMERICAN SOCIETY OF MECHANICAL ENGINEERS for publication in the ASME JOURNAL OF APPLIED MECHANICS.

Discussion on this paper should be addressed to the Technical Editor, Professor Lewis T. Wheeler, Department of Mechanical Engineering, University of Houston, Houston, TX 77204-4792, and will be accepted until four months after final publication of the paper itself in the ASME JOURNAL OF APPLIED MECHANICS.

Manuscript received by the ASME Applied Mechanics Division, Apr. 4, 1991; 1991; final revision Oct 21, 1992. Associate Technical Editor: C. F. Shih.

Copyright © 1994 by ASME
Downloaded 03 May 2010 to 171.66.16.20. Redistribution subject to ASME license or copyright; see http://www.asme.org/terms/Terms_Use.cfm

The shear stresses $\sigma_{\theta z}(r, \theta)$ and $\sigma_{rz}(r, \theta)$ in each material are given by

$$\sigma_{\theta zi}(r, \theta) = \mu_i \frac{1}{r} \frac{\partial}{\partial \theta} W(r, \theta), \quad i = 1, 2, \tag{2}$$

$$\sigma_{rzi}(r, \theta) = \mu_i \frac{\partial}{\partial r} W(r, \theta), \quad i = 1, 2. \tag{3}$$

Here the subscript $i = 1$ signifies the material 1 and $i = 2$ the material 2. The boundary conditions are written as

$$\sigma_{\theta z}(r, \pi) = \sigma_{\theta z}(r, -\pi) = Q\delta(r - l), \tag{4a}$$

$$\sigma_{\theta z}(r, \omega^+) = \sigma_{\theta z}(r, \omega^-) = 0, \quad 0 \le r < b, \tag{4b}$$

where δ is the Dirac function.

The continuity of the traction and displacement requires

$$\sigma_{\theta z}(r, \omega^+) = \sigma_{\theta z}(r, \omega^-), \quad b \le r \tag{4c}$$

$$W(r, \omega^+) = W(r, \omega^-), \quad b \le r \tag{4d}$$

$$\sigma_{\theta z}(r, 0^+) = \sigma_{\theta z}(r, 0^-), \quad 0 \le r \tag{4e}$$

$$W(r, 0^+) = W(r, 0^-), \quad 0 \le r. \tag{4f}$$

The asymptotic behavior of the stresses $\sigma_{\theta z}$ and σ_{rz} is

$$\sigma_{\theta z},\ \sigma_{rz} = \begin{cases} 0(r^{-\lambda}),\ 0 < \lambda < 1 & \text{as } r \to 0 \quad (5a) \\ 0(r^{-3/2}) & \text{as } r \to \infty \quad (5b) \\ 0((r-b)^{-1/2}) & \text{as } r \to b^+ \text{ and } \theta \to \omega. \quad (5c) \end{cases}$$

The Mellin transform of $W(r, \theta)$ is defined by

$$\hat{W}(p, \theta) \equiv \int_0^\infty W(r, \theta) r^{p-1} dr, \quad \lambda - 1 < Rlp < 1/2, \tag{6a}$$

from which (1) is rewritten as

$$\left(\frac{d^2}{d\theta^2} + p^2\right) \hat{W}(p, \theta) = 0. \tag{6b}$$

The range of Rlp in (6a) is determined from (5a) and (5b). The solution to (6b) is now written as

$$\hat{W}(p, \theta) = \begin{cases} A_1(p)\cos(\theta - \omega)p + B_1(p)\sin(\theta - \omega)p, \\ \qquad \omega \le \theta \le \pi \text{ (Region I, Fig. 1)} \quad (7a) \\ A_2(p)\cos(\theta - \omega)p + B_2(p)\sin(\theta - \omega)p, \\ \qquad -\pi \le \theta \le 0 \text{ (Region II, Fig. 1)} \quad (7b) \\ A_3(p)\cos(\theta - \omega)p + B_3(p)\sin(\theta - \omega)p, \\ \qquad 0 \le \theta \le \omega \text{ (Region III, Fig. 1).} \quad (7c) \end{cases}$$

With $A_i(p)$ and $B_i(p)$ $(i = 1, 2, 3)$ determined from the solution procedure described in the following section, the displacement $W(r, \theta)$ is given by

$$W(r, \theta) = \frac{1}{2\pi i} \int_{c-i\infty}^{c+i\infty} \hat{W}(p, \theta) r^{-p} dp, \quad \lambda - 1 < c < 1/2. \tag{8}$$

3 Solution Procedure

We employed the Wiener-Hopf technique (Noble, 1958) to determine $A_i(p)$ and $B_i(p)$ in (7a), (7b), and (7c). Using (4a) to (4f), we finally get (see Appendix A for details)

$$T_+(p) = K(p)[G_-(p) - E(p)/\cos(\pi p)], \tag{9}$$

where

$$K(p) = \frac{\sin(2\pi p)}{\mu_1 p \sin(\pi - \omega)p[\sin(\pi + \omega)p + \gamma \sin(\pi - \omega)p]}, \tag{10}$$

$$E(p) = Q\left(\frac{l}{b}\right)^p \cos(\omega p), \tag{11}$$

$$T_+(p) = \int_0^1 [W(r, \omega^+) - W(r, \omega^-)](r/b)^{p-1} d(r/b), \tag{12}$$

$$G_-(p) = b\int_1^\infty \sigma_{\theta z}(r, \omega)(r/b)^p d(r/b), \tag{13}$$

$$\gamma = (\mu_2 - \mu_1)/(\mu_2 + \mu_1). \tag{14}$$

Equation (9) is solved using the Wiener-Hopf technique to determine the unknown functions $T_+(p)$ and $G_-(p)$. The unknowns $A_i(p)$ and $B_i(p)$ $(i = 1, 2, 3)$ are given in terms of $G_-(p)$ as follows (see Appendix A):

$$A_1(p) = \frac{b^p G_-(p)\cos(\pi - \omega)p - Ql^p}{\mu_1 p \sin(\pi - \omega)p}, \tag{15a}$$

$$B_1(p) = b^p G_-(p)/\mu_1 p, \tag{15b}$$

$$A_2(p) = \frac{-2\alpha b^p G_-(p)\cos(\pi + \omega)p + Ql^p\{(\alpha + 1) + (\alpha - 1)\cos 2\omega p\}}{\mu_2 p F(p)}, \tag{15c}$$

$$B_2(p) = \frac{2\alpha b^p G_-(p)\sin(\pi + \omega)p + Ql^p(1 - \alpha)\sin 2\omega p}{\mu_2 p F(p)}, \tag{15d}$$

$$A_3(p) = \frac{-b^p G_-(p)\{(\alpha + 1)\cos(\pi + \omega)p + (1 - \alpha)\cos(\pi - \omega)p\} + 2Ql^p}{\mu_1 p F(p)}, \tag{15e}$$

$$B_3(p) = \frac{b^p G_-(p)}{\mu_1 p}, \tag{15f}$$

where

$$F(p) = (\alpha + 1)\sin(\pi + \omega)p + (\alpha - 1)\sin(\pi - \omega)p, \tag{15g}$$

$$\alpha = \mu_2/\mu_1. \tag{15h}$$

From (5a) and (5b), we know that $T_+(p)$ is analytic for $Rlp > \lambda - 1$ $(0 < \lambda < 1)$ while $G_-(p)$ is analytic for $Rlp < 1/2$.

Now $K(p)$ in (9) is decomposed as (see Appendix B)

$$K(p) = K_-(p)/K_+(p), \tag{16a}$$

where $K_+(p)$, analytic in the region $Rlp > -1/2$, is given by

$$K_+(p) = \mu_1 \pi \left(1 + \frac{\pi - \omega}{\pi + \omega}\gamma\right) \times p e^{\chi p} \frac{\Gamma(2p)}{\Gamma\left(\frac{\pi + \omega}{\pi}p\right)\Gamma\left(\frac{\pi - \omega}{\pi}p\right)} \prod_{k=1}^{\infty} \frac{1 + \frac{p}{p_k}}{1 + \frac{\pi + \omega}{k\pi}p} = \frac{\mu_1(\pi^2 - \omega^2)}{2\pi}\left(1 + \frac{\pi - \omega}{\pi + \omega}\gamma\right) p^2/K_-(-p). \tag{16b}$$

Here

$$\chi = -2\ln 2 + \frac{\pi + \omega}{\pi}\ln\frac{\pi + \omega}{\pi} + \frac{\pi - \omega}{\pi}\ln\frac{\pi - \omega}{\pi}, \tag{16c}$$

and p_k is the root in the right half of the p-plane (excluding zero) for

$$\sin(\pi + \omega)p + \gamma \sin(\pi - \omega)p = 0, \tag{16d}$$

which can be shown as

$$p_k = \frac{k + a_k}{\pi + \omega}\pi, \quad k = 1, 2, 3, \cdots, \ -1/2 < a_k < 1/2. \tag{16e}$$

The function $K_-(p)$ is analytic in the region $Rlp < 1/2$.

Downloaded 03 May 2010 to 171.66.16.20. Redistribution subject to ASME license or copyright; see http://www.asme.org/terms/Terms_Use.cfm

Equation (9) is now rearranged as

$$K_+(p)T_+(p)=K_-(p)G_-(p)-L(p), \tag{17a}$$

where

$$L(p)=K_-(p)E(p)/\cos\pi p, \tag{17b}$$

which is decomposed into (see Appendix B)

$$L(p)=L_-(p)+L_+(p)$$
$$=L_-(p)+\frac{1}{\pi}\sum_{n=1}^{\infty}\frac{(-1)^{n+1}}{p+\zeta_n}K_-(-\zeta_n)E(-\zeta_n). \tag{17c}$$

Here,

$$\zeta_n=n-1/2. \tag{17d}$$

The function $L_-(p)$ is analytic for $Rlp<1/2$ while $L_+(p)$ is analytic for $Rlp>-1/2$. We therefore rewrite (17a) as

$$K_+(p)T_+(p)+L_+(p)=K_-(p)G_-(p)-L_-(p), \tag{18}$$

where the left side is analytic for $Rlp>\text{Max}(-1/2, \lambda-1)$ and the right side for $Rlp<1/2$.

The argument of analytic continuation requires

$$K_+(p)T_+(p)+L_+(p)=K_-(p)G_-(p)-L_-(p)=C. \tag{19}$$

The constant C is easily determined from the behavior of $K_-(p)$, $G_-(p)$, and $L_-(p)$ at $p=0$, yielding

$$C=L_+(0). \tag{20}$$

Consequently, the unknown functions $T_+(p)$ and $G_-(p)$ are given by

$$T_+(p)=[L_+(0)-L_+(p)]/K_+(p), \tag{21a}$$

$$G_-(p)=[L_+(0)+L_-(p)]/K_-(p). \tag{21b}$$

Substituting (21b) into (15a) to (15f), $A_i(p)$ and $B_i(p)$ ($i=1, 2, 3$) are obtained, which in turn yields $\hat{W}(p, \theta)$ as in (7a) to (7c). Inversion of the Mellin transform using (8) results in

$$W(r,\theta)=\begin{cases}\dfrac{1}{2\pi i}\displaystyle\int_{c-i\infty}^{c+i\infty}\left\{\frac{[\sin(\pi+\omega)p+\gamma\sin(\pi-\omega)p]\cos(\pi-\theta)p}{\sin 2\pi p}b^pT_+(p)\right.\\ \qquad\left.+\dfrac{\sin\theta p}{\mu_1 p\cos\pi p}Ql^p\right\}r^{-p}dp, \quad \omega\le\theta\le\pi \text{ (Region I)}, & (22a)\\ \dfrac{1}{2\pi i}\displaystyle\int_{c-i\infty}^{c+i\infty}\left\{\frac{-2\cos(\pi+\theta)p\sin(\pi-\omega)p}{(1+\alpha)\sin 2\pi p}b^pT_+(p)\right.\\ \qquad\left.+\dfrac{\sin\theta p}{\mu_2 p\cos\pi p}Ql^p\right\}r^{-p}dp, \quad -\pi\le\theta\le 0 \text{ (Region II)}, & (22b)\\ \dfrac{1}{2\pi i}\displaystyle\int_{c-i\infty}^{c+i\infty}\left\{\frac{[-\cos(\pi+\theta)p+\gamma\cos(\pi-\theta)p]\sin(\pi-\omega)p}{\sin 2\pi p}b^pT_+(p)\right.\\ \qquad\left.+\dfrac{\sin\theta p}{\mu_1 p\cos\pi p}Ql^p\right\}r^{-p}dp, \quad 0\le\theta\le\omega \text{ (Region III)}, & (22c)\end{cases}$$

where

$$\lambda-1<c<1/2\ (0<\lambda<1),\ \alpha=\mu_2/\mu_1,\ \gamma=(\mu_2-\mu_1)/(\mu_2+\mu_1).$$

When $\mu_1=\mu_2$, (22b) is identical to (22c), and this result is in agreement with Choi and Earmme (1990). When $b=0$, this expression is the same as the one by Bassani and Erdogan (1979) if their result is applied to this problem.

4 Displacement and Stress Intensity Factor

The displacement and stress intensity factor are obtained as follows.

4.1 Case of Finite Kinked Length b. First let us consider the case ω (kink angle) $\neq 0$. The displacement near the crack tip is obtained by employing the local coordinate (ρ, Θ) as in Fig. 1 and expressing

$$r=b\left(1+\frac{\rho}{b}\cos\Theta\right)+0\left[\left(\frac{\rho}{b}\right)^2\right], \tag{23a}$$

$$\theta-\omega=\frac{\rho}{b}\sin\Theta+0\left[\left(\frac{\rho}{b}\right)^2\right] \quad \text{as } r\to b \text{ and } \theta\to\omega. \tag{23b}$$

The displacements $W(r, \theta)$ given in (22a) and (22c), respectively, are evaluated as $\rho\to 0$, both yielding

$$W(\rho,\Theta)=c_0+\frac{2L_+(0)}{\mu_1\sqrt{\pi^2-\omega^2}\left[1+\dfrac{\pi-\omega}{\pi+\omega}\gamma\right]^{1/2}}\left(\frac{\rho}{b}\right)^{1/2}\sin\frac{\Theta}{2}$$
$$+0(\rho), \quad -\pi\le\Theta\le\pi, \tag{24a}$$

where c_0 represents a rigid-body motion.

When $\omega=0$, region III disappears and the similar method with $W(r, \theta)$ in (22a) and (22b), respectively, leads to

$$W(\rho,\Theta)=\frac{2L_+(0)}{\mu_1\pi}\left(\frac{\rho}{b}\right)^{1/2}\sin\left(\frac{\Theta}{2}\right)+0(\rho), \quad 0\le\Theta\le\pi \text{ (Region I)},$$

$$=\frac{2L_+(0)}{\mu_2\pi}\left(\frac{\rho}{b}\right)^{1/2}\sin\left(\frac{\Theta}{2}\right)+0(\rho), \quad -\pi\le\Theta\le 0 \text{ (Region II)}. \tag{24b}$$

From (24a) and (24b) it can be shown that for any ω (including $\omega=0$) and $-\pi\le\Theta\le\pi$,

$$\sigma_{\Theta z}(\rho,\Theta)=\frac{K_{\text{III}}(b,\omega;\gamma)}{\sqrt{2\pi\rho}}\cos\frac{\Theta}{2}+0(1), \tag{25a}$$

$$\sigma_{\rho z}(\rho,\Theta)=\frac{K_{\text{III}}(b,\omega;\gamma)}{\sqrt{2\pi\rho}}\sin\frac{\Theta}{2}+0(1), \tag{25b}$$

where $K_{\text{III}}(b, \omega; \gamma)$ is defined by

$$K_{\text{III}}(b,\omega;\gamma)=\lim_{\rho\to 0}\sqrt{2\pi\rho}\,\sigma_{\Theta z}(\rho,0), \tag{25c}$$

whose value is evaluated using (24a) for $\omega\neq 0$ and (24b) for $\omega=0$, as

$$K_{\text{III}}(b,\omega;\gamma)=\frac{\sqrt{2\pi}L_+(0)}{\sqrt{\pi^2-\omega^2}\left(1+\dfrac{\pi-\omega}{\pi+\omega}\gamma\right)^{1/2}b^{1/2}}, \text{ for } \omega\neq 0 \tag{26a}$$

Downloaded 03 May 2010 to 171.66.16.20. Redistribution subject to ASME license or copyright; see http://www.asme.org/terms/Terms_Use.cfm

$$= \frac{\sqrt{2}\,L_+(0)}{\sqrt{\pi b}}, \quad \text{for } \omega = 0. \tag{26b}$$

From (26*a*) and (26*b*), it is seen that

$$\lim_{\omega \to 0} K_{\mathrm{III}}(b, \omega; \gamma) = K_{\mathrm{III}}(b, 0; \gamma)/(1+\gamma)^{1/2}, \tag{26c}$$

which shows that the stress intensity factor is discontinuous at $\omega = 0$. Formal similarity of (24*a*) and (26*a*) for the displacement and the shear stresses when $\omega \neq 0$ to the corresponding quantities of kinked crack in homogeneous materials (Choi and Earmme, 1990) is noted.

In particular, when $\omega = 0$, i.e., the crack lies in the interface without kink, it is known that the Mode III stress intensity factor is independent of the material constants of the bi-material (Sih and Chen, 1981) and that, accordingly, it is the same as for the crack in homogeneous material, which is in agreement with our result (26*b*). For the case of $\mu_1 = \mu_2$ ($\gamma = 0$), the results such as (24*a*), (24*b*), (25*a*), (25*b*), (26*a*), and (26*b*) are identical to those of Choi and Earmme (1990).

Denoting $K_{\mathrm{III}}^{\mathrm{nor}}(b, \omega; \gamma)$ by

$$K_{\mathrm{III}}^{\mathrm{nor}}(b, \omega; \gamma) = K_{\mathrm{III}}(b, \omega; \gamma)/K_{\mathrm{III}}^0, \tag{27}$$

where $K_{\mathrm{III}}^0 = \sqrt{2}Q/\sqrt{\pi l}$, which is the stress intensity factor for $b = 0$ (without kink), irrespective of whether the crack lies in the interface or in the homogeneous material. Using (16*b*) and (17*c*), it can be seen that

$$K_{\mathrm{III}}^{\mathrm{nor}}(b, \omega; \gamma) = \frac{\left(\frac{\pi-\omega}{\pi+\omega}\right)^{\omega/2\pi}}{\left[1+\frac{\pi-\omega}{\pi+\omega}\gamma\right]^{1/2}} \prod_{k=1}^{\infty} \frac{1+\frac{\pi+\omega}{2k\pi}}{1+\frac{1}{2p_k}}$$

$$+ \frac{\sqrt{\pi^2-\omega^2}}{2\pi^2\left[1+\frac{\pi-\omega}{\pi+\omega}\gamma\right]^{1/2}} \sum_{n=2}^{\infty}$$

$$\times \left[(-1)^{n+1} e^{-\chi\zeta_n} \frac{\Gamma\left(\frac{\pi-\omega}{\pi}\zeta_n\right)\Gamma\left(\frac{\pi+\omega}{\pi}\zeta_n\right)}{\Gamma(2\zeta_n)} \left(\frac{b}{l}\right)^{\zeta_n - 1/2} \right.$$

$$\left. \times \cos(\omega\zeta_n) \prod_{k=1}^{\infty} \frac{1+\frac{\pi+\omega}{k\pi}\zeta_n}{1+\frac{\zeta_n}{p_k}} \right]$$

$$= \left(1+\frac{b}{l}\right)^{-1/2} \quad \text{for } \omega \neq 0 \tag{28a}$$

$$\text{for } \omega = 0. \tag{28b}$$

Here, χ, p_k, and ζ_n are given in (16*c*), (16*e*), and (17*d*), respectively. Equations (28*a*) and (28*b*) reduce to the stress intensity factor for the case of a kinked crack in a homogeneous material (Choi and Earmme (1990)) for $\mu_1 = \mu_2$ ($\gamma = 0$).

4.2 Case of Kinked Length $b \to 0$. Choi and Earmme (1990) showed that as $b \to 0$, the stress intensity factor, which inherently involves the limit as ρ (the distance from the crack tip) $\to 0$, depends on the order of performing the two limiting processes, i.e., $b \to 0$ and $\rho \to 0$. The displacements in (22*a*) and (22*c*) are expressed in the local coordinate system (ρ, Θ) to obtain the stress intensity factor as

$$\lim_{b \to 0} K_{\mathrm{III}}(b, \omega; \gamma) = \lim_{\substack{\rho \to 0 \\ b \to 0}} \sqrt{2\pi\rho}\, \sigma_{\Theta z}(\rho, 0)$$

$$= \lim_{\substack{\rho \to 0 \\ b \to 0}} \sqrt{2\pi\rho}\, \mu_1 \frac{1}{\rho} \frac{\partial}{\partial \Theta} W(\rho, 0). \tag{29}$$

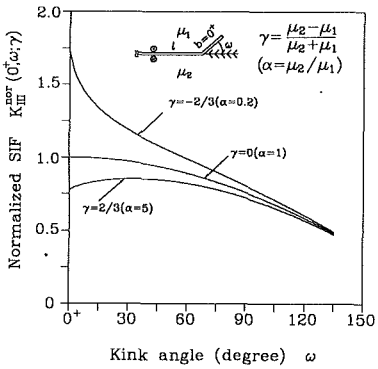


Fig. 2 Normalized stress intensity factor, $K_{\mathrm{III}}^{\mathrm{nor}}(0^+, \omega; \gamma)$ with kinked length b approaching zero is plotted against kink angle ω for various values of α

In performing the limit process, we take $\rho \to 0$ first and $b \to 0$ next, which means $\rho/b = o(1)$, $b \to 0$. Although there can be other methods in regard to the order of the limit processes, as described by Choi and Earmme (1990), the procedure we employed is preferred since it has physical meaning if we are interested in whether an existing crack will tend to propagate in the crack plane or kink out. Also, it will be seen later in Section 5 that the energy release rate $G(b = 0^+, \omega; \gamma)$ is related to the stress intensity factor as in (35*a*) only if we compute (29) based on the present method of taking the limit. It is, therefore, justified that we put $b = 0$ in (28*a*) and (28*b*) for this case of $b \to 0$, which results in

$$K_{\mathrm{III}}^{\mathrm{nor}}(0^+, \omega; \gamma) = \frac{\left(\frac{\pi-\omega}{\pi+\omega}\right)^{\omega/2\pi}}{\left[1+\frac{\pi-\omega}{\pi+\omega}\gamma\right]^{1/2}} \prod_{k=1}^{\infty} \frac{1+\frac{\pi+\omega}{2k\pi}}{1+\frac{1}{2p_k}}, \quad \omega \neq 0, \tag{30}$$

$$= 1, \quad \omega = 0. \tag{31}$$

4.3 Results. The normalized stress intensity factor, $K_{\mathrm{III}}^{\mathrm{nor}}(b, \omega; \gamma)$ as $b \to 0$ as evaluated from (30) and (31) is shown in Fig. 2 for various values of α. Figure 3(*a*) shows $K_{\mathrm{III}}^{\mathrm{nor}}(b, \omega; \gamma)$ given by (28*a*) and (28*b*) for finite b as a function of b, varying the kink angle ω with α ($= \mu_2/\mu_1$) $= 5$ ($\gamma = 2/3$). Notice the discontinuity of $K_{\mathrm{III}}^{\mathrm{nor}}$ at $\omega = 0$. Figure 3(*b*) shows $K_{\mathrm{III}}^{\mathrm{nor}}(b, \omega; \gamma)$ with the same condition as in Fig. 3(*a*) except for $\alpha = 0.2$ here. The normalized stress intensity factor $K_{\mathrm{III}}^{\mathrm{nor}}(b, \omega; \gamma)$ is plotted in Fig. 4(*a*) and 4(*b*) as a function of ω, varying b/l for $\alpha = 5$ and $\alpha = 0.2$, respectively.

5 Energy Release Rate

Since we are interested in the direction of an interfacial crack (initially straight) propagation, we focus our attention to the energy release rate when $b = 0$. As dealt with by Choi and Earmme (1990), the energy release rate $G(b = 0^+, \omega; \gamma)$ when the crack propagates in the direction of ω is given by

$$G(b = 0^+, \omega; \gamma) = \lim_{b \to 0} \frac{U(b) - U(0)}{b}, \tag{32}$$

where

$$U(b) - U(0) = \frac{1}{2} Q[\Delta W(l, \pi) - \Delta W(l, -\pi)], \tag{33}$$

Δ being the difference between a crack of kinked length b and a crack of $b = 0$.

Using (22*a*) and (22*b*), we can show that

Downloaded 03 May 2010 to 171.66.16.20. Redistribution subject to ASME license or copyright; see http://www.asme.org/terms/Terms_Use.cfm

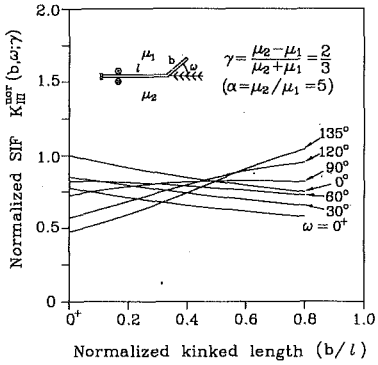


Fig. 3(*a*) Normalized stress intensity factor, $K_{III}^{nor}(b, \omega; \gamma)$ ((28*a*) and (28*b*)) as a function of *b/l*, for $\alpha = 5$

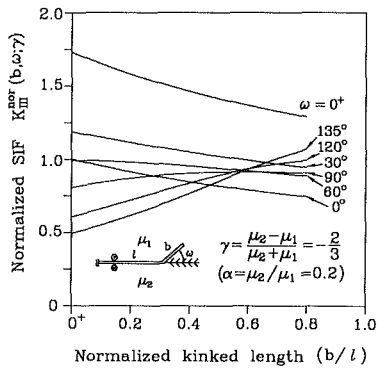


Fig. 3(*b*) Normalized stress intensity factor, $K_{III}^{nor}(b, \omega; \gamma)$ ((28*a*) and (28*b*)) as a function of *b/l*, for $\alpha = 0.2$

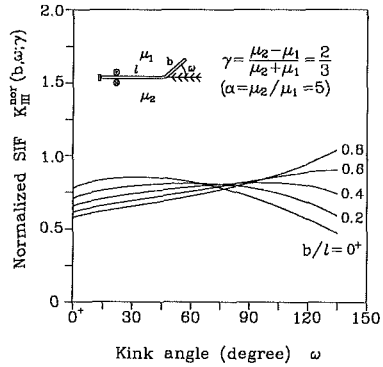


Fig. 4(*a*) Normalized stress intensity factor, $K_{III}^{nor}(b, \omega; \gamma)$ ((28*a*) and (28*b*)) as a function of ω, for $\alpha = 5$

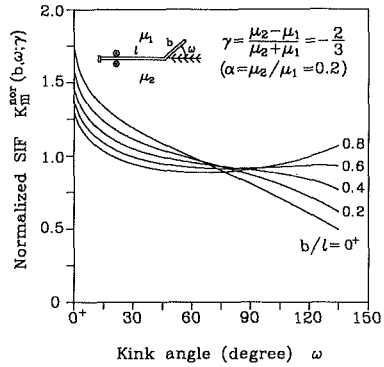


Fig. 4(*b*) Normalized stress intensity factor, $K_{III}^{nor}(b, \omega; \gamma)$ ((28*a*) and (28*b*)) as a function of ω, for $\alpha = 0.2$

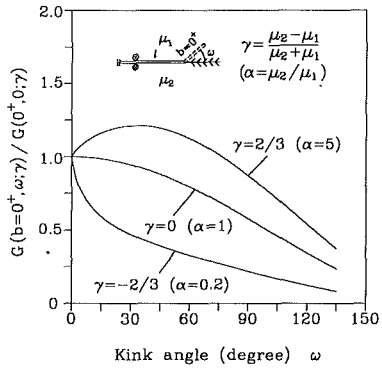


Fig. 5 Normalized energy release rate $G(0^+, \omega; \gamma)/G(0^+, 0; \gamma)$ ((34*a*) and (34*b*)) is plotted as a function of ω for various values of α

$$G(0^+, \omega; \gamma)=\frac{\left(\frac{\pi-\omega}{\pi+\omega}\right)^{\omega/\pi}}{2\mu_1\left[1+\frac{\pi-\omega}{\pi+\omega}\gamma\right]}\left[\prod_{k=1}^{\infty}\frac{1+\frac{\pi+\omega}{2k\pi}}{1+\frac{1}{2p_k}}\right]^2\frac{2Q^2}{\pi l},\quad \omega\neq 0, \tag{34a}$$

$$=\frac{1}{2\mu_1(1+\gamma)}\frac{2Q^2}{\pi l},\quad \omega=0. \tag{34b}$$

Comparison of (34*a*) with (34*b*) shows that the energy release rate G is continuous at $\omega=0$ while the stress intensity factor K_{III}^{nor} is discontinuous as seen in Sections 4.1 and 4.2. The energy release rate G in (34*a*) and (34*b*) can be written as

$$G(0^+, \omega; \gamma)=\frac{1}{2\mu_1}[K_{III}(0^+, \omega; \gamma)]^2,\qquad \omega\neq 0, \tag{35a}$$

$$=\frac{1}{4}\left(\frac{1}{\mu_1}+\frac{1}{\mu_2}\right)[K_{III}(0^+, \omega; \gamma)]^2,\quad \omega=0, \tag{35b}$$

where

$$K_{III}(0^+, \omega; \gamma)=K_{III}^{nor}K_{III}^{0}=K_{III}^{nor}(0^+, \omega; \gamma)\frac{\sqrt{2}}{\sqrt{\pi l}}Q.$$

Formal similarities of (35*a*) to the well-known relation in a homogeneous straight crack and (35*b*) to the result of a straight interfacial crack are also noted.

The kinked crack, as $b\to 0$, has been studied in conjunction with the direction of the interfacial crack propagation. One of the widely used criteria is the "Maximum Energy Release Rate Criterion." It is therefore important to determine G as a function of kink angle ω and the material constants. In Fig. 5, $G(0^+, \omega; \gamma)/G(0^+, 0; \gamma)$, where $G(0^+, 0; \gamma)(=1/2(1/\mu_1+1/\mu_2)Q^2/\pi l)$ is the energy release rate for the straight interfacial crack is plotted as a function of ω for $\alpha\,(=\mu_2/\mu_1)=0.2$, 1, and 5. For $\alpha=5$, i.e., kinking into the more compliant material it is larger than 1 for some ω, which is also observed by He and Hutchinson (1989) and Mukai et al. (1990) for an in-plane problem.

6 Conclusion

A kinked interfacial crack under antiplane loading is analyzed and a closed-form solution is obtained. Various limiting cases of kinked length $b\to 0$, kink angle $\omega\to 0$, and $\mu_1=\mu_2$, respectively, are studied and some of the results are compared with the existing solutions if any, confirming the validity of the solution.

It is found that

(i) the stresses near the tip have the $r^{-1/2}$ singularity in contrast to the result by Theocaris and Makrakis (1987);

Downloaded 03 May 2010 to 171.66.16.20. Redistribution subject to ASME license or copyright; see http://www.asme.org/terms/Terms_Use.cfm

(ii) as the kink angle $\omega \to 0$, the stress intensity factor K_{III} is different from the value at $\omega = 0$, showing the discontinuous behavior at $\omega = 0$. On the other hand, the energy release rate G is continuous at $\omega = 0$;

(iii) the energy release rate G becomes larger when the interfacial crack kinks into the more compliant material, suggesting the possible kinking of the interfacial crack.

References

Bassani, J. B., and Erdogan, F., 1979, "Stress Intensity Factors in Bonded Half Planes Containing Inclined Cracks Subjected to Antiplane Shear Loading," *Int. Journal of Fracture*, Vol. 15, pp. 145–158.

Choi, S. R., and Earmme, Y. Y., 1990, "Analysis of a Kinked Crack in Anti-Plane Shear," *Mechanics of Materials*, Vol. 9, pp. 195–204.

Hayashi, K., and Nemat-Nasser, S., 1981, "On Branched, Interface Cracks," ASME JOURNAL OF APPLIED MECHANICS, Vol. 48, pp. 529–533.

He, M. Y., and Hutchinson, J. W., 1989, "Kinking of a Crack out of an Interface," ASME JOURNAL OF APPLIED MECHANICS, Vol. 56, pp. 270–278.

Karihaloo, B. L., 1982, "On Crack Kinking and Curving," *Mechanics of Materials*, Vol. 1, pp. 189–201.

Mukai, D. J., Ballarini, R., and Miller, G. R., 1990, "Analysis of Branched Interface Cracks," ASME JOURNAL OF APPLIED MECHANICS, Vol. 57, pp. 887–893.

Noble, B., 1958, *Methods Based on the Wiener-Hopf Technique*, Pergamon Press, London.

Rice, J. R., 1988, "Elastic Fracture Mechanics Concepts for Interfacial Cracks," ASME JOURNAL OF APPLIED MECHANICS, Vol. 55, pp. 98–103.

Sih, G. C., and Chen, E. P., 1981, "Interface Cracks in Bimaterial Systems," *Mechanics of Fracture*, Vol. 6, G. C. Sih, ed., Martinus Nijhoff Publishers, The Hague, pp. 117–177.

Theocaris, P. S., and Makrakis, G., 1987, "Crack Kinking in Anti-plane Shear Solved by the Mellin Transform," *Int. Journal of Fracture*, Vol. 34, pp. 251–262.

Williams, M. L., 1959, "The Stress Around a Fault or Crack in Dissimilar Media," *Bull. Seismological Soc. America*, Vol. 49, pp. 199–204.

APPENDIX A

Derivation of Wiener-Hopf Eq. (9)

By Mellin transforming $r\sigma_{\theta zi}$ and $r\sigma_{rzi}$ given in (2) and (3), respectively, we obtain

$$M\{r\sigma_{\theta zi};\, p\} = \mu_i \frac{d}{d\theta}\hat{W}(p,\, \theta), \tag{A1}$$

$$M\{r\sigma_{rzi};\, p\} = -\mu_i p \hat{W}(p,\, \theta), \tag{A2}$$

where $\hat{W}(p, \theta)$ is given in (6a).

The first equality of (4a) is used, yielding

$$\mu_1 \frac{d}{d\theta}\hat{W}(p,\, \pi) = Q l^p. \tag{A3}$$

Equation (7a) is substituted into (A3), to give

$$-\mu_1 p A_1(p)\sin(\pi-\omega)p + \mu_1 p B_1(p)\cos(\pi-\omega)p = Q l^p. \tag{A4}$$

Similarly, from the second equality of (4a), we have

$$\mu_2 p A_2(p)\sin(\pi+\omega)p + \mu_2 p B_2(p)\cos(\pi+\omega)p = Q l^p. \tag{A5}$$

From (4e) it is seen that

$$\mu_1 \frac{d}{d\theta}\hat{W}(p,\, 0^+) = \mu_2 \frac{d}{d\theta}\hat{W}(p,\, 0^-). \tag{A6}$$

Substituting (7b) and (7c) into (A6) we have

$$\mu_1 p A_3(p)\sin\omega p + \mu_1 p B_3(p)\cos\omega p = \mu_2 p A_2(p)\sin\omega p + \mu_2 p B_2(p)\cos\omega p. \tag{A7}$$

Equations (4f) results in

$$\hat{W}(p,\, 0^+) = \hat{W}(p,\, 0^-). \tag{A8}$$

Substituting (7b) and (7c) into (A8), we have

$$A_3(p)\cos\omega p - B_3(p)\sin\omega p = A_2(p)\cos\omega p - B_2(p)\sin\omega p. \tag{A9}$$

Let us define $G_-(p)$ by

$$G_-(p) \equiv b\int_1^\infty \sigma_{\theta z}(r,\, \omega)(r/b)^p d(r/b). \tag{A10}$$

Then it is seen from (5b) that $G_-(p)$ is analytic in the region of $Rlp < 1/2$. From the first equality of (4b) together with (A1), we are led to

$$\mu_1 p B_1(p) = b^p G_-(p). \tag{A11}$$

In an analogous way we can also prove that

$$\mu_1 p B_3(p) = b^p G_-(p). \tag{A12}$$

Let us define $T_+(p)$ as

$$T_+(p) \equiv \int_0^1 [W(r,\, \omega^+) - W(r,\, \omega^-)](r/b)^{p-1} d(r/b). \tag{A13}$$

From (4d) together with (7a) and (7c), we get

$$A_1(p) - A_3(p) = b^p T_+(p). \tag{A14}$$

It is easily seen from (5a) that $T_+(p)$ is analytic in the region, $Rlp > \lambda - 1$. Substituting (A4), (A5), (A7), (A9), (A11), and (A12) into (A14), we obtain (9). The relations of $A_i(p)$ and $B_i(p)$ $(i = 1, 2, 3)$ with $G_-(p)$ as shown in (15a) to (15f) are obtained during this procedure.

APPENDIX B

Decomposition of $K(p)$, (16a) and $L(p)$, (17c)

Equation (10) is reproduced here as

$$K(p) = \frac{\sin(2\pi p)}{\mu_1 p \sin(\pi-\omega)p\,[\sin(\pi+\omega)p + \gamma\sin(\pi-\omega)p]}.$$

Expressing the trigonometric functions in terms of infinite product,

$$K(p) = \frac{2\pi}{\mu_1(\pi^2-\omega^2)\left(1+\frac{\pi-\omega}{\pi+\omega}\gamma\right)p^2}\prod_{k=1}^{\infty} \times \frac{\left(1-\frac{2p}{k}\right)\left(1+\frac{2p}{k}\right)}{\left(1-\frac{\pi-\omega}{k\pi}p\right)\left(1+\frac{\pi-\omega}{k\pi}p\right)\left(1-\frac{p}{p_k}\right)\left(1+\frac{p}{p_k}\right)} \tag{B1}$$

from which we can write

$$K(p) = K_-(p)/K_+(p), \tag{B2}$$

where

$$K_+(p) = \frac{\mu_1(\pi^2-\omega^2)}{2\pi}\left(1+\frac{\pi-\omega}{\pi+\omega}\gamma\right)p^2 e^{xp}\prod_{k=1}^{\infty} \times \frac{\left(1+\frac{\pi-\omega}{k\pi}p\right)\left(1+\frac{p}{p_k}\right)}{\left(1+\frac{2}{k}p\right)} \tag{B3}$$

and

$$K_-(p) = e^{xp}\prod_{k=1}^{\infty} \frac{\left(1-\frac{2p}{k}\right)}{\left(1-\frac{\pi-\omega}{k\pi}p\right)\left(1-\frac{p}{p_k}\right)}. \tag{B4}$$

Here p_k is the root in the right half of the p plane (excluding zero) for

$$\sin(\pi+\omega)p + \gamma\sin(\pi-\omega)p = 0, \tag{B5}$$

Downloaded 03 May 2010 to 171.66.16.20. Redistribution subject to ASME license or copyright; see http://www.asme.org/terms/Terms_Use.cfm

which can be written as

$$p_k = \frac{t_k}{\pi+\omega}\pi, \tag{B6}$$

where $t_k = k + a_k$, $-1/2 < a_k < 1/2$. The value χ given in (B3) and (B4) is to be determined from the behavior of $K_+(p)$ and $K_-(p)$ as $|p| \to \infty$. Expressing $K_+(p)$ in terms of the gamma function, we have

$$K_+(p) = \mu_1 \pi \left(1 + \frac{\pi-\omega}{\pi+\omega}\gamma\right) p e^{\chi p} \times \frac{\Gamma(2p)}{\Gamma\left(\frac{\pi+\omega}{\pi}p\right)\Gamma\left(\frac{\pi-\omega}{\pi}p\right)} \prod_{k=1}^{\infty} \frac{1+\frac{p}{p_k}}{1+\frac{\pi+\omega}{k\pi}p}. \tag{B7}$$

In passing we mention that the term of the infinite product on the right side of (B7) has constant value as $|p| \to \infty$. In order to have the nonexponential behavior of $K_+(p)$ as $|p| \to \infty$, χ turns out to be

$$\chi = -2\ln 2 + \frac{\pi+\omega}{\pi}\ln\left(\frac{\pi+\omega}{\pi}\right) + \frac{\pi-\omega}{\pi}\ln\left(\frac{\pi-\omega}{\pi}\right). \tag{B8}$$

On the other hand, the decomposition of $L(p)$, (17c) is performed as follows. Equation (17b) is reproduced here as

$$L(p) = K_-(p)E(p)/\cos \pi p, \tag{B9}$$

where $K_-(p)$ and $E(p)$ are given in (B4) and (11), respectively. Therefore, we write

$$\begin{aligned} L(p) &= L_+(p) + L_-(p) \\ &= K_-(p)E(p)\left[\frac{1}{\pi}\sum_{n=1}^{\infty}\frac{(-1)^n}{p-\zeta_n} - \frac{1}{\pi}\sum_{n=1}^{\infty}\frac{(-1)^n}{p+\zeta_n}\right] \\ &= K_-(p)E(p)\frac{1}{\pi}\sum_{n=1}^{\infty}\frac{(-1)^n}{p-\zeta_n} - \frac{1}{\pi}\sum_{n=1}^{\infty}\frac{(-1)^n}{p+\zeta_n} \\ &\quad \times \{K_-(p)E(p) - K_-(-\zeta_n)E(-\zeta_n)\} \\ &\quad - \frac{1}{\pi}\sum_{n=1}^{\infty}\frac{(-1)^n}{p+\zeta_n}K_-(-\zeta_n)E(-\zeta_n) \end{aligned} \tag{B10}$$

where

$$\zeta_n = n - \frac{1}{2}.$$

From (B10) we can see that

$$\begin{aligned} L_+(p) &= -\frac{1}{\pi}\sum_{n=1}^{\infty}\frac{(-1)^n}{p+\zeta_n}K_-(-\zeta_n)E(-\zeta_n) \\ &= L(p) - L_-(p). \end{aligned} \tag{B11}$$

Here $L_+(p)$ is analytic in the region $Rlp > -1/2$, while $L_-(p)$ is analytic in the region $Rlp < 1/2$.

Downloaded 03 May 2010 to 171.66.16.20. Redistribution subject to ASME license or copyright; see http://www.asme.org/terms/Terms_Use.cfm

A Progressive Damage Modeling Based on the Continuum Damage Mechanics and its Finite Element Analysis

Seung Jo Kim
Assoc. Professor.

Wie Dae Kim
Post Doctoral Fellow.

Department of Aerospace Engineering,
Seoul National University,
Kwanak-Ku, Seoul, 151-742, Korea

A continuum damage modeling based on the theory of materials of type N *is proposed and its nonlinear finite element approximation and numerical simulation are carried out. To solve the finite elastoplasticity problems, the reasonable kinematical strain measure for large deformed solids are introduced and constitutive relations based on the theory of materials of type* N *are derived. These highly nonlinear equations are reduced to the incremental weak formulation and approximated by the theory of nonlinear finite element method. To verify the theory and the computer code, the computational simulation of the uniaxial elongation is carried out and the results are compared with the actual experiment. Two example problems, bending problem and billet forming problem, are simulated, and the deformed shapes and the progressive results of the damage variable are presented.*

1 Introduction

Engineering materials under severe and repeated loads produce microscopic cracks and defects. These cracks and defects which are moved and coalesced through plastic deformation cause the decrease of strength, stiffness, toughness, stability, and residual life of structures. The detail process of deterioration in mechanical properties of a material is not so simple and clear. But in macroscopic sense, it can be assumed that micro defects and cracks are continuously distributed in a material. So, the continuum mechanics approach can be used for the analysis of damage progress of a material.

Continuum damage modeling, pioneered by Kachanov (1958), has become one of active subject of researches in recent years. Kachanov introduced a damage variable and it was used to set up inelastic constitutive equations for creep materials. Many other researchers introduced damage variable as a scalar, vector, or tensor quantity for the effective representation of damage phenomena of several kinds of materials under creep, fatigue, or other loading conditions.

Leckie and Hayhurst (1974) studied the creep rupture of structures with a scalar damage variable. Dragon and Mroz (1979) proposed a continuum damage model with a second-order damage tensor and used the flow potential concept for rock-like material. Krajcinovic (1979, 1981, 1984) studied the damage of brittle material and reviewed (1984, 1985) continuum damage mechanics pertaining to damage variable and kinetic equations. Chaboche presented the general damage theory (1982) and reviewed the general concept of damage mechanics (1988) relating to damage measure, description of the mechanical behavior of the damaged material, and damage evolution equations. This review shows the guideline of research on the continuum damage mechanics. Simo and Ju (1987) developed general continuum elastoplastic damage models employing irreversible thermodynamics and internal state variable within two alternative dual states, strain and stress-based formulation, and showed that computational results were in good agreement with experiments. Lemaitre and Dufailly (1987) proposed direct and nondirect measurement of damage with eight different methods. Combescure and Jiaju (1990) generalized the discrete Kirchhoff theory to the analysis for larger displacement/rotation and large strain elasto-plastic response of general shell structures and developed a ductile damage model. A generalization of the theory of materials of type N to continuum damage mechanics was presented by Kim and Oden (1988).

The aforementioned papers tried to make the foundations in the following aspects:

(a) definition and measure of damage by appropriate mechanical variables,
(b) description of the mechanical behavior of a damaged material by effective and reasonable framework of theory, and
(c) formulation of damage evolution equations.

To define the damaged state the following quantities were used: damaged area reduction ratio, effective stress concept,

Contributed by the Applied Mechanics Division of The American Society of Mechanical Engineers for publication in the ASME Journal of Applied Mechanics.

Discussion on this paper should be addressed to the Technical Editor, Professor Lewis T. Wheeler, Department of Mechanical Engineering, University of Houston, Houston, TX 77204-4792, and will be accepted until four months after final publication of the paper itself in the ASME Journal of Applied Mechanics.

Manuscript received by the ASME Applied Mechanics Division, July 5, 1991; final revision, June 22, 1992. Associate Technical Editor: A. K. Noor.

Copyright © 1994 by ASME
Downloaded 03 May 2010 to 171.66.16.20. Redistribution subject to ASME license or copyright; see http://www.asme.org/terms/Terms_Use.cfm

or residual life in fatigue damage, etc. Since the damage propagation phonomenon is an irreversible process, thermodynamic theory would be adequate to describe the mechanical behavior of a damaged material. Also, elaborate kinematics would be required to describe the large deformation of a material under damaging process.

In this paper, a progressive damage modeling based on the theory of materials of type N, which is the formalization of the continuum damage mechanics, is attempted. To accommodate the expected large deformation, the strain measures are introduced by defining appropriate intermediate configurations. It is necessary to characterize material damage constants appearing in the constitutive relations by experiments. But in a practical situation, the characterization of damage constants is not easy even in the case of isotropic damage assumption. We also attempted to characterize the damage constants by experiments under the assumption of isotropic damage, and this result is used for the analysis of damage progress. The stiffness degradation is chosen as a damage measure for the quantification of damaged states and for the computation by macroscopic variable, and experiments are performed to obtain the material constants. The derived nonlinear equations are reduced to the incremental weak formulation and approximated by the theory of the nonlinear finite element method. To verify the theory and the computer code, a computational simulation of the uniaxial elongation is compared with the experimental result and two example problems, bending and forming problem, are simulated.

2 Elasto-plastic Damage Model

2.1 Kinematics. Anticipating very large deformations we start from new kinematical definitions. These might solve the issues on the objective stress rates and its conjugate strain measures.

A material body B moves through space R^3. To trace the motion of body B we establish an absolutely fixed frame of reference so that each point X in the body B can be identified by their corresponding positions $\mathbf{X}$ through the map

$$\begin{aligned} &\mathbf{k}_o : B \to R^3 \\ &\mathbf{X} = \mathbf{k}_o(X). \end{aligned} \tag{1}$$

The image of this mapping $\mathbf{k}_o(B)$ will be denoted by C_o, which is named reference configuration. The spatial position $\mathbf{x}$ of a particle X at time t is then given by a relation of the type

$$\begin{aligned} &\mathbf{x} = \chi(\mathbf{X}, t) \\ &\mathbf{X} \in C_o,\ t \geq 0 \end{aligned} \tag{2}$$

and χ a continuous invertable map from C_o into R^3. The image $\chi(\mathbf{X}, t)$ will be called the spatial configuration or current configuration C_t at time t. The deformation gradient $\mathbf{F}$ as a measure of deformation at $\mathbf{X}$ at time t is defined by

$$\mathbf{F} = \nabla_{\mathbf{X}} \mathbf{x} = \frac{\partial \chi}{\partial \mathbf{X}}. \tag{3}$$

According to the polar decomposition theorem (Gurtin, 1981), the deformation gradient $\mathbf{F}$ can be represented as the decomposition

$$\mathbf{F} = \mathbf{RU} = \mathbf{VR}, \tag{4}$$

where $\mathbf{U}(\mathbf{V})$ is a right (left) stretch tensor of $\mathbf{F}$ and $\mathbf{R}$ is a positive definite orthogonal rotation tensor.

Having in mind these issues, we start decomposition by introducing the rotation-free current configuration C_{t-} as in Fig. 1. Here

$$\overline{OA}_{C_o} = \mathbf{X} + \Delta\mathbf{X} \tag{5}$$

and

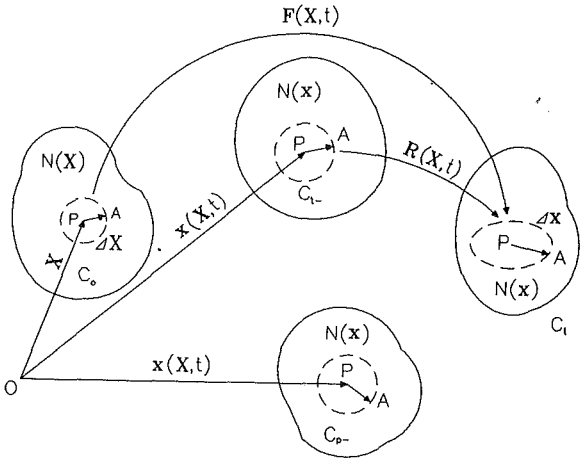


Fig. 1 Configurations by the right polar decomposition

$$\begin{aligned} \overline{OA}_{C_{t-}} &= \mathbf{x} + \mathbf{R}^{-1}\Delta\mathbf{x} \\ &= \chi(\mathbf{X}, t) + \mathbf{U}(\mathbf{X}, t)\Delta\mathbf{X} + \mathbf{W}_1(\mathbf{X}, t, \Delta\mathbf{X}), \end{aligned} \tag{6}$$

where

$$\lim_{\|\Delta X\| \to 0} \frac{1}{\|\Delta\mathbf{X}\|} \|\mathbf{W}_1(\mathbf{X}, t, \Delta\mathbf{X})\| = 0 \tag{7}$$

and $\|\cdot\|$ denotes the Euclidean norm.

Now let us consider an intermediate configuration C_{p-} which may correspond to a rotation-free state at the initial stress level σ_o. Then

$$\overline{OA}_{p-} = \chi(\mathbf{X}, t) + \mathbf{U}^p(\mathbf{X}, t)\Delta\mathbf{X} + \mathbf{W}_2(\mathbf{X}, t, \Delta\mathbf{X}) \tag{8}$$

and $\mathbf{W}_2$ has the same asymptotic behavior with respect to $\|\Delta\mathbf{X}\|$ as does $\mathbf{W}_1$.

We next introduce a second-order tensor $\mathbf{U}^e$ which represents the elastic stretch tensor and is defined by

$$\begin{aligned} \mathbf{U}^e(\mathbf{X}, t)\Delta\mathbf{X} - \Delta\mathbf{X} &= \overline{OA}_{C_{t-}} - \overline{OA}_{C_{p-}} \\ &= [\mathbf{U}(\mathbf{X}, t) - \mathbf{U}^p(\mathbf{X}, t)]\Delta\mathbf{X} + \mathbf{W}_1(\mathbf{X}, t, \Delta\mathbf{X}) \\ &\quad - \mathbf{W}_2(\mathbf{X}, t, \Delta\mathbf{X}). \end{aligned} \tag{9}$$

Thus, in the limit as $|\Delta\mathbf{X}| \to 0$, we have

$$\mathbf{U} = \mathbf{U}^e + \mathbf{U}^p - \mathbf{I} \tag{10}$$

and the relation (3) gives

$$\mathbf{F} = \mathbf{RU}^e + \mathbf{RU}^p - \mathbf{R} \tag{11}$$

and

$$\mathbf{L} = \dot{\mathbf{F}}\mathbf{F}^{-1} = \dot{\mathbf{R}}\mathbf{R}^t + \mathbf{R}(\dot{\mathbf{U}}^e\mathbf{U}^{-1} + \dot{\mathbf{U}}^p\mathbf{U}^{-1})\mathbf{R}^t \tag{12}$$

$$\mathbf{D} = \mathbf{L}|_{\text{sym}} = \mathbf{R}(\dot{\mathbf{U}}^e\mathbf{U}^{-1}|_{\text{sym}} + \dot{\mathbf{U}}^p\mathbf{U}^{-1}|_{\text{sym}})\mathbf{R}^t. \tag{13}$$

Here $\mathbf{L}|_{\text{sym}}$ represents the symmetric part of $\mathbf{L}$.

One can define the elastic and the plastic strain rates as

$$\dot{\mathbf{E}} = \dot{\mathbf{U}}^e\mathbf{U}^{-1}|_{\text{sym}} \tag{14}$$

$$\dot{\mathbf{P}} = \dot{\mathbf{U}}^p\mathbf{U}^{-1}|_{\text{sym}} \tag{15}$$

and

$$\mathbf{R}^t\mathbf{D}\mathbf{R} = \dot{\mathbf{E}} + \dot{\mathbf{P}}. \tag{16}$$

The elastic and the plastic strain tensors can be defined by

$$\mathbf{E} = \int_0^t \dot{\mathbf{U}}^e\mathbf{U}^{-1}|_{\text{sym}} dt \tag{17}$$

$$\mathbf{P} = \int_0^t \dot{\mathbf{U}}^p\mathbf{U}^{-1}|_{\text{sym}} dt. \tag{18}$$

Of course, it may be argued that this decomposition is still

Downloaded 03 May 2010 to 171.66.16.20. Redistribution subject to ASME license or copyright; see http://www.asme.org/terms/Terms_Use.cfm

imperfect since the definition involves the total stretch $\mathbf{U}$, but $\mathbf{U}$ is a well-defined kinematical property of the motion independent of the choice of C_p and (16) is a natural consequence of this formulations.

2.2 Theory of Materials of Type N. The theory of materials of type N (Kim, 1984, 1985) consists of field equations and two potentials from which the necessary constitutive equations result.

The thermomechanical behavior of the body B is governed by the principles of conservation of mass, energy, balance of linear and angular momentum, and the law of entropy production. Local forms of these principles can be written as follows:

- conservation of mass

$$\rho \mathrm{Det}\mathbf{F} = \rho_o \tag{19}$$

- balance of linear and angular momentum

$$\mathrm{div}\sigma + \rho\mathbf{b} = \rho\ddot{\mathbf{x}} \tag{20}$$

$$\sigma = \sigma^t \tag{21}$$

- conservation of energy

$$\rho\dot{e} = \mathrm{tr}(\sigma\mathbf{L}) - \mathrm{div}\mathbf{q} + \rho r \tag{22}$$

- law of entropy production—Clausius-Duhem inequality

$$\rho\dot{\eta} + \mathrm{div}\,\frac{\mathbf{q}}{\theta} - \rho\frac{r}{\theta} \geq 0. \tag{23}$$

Here, ρ_o is the mass density in the reference configuration, ρ the mass density, σ the Cauchy stress, $\mathbf{b}$ the body force per unit mass, e the specific internal energy, $\mathbf{q}$ the heat flux vector, r the heat supply per unit mass per unit time, η the specific entropy, and θ the absolute temperature. It is convenient to introduce free-energy density ϕ instead of the internal energy density e by

$$\phi = e - \eta\theta. \tag{24}$$

The second assumption is the existence of the following functions.

(i) There exist functions ϕ, Σ, N, and $\mathbf{Q}$ of $(\mathbf{E}, \theta, \mathbf{g}, \alpha, \mathbf{d})$ which define the free energy, stress, entropy, and heat flux at each particle $\mathbf{X} \in B$ and at each time t such that

$$\phi = \Phi(\mathbf{E}, \theta, \mathbf{g}, \alpha, \mathbf{d})$$

$$\sigma = \Sigma(\mathbf{E}, \theta, \mathbf{g}, \alpha, \mathbf{d})$$

$$\eta = N(\mathbf{E}, \theta, \mathbf{g}, \alpha, \mathbf{d})$$

$$\mathbf{q} = \mathbf{Q}(\mathbf{E}, \theta, \mathbf{g}, \alpha, \mathbf{d}). \tag{25}$$

Here, $\mathbf{g} = \mathrm{grad}\,\theta$, α is an internal variable introduced to model possible changes in the microstructure of the material and $\mathbf{d}$ is another internal state variable which monitors the degree of damage of a solid.

(ii) There exists a potential

$$\psi : \mathbf{W} \to (-\infty, \infty] \tag{26}$$

which has a nonempty generalized subdifferential such that

$$\dot{\mathbf{P}} = \frac{\partial\psi}{\partial\mathbf{S}} \tag{27}$$

$$\dot{\mathbf{d}} = -\frac{\partial\psi}{\partial\mathbf{B}} \tag{28}$$

$$\dot{\alpha} = -\frac{\partial\psi}{\partial\mathbf{A}}. \tag{29}$$

Here, $\mathbf{W}$ is a function space where $\mathbf{E}$, θ, $\mathbf{g}$, α, $\mathbf{d}$ belong, $\mathbf{S}$ the rotation free stress, and $\mathbf{A}$, $\mathbf{B}$, conjugate forces on α, $\mathbf{d}$, respectively. Eliminating r between (22) and (23), and taking into account (24), we obtain

$$\sigma : \mathbf{L} - \rho\dot{\phi} - \rho\dot{\theta}\eta - \frac{1}{\theta}\,\mathbf{q}\cdot\nabla\theta \geq 0. \tag{30}$$

Assume that the map: $(\mathbf{E}, \theta, \mathbf{g}, \alpha, \mathbf{d}) \to \phi(\mathbf{E}, \theta, \mathbf{g}, \alpha, \mathbf{d})$ is C^1 in each argument. Then the rate of change of the free energy is given by

$$\dot{\phi} = \frac{\partial\phi}{\partial\mathbf{E}} : \dot{\mathbf{E}} + \frac{\partial\phi}{\partial\theta}\,\dot{\theta} + \frac{\partial\phi}{\partial\mathbf{g}}\cdot\dot{\mathbf{g}} + \frac{\partial\phi}{\partial\alpha} : \dot{\alpha} + \frac{\partial\phi}{\partial\mathbf{d}} : \dot{\mathbf{d}}. \tag{31}$$

Introducing (16) and (31) into (30) gives

$$\left(\mathbf{S} - \rho\frac{\partial\phi}{\partial\mathbf{E}}\right) : \dot{\mathbf{E}} + \mathbf{S} : \dot{\mathbf{P}} - \rho\left(\frac{\partial\phi}{\partial\theta} + \eta\right)\dot{\theta} - \rho\frac{\partial\phi}{\partial\mathbf{g}}\cdot\dot{\mathbf{g}} - \rho\frac{\partial\phi}{\partial\alpha} : \dot{\alpha} - \rho\frac{\partial\phi}{\partial\mathbf{d}} : \dot{\mathbf{d}} - \frac{1}{\theta}\,\mathbf{q}\cdot\nabla\theta \geq 0. \tag{32}$$

Utilization of the new strain measures $\dot{\mathbf{E}}$ and $\dot{\mathbf{P}}$ naturally defines the rotation-free stress $\mathbf{S}$ (Dienes stress) by

$$\mathbf{S} = \mathbf{R}^t\sigma\mathbf{R}. \tag{33}$$

We note that the set of constitutive variables characterizing materials of type N do not include $\dot{\theta}$ and $\dot{\mathbf{g}}$. For this reason, the variables $\dot{\theta}$ and $\dot{\mathbf{g}}$ can be changed without changing the other argument. This fact leads to the following equations from (32):

$$\mathbf{S} = \rho\frac{\partial\phi}{\partial\mathbf{E}} \tag{34}$$

$$\eta = -\frac{\partial\phi}{\partial\theta} \tag{35}$$

$$0 = \frac{\partial\phi}{\partial\mathbf{g}} \tag{36}$$

and the ensuing inequality

$$\mathbf{S} : \dot{\mathbf{P}} + \mathbf{A} : \dot{\alpha} + \mathbf{B} : \dot{\mathbf{d}} - \frac{1}{\theta}\,\mathbf{q}\cdot\nabla\theta \geq 0. \tag{37}$$

Here the conjugate forces $\mathbf{A}$ and $\mathbf{B}$ can be defined by

$$\mathbf{A} = -\rho\frac{\partial\phi}{\partial\alpha} \tag{38}$$

$$\mathbf{B} = -\rho\frac{\partial\phi}{\partial\mathbf{d}}. \tag{39}$$

It remains to be shown how this theory can be applied to concrete cases. It is represented in the next section.

2.3 Introduction of Potentials and Constitutive Equations. Bodner and Partom (1972, 1975) proposed a flow rule which was drawn from the classical Prandtl-Reuss flow rule and improved by phenomenological observations, but does not involve specification of a yield surface. This theory attempts to characterize isotropic hardening of certain materials. This flow rule was modified and extended to simulate damage effect. We amend the constitutive functions for free energy to account for loss of stiffness due to damage in a manner suggested by the work of Lemaitre (1985). The resulting potentials assume the following forms:

- free energy functional

$$\phi = \frac{(1-d)}{2\rho_o}\{[\lambda(\mathrm{tr}\mathbf{E})^2 + 2\mu\mathrm{tr}\mathbf{E}^2] - h_1 z - \frac{1}{m}(h_1 - h_o)\exp(-mz)\} \tag{40}$$

- flow potential functional

$$\psi = D_o\sum_{i=0}^{\infty}(-1)^{i+1}\frac{(\beta^i h^{2i-1})}{i!(2i-1)J_2^{i-1/2}} - \frac{1}{2}\,C_1 B^2\exp\left(\frac{1}{1-d}\right). \tag{41}$$

Downloaded 03 May 2010 to 171.66.16.20. Redistribution subject to ASME license or copyright; see http://www.asme.org/terms/Terms_Use.cfm

Table 1 Mechanical properties of aluminum 2024

Young's Modulus	E	7.24×10^4 : [N/mm^2]
Poisson's Ratio	υ	0.32 : [-]
Shear Modulus	G	2.74×10^4 : [N/mm^2]
Initial Damage Threshold	D_0	1.35×10^7 : [N/mm^{2}sec^{-1}]
Hardening Constant	m	25 : [-]
Initial Hardness Constant	h_0	1150 : [N/mm^2]
Ultimate Hardness Constant	h_1	1450 : [N/mm^2]
Damage Constant	C_1	0.000185 : [N^{-1}mm^{2}sec^{-1}]

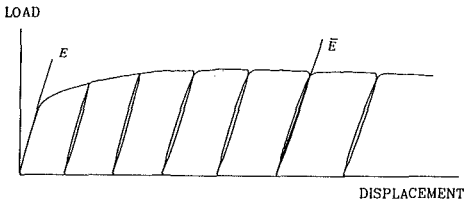


Fig. 2 Experimental results of loading, unloading, and reloading

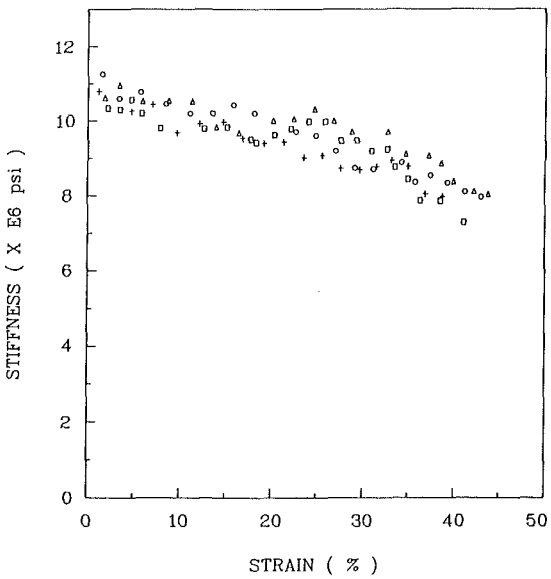


Fig. 3 Experimental results of the stiffness degradation

Here the internal state variables α and $\mathbf{d}$ are considered as scalar tensors, i.e.,

$$\alpha = z\mathbf{I} \tag{42}$$

$$\mathbf{d} = d\mathbf{I}. \tag{43}$$

Here, $0 \le d \le 1$, and corresponding conjugate forces can be written as

$$\mathbf{A} = h\mathbf{I} \tag{44}$$

$$\mathbf{B} = B\mathbf{I}. \tag{45}$$

Equation (42) means isotropic plasticity and Eq. (43) means isotropic damage. If $d = 0$, there is no damage and only elastic plastic deformation can occur. If d is greater than zero, there exists damage effect. When $d = 1$, the load-bearing capacity of the material disappears and, namely, the material can be considered as fractured. Then this model has a singularity. But in a real situation, a material is considered as fractured if the

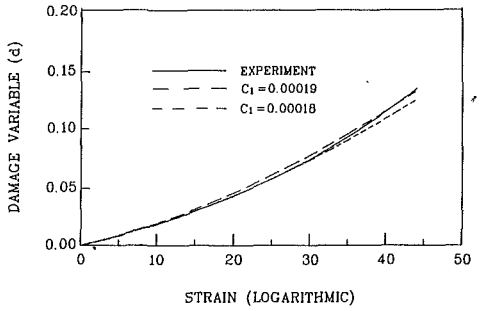


Fig. 4 Comparison of experimental result with computational results for damage variable

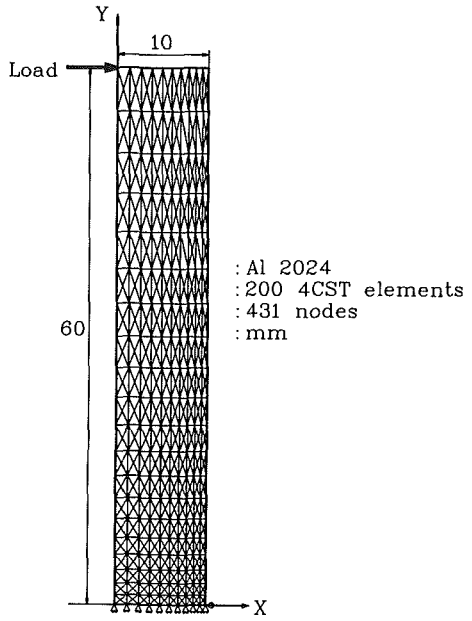


Fig. 5 Finite element model of bending problem

value of d is about 0.6 or 0.7. Here, J_2 is the second invariant of deviatoric rotation-free stress $\mathbf{S}'$, namely $J_2 = 1/2\text{tr}\,(\mathbf{S}')^2$, $\mathbf{S}' = \mathbf{S} - 1/3\text{tr}\,(\mathbf{S})\mathbf{I}$, and $\beta = 1/3^n(n+1)/n$. Generally n is taken as 1. Also, z is an internal state variable (since these potentials will characterize an isotropic hardening effect, the internal state variable is scalar valued), h is a hardness variable which is conjugate to the internal variable, λ and μ are Lame constants, and D_o, h_o, h_1, m, C_1 are material constants.

Applying the axioms (27)–(29) along with the potentials (40)–(41) and the results of (34), (38), and (39), we obtain the following constitutive relations:

$$\mathbf{S} = \frac{\rho}{\rho_o}(1-d)[\lambda(\text{tr}\mathbf{E})\mathbf{I} + 2\mu\mathbf{E}] \tag{46}$$

$$B = \frac{\rho}{2\rho_o}[\lambda(\text{tr}\mathbf{E})^2 + 2\mu(\text{tr}\mathbf{E}^2)] \tag{47}$$

$$h = \frac{\rho}{\rho_o}(1-d)[h_1 + (h_o - h_1)\exp(-mz)] \tag{48}$$

$$\dot{\mathbf{P}} = D_o \frac{1}{2h\sqrt{J_2}} \exp\left(-\frac{\beta h^2}{J_2}\right)\mathbf{S}' \tag{49}$$

$$\dot{d} = C_1 B \exp\left(\frac{1}{1-d}\right) \tag{50}$$

$$\dot{z} = \frac{1}{h}\mathbf{S}' : \dot{\mathbf{P}}. \tag{51}$$

Downloaded 03 May 2010 to 171.66.16.20. Redistribution subject to ASME license or copyright; see http://www.asme.org/terms/Terms_Use.cfm

Equation (50) is a damage evolution equation which describes the damage progression.

3 Finite Element Formulation and Approximation

(*1*) *Formulations.* We limit ourselves to quasi-static problems involving no body forces and no temperature dependence and that the equation of momentum balance in the reference configuration will be of the form

$$\nabla_x \cdot \mathbf{T} = 0 \text{ in } C_o \tag{52}$$

where $\mathbf{T}$ is the first Piola-Kirchhoff stress and its relation with the Cauchy stress σ and the rotation-free stress $\mathbf{S}$ can be written as

$$\mathbf{T} = J\sigma(\mathbf{F}^{-1})^t \tag{53}$$

$$= J\mathbf{R}\mathbf{S}\mathbf{U}^{-1}. \tag{54}$$

Here we adopt the incremental total Lagrangian formulation where the reference configuration is always the computational domain. Let $\mathbf{q}$ denote a test function which belongs to a set of admissible displacement increments, V. Then a weak form of Eq. (52) can be written as

$$\int_{\Omega_0} \mathbf{T} : \nabla \mathbf{q} d\mathbf{x} = \int_{\partial\Omega_o} \mathbf{T}\mathbf{N} \cdot \mathbf{q} ds \quad \forall \mathbf{q} \in V \tag{55}$$

where $\Omega_o \equiv \mathbf{k}_o(B)$, $\partial\Omega_o$ is boundary of Ω_o, and $\mathbf{N}$ is the outward normal unit vector in the reference configuration C_o.

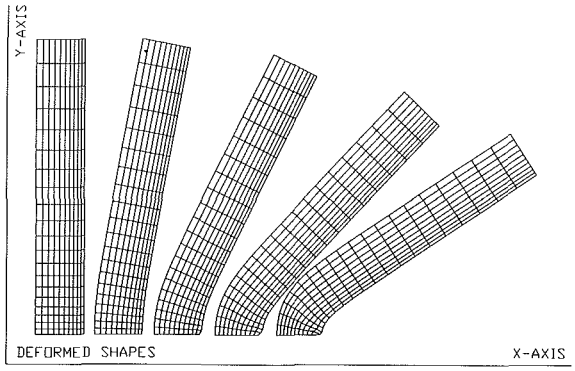


Fig. 6 Deformed shapes of the bending model

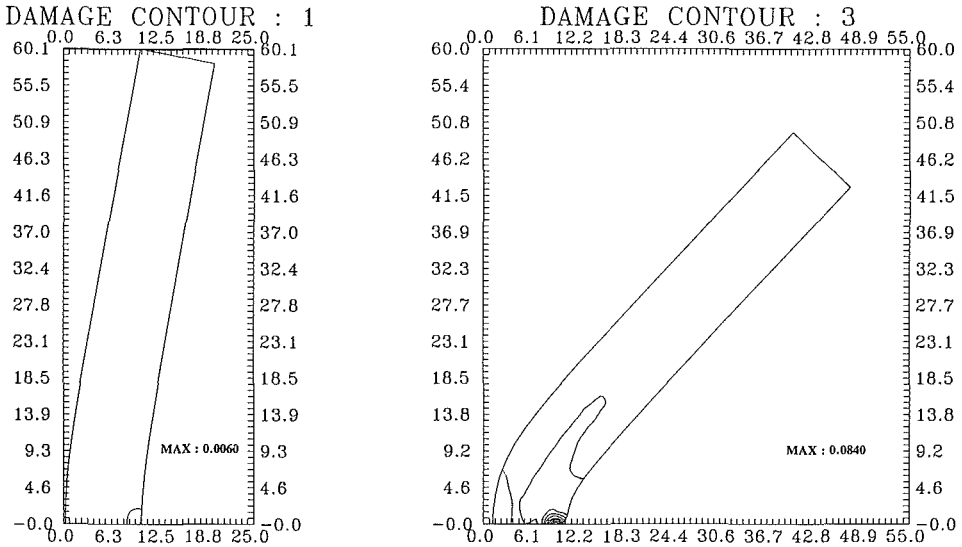


Fig. 7(*a*) Progressive drawings of damage variable for the bending problem (continued)

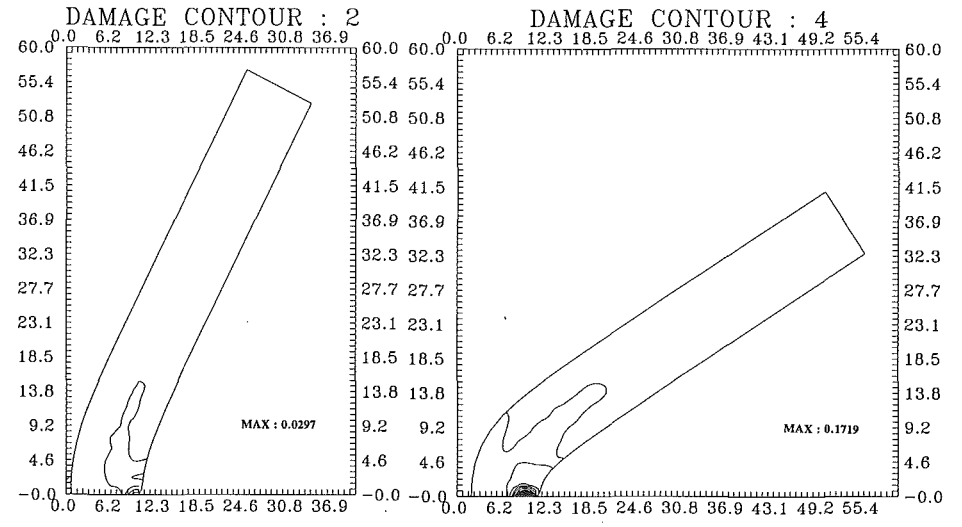


Fig. 7(*b*) Progressive drawings of damage variable for the bending problem

Downloaded 03 May 2010 to 171.66.16.20. Redistribution subject to ASME license or copyright; see http://www.asme.org/terms/Terms_Use.cfm

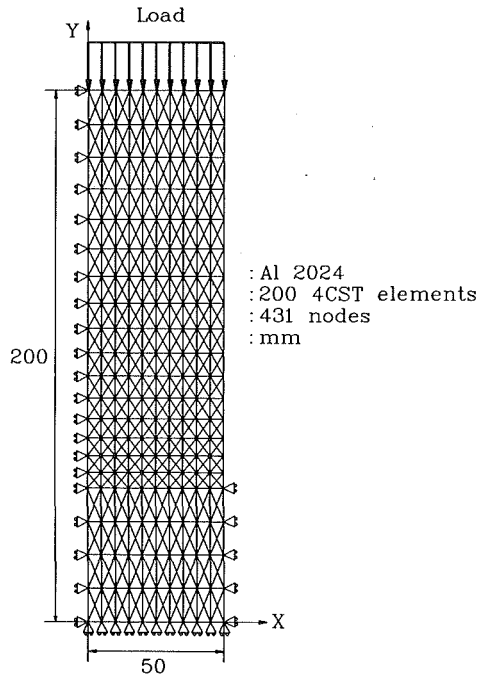


Fig. 8 Finite element model of billet-forming problem

We assume that the equilibrium state is achieved at $(n-1)$th incremental step, i.e.,

$$\int_{\Omega_o} \mathbf{T}_{n-1} : \nabla \mathbf{q} d\mathbf{x} = \int_{\partial\Omega_o} \mathbf{T}_{n-1}\mathbf{N} \cdot \mathbf{q} ds \quad \forall \mathbf{q} \in V. \tag{56}$$

Then at the (n)th step,

$$\mathbf{T}_n = \sum_{i=1}^{n} \Delta\mathbf{T}_i = \mathbf{T}_{n-1} + \Delta\mathbf{T}_n \tag{57}$$

$$\mathbf{t}_n = \mathbf{T}_n\mathbf{N} = \mathbf{t}_{n-1} + \Delta\mathbf{t}_n \tag{58}$$

and

$$\int_{\Omega_o} \Delta\mathbf{T}_n : \nabla \mathbf{q} d\mathbf{x} = \int_{\partial\Omega_o} \Delta\mathbf{t}_n \cdot \mathbf{q} ds \quad \forall \mathbf{q} \in V. \tag{59}$$

From the definition of the first Piola-Kirchhoff stress and Eqs. (15) and (33) we have

$$\begin{aligned}\Delta\mathbf{T} &= \Delta(J\mathbf{R}\mathbf{S}\mathbf{U}^{-1}) = \Delta(\lambda(\mathrm{tr}\mathbf{E})\mathbf{F}^{-t} + 2\mu\mathbf{R}\mathbf{E}\mathbf{U}^{-1}) \\ &= \lambda(\mathrm{tr}\Delta\mathbf{E})\mathbf{F}^{-t} + 2\mu\mathbf{R}\Delta\mathbf{E}\mathbf{U}^{-1} + \lambda(\mathrm{tr}\mathbf{E})\Delta\mathbf{F}^{-t} \\ &\quad + 2\mu\Delta\mathbf{R}\mathbf{E}\mathbf{U}^{-1} + 2\mu\mathbf{R}\mathbf{E}\Delta\mathbf{U}^{-1}. \end{aligned} \tag{60}$$

By using (15) and (60), Eq. (59) becomes

$$\begin{aligned}&\int_{\Omega_o} [\lambda\mathrm{tr}(\Delta t\mathbf{D}_n)\mathbf{F}_n^{-t} + 2\mu\Delta t\mathbf{D}_n\mathbf{F}_n^{-t}] : \nabla \mathbf{q} d\mathbf{x} \\ &\quad - \int_{\Omega o} [\lambda\mathrm{tr}(\Delta\mathbf{P})\mathbf{F}^{-t} + 2\mu(\mathbf{R}\Delta\mathbf{P}\mathbf{U}^{-1})]_n : \Delta\mathbf{q} d\mathbf{x} \\ &\quad + \int_{\Omega o} [\lambda\mathrm{tr}(\mathbf{E})\Delta\mathbf{F}^{-t} + 2\mu(\Delta\mathbf{R}\mathbf{E}\mathbf{U}^{-1} + \mathbf{R}\mathbf{E}\Delta\mathbf{U}^{-1})]_n : \nabla \mathbf{q} d\mathbf{x} \\ &\quad = \int_{\partial\Omega_o} \Delta\mathbf{t}_n \cdot \mathbf{q} ds \quad \forall_{\mathbf{q}} \in V. \end{aligned} \tag{61}$$

Now we apply the tangent stiffness scheme with the idea of successive approximation during iterations in an incremental step. We arrive at the following linearized form at the (i)th iteration in the (n)th increment:

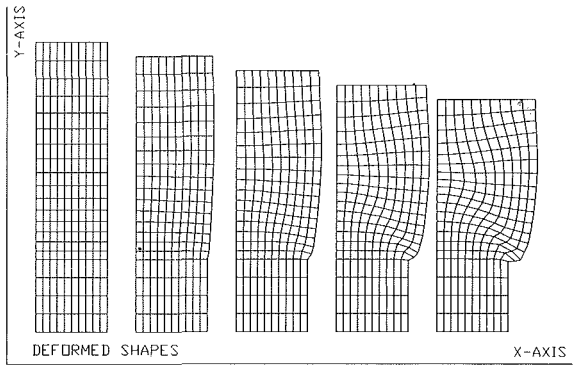


Fig. 9 Deformed shapes of the billet-forming model

$$\begin{aligned}&\int_{\Omega_o} [\lambda\mathrm{tr}(\Delta t\mathbf{D}_n^i)\mathbf{I} + 2\mu\Delta t\mathbf{D}_n^i](\mathbf{F}^{-t})_n^{i-1} : \nabla \mathbf{q} d\mathbf{x} \\ &\quad = \int_{\Omega_o} [\lambda\mathrm{tr}(\Delta\mathbf{P})\mathbf{F}^{-t} + 2\mu(\mathbf{R}\Delta\mathbf{P}\mathbf{U}^{-1})]_n^{i-1} : \nabla \mathbf{q} d\mathbf{x} \\ &\quad - \int_{\Omega_o} [\lambda\mathrm{tr}(\mathbf{E})\Delta\mathbf{F}^{-t} + 2\mu(\Delta\mathbf{R}\mathbf{E}\mathbf{U}^{-1} + \mathbf{R}\mathbf{E}\Delta\mathbf{U}^{-1})]_n^{i-1} : \nabla \mathbf{q} d\mathbf{x} \\ &\quad + \int_{\partial\Omega_o} \Delta\mathbf{t}_n^i \cdot \mathbf{q} ds - \int_{\Omega_o} \Delta\mathbf{T}_n^{i-1} : \nabla \mathbf{q} d\mathbf{x} \quad \forall \mathbf{q} \in V. \end{aligned} \tag{62}$$

Here the last integrals on the right-hand side of (62) is the left-hand side of (61) at the (i)th iteration, and the first two integrals of (62) are obtained by taking $\Delta\mathbf{P}$, $\Delta\mathbf{R}$ and $\Delta\mathbf{U}^{-1}$ as functions of $\mathbf{U}$ and transferring these to the right-hand side, i.e.,

$$\Delta\mathbf{P}_n^{i-1} = \frac{\partial\Delta\mathbf{P}}{\partial\Delta\mathbf{U}}\bigg|_n^{i-1} \Delta\mathbf{U}_n^i$$

$$\Delta\mathbf{R}_n^{i-1} = \frac{\partial\Delta\mathbf{R}}{\partial\Delta\mathbf{U}}\bigg|_n^{i-1} \Delta\mathbf{U}_n^i \quad \text{etc} \tag{63}$$

Note that $\Delta\mathbf{P}_n^{i-1}$, etc., go to zero when the iteration converges since $\mathbf{P}_n$, $\mathbf{R}_n$, etc. are defined in the following fashion:

$$\mathbf{P}_n = \mathbf{P}_{n-1} + \sum_{i}^{M} \Delta\mathbf{P}_n^i \quad \text{etc} \tag{64}$$

Adding (56) to (62) gives

$$\begin{aligned}&\int_{\Omega_o} [\lambda\mathrm{tr}(\Delta t\mathbf{D}_n^i)\mathbf{I} + 2\mu\Delta t\mathbf{D}_n^i](\mathbf{F}^{-t})_n^{i-1} : \nabla \mathbf{q} d\mathbf{x} \\ &\quad = \int_{\Omega_o} [\lambda\mathrm{tr}(\Delta\mathbf{P})\mathbf{F}^{-t} + 2\mu(\mathbf{R}\Delta\mathbf{P}\mathbf{U}^{-1})]_n^{i-1} : \nabla \mathbf{q} d\mathbf{x} \\ &\quad - \int_{\Omega_o} [\lambda\mathrm{tr}(\mathbf{E})\Delta\mathbf{F}^{-t} + 2\mu(\Delta\mathbf{R}\mathbf{E}\mathbf{U}^{-1} + \mathbf{R}\mathbf{E}\Delta\mathbf{U}^{-1})]_n^{i-1} : \Delta\mathbf{q} d\mathbf{x} \\ &\quad + \int_{\partial\Omega_o} \mathbf{t}_n^i \cdot \mathbf{q} ds - \int_{\Omega_o} \mathbf{T}_n^{i-1} : \nabla \mathbf{q} d\mathbf{x} \end{aligned} \tag{65}$$

(2) *Finite Element Approximation.* The unknown functions $\Delta\mathbf{u}_n^i$ at each incremental step and test functions $\mathbf{q}$ are interpolated in two-dimensional problems as follows:

$$\Delta\mathbf{u}_n^i = \mathbf{u}_\alpha\phi_\alpha(x), \quad \mathbf{u}_\alpha = \begin{Bmatrix} u_\alpha^1 \\ u_\alpha^2 \end{Bmatrix} \tag{66}$$

and

$$\mathbf{q} = \mathbf{q}_\alpha\phi_\alpha(x), \quad \mathbf{q}_\alpha = \begin{Bmatrix} q_\alpha^1 \\ q_\alpha^2 \end{Bmatrix}, \tag{67}$$

Downloaded 03 May 2010 to 171.66.16.20. Redistribution subject to ASME license or copyright; see http://www.asme.org/terms/Terms_Use.cfm

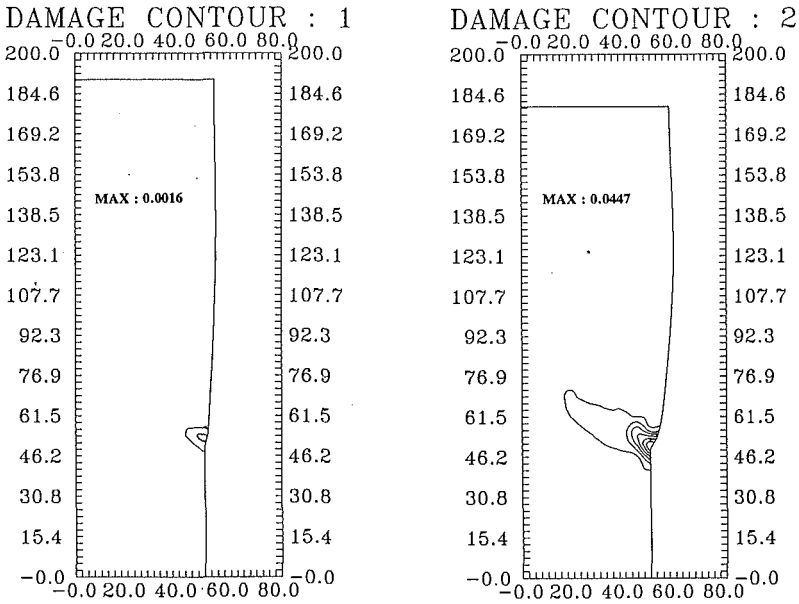


Fig. 10(*a*) Progressive drawings of damage variable for the billet-forming problem (continued)

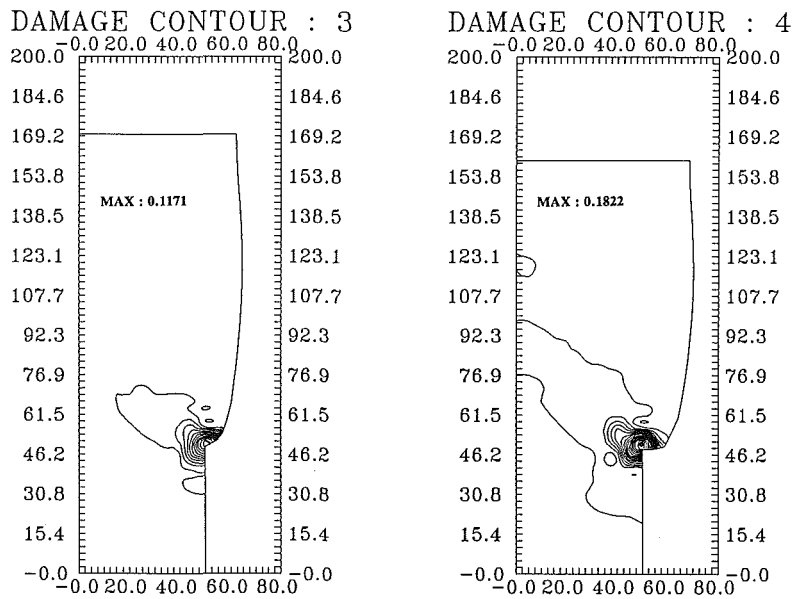


Fig. 10(*b*) Progressive drawings of damage variable for the billet-forming problem

where $\phi_\alpha(x)$ is a shape function and we have used the summation convention. Therefore,

$$\mathbf{u}_n = \mathbf{u}_{n-1} + \sum_{i=1}^{M} \Delta \mathbf{u}_n^i, \tag{68}$$

M being the iteration index.

The resulting simultaneous equations are solved by the band solver, and the constitutive relations (46)–(51) were reduced by the obtained displacements $\mathbf{u}$. Since the above constitutive equations assume incompressibility in the plastic deformation, the rectangular element which consists of four 3-node triangles (so-called four constant strain triangles (4CST element)) is used. This element is known to avoid the difficulties due to the incompressibility. A mathematical issues on this 4CST element can be found in Oden, Kikuchi, and Song (1982) and Kikuchi (1983).

4 Experiments

The proposed set of constitutive Eqs. (46)–(51) contains seven material constants to be determined from experiments. The two elastic constants can be determined by the uniaxial elongation test, but the four plastic constants require at least two uniaxial tests at different strain rates. The remaining damage constant, C_1, can be determined by comparing the experimental result with the computational simulations. This procedure is described in Section 5.

The used material was aluminum 2024 and test specimens were prepared by the ASTM standard. Maximum strain was about 40 percent and displacement control was used in the test. The mechanical properties of the material are listed in Table 1.

We adopt the definition of the value of damage variable, d, as $d = 1 - \bar{E}/E$, here E is the Young's modulus and $\bar{E}$ is the

Downloaded 03 May 2010 to 171.66.16.20. Redistribution subject to ASME license or copyright; see http://www.asme.org/terms/Terms_Use.cfm

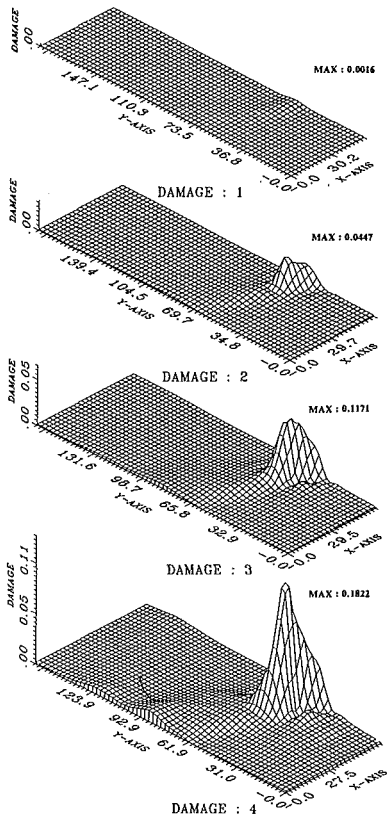


Fig. 11 Three-dimensional contours of damage variable

tangent modulus at each unloading and reloading process which is necessary to determine the damage constant, C_1. Several unloading-reloading processes were carried out to measure the degree of stiffness degradation of the specimen by using an extensometer. The test result of loading, unloading, and reloading is shown in Fig. 2 and the experimental results of gradual stiffness degradation are represented in Fig. 3.

5 Numerical Simulations

To verify the algorithm described previously and to fit with the experimental result, the homogeneous deforming states were computed by changing damage constant, C_1. The calculated result was in good agreement with the experimental at $C_1 = 0.000185$. This result is represented in Fig. 4.

Two example problems were chosen for numerical simulations. The first example is a bending problem with a size of 10mm by 60mm, and its finite element model is shown in Fig. 5. It contains 200 4CST elements, 431 nodes, and force is applied at the top left corner. All the bottom nodes can slide in the X-direction except for the right bottom node which is fixed.

Since the 4CST element has 5 nodes, the static condensation method was used to reduce the degree-of-freedoms of the center nodes of the element. The solutions of the remained nodes were obtained by a band solver, and the values at the center nodes were recovered from the solutions. Deformed shapes are represented in Fig. 6, which show that plastic deformation occurs mainly at the bottom right corner and, accordingly, the upper part of the model moves by large rotation with the elastic deformation. Therefore, it can be stated that the proposed kinematics is suitable to describe a large deformation of a solid. The damage contours are shown in Fig. 7. As the deformation increases, damage is concentrated at the fixed corner and gradually propagates inward. This is a reasonable result which we can expect in a practical situation.

The second example is a billet-forming problem whose finite element model is shown in Fig. 8. The Y-axis is the axis of symmetry of the model and compressive forces are applied at the top surface. The right boundary nodes can slide in the Y-direction. This model has 200 4CST elements, 401 nodes, and has a size of 50mm by 200mm. The deformed shapes are represented in Fig. 9. This shows a typical bulging shape by press as expected. The progressive damage contours are represented in Fig. 10, and damage is localized at the starting point of the bulging shape and gradually propagates inward. The damage contours are visualized in a three-dimensional pattern in Fig. 11. Damage propagation depends on the plastic deformation because it has a relation to the second invariant of the deviatoric rotation-free stress, J_2.

From these results, it can be said that the proposed damage model is reasonable to describe the damage propagation of an isotropic hardening materials, and the proposed kinematics is appropriate to describe the large deformation of a solid.

6 Concluding Remarks

In this paper we proposed a damage model to analyze isotropic hardening materials with large deformation and damage effect. The stiffness degradation was adopted as a damage measure and reasonable kinematics was considered for the analysis of a large deformation. The proposed damage model was based on the thermodynamical framework to analyze the irreversible process of damage propagation and two types of numerical simulations were presented.

Damage depends on the plastic deformation and is critical at the points where the plastic deformation is large. Load redistribution occurs by this damage propagation in a material. From these results it can be concluded that the proposed kinematics is reasonable to describe the large deformation problems with large rotation, elastic, plastic, and damage effect, and the proposed damage model can be applied to the simulation of damage propagation of isotropic hardening materials.

It is expected that this damage computer code will be extended to solve three-dimensional problems, and anisotropic damage effects may be considered in the future if experimental results for anisotropic damage are reasonable.

Acknowledgment

This research was supported by the Non Directed Research Fund of the Korea Research Foundation and by the University R & D Grant Program of Cray Research, Inc.

References

Bodner, S. R., and Partom, Y., 1972, "A Large Deformation Elastic-Viscoplastic Analysis of a Thick-Walled Spherical Shell," ASME JOURNAL OF APPLIED MECHANICS, Vol. 39, pp. 751–757.

Bodner, S. R., and Partom, Y., 1975, "Constitutive Equations for Elastic-Viscoplastic Strain-Hardening Materials," ASME JOURNAL OF APPLIED MECHANICS, Vol. 42, No. 2, pp. 385–389.

Chaboche, J. L., 1988, "Continuum Damage Mechanics: Part I—General Concepts," ASME JOURNAL OF APPLIED MECHANICS, Vol. 55, pp. 59–64.

Chaboche, J. L., 1982, "Continuous Damage Mechanics—A Tool to Describe Phenomena before Crack Initiation," *Nuclear Engineering and Design*, Vol. 64, pp. 233–247.

Combescure, A., and Jiaju, Y., 1990, "Finite Element Method for Large Displacement and Large Strain Elasto-Plastic Analysis of Shell Structures and Some Application of Damage Mechanics," *Eng. Fract. Mech.*, Vol. 36, No. 2, pp. 219–231.

Dragon, A., and Mroz, Z., 1979, "A Continuum Model for Plastic-Brittle Behavior of Rock and Concrete," *Int. J. Eng. Sci.*, Vol. 17, pp. 121–137.

Gurtin, M. E., 1981, *An Introduction to Continuous Mechanics*, Academic Press, New York.

Kachanov, M. L., 1958, "On the Creep Fracture Time," *Izv. Akad. Nauk. SSR.*, Vol. 8, pp. 26–31.

Kikuchi, N., 1983, "Remarks on 4CST-Elements for Incompressible Materials," *Comput. Meths. Appl. Mech. Eng.*, Vol. 37, pp. 109–123.

Kim, S. J., and Oden, J. T., 1984, "Generalized Potentials in Finite Elastoplasticity," *Int. J. Eng. Sci.*, Vol. 22, No. 11–22, pp. 1235–1257.

Kim, S. J., and Oden, J. T., 1985, "Finite Element Analysis of a Class of

Downloaded 03 May 2010 to 171.66.16.20. Redistribution subject to ASME license or copyright; see http://www.asme.org/terms/Terms_Use.cfm

Problems in Finite Elastoplasticity Based on the Thermodynamical Theory of Materials of Type-N," *Comput. Meths. Appl. Mech. Eng.*, Vol. 53, pp. 277–302.

Kim, S. J., and Oden, J. T., 1985, "Generalized Potentials in Finite Elastoplasticity, II. Example," *Int. J. Eng. Sci.*, Vol. 23, No. 5, pp. 515–530.

Kim, S. J., and Oden, J. T., 1988, "A Note on the Numerical Analysis of Material Damage Based on the Theory of Materials of Type N," *Comput. Maths. Applic.*, Vol. 15, pp. 169–174.

Krajcinovic, D., 1979, "Distributed Damage Theory of Beam in Pure Bending," ASME JOURNAL OF APPLIED MECHANICS, Vol. 46, pp. 592–596.

Krajcinovic, D., and Fonseka, G. U., 19081, "The Continuous Damage Theory of Brittle Materials, Part 1: General Theory," ASME JOURNAL OF APPLIED MECHANICS, Vol. 48, pp. 809–815.

Krajcinovic, D., and Selvaraj, S., 1984, "Creep Rupture of Metals—An Analytical Model," ASME *Journal of Engineering Materials and Technology*, pp. 1–5.

Krajcinovic, D., 1984, "Continuous Damage Mechanics" ASME *Applied Mechanics Reviews*, Vol. 37, No. 1, pp. 1–6.

Krajcinovic, D., 1985, "Continuous Damage Mechanics Revisited: Basic Concepts and Definitions," ASME JOURNAL OF APPLIED MECHANICS, pp. 1–6.

Leckie, F. A., and Hayhurst, D. R., 1974, "Creep Rupture of Structure," *Proc. Royal Soc. Lond., 340*, pp. 323–347.

Lemaitre, J., 1985, "Coupled Elasto-Plasticity and Damage Constitutive Equations," *Comput. Meths. Appl. Mech. Eng.*, Vol. 51, pp. 31–49.

Lemaitre, J., and Dufailly, J., 1987, "Damage Measurements," *Eng. Fract. Mech.*, Vol. 28, No. 5–6, pp. 643–661.

Oden, J. T., Kikuchi, N., and Song, Y. J., 1982, "Penalty-Finite Element Methods for the Analysis of Stokesian Flows," *Comput. Meths. Appl. Mech. Eng.*, Vol. 31, pp. 297–329.

Simo, J. C., and Ju, J. W., 1987, "Strain- and Stress-Based Continum Damage Models—I. Formulation," *Int. J. Solids Structures*, Vol. 23, No. 7, pp. 821–840.

Downloaded 03 May 2010 to 171.66.16.20. Redistribution subject to ASME license or copyright; see http://www.asme.org/terms/Terms_Use.cfm

V. L. Rabinovich
Department of Manufacturing Engineering,

S. R. Sipcic
Department of Aerospace and Mechanical Engineering,
Mem. ASME.

V. K. Sarin
Department of Manufacturing Engineering,

Boston University,
Boston, MA 02215

Three-Dimensional Unilateral Frictionless Contact Problem for Finite Bodies

The numerical solution of the three-dimensional frictionless contact problem is obtained by means of a boundary element discretization of a variational inequality and its related extremum principle. The discretization leads to a finite dimensional quadratic programming problem, solved by a modification of the gradient projection method. The associated Green's function is approximated using a standard direct boundary element procedure. The numerical method is applicable to any type of contacting bodies geometry under arbitrary loading. The examples considered were chosen such as to illustrate a distinct ability of the method to capture the influence of a body shape on the contact area and pressure acting in it. It has been demonstrated that the symmetry properties of the Green's operator hold only asymptotically for the discretized problem.

1 Introduction

In recent years, much interest has been devoted to the mathematical formulation of structural problems involving unilateral constraints (Panagiotopoulos, 1985; Kikuchi and Oden, 1988; Alliney et al., 1990). An important class of these problems is the frictionless contact between two elastic bodies. More specifically, given the surface geometry of both bodies, their elastic properties, and the total compressive force, the objective is to find the contact area and the pressure acting in it. Since the contact area is a priori unknown, unilateral conditions must be imposed on the relative displacement and the mutual reactions.

The first successful attempt to analyze such contacts was made by Hertz (1882). Hertz considered the equilibrium of two elastic bodies with quadratic surfaces in contact, and obtained analytical solutions for the contact pressure and the indentation under the assumption that the contact area was contained within an ellipse. For a limited class of geometries of which the half-space is a preeminent member, the exact solutions via integral equations are possible; an excellent treatise on the analysis of contact problems by classical methods is given by Gladwell (1980). For more general shapes the usual finite element method in connection with a suitable iteration for the contact pressure may be employed; e.g., Chan and Tuba (1971). A rigorous numerical treatment of contact problems, however, has to start from the variational inequalities (Fichera, 1972; Kikuchi, 1979).

The first variational formulations defined on the contact area were proposed in the 1970s. A variety of variational principles for contact problems and an extensive bibliography is given in Kalker (1975). A systematic and rigorous mathematical treatment of the variational boundary formulations in terms of Green's function is reported in Kikuchi and Oden (1988). A class of contact problems with an unknown contact zone for the laminated half-space was analyzed by Buffer et al. (1982). Recently, Panagiotopoulos and Lazaridis (1987) and Alliney et al. (1990), have proposed a numerical scheme, similar to the one presented in this paper, for the contact problem with unilateral constraints for two-dimensional homogeneous bodies.

The numerical method presented herein is applicable to any type of contacting bodies geometry under arbitrary loading. The method is based on the rigorous variational formulation and application of a direct boundary element procedure for the approximation of the related Green's function. The examples illustrate the distinct ability of the method to capture the influence of the shape and size of a body on the contact area and the pressure acting in it.

2 Formulation of the Problem

Two three-dimensional linearly elastic bodies, $\bar{\Omega}^\alpha$ ($\alpha = 1, 2$), are pressed together as in Fig. 1. Note that upper Greek indices will be used throughout the paper to denote bodies, and that no summation convention is assumed on a repeated Greek index. The boundary $\Gamma^\alpha \equiv \partial\Omega^\alpha$ is assumed to be piecewise continuous, and composed of three mutually disjoint open manifolds Γ^α_D, Γ^α_F, and Γ^α_C. We demand that on Γ^α_F the

Contributed by the Applied Mechanics Division of THE AMERICAN SOCIETY OF MECHANICAL ENGINEERS for presentation at the ASME Winter Annual Meeting, New Orleans, LA, Nov. 28–Dec. 3, 1993.

Discussion on this paper should be addressed to the Technical Editor, Professor Lewis T. Wheeler, Department of Mechanical Engineering, University of Houston, Houston, TX 77204-4792, and will be accepted until four months after final publication of the paper itself in the ASME JOURNAL OF APPLIED MECHANICS.

Manuscript received by the ASME Applied Mechanics Division, June 9, 1992; final revision, Mar. 11, 1993. Associate Technical Editor: F. Y. M. Wan.

Paper No. 93-WA/APM-20.

Copyright © 1994 by ASME
Downloaded 03 May 2010 to 171.66.16.20. Redistribution subject to ASME license or copyright; see http://www.asme.org/terms/Terms_Use.cfm

surface traction $\mathbf{t}^\alpha$ be specified and that on Γ_D^α the displacement be specified. The contact area is assumed to be small so that only displacements perpendicular to the common tangential plane at a representative contact point have to be taken into account. Furthermore, the two surfaces Γ_C^α, ($\alpha = 1, 2$), can be identified with their projection Γ_C to the tangential plane (contact plane). We will assume that the normal $\mathbf{n}$ to the tangential plane is oriented from the region Ω^1 to the region Ω^2 as shown in Fig. 1.

Assuming that the bodies are in equilibrium, the problem becomes one of finding a displacement field u_i^α, stress field σ_{ij}^α, and the contact pressure p, that satisfy the equilibrium conditions

$$-(E_{ijkm}^\alpha u_{m,k}^\alpha)_{,j} = 0 \text{ in } \Omega^\alpha. \tag{1}$$

The associated natural, essential, and frictionless contact conditions are given as, respectively,

$$t_i^\alpha = (t_i^\alpha)_0 \text{ on } \Gamma_F^\alpha \tag{2}$$

$$u_i^\alpha = 0 \text{ on } \Gamma_D^\alpha \tag{3}$$

$$\left.\begin{array}{l} \sigma_{T_i} = 0 \\ p = 0 \quad \text{for} \quad u_n^R < g_0 \\ p \le 0 \quad \text{for} \quad u_n^R = g_0 \end{array}\right\} \text{ on } \Gamma_C \tag{4}$$

where σ_{T_i} denotes the tangential component of stress vector, p is the contact pressure, $u_n^R = u_n^1 - u_n^2$ is the relative displacement perpendicular to the common tangential plane at a contact point, and g_0 is the "gap" function between the two surfaces Γ_C^1 and Γ_C^2, as measured along the normal $\mathbf{n}$ before the deformation. Since the contact zone is not known in advance, the problem is nonlinear.

3 Equivalent Variational Formulation

We shall now introduce a reciprocal variational principle for the problem considered. An advantage of such a formulation, from the point of view of approximations, is that the problem can be completely defined in terms of the contact pressure exerted on the surface Γ_C if Green's operators related to the boundary conditions are known. Suppose that for any $p \in ((H^{1/2}(\Gamma_C))'$ and for a given essential boundary condition (3) we have determined the Green's operators $\mathbf{G}^\alpha(\mathbf{x}, \eta)$ ($\alpha = 1, 2$), such that the displacements at $\mathbf{x} \in \Omega^\alpha$ introduced by $p(\eta)\mathbf{n}^\alpha(\eta)$ can be expressed as $\mathbf{G}^\alpha(\mathbf{x}, \eta) \cdot p(\eta)\mathbf{n}(\eta)$, then the displacement fields introduced by the contact pressure can be expressed as

$$\mathbf{u}^\alpha(\mathbf{x}) = \int_{\Gamma_C} \mathbf{G}^\alpha(\mathbf{x}, \eta) \cdot p(\eta)\mathbf{n}(\eta) dS_\eta \quad \forall \mathbf{x} \in \Omega^\alpha. \tag{5}$$

Here $\mathbf{u}^\alpha(\mathbf{x}) \in \mathbf{H}^1(\Omega^\alpha)$, and $(H^{1/2}(\Gamma_C))' = H^{-1/2}(\Gamma_C)$ is dual space for Sobolev's space $H^{1/2}(\Gamma_C)$. Furthermore, if $\Omega \in C^{1,1}$ and for $\Gamma_C \subset \Sigma = \Gamma^\alpha - \Gamma_D^\alpha - \Gamma_F^\alpha$, the normal trace $u_n^\alpha = \gamma_{\Sigma_n}^0(\mathbf{u}^\alpha)$ and the relative normal trace

$$w = \gamma_{\Sigma_n}^0(\mathbf{u}^1) - \gamma_{\Sigma_n}^0(\mathbf{u}^2) \tag{6}$$

belong to $H^{1/2}(\Gamma_C)$. Therefore, the contact condition (4) leads to the variational inequality

$$p \in K: \langle q - p, w - \hat{g} \rangle_{\Gamma_C} > 0 \quad \forall q \in K \tag{7}$$

where $K = \{q \in (H^{1/2}(\Gamma_C))' \mid q \le 0\}$ and the gap function is modified by the relative normal displacement $\hat{u}_n^R$, where $\hat{\mathbf{u}}^\alpha$ are the displacement fields in the bodies Ω^α constrained at Γ_D^α and loaded with the boundary tractions $\mathbf{t}^\alpha$ along Γ_F^α, i.e.,

$$\hat{g} = g_0 - \hat{u}_n^R. \tag{8}$$

Here $\langle \cdot, \cdot \rangle_{\Gamma_C}$ is the duality pairing on $H^{-1/2}(\Gamma_C) \times H^{1/2}(\Gamma_C)$. The variational inequality (7) is equivalent to the following constrained minimization problem:

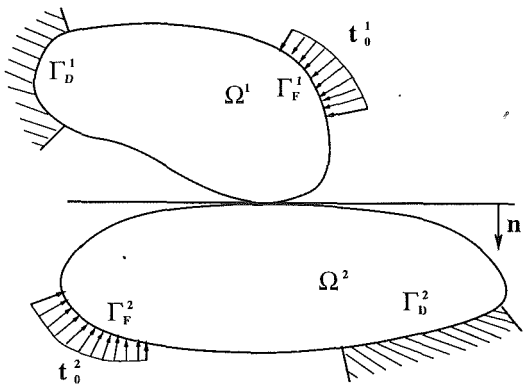


Fig. 1 A model of two-body contact problems

$$\min_{p \le 0} \Phi(p) = \frac{1}{2} \langle p, w \rangle_{\Gamma_C} - \langle p, \hat{g} \rangle_{\Gamma_C}. \tag{9}$$

Since the Green's operators are elliptic on $(H^{1/2}(\Gamma_C))'$ according to Kikuchi and Oden (1988, pp. 217, Eq. (8.80)), it can be easily proved that the variational inequality (7), or equivalently, the minimization problem (9), have a unique solution $p \in K$ whenever $\text{mes}(\Gamma_D^1) > 0$ and $\text{mes}(\Gamma_D^2) > 0$.

4 Numerical Solution of the Problem

4.1 Approximation of the Variational Inequality. A direct boundary element technique was adopted as a method for discretization of the continuous variational problem (9). In order to obtain a discrete version of a problem we have to approximate both, the ambient space $H^{-1/2}(\Gamma_C)$, and the possible contact surface Γ_C.

We partition the candidate contact surface Γ_C, a projection of the real contact surfaces Γ_C^α ($\alpha = 1, 2$) on the tangential plane at a representative contact point, into M_C flat polygonal regions $\{\Gamma_C^i\}_{i=1}^{M_C}$. Note that the shape of the real contact surfaces will be taken into consideration though the gap function g_0. We approximate the space $H^{-1/2}(\Gamma_C)$ with its finite dimensional subspace of all linear combinations of the zero-order shape functions which are constant over any boundary element Γ_C^i in Γ_C, namely

$$p(\mathbf{x}) = \sum_{i=1}^{M_C} \phi_i(\mathbf{x}) p_i \tag{10}$$

where $p_i \le 0 \in \mathbb{R}$, and $\phi_i(\mathbf{x})$ is indicator function for the boundary element Γ_C^i

$$\phi_i(\mathbf{x}) = \begin{cases} 1 \text{ if } \mathbf{x} \in \Gamma_C^i \\ 0 \text{ if } \mathbf{x} \notin \Gamma_C^i. \end{cases} \tag{11}$$

For a chosen approximation p, the relative displacement (6) can be written as

$$w(\mathbf{x}) = \sum_{j=1}^{M_C} w_j(\mathbf{x}) p_j \tag{12}$$

where

$$w_j(\mathbf{x}) = \int_{\Gamma_C} \mathbf{n}(\mathbf{x}) \cdot \mathbf{G}(\mathbf{x}, \eta) \cdot \mathbf{n}(\eta) \phi_j(\eta) dS_\eta \quad \forall \mathbf{x} \in \Gamma_C \tag{13}$$

and $\mathbf{G}(\mathbf{x}, \eta) = \mathbf{G}^1(\mathbf{x}, \eta) - \mathbf{G}^2(\mathbf{x}, \eta)$.

Using the approximations for p and w, the minimization problem (9) turns into the following finite dimensional quadratic programming problem,

Downloaded 03 May 2010 to 171.66.16.20. Redistribution subject to ASME license or copyright; see http://www.asme.org/terms/Terms_Use.cfm

$$\min_{\mathbf{p}\in\mathbf{K}^{M_C}} \Phi_{M_C}(\mathbf{p}) = \frac{1}{2}\sum_{i=1}^{M_C}\sum_{j=1}^{M_C} A_{ij}p_ip_j - \sum_{i=1}^{M_C} B_ip_i \qquad (14)$$

where $\mathbf{K}^{M_C} = \{\mathbf{p} \in \mathbb{R}^{M_C} | \forall i\ p_i \le 0\}$ and

$$A_{ij} = \int_{\Gamma_C} \phi_i(\mathbf{x}) w_j(\mathbf{x}) dS_x$$

$$B_i = \int_{\Gamma_C} \phi_i(\mathbf{x}) \hat{g}(\mathbf{x}) dS_x. \qquad (15)$$

In general, the Green's matrix is not available in explicit closed-form, except for a few simple cases such as for semi-infinite domains. Thus the relative displacement (13) must generally be approximated numerically for application in (15). Integrals (13) will be calculated numerically by the evaluation of the left-hand side using the direct boundary element method.

4.2 Approximation of the Green's Matrix: Boundary Integral Equation. According to the definition of a Green's function, integral (13) is nothing but the distribution of the normal relative displacements in Γ_C due to a uniform unit contact load over the element Γ_C^j. Therefore, the problem becomes one of finding the displacement fields $(\mathbf{u}_j)^\alpha$ in the bodies Ω^α, ($\alpha = 1, 2$), that satisfy the equilibrium conditions (1), the essential boundary condition (3) and with the following setup in Γ_C^j:

$$\left.\begin{aligned}(\mathbf{t}_j)^1(\mathbf{x}) &= -\phi_j(\mathbf{x})\mathbf{n}(\mathbf{x})\\ (\mathbf{t}_j)^2(\mathbf{x}) &= \phi_j(\mathbf{x})\mathbf{n}(\mathbf{x})\end{aligned}\right\} \forall \mathbf{x} \in \Gamma_C, \qquad (16)$$

for every $j = 1, \ldots, M_C$. Let $\text{mes}(\Gamma_D^\alpha) > 0$, ($\alpha = 1, 2$), then using Korn's inequality, it can be shown that this mixed boundary value problem has a unique solution that admits the representation

$$(\mathbf{u}_j)^\alpha(\mathbf{x}) + \int_{\Gamma^\alpha} \mathbf{T}^\alpha(\mathbf{x}, \xi)\cdot(\mathbf{u}_j)^\alpha(\xi)d\Gamma = \int_{\Gamma^\alpha} \mathbf{U}^\alpha(\mathbf{x}, \xi)\cdot(\mathbf{t}_j)^\alpha(\xi)d\Gamma \qquad (17)$$

where subscript j indicates that the uniform unit contact load has been applied over element Γ_C^j, according to (16). The matrix components of $\mathbf{U}^\alpha$ and $\mathbf{T}^\alpha$ in (17) are given by

$$U_{mn}^\alpha = \frac{1}{16\pi\mu(1-\nu)}\frac{1}{r}[(3-4\nu)\delta_{mn} + r_{,m}r_{,n}]$$

$$T_{mn}^\alpha = -\frac{1-2\nu}{8\pi(1-\nu)}\frac{1}{r^2}\left[\frac{\partial r}{\partial n}\left(\delta_{mn} + \frac{3}{1-2\nu}r_{,m}r_{,n}\right) - n_nr_{,m} + n_mr_{,n}\right], \qquad (18)$$

respectively, with $1 \le m, n \le 3$. In addition, λ and μ are Lame coefficients, and $\nu = \lambda/2(\lambda+\mu)$ is the Poisson ratio, of a body Ω^α. In addition, r is the distance between the field point $\mathbf{x}$ and the load point ξ, and the comma indicates differentiation with respect to the field point.

If we take the boundary values of both sides of (17) on Γ^α then we find

$$\frac{1}{2}(\mathbf{u}_j)^\alpha(\mathbf{x}) + \int_{\Gamma^\alpha} \mathbf{T}^\alpha(\mathbf{x}, \xi)\cdot(\mathbf{u}_j)^\alpha(\xi)d\Gamma = \int_{\Gamma^\alpha} \mathbf{U}^\alpha(\mathbf{x}, \xi)\cdot(\mathbf{t}_j)^\alpha(\xi)d\Gamma \qquad (19)$$

where the integrals are interpreted in the Cauchy Principal Value sense.

Equation (19) can be viewed as a constrained equation relating surface tractions to surface displacements. A general analytical solution of these integral Eqs. (19) is not available and it is necessary to approximate them numerically.

Consider discretizing Γ into M plane triangular elements, $\{\Gamma^l\}_{l=1}^M$, such that $\{\Gamma_C^i\} \subset \{\Gamma^l\}$. Let the boundary data be approximated by

$$\mathbf{u}^\alpha(\mathbf{x}) = \sum_{l=1}^{M} \phi_l(\mathbf{x})\mathbf{u}_l^\alpha$$

$$\mathbf{t}^\alpha(\mathbf{x}) = \sum_{l=1}^{M} \phi_l(\mathbf{x})\mathbf{t}_l^\alpha, \qquad (20)$$

where $\mathbf{u}_l^\alpha, \mathbf{t}_l^\alpha \in \mathbb{R}^3$, and the indicator function for the boundary element Γ^l is defined as in (11). Then, substituting these functions into (19), we arrive at a linear algebraic system of the form

$$\frac{1}{2}(\mathbf{u}_j)^\alpha(\mathbf{x}_k) + \sum_{l=1}^{M} \mathbf{T}_{kl}^\alpha\cdot(\mathbf{u}_j)_l^\alpha = \sum_{l=1}^{M} \mathbf{U}_{kl}^\alpha\cdot(\mathbf{t}_j)_l^\alpha \quad (\alpha = 1, 2) \qquad (21)$$

where

$$\mathbf{T}_{kl}^\alpha = \int_{\Gamma^\alpha} \mathbf{T}(\mathbf{x}_k, \xi)\phi_l(\xi)d\Gamma$$

$$\mathbf{U}_{kl}^\alpha = \int_{\Gamma^\alpha} \mathbf{U}(\mathbf{x}_k, \xi)\phi_l(\xi)d\Gamma, \qquad (22)$$

and where $\mathbf{x}_k$, ξ_l are centroids of the elements Γ^k and Γ^l, respectively. In general, the solution of the mixed boundary value problem is obtained by first appropriately rearranging the columns in Eq. (21), in accordance with classical boundary integral solution strategies (see Cruse, 1988, for details). The set of algebraic equations obtained in this way has been solved by a standard Gauss elimination scheme.

Finally, after solving Eqs. (21), one can obtain the normal displacements in $\{\Gamma_C^i\}_{i=1}^{M_C}$ due to a unit pressure distribution over Γ_C^j (see Eq. (16)) as

$$w_j(\mathbf{x}_i) = [(\mathbf{u}_j)^1(\mathbf{x}_i) - (\mathbf{u}_j)^2(\mathbf{x}_i)]\cdot\mathbf{n}(\mathbf{x}_i). \qquad (23)$$

In order to establish Eq. (23) for all $(\mathbf{t}_j)^\alpha$, ($j = 1, \ldots, M_C$, $\alpha = 1, 2$), as required by (15), Eqs. (21) ought to be solved $2 \times M_C$ times, with defined boundary conditions on Γ_D^α.

4.3 Numerical Solution of the Variational Problems. Let us now return to the computation of the coefficients in (14), given by (15). Approximations (10) and (12) placed into (15) yield for the coefficients of a quadratic term in (14)

$$A_{ij} \simeq \int_{\Gamma_C} \phi_i(\mathbf{x})w_j(\mathbf{x})dS_x = \text{mes}(\Gamma_i)w_j(\mathbf{x}_i) \qquad (24)$$

and for the coefficients of a linear term in (14)

$$B_i \simeq \text{mes}(\Gamma_i)\hat{g}(\mathbf{x}_i). \qquad (25)$$

Note again that $w_j(\mathbf{x}_i)$ stands for a displacement in the center of the element Γ_C^i due to unit pressure distribution over Γ_C^j. Since the structure of the constraints in the minimization problem (14) is simple, a modification of the gradient-projection method has been implemented for its solution, as in Rabinovich and Spector (1985).

5 Rigid Punch Problem

A special and important class of contact problems involves the indentation of a deformable body by a rigid "punch", i.e., a rigid body of specified shape. Mathematically, rigid punch problems have certain features which distinguish them from the general problem discussed in the previous sections.

Let us assume that one of the bodies in the general contact problem given in Fig. 1, say body Ω^1, is rigid, we will call it the punch. A body of interest, we will call it the foundation, is then $\Omega^2 \equiv \Omega$, and will be assumed linearly elastic. Furthermore, we will assume that the punch is not fixed, i.e., $\Gamma_D = \emptyset$ for the punch, and that it can only translate perpendicular to the contact plane (indentation). Assuming that the geometry

Downloaded 03 May 2010 to 171.66.16.20. Redistribution subject to ASME license or copyright; see http://www.asme.org/terms/Terms_Use.cfm

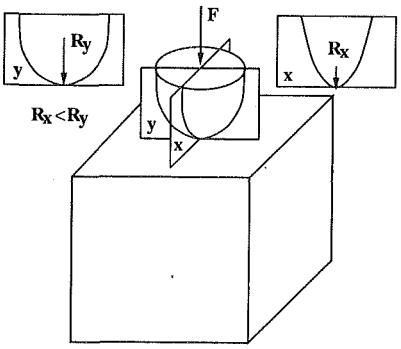


Fig. 2 Indentation of an elastic unit cube by a rigid punch with the shape of a second-degree paraboloid

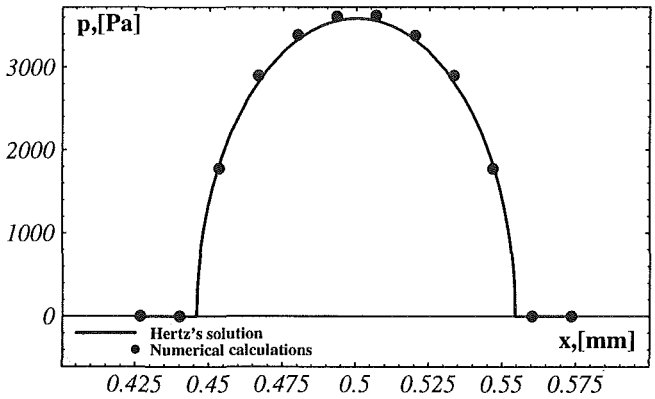


Fig. 3 Contact pressure in the *x*-plane of Fig. 2

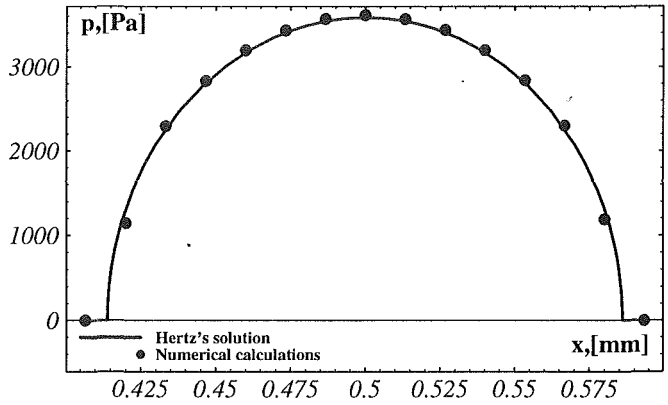


Fig. 4 Contact pressure in the *y*-plane of Fig. 2

of the surfaces of both bodies are known, that the rigid-body motion of the punch (indentation) is given, and for given boundary conditions at the foundation, the objective is to find the contact area and the pressure acting in it. Obviously, the original boundary value problem now becomes one of finding a displacement field, $\mathbf{u}$, and a stress field, σ_{ij}, in the foundation Ω that satisfies the equilibrium conditions (1), the natural and the essential boundary conditions (2) and (3), respectively, as well as the contact condition (4) with the following expression for the gap function

$$\hat{g}(\mathbf{x}) = g_0(\mathbf{x}) - \delta(\mathbf{x}) \quad \forall \mathbf{x} \in \Gamma_C \tag{26}$$

where $\delta(\mathbf{x})$ is a rigid-body displacement (indentation) of a material point $\mathbf{x} \in \Gamma_C$ of the punch measured along the normal $\mathbf{n}$ to the contact plane.

The variational inequality (7), or equivalently the minimization problem (9), has the same form with a relative displacement given as $w = \gamma^0_{\Sigma_n}(\mathbf{u}^2)$. The existence and uniqueness of the solution is then guaranteed by Theorem 8.8 (pp. 228–229) of Kikuchi and Oden (1988).

6 Numerical Results

Series of boundary value problems were solved to verify the accuracy of the approximations discussed in the previous sections. The computed results are given for the indentation of a rigid frictionless punch into a deformable cube with unit dimensions. In all cases sufficient displacements were set to zero, i.e., $\text{mes}(\Gamma_D) > 0$, to eliminate the rigid-body motion. The results presented are for the case of 108 boundary elements and values of Poisson's ratio $\nu = 0.3$. Additionally the surface element arrangement in the candidate contact surface Γ_C and the indentation are required. The results consist of the contact area, the pressure acting in it, as well as stresses and displacements where required.

6.1 Half-Space Contact Problems. For test examples to estimate the accuracy of the calculation, we consider two problems involving indentation of a rigid frictionless punch into a center of an elastic unit cube, as shown in Fig. 2. The shape of the punch will be a second-degree paraboloid and a fourth-degree paraboloid, respectively. These are two well-known three-dimensional contact problems, which in the case of an semi-infinite foundation have analytical solutions, namely Hertz problem (Johnson, 1985, pp. 90–104), and the blunt punch problem (Lur'e, 1964, pp. 279–284). It may be expected that the influence of the free sides of a cube will be negligible in these cases, and the solutions should be close to the analytical ones.

First consider the Hertz problem. The results presented here are for the depth of indentation of $d = 1.66 \times 10^{-3}$, and for the case of $15 \times 12 \times 2$ triangles in the candidate contact zone Γ_C. The contact pressure in the planes x and y of Fig. 2 are presented in Figs. 3 and 4, respectively. Numerical results are plotted along with the analytical solutions of Hertz for the half-space (see Johnson, 1985, pp. 90–104). As expected, the results of the numerical calculations are in good agreement with the analytical solution, indicating that the influence of the free boundary is negligible.

Next consider the blunt punch problem. It is well known that in the contact problems local pressure maxima occur on segments where the curvature of the profile of the contacting surfaces changes sharply. For the punch profile given by a fourth-degree paraboloid, the local pressure maxima occur in the neighborhood of the edge zone as shown in Lur'e (1964, pp. 279–284). The ability of our method to deal with this type of contact problem, where the solution for integral equations exhibit a "boundary layer" nature, will be tested here. The results presented are for the depth of indentation of $d = 1.64 \times 10^{-5}$ and for the case of $16 \times 16 \times 2$ triangles in the candidate contact zone Γ_C. The contact pressure is presented in Fig. 5. Numerical results are plotted along with the analytical solution obtained for the half-space by Lur'e (1964, pp. 279–284). Two observations may be made. First, it is seen that the results of the numerical calculations are in good agreement with the analytical solution for the half-space, indicating that the influence of the free boundary is negligible. Secondly, the results demonstrate the ability of a model to describe a "boundary layer" nature of the solution.

6.2 Finite Bodies Contact Problems. In order to examine the free boundary effect, we have performed a series of calculations for the axisymmetrical rigid punch with the shape of a fourth-order paraboloid. The punch is indenting at the corner of the cube as shown in Fig. 6. The results presented are for

Downloaded 03 May 2010 to 171.66.16.20. Redistribution subject to ASME license or copyright; see http://www.asme.org/terms/Terms_Use.cfm

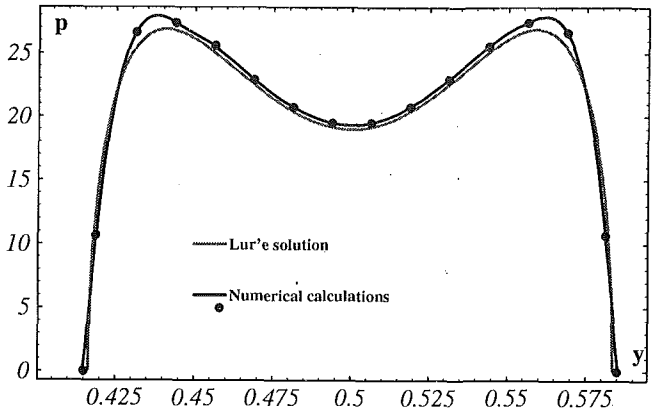


Fig. 5 Indentation of an elastic unit cube by a rigid punch with the shape of a fourth-order paraboloid: contact pressure

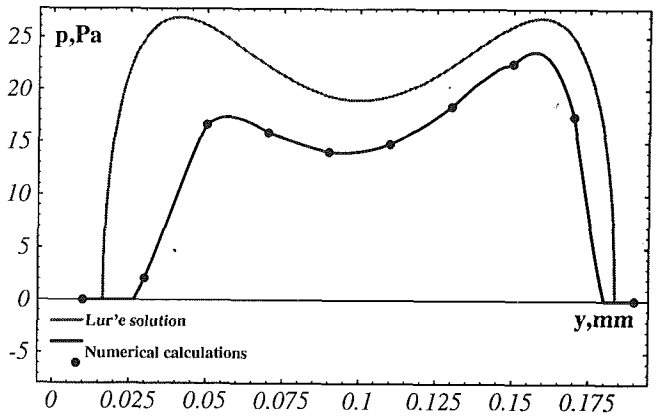


Fig. 7 Contact pressure in the y-plane of Fig. 6: illustration of the influence of the free boundary

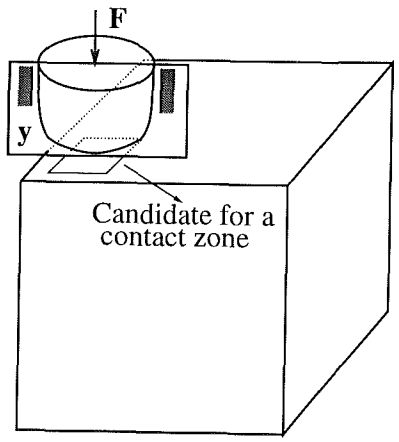


Fig. 6 Indentation of a corner of an elastic unit cube by a rigid punch with the shape of a fourth-order paraboloid

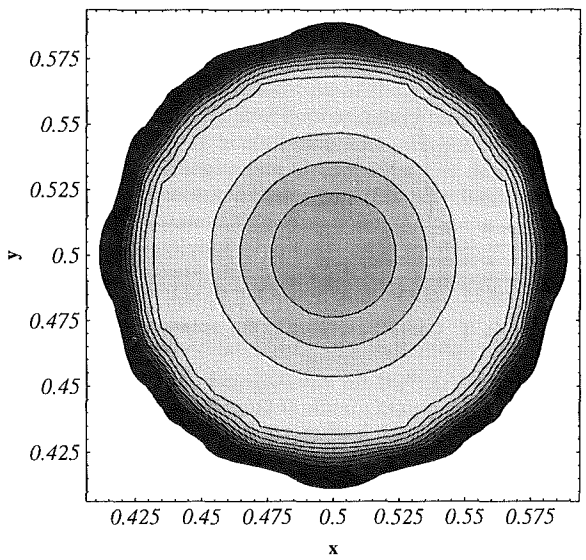


Fig. 8 Contact zone for the case given in Fig. 5

the depth of indentation $d = 1.64 \times 10^{-5}$, and for $10 \times 10 \times 2$ triangles in the candidate contact zone Γ_C. A contact pressure in the plane y of Fig. 6 is presented in Fig. 7. For comparison, numerical results are plotted along with the analytical solution for the half-space problem (Lur'e, 1964, pp. 279–284). One can see that the pressure is lower at the points close to the free surface, as what should be expected on the physical ground; the material is "softer" close to the free boundary.

6.3 The Contact Area. In Figure 8, a contact area and several isobars are given for the axisymmetrical rigid punch with the shape of a fourth-order paraboloid; the corresponding pressure distribution is given in Fig. 5. Note that the lighter shaded regions correspond to higher pressure and darker shaded regions to lower pressure. The outermost isobar is the numerically obtained boundary of the contact area. It is seen that the shape of the contact zone is quite satisfactory; the slight irregularities in the shape of the contact zone are the consequence of the discretization.

The influence of the free boundary on a structure of the contact zone for a rigid blunt punch problem is illustrated in Fig. 9. Again, the lighter shaded regions correspond to higher pressure and darker shaded regions to lower pressure. It is seen that the contact zone is symmetric with respect to the diagonal plane and that the region of higher pressure is shifted towards the bulk of the material.

6.4 Some Remarks Regarding the Symmetry. The approximations involved in the discretization and collocation processes amount to an imperfect evaluation of the bilinear

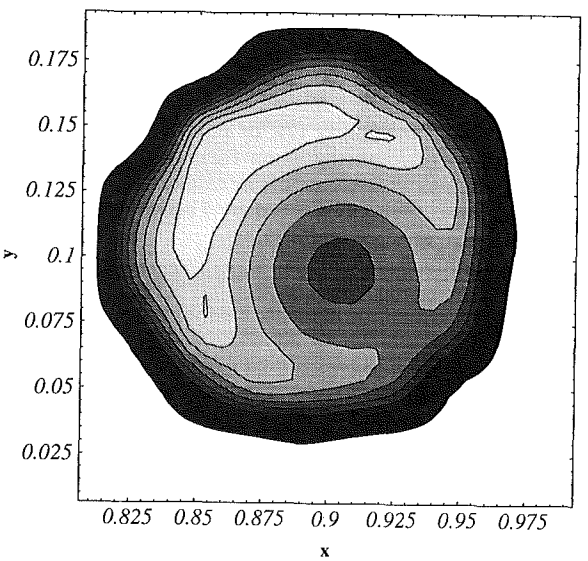


Fig. 9 Contact zone for the case given in Fig. 6: illustration of the influence of the free boundary

Downloaded 03 May 2010 to 171.66.16.20. Redistribution subject to ASME license or copyright; see http://www.asme.org/terms/Terms_Use.cfm

Table 1 Symmetry properties

No. elem.	Asym. (percent)	Diff. in press. (percent)	Ratio of norms $\|A_{ij}\| / \|A_j^{sym}\|$	Equilibrium percent $[A_{ij}]$	Equilibrium percent $[A_{ij}]^{sym}$
474	12.6	1.7	0.0165	−1.428	−1.437
942	8.0	0.97	0.0106	−0.87	−0.88

form in (14). Consequently, the symmetry properties of the Green's operator hold only asymptotically for the discretized problem.

To test the asymmetry of the quadratic part of the functional $\Phi_{M_C}(p)$, A_{ij}, and its influence on the results obtained two different discretization of the surface $\Gamma - \Gamma_C$ were used in the experiment described in Section 6.2 (474 and 942 elements). The measure of the asymmetry of the A_{ij} matrix is computed by means of Bauer-Roy scaling,

$$\max \left| \frac{A_{ij} - A_{ji}}{\sqrt{|A_{ii}|}\sqrt{|A_{jj}|}} \right|.$$

Maximum deviation from symmetry was 12.6 percent for 476 elements, and 8 percent for 942 elements, as given in Table 1. In order to estimate the influence of this local asymmetry to the contact pressure, the contact pressure is obtained first with the matrix $[A_{ij}]$ and then with its symmetric part, $[A_{ij}]^{sym}$. The relative difference is 1.7 percent in the first discretization and 0.97 percent in the second discretization, as shown in the third column of Table 1. Furthermore, the ratios of the Frobenious norms of these two matrices are equal to 0.0165 for the first discretization, and 0.0106 for the second discretization.

Finally, in columns five and six we address the concern that boundary element method results satisfy equilibrium not exactly but in an asymptotic way. The error in computing equilibrium in the vertical direction was 1.428 percent of the total reaction for the first discretization and 0.87 percent for the second discretization. Similar errors were found in the calculations based on the symmetric part the matrix $[A_{ij}]$.

7 Conclusion

A method for the numerical solution of the frictionless contact between two elastic bodies having arbitrary shape and loading is presented. Starting from a rigorous variational formulation for the contact problem and its related extremum principle, a numerical method is defined by means of boundary element discretization. More specifically, the Green's function associated with the formulation is approximated by means of standard direct boundary element procedure. The discretization leads to the finite dimensional quadratic programming problem which was solved by a modification of the gradient-projection method.

A variety of problems including Hertzian and non-Hertzian contact problems were investigated numerically. The results of our calculations are in good agreement with existing analytical results. It has been demonstrated that the symmetry properties of the Green's operator hold only asymptotically for the discretized problem. Finally, important new sets of results for three-dimensional finite-bodies contact problems are reported.

References

Alliney, S., Tralli, A., and Alessandri, C., 1990, "Boundary Variational Formulations and Numerical Solution Techniques for Unilateral Contact Problems," *Computational Mechanics*, Vol. 6, pp. 247–257.

Bufler, H., Lieb, H., and Meier, G., 1982, "Frictionless Contact Between an Elastic Stamp and an Elastic Foundation," *Ingenieur-Archiv*, Vol. 52, pp. 63–76.

Chan, S. K., and Tuba, I. S., 1971, "A Finite Element Method for Contact Problems of Solid Bodies—Part I. Theory and Validation," *International Journal of Mechanical Sciences*, Vol. 13, pp. 615–625.

Cruse, T. A., 1988, *Boundary Element Analysis in Computational Fracture Mechanics*, Kluwer.

Cruse, T. A., 1969, "Numerical Solutions in Three Dimensional Elastostatics," *International Journal of Solids Structures*, Vol. 5, pp. 1259–1274.

Fichera, G., 1972, "Boundary Value Problems of Elasticity with Unilateral Constraints," *Encyclopedia of Physics*, Vol. VI a/2, S. Flügge, ed., Springer, Berlin.

Gladwell, G. M. L., 1980, *Contact Problems in the Classical Theory of Elasticity*, Sijthoff and Nordhoff.

Hertz, H. R., 1882, *Hertz's Miscellaneous Papers*, MacMillan Press, London, Chapters 5, 6.

Johnson, K. L., 1985, *Contact Mechanics*, Cambridge University Press, pp. 452.

Kalker, J. J., 1975, "The Mechanics of the Contact Between Deformable Bodies," *Proceedings of the IUTAM Symposium*, A. D. de Pater and J. J. Kalker, eds., Delft Univ. Press, Delft, The Netherlands.

Kikuchi, N., 1979, "A Class of Rigid Punch Problems Involving Forces and Moments," *International Journal of Mechanical Sciences*, Vol. 17, pp. 1129–1140.

Kikuchi, N., and Oden, J. T., 1988, *Contact Problems in Elasticity: A Study of Variational Inequalities and Finite Element Methods*, SIAM, Philadelphia.

Lur'e, A. I., 1964, *Three-Dimensional Problems of the Theory of Elasticity*, John Wiley and Sons, New York.

Panagiotopoulos, P. D., 1985, *Inequality Problems in Mechanics and Applications*, Birkhäuser, Basel.

Panagiotopoulos, P. D., and Lazaridis, P. P., 1987, "Boundary Minimum Principles for the Unilateral Contact Problems," *International Journal of Solids Structures*, Vol. 23, pp. 1465–1484.

Rabinovich, V. L., and Spector, A. A., 1985, "Solution of Some Classes of Three Dimensional Contact Problems With An Unknown Boundary," *Mechanics of Solids*, Vol. 20, pp. 89–97.

Downloaded 03 May 2010 to 171.66.16.20. Redistribution subject to ASME license or copyright; see http://www.asme.org/terms/Terms_Use.cfm

The Contact Behavior Between Laminated Composite Plates and Rigid Spheres

Enboa Wu
Associate Professor,
Assoc. Mem. ASME

Ching-Shih Yen
Graduate Student.

Institute of Applied Mechanics,
National Taiwan University,
Taipei, Taiwan 10764,
Republic of China

The contact behavior between a composite laminate and a rigid sphere is discussed in this paper using a method derived from the three-dimensional anisotropic elasticity theory. Response of the plate and the force-indentation $(F-\alpha)$ *relationship were obtained by constructing an exact Green's function of the laminate. Agreement between the prediction and the experimental data reported by others is excellent before laminates are damaged. The* $F-\alpha$ *relationship is approximately proportional to the out-of-plane Young's modulus and is influenced by the plate thickness. The effects of changing the in-place Young's moduli, all the shear moduli, stacking sequences and span of the laminates are insignificant unless identation is large. Further, the modified Hertz law underestimates the contact force for the same indentation.*

1 Introduction

It was shown by Tan and Sun (1985) that the contact law of a laminate indented by a rigid sphere obtained from a quasi-static test can be applied to study low velocity impact. However, if the contact law is obtained by experiment, changes of the relevant parameters, such as indentor sizes, material properties, stacking sequence, span or thickness of the laminates require a new identation test to be done. Because the test is complicated and time-consuming, it is worthwhile constructing the force-indentation relationship using an analytical method and studying the effect due to these parameter changes.

The analytical contact law between two isotropic bodies, of which the profiles of both bodies near the contact zone can be approximated by quadratic surfaces, was first developed by Hertz (1881). This famous law was widely applied to study contact between a rigid sphere and an elastic, isotropic half-space. Willis (1966) investigated the contact behavior between a transversely isotropic half-space and a rigid sphere. They both found that the contact force is proportional to 1.5 power of indentation. However, when a composite laminate with finite dimensions is in contact with a rigid indentor, the behavior may deviate drastically from that predicted by the half-space solution. In the two-dimensional contact problem, which is quite often encountered in the short beam shear and three- or four-point flexural test for isotropic, orthotropic, or laminated beams, various methods have been used to investigate the contact pressure profile. It is found that the pressure profile may change from a semi-ellipse to a saddle shape (Keer and Miller, 1983; Sankar and Sun, 1983; Sankar, 1989). Among these analyses, the methods combining an elasticity solution describing the local contact phenomenon with a beam solution for the global response were mostly used. For example, Keer and Miller (1983) studied the contact behavior of an orthotropic beam by a cylinder using an infinite layer solution. Another popular method for beam types of problems was to use a Green's function and integral equations to correlate the applied force and the beam response. For example, Sankar (1989) superposed an orthotropic half-space solution on a beam solution to construct an approximate Green's function. On the other hand, Cairns and Lagace (1987) investigated the contact behavior between a composite plate and a rigid sphere by adopting Hertzian pressure distribution. They used a series of Bessel functions and converted a laminated plate to that with axisymmetric properties.

To avoid the limitations by using an approximate Green's function (Sankar, 1989) and the Hertzian pressure profile (Cairns and Lagace, 1987), we constructed an exact Green's function based on an exact solution developed by Pagano (1970). The present method allows arbitrary loads to be applied to a laminated plate of simple supports, provided that the loads can be represented by double Fourier sine series. Since both the contact area and the pressure are unknowns, the exact solution is not attainable. Therefore, a numerical procedure is developed in this study. In the numerical procedure, the contact area is discretized into small rectangular patches and the load inside each patch is represented using double Fourier series. Laminate responses to this discrete loading are then calculated using a Green's function. Iterations are needed to obtain the final contact pressure distribution and the contact area as well as the overall plate response to a known indentor

Contributed by the Applied Mechanics Division of THE AMERICAN SOCIETY OF MECHANICAL ENGINEERS for publication in the ASME JOURNAL OF APPLIED MECHANICS.

Discussion on this paper should be addressed to the Technical Editor, Professor Lewis T. Wheeler, Department of Mechanical Engineering, University of Houston, TX 77204-4792, and will be accepted until four months after final publication of the paper itself in the ASME JOURNAL OF APPLIED MECHANICS.

Manuscript received by the ASME Applied Mechanics Division, Dec. 12, 1991; final revision, Dec. 31, 1992. Associate Technical Editor: G. J. Dvorak.

Copyright © 1994 by ASME
Downloaded 03 May 2010 to 171.66.16.20. Redistribution subject to ASME license or copyright; see http://www.asme.org/terms/Terms_Use.cfm

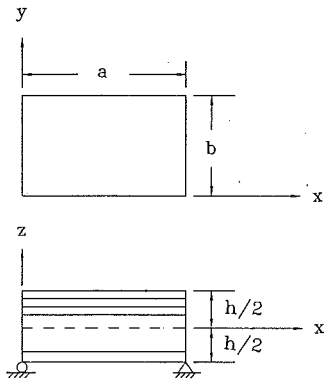


Fig. 1 Schematic of an orthotropic laminated plate of simple supports

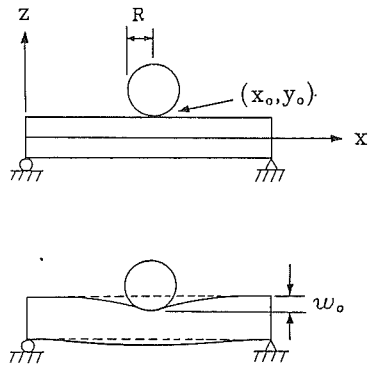


Fig. 2 Contact schematic between a laminated plate and a rigid sphere

movement. Effects of changing the material properties, stacking sequence, span and thickness of the plate, and the indentor size on the force-indentation relationships are also studied.

2 Method of Solution

The method developed in this section is applicable to a laminated plate composed of orthotropic plys such that the material axes for each ply are parallel to the plate axes (Fig. 1), or with a balanced stacking sequence (Jones, 1975) and is modeled as a nonlaminated orthotropic continuum such that the material axes of the plate are aligned with the plate axes. From the analysis point of view, the latter is a special case of the former. Thus only the derivation of the orthotopic laminated plate is considered in this section. The constitutive relationship for each orthotropic ply is

$$\begin{Bmatrix} \sigma_x \\ \sigma_y \\ \sigma_z \\ \tau_{yz} \\ \tau_{xz} \\ \tau_{xy} \end{Bmatrix} = \begin{bmatrix} C_{11} & C_{12} & C_{13} & 0 & 0 & 0 \\ C_{12} & C_{22} & C_{23} & 0 & 0 & 0 \\ C_{13} & C_{23} & C_{33} & 0 & 0 & 0 \\ 0 & 0 & 0 & C_{44} & 0 & 0 \\ 0 & 0 & 0 & 0 & C_{55} & 0 \\ 0 & 0 & 0 & 0 & 0 & C_{66} \end{bmatrix} \begin{Bmatrix} \epsilon_x \\ \epsilon_y \\ \epsilon_z \\ \gamma_{yz} \\ \gamma_{xz} \\ \gamma_{xy} \end{Bmatrix} \tag{1}$$

where x, y, and z are the plate axes (Fig. 1) and C_{ij} is the stiffness constant. If the infinitesimal strain theory of elasticity is used, the governing equations for each orthotropic lamina in terms of displacements and in the absence of body forces can be written as follows:

$$C_{11}u_{,xx} + C_{66}u_{,yy} + C_{55}u_{,zz} + (C_{12} + C_{66})v_{,xy} + (C_{13} + C_{55})w_{,xz} = 0 \tag{2}$$

$$C_{66}v_{,xx} + C_{22}v_{,yy} + C_{44}v_{,zz} + (C_{12} + C_{66})u_{,xy} + (C_{23} + C_{44})w_{,yz} = 0 \tag{3}$$

$$C_{55}w_{,xx} + C_{44}w_{,yy} + C_{33}w_{,zz} + (C_{13} + C_{55})u_{,xz} + (C_{23} + C_{44})v_{,yz} = 0 \tag{4}$$

where u, v, and w are the displacements of the plate in the x, y, and z directions, respectively. Let the following loading be applied to such a laminate:

$$\sigma_z(x, y, h/2) = p_0 \sin\frac{n\pi x}{a} \sin\frac{m\pi y}{b} \tag{5}$$

$$\sigma_z(x, y, -h/2) = \tau(x, y, \pm h/2) = \tau(x, y, \pm h/2) = 0. \tag{6}$$

Here, p_0 is a constant, m and n are arbitrary integers, a and b are the in-plane dimensions, and h is the laminate thickness, as exemplified in Fig. 1. If simply-supported boundaries are assumed, the boundary conditions are given by

$$\sigma_x = v = w = 0, \text{ at } x = 0, a \tag{7}$$

$$\sigma_y = u = w = 0, \text{ at } y = 0, b. \tag{8}$$

The exact solution to this problem was obtained previously by Pagano (1970) using the three-dimensional linear anisotropic elasticity theory. Therefore, for any point, (x, y), located on the upper surface of such a plate and subjected to $\sin n\pi x/a \sin m\pi y/b$ loading on its upper surface, the lateral displacement, $w_{mn} \sin n\pi x/a \sin m\pi y/b$ is known. Since linear elasticity is used, the superposition principle holds for the applied loading and the corresponding plate response. For such a laminate subject to arbitrary lateral loading, $P(x, y)$, expressed by double Fourier series, the lateral displacement becomes

$$w(x, y) = \sum_{m,n} P_{mn} w_{mn} \sin\frac{n\pi x}{a} \sin\frac{m\pi y}{b}. \tag{9}$$

In the above equation, P_{mn} is the Fourier coefficient of loading $P(x, y)$, i.e.,

$$P(x, y) = \sum_{m,n} P_{mn} \sin\frac{n\pi x}{a} \sin\frac{m\pi y}{b} \tag{10}$$

where m and n vary from 1 to ∞.

For a laminated plate in contact with a rigid indentor, Eq. (9) represents exactly the lateral displacement on the loading surface of the plate if the contact pressure is equal to $P(x, y)$ in Eq. (10). However, the contact region and the pressure distribution both appear as unknown for a known indentor movement, w_0, as shown in Fig. 2. To the best of our knowledge, the exact solution is still not available.

From Eq. (9) and the orthogonality condition of Fourier series, the lateral displacement on the upper surface of the plate subject to $P(x, y)$ in the contact region, Ω, is

$$w(x, y) = \sum_{m,n} w_{mn} \left(\frac{4}{ab} \int_\Omega P(\xi, \eta) \sin\frac{n\pi\xi}{a} \sin\frac{m\pi\eta}{b} d\xi d\eta \right). \tag{11}$$

$$\sin\frac{n\pi x}{a} \sin\frac{m\pi y}{b} = \int_\Omega G(x, y; \xi, \eta) P(\xi, \eta) d\xi d\eta \tag{12}$$

where

$$G(x, y; \xi, \eta) = \frac{4}{ab} \sum_{m,n} w_{mn} \sin\frac{n\pi\xi}{a} \sin\frac{m\pi\eta}{b} \sin\frac{n\pi x}{a} \sin\frac{m\pi y}{b} \tag{13}$$

is the Green's function. It is the lateral displacement at (x, y) due to unit loading applied at (ξ, η) on the upper surface of the plate.

At indentor movement w_0, the indentor profile is

$$z - \frac{h}{2} = f(x, y). \tag{14}$$

Thus, for any point $(x, y) \in \Omega$, we have

Downloaded 03 May 2010 to 171.66.16.20. Redistribution subject to ASME license or copyright; see http://www.asme.org/terms/Terms_Use.cfm

$$f(x, y) = \int_{\Omega} G(x, y; \xi, \eta) P(\xi, \eta) d\xi d\eta. \quad (15)$$

The physical meaning of the above equation is that the upper surface of the plate within the contact region conforms to the indentor profile. In fact, there are other conditions to be satisfied for meaningful contact:

$$P(x, y) < 0, \quad (x, y) \in \Omega \quad (16)$$

$$P(x, y) = 0, \quad (x, y) \in (\Phi - \Omega) \quad (17)$$

$$(x, y) \notin B, \quad (x, y) \in (\Phi - \Omega) \quad (18)$$

where Φ and B are the regions representing the upper surface of the plate and the indentor, respectively. Equation (16) requires that only compressive contact pressure be allowed. Equation (17) expresses the fact that the area outside the contact region is loading free. Equation (18) represents the noninterpenetration condition outside the contact area.

Because the exact solution is difficult, if not impossible, to be obtained analytically from the above formulation, a numerical procedure was employed to solve Eq. (15). In the numerical procedure, an initial contact area is first assumed. This area should be sufficiently large to include the actual contact zone between the indentor and the laminate upper surface. The area is then divided into N small rectangular patches each with dimensions of s and t. By assuming constant pressure inside each of these patches, Eq. (15) can be expressed as

$$f(x, y) = \sum_{j=1}^{N} P_j \int_{y_j - t/2}^{y_j + t/2} \int_{x_j - s/2}^{x_j + s/2} G(x, y; \xi, \eta) d\xi d\eta \quad (19)$$

where (x_j, y_j) is the center of the small rectangular patch. Equation (19) can be integrated to give

$$f(x, y) = \sum_{j=1}^{N} \left[\sum_{m, n} K_{mn}(x, y) \sin \frac{n\pi x_j}{a} \sin \frac{m\pi y_j}{b} \right] P_j \quad (20)$$

where

$$K_{mn}(x, y) = \frac{16 w_{mn}}{mn\pi^2} \sin \frac{n\pi s}{2a} \sin \frac{m\pi t}{2b} \sin \frac{n\pi x}{a} \sin \frac{m\pi y}{b}. \quad (21)$$

Now, if a rigid sphere is used as the indentor, the profile function, $f(x, y)$, has the following form:

$$f(x, y) = w_0 - R + \sqrt{R^2 - r^2} \quad (22)$$

where R is the radius of the sphere, $r = \sqrt{(x - x_0)^2 + (y - y_0)^2}$, and (x_0, y_0) is the initial contact point, as shown in Fig. 2.

Equations (20) and (22) are the main equations to be solved for the smooth contact problem between a rigid sphere and an orthotropic laminate with simple supports.

In order to solve for the N unknown pressure values, P_i, $i = 1, \ldots, N$, at least N linear independent equations are needed. However, because the solution to Eq. (20) is approximate due to discretization, randomly distributed errors may result. Thus, if we construct more than N equations, the error could be reduced using the least-square method. This is the idea of the method of redundant field points which has been successfully employed to solve the contact problem of an isotropic half-space (Singh and Paul, 1974; Ahmadi et al., 1983). In this paper, we chose all patch nodes and centers as the field points to construct $2N$ equations to solve Eq. (20) for P_i.

As the values of P_i are determined, Eq. (16) is checked. If there are patches where Eq. (16) is violated, the patches are removed and the solution procedure is repeated. The solution is deemed final when Eq. (16) is satisfied for all patches. Normally, in our calculations it took three to five iterations to reach the final solution. The effect of the patch size in the determination of the results will be discussed in the next section.

3 Results

Experimental results obtained from Tan and Sun (1985) were employed to check the validity of the analytical method developed in the above section. Each of the $[0°/45°/0°/-45°/0°]_{2s}$ graphite/epoxy laminae made of unidirectional pre-pregs has the following material properties:

$$E_1 = 120\text{GPa } (17.5 \times 10^6\text{psi})$$

$$E_2 = 7.9\text{GPa } (1.15 \times 10^6\text{psi}) = E_3$$

$$G_{12} = 5.5\text{GPa } (0.8 \times 10^6\text{psi}) = G_{13}$$

$$\nu_{12} = 0.30 = \nu_{13} \quad (23)$$

where E_1 and E_2 are the Young's moduli in the longitudinal and transverse directions, respectively; G_{12} is the in-plane shear modulus and ν_{12} is the Poisson's ratio of the lamina. Because the Poisson's ratio, ν_{23}, was not specified in Tan and Sun (1985), three different Poisson's ratios, $\nu_{23} = 0.3$, 0.4 and 0.45 that cover a reasonable range of graphite/epoxy pre-pregs were selected. In addition, because of transverse isotropy of unidirectional pre-pregs, the corresponding transverse shear moduli, G_{23}, are obtained by $G_{23} = E_3/2(1 + 2\nu_{23})$. The values are 3.04., 2.82 and 2.72 Gpa, respectively. Also, because the derivation is limited to an orthotropic laminate or a balanced laminate which is modeled as an orthotropic continuum, the material properties for this $[0°/45°/0°/-45°/0°]_{2s}$ laminate were averaged and formed only one layer in the analysis. The averaging process is: (1) form the stiffness coefficients, C_{ij}, for each lamina; (2) perform tensor transformation for each lamina to obtain $\bar{C}_{ij}$ referred to the $x-y$ coordinate system (Fig. 1); and (3) obtain the average material properties, which are equivalent to those for an orthotropoic plate due to the balanced stacking sequence. The average material properties for $\nu_{23} = 0.3$ are listed below:

$$E_{xx} = 80.2\text{GPa}(11.7 \times 10^6\text{psi})$$

$$E_{yy} = 18.5\text{GPa}(2.70 \times 10^6\text{psi})$$

$$E_{zz} = 8.36\text{GPa}(1.22 \times 10^6\text{psi})$$

$$G_{xy} = 15.7\text{GPa}(2.29 \times 10^6\text{psi})$$

$$G_{yz} = 3.52\text{GPa}(0.514 \times 10^6\text{psi})$$

$$G_{xz} = 4.99\text{GPa}(0.728 \times 10^6\text{psi})$$

$$\nu_{xy} = 0.62 \ \nu_{yz} = 0.27 \ \nu_{xz} = 0.018. \quad (24)$$

The material properties for using $\nu_{23} = 0.4$ and 0.45 were calculated accordingly. The dimensions of the laminated plate are 50.8 mm × 50.8mm × 2.7mm. In the following discussions, the indentation, α, is defined as

$$\alpha = w(x_0, y_0, -h/2) - w(x_0, y_0, h/2) \quad (25)$$

where w is the lateral displacement of the plate. Note that the positive value of w is in the upper direction, and contact occurs on the upper surface of the plate where $z = h/2$, as illustrated in Fig. 2.

As a first check, we compared the solutions obtained from two different types of discretization. The indentor used was 19.1 mm in diameter. From Fig. 3, use of 70 × 70 double Fourier sine series and square patches, each with dimension ratio of $r = 0.006$, gave the same $F - \alpha$ relationship as that obtained using 200 × 200 double Fourier terms and $r = 0.004$, where r is the ratio of the selected patch size to the plate span. Therefore, 70×70 Fourier series and $r = 0.006$ were enough for the analysis. A direct way to check convergence of the numerical results is to re-analyze the problem using refined patches and more Fourier terms. It is then to compare the results obtained from two discretization procedures. In general, more Fourier terms and smaller r are needed for indentors

Downloaded 03 May 2010 to 171.66.16.20. Redistribution subject to ASME license or copyright; see http://www.asme.org/terms/Terms_Use.cfm

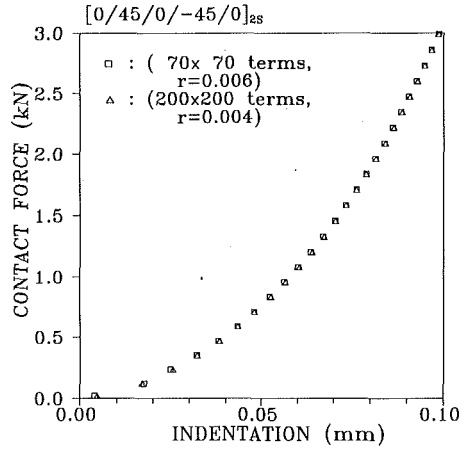


Fig. 3 Convergence test for force-indentation analyses

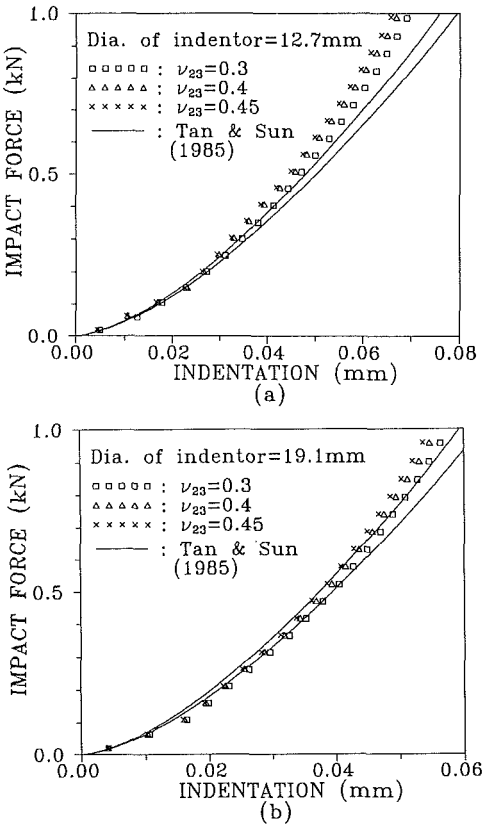


Fig. 4 Comparison of the prediction and the experimental results. The rigid spheres used are (*a*) 12.7 mm and (*b*) 19.1 mm in diameters. The stacking sequence is [0/45/0/-45/0]2s.

with smaller diameters. In this paper, convergence was obtained for all the calculations using 70×70 to 200×200 Fourier terms for $r=0.006$ to $r=0.004$, respectively.

A second check was to compare the prediction with the experimental results obtained from Tan and Sun (1985). Figures 4(*a*) and (*b*) show results for 12.7 mm and 19.1 mm diameter indentors, respectively. In each figure, there are two solid curves representing the experimental results. These results are for two clamped supports along and perpendicular to the 0 deg lamina of the laminates, with the rest two edges of the plate being free to move. Excellent agreement was found for $F\leq0.41kN$ and $F\leq0.79kN$ for indentation by 12.7 mm and 19.1 mm diameter indentors, respectively. Further, change of Poisson's ratio, ν_{23}, affected the F-α relationship insignificantly. The deviation beyond these forces is believed to be due

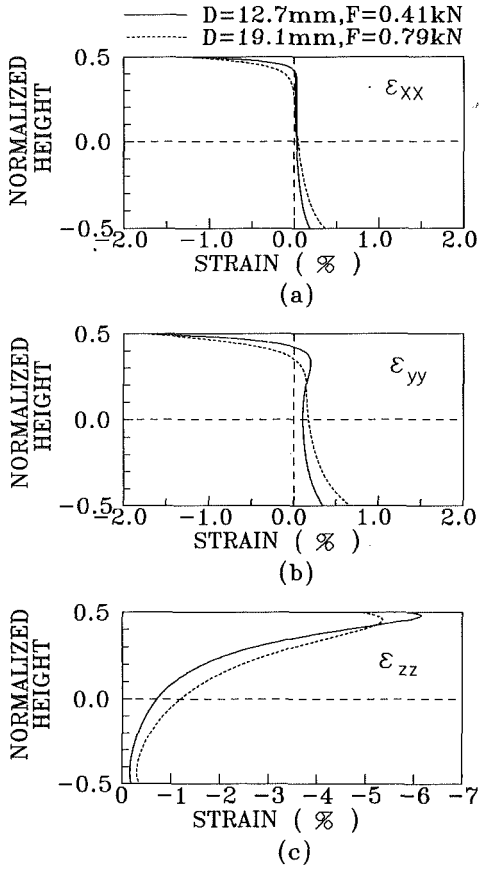


Fig. 5 Three normal strains at the center of the laminated plate. The loads are 0.41 *kN* and 0.79*kN* for 12.7 mm and 19.1 mm diameter indentors, respectively. In these figures, ν_{23} = 0.3 was used.

to damage of laminae within the contact region. To prove this, three normal strains at the center of the laminates along the thickness direction are plotted in Fig. 5 for both cases, i.e., $F=0.41kN$ and $0.79kN$ for 12.7 mm and 19.1 mm diameter indentors, respectively. In these figures $\nu_{23}=0.3$ was used. The strengths in terms of the strains for typical graphite/epoxy composites used in the aerospace industry are approximately $+1$ percent and -1 percent parallel, and $+0.6$ percent and -2.4 percent perpendicular to the fibers (Tsai, 1988). Therefore, the calculated ϵ_{zz} is much larger than the maximum compressive strain for typical graphite/epoxy laminates. Because of this large ϵ_{zz} underneath the indentor, the laminate has been crushed in the thickness direction, which is also one of the major reasons why permanent indentation was always found in the experimental results (Tan and Sun, 1985; Yang and Sun, 1982; Wu and Shyu, 1993). Thus, the analyses were able to predict the experimental result before the specimens were damaged.

4 Parametric Study

In this section, we study the effects on the force-indentation relationship due to changes of stacking sequence, Young's moduli, span and thickness of the laminates, and size of the indentor. The material properties of the laminate are the same as those used in the previous section with $\nu_{23}=0.3$, i.e., given by Eq. (23). The indentors used are 19.1 mm in diameter.

4.1 Change of Stacking Sequence. The $F-\alpha$ relationships for composite plates of the same thickness but with stacking sequences of $[0°]_{20}$, $[(0°_5)/(90°)_5]_s$, $[(0°)/(90°)]_{10}$ and $[0°/45°/0°/-45°/0°]_{2s}$ laminates are shown in Fig. 6. These laminates are composed of 1, 3, 20, and 17 layers, respectively. The span and the thickness of the square plate are 50.8 mm

Downloaded 03 May 2010 to 171.66.16.20. Redistribution subject to ASME license or copyright; see http://www.asme.org/terms/Terms_Use.cfm

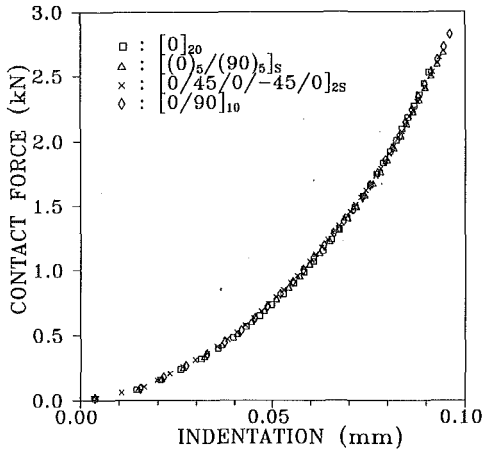


Fig. 6 Effect of stacking sequence change on the $F-\alpha$ relationships. The indentor is 19.1 mm in diameter.

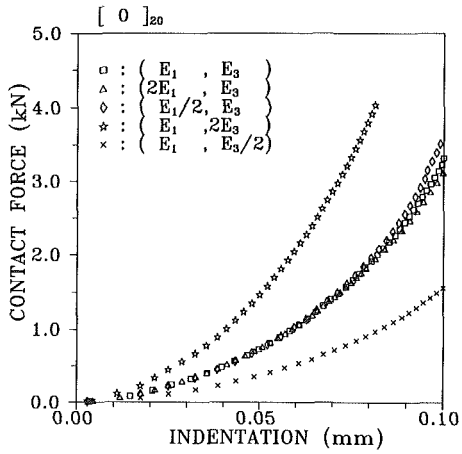


Fig. 7 Effect of Young's modulus change on the $F-\alpha$ relationships. The indentor is 19.1 mm is diameter.

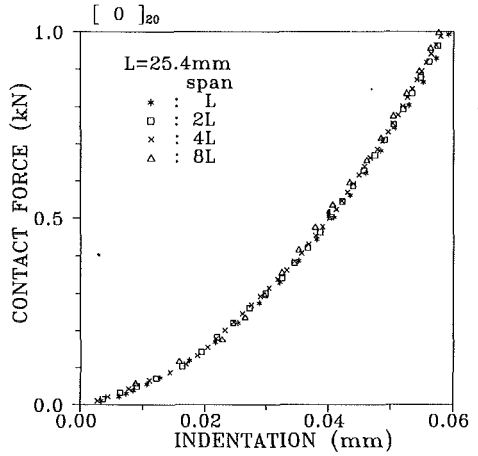


Fig. 8 Effect of plate span change on the $F-\alpha$ relationships. The indentor is 19.1 mm in diameter.

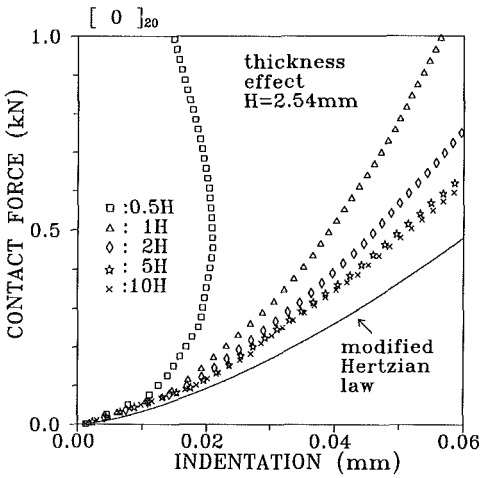


Fig. 9 Effect of laminate thickness change on the $F-\alpha$ relationships. The span of the square plates used is 101.6 mm. The indentor is 19.1 mm in diameter. Also shown is the prediction of the modified Hertzian law.

and 2.7 mm, respectively. The first three cases were analyzed layer by layer using the elasticity method derived in Section 2. The $[0°/45°/0°/-45°/0°]_{2s}$ plate was analyzed by averaging the material properties so that only one layer was considered in the analysis. As shown in Fig. 6, essentially no difference could be found in the force-indentation relationship even when the contact force is large. Thus the change of stacking sequence only has a negligible effect on the $F-\alpha$ relationship for orthotropic laminates and balanced laminates which are modeled as orthotropic plates. Therefore, only unidirectional composite plates were used in the subsequent analyses.

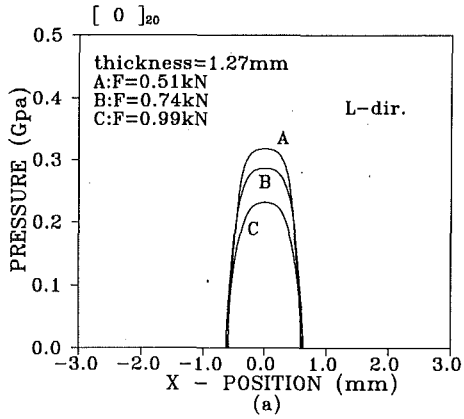
4.2 Change of Young's Moduli. Figure 7 depicts the $F-\alpha$ relationships for five unidirectional composite plates, each with the same dimensions of 50.8 mm × 50.8 mm × 2.7 mm, but with different Young's moduli, E_1 and E_3 ($=E_2$). The material properties for the curve consisting of square blocks were identical to the ones used in the previous section. It was found that the force-indentation relationship is approximately proportional to the magnitude of E_3, while increasing the value of E_1 has no effect on the $F-\alpha$ relationship until indentation is relatively large. Among the three curves using the same value of E_3, the one with $E_1/2$ has a stiffer $F-\alpha$ relationship. This is due to smaller bending and membrane rigidities of that plate so that larger curvatures occur in the contact neighborhood. It then creates a larger contact area. Therefore, the applied force is slightly larger for the same indentation. It is also shown in Fig. 4 that the effect due to change of G_{23} on the $F-\alpha$ relationship is insignificant.

Further, although not shown in Fig. 7, the effect due to change of $G_{12}(=G_{13})$ is found negligible. Use of $G_{12}/2$ instead of G_{12} in the analysis only results in slightly larger contact force when the indentor goes very deep.

4.3 Change of Plate Span. Four different spans, L, $2L$, $4L$, and $8L$ were employed to study the effect on the $F-\alpha$ relationship for 2.7 mm thick unidirectional composites plates with square dimensions, where $L=25.4$ mm. The plate used in the previous section corresponds to the case of span equal to $2L$. From Fig. 8, the difference among the cases considered is small. The slightly stiffer curve for the $8L$ plate is again due to its relatively smaller rigidity in resisting the lateral contact load.

4.4 Change of Plate Thickness. In Fig. 9, the slopes of the $F-\alpha$ curves are stiffer when the plate thickness decreases from 10 H to $0.5H$, where H is equal to 2.54 mm. However, the force-indentation relationship in the initial contact stage is independent of plate thickness. This is because the contact area is small in comparison to the plate thickness and the solution is similar to indentation of a half-space by a rigid sphere. As the indentor moves deeper, the one corresponding to the thinnest plate first deviates from the rest curves. The indentation magnitude even decreases when additional contact force is added to the load of larger than $0.5kN$. To investigate

Downloaded 03 May 2010 to 171.66.16.20. Redistribution subject to ASME license or copyright; see http://www.asme.org/terms/Terms_Use.cfm



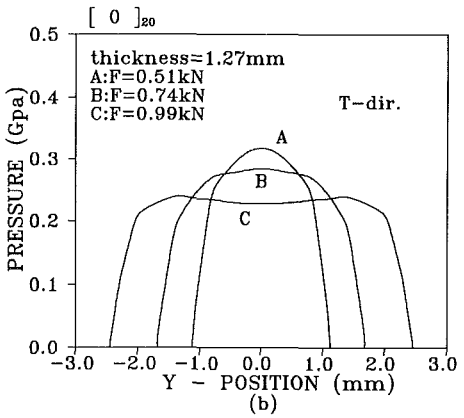


Fig. 10 Contact pressure distribution on the unidirectional composite plate of 1.27 mm in thickness. The indentor is 19.1 mm in diameter. (*a*) in the longitudinal direction and (*b*) in the transverse direction.

this peculiar contact phenomenon, the pressure distribution for loads at $0.51kN$, $0.74kN$, and $0.99kN$ were plotted in Figs. 10(*a*) and (*b*). It can be seen that the peak pressure decreases with additional load. On the other hand, difference between the pressure profiles in the longitudinal and transverse directions of the fibers becomes more significant. Further, this profile changes from a semi-ellipsoid to that with a plateau in the direction perpendicular to the fibers. This phenomenon results from the relatively small transverse Young's modulus, E_2. It causes the contact neighborhood of the plate easier to conform to the spherical indentor in this direction at relatively large indentation. Thus, the size of the contact area increases when small amount of additional force acts on the plate. The increase of the contact area, in turn, decreases the peak pressure. The difference for contact pressure distribution in the directions parallel and perpendicular to the fibers is, however, strongly dependent on the in-plane orthotropy of composite plates.

Figure 9 also shows the result of the modified contact law proposed in Yang and Sun (1983). The form of the contact law is given by

$$F=(4/3)(R_s)^{1/2}\left[\frac{1-\nu_s^2}{E_s}+\frac{1}{E_3}\right]^{-1}\alpha^{3/2} \tag{26}$$

where R_s, ν, and E_s are the radius, Poisson's ratio, and Young's modulus of the indentor, and E_3 is the Young's modulus of the plate in the thickness direction. Because of rigid indentors used in the analysis, E_s is equal to infinity and only the second term in the bracket was considered. The modified contact law deviates from the rest curves at the very beginning of the indentation. The underestimation of the contact force becomes more significant as the indentor goes deeper. Further, because

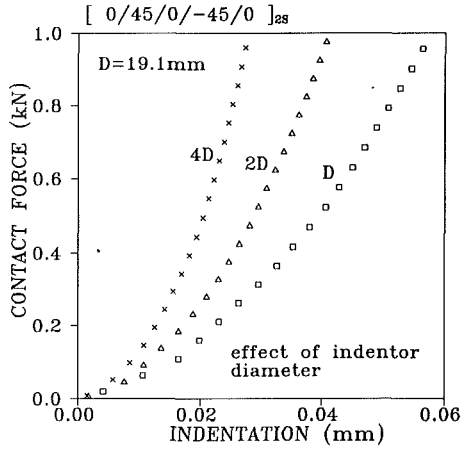


Fig. 11 Effect of indentor size change on the $F-\alpha$ relationships.

there is no thickness parameter in Eq. (26), use of this law in the contact and low velocity impact analyses of composite plates is questionable.

4.5 Change of Indentor Sizes. In Hertz contact law, the applied loading is proportional to square root of the indentor size. The same relationship was also proposed in the modified contact law. To check whether this relationship is applicable to a laminate of finite thickness, the $F-\alpha$ relationships between a $[0°/45°/0°/-45°/0°]_{2s}$ laminated plate and three rigid spheres were plotted in Fig. 11. The plate dimensions are 50.8 mm × 50.8 mm × 2.7 mm. The indentor diameters are 19.1, 38.2, and 76.4 mm. Take $\alpha = 18$ μm as one example, the contact forces are $0.127kN$, $0.270kN$ and $0.400kN$ for indentors of D, $2D$, and $4D$ in diameters, respectively. These deviate from the $\sqrt{R_s}$ relationship by more than 50 percent. As indentor goes deeper, the deviation becomes more significant. Apparently, the $F-\alpha$ relationship is not proportional to the $\sqrt{R_s}$ for plates with finite thickness.

5 Conclusions

The analytical method developed in this paper is based on an exact Green's function derived from the three-dimensional linear anisotropic elasticity theory. The method is applicable to orthotropic laminates and balanced laminates which are modeled as orthotropic plates. This method has successfully predicted the force-indentation relationships before the laminates are damaged. Based on the analyses it is concluded that:

(1) The contact force is approximately proportional to E_3 for the same indentation. On the other hand, changes of in-plane Young's moduli and three shear moduli, G_{12}, G_{13}, and G_{23}, have insignificant influence on the $F-\alpha$ relationship.

(2) Changes of stacking sequence and span of the laminated plates have a negligible effect on the $F-\alpha$ relationship within the analysis scope.

(3) Change of the plate thickness does affect the $F-\alpha$ relationship. The thinner plate has smaller indentation for a given applied load. The modified contact law significantly underestimates the contact force for a given indentation. Also, the $F-\alpha$ relationship is no longer proportional to the square root of the indentor diameter.

(4) By changing Eq. (22), the contact behavior between laminated plates and any indentors of smooth profiles can be studied using the method reported in this paper.

Acknowledgments

The authors would like to express their sincere appreciation to the reviewers and Prof. Kuang-Chong Wu for many valuable

Downloaded 03 May 2010 to 171.66.16.20. Redistribution subject to ASME license or copyright; see http://www.asme.org/terms/Terms_Use.cfm

suggestions. This work was supported by National Science Council of the Republic of China under Contract number NSC-79-0401-E-002-33.

References

Ahmadi, N., Keer, L. M., and Mura, T., 1983, "Non-Hertzian Contact Stress Analysis for an Elastic Half Space-Normal and Sliding Contact," *Int. J. Solids Structures*, Vol. 19, No. 4, pp. 357–373.

Cairns, D. S., and Lagace, P. A., 1987, "Thick Composite Plates Subjected to Lateral Loading," ASME JOURNAL OF APPLIED MECHANICS, Vol. 54, pp. 611–615.

Hertz, H., 1881, "Uber die Beruhrung fester Elastischer Korper," *Journal for die reine und angewandte mathematik*, Vol. 92, pp. 156–171, translated by D. E. Jones and G. A. Schott, MacMillan and Co., London, 1896.

Jones, R. M., 1975, *Mechanics of Composite Materials*, McGraw-Hill Book Co., New York.

Keer, L. M., and Miller, G. R., 1983 "Smooth Indentation of a Finite Layer," *ASCE Journal of Engineering Mechanics*, Vol. 109, pp. 706–717.

Pagano, N. J., 1970, "Exact Solutions for Rectangular Bidirectional Composites and Sandwich Plates," *J. Composite Materials*, Vol. 4, pp. 20–34.

Sankar, B. V., and Sun, C. T., 1983, "Indentation of a Beam by a Rigid Cylinder," *Int. J. Solids Structures*, Vol. 19, No. 4, pp. 293–303.

Sankar, B. V., 1989, "Smooth Indentation of Orthotropic Beams," *Composites Science and Technology*, Vol. 34, pp. 95–111.

Singh, K. P., and Paul, B., 1974, "Numerical Solution of Non-Hertzian Elastic Contact Problems," ASME JOURNAL OF APPLIED MECHANICS, Vol. 41, pp. 484–490.

Tan, T. M., and Sun, C. T., 1985, "Use of Statical Indentation Laws in the Impact Analysis of Laminated Composite Plates," ASME JOURNAL OF APPLIED MECHANICS, Vol. 52, pp. 6–12.

Tsai, S., 1988, *Composites Design*, 4th ed., Think Composites, Dayton, OH, pp. 11–8, 9.

Willis, J. R., 1966, "Hertzian Contact of Anisotropic Bodies," *Journal of Mechanics and Physics of Solids*, Vol. 14, pp. 163–176.

Wu, E., and Shyu, K., 1993, "Response of Composite Laminates to Contact Loads and Relationship to Low-Velocity Impact," *J. Composite Materials*, Vol. 27, pp. 1443–1464.

Yang, S. H., and Sun, C. T., 1983, "Indentation Law for Composite Laminates," *Composite Materials: Testing and Design*, ASTM STP787, American Society for Testing and Materials, pp. 425–449.

Downloaded 03 May 2010 to 171.66.16.20. Redistribution subject to ASME license or copyright; see http://www.asme.org/terms/Terms_Use.cfm

ERRATUM

Erratum on "Steady-State Transonic Motion of a Line Load Over an Elastic Half-Space: The Corrected Cole/Huth Solution," by H. G. Georgiadis and J. R. Barber, published in the Sept. 1993 issue of ASME JOURNAL OF APPLIED MECHANICS, Vol. 60, pp. 772–774.

On page 773, the factor $(1-m_2^4)^4$ in Eq. (11) should read: $(1-m_2^4)$.

Copyright © 1994 by ASME
Downloaded 03 May 2010 to 171.66.16.20. Redistribution subject to ASME license or copyright; see http://www.asme.org/terms/Terms_Use.cfm

H. C. Chiu

R. C. Benson
Mem. ASME

Department of Mechanical Engineering,
University of Rochester,
Rochester, NY 14627

M. D. Fiscella
Photographic Research Laboratory,
Eastman Kodak Company,
Rochester, NY 14650
Mem. ASME

S. J. Burns
Department of Mechanical Engineering,
University of Rochester,
Rochester, NY 14627
Mem. ASME

Mechanical and Thermal Wrinkling of Polymer Membranes

A finite element method by Roddeman was modified in order to study wrinkling of polymer membranes due to mechanical loads and thermal shrinkage. Thermal shrinkage was incorporated as a prestrain and the elastic modulus was allowed to be dependent on temperature. The following wrinkling cases were studied: (1) a circular membrane with a heated spot at the center and a uniform radial displacement at the outer edge, (2) a rectangular membrane with wrinkles emanating from an imperfection in the boundary, and (3) a rectangular membrane with wrinkles emanating from a heated spot at the center.

1 Introduction

Wrinkling of membranes has received increasing attention because of important uses of membranes in space structures, biomechanics, data storage, and other industrial applications with lightweight requirements. An early study on wrinkling was by Wagner in 1929 on airplane wing design. In this work, a form of "tension field theory" was derived. The key point of the theory is that the structure is too thin to bear any in-plane compression. The conventional plane stress field is rearranged through out-of-plane displacement to attain a state with only tensile stress components. Kondo et al. (1955) and Mansfield (1968, 1970, 1977) contributed to the theory by a geometrical ray analysis. Wu (1975) presented a different approach that could be used to analyze partly wrinkled structures. The strains of wrinkled and taut parts could be solved separately, with continuity of stresses and displacements at the wrinkled/taut transition. Pipkin (1986) and Pipkin and Steigmann (1989) provided a mathematical foundation to define the relaxation strain energy of isotropic elastic membranes with wrinkling deformation. A finite element method was built by Miller and Hedgepeth (1982, 1985) to model the partial wrinkling of thin plates. In their algorithm, Poisson's ratio was not regarded as a fixed material property, but rather as an adjustable parameter chosen to ensure zero stress across the wrinkles.

Recently Roddeman et al. (1987a,b) presented an alternative finite element method for wrinkling problems. This approach utilizes weighted residual functions and a variation of nodal displacements due to wrinkle formation. It can be applied to nonlinear and anisotropic membranes.

We are concerned with the wrinkling of polymer webs in a thermal printing process (Fiscella et al., 1990). A thin polymer membrane is used as a dye carrier. Locally applied heat causes dye migration to adjacent "receiver paper" while digitally constructing a color image. This process causes the heated spot of the membrane to shrink, and this in turn may cause wrinkles.

The problem is geometrically nonlinear due to the lack of prior knowledge of which membrane segments are wrinkled, taut, or slack. We solve for the deformation and the induced stresses and strains with a modification of Roddeman's finite element model. To incorporate a thermal shrinkage capability, we introduce a temperature-dependent prestrain. Other material parameters, such as Young's modulus, may also be a function of temperature. Using this model we study a number of problems. We find that the manner in which the membrane is supported on its boundary can have a significant effect on the wrinkling that results from thermal stress.

2 Material Thermal Properties

Polymer films such as polyester polyethylene terephthalate (PET) can deform due to reversible thermal expansion and irreversible thermal recovery, i.e., shrinkage. The shrinkage is a partial relaxation of residual strains induced during the manufacture of the films. Once these strains are relieved at a specific

Contributed by the Applied Mechanics Division of THE AMERICAN SOCIETY OF MECHANICAL ENGINEERS for presentation at the ASME Winter Annual Meeting, New Orleans, LA, Nov. 28–Dec. 3, 1993.

Discussion on this paper should be addressed to the Technical Editor, Professor Lewis T. Wheeler, Department of Mechanical Engineering, University of Houston, Houston, TX 77204-4792, and will be accepted until four months after final publication of the paper itself in the ASME JOURNAL OF APPLIED MECHANICS.

Manuscript received by the ASME Applied Mechanics Division, Feb. 7, 1992; final revision, Mar. 9, 1993. Associate Technical Editor: A. K. Noor.

Paper No. 93-WA/APM-25.

Copyright © 1994 by ASME

Downloaded 03 May 2010 to 171.66.16.20. Redistribution subject to ASME license or copyright; see http://www.asme.org/terms/Terms_Use.cfm

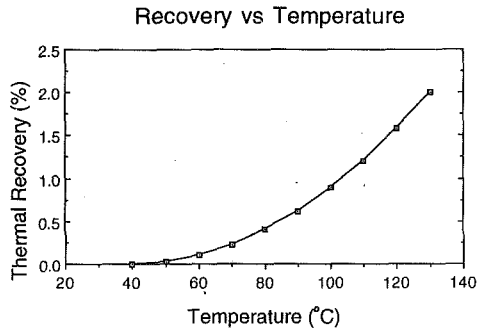


Fig. 1(*a*)

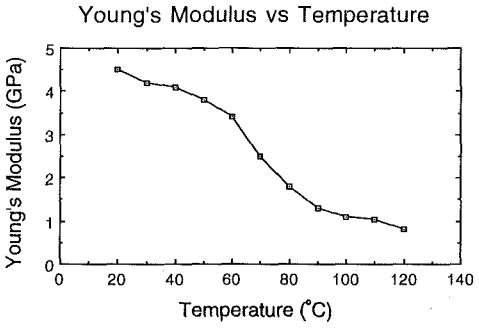


Fig. 1(*b*)

Fig. 1 Thermal properties of polymer (PET) material; (*a*) thermal recovery (data reproduced from DuPont (1989)), (*b*) Young's modulus versus temperature

temperature, the film will not return to its original shape. The deformation is permanent.

Recovery is typically more complicated than simple linear thermal expansion or contraction. Refer to the thermal recovery graph in Fig. 1(*a*) which was redrawn from a DuPont (1989) technical information report. The thermal expansion coefficient of PET is about $1.9\times10^{-5}/°C$. This value is much smaller than thermal shrinkage per unit of temperature change at an elevated temperature, thus the deformation from thermal expansion can be neglected in the following analysis. Our experiments also show that the Young's modulus is strongly dependent on temperature (Fig. 1(*b*)). In light of these observations, in this analysis the heated membrane will be treated as an elastic "tension field" structure with a nonlinear temperature-dependent Young's modulus and thermal shrinkage.

The thermal conductivity is approximately 0.13 $J/ms°C$. The creep strain at 100°C, and under 10 MPa is 0.9 percent. Thus we regard the film to be highly resistant to thermal conductivity and creep. The heating time for the dye transport in the thermal printing process is very short; less than 30 ms. As the thermal conductivity is small, most heat transfer occurs in conduction to the air, while in the plane of the membrane the heated spot remains quite localized. Consequently, we assume that thermal shrinkage takes place only in the area where heat was applied.

3 Mechanical Model

The finite element method by Roddeman (1987a,b) can be modified as follows to simulate the equivalent structural prestrain due to temperature change.

Step 1—Element Modification for Wrinkling. A triangular finite element is created to solve for a uniform strain and stress state on the element and to ascertain if wrinkle lines exist in it. Given a deformation tensor $\mathbf{F}$, the principal stress can be obtained by conventional methods. If one of the principal stresses is negative, two parameters are introduced: α, the direction of the wrinkling line; and β, the extra strain normal to wrinkle lines due to out-of-plane displacement. The wrinkling deformation tensor $\mathbf{R}$ can then be obtained with the following equation:

$$\mathbf{R}=(\beta n_1 n_1+\mathbf{I})\mathbf{F}, \tag{1}$$

where n_1 is the unit vector normal to the wrinkle lines and $\mathbf{I}$ is the second-order identity tensor. In this section, the notation parallels Roddeman's. The vector n_1 is a function of α. The stress tensor, σ, is then derived as

$$\sigma=J^{-1}\mathbf{R}\mathbf{H}(\mathbf{E}')\mathbf{R}^{\mathrm{T}},\quad \mathbf{H}={}^4\mathbf{M}\mathbf{E}'(\mathbf{R}) \tag{2}$$

where J is Jacobian of the wrinkling deformation tensor, $\mathbf{H}$ is the Kirchhoff's stress tensor, $\mathbf{E}'$ is the Green-Lagrange strain tensor of the element with wrinkling, and ${}^4\mathbf{M}$ is a fourth-order constitutive tensor relating elastic stresses and strains. The normal stress perpendicular to wrinkle lines and shear stress should both be zero. Thus we have two constraint equations

$$n_1\cdot\sigma\cdot n_2=0,\quad n_1\cdot\sigma\cdot n_1=0 \tag{3}$$

where n_2 is the unit vector in the plane of the sheet along the wrinkling direction.

Step 2—Equilibrium by Variational Methods. In Step 2, the relation of nodal displacements and nodal forces is constructed with dependence on α's and β's in the elements. The equilibrium of an element can be expressed as

$$\nabla\cdot\sigma=\mathbf{0}. \tag{4}$$

Taking the integral of Eq. (4) over the volume of the element, gives

$$\int_V(\nabla\cdot\sigma)\cdot h\,dV=0 \tag{5}$$

where h is an arbitrary residual vector, and V is the deformed volume of the element. Through Gauss' theorem, we get

$$\int_V(\sigma:(\nabla h)^T)dV=\int_A n_A\cdot(\sigma\cdot h)\,dA \tag{6}$$

where n_A is the unit vector perpendicular to the membrane surface, and A is the surface area of the deformed element. This formula can be rewritten in terms of the original element geometry as

$$\int_{V_o}\pi:(\nabla_o h)^T\,dV_o=\int_{A_o}k_o\cdot h\,dA_o. \tag{7}$$

where $\pi\equiv\mathbf{R}\mathbf{J}\sigma$ is the first Piola-Kirchhoff stress tensor, V_o is the original volume of the element, $k_o=J^a\sigma\cdot n_A$ is the load on the deformed surface as referred to the undeformed surface, A_o is the original surface area of the element, and J^a is the Jacobian of the area change.

The numerical estimates of π, $\mathbf{F}$, and other variables will be different from the "exact" analytical ones. Their relations are $\pi=\pi^*+\delta\pi$, etc., where * represents approximation by numerical methods and δ represents a deviation from the theoretically exact value. The variation in the stress state, $\delta\sigma$, found from Eq. (7), can be formally expressed as a function of $\delta\mathbf{F}$, $\delta\mathbf{R}$, and δn_1,

$$\delta\sigma=\delta\sigma(J,\ \delta\mathbf{F},\ \delta\mathbf{R},\ \delta n_1). \tag{8}$$

From Eq. (1), the variation of $\mathbf{R}$ can be obtained as

$$\delta\mathbf{R}=(\delta\beta n_1 n_1+\beta\delta n_1 n_1+\beta n_1\delta n_1)\mathbf{F}+(\beta n_1 n_1+\mathbf{I})\delta\mathbf{F}. \tag{9}$$

Every variation term in this equation may be related to the variation of nodal displacements of the element through geometrical calculations. After much algebra we can obtain the relationship between variation of nodal displacements and variation of the stress in the element,

$$\delta\sigma={}^3\mathbf{M}_\mathbf{k}\delta\mathbf{u}_\mathbf{k} \tag{10}$$

where ${}^3\mathbf{M}_\mathbf{k}$ is a third-order tensor determined by the membrane geometry, material properties, and the wrinkling state. By taking the variation of Eq. (7), the incremental nodal forces and displacements of an element can be obtained. The right-hand side of Eq. (7) can be derived as nodal forces. The left-hand side can be expressed as a function of displacements through

Downloaded 03 May 2010 to 171.66.16.20. Redistribution subject to ASME license or copyright; see http://www.asme.org/terms/Terms_Use.cfm

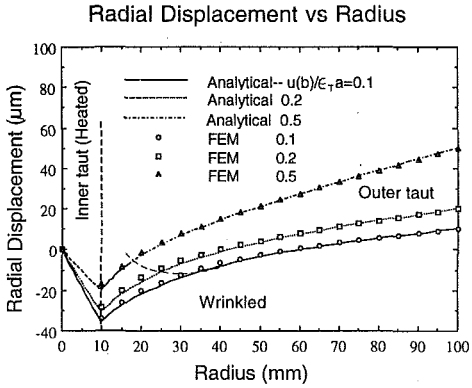


Fig. 2 Heated circle membrane example: radial displacement

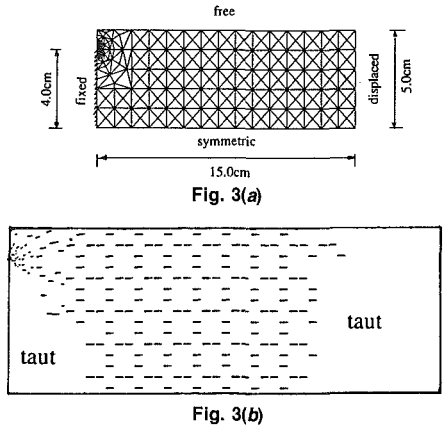


Fig. 3(*a*)

Fig. 3(*b*)

Fig. 3 Rectangular membrane with an imperfect clamp; (*a*) FEM mesh, (*b*) wrinkle lines

Eqs. (8) and (9). The following functional relationship is then obtained:

$$\mathbf{K}_w \cdot \delta d = \delta f, \tag{11}$$

where $\mathbf{K}_w$ is a local stiffness matrix of the element, δd is the variation of nodal displacements, and δf is the variation of nodal forces. Combining the local matrices for all of the elements, the global stiffness matrix of the whole structure is obtained. Further details of the variational derivation can be found in Roddeman (1988).

Step 3—Thermal Modification. Thermal shrinkage is now introduced into the wrinkling analysis. The thermal deformation of an element is transferred into equivalent nodal forces. A heated area tends to shrink, and because it is connected to surrounding material it experiences a resisting tension. The surrounding material feels equivalent nodal forces pulling the membrane into the heated area. Nodal displacements in the structure include mechanical and thermal parts, respectively,

$$d = d_m + d_t. \tag{12}$$

For wrinkling analysis, the thermal deformation is treated as a shift of the true stress-free initial state of the membrane. The deformation tensor used in the Roddeman process is thus modified by a thermal prestrain,

$$\mathbf{F}_t = \mathbf{T}^{-1}\mathbf{F}, \quad \mathbf{R}_t = \mathbf{T}^{-1}\mathbf{R} \tag{13}$$

where $\mathbf{T}$ is the deformation tensor describing thermal shrinkage.

The final wrinkled result requires iteration, as we do not have prior knowledge of which elements are taut, wrinkled, or slack. The elements with both principal stresses positive are taut and are treated with conventional analysis. Elements with two negative values are slack and are given a completely zero local stiffness matrix. Elements with one positive stress and one negative stress are wrinkled elements and are treated with the method described above. Nodal displacements will converge after iteration, and the strain energy of the structure will attain a converged value.

4 Applications

Comparison to Closed-Form Solutions. To confirm that the numerical program is accurate we applied it to a geometrically simple case. A circular membrane of radius b is displaced radially outward by an amount u_b on its perimeter. A concentric "hot" spot of radius a experiences a thermal shrinkage strain of ϵ_T. Using conventional tension field analysis we may compute in closed form the stresses and strains of this axisymmetric problem. Space limitations present a derivation of results here. Details may be found in Chiu et al. (1992).

On the domain $0 < r < a$, the membrane will be taut because of the thermal shrinkage. On the domain $a < r < l$, the membrane will have radially directed wrinkles, and on the domain $l < r < b$, the membrane will again be taut. The transition radius l depends on ϵ_T and u_b and is found from the following transcendental equation:

$$l^2 + \frac{2bu_b l}{\epsilon_T a}\left[\frac{\nu}{1+\nu} - \frac{\ln l/a}{1+\nu} + \frac{E(1-\nu)}{E_h(1+\nu)}\right] - b^2\frac{1-\nu}{1+\nu} = 0. \tag{14}$$

Here E is the Young's modulus of the membrane when "cool." E_h is the (possibly different) value when "hot." The radial membrane displacement is given in the heated, wrinkled, and outer taut regions by the following respective expressions:

$$u_h = \left[\frac{2Eu_b(1-\nu)}{E_h abl(1+\nu)\left(\frac{1-\nu}{1+\nu}\frac{1}{l^2} - \frac{1}{b^2}\right)} - \epsilon_T\right] r, \tag{15}$$

$$u_w = \left[\frac{2u_b}{bl(1+\nu)\left(\frac{1-\nu}{1+\nu} - \frac{1}{b^2}\right)}\right](\ln r/l - \nu), \tag{16}$$

$$u_t = \left[\frac{bu_b}{\frac{1-\nu}{1+\nu}b^2 - l^2}\right]\left[\left(\frac{1-\nu}{1+\nu}\right) r - \frac{l^2}{r}\right]. \tag{17}$$

The closed-form results are compared to the finite element model predictions in Fig. 2 using specifications: $a = 10$ mm, $b = 100$ mm, $E = 4500$ MPa, $E_h = 1000$ MPa, $\nu = 0.3$, and $\epsilon_T = 0.01$ (which corresponds to a temperature of $103°C$ in Fig. 1). Finite element nodes were placed every 5 mm in the radial direction, and every $\pi/16$ radians in the circumferential direction. The result is very close to the closed-form result.

Mechanical Wrinkling of a Rectangular Membrane. The finite element method (FEM) program is now used on a rectangular membrane (150 mm × 100 mm) subjected to stretch. The left edge, as shown in Fig. 3(*a*), is clamped over a central 80 mm length, with the outlying 10 mm lengths left free. A uniform horizontal displacement of 1.5 mm is applied to the right edge. The two long edges are taken to be free. The FEM mesh covers only half of the structure as it is a symmetrical problem. The singular stress on the upper left clamped corner is the wrinkle ray source. This singularity causes extensive wrinkling in the membrane as seen in Fig. 3(*b*). The contours of the major principal stress are plotted in Fig. 4. In general, an imperfection in a boundary condition can create a singularity in the stress field. When a membrane is allowed to wrinkle, the stress perpendicular to the wrinkles will be zero, and the normal stresses along the wrinkles will be generally higher than those calculated in a conventional analysis. Thus the order of singularity as calculated by a wrinkling FEM may be expected to be greater than that calculated by a conventional analysis.

Thermal Wrinkling of a Rectangular Membrane. A rec-

Downloaded 03 May 2010 to 171.66.16.20. Redistribution subject to ASME license or copyright; see http://www.asme.org/terms/Terms_Use.cfm

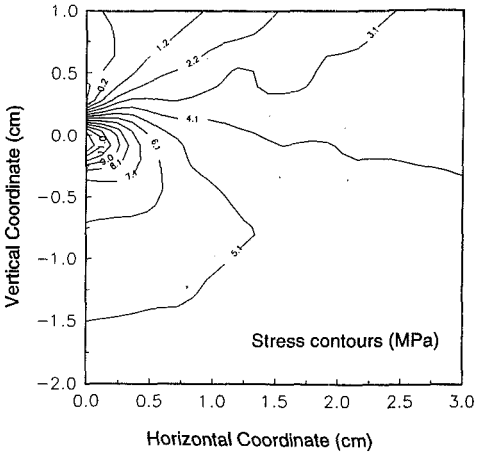


Fig. 4 Rectangular membrane with an imperfect clamp: major principal stress contours

tangular membrane (200 mm × 160 mm) has long edges free and short edges fixed. It is heated on a small 10.0 mm radius spot at the center. A stretch is applied on the short edges to reduced wrinkling, either as a uniform displacement of 0.14 mm or a uniform stress of 7.0 MPa on the two fixed sides. For the sake of comparison, the resultant stretching forces in the two cases are both about 3.9N. The FEM mesh takes advantage of quarter symmetry (Fig. 5(*a*)). When the applied stretch is zero, the wrinkles are in a ray form emanating from the heated spot, as seen in Fig. 5(*b*). A slack region occurs in the upper left corner. Figures 5(*c*) and 5(*d*) show the different effects of applied uniform stress (7.0 MPa) and applied uniform displacement (0.14 mm). Both reduce the extent of wrinkles in the membrane and change the wrinkling directions within the membrane. The applied uniform displacement reduced the wrinkling area to a greater extent than the applied uniform stress.

5 Summary

Thermally induced wrinkling can be modeled with a finite element method by incorporating a temperature-dependent prestrain and temperature-dependent material parameters into the model. The FEM results compare favorably with a closed-form results for an axisymmetric, circular membrane. The thermal wrinkling of membranes can be reduced by externally applied stresses or displacements. In a rectangular membrane with an interior wrinkle source, a stretch of uniform displacement appeared to reduce wrinkling more effectively than a stretch of uniform stress. The geometry of membranes is very important in wrinkling deformation. Sharp corners and irregular boundaries can initiate wrinkles.

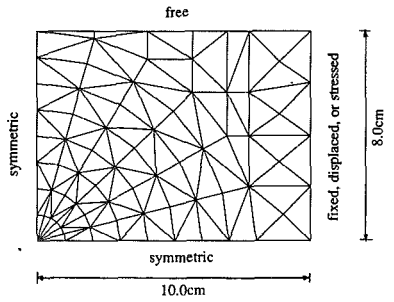


Fig. 5(*a*)

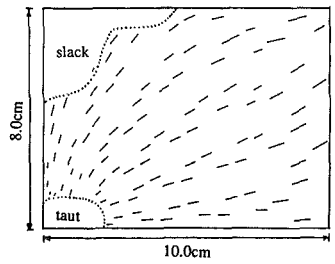


Fig. 5(*b*)

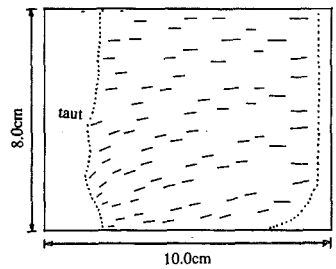


Fig. 5(*c*)

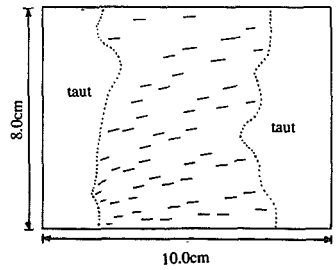


Fig. 5(*d*)

Fig. 5 Wrinkling of a 200 mm × 160 mm rectangular membrane with a heated spot at the center: (*a*) FEM mesh, (*b*) right edge fixed, (*c*) right edge stressed 7.0MPa, (*d*) right edge displaced 0.14 mm

References

Chiu, H. C., Benson, R. C., Fiscella, M. D., and Burns, S. J., 1992, "Mechanical and Thermal Wrinkling of Polymer Membranes," *Proceedings of the Symposium on Web Handling*, ASME Winter Annual Meeting, AMD Vol. 149, pp. 37-50.

DuPont Company, 1989, "Technical Information, Mylar Polyester Film, Physical-Thermal Properties," Wilmington, DE.

Fiscella, M. D., Brownstein, S. A., and Johnson, D. A., 1990, "Pulse Count Modulation: a Novel Head Drive Method for Thermal Printing," *Hard Copy and Printing Technologies, SPIE Proceedings*, Vol. 1252, pp. 156-167.

Kondo, K., Iai, T., Moriguri, S., and Murasaki, T., 1955, "Tension Field Theory," *Memoirs of the Unifying Study of the Basic Problems in Engineering Science by Means of Geometry*, Vol. I, pp. 417-441.

Mansfield, E. H., 1968, "Tension Field Theory," *Proc. XII Int. Congress of Applied Mechanics*, pp. 305-329.

Mansfield, E. H., 1970, "Load Transfer via a Wrinkled Membrane," *Proc. Royal Society of London A*, Vol. 316, pp. 269-289.

Mansfield, E. H., 1977, "Analysis of Wrinkled Membranes with Anisotropic and Nonlinear Elastic Properties," *Proc. Royal Society of London*, Vol. A353, pp. 475-498.

Miller, R. K., and Hedgepeth, J. M., 1982, "An Algorithm of Finite Element Analysis of Partly Wrinkled Membranes," *AIAA J.*, Vol. 20, pp. 1761-1763.

Miller, R. K., and Hedgepeth, J. M., 1985, "Finite Element Analysis of Partly Wrinkled Membranes," *Computers and Structures*, Vol. 20, pp. 631-634.

Pipkin, A. C., 1986, "The Relaxed Energy Density for Isotropic Elastic Membranes," *Arch. Rational Mech. Anal.*, Vol. 95, pp. 93-115.

Roddeman, D. G., Oomens, C. W., Janssen, J. D., and Drukker, J., 1987, "The Wrinkling of Thin Membranes: Part I—Theory," ASME JOURNAL OF APPLIED MECHANICS, Vol. 54, pp. 884-887.

Roddeman, D. G., Oomens, C. W., Janssen, J. D., and Drukker, J., 1987, "The Wrinkling of Thin Membranes: Part II—Numerical Analysis," ASME JOURNAL OF APPLIED MECHANICS, Vol. 54, pp. 888-892.

Roddemann, D. G., 1988, "Force Transmission in Wrinkled Membranes," Ph.D. Thesis, The Technical Univeristy, Eindhoven, The Netherlands.

Steigmann, D. J., and Pipkin, A. C., 1989, "Wrinkling of Pressurized Membranes," ASME JOURNAL OF APPLIED MECHANICS, Vol. 56, pp. 624-628.

Wagner, H., 1929, "Flat Sheet Metal Girders with a Very Thin Metal Web," *Zeitschrift Flugtechne Motor.*, Vol. 20, pp. 8-12.

Wu, C. H., 1978, "Nonlinear Wrinkling of Nonlinear Membranes of Revolution," ASME JOURNAL OF APPLIED MECHANICS, Vol. 45, pp. 533-538.

Downloaded 03 May 2010 to 171.66.16.20. Redistribution subject to ASME license or copyright; see http://www.asme.org/terms/Terms_Use.cfm

V. K. Kinra
Professor,
Fellow ASME.

K. B. Milligan
Graduate Research Assistant.

Center for Mechanics of Composites and Department of Aerospace Engineering, Texas A&M University, College Station, TX 77843

A Second-Law Analysis of Thermoelastic Damping

In accordance with the Thomson effect (Thomson, 1853), when a thermoelastic solid is subjected to a tensile stress, it cools. Similarly, when a homogeneous material is subjected to an inhomogeneous stress field or when an heterogeneous material is subjected to any stress field (homogeneous or inhomogeneous), different parts of the material undergo different temperature changes. As a result irreversible heat conduction occurs and entropy is produced. In this paper we take the second law of thermodynamics as our starting point and develop a general theory for calculating the thermoelastic damping from the entropy produced.

Introduction

It is well known that for most engineering materials, the higher the damping, the lower the stiffness and strength. Moreover, in a majority of techniques currently under development for damping enhancement, it has been observed that an increase in damping is accompanied by an undesirable decrease in stiffness. Thermoelastic damping offers an attractive alternative. In this case the damping is due to thermal currents within the material, and, therefore, it is not accompanied by a loss of stiffness or strength. The thermoelastic damping is *in addition to* all other sources of material damping present in the material. Moreover, for multiphase materials such as alloys, fiber-reinforced composites, and particulate composities it is envisioned that the thermoelastic damping can be tailored in a manner analogous to that used for tailoring stiffness, strength, coefficient of thermal expansion, etc.

In a seminal text, Clarence Zener (1948) considered transverse vibrations of an isotropic, *homogeneous*, and thermoelastic beam. He argued that irreversible heat transfer occurs in the beam due to the cooling of the tensile side and the heating of the compressional side. From this argument Zener postulated the existence of thermoelastic damping, which he modeled as three-parameter standard anelastic solids; his result is

$$\psi = \psi_o \frac{\omega\tau}{1+(\omega\tau)^2} \tag{1}$$

where

$$\psi_o = \frac{2\pi\alpha^2 E_R T_o}{\rho c} \tag{2}$$

$$\tau = \frac{\rho c h^2}{\pi^2 k} \tag{3}$$

and where ω is the circular frequency, τ is a characteristic time of the beam, ψ_o is a characteristic damping, α is the coefficient of thermal expansion, E_R is the relaxed (isothermal) modulus of elasticity, T_o is the absolute equilibrium temperature, ρ is the mass per unit volume, c is the specific heat per unit mass, k is the (isotropic) thermal conductivity, and h is the thickness of the beam. More recently, Alblas (1961, 1981) and Chadwick (1962) have extended Zener's one-dimensional analysis to three-dimensional thermoelastic damping in linear, isotropic, and homogeneous materials. They obtained solutions to the coupled thermoelastic equations in the form of series expansions in terms of orthonormal eigenfunctions. Shieh (1975, 1979) has solved the eigenvalue problem of lateral vibrations of Timoshenko beams with circular cross-section. Unfortunately, these theories are confined to *isotropic and homogeneous* materials and cannot be extended to heterogeneous materials.

We present a fundamental theory for thermoelastic damping which takes as its starting point the second law of thermodynamics. The solution is sought within the framework of the field equations of classical thermoelasticity. It is well known that entropy is created when heat flows across a temperature gradient and, consequently, work is converted into heat, this process is the origin of thermoelastic damping. By way of illustration, two specific boundary value problems are solved:

1. First, the problem treated by Zener is revisited.
2. Second, we consider two rods of thermoelastically different materials in welded contact subjected to a uniform longitudinal stress.

General Theory

The thermomechanical behavior of a linear, isotropic, and homogeneous thermoelastic medium is governed by the following equations.

First law of thermodynamics:

$$\rho\frac{\partial u}{\partial t} = \sigma_{ij}\frac{\partial \epsilon_{ij}}{\partial t} - q_{i,i}. \tag{4}$$

Newton's law of motion:

Contributed by the Applied Mechanics Division of THE AMERICAN SOCIETY OF MECHANICAL ENGINEERS for publication in the ASME JOURNAL OF APPLIED MECHANICS.

Discussion on this paper should be addressed to the Technical Editor, Professor Lewis T. Wheeler, Department of Mechanical Engineering, University of Houston, Houston, TX 77204-4792, and will be accepted until four months after final publication of the paper itself in the ASME JOURNAL OF APPLIED MECHANICS.

Manuscript received by the ASME Applied Mechanics Division, Feb. 27, 1992; final revision, Dec. 31, 1992. Associate Technical Editor: G. J. Dvorak.

Copyright © 1994 by ASME
Downloaded 03 May 2010 to 171.66.16.20. Redistribution subject to ASME license or copyright; see http://www.asme.org/terms/Terms_Use.cfm

$$\sigma_{ji,j}=\rho\frac{\partial^2 u_i}{\partial t^2}. \tag{5}$$

Kinematic equations of linear thermoelasticity:

$$\epsilon_{ij}=\frac{1}{2}(u_{i,j}+u_{j,i}). \tag{6}$$

Thermoelastic Hooke's law:

$$\sigma_{ij}=\frac{E}{1+\nu}\left(\epsilon_{ij}+\frac{\nu}{1-2\nu}\epsilon_{kk}\delta_{ij}\right)-\frac{E}{1-2\nu}\alpha\delta_{ij}(T-T_o). \tag{7}$$

Fourier law of heat conduction:

$$q_i=-kT_{,i}. \tag{8}$$

where σ_{ij} is the stress tensor, ϵ_{ij} is the linear strain tensor, u_i is the displacement vector, ν is the Poisson's ratio, E is the Young's modulus, T is the absolute temperature, q_i is the heat flux vector, u is the internal energy per unit mass, δ_{ij} is the Kronecker delta, and the indices i, j, k each have a range of 1, 2, 3.

The entropy created due to irreversible heat conduction in a solid can be calculated from the second law of thermodynamics (Coleman and Noll, 1961; Coleman and Mizell, 1964)

$$\frac{\partial s_p}{\partial t}=\frac{k}{\rho T^2}T_{,i}T_{,i} \tag{9}$$

where s_p is the entropy produced per unit mass. When entropy is created, mechanical energy is necessarily converted into heat; the connection between the two is given by the Gouy-Stodola Theorem (Bejan, 1988)

$$\Delta W=\rho T_o s_p. \tag{10}$$

The stored elasic energy per unit volume is given by

$$W=\frac{1}{2}\sigma_{ij}\epsilon_{ij}. \tag{11}$$

We now consider a thermoelastic solid undergoing a steady time-harmonic deformation. ΔW may be identified with the dissipation of mechanical energy during one cycle, and W may be identified with the maximum stored elastic energy during the cycle. We define a local specific damping capacity (SDC) as

$$\psi_L=\frac{\Delta W}{W}. \tag{12}$$

The volume-averaged damping of a structure of a finite extent may be defined as

$$\psi=\frac{\int_V \Delta W\,dV}{\int_V W\,dV}=\frac{\int_V \psi_L W\,dV}{\int_V W\,dV}. \tag{13}$$

Finally, the two-way coupled heat-conduction equation (Frederick and Chang, 1972) is

$$T_{,ii}=\frac{\rho c}{k}\frac{\partial T}{\partial t}+\frac{E\alpha}{k(1-2\nu)}T\frac{\partial \epsilon_{kk}}{\partial t}. \tag{14}$$

For the class of problems under considerations, the variations in temperature are very small, $\Delta T=O(10^{-2}\ \mathrm{K})$. Therefore, in the coupling term, T may be replaced by the equilibrium temperature, T_o, to obtain the one-way coupled heat-conduction equation

$$T_{,ii}=\frac{\rho c}{k}\frac{\partial T}{\partial t}+\frac{E\alpha}{k(1-2\nu)}T_o\frac{\partial \epsilon_{kk}}{\partial t}. \tag{15}$$

Equations (4) through (15) constitute the general theory of thermoelastic damping. In the following we solve two specific boundary value problems.

Boundary Value Problem 1: Flexural Vibrations of a Bernoulli-Euler Beam

Consider an isotropic, homogeneous, thermoelastic, Bernoulli-Euler beam of constant rectangular cross-section and height h undergoing time-harmonic flexural vibrations in the x-y plane. We assume that the centroidal axis occupies the x-axis and the displacement is confined to the y-axis. The curvature of the beam is given by $\kappa=\kappa_o e^{i\omega t}$ where ω is the circular frequency in radians per second. We will view the curvature as the *cause* and the fluctuating temperature as its *effect*. Now, $\epsilon_{yy}=\epsilon_{zz}=-\nu\epsilon_{xx}$ and $\epsilon_{xx}=-y\kappa$; therefore, $\epsilon_{kk}=-(1-2\nu)\kappa_o y e^{i\omega t}$ and Eq. (15) reduces to

$$\frac{\partial^2 T}{\partial y^2}-\frac{\rho c}{k}\frac{\partial T}{\partial t}=-i\omega\frac{E\alpha T_o}{k}\kappa_o y e^{i\omega t}. \tag{16}$$

The beam surfaces are assumed to be adiabatic; therefore, the boundary conditions at $y=\pm(h/2)$ are

$$\frac{\partial T}{\partial y}\left(-\frac{h}{2},\,t\right)=\frac{\partial T}{\partial y}\left(\frac{h}{2},\,t\right)=0. \tag{17}$$

It is convenient to introduce a complex temperature

$$T=T_o\sqrt{2}e^{i\pi/4}+V^*(y)e^{i\omega t} \tag{18}$$

where T_o is the absolute equilibrium temperature of the undisturbed beam and $V^*(y)$ is the unknown spatial variation of the temperature. Now, when a material point is subjected to a uniaxial tensile stress, it cools. Its decrease in temperature can be readily calculated from Eq. (15)

$$\Delta T=-\frac{\alpha}{\rho c}\sigma T_o. \tag{19}$$

This is the well-known Thomson effect (Thomson, 1853). In the present case when the beam is subjected to a positive curvature ($\kappa_o>0$), the compressive stress at the upper surface is given by $\sigma_{xx}=-Eh\kappa_o/2$ and $\Delta T=(\alpha hET_o\kappa_o/2\rho c)$. We now introduce a normalized temperature $\hat{V}^*=V^*/\Delta T$, a normalized coordinate $Y=(y/h)$, and a normalized frequency $\Omega=\omega\tau$. Equation (16) reduces to

$$\frac{d^2\hat{V}^*}{dY^2}-i\Omega\pi^2\hat{V}^*=-2i\pi^2\Omega Y. \tag{20}$$

The preceding equation can be readily solved to give

$$\hat{V}^*(Y)=2Y-2\frac{(1-i)}{\Gamma}\left[\frac{\sinh\left(\frac{1}{2}\Gamma\right)\cos\left(\frac{1}{2}\Gamma\right)+i\cosh\left(\frac{1}{2}\Gamma\right)\sin\left(\frac{1}{2}\Gamma\right)}{\sinh(\Gamma)\cos(\Gamma)+i\cosh(\Gamma)\sin(\Gamma)}\right]\cdot[\sinh(\Gamma Y)\cos(\Gamma Y)+i\cosh(\Gamma Y)\sin(\Gamma Y)] \tag{21}$$

where, for brevity, $\Gamma=\pi(\Omega/2)^{1/2}$. As expected, $V^*(Y)$ is an odd function of Y.

Using Eqs. (9) through (12), it can be readily shown that the *local* SDC is

$$\begin{aligned}\psi_L=\frac{\psi_o}{2\Gamma^2Y^2}\Bigg\{1-\frac{1}{\cosh(2\Gamma)-\cos(2\Gamma)}\times\Bigg[&2\cos\left[\Gamma\left(Y-\frac{1}{2}\right)\right]\cosh\left[\Gamma\left(Y+\frac{3}{2}\right)\right]\\&+2\cos\left[\Gamma\left(Y+\frac{1}{2}\right)\right]\cosh\left[\Gamma\left(Y-\frac{3}{2}\right)\right]\\&-2\cos\left[\Gamma\left(Y+\frac{3}{2}\right)\right]\cosh\left[\Gamma\left(Y-\frac{1}{2}\right)\right]\\&-2\cos\left[\Gamma\left(Y-\frac{3}{2}\right)\right]\cosh\left[\Gamma\left(Y+\frac{1}{2}\right)\right]\\&+2\cos(\Gamma)\cosh(2\Gamma Y)\end{aligned}$$

Downloaded 03 May 2010 to 171.66.16.20. Redistribution subject to ASME license or copyright; see http://www.asme.org/terms/Terms_Use.cfm

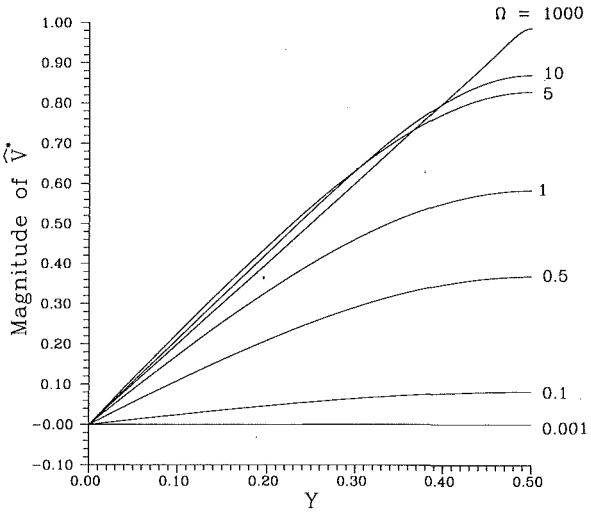


Fig. 1(*a*) Spatial dependence of the magnitude of the normalized temperature for fixed frequencies

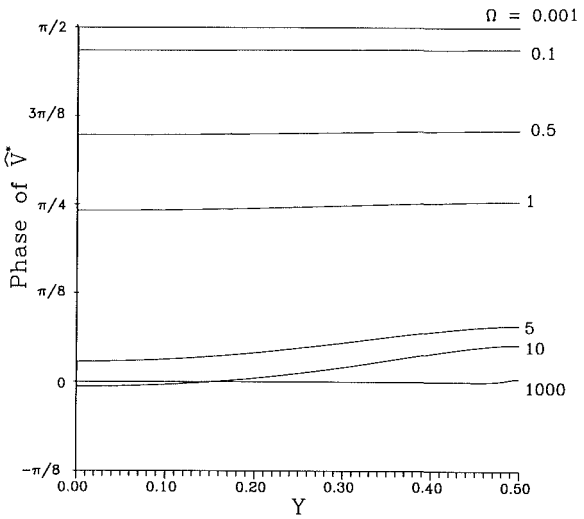


Fig. 1(*b*) Spatial dependence of the phase of the normalized temperature for fixed frequencies

$$-2\cos(2\Gamma Y)\cosh(\Gamma) + \cos\left[2\Gamma\left(Y+\frac{1}{2}\right)\right] + \cos\left[2\Gamma\left(Y-\frac{1}{2}\right)\right] - \cosh\left[2\Gamma\left(Y+\frac{1}{2}\right)\right] - \cosh\left[2\Gamma\left(Y-\frac{1}{2}\right)\right]\Bigg]\Bigg\} \quad (22)$$

and the volume-averaged damping, defined by Eq. (13), is

$$\psi = \frac{6\psi_o}{\Gamma^2}\left\{1 - \frac{1}{\Gamma}\left[\frac{\sinh(2\Gamma) - \sin(2\Gamma) - 2\cos(\Gamma)\sinh(\Gamma) + 2\sin(\Gamma)\cosh(\Gamma)}{\cosh(2\Gamma) - \cos(2\Gamma)}\right]\right\}. \quad (23)$$

Our exact solution is algebraically far more complicated than that of Zener; however, it is not difficult to show that the temperature distribution assumed by Zener is the first term in the Fourier series expansion of our exact solution for the temperature, Eq. (21).

Boundary Value Problem 1: Numerical Results

In Eq. (21) let V and ϕ be, respectively, the magnitude and phase of $\hat{V}^*$, i.e., $\hat{V}^* = Ve^{i\phi}$. Figure 1(*a*) shows V as a function of Y; we note that V is an even function of Y. When the frequency is very small, the heat generated in the beam has sufficient time to conduct from regions of elevated temperature to regions of lowered temperature. As a result, the temperature remains at the reference temperature, hence, $V \approx 0$ at $\Omega = 10^{-3}$ (essentially isothermal conditions). Conversely, when the frequency is very large, the heat has no time to conduct; therefore, the temperature corresponds to adiabatic conditions. From Eq. (21), as $\Omega \to \infty$, $\hat{V}^* = 2Y$; this is evidenced by a nearly linear variation of V with Y at $\Omega = 10^3$. Figure 1(*b*) shows the phase, ϕ, as a function of Y. Since $\hat{V}^*$ is an odd function of Y, $\phi(Y) = \phi(-Y) + \pi$. Accordingly, we have considered $0 \le Y \le 1/2$ only. As $\Omega \to 0$, $\phi \to \pi/2$ (i.e., the temperature leads the curvature by $\pi/2$) and is essentially independent of Y. As $\Omega \to \infty$, the temperature is in phase with the curvature, as expected. Figure 2 shows the frequency dependence of $\hat{V}^*$ for fixed values of Y; since V is an even function of Y, we have considered only $0 \le Y \le 1/2$. In Fig. 2(*a*) we have plotted the magnitude; the only unexpected result is a slight overshoot

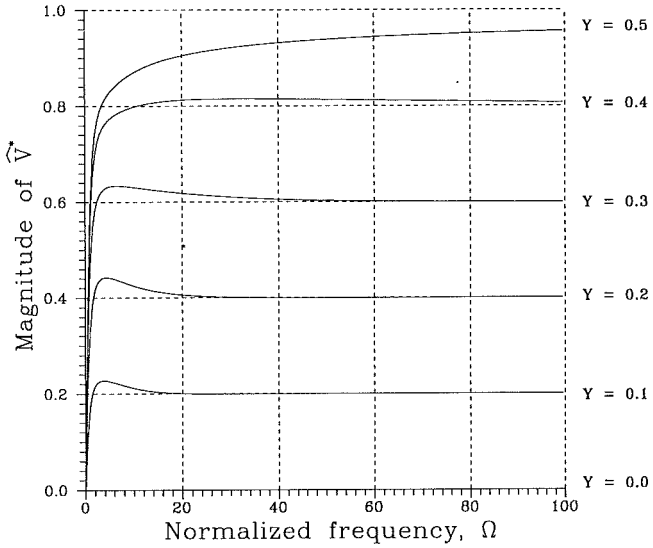


Fig. 2(*a*) Frequency dependence of the magnitude of the normalized temperature for fixed *Y*

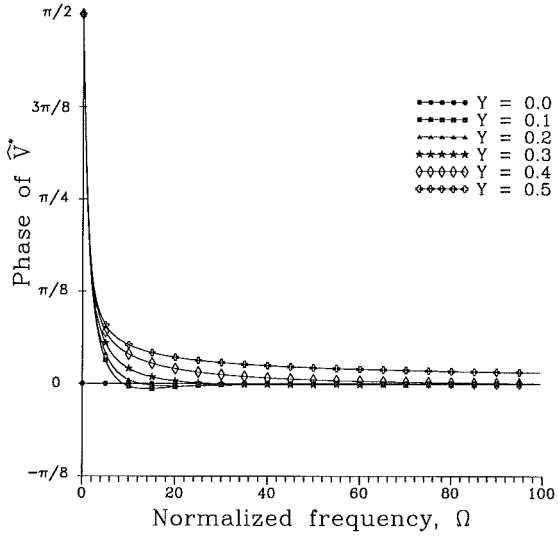


Fig. 2(*b*) Frequency dependence of the phase of the normalized temperature for fixed *Y*

Downloaded 03 May 2010 to 171.66.16.20. Redistribution subject to ASME license or copyright; see http://www.asme.org/terms/Terms_Use.cfm

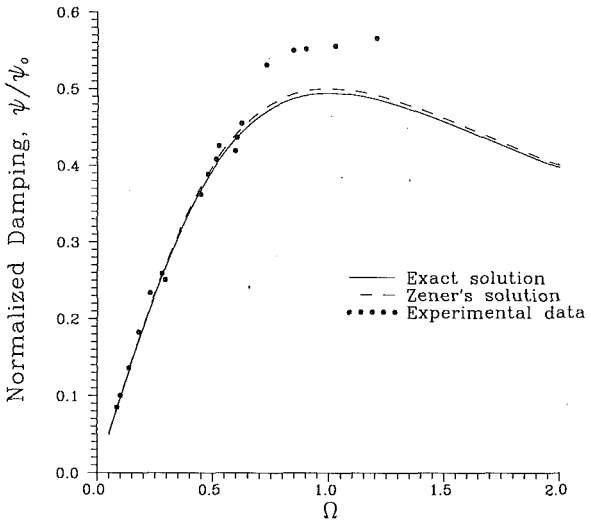


Fig. 3 A comparison of the present exact solution with the solution of Zener and with experimental data

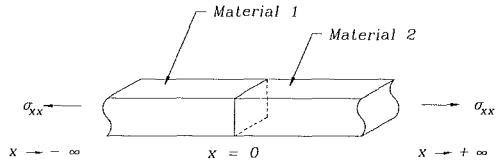


Fig. 4 A thermoelastic interface under uniaxial stress

around $\Omega = O(1)$ for the smaller values of Y. The phase plots are shown in Fig. 2(b). At very high frequencies, $\phi \to 0$ for all Y.

Next we consider the volume-averaged damping, Eq. (23). Our exact solution is compared with the approximate solution of Zener, Eq. (1), in Fig. 3. It is important to note that these are universal curves for all thermoelastic beams in flexure; each beam is classified by two of its thermoelastic properties: the characteristic damping, ψ_o, which is a *material* property, and the characteristic time, τ, which is a combination of material properties and a structural property (h). We have also included some experimental results for aluminum beams obtained by Bishop and Kinra (1991). The precision of these measurements was estimated to be of the order of 10^{-4}; therefore, the size of the circle chosen to plot the data is considerably larger than the precision. Aluminum was chosen for comparison because of its extremely low intrinsic material damping, $\psi_{\text{intrinsic}} = O(10^{-5})$ (Wren and Kinra, 1990). Therefore, the measured damping may reasonably be assumed to be entirely due to thermoelastic effects. In view of the fact that damping is a notoriously difficult quantity to measure, the agreement between the theory and the experiment is considered excellent.

Boundary Value Problem 2: A Thermoelastic Interface Under Uniform Uniaxial Stress

Consider a pair of semi-infinite, thermoelastic rods of equal cross-sectional area in welded contact at $x = 0$ as shown in Fig. 4. The welded rod is subjected to a spatially constant, time-harmonic, uniaxial stress $\sigma_{xx} = \sigma_o e^{i\omega t}$. It is recognized that very near the interface the stress field will be three-dimensional due to unequal Poisson's contractions. However, the influence of this phenomenon on damping is anticipated to be negligibly small. Therefore, to keep the problem tractable, this effect is neglected. Then $\epsilon_{xx} = \sigma_o e^{i\omega t}/E$, and $\epsilon_{yy} = \epsilon_{zz} = -\nu\epsilon_{xx}$; therefore, $\epsilon_{kk} = (1-2\nu)\,\sigma_o e^{i\omega t}/E$, and Eq. (15) reduces to

$$\frac{\partial^2 T}{\partial x^2} - \frac{\rho c}{k}\frac{\partial T}{\partial t} = i\omega \frac{\alpha T_o \sigma_o}{k} e^{i\omega t}. \tag{24}$$

The boundary conditions at the interface are the continuity of temperature

$$T(0^-, t) = T(0^+, t), \tag{25}$$

the continuity of heat flux

$$k_1 \frac{\partial T}{\partial x}(0^-, t) = k_2 \frac{\partial T}{\partial x}(0^+, t), \tag{26}$$

and as $x \to -\infty$

$$T(x, t) \to T_o - \frac{\alpha_1}{\rho_1 c_1} T_o \sigma_o e^{i\omega t}, \tag{27}$$

and as $x \to +\infty$

$$T(x, t) \to T_o - \frac{\alpha_2}{\rho_2 c_2} T_o \sigma_o e^{i\omega t}. \tag{28}$$

Once again, we write T as in Eq. (18). We introduce the normalized temperatures

$$\hat{V}_1^* = V_1^*/(-\sigma_o T_o \alpha_1/\rho_1 c_1) \quad x < 0 \tag{29}$$

$$\hat{V}_2^* = V_2^*/(-\sigma_o T_o \alpha_2/\rho_2 c_2) \quad x > 0. \tag{30}$$

Since the geometry does not have a characteristic length, we will introduce a diffusion length $l = (2k/\omega\rho c)^{1/2}$. Next, two normalized coordinates are introduced: $\xi_1 = x/l_1$ for $x < 0$, and $\xi_2 = x/l_2$ for $x > 0$. It is easy to show that Eq. (15) reduces to the following pair of ordinary differential equations:

$$\frac{d^2 \hat{V}_1^*}{d\xi_1^2} - 2i\hat{V}_1^* = -2i \quad \xi_1 < 0 \tag{31}$$

$$\frac{d^2 \hat{V}_2^*}{d\xi_2^2} - 2i\hat{V}_2^* = -2i \quad \xi_2 > 0 \tag{32}$$

The boundary conditions at the interface become

$$Z_1 \hat{V}_1^* = Z_2 \hat{V}_2^* \tag{33}$$

$$Z_1 K_1 \frac{d\hat{V}_1^*}{d\xi_1} = Z_2 K_2 \frac{d\hat{V}_2^*}{d\xi_2} \tag{34}$$

where we have introduced $Z = \alpha/\rho c$ and the coefficient of heat penetration $K = (\rho c k)^{1/2}$ (Grigull and Sander, 1984). At infinity the boundary conditions are as follows: as $\xi_1 \to -\infty$, $\hat{V}_1^* \to 1$; and as $\xi_2 \to +\infty$, $\hat{V}_2^* \to 1$. The solution to the ordinary differential equations is

$$\hat{V}_1^*(\xi_1) = 1 - \left(1 - \frac{Z_2}{Z_1}\right)\frac{K_2}{K_1 + K_2} e^{(1+i)\xi_1} \tag{35}$$

$$\hat{V}_2^*(\xi_2) = 1 - \left(1 - \frac{Z_1}{Z_2}\right)\frac{K_1}{K_1 + K_2} e^{-(1+i)\xi_2}. \tag{36}$$

As in boundary value problem 1, using Eqs. (9) through (12) it can be readily shown that the local specific damping capacity is

$$\psi_{L1} = \psi_{o1}\left[\frac{K_2}{K_1 + K_2}\left(1 - \frac{Z_2}{Z_1}\right)e^{\xi_1}\right]^2 \tag{37}$$

$$\omega_{L2} = \psi_{o2}\left[\frac{K_1}{K_1 + K_2}\left(1 - \frac{Z_1}{Z_2}\right)e^{-\xi_2}\right]^2 \tag{38}$$

where ψ_o is given by Eq. (2) and the subscript on ψ_o refers to material 1 or 2.

From Eqs. (35) and (36) we observe that when $Z_1 = Z_2$, $\hat{V}_1^* = \hat{V}_2^* = 1$, i.e., $\hat{V}^*(x)$ is constant for all x. Under these circumstances the two rods experience identical temperature fluctuations and there is no heat transfer anywhere. As expected, Eqs. (37) and (38) reduce to $\psi_{L1} = \psi_{L2} = 0$ for all x, i.e., there is no damping. Clearly the material property combination $Z = \alpha/\rho c$ is the quintessential physical property governing the physics of this problem. In honor of Zener, we would like to call it the Zener coefficient. Physically, Z is the negative of the normalized change in temperature due to one unit stress; see Eq. (19).

Downloaded 03 May 2010 to 171.66.16.20. Redistribution subject to ASME license or copyright; see http://www.asme.org/terms/Terms_Use.cfm

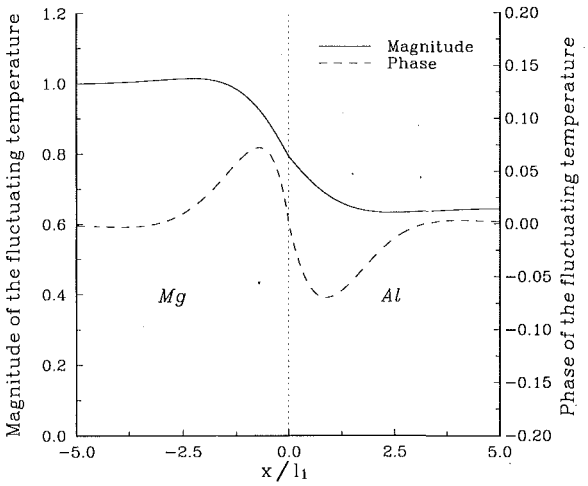


Fig. 5 Spatial dependence of the magnitude and phase of the normalized fluctuating temperature for a pair of thermoelastically similar materials

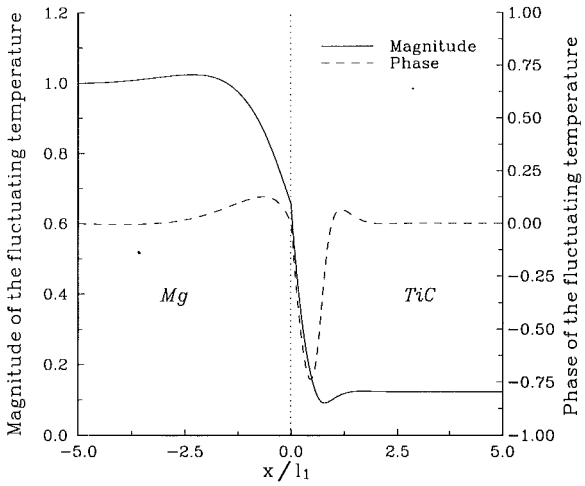


Fig. 6 Spatial dependence of the magnitude and phase of the normalized fluctuating temperature for a pair of thermoelasticically dissimilar materials

As expected, ψ_{L1} and ψ_{L2} are symmetric in the exchange of indices 1 and 2. It is interesting to note that even though the temperature and the heat flux are equal at the interface, the damping on the two sides of the interface is unequal due to the difference in the thermal conductivity and the temperature gradient. Furthermore, the damping considered here is due solely to the presence of the interface; far away from the interface the temperature field is uniform and, therefore, the thermoelastic damping is zero. Accordingly, we will designate this phenomenon as *interface damping*.

Boundary Value Problem 2: Numerical Results

The use of the normalized variables $\hat{V}_1^*(\xi_1)$ and $\hat{V}_2^*(\xi_2)$ was very convenient from the viewpoint of algebraic manipulation; however, their use in reporting numerical results would mask the relative magnitude of the temperatures as well as their spatial dependence. Therefore, for plotting purposes we shall use the unsubscripted $\hat{V}^* = V^*/(-\sigma_o T_o \alpha_1/\rho_1 c_1)$ and x/l_1 for $-\infty < x < \infty$. Then

$$\hat{V}^* = \begin{cases} \hat{V}_1^* & x<0 \\ \dfrac{Z_2}{Z_1}\hat{V}_2^* & x>0 \end{cases} \tag{39}$$

or

$$\hat{V}^* = 1 - \left(1 - \frac{Z_2}{Z_1}\right)\frac{K_2}{K_1+K_2} e^{(1+i)(x/l_1)} \quad x<0 \tag{40}$$

$$\hat{V}^* = \frac{Z_2}{Z_1} + \left(1 - \frac{Z_2}{Z_1}\right)\frac{K_1}{K_1+K_2} e^{-(1+i)(l_1/l_2)(x/l_1)} \quad x>0. \tag{41}$$

As in boundary value problem 1, let V and ϕ be, respectively, the magnitude and phase of $\hat{V}^*$, i.e., $\hat{V}^* = Ve^{i\phi}$. In Fig. 5, V and ϕ are plotted against x/l_1 for a pair of thermoelastically *similar* materials, namely, Mg/Al with $Z_{Al}/Z_{Mg} = 0.64$. From Eqs. (40) and (41), as $x \to -\infty$, $\hat{V}^* \to 1$, i.e., $V \to 1$ and $\phi \to 0$; as $x \to +\infty$, $\hat{V}^* \to Z_2/Z_1$, i.e., $V \to Z_2/Z_1$ and $\phi \to 0$. At the interface $\hat{V}^*(0^-) = \hat{V}^*(0^+) = (Z_1K_1 + Z_2K_2)/(K_1+K_2)$. The form of this equation is rather interesting. In the parlance of mechanics of composite materials, the interface temperature is the "modulus-weighted mean" of the two remote temperatures, Z_1 and Z_2; here K_1 and K_2 play the role of the "moduli." Also note that ϕ is zero at the interface, i.e., the interface temperature is always in phase with the applied stress. Similar results are presented in Fig. 6 for a pair of thermoelastically *dissimilar* materials, namely, Mg/TiC: $Z_{TiC}/Z_{Mg} = 0.12$. Note that the slope of the temperature at the interface is discontinuous; this is a consequence of the requirement of the continuity of heat flux, $q = -k\partial T/\partial x$. The diffusion length at 100 Hz for Al is 0.54 mm, for Mg it is 0.52 mm, and for TiC it is only 0.16 mm. This explains the relative localization of the diffusion in TiC when in contact with Mg. Now, $Z_{Mg} > Z_{Al}$, i.e., when subjected to the same compressional stress, Mg will become "hotter" than Al. For ease of communication we will call Mg the "donor" and Al the "acceptor." At the interface, the temperature in the donor leads the applied stress whereas the temperature in the acceptor lags. In Fig. 6, observe that the slope of the V versus x/l_1 curve is zero at about $x/l_1 = 0.8$. At first sight this would suggest a plane of zero heat conduction in the rod. It is worth pointing out that this is not the case. The slope of the phase at the same location, $x/l_1 = 0.8$, is not zero. Therefore, even though two neighboring material points experience the same temperature amplitude, they are out of phase, and this leads to nonzero heat conduction. It is a trivial exercise to verify that over the entire real axis $\partial \hat{V}^*/\partial x \neq 0$. The Nyquist plot (i.e., the plot in the complex plane) of $\hat{V}^*$ with x/l_1 as the parameter is presented in Fig. 7. The phase for the donor is (generally) positive while that of the acceptor is (generally) negative; the magnitude for the donor is always greater than the magnitude of the acceptor. (Note that the origin lies on the vertical axis.)

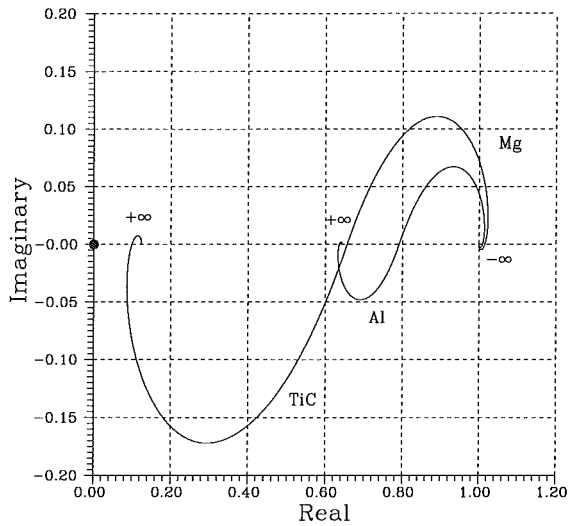


Fig. 7 The Nyquist plot of $\hat{V}^*$ with x/l_1 as the parameter

Attention is now turned to interface damping; see Eqs. (37) and (38). All numerical results will be presented at a frequency

Downloaded 03 May 2010 to 171.66.16.20. Redistribution subject to ASME license or copyright; see http://www.asme.org/terms/Terms_Use.cfm

Table 1 Thermoelastic properties for selected materials

Material	ρ (10^3 kg/m^3)	E (GPa)	k (J/s-m-K)	c (J/kg-K)	α (10^{-6} /K)	Z (10^{-12} m^2/N)	ψ_o at 300 K	l at 100 Hz (mm)
Al	2.70	70	222	900	23.6	9.71	0.0302	0.54
Mg	1.74	44	154	1030	27.1	15.1	0.0340	0.52
Ti	4.51	116	38.9	519	8.41	3.59	0.0066	0.23
Al_2O_3	3.80	350	29.3	840	9.0	2.82	0.0167	0.17
TiC	4.50	350	30.3	840	7.0	1.85	0.0086	0.16
SiC	3.26	460	90.0	1330	4.3	0.99	0.0037	0.26

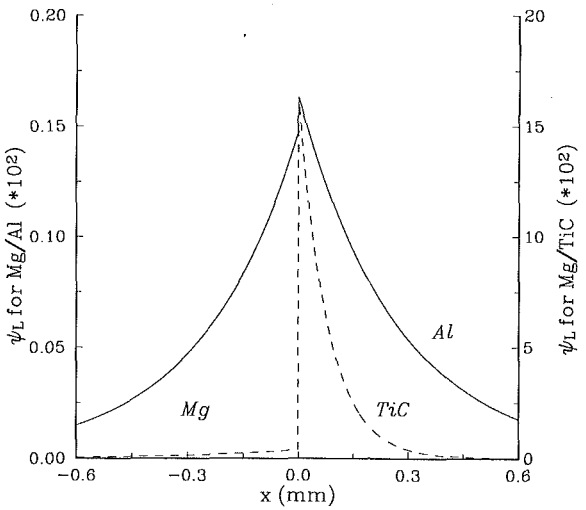


Fig. 8 Specific damping capacity near the interface as a function of position

of $f = 100$ Hz. The local specific damping capacities for Mg/Al and Mg/TiC are shown in Fig. 8. (Note the use of different scales.) Since Z_{Mg} (15.12) and Z_{Al} (9.71) are not very different, the damping is rather small; $\psi = O(0.1$ percent). On the other hand, in the case of Mg/TiC, $Z_{Mg}/Z_{TiC} = 15.1/1.85 \approx 10$. With reference to Eqs. (37) and (38), the SDC depends upon the square of $(Z_1\text{-}Z_2)$; this explains the very high interface damping for the case of Mg/TiC. This is the most encouraging result of the present investigation: by a proper *tailoring* of the two constituents, one can obtain interface damping as high as 20 percent. For a variety of material combinations, interface damping is given in Table 2. From a design point of view, we observe that high damping is achieved when a ceramic (Al_2O_2, SiC, TiC) is "interfaced" with a high-conductivity metal (Al, Mg).

As a minor aside we note that $\psi_L(0^+)/\psi_L(0^-)$ is very nearly unity for the similar materials (Mg/Al) and quite large for the dissimilar materials (Mg/TiC); this may be explained by the following. From Eqs. (37) and (38)

$$\psi_L(0^+)/\psi_L(0^-) = (E_2/k_2)/(E_1/k_1), \qquad (42)$$

i.e., (E/k) is the relevant physical property. With reference to Table 1, $(E/k)_{Al} = 0.315 \cdot 10^9$ s-K/m^2, $(E/k)_{Mg} = 0.286 \cdot 10^9$ s-Km^2, whereas $(E/k)_{TiC} = 11.5 \cdot 10^9$ s-K/m^2.

Conclusions

Taking the second law of thermodynamics as our starting point, we have developed a theory for thermoelastic damping in elastic solids. In this theory the applied stress field is viewed as the cause which results in a temperature field (see Thomson effect). This causes irreversible heat transfer and entropy is created as a result thereof. The entropy produced is a measure of the amount of work converted into heat, i.e., mechanical damping. The theory is quite general and can be used to predict damping either due to the application of an inhomogeneous stress field to a homogeneous body or due to the application of a homogeneous (or inhomogeneous) stress field to a heterogeneous material. By way of illustration, we have solved two problems: (1) flexural vibrations of a Bernoulli-Euler beam, and (2) interface damping.

Table 2 Local specific damping capacity at the interface for various material combinations

Damping in ($\psi_L \cdot 10^2$)	When against: Al	Mg	Ti	Al_2O_3	TiC	SiC
Al	0.000	0.163	0.102	0.132	0.197	0.515
Mg	0.148	0.000	0.263	0.305	0.402	0.876
Ti	0.963	2.744	0.000	0.008	0.043	0.157
Al_2O_3	4.987	12.731	0.031	0.000	0.054	0.317
TiC	7.220	16.242	0.168	0.053	0.000	0.078
SiC	8.348	15.662	0.270	0.136	0.034	0.000

Acknowledgments

This research is supported by the Office of Naval Research through Grant Number N00014-90-J-1130 to Texas A&M University, College Station, Texas. The continued and keen interest taken by the program managers, Ms. Cathy Wong, Dr. Don Polk, and Dr. L. Kabacoff, in the evolution of this work is gratefully acknowledged. Thanks are due to Professor Kalyan Annamalai for many helpful discussions.

References

Albas, J. B., 1961, "On the General Theory of Thermo-Elastic Friction," *Apl. Sci. Res.*, Section A, Vol. 10, pp. 349-362.

Alblas, J. B., 1981, "A Note on the Theory of Thermoelastic Damping," *Journal of Thermal Stresses*, Vol. 4, pp. 333-355.

Bejan, A., 1988, *Advanced Engineering Thermodynamics*, John Wiley and Sons, New York, New York, p. 114.

Bishop, J. E., and Kinra, V. K., 1992, "Some Improvements in the Flexural Damping Measurement Technique," *M^{3}D: Mechanics and Mechanisms of Material Damping*, ASTM STP 1169, V. K. Kinra and A. Wolfenden, eds., American Society for Testing and Materials, Philadelphia, pp. 457-470.

Chadwick, P., 1962, "Thermal Damping of a Vibrating Elastic Body," *Mathematika*, Vol. 9, pp. 38-48.

Coleman, B. D., and Noll, W., 1961, "Foundations of Linear Viscoelasticity," *Review of Modern Physics*, Vol. 33, pp. 239-249.

Coleman, B. D., and Mizel, V. J., 1964, "Existence of Caloric Equations of State in Thermodynamics," *Journal of Chemistry and Physics*, Vol. 40, pp. 1116-1125.

Frederick, D., and Chang, T. S., 1972, *Continuum Mechanics*, Scientific Publishers, Cambridge, MA, p. 169.

Grigull, U., and Sander, H., 1984, *Heat Conduction*, Springer-Verlag, New York, p. 18.

Shieh, R. C., 1975, "Thermoelastic Vibration and Damping for Circular Timoshenko Beams," ASME JOURNAL OF APPLIED MECHANICS, Vol. 42, pp. 405-410.

Shieh, R. C., 1979, "Eigensolutions for Coupled Vibrations of Timoshenko Beams," ASME JOURNAL OF APPLIED MECHANICS, Vol. 46, pp. 169-174.

Thomson, W., 1853, "On the Dynamical Theory of Heat," *Transactions of the Royal Society of Edinburgh*, Vol. 20, pp. 261-283.

Wren, G. G., and Kinra, V. K., 1990, "An Experimental Study of the Complex Dynamic Modulus," *Dynamic Elastic Modulus Measurements in Materials*, ASTM STP 1045, A. Wolfenden, ed., American Society for Testing and Materials, Philadelphia, pp. 58-74.

Zener, C., 1948, *Elasticity and Anelasticity of Metals*, University of Chicago Press, Chicago, Illinois.

Downloaded 03 May 2010 to 171.66.16.20. Redistribution subject to ASME license or copyright; see http://www.asme.org/terms/Terms_Use.cfm

Characteristics of Modal Coupling in Nonclassically Damped Systems Under Harmonic Excitation

I. W. Park
Research Assistant.

J. S. Kim
Research Assistant.

F. Ma
Associate Professor of Applied Mechanics, Mem. ASME.

Department of Mechanical Engineering, University of California, Berkeley, CA 94720

The normal coordinates of a nonclassically damped system are coupled by nonzero off-diagonal elements of the modal damping matrix. The purpose of this paper is to study the characteristics of modal coupling, which is amenable to a complex representation. An analytical formulation is developed to facilitate the evaluation of modal coupling. Contrary to widely accepted beliefs, it is shown that enhancing the diagonal dominance of the modal damping matrix or increasing the frequency separation of the natural modes need not diminish the effect of modal coupling. The effect of modal coupling may even increase. It is demonstrated that, within the practical range of engineering applications, neither diagonal dominance of the modal damping matrix nor frequency separation of the natural modes would be sufficient for neglecting modal coupling.

1 Introduction

The equation of motion of an n-degree-of-freedom system under external excitation can be written as

$$M\ddot{x}+C\dot{x}+Kx=g(t),\ x(0)=x_0,\ \dot{x}(0)=\dot{x}_0,\ t\geq 0, \qquad (1)$$

where the mass matrix M, the damping matrix C, and the stiffness matrix K are of order $n\times n$. The displacement $x(t)$ and external excitation $g(t)$ are n-dimensional vectors. For passive systems, the matrices M, C, and K are real, symmetric, and positive definite. These assumptions are not arbitrary, but in fact have solid footing in the theory of Lagrangian dynamics. In the last several decades, passive systems have constituted a subject of intense investigation in structural mechanics.

Let U denote the $n\times n$ modal matrix associated with system (1). The modal matrix is a real nonsingular matrix whose columns are the eigenvectors of the symmetric eigenvalue problem

$$Ku^{(i)}=\omega_i^2\, Mu^{(i)}, \qquad (2)$$

where $\omega_i^2>0$ and $u^{(i)}$ $(i=1,\ \ldots,\ n)$ are, respectively, the eigenvalues and eigenvectors. The modal matrix is usually orthonormalized according to $U^TMU=I$, where U^T denotes the transpose of U, and I is the identity matrix of order n. In addition, $U^TKU=\Omega=\text{diag}[\omega_1^2,\ \cdots,\ \omega_n^2]$. By the linear transformation $x(t)=Uq(t)$, Eq. (1) can be written in the normalized form

$$\ddot{q}+D\dot{q}+\Omega q=f(t),\ q(0)=U^TMx_0, \qquad (3)$$

where $f(t)=U^Tg(t)$, and $q(t)$ is the n-dimensional vector of normal coordinates. The symmetric matrix $D=U^TCU$ is called the modal damping matrix. If D is diagonal, the system is said to be classically damped. It has been shown by Caughey and O'Kelly (1965) that system (1) is classically damped if and only if $CM^{-1}K=KM^{-1}C$. In general, this condition is not satisfied, and the modal matrix D is not diagonal. The normalized equations of motion are then coupled by the nonzero off-diagonal elements of D, and the system is said to be nonclassically damped. It is with this type of linear systems that the present paper is concerned.

Various exact and approximate techniques have been proposed for the study of nonclassically damped systems. For instance, Foss (1958) and others expounded a state-space approach which is based upon the orthogonality between complex eigenvectors. However, this complex-mode method is computationally intensive, and the physical significance of the different elements of this exact method is not well clarified. Approximate solution of a nonclassically damped system by perturbation techniques was proposed by Cronin (1976), Chung and Lee (1986), and others. Prater and Singh (1986), and Nair and Singh (1986) developed several indices to determine quantitatively the extent of nonclassical damping in discrete vibratory systems. Ozguven (1982, 1987) used the concept of receptance to study nonclassically damped structures in the frequency domain. Bellos and Inman (1990) examined modal coupling in linear systems by employing nonproportionality indices. A survey of the various methods that are applicable to nonclassically damped systems has recently been given by Bellos and Inman (1989).

A common procedure in the solution of a nonclassically damped linear system is to neglect the off-diagonal elements of the modal damping matrix. This procedure, herein called the decoupling approximation, is widely used in industry for the solution of large-scale systems. A whole body of literature

Contributed by the Applied Mechanics Division of THE AMERICAN SOCIETY OF MECHANICAL ENGINEERS for publication in the ASME JOURNAL OF APPLIED MECHANICS.

Discussion on this paper should be addressed to the Technical Editor, Professor Lewis T. Wheeler, Department of Mechanical Engineering, University of Houston, Houston, TX 77204-4792, and will be accepted until four months after final publication of the paper itself in the ASME JOURNAL OF APPLIED MECHANICS.

Manuscript received by the ASME Applied Mechanics Division, Nov. 1, 1991; final revision, June 8, 1992. Associate Technical Editor: D. J. Inman.

Copyright © 1994 by ASME
Downloaded 03 May 2010 to 171.66.16.20. Redistribution subject to ASME license or copyright; see http://www.asme.org/terms/Terms_Use.cfm

has been devoted to this rather appealing method of approximate solution. Clearly, decoupling approximation is valid if modal coupling can somehow be ignored.

It is widely believed that the off-diagonal elements of the modal damping matrix D can be neglected if their relative magnitudes are small. Mathematically, this means some form of diagonal dominance of D can justify the omission of its off-diagonal elements. The concept of diagonal dominance may be explained in the following way. Denote the row sum of the absolute values of the off-diagonal elements of D by

$$\sigma_i = \sum_{\substack{j=1 \\ j\neq i}}^{n} |d_{ij}|, \tag{4}$$

where d_{ij} are the elements of D. The matrix D is diagonally dominant if $\sigma_i \leq |d_{ii}|$ $(i=1, \cdots, n)$. It is said to be strictly diagonally dominant if $\sigma_i < |d_{ii}|$ $(i=1, \cdots, n)$. Moreover, if $\sigma_i \ll |d_{ii}|$ for all i, then D is said to be strongly diagonally dominant. A rigorous demonstration that diagonal dominance of D always leads to small errors in the decoupling approximation has not been reported. In the event that D is diagonally dominant, and if system (3) is to be decoupled by replacing D by an arbitrary diagonal matrix, Shahruz and Ma (1988) have proved that neglecting the off-diagonal elements of D will minimize the error bound. Although somewhat relevant, this does not ensure small errors in the decoupling approximation. Perhaps it should be stated that the interplay between diagonal dominance and modal coupling is still not well understood.

An alternative criterion for neglecting modal coupling, suggested by Hasselman (1976), is to require adequate frequency separation between the natural modes. A similar observation was made by Warburton and Soni (1977). Over the years, frequency separation of the natural modes has generally been accepted as a sufficient condition for the decoupling approximation.

The purpose of this paper is to characterize modal coupling in nonclassically damped linear systems under harmonic excitation. It will be shown that, within the practical range of engineering applications, neither diagonal dominance of the modal damping matrix nor frequency separation of the natural modes would be sufficient for neglecting modal coupling. The organization of the paper is as follows. In Section 2, an analytical formulation is developed to facilitate the evaluation of modal coupling. The concepts of coupling coefficients and coupling indices are introduced, and their basic properties are described. In Section 3, the issue of diagonal dominance of the modal damping matrix is examined in terms of coupling indices. A multi-degree-of-freedom system is employed to demonstrate that modal coupling can even increase as the degree of diagonal dominance increases. The issue of frequency separation is taken up in Section 4. Several expressions are derived to highlight the functional dependence of modal coupling on both the natural and excitation frequencies. For two-degree-of-freedom systems, the analysis is carried out in detail. A numerical example is also furnished. In Section 5, a summary of the findings is provided.

2 Characterization of Modal Coupling

An index for measuring the effect of modal coupling quantitatively will be introduced. This complex parameter, called the coupling index, clarifies the role that harmonic excitation plays in influencing modal coupling. Various numerical indices have already been devised by other authors to quantify the extent of nonclassical damping. Of particular relevance are the indices proposed by Warburton and Soni (1977), and by Bellos and Inman (1990). However, this work is new, and it represents the first significant use of a complex formulation in the characterization of modal coupling. It will be seen that the complex formulation has crucial implications on the precise nature of modal coupling. This concept of coupling index will be employed in the next section to explain how modal coupling may increase as the off-diagonal elements of the modal damping matrix decrease in magnitude.

Consider system (3) subjected to harmonic excitation. Let

$$f(t) = au(t) \tag{5}$$

where $a = (f_1, f_2, \cdots, f_n)^T$ and f_i $(i=1, \cdots, n)$ are nonzero constants. The scalar $u(t)$ is a harmonic function of unit amplitude. Since the main focus of this study is the investigation of modal coupling in the steady-state solution, it may be assumed, for convenience, that $x_0 = \dot{x}_0 = 0$. From system (3), the equation of motion associated with the i-th modal coordinate is

$$\ddot{q}_i + d_{ii}\dot{q}_i + \omega_i^2 q_i + \sum_{\substack{j=1 \\ j\neq i}}^{n} d_{ij}\dot{q}_j = f_i u(t), \tag{6}$$

where d_{ij} $(i, j=1, \cdots, n)$ are elements of the modal damping matrix D. Applying the Laplace transform to Eq. (6), we have

$$\left\{ s^2 + \left(d_{ii} + \sum_{\substack{j=1 \\ j\neq i}}^{n} d_{ij} \frac{Q_j(s)}{Q_i(s)} \right) s + \omega_i^2 \right\} Q_i(s) = f_i U(s), \tag{7}$$

where $Q_k(s)$ and $U(s)$ are the Laplace transforms of $q_k(t)$ and $u(t)$, respectively. Since the Laplace variable s is complex, each $Q_k(s)$ is also complex. Define the ith nonproportionality factor $\Delta_i(s)$ by

$$\Delta_i(s) = \sum_{\substack{j=1 \\ j\neq i}}^{n} d_{ij} \frac{Q_j(s)}{Q_i(s)}. \tag{8}$$

If the system is classically damped, $\Delta_i(s)$ is zero. Moreover, the nonproportionality factor $\Delta_i(s)$ is independent of the transformed excitation $U(s)$, even though each $Q_k(s)$ must depend on $U(s)$. To prove this independence, transform Eq. (3) into

$$(Is^2 + Ds + \Omega) Q(s) = aU(s), \tag{9}$$

where $Q(s)$ is the Laplace transform of $q(t)$. It follows that

$$Q(s) = (Is^2 + Ds + \Omega)^{-1} aU(s). \tag{10}$$

Let $g_i(s)$ denote the ith element of the column vector $(Is^2 + Ds + \Omega)^{-1}a$. Obviously, $g_i(s)$ depends on the system parameters and a only and is independent of $U(s)$. Since

$$Q_i(s) = g_i(s) U(s), \tag{11}$$

therefore

$$\frac{Q_j(s)}{Q_i(s)} = \frac{g_j(s)}{g_i(s)}, \tag{12}$$

showing that $Q_j(s)/Q_i(s)$ is independent of $U(s)$. From Eq. (8), $\Delta_i(s)$ is independent of $U(s)$. In other words, the nonproportionality factor $\Delta_i(s)$ is not affected by changes in the functional form of $u(t)$. However, for the purpose of this investigation, $u(t)$ remains a harmonic function of unit amplitude.

It is tempting to use the nonproportionality factor as an indicator of the effect of modal coupling. It should be stressed, however, that nonproportionality factors does not provide a direct measure of the influence of modal coupling on the system response. As will be demonstrated in a subsequent section, a nonproportionality factor of large magnitude may not imply correspondingly significant effect of modal coupling on the system response. Further development is needed to generate a more realistic indicator of the effect of modal coupling. To this end, observe that

$$Q_i(s) = \left\{ \frac{f_i}{s^2 + (d_{ii} + \Delta_i(s))s + \omega_i^2} \right\} U(s). \tag{13}$$

Downloaded 03 May 2010 to 171.66.16.20. Redistribution subject to ASME license or copyright; see http://www.asme.org/terms/Terms_Use.cfm

Writing j for i in the above and substituting into Eq. (7), we obtain

$$Q_i(s) = \frac{1}{s^2 + d_{ii}s + \omega_i^2} \times \left\{ f_i - \sum_{\substack{j=1 \\ j \neq i}}^{n} d_{ij} \frac{sf_j}{s^2 + (d_{jj} + \Delta_j(s))s + \omega_j^2} \right\} U(s). \quad (14)$$

Since each $\Delta_j(s)$ is independent of $U(s)$, the expression premultiplying $U(s)$ in the above equation can be viewed as a transfer function of the modal response $Q_i(s)$.

Define a quantity called the coupling coefficient by

$$\gamma_{ij}(s) = -d_{ij} \frac{sf_j}{s^2 + (d_{jj} + \Delta_j(s))s + \omega_j^2}, \quad (15)$$

where $i \neq j$ $(i, j = 1, \cdots, n)$. Furthermore, define the coupling index $\Gamma_i(s)$ associated with the ith modal response by

$$\Gamma_i(s) = \sum_{\substack{j=1 \\ j \neq i}}^{n} \gamma_{ij}(s). \quad (16)$$

The coupling coefficient $\gamma_{ij}(s)$ is a measure of the effect of coupling exerted by the jth mode on the ith modal response. These coefficients are complex quantities. The coupling index $\Gamma_i(s)$ is the vector sum of $n-1$ constituent coefficients in the complex plane. If the system is classically damped, each coupling index $\Gamma_i(s)$ must be zero. Moreover, from Eq. (14), $\Gamma_i(s)$ can be regarded as a correction factor that accounts for nonclassical damping in the modal transfer function. In contrast to the nonproportionality factor, it can be shown that a coupling index $\Gamma_i(s)$ of large magnitude always implies correspondingly significant effect of modal coupling on the ith modal response. This point will be demonstrated in the next section. It is important to note that determination of $\Gamma_i(s)$ requires the prior calculation of the nonproportionality factors $\Delta_j(s)$.

3 Diagonal Dominance

In a system with a large number of degrees-of-freedom, there are many ways that modal coupling can become appreciable. The overall effect of coupling on the ith modal response can be directly measured by Γ_i, defined by Eq. (16). In the complex plane, the coupling index Γ_i is the vector sum of a large number of coupling coefficients γ_{ij} $(j = 1, \cdots, i-1, i+1, \cdots, n)$. Therefore, Γ_i is determined not only by the magnitudes of the constituent coupling coefficients, but also by their angular orientations in the complex plane. Even when the individual coupling coefficients are small, their sum can be large if their directions allow them to add up. On the other hand, summing relatively large coupling coefficients may result in a coupling index with negligible magnitude if there are cancellations among a significant number of them. To predict the extent of modal coupling, an explicit evaluation of the coupling index is necessary.

It is widely believed that some form of diagonal dominance of the modal damping matrix D is sufficient for neglecting modal coupling. This belief is explicit or implicit in papers by Warburton and Soni (1977), Xu and Igusa (1991), Hwang and Ma (1992), and many others. However, within the practical range of engineering applications, diagonal dominance of the modal damping matrix D is not a sufficient condition for ignoring modal coupling. That means it is not sufficient to ensure small errors in the decoupling approximation. The following concrete example will illustrate this point. In addition, this example will demonstrate that the larger the coupling index, the greater is the error due to decoupling approximation.

Example 1. Consider a six-degree-of-freedom system whose normalized equation of motion is

$$\ddot{q} + D\dot{q} + \Omega q = a \sin \omega_f t, \quad q(0) = \dot{q}(0) = 0, \quad t \geq 0, \quad (17)$$

where $a = (1, 1, 1, 1, 1, 1)^T$, $\omega_f = 4.14$, and

$$\Omega = \text{diag}[3.95^2, 3.98^2, 4.0^2, 4.1^2, 4.17^2, 4.25^2]. \quad (18)$$

The modal damping matrix is specified in three separate cases.

Case (i):

$$D = \begin{bmatrix} 1.61 & 0.5 & 0.3 & -0.5 & 0.0 & -0.3 \\ 0.5 & 1.7 & 0.0 & -0.3 & -0.5 & 0.3 \\ 0.3 & 0.0 & 1.8 & 0.5 & -0.3 & -0.5 \\ -0.5 & -0.3 & 0.5 & 1.75 & 0.3 & 0.0 \\ 0.0 & -0.5 & -0.3 & 0.3 & 1.65 & 0.5 \\ -0.3 & 0.3 & -0.5 & 0.0 & 0.5 & 1.8 \end{bmatrix}. \quad (19)$$

Case (ii):

$$D = \begin{bmatrix} 1.61 & 0.06 & 0.08 & 0.07 & 0.05 & 0.04 \\ 0.06 & 1.7 & 0.02 & 0.05 & 0.06 & 0.03 \\ 0.08 & 0.02 & 1.8 & 0.03 & 0.07 & 0.05 \\ 0.07 & 0.05 & 0.03 & 1.75 & 0.04 & 0.02 \\ 0.05 & 0.06 & 0.07 & 0.04 & 1.65 & 0.05 \\ 0.04 & 0.03 & 0.05 & 0.02 & 0.05 & 1.8 \end{bmatrix}. \quad (20)$$

It is easy to see that the modal damping matrices in both cases are diagonally dominant. In Case (i), each row sum of the absolute values of the off-diagonal elements of D is only slightly less than the corresponding diagonal element. However, the damping matrix in Case (ii) is strongly diagonally dominant, with each row sum of the absolute values of the off-diagonal elements an order-of-magnitude smaller than the corresponding diagonal element. If diagonal dominance of D could serve as a sufficient criterion for neglecting modal coupling, then Case (ii) would be more suited for solution by decoupling approximation. A comparison is made between the exact solution and the solution obtained by decoupling approximation for the two cases, using the first mode. According to Fig. 1, the exact and approximate solutions are almost identical in Case (i). However, Fig. 2 shows that the approximate solution in Case (ii) has as much as 15 percent error compared to the exact solution. In fact, over a finite range, the effect of modal coupling can increase as the degree of diagonal dominance increases.

To explain the unexpectedly large error in Case (ii), coupling coefficients associated with the first mode are plotted in the

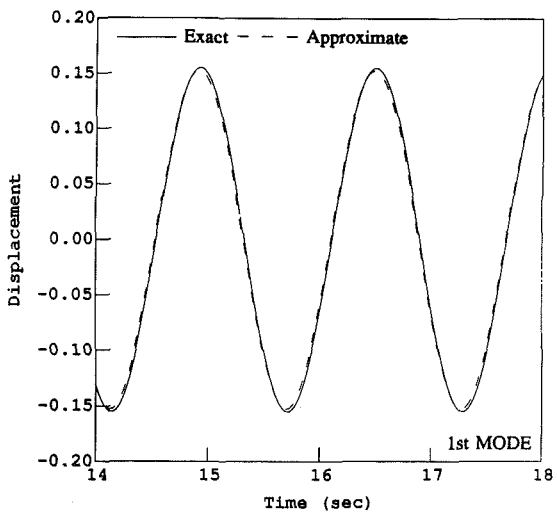


Fig. 1 Exact versus approximate solution for Case (i)

Downloaded 03 May 2010 to 171.66.16.20. Redistribution subject to ASME license or copyright; see http://www.asme.org/terms/Terms_Use.cfm

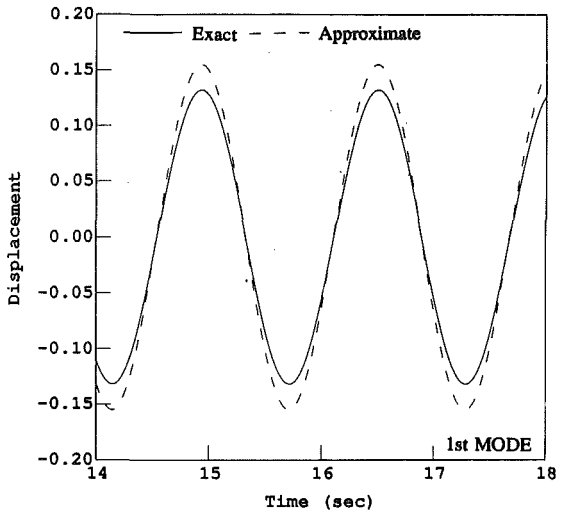


Fig. 2 Exact versus approximate solution for Case (ii)

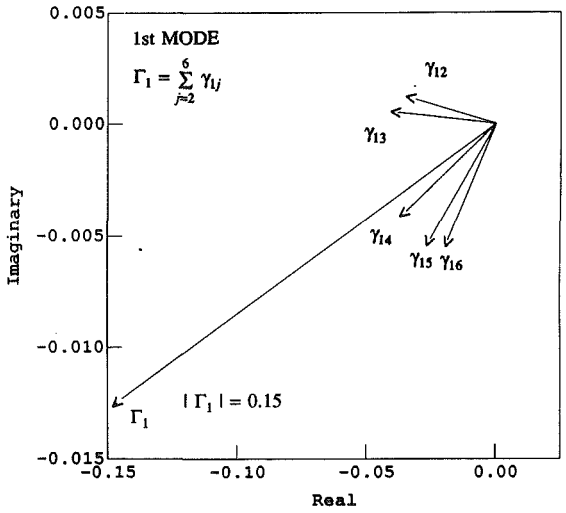


Fig. 4 Vector sum of coupling coefficients in the complex plane for Case (ii)

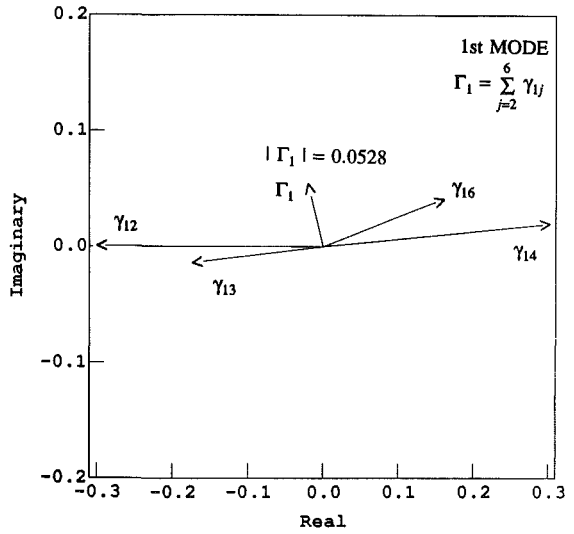


Fig. 3 Vector sum of coupling coefficients in the complex plane for Case (i)

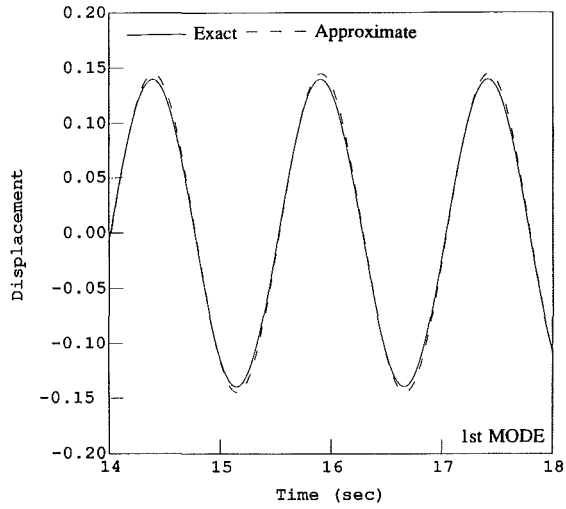


Fig. 5 Exact versus approximate solution for Case (iii)

complex plane. In Case (i), the magnitudes of individual coupling coefficients are large, as may be surmised from the relatively large off-diagonal damping elements. This is shown in Fig. 3. However, the vector sum of the coupling coefficients is quite small due to cancellations among the constituent terms. As a result, the coupling index Γ_1 associated with the first mode is relatively small. In Case (ii), the coupling coefficients, although individually smaller, are aligned such that they add up to a much larger coupling index Γ_1, as exhibited in Fig. 4. The larger coupling index in Case (ii) leads to a greater error of decoupling approximation.

What has been observed above can be reinforced by further increasing the row sums of the absolute values of the off-diagonal damping elements.

Case (iii):

$$D = \begin{bmatrix} 1.61 & 0.53 & 0.39 & -0.5 & -0.26 & -0.05 \\ 0.53 & 1.7 & 0.08 & -0.35 & -0.4 & 0.3 \\ 0.39 & 0.08 & 1.8 & 0.47 & -0.38 & -0.57 \\ -0.5 & -0.35 & 0.47 & 1.75 & 0.52 & -0.15 \\ -0.26 & -0.4 & -0.38 & 0.52 & 1.65 & 0.56 \\ -0.05 & 0.3 & -0.57 & -0.15 & 0.56 & 1.8 \end{bmatrix}. \quad (21)$$

The modal matrix in this case is not even diagonally dominant. Yet, the error in the first mode due to decoupling approximation is generally less than four percent of the exact solution, as shown in Fig. 5. A simple calculation will reveal that the coupling index Γ_1 in Case (iii) is small compared to Case (ii), owing to cancellations among the constituent terms.

4 Frequency Separation

Using harmonic excitation in their analysis, several authors have suggested that adequate frequency separation between the natural modes is a sufficient condition for neglecting modal coupling. This issue is now examined. It will be demonstrated that frequency separation between the excitation and natural modes, and not the separation between the modes themselves, primarily determines the extent of modal coupling. Analysis in this section will be conducted in the frequency domain.

Recall that modal coupling can be measured by the coupling indices $\Gamma_i(J\omega_f)$, where J denotes $\sqrt{-1}$ and ω_f is the driving frequency. The dependence of $\Gamma_i(J\omega_f)$ on ω_f and the natural frequencies ω_j $(j=1, \cdots, n)$ can be uncovered if the dependence of the coupling coefficients $\gamma_{ij}(J\omega_f)$ on these frequencies is first investigated. For this purpose, let $\alpha_i = \mathrm{Re}[\Delta_i(J\omega_f)]$, $\beta_i = \mathrm{Im}[\Delta_i(J\omega_f)]$, where Re and Im represent the real and imaginary parts of a complex quantity. For a harmonic excitation

Downloaded 03 May 2010 to 171.66.16.20. Redistribution subject to ASME license or copyright; see http://www.asme.org/terms/Terms_Use.cfm

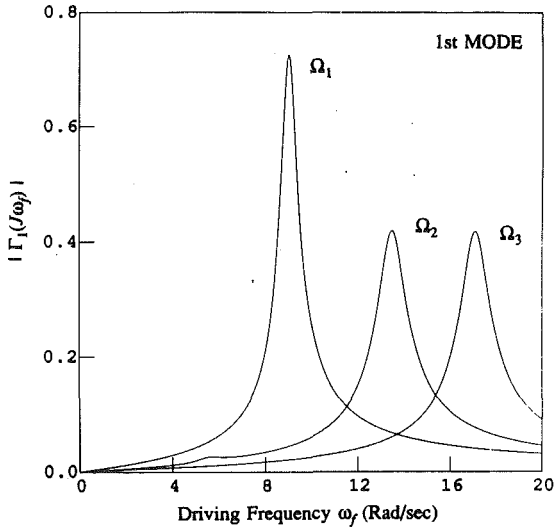


Fig. 6 Amplitudes of $\Gamma_1(J\omega_f)$ corresponding to different natural frequencies

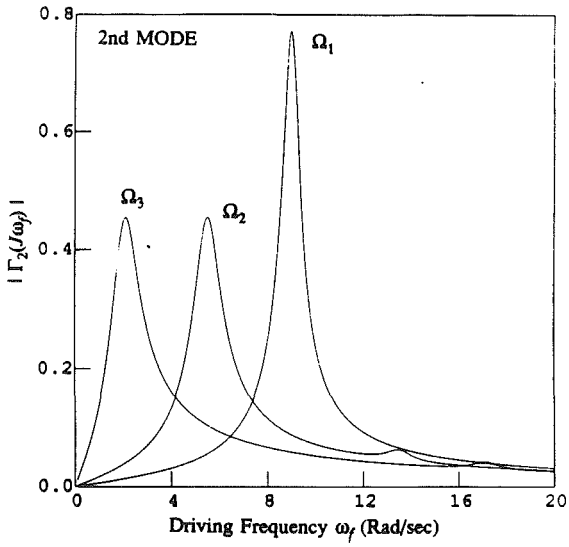


Fig. 7 Amplitudes of $\Gamma_2(J\omega_f)$ corresponding to different natural frequencies

of the type (5), the magnitude $|Q_i|$ and phase angle $\arg(Q_i)$ of the ith modal response $Q_i(J\omega_f)$ $(i=1, \cdots, n)$ can be calculated from expression (13). They are given by

$$|Q_i| = \frac{|f_i|}{[(\omega_i^2 - \omega_f^2 - \beta_i\omega_f)^2 + (d_{ii}+\alpha_i)^2\omega_f^2]^{1/2}}, \tag{22}$$

$$\arg(Q_i) = -\tan^{-1}\frac{(d_{ii}+\alpha_i)\omega_f}{\omega_i^2 - \omega_f^2 - \beta_i\omega_f} - \frac{1}{2}[1-\operatorname{sgn}(f_i)]\pi, \tag{23}$$

where the phase angle is measured with respect to $u(t)$. In the above, $\operatorname{sgn}(f_i)$ is 1 or -1 depending on whether f_i is positive or negative, and use has been made of the relation $e^{-J\pi} = -1$. Although $\arg(Q_i)$ has two possible values depending on the sign of f_i, both values correspond to the same straight line in the complex plane. From Eq. (15), the magnitude $|\gamma_{ij}|$ and phase angle $\arg(\gamma_{ij})$ of the coupling coefficient $\gamma_{ij}(J\omega_f)$ can be found, and

$$|\gamma_{ij}| = \frac{|d_{ij}f_j|\omega_f}{[(\omega_j^2 - \omega_f^2 - \beta_j\omega_f)^2 + (d_{jj}+\alpha_j)^2\omega_f^2]^{1/2}}, \tag{24}$$

$$\arg(\gamma_{ij}) = \arg(Q_j) - \operatorname{sgn}(d_{ij})\frac{\pi}{2}, \tag{25}$$

where $i \neq j$ $(i, j=1, \cdots, n)$. Because of the occurrence of $\omega_j^2 - \omega_f^2$, these equations already suggest that modal coupling can depend heavily on the separation between the natural and excitation frequencies.

For simplicity, further analysis will be carried out for two-degree-of-freedom systems. With only two modes present, a coupling coefficient and the associated coupling index are identical, so that

$$\gamma_{ij}(J\omega_f) = \Gamma_i(J\omega_f), \tag{26}$$

where $i \neq j$ $(i, j=1, 2)$. Hence, $|\Gamma_i|$ is also given by Eq. (24). In addition, it can be deduced from Eq. (8) that

$$\arg(\Delta_i) = \arg(Q_j) - \arg(Q_i) - \frac{1}{2}[1-\operatorname{sgn}(d_{ij})]\pi, \tag{27}$$

where $i \neq j$ $(i, j=1, 2)$. The following four mutually exclusive situations are considered.

(a) $\omega_f \ll \omega_1 \ll \omega_2$ or $\omega_1 \ll \omega_f \ll \omega_2$ or $\omega_1 \ll \omega_2 \ll \omega_f$. This corresponds to the case when the natural and excitation frequencies are all well-separated. From Eq. (24),

$$|\Gamma_1| = \frac{|d_{12}f_2|}{[[(\omega_2-\omega_f)(1+(\omega_2/\omega_f)) - \beta_2]^2 + (d_{22}+\alpha_2)^2]^{1/2}}, \tag{28}$$

$$|\Gamma_2| = \frac{|d_{21}f_1|}{[[(\omega_1-\omega_f)(1+(\omega_1/\omega_f)) - \beta_1]^2 + (d_{11}+\alpha_1)^2]^{1/2}}, \tag{29}$$

and thus $|\Gamma_1|$ and $|\Gamma_2|$ are small if $|\omega_i - \omega_f| \gg 1$ $(i=1, 2)$, provided $|\beta_i|$ will not grow. That each $|\beta_i|$ is small can be explained in the following way. In the frequency domain, the two modes are distinct and both are very far from resonance. Their phase angles are then close to 0 or $-\pi$, implying that $\arg(Q_i) \approx 0$ or $-\pi$ $(i=1, 2)$. By Eq. (27), $\arg(\Delta_i) \approx 0$ or $-\pi$ in principal value. That means the imaginary part of the nonproportionality factor Δ_i must be very small, or $\beta_1 \approx \beta_2 \approx 0$. It can now be concluded that each coupling index, and hence modal coupling, is small when there is adequate frequency separation between the excitation and natural modes.

(b) $\omega_f \approx \omega_1 \approx \omega_2$. This is the situation in which all frequencies are clustered. Since both modes are near resonance, their phase angles are close to $-\pi/2$ in principal value, or $\arg(Q_i) \approx \arg(Q_2) \approx -(\pi/2)$. By Eq. (27), $\arg(\Delta_i) \approx 0$ or $-\pi$ in principal value, implying that $\beta_1 \approx \beta_2 \approx 0$. Hence, the magnitudes of the coupling indices are

$$|\Gamma_1| = \left|\frac{d_{12}f_2}{|d_{22}+\alpha_2|}\right|, \tag{30}$$

$$|\Gamma_2| = \left|\frac{d_{21}f_1}{|d_{11}+\alpha_1|}\right|. \tag{31}$$

In the above, d_{11} and d_{22} must be positive because of the positive definiteness of the damping matrix. Also note that $\alpha_1 \approx \Delta_1$ and $\alpha_2 \approx \Delta_2$. If it is assumed that α_1 and α_2 are positive, then the coupling indices decrease in magnitude as the nonproportionality factors increase. Thus the nonproportionality factor Δ_i is not a true indicator of modal coupling. As will be shown by an example, $|\Gamma_1|$ and $|\Gamma_2|$, and hence modal coupling, can become rather large if the frequencies are clustered around each other.

(c) $\omega_f \gg \omega_2 \approx \omega_1$ or $\omega_f \ll \omega_1 \approx \omega_2$. In this case the natural frequencies are clustered, but are otherwise separated from the excitation frequency. In the frequency domain, the two modes are close to each other, but are still very far from resonance. The same argument as in Case (a) applies, and $|\Gamma_1|$ and $|\Gamma_2|$ are small as long as $|\omega_i - \omega_f| \gg 1$ $(i=1, 2)$. Thus modal coupling can be small even when $\omega_1 \approx \omega_2$, provided ω_f is well separated from ω_1 and ω_2. This will be illustrated by an example later in this section.

(d) $\omega_f \approx \omega_1 \ll \omega_2$ or $\omega_f \approx \omega_2 \gg \omega_1$. In this case the natural

Downloaded 03 May 2010 to 171.66.16.20. Redistribution subject to ASME license or copyright; see http://www.asme.org/terms/Terms_Use.cfm

frequencies are separated, but the excitation frequency is clustered around one natural frequency. Without loss of generality, let $\omega_1 \approx \omega_f$. Then the first mode is near resonance, and $\arg(Q_1) \approx -(\pi/2)$. However, the second mode is far from resonance, and $\arg(Q_2) \approx 0$ or $-\pi$. From Eq. (27), $\arg(\Delta_i) \approx (\pi/2)$ or $-(\pi/2)$ $(i=1, 2)$. That means the real part of the nonproportionality factor Δ_i must be small, or $\alpha_1 \approx \alpha_2 \approx 0$. Hence, the magnitudes of the coupling indices become

$$|\Gamma_1| = \frac{|d_{12} f_2|}{[[(\omega_2 - \omega_1)(1 + (\omega_2/\omega_1)) - \beta_2]^2 + d_{22}^2]^{1/2}}, \quad (32)$$

$$|\Gamma_2| \approx \frac{|d_{21} f_1|}{[d_{11}^2 + \beta_1^2]^{1/2}}. \quad (33)$$

Since $|\Gamma_2|$ is independent of $\omega_2 - \omega_1$, a large magnitude of Γ_2 can remain large even when $|\omega_2 - \omega_1| \gg 1$. Thus, a wide frequency separation between the natural modes does not preclude substantial effect of modal coupling. A similar argument applies if $\omega_f \approx \omega_2 \gg \omega_1$.

The preceding analysis shows that the most important parameter for modal coupling is the location of the excitation frequency with respect to the natural frequencies and not the frequency separation between the natural modes. The findings of this section explain the data reported by Ozguven (1987), but contradict the results derived by Hasselman (1976). The statement that modal coupling is negligible for widely separated modes even when the modal damping matrix is not diagonally dominant should be negated. Although frequency separation between the natural modes does impart some influence, situations (c) and (d) unambiguously demonstrate that it is the frequency separation between the excitation and natural modes, and not the separation between the modes themselves, that primarily determines the extent of modal coupling. Numerical corroboration of the preceding analysis is provided in the following example.

Example 2. Consider a two-degree-of-freedom system whose equation of motion is

$$\ddot{q} + D\dot{q} + \Omega q = a \cos \omega_f t, \quad q(0) = \dot{q}(0) = 0, \quad t \geq 0, \quad (34)$$

where $a = (1, 1)^T$ and

$$D = \begin{bmatrix} 1.1 & -0.5 \\ -0.5 & 1.2 \end{bmatrix}. \quad (35)$$

The modal stiffness matrix is specified in the following three separate cases with increasing levels of frequency separation between the natural modes.

Case (i):

$$\Omega = \text{diag}[8.9^2, 9.1^2] = \Omega_1. \quad (36)$$

Case (ii):

$$\Omega = \text{diag}[5.5^2, 13.5^2] = \Omega_2. \quad (37)$$

Case (iii):

$$\Omega = \text{diag}[2.1^2, 17.1^2] = \Omega_3. \quad (38)$$

The effect of modal coupling is measured by $\Gamma_i(J\omega_f)$ $(i=1, 2)$. In Figs. 6 and 7, $|\Gamma_1|$ and $|\Gamma_2|$ are plotted against the excitation frequency ω_f for the above three cases. Identical features would be observed if amplitudes of the errors associated with decoupling approximation are used instead of $|\Gamma_1|$ and $|\Gamma_2|$ in these figures. A marked dependence of the coupling indices on ω_f is observed in all cases. With only two modes, $|\Gamma_1|$ is a measure of coupling exerted by the second mode on the first modal response. A corresponding statement can be made for $|\Gamma_2|$. For each case in Fig. 6, $|\Gamma_1|$ possesses a peak value when $\omega_f \approx \omega_2$. This phenomenon arises because the resonant second mode imparts significant influence on the nonresonant first modal response through coupling. In contrast, at $\omega_f \approx \omega_2$, each $|\Gamma_2|$ is much smaller than the corresponding $|\Gamma_1|$, as a comparison of Figs. 6 and 7 unveils. The reason is that the first mode, possessing smaller amplitude of motion, imparts only modest influence on the resonant second mode. As expected, each $|\Gamma_2|$ in Fig. 7 exhibits a peak value when $\omega_f \approx \omega_1$, this time due to the resonant first mode. Both $|\Gamma_1|$ and $|\Gamma_2|$ rapidly decrease as $|\omega_1 - \omega_f|$ and $|\omega_2 - \omega_f|$ increase. Comparing the three cases, the greatest peaks are observed for Case (i) due to an additional effect of having $\omega_1 \approx \omega_2$. But clearly, this effect is secondary; even for Case (i), there is steep decline in modal coupling as the separation between ω_f and ω_1, ω_f and ω_2, increases.

If modal coupling is negligible for modes that are widely separated in frequency, then the coupling indices in Case (iii) should have negligible magnitudes. As shown in the figures, this is not true if ω_f is in the vicinity of one of the natural frequencies. Moreover, the peak values of $|\Gamma_1|$ and $|\Gamma_2|$ for Case (iii) are not any smaller than those for Case (ii). As long as ω_f is clustered around ω_1 or ω_2 further increase in $|\omega_2 - \omega_1|$ would not reduce the effect of modal coupling. It would simply shift the locations at which the coupling indices assume their maximum magnitudes.

5 Conclusions

The normal coordinates of a nonclassically damped system are coupled by nonzero off-diagonal elements of the modal damping matrix. In the presence of harmonic excitation, the characteristics of modal coupling have been investigated in this paper. An analytical formulation has been developed to facilitate the evaluation of modal coupling. The complex nature of the formulation and its implications on the quantification of modal coupling have been elucidated. The major results are summarized in the following.

(1) Modal coupling in a linear system can be measured by coupling indices defined by Eq. (16). The extent of nonclassical damping can be quantified through the use of these complex coupling indices and constituent coupling coefficients.

(2) Within the practical range of engineering applications, diagonal dominance of the modal damping matrix would not be sufficient for neglecting modal coupling. The effect of modal coupling on system response can even increase as the off-diagonal elements of the modal damping matrix decrease in magnitude.

(3) Adequate frequency separation between the natural modes alone is not sufficient for neglecting modal coupling. It is the frequency separation between the excitation and natural modes, and not the separation between the modes themselves, that primarily determines the effect of modal coupling.

Since the analysis of modal coupling has been pursued in the frequency domain, all results apply to steady-state solutions only. Two examples have been employed to illustrate the theoretical developments. Although a limited set of data is presented here, extensive calculations have been performed by the authors, and numerous other simulations have yielded qualitatively identical results.

Acknowledgment

This research has been supported in part by the National Science Foundation under Grant No. MSS-8657619 and by the Alexander von Humboldt Foundation. Opinions, findings, and conclusions expressed in this paper are those of the authors and do not necessarily reflect the views of the National Science Foundation.

References

Bellos, J., and Inman, D. J., 1989, "A Survey of Nonproportional Damping," *Shock and Vibration Digest*, Vol. 21, pp. 7-12.

Downloaded 03 May 2010 to 171.66.16.20. Redistribution subject to ASME license or copyright; see http://www.asme.org/terms/Terms_Use.cfm

Bellos, J., and Inman, D. J., 1990, "Frequency Response of Nonproportionally Damped, Lumped Parameter, Linear Dynamic Systems," ASME *Journal of Vibration and Acoustics*, Vol. 112, pp. 194–201.

Caughey, T. K., and O'Kelly, M. E. J., 1965, "Classical Normal Modes in Damped Linear Dynamic Systems," ASME JOURNAL OF APPLIED MECHANICS, Vol. 32, pp. 583–588.

Chung, K. R., and Lee, C. W., 1986, "Dynamic Reanalysis of Weakly Nonproportionally Damped Systems," *J. Sound and Vibration*, Vol. 111, pp. 37–50.

Cronin, D. L., 1976, "Approximation for Determining Harmonically Excited Response of Nonclassically Damped Systems," ASME *Journal of Engineering for Industry*, Vol. 98, pp. 43–47.

Foss, K. A., 1958, "Coordinates which Uncouple the Equations of Motion of Damped Linear Dynamic System," ASME JOURNAL OF APPLIED MECHANICS, Vol. 25, pp. 361–364.

Hasselman, T. K., 1976, "Modal Coupling in Lightly Damped Structures," *AIAA J.*, Vol. 14, pp. 1627–1628.

Hwang, J. H., and Ma, F., 1993, "On the Approximate Solution of Nonclassically Damped Linear Systems," ASME JOURNAL OF APPLIED MECHANICS, Vol. 60, pp. 695–701.

Nair, S. S., and Singh, R., 1986, "Examination of the Validity of Proportional Damping Approximations with Two Further Numerical Indices," *J. Sound and Vibration*, Vol. 104, pp. 348–350.

Ozguven, H. N., 1982, "Receptances of Non-Proportionally and Continuously Damped Plates—Reduced Dampers Method," *J. of Sound and Vibration*, Vol. 85, pp. 383–395.

Özguven, H. N., 1987, "On the Harmonic Response of Non-Proportionally Damped Structures," *Proc. 11th ASME Biennial Conference on Mechanical Vibration and Noise*, Vol. 5, pp. 117–124.

Prater, G., Jr., and Singh, R., 1986, "Quantification of the Extent of Non-proportional Viscous Damping in Discrete Vibratory Systems," *J. Sound and Vibration*, Vol. 104, pp. 109–125.

Shahruz, S. M., and Ma, F., 1988, "Approximate Decoupling of the Equations of Motion of Linear Underdamped Systems," ASME JOURNAL OF APPLIED MECHANICS, Vol. 55, pp. 716–720.

Warburton, G. B, and Soni, S. R., 1977, "Errors in Response Calculations for Non-Classically Damped Structures," *Earthq. Engng. Struct. Dyn.*, Vol. 5, pp. 365–376.

Xu, K., and Igusa, T., 1991, "Dynamic Characteristics of Non-Classically Damped Structures," *Earthq. Engng. Struct. Dyn.*, Vol. 20, pp. 1127–1144.

Downloaded 03 May 2010 to 171.66.16.20. Redistribution subject to ASME license or copyright; see http://www.asme.org/terms/Terms_Use.cfm

Distributed Transfer Function Analysis of Complex Distributed Parameter Systems

B. Yang
Assistant Professor,
Department of Mechanical Engineering,
University of Southern California,
Los Angeles, CA 90089-1453
Mem. ASME

This paper presents a new analytical and numerical method for modeling and synthesis of complex distributed parameter systems that are multiple continua combined with lumped parameter systems. In the analysis, the complex distributed parameter system is first divided into a number of subsystems; the distributed transfer functions of each subsystem are determined in exact and closed form by a state space technique. The complex distributed parameter system is then assembled by imposing displacement compatibility and force balance at the nodes where the subsystems are interconnected. With the distributed transfer functions and the transfer functions of the constraints and lumped parameter systems, exact, closed-form formulation is obtained for various dynamics and vibration problems. The method does not require a knowledge of system eigensolutions, and is valid for non-self-adjoint systems with inhomogeneous boundary conditions. In addition, the proposed method is convenient in computer coding and suitable for computerized symbolic manipulation.

1 Introduction

Complex distributed parameter systems that are composed of multiple distributed and lumped parameter subsystems have wide engineering applications. The dynamics and vibration of complex distributed parameter systems have been extensively studied by many authors in the last several decades, and are of increased research interest today. Methods developed in the past include the receptance method (Gladwell and Bishop, 1960), the transfer matrix method (Pestel and Leckie, 1963; Lin, 1969), eigenvalue modification (Jacquot and Soedel, 1970), the Lagrange multiplier method (Dowell, 1971 and 1972; Hallquist and Snyder, 1973), wave propagation analysis (Mead, 1971; Mead and Yaman, 1990), modal analysis (Chen, Y., 1963; Bergman and Nicholson, 1985), the impedance method (Jacquot, 1976), the Rayleigh quotient (Nour-Omid et al., 1983), the Green's function method (Nicholson and Bergman, 1986; Bergman and McFarland, 1988), matrix perturbation (Zhou and Sackman, 1989), and the distributed transfer function formulation (Butkoviskiy, 1983; Yang, 1991, 1992; Tan and Chung, 1991).

Instead of the rich literature on complex distributed parameter systems, there remain a few research problems warranting attention. First, the distributed system in the previous study is usually a single, nonbranched continuum; multibranched flexible bodies assembled through pointwise and distributed connections are rarely addressed, with notable exceptions in Pestel and Leckie (1963) and Butkoviskiy (1983). Second, the distributed system is often modeled as a self-adjoint system with orthogonal eigenfunctions; non-self-adjoint effects due to nonproportional damping, mass transport, coriolis acceleration, and circulatory forces have not been well studied. Third, while classical boundary value approaches yield exact eigensolutions for some simple flexible systems (Meirovitch, 1967), they are not practical for complex systems, partially because of formidable labor and a large number of unknowns involved in the analysis. Fourth, in estimating the response of complex distributed parameter systems, most work relies on discretization or truncated eigenfunction expansions. Although exact, closed-form evaluation of frequency response of certain complex systems is recently available (Yang, 1992), it is not valid for multibranched complex distributed parameter systems. In addition, many existing techniques require different derivation in different cases of system type, constraints, boundary conditions and external disturbances. As such, computer coding for general complex distributed parameter systems is difficult.

The objective of this work is to develop an exact, closed-form method for modeling and analysis of complex distributed parameter systems. The complex distributed parameter system in consideration is an assembly of multiple one-dimensional continua that are interconnected at certain points and/or in certain regions. Each continuum may be under constraints, combined with lumped parameter systems, and subject to external and boundary disturbances. The structure in Fig. 1 is an example. The structure consists of five beams that are interconnected at points 4, 6, 9, and 15 as well as in the region 7-8-14-13-7. There are a pointwise constraint at point 2, a

Contributed by the Applied Mechanics Division of THE AMERICAN SOCIETY OF MECHANICAL ENGINEERS for publication in the ASME JOURNAL OF APPLIED MECHANICS.

Discussion on this paper should be addressed to the Technical Editor, Professor Lewis T. Wheeler, Department of Mechanical Engineering, University of Houston, Houston, TX 77204-4792, and will be accepted until four months after final publication of the paper itself in the ASME JOURNAL OF APPLIED MECHANICS.

Manuscript received by the ASME Applied Mechanics Division, June 11, 1992; final revision, Feb. 3, 1993. Associate Technical Editor: D. J. Inman.

Copyright © 1994 by ASME
Downloaded 03 May 2010 to 171.66.16.20. Redistribution subject to ASME license or copyright; see http://www.asme.org/terms/Terms_Use.cfm

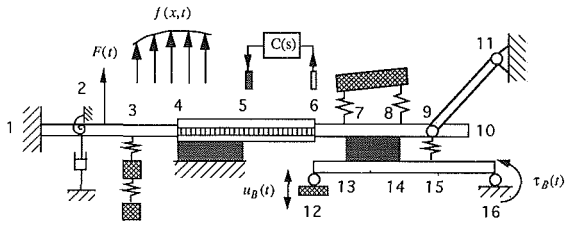


Fig. 1 An example of complex distributed parameter systems

distributed constraint (e.g., elastic foundation) in region 4-5, an oscillator connected at point 3, a rigid body elastically mounted at points 7 and 8, and an active controller with a sensor at point 6 and an actuator at point 5. The structure is subject to a distributed force $f(x, t)$ and a pointwise force $F(t)$ in its interior and displacement and torque excitations ($u_B(t)$ and $\tau_B(t)$) at its boundaries (points 12 and 16). Material and geometry discontinuities (E, I, A, ρ, etc.) occur at points 4 and 6. Also, the segment 4–6 may contain embedded actuators and sensors (for smart structure design).

This research proposes a distributed transfer function synthesis for complex distributed parameter systems. In the analysis, the complex distributed parameter system is first divided into a number of flexible subsystems; the distributed transfer functions of each subsystem are determined in exact and closed form by a state space technique given in Yang and Tan (1992). The complex distributed parameter system is then assembled from these subsystems using the distributed transfer functions and the transfer functions describing the constraints and combined lumped parameter systems. Displacement compatibility and force balance are imposed at the "nodes" where the subsystems are interconnected, leading to a global dynamic equilibrium equation. The synthesis does not make use of approximation or series truncation. Thus, solution of the dynamic equilibrium equation gives precise prediction of the system eigenvalues and eigenfunctions, and forced response. The proposed method deals with the complex distributed parameter system in a unified manner, and is convenient for computer coding.

2 Transfer Functions of Distributed Subsystem

The response $w(x, t)$ of the distributed subsystem is governed by the nth order, linear partial differential equation

$$\sum_{k=0}^{n}\left\{a_k\frac{\partial^k}{\partial x^k}\frac{\partial^2}{\partial t^2}+b_k\frac{\partial^k}{\partial x^k}\frac{\partial}{\partial t}+c_k\frac{\partial^k}{\partial x^k}\right\}w(x,t)=f(x,t),$$

$$x\in(0,1),\quad t>0 \qquad (1a)$$

with the inhomogeneous boundary conditions

$$M_j w(x,t)|_{x=0}+N_j w(x,t)|_{x=1}=\gamma_j(t),$$

$$t\geq 0,\quad j=1,2,\ldots,n. \qquad (1b)$$

Here $f(x, t)$ is the external disturbance, a_k, b_k, and c_k are constants, $|a_n|^2+|b_n|^2+|c_n|^2\neq 0$, M_j and N_j are linear temporal-spatial differential operators of proper order, and $\gamma_j(t)$ are known functions representing the external disturbances at the boundaries. The coefficients a_k, b_k, and c_k represent inertia, damping, distributed constraints (e.g., elastic foundation), coriolis acceleration, mass transport, axial loads, centrifugal forces, and circulatory effects. Equations (1), nonself-adjoint in general, describe many vibrating continua such as strings, bars, beams, beam-columns, rotating shafts, slewing flexible arms, and axially moving materials (Meirovitch, 1967; Mote, 1972).

Transfer functions of distributed subsystems have been derived by Yang and Tan (1992). In the remainder of this section, the results from Yang and Tan (1992) are briefly reviewed. Equations (1) are Laplace transformed with respect to t, and cast into a state space form

$$\frac{\partial}{\partial x}\eta(x,s)=F(s)\eta(x,s)+\upsilon(x,s),\quad x\in(0,1) \qquad (2a)$$

$$M(s)\eta(0,s)+N(s)\eta(1,s)=\gamma(s) \qquad (2b)$$

with

$$\eta(x,s)=\{\bar{w}(x,s)\ \bar{w}^{(1)}(x,s)\ \ldots\ \bar{w}^{(n-1)}(x,s)\}^T\in C^n$$

$$\upsilon(x,s)=\{\dot{0}\ \ldots\ 0\ \bar{f}(x,s)/(a_n s^2+b_n s+c_n)\}^T\in C^n$$

$$\gamma(s)=\{\bar{\gamma}_1(s)\ \bar{\gamma}_2(s)\ \ldots\ \bar{\gamma}_n(s)\}^T\in C^n.$$

The overbar denotes Laplace transformation, $(\ )^{(k)}=\partial^k(\ )/\partial x^k$; $F(s)\in C^{n\times n}$ is composed of the constants a_k, b_k, and c_k; and $M(s)$ and $N(s)\in C^{n\times n}$ contain the coefficients of the operators M_j and N_j, respectively. The solution to (2) is obtained as

$$\eta(x,s)=\int_0^1 G(x,\xi,s)\upsilon(\xi,s)d\xi+H(x,s)\gamma(s),\quad x\in(0,1) \qquad (3a)$$

where

$$G(x,\xi,s)=\begin{cases}e^{F(s)x}(M(s)+N(s)e^{F(s)})^{-1}M(s)e^{-F(s)\xi}, & \xi<x\\ -e^{F(s)x}(M(s)+N(s)e^{F(s)})^{-1}N(s)e^{F(s)(1-\xi)}, & \xi>x\end{cases} \qquad (3b)$$

$$H(x,s)=e^{F(s)x}(M(s)+N(s)e^{F(s)})^{-1} \qquad (3c)$$

and $e^{F(s)x}$ is the fundamental matrix of (2a). Following Butkovskiy (1983), we shall call $G(x, \xi, s)\in C^{n\times n}$ and $H(x, s)\in C^{n\times n}$ the transfer functions of the subsystem.

The fundamental matrix $e^{F(s)x}$, with low order in general (for example, for vibration and wave propagation in continua, usually $n\leq 4$), can be accurately calculated (Moler and Van Loan, 1978; Yang and Tan, 1992). Thus, $G(x, \xi, s)$ and $H(x, s)$ are precisely evaluated in closed form. With the state space formulation the subsystem (1) is treated systematically through easy formation of the matrices $F(s)$, $M(s)$ and $N(s)$, which is convenient for computer coding.

3 Transfer Function Synthesis

In the transfer function synthesis, the complex distributed parameter system is first divided into a number of subsystems; the response of each subsystem is specified in terms its nodal displacements using the distributed transfer functions $G(x, \xi, s)$ and $H(x, s)$. The complex distributed parameter system is then assembled from these subsystems by imposing the displacement compatibility and force balance (the finite element concept) at the nodes where the subsystems are interconnected. In the following discussion the terms such as "displacement", "strain", "internal force" and "external force" will be borrowed from structural mechanics although the proposed method is not limited to structures.

3.1 Representation of System Response by Nodal Displacements. Define

$$\alpha(x,s)=\{\bar{w}(x,s)\ \bar{w}^{(1)}(x,s)\ \ldots\ \bar{w}^{(n/2-1)}(x,s)\}^T\in C^{n/2} \qquad (4a)$$

$$\epsilon(x,s)=\{\bar{w}^{(n/2)}(x,s)\ \bar{w}^{(n/2+1)}(x,s)\ \ldots\ \bar{w}^{(n-1)}(x,s)\}^T\in C^{n/2} \qquad (4b)$$

as the displacement and strain vectors of the subsystem (1), respectively. Note that

$$\eta(x,s)=\{\alpha^T(x,s)\ \epsilon^T(x,s)\}^T. \qquad (5)$$

Assume that the internal force vector $\sigma(x, s)$ is described by

$$\sigma(x,s)=E(s)\epsilon(x,s) \qquad (6)$$

Downloaded 03 May 2010 to 171.66.16.20. Redistribution subject to ASME license or copyright; see http://www.asme.org/terms/Terms_Use.cfm

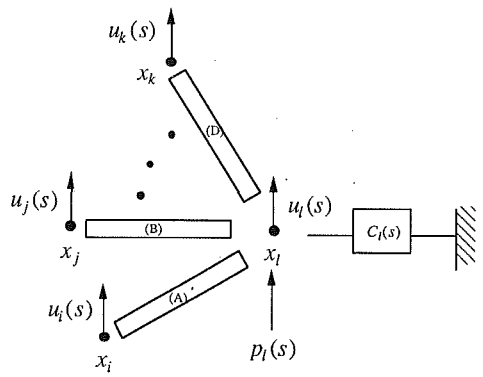


Fig. 2 Assembly of distributed subsystems (A), (B), . . . , (D) at node x_l

where $E(s) \in C^{n/2\times n/2}$ is a given constitutive matrix. Set $\gamma(s)$, $M(s)$, and $N(s)$ in (2*b*) as

$$\gamma(s)=\begin{Bmatrix}\alpha_0(s)\\ \alpha_1(s)\end{Bmatrix},\quad M(s)=\begin{bmatrix}I_{n/2} & 0\\ 0 & 0\end{bmatrix},\quad N(s)=\begin{bmatrix}0 & 0\\ I_{n/2} & 0\end{bmatrix} \tag{7}$$

where $\alpha_0(s) = \alpha(0, s)$ and $\alpha_1(s) = \alpha(1, s)$ are called nodal displacement vectors, and $I_{n/2}$ is the identity matrix of order $n/2$. A similar setting was used in Tan and Chung (1991) for a free vibration analysis of nonbranched, constrained distributed systems. By (3), (4), (6), and (7)

$$\alpha(x, s)=\int_0^1 G_\alpha(x, \xi, s)\bar{f}(\xi, s)d\xi + H_{\alpha 0}(x, s)\alpha_0(s) + H_{\alpha 1}(x, s)\alpha_1(s) \tag{8a}$$

$$\sigma(x, s)=E(s)\left\{\int_0^1 G_\epsilon(x, \xi, s)\bar{f}(\xi, s)d\xi + H_{\epsilon 0}(x, s)\alpha_0(s)+H_{\epsilon 1}(x, s)\alpha_1(s)\right\} \tag{8b}$$

where $\bar{f}(\xi, s)$ is the external force, $G_\alpha(x, \xi, s)$ and $G_\epsilon(x, \xi, s) \in C^{n/2}$, and $H_{\alpha 0}(x, s)$, $H_{\alpha 1}(x, s)$, $H_{\epsilon 0}(x, s)$ and $H_{\epsilon 1}(x, s) \in C^{n/2\times n/2}$ are the submatrices obtained from proper partition of $G(x, \xi, s)$ and $H(x, s)$, respectively. So, the response ($\alpha(x, s)$ and $\sigma(x, s)$) of the subsystem is completely determined once the nodal displacements ($\alpha_0(s)$ and $\alpha_1(s)$) of the subsystem are known.

3.2 Assembly of Subsystems. Assume that the complex distributed parameter system has N nodes, x_k, $k = 1, 2, \ldots, N$, where the subsystems are interconnected. Denote the displacement vector of the complex distributed parameter system at the node x_k by $u_k(s)$, which is described in a global coordinate system. Suppose that at the lth node x_l, subsystems (A), (B), . . . , (D) are interconnected; see Fig. 2. Also at the node are some pointwise constraints, combined lumped parameter systems (including active controllers), and external forces. The resultant constraint forces due to the constraints and lumped systems have the form $-C_l(s)u_l(s)$, where $C_l(s)$ is a matrix transfer function. The $C_l(s)$ for various constraints and lumped systems has been fully studied in Yang (1992). Force balance at the node x_l requires

$$Q_A(s)+Q_B(s)+\ldots+Q_D(s)-C_l(s)u_l(s)+p_l(s)=0 \tag{9}$$

where $Q_A(s)$, $Q_B(s)$, . . . , and $Q_D(s)$ are the vectors of the forces applied at x_l by the subsystems (A), (B), . . . , (D), respectively, and $p_l(s)$ is the vector of nodal external forces.

Denote the displacement and internal force vectors of subsystem (A) by $\alpha_A(x, s)$ and $\sigma_A(x, s)$, respectively. Denote the distributed transfer functions of the subsystem by $G^{(A)}(x, \xi, s)$ and $H^{(A)}(x, s)$. Subsystem (A) exerts a force $-\sigma_A(x_l, s)$ on the node x_l. Recall that $\sigma_A(x_l, s)$ is defined in a local coordinate system associated with the subsystem. In the global coordinate system, the force $Q_A(s)$ is

$$Q_A(s)=-R_A\sigma_A(x_l, s) \tag{10}$$

where R_A is a coordinate transformation matrix. On the other hand, $\sigma_A(x_l, s)$ in (8*b*) is expressed by the nodal displacement vectors $\alpha_A(x_l, s)$ and $\alpha_A(x_i, s)$, which are also defined in the local coordinates. The $\alpha_A(x_l, s)$ and $\alpha_A(x_i, s)$ are related to the global nodal displacements $u_l(s)$ and $u_i(s)$ by appropriate coordinate transformation matrices S_A and T_A, i.e.,

$$\alpha_A(x_l, s)=S_Au_l(s)\quad \alpha_A(x_i, s)=T_Au_i(s). \tag{11}$$

Substituting (8*b*) and (11) into (10) gives

$$Q_A(s)=-K_{ll}^{(A)}(s)u_l(s)-K_{li}^{(A)}u_i(s)-f_l^{(A)}(s) \tag{12a}$$

where the stiffness matrices $K_{ll}^{(A)}(s)$ and $K_{li}^{(A)}$ are given in terms of R_A, S_A, T_A, $H^{(A)}(x_l, s)$, and $f_l^{(A)}(s) = R_AE_A(s) \times \int_0^1 G_\epsilon^{(A)}(x_l, \xi, s)\bar{f}^{(A)}(\xi, s)d\xi$. Physically $f_l^{(A)}(s)$ represents the transmitted forces at the node x_l due to the external force $\bar{f}^{(A)}(\xi, s)$ applied to subsystem (A). Likewise, the nodal forces by subsystems (B), . . . , (D) are

$$Q_B(s)=-K_{ll}^{(B)}(s)u_l(s)-K_{lj}^{(B)}u_j(s)-f_l^{(B)}(s) \tag{12b}$$

$$\vdots \qquad\qquad \vdots$$

$$Q_D(s)=-K_{ll}^{(D)}(s)u_l(s)-K_{lk}^{(D)}u_k(s)-f_l^{(D)}(s). \tag{12c}$$

Here Eqs. (12) automatically guarantee displacement compatibility at the node x_k.

Substituting (12) into (9) yields

$$K_{ll}(s)u_l(s)+K_{li}u_i(s)+K_{lj}u_j(s)+\ldots+K_{lk}u_k(s)=q_l(s) \tag{13}$$

where

$$K_{ll}(s)=C_l(s)+K_{ll}^{(A)}(s)+K_{ll}^{(B)}(s)+\ldots+K_{ll}^{(D)}(s)$$

$$K_{li}(s)=K_{li}^{(A)}(s),\quad K_{lj}(s)=K_{lj}^{(B)}(s),\ \ldots,\ K_{lk}(s)=K_{lk}^{(D)}(s)$$

$$q_l(s)=p_l(s)-f_l^{(A)}(s)-f_l^{(B)}(s)-\ldots-f_l^{(D)}(s).$$

Force balance at all the nodal points yields a matrix dynamic equilibrium equation

$$K(s)u(s)=q(s) \tag{14}$$

where $u(s) = \{u_1^T(s) \ldots u_N^T(s)\}^T$, $q(s) = \{q_1^T(s) \ldots q_N^T(s)\}^T$, $K(s) = [K_{jk}(s)]$. The $K(s)$, $u(s)$, and $q(s)$ are the global dynamic stiffness matrix, nodal displacement, and force vectors of the complex distributed parameter system, respectively.

3.3 Boundary Conditions. In the finite element analysis, the global equilibrium equation cannot be solved before the prescribed boundary conditions are substituted. Unlike the finite element method, the proposed transfer function method substitutes the boundary conditions at the subsystem level so that the dynamic equilibrium Eq. (14) can be directly solved upon its formation.

Suppose that subsystem (A) in Fig. 2 has the prescribed boundary conditions at point x_i

$$B(s)\eta(x_i, s)=\kappa(s) \tag{15}$$

where $B(s) \in C^{n/2\times n}$ and $\kappa(s) \in C^{n/2}$ are given. Equation (15) represents general boundary conditions (essential or natural, homogeneous or inhomogeneous). For instance, the boundary conditions of an Euler-Bernoulli beam in Fig. 3 can be described by (15):

(a) free end:

$$B(s)=\begin{bmatrix}0 & 0 & EI & 0\\ 0 & 0 & 0 & -EI\end{bmatrix}\quad \kappa(s)=\begin{pmatrix}M_0\\ V_0\end{pmatrix};$$

(b) simply supported

Downloaded 03 May 2010 to 171.66.16.20. Redistribution subject to ASME license or copyright; see http://www.asme.org/terms/Terms_Use.cfm

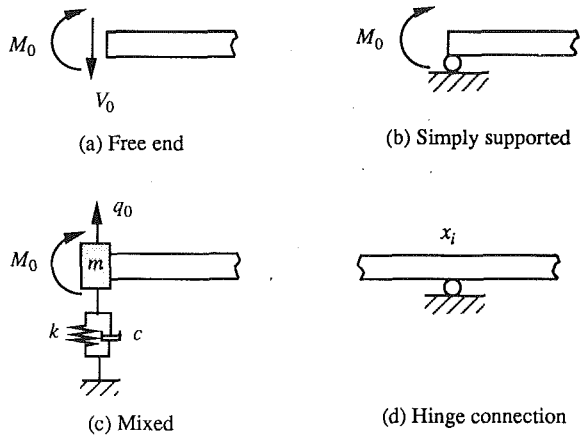


Fig. 3 Boundary conditions of an Euler-Bernoulli beam

$$B(s)=\begin{bmatrix}0 & 0 & EI & 0\\ 1 & 0 & 0 & 0\end{bmatrix}\quad \kappa(s)=\begin{pmatrix}M_0\\ 0\end{pmatrix};$$

(c) mixed

$$B(s)=\begin{bmatrix}0 & 0 & EI & 0\\ ms^2+cs+k & 0 & 0 & -EI\end{bmatrix}\quad \kappa(s)=\begin{pmatrix}M_0\\ q_0\end{pmatrix}.$$

Here $\eta(x, s) = \{\overline{w}(x, s)\ \overline{w}^{(1)}(x, s)\ \overline{w}^{(2)}(x, s)\ \overline{w}^{(3)}(x, s)\}^T$, $\overline{w}(x, s)$ and EI are the transverse displacement and bending stiffness of the beam, respectively.

Now, set $\gamma(s)$, $M(s)$, and $N(s)$ in (2*b*) as

$$\gamma(s)=\begin{pmatrix}\kappa(s)\\ \alpha(x_l, s)\end{pmatrix}\in C^n,\quad M(s)=\begin{bmatrix}B(s)\\ 0\end{bmatrix}\in C^{n\times n},$$

$$N(s)=\begin{bmatrix}0 & 0\\ I_{n/2} & 0\end{bmatrix}\in C^{n\times n}. \tag{16}$$

By (8), the response of the subsystem is given by

$$\alpha(x, s)=\int_0^1 G_\alpha(x, \xi, s)\bar{f}(\xi, s)d\xi + H_{\alpha 0}(x, s)\kappa(s)+H_{\alpha 1}(x, s)\alpha(x_l, s) \tag{17a}$$

$$\sigma(x, s)=E(s)\left\{\int_0^1 G_\epsilon(x, \xi, s)\bar{f}(\xi, s)d\xi + H_{\epsilon 0}(x, s)\kappa(s)+H_{\epsilon 1}(x, s)\alpha(x_l, s)\right\}. \tag{17b}$$

Equations (17) show that evaluation of the response of the subsystem does not need to know the displacements at the boundary x_i. In other words, the global dynamic equilibrium Eq. (14) will not involve any unknown variables at the boundaries of the complex distributed parameter system. In this way, the number of unknowns in the dynamic equilibrium (14) is reduced.

Equation (15) can also be applied to those nodes with both boundary and interface conditions. For instance, consider the hinge connection of the beam in Fig. 3(*d*) where the boundary condition is $\overline{w}(x_i, s) = 0$ and the interface condition is $\overline{w}^{(1)}(x_i^-, s) = \overline{w}^{(1)}(x_i^+, s)$. In this case $B(s)$ and $\kappa(s)$ in (15) are specified as

$$B(s)=\begin{bmatrix}1 & 0 & 0 & 0\\ 0 & 1 & 0 & 0\end{bmatrix}\quad \kappa(s)=\begin{pmatrix}0\\ \overline{w}^{(1)}(x_i, s)\end{pmatrix}.$$

The unknown nodal displacement $\overline{w}^{(1)}(x_i, s)$ will appear in the dynamic equilibrium Eq. (14) due to bending moment balance at point x_i. A similar treatment is also applied to a coupled beam structure in Fig. 9 (see Sec. 6) where points 3 and 4 have both boundary and interface conditions.

4 Numerical Scheme and Applications

The numerical scheme for the transfer function synthesis consists of the following steps:

(i) Divide the complex distributed parameter system into a number of subsystems.

(ii) Calculate the stiffness matrices of each subsystems, e.g., $K_{ll}^{(A)}(s)$ and $K_{li}^{(A)}$ in (12*a*); the boundary conditions of the complex distributed parameter system are substituted through use of (16).

(iii) Assemble the dynamic equilibrium Eq. (14) based on (13).

(iv) Solve the dynamic equilibrium Eq. (14) for the nodal displacement vector $u(s)$.

(v) Substitute $u(s)$ into (8) and (11) to determine the response of every subsystem.

In the above transfer function synthesis, no approximation or series truncation has been made. Therefore, the solution is exact and of closed form. Some applications of the proposed method are listed as follows although detailed study of these topics will not be pursued in this paper:

(*a*) *Eigenvalue Problem.* Let all external disturbances be zero. Equation (14) becomes $K(s)u(s) = 0$. The characteristic equation of the complex distributed parameter system then is $\det K(s) = 0$, from which the system eigenvalues λ_k, $k = 1, 2, \ldots$, are determined. The corresponding system eigenfunctions are obtained in two steps: first, determine the nontrivial solution $u(\lambda_k)$ of $K(\lambda_k)u(\lambda_k) = 0$; second, substitute $u(\lambda_k)$ into (8*a*) ($\bar{f}(\xi, s) \equiv 0$) to give the "mode shape" distribution in each subsystem.

(*b*) *Frequency Response.* For the complex distributed parameter system under harmonic external excitations of frequency ω, the nodal displacements are determined as $u(J\omega) = K^{-1}(J\omega)q(J\omega)$, $J \equiv \sqrt{-1}$. Substituting $u(J\omega)$ into (8) and (11) gives the frequency response or steady state response of the complex distributed parameter system. If the external disturbances are periodic, expand them into series of harmonic time components (Fourier series). The forced response is the sum of the contributions of all harmonic components.

(*c*) *Transient Response.* With the eigensolutions, the transient response of the complex distributed parameter system to initial and external disturbances can be evaluated by modal superposition. Like in many time domain methods, truncation of infinite series has to be made. There is one thing different though: the eigensolutions used in the computation are exact, which may bring some more accuracy and efficiency.

(*d*) *Stability Analysis.* The frequency response function obtained from (b) can be used to predict the stability of the complex distributed parameter system subject to inertial, impact, damping, gyroscopic, and aerodynamic forces. Several well-developed frequency domain methods, including Nyquist plots and Bode diagrams, are ready to incorporate into the transfer formulation proposed here.

(*e*) *Active Control.* Transfer function modeling has important applications in active control of distributed parameter systems (Butkoviskiy, 1983; Yang and Mote, 1991a,b). Although exact transfer functions of some simple distributed systems have been obtained, exact transfer functions of general complex multibody distributed systems are not available in the literature. This research provides an exact, closed-form transfer function formulation for active control of a wide class of complex distributed parameter systems. In the proposed method, feedback controllers are treated as constraints imposed to the distributed system; the control scheme and the dynamics of sensors and actuators are conveniently described by the constraint transfer functions. The response and the stability of the closed-loop system can be accurately predicted. The frequency domain techniques developed for lumped systems can be extended for optimal control of complex distributed parameter systems. The transfer function synthesis

Downloaded 03 May 2010 to 171.66.16.20. Redistribution subject to ASME license or copyright; see http://www.asme.org/terms/Terms_Use.cfm

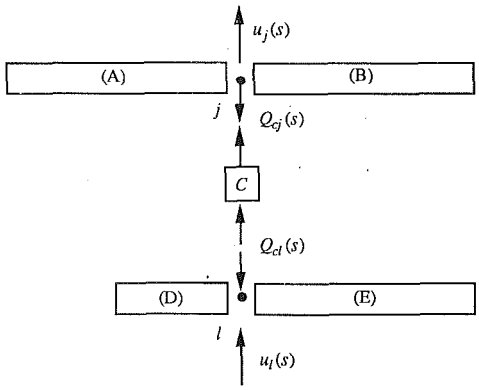


Fig. 4 Pointwise connection of distributed subsystems

developed is also applicable to combined passive/active control, and design of smart structures with embedded sensors and actuators.

5 Some Special Considerations

Section 3 outlines the general rules of the transfer function synthesis. This section discusses several important issues of the proposed method that are not mentioned in the previous sections.

5.1 Pointwise Connection of Subsystems. Figure 4 shows subsystems (A), (B), (D), and (E) connected through some mechanism C at points j and l. (One example is the spring connection at points 9 and 15 of the beam structure in Fig. 1.) Let $Q_{cj}(s)$ and $Q_{cl}(s)$ be the forces applied to nodes j and l, respectively, in order to maintain the connection. These forces are related to the nodal displacements by

$$\begin{pmatrix} Q_{cj}(s) \\ Q_{cl}(s) \end{pmatrix} = -\begin{bmatrix} C_{jj}(s) & C_{jl}(s) \\ C_{lj}(s) & C_{ll}(s) \end{bmatrix} \begin{pmatrix} u_j(s) \\ u_l(s) \end{pmatrix} \tag{18}$$

where $C_{jj}(s)$ et al. are the matrix transfer functions describing the connection. Force balance at node l requires inclusion of $Q_{cl}(s)$, i.e., the terms $C_{lj}(s)u_j(s) + C_{ll}(s)u_l(s)$, in (13). Similarly, force balance at node j leads to the addition of $C_{jj}(s)u_j(s) + C_{jl}(s)u_l(s)$ to the equilibrium equation. Thus pointwise connection of subsystems is described through modification of the stiffness matrix $K(s)$ with the matrix transfer functions $C_{jj}(s)$, $C_{jl}(s)$, $C_{lj}(s)$ and $C_{ll}(s)$.

5.2 Distributed Connection of Subsystems. Consider subsystems (I) and (II) connected throughout their domains; see Fig. 5(*a*). Such connection is also seen in Fig. 1 where the beam segments 7–8 and 13–14 are connected, say, by a uniform viscoelastic layer. This type of connection couples responses of the subsystems at every interior point. Assembly of the coupled subsystems using the model given in Sec. 2 will lead to coupled integral equations, which cannot be solved in exact and closed form. To overcome this difficulty, a new model for the coupled subsystems is derived.

Let state space equations of subsystems (I) and (II) be

$$\frac{\partial}{\partial x}\eta_i(x, s) = F_i(s)\eta_i(x, s) + v_i(x, s) + Q_{ci}(x, s), \quad x \in (0, 1) \tag{19a}$$

$$M_i(s)\eta_i(0, s) + N_i(s)\eta_i(1, s) = \gamma_i(s), \quad i = 1, 2 \tag{19b}$$

where $Q_{c1}(x, s)$ and $Q_{c2}(x, s)$ are distributed forces applied at (I) and (II), respectively, required to maintain the connection (Fig. 5(*b*)). Assume that the connection is uniformly distributed; i.e.,

$$\begin{pmatrix} Q_{c1}(x, s) \\ Q_{c1}(x, s) \end{pmatrix} = \begin{bmatrix} C_{11}(s) & C_{12}(s) \\ C_{21}(s) & C_{22}(s) \end{bmatrix} \begin{pmatrix} \eta_1(x, s) \\ \eta_2(x, s) \end{pmatrix} \tag{20}$$

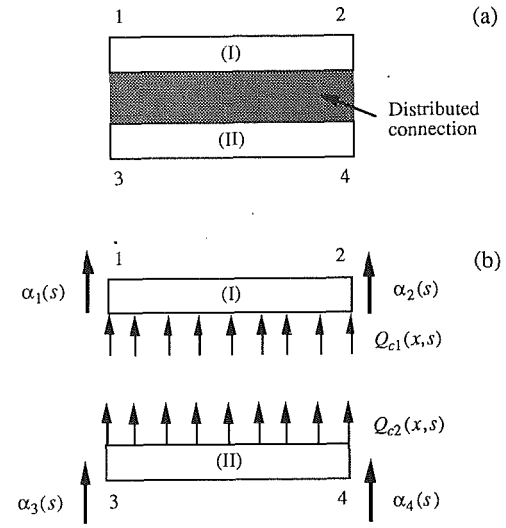


Fig. 5 Distributed connection of two distributed subsystems

where $C_{ij}(s)$ are the matrix transfer functions describing the connection. Substitution of (20) into (19) yields (2) with

$$F(s) = \begin{bmatrix} F_1(s) + C_{11}(s) & C_{12}(s) \\ C_{21}(s) & F_2(s) + C_{22}(s) \end{bmatrix},$$

$$\eta(x, s) = \begin{pmatrix} \eta_1(x, s) \\ \eta_2(x, s) \end{pmatrix}$$

$$v(x, s) = \begin{pmatrix} v_1(x, s) \\ v_2(x, s) \end{pmatrix}, \quad \gamma(s) = \begin{pmatrix} \gamma_1(s) \\ \gamma_2(s) \end{pmatrix}$$

$$M(s) = \begin{bmatrix} M_1(s) & 0 \\ 0 & M_2(s) \end{bmatrix}, \quad N(s) = \begin{bmatrix} N_1(s) & 0 \\ 0 & N_2(s) \end{bmatrix}. \tag{21}$$

Because the state space equation of the coupled subsystems has the same form as that of an uncoupled subsystem (Eqs. (2)), the response of the coupled subsystems can be determined using (3). Set

$$\gamma(s) \equiv \{\gamma_1^T(s) \quad \gamma_2^T(s)\}^T = \{\alpha_1^T(s) \quad \alpha_2^T(s) \quad \alpha_3^T(s) \quad \alpha_4^T(s)\}^T \tag{22}$$

where $\alpha_1(s)$ and $\alpha_2(s)$ are the nodal displacements of system (I) at points 1 and 2, $\alpha_3(s)$ and $\alpha_4(s)$ are the nodal displacements of system (II) at points 3 and 4; see Fig. 5(*b*). By (8), the displacements and internal forces of the coupled subsystems are expressed in terms of $\alpha_i(s)$, $i = 1, \ldots, 4$. The corresponding matrices G_α, G_ϵ, H_α, and H_ϵ from (8) can now be used to describe the distributed connection in the transfer function synthesis. Note that the internal forces of each coupled subsystem are related to the boundary displacements at nodes 1, 2, 3, and 4. The $K(s)$ in (14) has submatrices coupling the displacements at all these nodes.

5.3 Subsystems With Multiple Distributed Parameters. Equations (1) describe the dynamic behavior of a subsystem with one distributed parameter, namely $w(x, t)$. In many cases description of a subsystem requires multiple distributed parameters. The vibration of a Timoshenko beam is represented by its transverse deflection and angle of rotation at every point. The vibration of a spinning flexible shaft is described by transverse deflections along two perpendicular directions. Also, the dynamic equations of coupled thermomechanical and electromagneto-mechanical systems often involve more than one distributed parameter.

For a linear, uniformly distributed subsystem described by

Downloaded 03 May 2010 to 171.66.16.20. Redistribution subject to ASME license or copyright; see http://www.asme.org/terms/Terms_Use.cfm

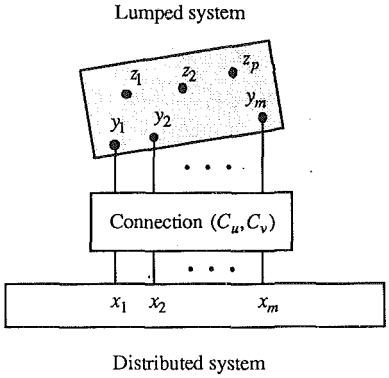


Fig. 6 Connection of a distributed subsystem and a lumped parameter system at multiple points

m parameters $w_1(x, t), \ldots, w_m(x, t)$, its dynamic equations can also be written in the form (1) where $w = \{w_1 \ldots w_m\}^T \in R^m, f = \{f_1 \ldots f_m\}^T \in R^m$ is the external disturbance vector, and a_k, b_k, and c_k are constant matrices. Let the highest order of the spatial differentiation of the parameter $w_k(x, t)$ in (1) be p_k. In the Laplace transform domain define the state space vector as

$$\eta = \{\overline{w}_1\ \overline{w}_1^{(1)} \ldots \overline{w}_1^{(p_1-1)} \ldots \overline{w}_m\ \overline{w}_m^{(1)} \ldots \overline{w}_m^{(p_m-1)}\}^T \in C^n \quad (23)$$

where $n = p_1 + \ldots + p_m$. With (23), the system Eqs. (1) can be cast into the state space form (2). Hence the matrix transfer functions of the subsystem can be evaluated in the closed form (3), and the transfer function synthesis in Sec. 3 can also be applied.

5.4 Transmitted Nodal Forces and Response to Distributed Forces. According to (3), determination of the transmitted nodal forces $f_l^{(A)}(s), f_l^{(B)}(s), \ldots, f_l^{(D)}(s)$ in (12) requires evaluation of the integral

$$I \equiv \int_0^1 e^{-F(s)\xi}\bar{f}(\xi, s)d\xi = V(s) \int_0^1 e^{-J(s)\xi}\bar{f}(\xi, s)d\xi\, V^{-1}(s) \quad (24)$$

where $\bar{f}(\xi, s)$ is the external force applied to the distributed subsystem, $V(s)$ is a nonsingular matrix related to the eigenvectors of $F(s)$, and $J(s)$ is the Jordan form of $F(s)$ consisting of the eigenvalues of $F(s)$. For given s, the eigenvalues $\lambda_l(s)$ of $F(s)$, $l = 1, 2, \ldots, n$, are the roots of

$$\sum_{k=0}^{n} (a_k s^2 + b_k s + c_k)\lambda^k(s) = 0.$$

Because of the special structure of $J(s)$, the integral I is represented in terms of $\int_0^1 \xi^m e^{-\lambda_l(s)\xi}\bar{f}(\xi, s)d\xi$, $0 \le m \le n-1$, $l = 1, \ldots, n$, which can be obtained in exact and explicit form. Thus, for given external force $\bar{f}(\xi, s)$, the transmitted nodal forces can be precisely calculated. The response of the complex distributed parameter system subject to a distributed force $\bar{f}(\xi, s)$, i.e., the integrals in Eqs. (8), can also be treated in a similar manner.

5.5 Connection of Lumped and Distributed Systems at Multiple Points. The term $-C_l(s)u_l(s)$ in (9) is valid only for connection of a lumped system and a distributed system at a *single* point. Quite often, lumped systems are connected to the distributed system at *multiple* points. The rigid body connected to points 7 and 8 in Fig. 1 is one example; a flexible structure controlled via multiple sensors and actuators is another. In this section, such connection is studied for the transfer function synthesis.

Figure 6 shows a schematic of the connection of a lumped system and a distributed system where the connecting points of the lumped system are $y_1, \ldots, y_m$ and those of the distributed system are $x_1, \ldots, x_m$. The lumped system also has p points $(z_1, \ldots, z_p)$ that are not connected to the distributed system.

Let the vector of the displacements of the distributed system at point x_k be $u_k(s)$, and the vector of the displacements of the lumped system at point y_k be $v_k(s)$, $k = 1, \ldots, m$. Denote the vector of the constraint forces at point x_k by $Q_k(s)$. Assume that the constraint forces at points $x_1, \ldots, x_m$ are related to the displacements at the connecting points by

$$Q(s) = C_v(s)v(s) - C_u(s)u(s) \quad (25)$$

where $Q(s) = \{Q_1^T(s) \ldots Q_m^T(s)\}^T$, $v(s) = \{v_1^T(s) \ldots v_m^T(s)\}^T$, $u(s) = \{u_1^T(s) \ldots u_m^T(s)\}^T$, and $C_v(s)$ and $C_u(s)$ are known matrices describing the connection. In the Laplace transform domain, the dynamic equations of the lumped system are in the matrix form

$$\begin{bmatrix} A_{11}(s) & A_{12}(s) \\ A_{21}(s) & A_{22}(s) \end{bmatrix} \begin{pmatrix} v(s) \\ \beta(s) \end{pmatrix} = \begin{pmatrix} -Q(s) + f_v(s) \\ f_\beta(s) \end{pmatrix} \quad (26)$$

where $\beta(s)$ is the vector of the displacements of the lumped system at points $z_1, \ldots, z_p$, $A_{jk}(s)$ are given matrices, and $f_v(s)$ and $f_\beta(s)$ are the vectors of the external forces applied to the lumped system at points $y_1, \ldots, y_m$ and $z_1, \ldots, z_p$, respectively. Note that $-Q(s)$ represents the constraint forces at the points $y_1, \ldots, y_m$. Eliminating $v(s)$ and $\beta(s)$ from (25) and (26) gives

$$Q(s) = -C(s)u(s) + f_T(s) \quad (27)$$

where

$$C(s) = C_u(s) - C_v(s)[A_{11}(s) - A_{12}(s)A_{22}^{-1}(s)A_{21}(s) + C_v(s)]^{-1}C_u(s)$$

$$f_T(s) = C_v(s)[A_{11}(s) - A_{12}(s)A_{22}^{-1}(s)A_{21}(s) + C_v(s)]^{-1} \times \{f_v(s) - A_{12}(s)A_{22}^{-1}(s)f_\beta(s)\}.$$

The $f_T(s)$ is the vector of the transmitted forces at $x_1, \ldots, x_m$ due to the external forces $f_v(s)$ and $f_\beta(s)$ applied to the lumped system. Write

$$C(s) = [C_{jk}(s)] \quad f_T(s) = \{f_{T1}(s) \ldots f_{Tm}(s)\}. \quad (28)$$

The constraint force vector $Q_k(s)$ (at point x_k) is then

$$Q_k(s) = -\sum_{j=1}^{m} C_{kj}(s)u_j(s) + f_{Tk}(s), \quad 1 \le k \le m. \quad (29)$$

It is seen that the constraint forces at any connecting point are related to the displacements at all the connecting points. In the transfer function synthesis, the multipoint connection is treated by replacing $-C_l(s)u_l(s)$ in (9) with $-\Sigma_{j=1}^m C_{lj}(s)u_j(s) + f_{Tl}(s)$.

5.6 Further Elimination of Unknown Nodal Displacements. As discussed in Sec. 3.3, the proposed method reduces the order of the equilibrium equation (14) by eliminating any unknown variables at the boundaries of the complex distributed parameter system. In this section, we show that further elimination of unknown nodal displacements is possible. Suppose that between nodes x_L and x_R there are $m + 1$ distributed subsystems serially connected at nodes x_k, $k = 1, 2, \ldots, m$ (Fig. 7). If no external forces are applied to these subsystems, the nodal displacement vectors $u_k(s)$, $k = 1, \ldots, m$, can be eliminated from (14) through a procedure similar to that of the transfer matrix method (Pestel and Leckie, 1963).

For each of the $m + 1$ subsystems, setting $\gamma(s) = \eta(0, s) = (\alpha^T(0, s)\epsilon^T(0, s))^T$, $M(s) = I$, $N(s) = 0$, and $\bar{f}(\xi, s) = 0$ in (3) leads to $\eta(1, s) = e^{F(s)}\eta(0, s)$. Let $Q_{k-1}^+(s)$ and $Q_k^-(s)$ be the forces applied by subsystem (k) at nodes x_{k-1} and x_k, respectively; see Fig. 8. It is easy to show that

$$\begin{pmatrix} u_k(s) \\ Q_k^-(s) \end{pmatrix} = J_k(s) \begin{pmatrix} u_{k-1}(s) \\ Q_{k-1}^+(s) \end{pmatrix} \quad (30)$$

Downloaded 03 May 2010 to 171.66.16.20. Redistribution subject to ASME license or copyright; see http://www.asme.org/terms/Terms_Use.cfm

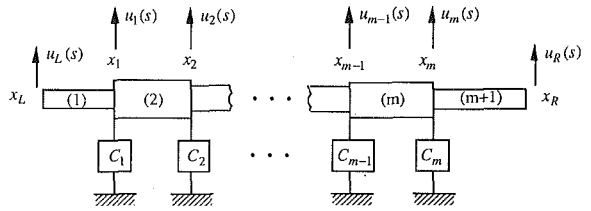


Fig. 7 Distributed subsystems serially connected

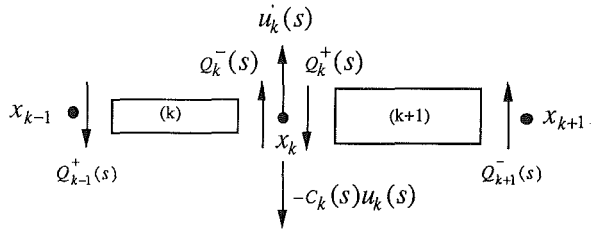


Fig. 8 Connection of two adjacent distributed subsystems

where $J_k(s) \in C^{n\times n}$ is given in terms of $e^{F(s)}$, $E(s)$ in (6), and the coordinate transformation matrices in (10) and (11). Force balance at node x_k yields $Q_k^+(s) = Q_k^-(s) - C_k(s)u_k(s)$, or

$$\begin{pmatrix} u_k(s) \\ Q_k^+(s) \end{pmatrix} = \begin{bmatrix} I & 0 \\ -C_k(s) & I \end{bmatrix} \begin{pmatrix} u_k(s) \\ Q_k^-(s) \end{pmatrix} = T_k(s) \begin{pmatrix} u_k(s) \\ Q_k^-(s) \end{pmatrix} \tag{31}$$

where the matrix $C_k(s)$ describes the constraint forces at x_k due to the constraints and lumped systems (Fig. 8). Successive use of (30) and (31) results in

$$\begin{pmatrix} u_R(s) \\ Q_R^-(s) \end{pmatrix} = T(s) \begin{pmatrix} u_L(s) \\ Q_L^+(s) \end{pmatrix} \tag{32}$$

where

$$T(s) = J_{m+1}(s)T_m(s)J_m(s) \ \ldots \ T_2(s)J_2(s)T_1(s)J_1(s). \tag{33}$$

Write

$$T(s) = \begin{bmatrix} T_{11}(s) & T_{12}(s) \\ T_{21}(s) & T_{22}(s) \end{bmatrix}. \tag{34}$$

It is found from (32) and (34) that

$$Q_L^+(s) = -T_{12}^{-1}(s)T_{11}(s)u_L(s) + T_{12}^{-1}(s)u_R(s) \tag{35a}$$

$$Q_R^-(s) = (T_{21}(s) - T_{22}(s)T_{12}^{-1}(s)T_{11}(s))u_L(s) + T_{22}(s)T_{12}^{-1}(s)u_R(s). \tag{35b}$$

Thus, the formation of Eq. (14) only needs to consider force balance at nodes x_L and x_R; the nodal displacement vectors $u_k(s)$, $k = 1, \ldots, m$, are eliminated by using (35).

Classical boundary value approaches require $(m + 1) \times n$ unknown parameters to impose the boundary and interface conditions for the serially connected subsystems. The aforementioned procedure only needs n unknown nodal displacements ($u_L(s)$ and $u_R(s)$) no matter how large the number of the subsystems is. This feature is particularly useful for analysis of nonbranched distributed systems under multiple pointwise constraints, such as multispan bridges, rotating shafts, and oil pipelines with supports.

6 Example

The proposed transfer function method is applied to determine the natural frequencies of a flexible structure shown in Fig. 9, where two cantilever beams are coupled by two linear springs. In the synthesis, the structure is divided into four subsystems (segments 1-2, 2-3, 4-5, and 5-6), with six nodes

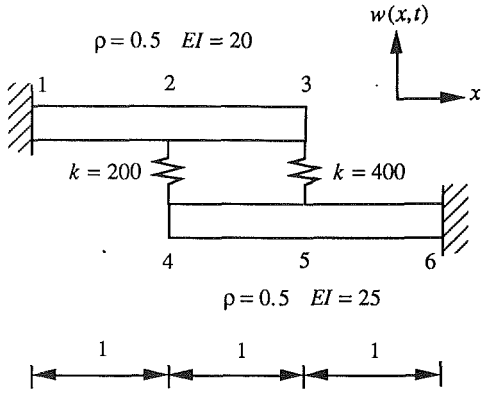


Fig. 9 A coupled beam structure

(points 1, 2, ..., 6). The Laplace-transformed equation of motion of each subsystem is

$$\left(\frac{\rho}{EI}s^2 + \frac{\partial^4}{\partial x^4}\right)\overline{w}(x, s) = 0, \quad x \in (0, 1) \tag{36}$$

where $\overline{w}(x, s)$ is the transverse displacement of the beam, and EI and ρ are the bending stiffness and linear density, respectively. The state space matrix $F(s)$ in (2a) has the form

$$F(s) = \begin{bmatrix} 0 & 1 & 0 & 0 \\ 0 & 0 & 1 & 0 \\ 0 & 0 & 0 & 1 \\ -\rho s^2/EI & 0 & 0 & 0 \end{bmatrix}. \tag{37}$$

The matrix $F(s)$ can be easily modified to include the effects of damping, axial tension, and coriolis acceleration. Interested readers are referred to Yang and Tan (1992) for detail. With $F(s)$, $M(s)$, and $N(s)$ specified in (7), the transfer functions $G(x, \xi, s)$ and $H(x, s)$ of the subsystems can be evaluated in the closed form (3).

The displacement, strain, and internal force vectors of each subsystem are

$$\alpha(x, s) = \begin{pmatrix} \overline{w}(x, s) \\ \overline{w}^{(1)}(x, s) \end{pmatrix}, \quad \epsilon(x, s) = \begin{pmatrix} \overline{w}^{(2)}(x, s) \\ \overline{w}^{(3)}(x, s) \end{pmatrix}, \quad \sigma(x, s) = \begin{pmatrix} M(x, s) \\ V(x, s) \end{pmatrix} \tag{38}$$

where $M(x, s)$ and $V(x, s)$ are the bending moment and shear force of the subsystem, respectively. The constitutive matrix in (6) is

$$E(s) = \begin{bmatrix} EI & 0 \\ 0 & -EI \end{bmatrix} \tag{39}$$

where EI is the beam bending stiffness. The boundary conditions of the structure are

at points 1 and 6, $\overline{w} = 0, \quad \partial\overline{w}/\partial x = 0$ (40a)

at points 3 and 4, $\partial^2\overline{w}/\partial x^2 = 0.$ (40b)

The spring connections at points 2 and 4, and 3 and 5 are treated by (18) with

$$C_{jj}(s) = C_{ll}(s) = \begin{bmatrix} k & 0 \\ 0 & 0 \end{bmatrix}, \quad C_{jl}(s) = C_{lj}(s) = \begin{bmatrix} -k & 0 \\ 0 & 0 \end{bmatrix} \tag{41}$$

where k is the spring coefficient.

Let w_k and θ_k be the transverse displacement $\overline{w}$ and rotation $\partial\overline{w}/\partial x$ at node k, respectively. According to Secs. 3.2 and 3.3, the forces at the nodes 2, 3, 4, and 5, applied by the subsystems, are expressed by the nodal displacement parameters w_2, θ_2, w_3, w_4, w_5, and θ_5. Force balance at those nodes yields a matrix dynamic equilibrium equation of six unknowns

Downloaded 03 May 2010 to 171.66.16.20. Redistribution subject to ASME license or copyright; see http://www.asme.org/terms/Terms_Use.cfm

Table 1 The natural frequencies of the coupled beam structure in Fig. 9 calculated by the proposed transfer function synthesis (TFS) and the finite element method (FEM)

Mode Number	TFS	FEM		
		14 Elements	34 Elements	66 Elements
1	16.4	16.3	16.4	16.4
2	40.9	41.1	41.0	40.9
3	54.6	52.0	54.2	54.5
4	79.2	76.7	78.9	79.1
5	144.7	133.6	143.1	144.3
6	157.0	145.9	155.4	156.6
7	273.9	246.8	269.9	272.9
8	305.2	275.8	289.9	304.1
9	448.7	385.1	440.4	446.6
10	500.5	430.4	491.2	498.1
11	669.1	509.4	653.7	665.3
12	747.5	569.7	730.5	743.3

$$K(s)u(s)=0, \quad K(s)\in C^{6\times 6} \tag{42}$$

where $u(s) = \{w_2\ \theta_2\ w_3\ w_4\ w_5\ \theta_5\}^T$. The parameters w_1, θ_1, θ_3, θ_4, w_6, and θ_6 have been eliminated from $u(s)$ through introduction of the boundary conditions (40) by the method given in Sec. 3.3. Note that classical boundary value approaches would lead to a set of homogeneous algebraic equations of 16 unknowns.

The natural frequencies of the coupled beam structure are the roots of the characteristic equation $\det K(J\omega) = 0$, $J = \sqrt{-1}$. Table 1 lists the first 12 natural frequencies of the coupled beam structure, calculated using the data given in Fig. 9. The result is justified by the finite element method. It is seen from Table 1 that as the number of elements increases, the finite element result converges to that obtained by the proposed method.

7 Concluding Remarks

A new analytical and numerical method for modeling and synthesis of complex distributed parameter systems has been presented. This method does not require a knowledge of system eigensolutions and is valid for non-self-adjoint systems with inhomogeneous boundary conditions. The proposed method can be applied to predict system eigensolutions, forced response and stability, and to design passive/active control schemes. Beside being exact and of closed form, the proposed method has the following features:

(i) The method is fairly general because it uses the same algorithm for different systems. The system type, boundary conditions, external disturbances, constraints, and connections are systematically treated through formation of the matrices $F(s)$, $M(s)$, and $N(s)$ of each distributed subsystem, and through assembly of the global stiffness matrix $K(s)$. As a result, the method is convenient in numerical simulation and is suitable for computerized symbolic manipulation.

(ii) The number of unknowns in the dynamic equilibrium Eq. (14) is minimized through elimination of the unknown variables at the boundaries (Sec. 3.3), and the unknown nodal displacements of those subsystems which are serially connected (Sec. 5.6).

(iii) Although the distributed transfer function formulation adopts the finite element concept, i.e., displacement compatibility and force balance at nodes, it is different from the conventional finite element method in several aspects: (a) it provides exact solutions; (b) it simultaneously determines the displacements and internal forces of the distributed system without taking spatial differentiation of the displacement functions (Eqs. (8)); and (c) it substitutes the boundary conditions of complex distributed parameter systems at the subsystem level (Sec. 3.3).

(iv) The proposed method is especially capable of handling systems with multiple branches and closed loops, distributed connection of flexible bodies, distributed disturbances, and multipoint connection of distributed and lumped systems, which otherwise may be difficult to deal with by other methods.

(v) The method can be combined with some experimental approaches. In many practical cases, the mathematical models of some subsystems or boundaries of the complex distributed parameter system are difficult to obtain. Nonetheless, the impedance functions of the uncertain subsystems or boundaries can be measured experimentally, and then directly incorporated into the transfer function formulation. This mixture of analytical and experimental efforts makes real engineering problems more tractable.

Although this paper has been focused on one-dimensional, uniformly distributed systems, the main results about the transfer function synthesis presented in Secs. 3 to 5 can be extended to multidimensional, nonuniformly distributed systems. The closed-form evaluation of the subsystem transfer functions given in Sec. 2, however, is invalid for multidimensional continua. In this case, approximate methods may be used to determine $G(x, \xi, s)$ and $H(x, s)$ (Yang and Fan, 1993). Also, it should be mentioned that the proposed method is not limited to vibrating continua. In fact, Eq. (1) can also be used to describe other important physical processes in continua such as diffusion, heat conduction, wave propagation, acoustics, hydrodynamics, and aerodynamics. It is hoped that the transfer function formulation developed in this work will provide a useful tool for modeling, analysis, and control of general distributed parameter systems.

Acknowledgments

This work was partially supported by the National Science Foundation and the U.S. Army Research Office. The numerical simulation of the example was conducted by Mr. H. Fang.

References

Bergman, L. A., and McFarland, D. M., 1988, "On the Vibration of a Point-Supported Linear Distributed System," ASME *Journal of Vibration, Acoustics, Stress, and Reliability in Design*, Vol. 110, pp. 485–492.

Bergman, L. A., and Nicholson, J. W., 1985, "Forced Vibration of a Damped Combined Linear System," ASME *Journal of Vibration, Acoustics, Stress, and Reliability in Design*, Vol. 107, pp. 275–281.

Butkoviskiy, A. G., 1983, *Structural Theory of Distributed Systems*, Halsted Press, John Wiley and Sons, New York.

Chen, Y., 1963, "On the Vibration of Beams or Rods Carrying a Concentrated Mass," ASME JOURNAL OF APPLIED MECHANICS, Vol. 30, pp. 310–311.

Dowell, E. H., 1971, "Free Vibrations of a Linear Structure with Arbitrary Support Conditions," ASME JOURNAL OF APPLIED MECHANICS, Vol. 38, pp. 595–600.

Dowell, E. H., 1972, "Free Vibrations of an Arbitrary Structure in Terms of Component Modes," ASME JOURNAL OF APPLIED MECHANICS, Vol. 39, pp. 727–732.

Gladwell, G. M. L., and Bishop, R. E. D., 1960, "Interior Receptances of Beams," *Journal of Mechanical Engineering Science*, Vol. 2, pp. 1–15.

Hallquist, J., and Snyder, V. W., 1973, "Linear Damped Vibratory Structures with Arbitrary Support Conditions," ASME JOURNAL OF APPLIED MECHANICS, Vol. 40, pp. 312–313.

Jacquot, R. G., 1976, "The Forced Vibration of Singly Modified Elastic Surface Systems," *Journal of Sound and Vibration*, Vol. 48, pp. 195–201.

Downloaded 03 May 2010 to 171.66.16.20. Redistribution subject to ASME license or copyright; see http://www.asme.org/terms/Terms_Use.cfm

Jacquot, R. G., and Soedel, W., 1970, "Vibration of Elastic Surface Systems Carrying Dynamic Elements," *Journal of the Acoustical Society of America*, Vol. 47, pp. 1354–1358.

Lin, Y. K., 1969, "Dynamics of Beam-Type Periodic Structures," ASME *Journal of Engineering for Industry*, Nov., pp. 1133–1141.

Mead, D. J., 1971, "Vibration Response and Wave Propagation in Periodic Structures," ASME *Journal of Engineering for Industry*, Aug., pp. 783–792.

Mead, D. J., and Yaman, Y., 1990, "The Harmonic Response of Uniform Beams on Multiple Linear Supports: a Flexural Wave Analysis," *Journal of Sound and Vibration*, Vol. 141, pp. 465–484.

Meirovitch, L., 1967, *Analytical Methods in Vibrations*, The Macmillan Company, London.

Moler, C., and Van Loan, C., 1978, "Nineteen Dubious Ways to Compute the Exponential of a Matrix," *SIAM Review*, Vol. 20, No. 4, Oct., pp. 801–836.

Mote, C. D., Jr., 1972, "Dynamic Stability of Axially Moving Materials," *Shock and Vibration Digest*, Vol. 4, No. 4, pp. 2–11.

Nicholson, J. W., and Bergman, L. A., 1986, "Free Vibration of Combined Dynamical Systems," *Journal of Engineering Mechanics*, Vol. 112, pp. 1–13.

Nour-Omid, B., Sackman, J. L., and Der Kiureghian, A., 1983, "Model Characterization of Equipment Continuous Structure Systems," *Journal of Sound and Vibration*, Vol. 88, pp. 459–472.

Pestel, E. C., and Leckie, F. A., 1963, *Matrix Methods in Elastomechanics*, McGraw-Hill, New York.

Tan, C. A., and Chung, C. H., 1991, "Transfer Function Formulation of Constrained Distributed Systems," ASME DE-Vol. 34, pp. 241–252.

Yang, B., 1991, "Eigenvalue Inclusion Principles for Distributed Gyroscopic Systems," ASME DE-Vol. 37, pp. 7–12. Also, ASME JOURNAL OF APPLIED MECHANICS, Vol. 59, No. 3, Sept. 1992, pp. 650–656.

Yang, B., 1992, "Transfer Functions of Constrained/Combined One-Dimensional Continuous Dynamic Systems," *Journal of Sound and Vibration*, Vol. 156, No. 3, Aug., pp. 425–443.

Yang, B., and Fang, H., 1993, "Transfer Function Formulation of Non-Uniformly Distributed Parameter Systems," ASME DE-Vol. 61, pp. 79–86; also to appear in the ASME *Journal of Vibration and Acoustics*.

Yang, B., and Mote, C. D., Jr., 1991a, "Active Vibration Control of the Axially Moving String in the s Domain," ASME JOURNAL OF APPLIED MECHANICS, Vol. 58, Mar., pp. 189–196.

Yang, B., and Mote, C. D., Jr., 1991a, "Active Vibration Control of the Axially Moving String in the s Domain," ASME JOURNAL OF APPLIED MECHANICS, Vol. 58, Mar., pp. 189–196.

Yang, B., and Mote, C. D., Jr., 1991b, "Frequency-Domain Vibration Control of Distributed Gyroscopic Systems," ASME *Journal of Dynamic Systems, Measurement and Control*, Vol. 113, Mar., pp. 18–25.

Yang, B., and Tan, C. A., 1992, "Transfer Functions of One-Dimensional Distributed Parameter Systems," ASME JOURNAL OF APPLIED MECHANICS, Vol. 59, No. 4, pp. 1009–1014.

Zhou, Y., and Sackman, J. L., 1989, "Modal Properties and Equipment Response in the Case of a Continuous Structure," *Journal of Sound and Vibration*, Vol. 128, pp. 25–38.

Downloaded 03 May 2010 to 171.66.16.20. Redistribution subject to ASME license or copyright; see http://www.asme.org/terms/Terms_Use.cfm

On Statistics of First-Passage Failure

G. Q. Cai
Research Associate.

Y. K. Lin
Schmidt Chair in Engineering and Director.

Center for Applied Stochastics Research, Florida Atlantic University, Boca Raton, FL 33431

The event in which the response of a randomly excited dynamical system passes, for the first time, a critical magnitude z_c is investigated. When the response variable in question can be modeled as a one-dimensional diffusion process, defined on $[z_l, z_c]$, the statistical moment of the first passage time of an arbitrary order is governed by the classical Pontryagin equation, subject to suitable boundary conditions. It is shown that, when a boundary is singular, it must be either an entrance, a regular boundary, or a repulsive natural boundary in order that a solution for the Pontryagin equation is physically meaningful. Boundary conditions are obtained for three types of singular boundaries and applied to the second-order oscillators in which the amplitude or energy process can be approximated as a Markov process. Illustrative examples are given of linear and nonlinear oscillators under additive and/or multiplicative random excitations.

Introduction

When analyzing a randomly varying phenomenon, be it physical, biological, sociological, or economical, one common concern is that the event that some important quantity reaches, for the first time, a critical value. This is known as the first-passage problem, and is one of the most difficult problems in the theory of stochastic processes. At present, possibility of solution exists only if the random phenomenon in question can be approximated as a diffusive Markov process. Still, known solutions are limited only to very few cases of one-dimensional Markov process (see e.g., Bharucha-Reid, 1960; Cox and Miller, 1965).

In mechanics, difficulty arises because the state space is often two-dimensional or higher. One powerful procedure to reduce the dimension of the state space is that of stochastic averaging due originally to Stratonovich (1963) and Khasminskii (1966). This method was applied to the first-passage problem by Ariaratnam and Pi (1973), Lennox and Fraser (1974), and Ariaratnam and Tam (1979) for the case of linear oscillators, and by Roberts (1978) for the case of oscillators with nonlinear damping. In these cases, failure of an oscillator was treated as the first passage of the response amplitude over a specified critical level. The case of second-order oscillator with nonlinear restoring force was considered by Roberts (1976) and Zhu and Lei (1989), using the logical generalization from amplitude to energy envelope, thus retaining the advantage of one-dimensional state space.

In this paper, the first-passage problem is examined from a unified viewpoint. Special attention is given to various boundary conditions, including those of singular boundaries.

Pontryagin Equation

A one-dimensional diffusive Markov process, say $Z(t)$, is governed by an Itô-type stochastic differential equation (Itô, 1951)

$$dZ(t) = m(Z)dt + \sigma(Z)dB(t) \tag{1}$$

where $B(t)$ is a unit Wiener process (e.g., Cox and Miller, 1965), and m and σ are known as the drift and diffusion coefficients, respectively. We shall limit our consideration for those cases, in which m and σ do not depend explicitly on time t, as implied in (1). We are concerned with the random time T when $Z(t)$ reaches, for the first time, a critical value z_c, on the condition that $Z(0) = z_0$. The statistical moments $\mu_{n+1}(z_0, z_c) = E[T^{n+1}]$ are governed by

$$\frac{1}{2}\sigma^2(z_0)\frac{d^2}{dz_0^2}\mu_{n+1} + m(z_0)\frac{d}{dz_0}\mu_{n+1} = -(n+1)\mu_n, \qquad n = 0, 1, 2, \ldots \tag{2}$$

where $m(z_0)$ and $\sigma(z_0)$ are the same coefficients appearing in (1), but with $Z(t)$ replaced by the conditional initial state $Z(0) = z_0$. Equation (2) is known as the Pontryagin equation (Andronov, Pontryagin, and Witt, 1933), and in most cases, it may be solved subject to the boundary conditions:

$$\mu_{n+1}(z_c, z_c) = 0 \tag{3}$$

$$\mu_{n+1}(z_l, z_c) = \text{finite} \tag{4}$$

where z_l is the left boundary for the initial state z_0. In principle, Eq. (2) may be solved recursively, beginning with $n = 0$ and $\mu_0 = 1$. Conditions (3) indicates the sure event that the first

Contributed by the Applied Mechanics Division of THE AMERICAN SOCIETY OF MECHANICAL ENGINEERS for publication in the ASME JOURNAL OF APPLIED MECHANICS.

Discussion on this paper should be addressed to the Technical Editor, Professor Lewis T. Wheeler, Department of Mechanical Engineering, University of Houston, Houston, TX 77204-4792, and will be accepted until four months after final publication of the paper itself in the ASME JOURNAL OF APPLIED MECHANICS.

Manuscript received by the ASME Applied Mechanics Division, May 1, 1992; final revision, Oct. 22, 1992. Associate Technical Editor: P. D. Spanos.

Copyright © 1994 by ASME
Downloaded 03 May 2010 to 171.66.16.20. Redistribution subject to ASME license or copyright; see http://www.asme.org/terms/Terms_Use.cfm

passage time is zero if the initial state is already critical. Condition (4) is based on an assumption that first passage will occur sooner or later, which is used also in deriving the Pontryagin equation. It is important to note that the Pontryagin equation is no longer valid when this assumption does not hold.

Condition (4) is "qualitative," rather than "quantitative." Nevertheless, it is useful to obtain closed-form solutions, when such solutions are possible (e.g., Ariaratnam and Tam, 1979). However, if Eq. (2) must be solved numerically, or numerical solutions are in fact more convenient and preferred, then a quantitative boundary condition is required.

Singular Boundaries

A boundary of a diffusive process is said to be singular if, at the boundary, the diffusion coefficient σ vanishes, or the drift coefficient m tends to infinity, or both. As shown later in several examples, singular boundary conditions are commonplace in stochastic dynamical systems. Therefore, their relations to the Pontryagin Eq. (2) should be examined with care.

According to Feller (1952, 1954), the boundaries of a diffusive process may be classified into four types: regular, exit, entrance and natural. These boundaries can be identified through two time measures, the time measure to reach a boundary, starting from an interior point, and the time measure to reach an interior point, starting from a boundary (Itô and McKean, 1965). A refinement has been proposed by Karlin and Taylor (1981) by splitting the class of natural boundaries into the class of attractive natural boundaries and the class of unattractive natural boundaries. However, for the present investigation, a further refinement is necessary in which the unattractive natural boundaries are divided into the repulsively natural boundaries and the strictly natural boundaries. Feller's classifications have been used, for example, by Sri Namachchivaya (1991) to investigate the effects of random excitation on co-dimension-two bifurcation.

The calculation of the two time measures is generally complicated, especially at a singular boundary. However, only their boundedness, which can be determined based on the limiting behaviors of the drift and diffusion coefficients near the boundary, is needed for the boundary classification. In the case of a singular boundary where the diffusion coefficient vanishes, Zhang and Kozin (1990) developed a set of equivalent, easier to apply criteria for the identification of these boundaries. A modified version of the Zhang-Kozin criteria will now be presented below, from the viewpoint of the present investigation of first passage failures. It should be noted, however, that these criteria apply only to those singular boundaries with vanishing diffusion coefficients.

Let z_l be a boundary on the left-hand side, and let $\sigma(z_l)=0$. The boundary z_l is said to be a shunt if $m(z_l)\neq 0$ and a trap if $m(z_l)=0$. Define the following limits as $Z(t)\to z_l$:

$$(1)\ \sigma^2(Z)\to 0|Z-z_l|^{\alpha_l}, \qquad \alpha_l \geq 0$$

$$(2)\ m(Z)\to 0|Z-z_l|^{\beta_l}, \qquad \beta_l \geq 0$$

$$(3)\ \frac{2m(Z)(Z-z_l)^{\alpha_l-\beta_l}}{\sigma^2(Z)}\to c_l$$

where $0|\cdot|$ denotes the order of magnitude of $|\cdot|$. The values α_l, β_l, and c_l are called the diffusion exponent, drift exponent, and character value of z_l, respectively. Singular boundaries associated with $\sigma(z_l)=0$ are classified in Table 1 in terms of α_l, β_l, and c_l. It should be noted that α_l and β_l are also called the shunt index and the trap index, respectively (Zhang and Kozin, 1990).

As shown in Table 1, a shunt can be either an entrance, an exit, or a regular boundary, and a trap can be either an entrance, an exit, a natural boundary, or a regular boundary. In

Table 1 Classification of singular boundary (modified from the original tables of Zhang and Kozin (1990))

STATE	CONDITIONS				CLASS
SHUNT	$\alpha_l < 1$				regular
$\sigma(z_l)=0$	$\alpha_l = 1$	$m(z_l) < 0$			exit
$(\alpha_l > 0)$		$m(z_l) > 0$	$0 < c_l < 1$		regular
			$c_l \geq 1$		entrance
$m(z_l)\neq 0$	$\alpha_l > 1$	$m(z_l) < 0$			exit
$(\beta_l = 0)$		$m(z_l) > 0$			entrance
TRAP	$\alpha_l < 1+\beta_l$	$\alpha_l < 1$			regular
$\sigma(z_l)=0$		$1 \leq \alpha_l < 2$			exit
$(\alpha_l > 0)$		$\alpha_l \geq 2$			attractively natural
	$\alpha_l > 1+\beta_l$	$\beta_l < 1$	$m(z_l^*) < 0$		exit
			$m(z_l^*) > 0$		entrance
		$\beta_l \geq 1$	$m(z_l^*) < 0$		attractively natural
			$m(z_l^*) > 0$		repulsively natural
$m(z_l)=0$	$\alpha_l = 1+\beta_l$	$\beta_l < 1$	$c_l > \beta_l$	$c_l \geq 1$	entrance
$(\beta_l > 0)$				$c_l < 1$	regular
			$c_l \leq \beta_l$		exit
		$\beta_l \geq 1$	$c_l > \beta_l$		repulsively natural
			$c_l \leq \beta_l$	$c_l \geq 1$	strictly natural
				$c_l < 1$	attractively natural

the case of an entrance, a regular boundary, or a repulsively natural boundary on the left-hand side, a sample path that begins at the boundary, can travel inward, thus it is capable of reaching the critical state. On the other hand, if the left boundary is an exit, attractively natural, or strictly natural, then not every sample path that begins at or near the boundary is to reach the critical state. Since the Pontryagin equation is derived on the assumption that first passage will occur sooner or later, a left-hand-side exit, attractively natural boundary, or strictly natural boundary is not compatible with any solution obtainable from the equation.

Three specific types of singular boundaries will now be considered:

(i) $\sigma^2(z_l)=0$ and $m(z_l)>0$. This boundary is either a regular shunt or an entrance shunt. In order that it is compatible with the solutions of Eq. (2), we obtain, directly from the equation,

$$\mu'_{n+1}(z_l) = -\frac{(n+1)\mu_n(z_l)}{m(z_l)}. \tag{4a}$$

In this case, condition (4a) is equivalent to condition (4), in the sense that either both are satisfied, or neither is satisfied. Condition (4a) has been suggested by Zhu and Lei (1989).

(ii) $\sigma^2(z_l)=$ finite and $m(z_0)\to\infty$ as $z_0\to z_l$. Such a boundary is not included in Table 1, but it is also singular by virtue of the unbounded drift at the boundary. Again, we obtain directly from Eq. (2)

$$\mu'_{n+1}(z_l)=0, \tag{4b}$$

indicating a reflecting boundary. When applicable, condition (4b) is equivalent to condition (4).

(iii) $\sigma^2(z_l)=0$ and $m(z_l)=0$. This boundary is a trap, and it must be either an entrance, a regular trap, or a repulsively natural trap in order to be admissible to the solution of the Pontryagin equation. In either case, we may impose the condition

$$0|m(z_0)\mu'_{n+1}(z_0)| \sim 0|\mu_n(z_0)|, \quad \text{as } z_0\to z_l. \tag{4c}$$

In particular, for $n=0$,

Downloaded 03 May 2010 to 171.66.16.20. Redistribution subject to ASME license or copyright; see http://www.asme.org/terms/Terms_Use.cfm

$$m(z_0)\mu_1'(z_0) = \text{finite}, \quad \text{as } z_0 \to z_l. \tag{4d}$$

Applications of these boundary conditions will now be illustrated in the following examples.

Example 1. As the first example, consider the problem of population genetics investigated by Karlin and Taylor (1981) and Sri Namachchivaya (1989), for which the Pontryagin equation reads

$$\frac{1}{2}z_0^2\frac{d^2}{dz_0^2}\mu_{n+1} + (1+z_0)\frac{d}{dz_0}\mu_{n+1} = -(n+1)\mu_n \tag{5}$$

subject to the boundary conditions

$$\mu_{n+1}(z_c) = 0 \tag{6}$$

$$\mu_{n+1}'(0) = -(n+1)\mu_n(0). \tag{7}$$

Condition (7) is deduced from (4*a*) since, from (5), the left boundary $z_l = 0$ can be easily identified as an entrance shunt. The solution may be expressed as follows:

$$\mu_{n+1}(z_0) = (n+1)\left[\int_{z_0}^{z_c}\mu_n(u)du + e^{2/z_0}\int_0^{z_0}\mu_n(u)e^{-2/u}du - e^{2/z_c}\int_0^{z_c}\mu_n(u)e^{-2/u}du\right]. \tag{8}$$

In particular, for $n = 0$,

$$\mu_1(z_0) = z_c - z_0 + e^{2/z_0}\int_0^{z_0}e^{-2/u}du - e^{2/z_c}\int_0^{z_c}e^{-2/u}du = 2\left[e^{2/z_0}Ei\left(-\frac{2}{z_0}\right) - e^{2/z_c}Ei\left(-\frac{2}{z_c}\right)\right] \tag{9}$$

and

$$\mu_1(0) = -2e^{2/z_c}Ei\left(-\frac{2}{z_c}\right) \tag{10}$$

where $Ei(-x)$ is an exponential integral, defined as

$$Ei(-x) = -\int_x^\infty \frac{1}{t}e^{-t}dt, \quad x > 0. \tag{11}$$

Equation (10) has been obtained previously by Sri Namachchivaya (1989).

Amplitude Envelope

The method of stochastic averaging of Stratonovich (1963) and Khasminskii (1966) is effective for investigating the case of an oscillator with linear restoring force, light damping, and weak excitations. The equation of motion for this case has the form of

$$\ddot{X} + \epsilon h(X, \dot{X}) + \omega_0^2 X = \epsilon^{1/2} g_j(X, \dot{X})\xi_j(t) \tag{12}$$

where h and g_j are generally nonlinear functions of X and $\dot{X}$, $\xi_j(t)$ are wide-band random excitations, and ϵ is a small parameter. In the stochastic averaging method, equation (12) is first replaced by two first-order equations for the amplitude process $A(t)$ and the phase process $\Theta(t)$, using the following transformation:

$$\begin{aligned} X(t) &= A(t)\cos[\omega_0 t + \Theta(t)] \\ \dot{X}(t) &= -\omega_0 A(t)\sin[\omega_0 t + \Theta(t)]. \end{aligned} \tag{13}$$

Recognizing that both $A(t)$ and $\Theta(t)$ are slowly varying, compared with the excitation processes $\xi_j(t)$, the excitation processes are averaged over the probability space and approximated by Gaussian white noises. Finally, a time averaging procedure is carried out to eliminate the oscillatory terms and decouple the amplitude $A(t)$ from the phase $\Theta(t)$. The decoupled amplitude process $A(t)$ is approximately a Markov process and governed by the following Itô equation:

$$dA = m(A)dt + \sigma(A)dB(t) \tag{14}$$

The statistical moments of the first-passage time can be obtained by solving the Pontryagin Eq. (2) with suitable boundary conditions.

Example 2. The following case of a linear oscillator under both additive and multiplicative random excitations has been studied by Ariaratnam and Tam (1979):

$$\ddot{X} + \omega_0[2\zeta + F(t)]\dot{X} + \omega_0^2[1 + G(t)]X = H(t) \tag{15}$$

where $F(t)$, $G(t)$, and $H(t)$ are wide-band stationary processes with zero mean values. It is implied that ζ is of order ϵ, and that $F(t)$, $G(t)$, and $H(t)$ are of order $\epsilon^{1/2}$. The amplitude $A(t) = [X^2(t) + \omega_0^{-2}\dot{X}^2(t)]^{1/2}$ is approximated by a Markov diffusive process and governed by Itô Eq. (14), where the drift coefficient $m(A)$ and the diffusion coefficient $\sigma(A)$ are obtained by applying the stochastic averaging procedure to yield

$$m(A) = -\alpha A + \frac{\beta}{2A} \tag{16}$$

$$\sigma^2(A) = \gamma A^2 + \beta. \tag{17}$$

The coefficients α, β, and γ in Eqs. (16) and (17) are given by

$$\alpha = \zeta\omega_0 - \frac{\pi\omega_0^2}{8}[2\Phi_{FF}(0) + 3\Phi_{FF}(2\omega_0) + 3\Phi_{GG}(2\omega_0) - 6\Psi_{GF}(2\omega_0)] \tag{18}$$

$$\beta = \frac{\pi}{\omega_0^2}\Phi_{HH}(\omega_0) \tag{19}$$

$$\gamma = \frac{\pi\omega_0^2}{4}[2\Phi_{FF}(0) + \Phi_{FF}(2\omega_0) + \Phi_{GG}(2\omega_0) + 2\Phi_{GF}(2\omega_0)] \tag{20}$$

$$\Phi_{\xi\eta}(\omega) = \frac{1}{2\pi}\int_{-\infty}^{\infty}E[\xi(t)\eta(t+\tau)]\cos(\omega\tau)d\tau \tag{21}$$

$$\Psi_{\xi\eta}(\omega) = \frac{1}{2\pi}\int_{-\infty}^{\infty}E[\xi(t)\xi(t+\tau)]\sin(\omega\tau)d\tau \tag{22}$$

where ξ and η in (21) and (22) can be either F, G, or H. Thus the Pontryagin equation reads

$$\frac{1}{2}(\gamma a_0^2 + \beta)\frac{d^2}{da_0^2}\mu_{n+1} + \left(-\alpha a_0 + \frac{\beta}{2a_0}\right)\frac{d}{da_0}\mu_{n+1} = -(n+1)\mu_n. \tag{23}$$

Since the drift coefficient tends to infinity, and the diffusion coefficient remains finite as $a_0 \to 0$, the two boundary conditions are

$$\mu_{n+1}'(0) = 0 \tag{24}$$

$$\mu_{n+1}(a_c) = 0. \tag{25}$$

Condition (24) indicates a reflective boundary. The first moment is obtained by letting $n = 0$, yielding

$$\mu_1(a_0) = \frac{1}{\eta\gamma}\int_{a_0}^{a_c}\frac{1}{u}\left[\left(1 + \frac{\gamma}{\beta}u^2\right)^\eta - 1\right]du, \quad \text{if } \eta = \frac{\alpha}{\gamma} + \frac{1}{2} \neq 0 \tag{26}$$

$$\mu_1(a_0) = \frac{1}{\gamma}\int_{a_0}^{a_c}\frac{1}{u}\ln\left(1 + \frac{\gamma}{\beta}u^2\right)du, \quad \text{if } \eta = 0. \tag{27}$$

These results were obtained by Ariaratnam and Tam (1979) previously. For a higher order moment, we obtain

$$\mu_{n+1}(a_0) = 2(n+1)\int_{a_0}^{a_c}\frac{(\gamma u^2 + \beta)^\eta}{u}\left[\int_0^u \frac{v\mu_n(v)}{(\gamma v^2 + \beta)^{\eta+1}}dv\right]du, \quad \text{if } \eta \neq 0 \tag{28}$$

Downloaded 03 May 2010 to 171.66.16.20. Redistribution subject to ASME license or copyright; see http://www.asme.org/terms/Terms_Use.cfm

$$\mu_{n+1}(a_0) = (n+1)\int_{a_0}^{a_c}\frac{1}{u}\left[\int_0^u \frac{v\mu_n(v)}{(\gamma v^2+\beta)}dv\right]du,$$

if $\eta = 0$. (29)

If the multiplicative excitations $F(t)$ and $G(t)$ are absent, then $\gamma = 0$ in Eq. (23), and Eqs. (26)–(29) are no longer applicable. However, the boundary conditions (24) and (25) remain valid, their imposition yields

$$\mu_1 = \frac{1}{\zeta\omega_0}\left[-\ln\frac{a_c}{a_0} + \int_{a_0}^{a_c}\frac{1}{u}\exp\left(\frac{\zeta\omega_0}{\beta}u^2\right)du\right]$$

$$= \frac{1}{2\zeta\omega_0}\left[\overline{Ei}\left(\frac{\zeta\omega_0}{\beta}a_c^2\right) - \overline{Ei}\left(\frac{\zeta\omega_0}{\beta}a_0^2\right) - \ln\left(\frac{a_c}{a_0}\right)^2\right] \quad (30)$$

where $\overline{Ei}$ is another exponential function defined as

$$\overline{Ei}(x) = -\int_{-x}^{\infty}\frac{1}{t}e^{-t}dt, \quad x>0. \quad (31)$$

The higher-order moments are obtained as

$$\mu_{n+1} = \frac{2(n+1)}{\beta}\int_{a_0}^{a_c}\frac{1}{u}\exp\left(\frac{\zeta\omega_0}{\beta}u^2\right)$$

$$\times\left[\int_0^u v\mu_n(v)\exp\left(-\frac{\zeta\omega_0}{\beta}v^2\right)dv\right]du. \quad (32)$$

Equation (30) has been obtained by Ariaratnam and Pi (1973) previously.

On the other hand, if the additive random excitation $H(t)$ is absent, then $\beta = 0$, and both the drift and diffusion coefficients vanish at $a_0 = 0$. As noted earlier, $a_0 = 0$ is now a trap. This case will be considered in Example 5.

Example 3. Consider the following van der Pol oscillator

$$\ddot{X} + 2\zeta\omega_0(1+\delta X^2)\dot{X} + \omega_0^2 X = H(t). \quad (33)$$

The drift and diffusion coefficients, obtained from stochastic averaging, are given by

$$m(A) = -\zeta\omega_0 A - \frac{1}{4}\zeta\omega_0\delta A^3 + \frac{\beta}{2A} \quad (34)$$

$$\sigma^2(A) = \beta \quad (35)$$

where β has been given in (19). Then the Pontryagin equation becomes

$$\frac{1}{2}\beta\frac{d^2}{da_0^2}\mu_{n+1} + \left(-\zeta\omega_0 a_0 - \frac{1}{4}\zeta\omega_0 a_0^3 + \frac{\beta}{2a_0}\right)\frac{d}{da_0}\mu_{n+1}$$

$$= -(n+1)\mu_n, \quad (36)$$

subject to boundary conditions (24) and (25). The solution is

$$\mu_{n+1}(a_0) = \frac{2(n+1)}{\beta}\int_{a_0}^{a_c}\frac{1}{u}\exp\left[\frac{\zeta\omega_0}{\beta}\left(u^2+\frac{\delta}{8}u^4\right)\right]$$

$$\times\left\{\int_0^u v\mu_n(v)\exp\left[-\frac{\zeta\omega_0}{\beta}\left(v^2+\frac{\delta}{8}v^4\right)\right]dv\right\}du. \quad (37)$$

The statistical moments $\mu_{n+1}(a_0)$ can be calculated by carrying out the integrations in (37) or solving numerically the boundary value problem defined in (36), (24), and (25).

It is of interest to note that if the first-passage problem of an oscillator is formulated in terms of the amplitude envelope, and if an additive wide-band excitation exists, then the boundary condition at $a_0 = 0$ for the Pontryagin Eq. (2) is always reflective, namely condition (24) holds, irrespective of the damping mechanism and the existence of multiplicative excitations.

Energy Envelope

The traditional method of stochastic averaging is not suitable if the restoring force of an oscillator is strongly nonlinear. This latter case has a typical governing equation of the form

$$\ddot{X} + \epsilon h(X, \dot{X}) + f(X) = \epsilon^{1/2} g_j(X, \dot{X}) W_j(t) \quad (38)$$

where f represents the nonlinear restoring force, assumed to be an odd function of X, and $W_j(t)$ will be treated as Gaussian white noises in what follows, with

$$E[W_j(t) W_l(t+\tau)] = 2\pi K_{jl}\delta(\tau). \quad (39)$$

The total energy of the oscillator is given by

$$\Lambda(t) = \frac{1}{2}\dot{X}^2 + U(X) \quad (40)$$

where

$$U(X) = \int_0^X f(u)du. \quad (41)$$

Differentiate Eq. (40) with respect to time, and combine the result with Eq. (38) to obtain

$$\dot{\Lambda} = \dot{X}[-\epsilon h(X, \dot{X}) + \epsilon^{1/2} g_j(X, \dot{X}) W_j(t)]. \quad (42)$$

Equation (42) may be replaced by the following Itô equation:

$$d\Lambda = m(\Lambda)dt + \sigma(\Lambda)dB(t), \quad (43)$$

where the drift and diffusion coefficients may be obtained approximately by use of another version of stochastic averaging, called quasi-conservative stochastic averaging (Landa and Stratonovich, 1962; Khasminskii, 1964), as follows:

$$m(\Lambda) = \epsilon\left\langle -\dot{X}h(X, \dot{X}) + \pi K_{jl}\dot{X} g_l(X, \dot{X})\frac{\partial}{\partial\Lambda}[\dot{X} g_j(X, \dot{X})]\right\rangle_t \quad (44)$$

$$\sigma^2(\Lambda) = 2\epsilon\pi K_{jl}\langle \dot{X}^2 g_j(X, \dot{X}) g_l(X, \dot{X})\rangle_t \quad (45)$$

in which $\langle[\cdot]\rangle_t$ denotes time-averaging of $[\cdot]$, and $\dot{X}$ is treated as a function of Λ and X; i.e.

$$\dot{X} = \pm\sqrt{2[\Lambda - U(X)]}. \quad (46)$$

In the quasi-conservative averaging procedure, each time averaging is substituted by averaging on X over a pseudo-period,

$$\langle[\cdot]\rangle = \frac{1}{T}\int_{-A}^{A}\frac{[\cdot]_{\dot{X}=\sqrt{2[\Lambda-U(X)]}} + [\cdot]_{\dot{X}=-\sqrt{2[\Lambda-U(X)]}}}{\sqrt{2[\Lambda-U(X)]}}dX \quad (47)$$

where

$$T = 4T_{1/4} = 4\int_0^A\frac{1}{\sqrt{2[\Lambda-U(X)]}}dX \quad (48)$$

and A is the would-be amplitude of free oscillation, if the oscillator were undamped and possessing a total energy Λ, or symbolically,

$$A = U^{-1}(\Lambda). \quad (49)$$

The same Pontryagin Eq. (2) and the boundary conditions apply, with z replaced by the state variable λ of the total energy.

Example 4. Roberts (1976) has considered the following oscillator:

$$\ddot{X} + 2\zeta\dot{X} + k|X|^\rho \operatorname{sgn}(X) = W(t); \quad k, \rho > 0. \quad (50)$$

This case involves only one additive white noise excitation. We assume that ζ and the spectral density K of $W(t)$ are of order ϵ. Applying Eqs. (44) and (45), we obtained after some algebra,

$$m(\Lambda) = -2\delta\zeta\Lambda + \pi K \quad (51)$$

$$\sigma^2(\Lambda) = 2\pi K\delta\Lambda \quad (52)$$

where $\delta = 2(\rho+1)/(\rho+3)$. The Pontryagin equation is now

$$\pi K\delta\lambda_0\frac{d^2}{d\lambda_0^2}\mu_{n+1} + (\pi K - 2\delta\zeta\lambda_0)\frac{d}{d\lambda_0}\mu_{n+1} = -(n+1)\mu_n. \quad (53)$$

It can be shown by using Table 1 that the boundary $\lambda_0 = 0$ is

Downloaded 03 May 2010 to 171.66.16.20. Redistribution subject to ASME license or copyright; see http://www.asme.org/terms/Terms_Use.cfm

an entrance shunt if $\delta \leq 1$ and a regular shunt if $\delta > 1$. In either case, condition (4*a*) is applicable. Therefore, the proper boundary conditions for (53) are

$$\mu'_{n+1}(0) = -\frac{(n+1)\mu_n(0)}{\pi K} \tag{54}$$

$$\mu_{n+1}(\lambda_c) = 0. \tag{55}$$

Its solution is given by

$$\mu'_{n+1}(\lambda_0) = -\frac{n+1}{\pi K \delta} e^{(2\zeta/\pi K)\lambda_0} \lambda_0^{-1/\delta} \times \int_0^{\lambda_0} \mu_n(v) v^{1/\delta - 1} e^{-(2\zeta/\pi K)v} dv \tag{56}$$

and

$$\mu_{n+1}(\lambda_0) = -\int_{\lambda_0}^{\lambda_c} \mu'_{n+1}(u)\, du. \tag{57}$$

It is of interest to compare the present result with that of the linear case, by letting $\delta = \rho = 1$. Upon carrying out the integration we obtain

$$\mu_1 = \frac{1}{2\zeta}\left[\overline{Ei}\left(\frac{2\zeta}{\pi K}\lambda_c\right) - \overline{Ei}\left(\frac{2\zeta}{\pi K}\lambda_0\right) - \ln\left(\frac{\lambda_c}{\lambda_0}\right)\right]. \tag{58}$$

Equation (58) coincides with Eq. (30), although the behaviors of the drift and diffusion coefficients are different between Eq. (23) and (53) at the left boundary and the respective boundary conditions (24) and (54) are also different. This is remarkable, since in the linear case energy Λ is exactly the amplitude squared, namely $\Lambda = A^2$, and the stability conditions for $E[A(t)]$ and $E[A^2(t)]$ are known to be different.

It is also remarkable that, if the first passage problem is formulated in terms of energy, then the boundary condition (54) is shared by all cases, whether the system is linear or nonlinear, and that none of the system parameters ζ, k, and ρ appears in the condition. In fact, this is true as long as an additive noise is present, irrespective of whether a multiplicative noise is also present. We note that Kozin (1982) has obtained a very simple result for an undamped linear system under additive Gaussian white noise excitation, which, in the present notation, reads

$$\mu_1 = \frac{\lambda_c - \lambda_0}{\pi K}. \tag{59}$$

Kozin's result was obtained by applying the so-called Dynkin's formula (Dynkin, 1965), and in fact it is also valid when the undamped system is nonlinear. Equation (59) shows that the slop of μ_1 remains unchanged at $-(\pi K)^{-1}$ if the system is undamped. Therefore, in terms of first passage to a critical energy level, all systems under additive random excitation begin with the same slope for μ_1 at the boundary $\lambda_0 = 0$ and damping can change the slope only after departing from the boundary.

Example 5. To illustrate the case of trap boundaries and their admissibility to solutions of the Pontryagin equation, consider the following oscillator excited by a parametric noise:

$$\ddot{X} + 2\zeta\dot{X} + f(X) = XW(t). \tag{60}$$

The drift and diffusion coefficients, obtained from Eqs. (44) and (45), are

$$m(\Lambda) = \frac{1}{T_{1/4}(\Lambda)}\left\{\pi K \int_0^A X^2[2\Lambda - 2U(X)]^{-1/2} dX - 2\zeta \int_0^A [2\Lambda - 2U(X)]^{1/2} dX\right\} \tag{61}$$

$$\sigma^2(\Lambda) = \frac{2\pi K}{T_{1/4}(\Lambda)} \int_0^A X^2[2\Lambda - 2U(X)]^{1/2} dX. \tag{62}$$

Examine first the special case of a linear system, corresponding to $f(X) = X$ and $U(X) = X^2/2$, since some closed-form results are obtainable. Upon carrying out the integrations in (61) and (62) for this linear case we obtain

$$m(\Lambda) = (-2\zeta + \pi K)\Lambda \tag{63}$$

$$\sigma^2(\Lambda) = \pi K \Lambda^2. \tag{64}$$

The Pontryagin equation is therefore

$$\frac{1}{2}\pi K \lambda_0^2 \frac{d^2}{d\lambda_0^2}\mu_{n+1} + (-2\zeta + \pi K)\lambda_0 \frac{d}{d\lambda_0}\mu_{n+1} = -(n+1)\mu_n \tag{65}$$

and one of the boundary conditions is

$$\mu_{n+1}(\lambda_c) = 0. \tag{66}$$

Clearly, $\lambda_0 = 0$ is a trap boundary. As such, it must be either a regular trap, a repulsively natural trap, or an entrance trap to be compatible with the Pontryagin equation. The diffusion exponent, drift exponent, and character value at $\lambda_0 = 0$ are, respectively, $\alpha_l = 2$, $\beta_l = 1$, and $c_l = 2 - (4\zeta/\pi K)$. Thus the boundary is repulsively natural if

$$c_l = 2 - \frac{4\zeta}{\pi K} > 1 \tag{67}$$

in which case condition (4*c*) is applicable. The left boundary is attractively natural if $c_l < 1$, or strictly natural if $c_l = 1$. In both cases, it is not admissible boundary for the first-passage problem.

Equation (65) is an Euler-type ordinary differential equation which can be solved easily to yield

$$\mu'_{n+1}(\lambda_0) = \lambda_0^{(4\zeta/\pi K)-2} \times \left[-\frac{2(n+1)}{\pi K}\int_0^{\lambda_0} \mu^n(v) v^{-(4\zeta/\pi K)} dv + C_{n+1}\right]. \tag{68}$$

For $n = 0$, we obtain

$$\mu'_1(\lambda_0) = C_1 \lambda_0^{(4\zeta/\pi K)-2} - \frac{1}{(\pi K - 4\zeta)\lambda_0}. \tag{69}$$

It follows upon imposing boundary condition (4*d*) that $C_1 = 0$. Imposing the remaining condition (66),

$$\mu_1(\lambda_0) = \frac{2}{\pi K - 4\zeta}\ln\frac{\lambda_c}{\lambda_0}. \tag{70}$$

For $n = 1$, we find that

$$\mu'_2(\lambda_0) = C_2 \lambda_0^{(4\zeta/\pi K)-2} - \frac{8}{(\pi K - 4\zeta)^2 \lambda_0}\left(\frac{\pi K}{\pi K - 4\zeta} + \ln\frac{\lambda_c}{\lambda_0}\right) \tag{71}$$

and that $C_2 = 0$ upon imposing boundary condition (4*c*). The second moment is obtained by performing another integration and imposing (66) to yield

$$\mu_2(\lambda_0) = \frac{4}{(\pi K - 4\zeta)^2}\ln\frac{\lambda_c}{\lambda_0}\left(\frac{2\pi K}{\pi K - 4\zeta} + \ln\frac{\lambda_c}{\lambda_0}\right). \tag{72}$$

Similarly, $C_{n+1} = 0$ for all $n = 0, 1, 2, \ldots$ and

$$\mu_{n+1}(\lambda_0) = \frac{2(n+1)}{\pi K}\int_{\lambda_0}^{\lambda_c} u^{(4\zeta/\pi K)-2}\left[\int_0^u \mu^n(v) v^{-(4\zeta/\pi K)} dv\right] du. \tag{73}$$

The same results, (70) and (73), can be obtained from Eqs. (26) and (28) by letting $\beta \to 0$, $\eta < 0$ and changing the state variable from a to λ. It shows, once again, the same statistical moments for the first-passage time are obtainable from either the amplitude or the energy envelope formulations.

Of course, the above results are valid only if the trap boundary at $\lambda_0 = 0$ is repulsively natural, which requires $c_l > 1$ or $4\zeta < \pi K$. Under this condition, the system is unstable at $\lambda = 0$; therefore, it is possible for a sample path beginning at near $\lambda_0 = 0$ to travel to the critical state λ_c. However, as seen from

Downloaded 03 May 2010 to 171.66.16.20. Redistribution subject to ASME license or copyright; see http://www.asme.org/terms/Terms_Use.cfm

(70), (72), and (73), the statistical moments of the first-passage time are very large if λ_0 is close to zero, since there exist only infinitesimal diffusion and infinitesimal positive rightward drift near the boundary.

To show that neither an attractively natural trap nor a strictly natural trap is admissible for the left boundary, let us return to the Pontryagin Eq. (65). If $4\zeta > \pi K$, then the left boundary is attractively natural, in which case the general solution of (65) has the form of

$$\mu_1(\lambda_0) = \frac{2}{4\zeta - \pi K} \ln \lambda_0 + C_1 \lambda_0^{(4\zeta/\pi K)-1} + D_1. \tag{74}$$

On the other hand, if $4\zeta = \pi K$ corresponds to a strictly natural trap, the general solution reads

$$\mu_1(\lambda_0) = -\frac{1}{\pi K} (\ln \lambda_0)^2 + C_1 \ln \lambda_0 + D_1. \tag{75}$$

For any finite C_1 and D_1 values, both (74) and (75) give rise to negative results for $\mu_1(\lambda_0)$ as $\lambda_0 \to 0$. In either case, the Pontryagin equation is no longer physically meaningful.

Next, consider a Duffing-type oscillator with a nonlinear restoring force $f(X) = X + \delta X^3$, where δ is a positive constant. The drift and diffusion coefficients obtained from (61) and (62) are as follows:

$$m(\Lambda) = A^2 \frac{\pi K \int_0^{\pi/2} \cos^2\phi (1 - \bar{k}^2 \sin^2\phi)^{-1/2} d\phi - 2\zeta(1+\delta A^2) \int_0^{\pi/2} \sin^2\phi (1 - \bar{k}^2 \sin^2\phi)^{1/2} d\phi}{\int_0^{\pi/2} (1 - \bar{k}^2 \sin^2\phi)^{-1/2} d\phi} \tag{76}$$

$$\sigma^2(\Lambda) = 2\pi K A^4 (1 + \delta A^2) \frac{\int_0^{\pi/2} \sin^2\phi \cos^2\phi (1 - \bar{k}^2 \sin^2\phi)^{1/2} d\phi}{\int_0^{\pi/2} (1 - \bar{k}^2 \sin^2\phi)^{-1/2} d\phi} \tag{77}$$

where

$$\bar{k} = A \sqrt{\frac{\delta}{2(1+\delta A^2)}}. \tag{78}$$

In Eqs. (76) through (78), A is treated as a function of Λ, and is the positive root of the equation

$$\delta A^4 + 2A^2 - 4\Lambda = 0. \tag{79}$$

As $\Lambda \to 0$, $m(\Lambda) \to (\pi K - 2\zeta)\Lambda$ and $\sigma^2(\Lambda) \to \pi K \Lambda^2$. It can be seen by comparing with (63) and (64), that the diffusion exponent, drift exponent, character value of the left boundary in this case are the same as those in the linear case. Therefore, the condition for a repulsively natural trap is still Eq. (67). Similar to the linear case, the Pontryagin equation may be integrated once to obtain

$$\mu'_{n+1}(\lambda_0) = \exp\left[-\int \frac{2m(\lambda_0)}{\sigma^2(\lambda_0)} d\lambda_0 \right] \times \left\{ -2(n+1) \int_0^{\lambda_0} \frac{\mu_n(u)}{\sigma^2(u)} \exp\left[\int_0^u \frac{2m(v)}{\sigma^2(v)} dv \right] du + C_{n+1} \right\}. \tag{80}$$

Upon imposing boundary condition (4c), $C_{n+1} = 0$, and it follows that

$$\mu'_{n+1}(\lambda_0) = -2(n+1) \exp\left[-\int \frac{2m(\lambda_0)}{\sigma^2(\lambda_0)} d\lambda_0 \right] \times \left\{ \int_0^{\lambda_0} \frac{\mu_n(u)}{\sigma^2(u)} \exp\left[\int_0^u \frac{2m(v)}{\sigma^2(v)} dv \right] du \right\}. \tag{81}$$

However, the above solution form is not suitable for numerical calculation since the integrations indicated in (81) are divergent at the origin.

To facilitate a direct numerical solution of the Pontryagin equation, the behavior of the solution near the left boundary must first be examined. When λ_0 is very small, the drift and diffusion coefficients may be approximated by (63) and (64). Thus we obtain, from the Pontryagin equation,

$$\mu'_{n+1}(\lambda_0) \approx -\frac{2(n+1)}{\pi K} \lambda_0^{(4\zeta/\pi K)-2} \int_0^{\lambda_0} \mu_n(v) v^{-(4\zeta/\pi K)} dv, \qquad \lambda_0 \ll 1. \tag{82}$$

Specifically, for $n = 0$,

$$\mu'_1(\lambda_0) \approx \frac{2}{(4\zeta - \pi K)\lambda_0}, \quad \lambda_0 \ll 1. \tag{83}$$

Condition (83) may be used in conjunction with the condition $\mu_1(\lambda_c) = 0$ in carrying out the numerical solution of the Pontryagin equation for μ_1. For the second moment μ_2, we obtain from integrating (82) by parts

$$\mu'_2(\lambda_0) \approx \frac{4}{(4\zeta - \pi K)\lambda_0} \left[\mu_1(\lambda_0) + \frac{2\pi K}{(4\zeta - \pi K)^2} \right], \quad \lambda_0 \ll 1. \tag{84}$$

Condition (84) may be used in conjunction with $\mu_2(\lambda_c) = 0$. Calculation of higher-order moments can proceed analogously.

Numerical results have been obtained, in three different ways, for the mean first-passage time μ_1 of the energy envelope for the Duffing oscillators with $\delta = 0.1$ and several combinations of ζ and K values. First, the Pontryagin equation was solved numerically with boundary conditions $\mu_1(\lambda_c) = 0$ and the one given approximately in (83). When applying the approximate boundary condition (83), two trial initial values 0.01 and 0.005 were selected for λ_0 to begin the computation and the results were found to be practically the same. These results are shown in Figs. 1 and 2 as solid and dashed lines. Next, Monte Carlo simulations were preformed on the basis of the original governing equation for a Duffing oscillator, and the results so obtained are represented by the crosses in Figs. 1 and 2. Finally, the Itô equation for the energy envelope of the averaged system was converted to its corresponding Stratonovich-type equation, which was then used as the basis to perform another set of Monte Carlo simulations. The results of the latter set of simulations are known as diamonds in Figs. 1 and 2. As expected, the simulation results for the averaged system are in excellent agreement with the analytical results obtained by solving the Pontryagin equation. The difference between the simulation results for the original and the averaged systems indicates that the error arising from the averaging procedure is of the order of the period of the oscillator. This error is considered insignificant because, for practical applications, the first-passage time is expected to be much longer than the period of a properly designed oscillator.

Concluding Remarks

The statistical moments of the first-passage time for a one-

Downloaded 03 May 2010 to 171.66.16.20. Redistribution subject to ASME license or copyright; see http://www.asme.org/terms/Terms_Use.cfm

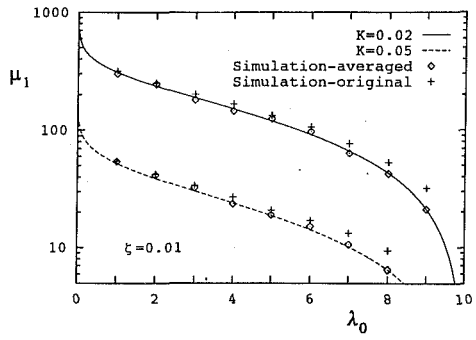


Fig. 1 The mean first-passage time of a Duffing oscillator under parametric white-noise excitation. Damping coefficient $\zeta = 0.01$, white-noise spectral level $K = 0.02, 0.05$.

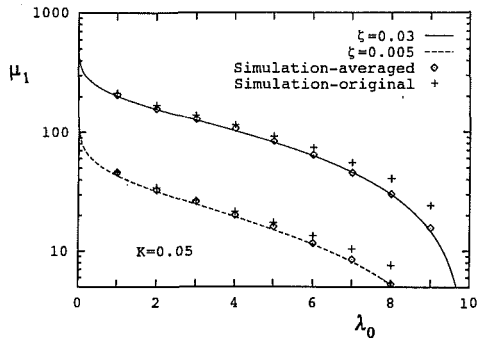


Fig. 2 The mean first-passage time of a Duffing oscillator under parametric white-noise excitation. Damping coefficient $\zeta = 0.03, 0.005$, white-noise spectral level $K = 0.05$.

dimensional diffusive Markov process are governed by the associated Pontryagin equations subject to appropriate boundary conditions. When the left-hand side boundary is singular, it must be either an entrance, a regular boundary, or a repulsively natural boundary to be admissible to the Pontryagin equation. In this paper, boundary conditions are formulated for three types of singular boundaries in order that the Pontryagin equation can be solved either analytically or numerically. For a second-order oscillator with light damping and under weak wide-band excitations, the left boundary is singular when the first-passage problem is formulated in terms of either amplitude or energy envelope of the system response. Examples are given of linear and nonlinear oscillators under additive and/or multiplicative random excitations.

It is shown that if an additive random excitation is present, then the slopes of the statistical moments of the first-passage time is always zero at the left boundary (a reflective boundary) when the problem is formulated in terms of the amplitude process but they are inversely proportional to the spectral density of the additive excitation when the problem is formulated in terms of the energy process. This is true irrespective of the damping mechanism and whether or not multiplicative random excitations are also present. Furthermore, the same statistical moments are obtained from either the amplitude or energy formulation, although their respective boundary conditions are very much different.

Acknowledgment

This paper is prepared under grant AFOSR-91-0073 from the Air Force Office of Scientific Research, Air Force Systems Command, USAF, monitored by Dr. Spender Wu. The U.S. Government is authorized to reproduce and distribute reprints for governmental purposes, notwithstanding any copyright notation thereon.

References

Andronov, A. A., Pontryagin, L. S., and Witt, A. A., 1933, "On the Statistical Consideration of Dynamic Systems," (in Russian), *Zhurnal Exper. Theoret. Fiz.*, Vol. 3, pp. 165–180.

Ariaratnam, S. T., and Pi, H. N., 1973, "On the First-Passage Time for Envelope Crossing for a Linear Oscillator," *Int. J. Control*, Vol. 18, pp. 89–96.

Ariaratnam, S. T., and Tam, D. S. F., 1979, "Random Vibration and Stability of a Linear Parametrically Excited Oscillator," *ZAMM*, Vol. 59, pp. 79–84.

Bharucha-Reid, A. T., 1960, *Elements of Markov Processes and their Applications*, McGraw-Hill, New York.

Cox, D. R., and Miller, H. D., 1965, *The Theory of Stochastic Processes*, Chapman and Hall, New York.

Dynkin, E. B., 1965, *Markov Process*, Vols. 1 and 2, Springer-Verlag, New York.

Feller, W., 1952, "The Parabolic Differential Equation and the Associated Semigroups of Transformations," *Ann. Math.*, Vol. 55, pp. 468–519.

Feller, W., 1954, "Diffusion Process in One Dimension," *Trans. of Amer. Math. Soc.*, Vol. 97, pp. 1–31.

Itô, K., 1951, "On Stochastic Differential Equations," *Mem. Amer. Math. Soc.*, Vol. 4, pp. 289–302.

Itô, K., and McKean, Jr. H. P., 1965, *Diffusion Processes and Their Sample Paths*, Academic Press, New York.

Karlin, S., and Taylor, H. M., 1981, A Second Course in Stochastic Processes, Academic Press, New York.

Khasminskii, R. Z., 1964, "On the Behavior of a Conservative System with Friction and Small Random Noise," (in Russian), *Prikladnaya Matematika i Mechanica* (Appl. Math and Mechanics), Vol. 28, No. 5, pp. 1126–1130.

Khasminskii, R. Z., 1966, "A Limit Theorem for the Solution of Differential Equations with Random Right Hand Sides," *Theory of Probability and Application*, Vol. 2, pp. 390–405.

Kozin, F., 1982, "First-Passage Times—Some Results," *Proceedings of the International Workshop on Structural Mechanics*, Innsbruck, Austria, pp. 28–32.

Landa, P. S., and Stratonovich, R. L., 1962, "Theory of Stochastic Transitions of Various Systems Between Different States," (in Russian) *Vestnik MGU* (Proc. of Moscow University), Series III (1), pp. 33–45.

Lennox, W. C., and Fraser, D. A., 1974, "On the First-Passage Distribution for the Envelope of a Nonstationary Narrow-Band Stochastic Process," ASME JOURNAL OF APPLIED MECHANICS, Vol. 41, pp. 793–797.

Roberts, J. B., 1976, "First Passage Probability for Nonlinear Oscillator," *ASCE Journal of Engineering Mechanics*, Vol. 102, pp. 851–866.

Roberts, J. B., 1978, "First-Passage Time for Oscillators with Nonlinear Damping," ASME JOURNAL OF APPLIED MECHANICS, Vol. 45, pp. 175–180.

Sri Namachchivaya, N., 1991, "Co-dimension Two Bifurcations in the Presence of Noise," ASME JOURNAL OF APPLIED MECHANICS, Vol. 58, pp. 259–265.

Sri Namachchivaya, N., 1989, "Instability Theorem Based on the Nature of the Boundary Behavior for One Dimensional Diffusion," *SM Archives*, Vol. 14, pp. 131–141.

Stratonovich, R. L., 1963, *Topics in the Theory of Random Noise*, Vol. 1, Gordon and Beach, New York.

Zhang, Z. Y., and Kozin, F., 1990, "On Almost Sure Sample Stability of Nonlinear Stochastic Dynamic Systems," *Proceedings of IEEE International Conference on System Engineering*, Pittsburgh, PA, Aug. 9–11.

Zhu, W. Q., and Lei, Y., 1989, "First Passage Time for State Transition of Randomly Excited Systems," *Proceedings of 47th International Statistical Institute Meeting*, Paris, Aug. 29–Sept. 6, pp. 517–531.

Downloaded 03 May 2010 to 171.66.16.20. Redistribution subject to ASME license or copyright; see http://www.asme.org/terms/Terms_Use.cfm

Component Modal Synthesis Methods Based on Hybrid Models, Part I: Theory of Hybrid Models and Modal Truncation Methods

L. Jezequel

H. D. Seito

Laboratoire de Tribologie et de Dynamique des Systemes, URA CNRS 855, Ecole Centrale de Lyon, 36, av. Guy de Collongue, 69131 Ecully Cedex, France

The assembly of structures along continuous boundaries poses great difficulties for expressing generalized boundary coordinates in modal synthesis, especially in the context of experiments. In order to solve such problems, a hybrid modal synthesis method is proposed in this study. This approach is based on the intermediate problem theory of Weinstein and brings out the duality between the formulation in displacement and the formulation in force. Generalized boundary coordinates are defined by introducing static deformations resulting from force distribution or displacement distribution along the boundaries depending on which formulation is to be used. By introducing integral operators associated with intermediate problems, two new methods of modal truncation can be proposed.

1 Introduction

The basic idea behind modal synthesis methods is to describe the behavior of a structure by using its first modes. The first method was proposed by Hurty (1965). In accordance with the Rayleigh-Ritz procedure, Hurty's method consists in describing the displacement of each substructure as a superposition both of the fixed-interface modes obtained by clamping the boundaries and of static deformations defined from the connection points and rigid-body modes in the case of a free structure. The second possibility which corresponds to the utilization of free modes was proposed by Goldman (1968). In this case, the assembly of the structure can be ensured either implicitly, by directly imposing the boundary conditions, or explicitly through the use of Lagrange multipliers Hou (1969).

The methods of modal synthesis which allow one to describe the dynamic behavior of complex structures with a low numerical cost have had a great number of applications. This success is primarily due to the possibility of applying them indifferently to substructure models resulting from a discretization by finite elements or from models constructed by experimental testing. In fact, the rise of these methods has coincided with the extension of numerical acquisition chains allowing an automatic and reliable identification of the mode characteristics based on dynamic testing. Yet the synthesis methods utilizing fixed-interface modes necessitate the measurement of static modes, which is experimentally hard to realize.

Furthermore, the methods in which the free modes are utilized need the identification of a large number of modes since the effective number of degrees-of-freedom of the models decreases when the number of linking compatibility equations increases. Thus the majority of applications of these methods has been limited to assemblies of mechanical systems with a low number of connecting points.

The methods of modal synthesis have been reformulated so as to make them compatible with the finite element method. This reformulation has been carried out by utilizing, to represent the boundary displacements, the constraint modes introduced by Craig and Bampton in the context of the fixed component modes synthesis method (Craig and Chang, 1977). Also in the free component mode synthesis method implemented in the current version of MCS/NASTRAN and COSMIC/NASTRAN, the first free modes of the component are reinterpreted in terms of physical coordinates at connecting points. The rigid-body modes are thus associated with inertia relief modes corresponding to static deflection patterns for the interior degree-of-freedom of the component with the fixed boundary induced by an inertia loading corresponding to the component being accelerated as a rigid body. Moreover, pressure modes can be introduced to produce a statically complete solution by using a component mode synthesis method (Allen, 1987).

The principal aim of the improvement in modal synthesis techniques has been to reduce the influence of the nonretained modes. Three types of procedures can be distinguished:

- *utilization of loaded modes*, which are obtained when adjacent substructures are replaced by boundary loadings obtained through Guyan dynamic condensation (Benfield and Hruda, 1991; Jezequel, 1980).

Contributed by the Applied Mechanics Division of THE AMERICAN SOCIETY OF MECHANICAL ENGINEERS for publication in the ASME JOURNAL OF APPLIED MECHANICS.

Discussion on this paper should be addressed to the Technical Editor, Professor Lewis T. Wheeler, Department of Mechanical Engineering, University of Houston, Houston, TX 77204-4792, and will be accepted until four months after final publication of the paper itself in the ASME JOURNAL OF APPLIED MECHANICS.

Manuscript received by the ASME Applied Mechanics Division, Jan. 30, 1991; final revision, June 29, 1992. Associate Technical Editor: P. D. Spanos.

Copyright © 1994 by ASME

Downloaded 03 May 2010 to 171.66.16.20. Redistribution subject to ASME license or copyright; see http://www.asme.org/terms/Terms_Use.cfm

• *utilization of residual terms*, which correspond to an asymptotic development of the spectral problem's resolvent, to approximate the participation of the nonretained modes (Craig, 1987; Craig and Chang, 1976, 1977; Jezequel, 1985a, b; MacNeal, 1971; Rubin, 1975).
• *utilization of a subspace iteration method*, which consists of using an iterative procedure to approximate the exact modes of the assembly. At each stage, the set of substructure admissible vectors is improved by calculating the dynamic response to the interface forces exerted by the rest of the structure as it vibrates in the computed lower modes (Beninghof, 1987; Hale and Meirovitch, 1982a, b; Kline, 1986).

Furthermore, the procedures employed to reduce the influence of modal truncation are difficult to apply in an experimental context. Thus the efficiency of the substructure method based on the utilization of loaded modes is only assured for stiffness and mass loading which allow one to approach the dynamic behavior of the adjacent component, and which are practically impossible to realize during vibration testing.

Nevertheless, a study of a space shuttle configuration carried out by Goldenberg and Shapiro (1973) has shown an interest in introducing mass loading at the connection points. This procedure provides the least complicated means of deforming the local structure near interface boundaries in the lower component modes (Coleman et al., 1988). The subspace iteration method can only be used in a numerical context. The residual flexibility matrices identified from vibration testing contain many errors and are virtually unusable in the case of a great number of boundary degrees-of-freedom. In the case of a modal synthesis based on the fixed interface modes, the residual terms appear inaccessible unless one introduces static solutions, which are always difficult to obtain experimentally.

In order to avoid these difficulties, the modal hybrid synthesis method proposed in Jezequel (1985a) utilizes generalized boundary coordinates to describe substructure connections along continuous boundaries. This procedure, originally inspired by the works of Meirovitch on intermediate structures (Hale and Meirovitch, 1982a, b), is based on the intermediate problem theory of Weinstein and Stenger (1972). In Jezequel (1985a), the method is explained for the case of a synthesis with free modes, thus using an individual flexibility matrix corrected with the aid of vibration testing. The generalized boundary coordinates, defined thanks to the introduction of loaded modes, proved to be highly representative of the boundary deformability in the low-frequency field. This procedure can then be presented as a *double modal synthesis*. The first modal synthesis is classical. It consists of representing the displacements of interior points of the structure by free or fixed-interface modes. The second modal synthesis consists of describing the boundary forces through the use of a set of loaded modes. The modal models thus obtained, despite the low number of degrees-of-freedom they possess, have proved to be quite efficient (Sehmi, 1985). Furthermore, in the case of the fixed-interface component modes method, the procedure proposed in Jezequel (1980) utilizes (in similar way) boundary loading to describe boundary displacement. It has given very good results in the case of highly damped plates. Thus the introduction of loading modes, called *branch modes* in Gladwell (1964) and Jezequel (1980, 1985a), has proved to be an efficient means of avoiding the difficulty in assuring compatibility conditions at the connection in the case in which substructures are identified by vibration testing. In order to analyze the convergence of this double modal synthesis, we linked it to the intermediate problems of the first type introduced by Weinstein. This approach will be the basis of the modal synthesis theory which we propose in this study. The theory brings out the duality between the formulation in displacement linked to the free component mode method and the formulation in force linked to the fixed component mode method (Jezequel, 1985b). In light of this analysis, new coupling procedures which are applicable in modal synthesis will be obtained by applying methods developed in a classical way for the displacement formulation in the context of the constraint formulation and vice versa.

Moreover, the introduction of integral operators associated with intermediate problems will allow us to propose two new methods of truncation and to explain the more or less close relationship of the diverse methods of modal synthesis usually used. In particular, we will introduce a truncation by projection, which to our knowledge has never been introduced in the framework of modal synthesis. However, we will see that this technique allows us to obtain a good estimation of resonance frequency when fixed-interface modes are utilized and a lower bound frequency when free modes are utilized. The general formalism which is introduced allows us to group all of the structural dynamics problems. The accompanying paper (Jezequel and Setio, 1994) will attempt to present the construction of the modal models defined in this paper in a numerical context and will examine their identification based on vibration tests when no numerical model is available. The assembly process of the substructures will also be studied and tested in simple case.

2 Equilibrium Equation of a Substructure

2.1 Formulation in Displacement. According to the classic linearity hypothesis, the free vibration of an elastic medium satisfies an equilibrium equation where an elliptical operator A of order $2m$ appears:

$$A\bar{u} = -\rho \frac{\partial^2 \bar{u}}{\partial t^2} \quad \forall M \in \Omega. \tag{1}$$

We denote by Ω a bounded space of R^N of boundary S, a variety differentiable of class C^m. As the substructure considered will be part of an assembly, it is interesting to show in the boundary conditions the particular interface Γ_i where coupling forces with adjacent substructures work like that shown in Fig. 1.

$$\forall M \in S_{1i} \quad D_i \bar{u} = 0 \tag{2a}$$

$$\forall M \in S_{2i} \quad F_i T \bar{u} = 0 \tag{2b}$$

$$\Gamma_i \qquad F_i T \bar{u} = -f_i \tag{2c}$$

The boundary operators D_i, which are of order less than m, correspond to the kinematic conditions on m parts of S_{1i} (eventually $S_{1i} = \phi$) and consists of a normal system on S. The boundary operators $F_i T$, of order between m and $2m-1$, are adjoint to the operator A and to a Green formula of the system $\{D_i\}$, thus proving

$$a(u, v) = (Au, v) - \sum_{i=1}^{m} (F_i T u, D_i v)_{Si}. \tag{3}$$

The bilinear form $a(.\ ,\ .)$ is associated with the elastic energy, and the scalar product $(.\ ,\ .)_{Si}$ is associated with all functions that are defined along the boundary S_i and that are square integrable. The operator T gives generalized stress from the displacement field. This operator allows one to link the elastic

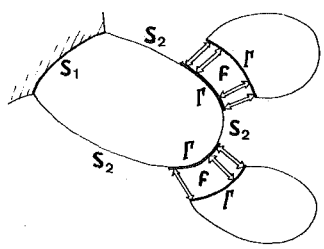


Fig. 1 Substructure assembly

Downloaded 03 May 2010 to 171.66.16.20. Redistribution subject to ASME license or copyright; see http://www.asme.org/terms/Terms_Use.cfm

energy expressed as a function of stress to the elastic energy expressed as a function of displacements.

$$a(u, v) = t(Tu, Tv) \tag{4}$$

Let $\overline{E}$ be the stress space completed by the scalar product $t(.\ ,\ .)$. The operator T appears in the canonical decomposition of the operator A

$$A = T^* T. \tag{5}$$

The coupling force distribution f_i can be introduced in a condensed form by adding the following formal scalar product:

$$\sum_{i=1}^{m} (F_i Tu, D_i v)_{\Gamma_i} = \langle FTu, Dv \rangle, \tag{6}$$

that is

$$\sum_{i=1}^{m} (f_i, D_i v)_{\Gamma_i} = \langle f, Dv \rangle. \tag{7}$$

Given boundary conditions (2*a*) and (2*b*), the Green's formula becomes

$$a(u, v) = (Au, v) + \langle f, Dv \rangle. \tag{8}$$

Let $\tilde{U}_L$ be the space of admissible displacements obtained by completing the space U_L, which consists of functions that are sufficiently differentiable and which satisfy the kinematic conditions (2*a*), with the aid of scalar product defined by

$$\tilde{a}(u, v) = a(u, v) + (\rho u, v). \tag{9}$$

In order to apply these methods to vibration problems associated with differential inertia operators, the space engendered by the scalar product $(\rho\ .\ ,\ .)$ with be termed $\overline{L}$.

Let $\tilde{U}_E$ be the complete space obtained by closing with the scalar product $\tilde{a}(.\ ,\ .)$, the set of functions which are sufficiently differentiable and satisfy the kinematic conditions (2*a*) and which give zero generalized displacement along boundaries Γ_i.

$$\tilde{U}_E = \{u/u \in \tilde{U}_L,\ M \in \Gamma_i:\ D_i u = 0\} \tag{10}$$

This space is a closed subspace of $\tilde{U}_L$.

$$\tilde{U}_E \subset \tilde{U}_L \tag{11}$$

It is important to introduce the space L_R which corresponds to displacement fields that do not induce any stress.

$$L_R = \{u/u \in \overline{L},\ Tu = 0\} \tag{12}$$

The orthogonal complement of this space with respect to the scalar product $\overline{L}$ is termed $L_R^{\perp}$. That is

$$L_R^{\perp} = \overline{L} \ominus L_R. \tag{13}$$

In the case where the kernel of L_R is not empty, the following spaces of admissible displacements must be introduced:

$$\overline{U}_L = \tilde{U}_L \cap L_R^{\perp} \tag{14a}$$

$$\overline{U}_E = \tilde{U}_E \cap L_R^{\perp} \tag{14b}$$

In the framework of a formulation in displacement, the solution of the dynamic problem is associated to a compact operator defined with the aid of the Reisz theorem:

$$a(G_L u, v) = (\rho u, v) \quad \forall u,\ \forall v \in \overline{U}_L. \tag{15}$$

This compact operator is self-adjoint with respect to the scalar products used to build spaces $\overline{L}$ and $\overline{U}_L$

$$a(G_L u, v) = a(u, G_L) \quad \forall u,\ \forall v \in \overline{U}_L \tag{16a}$$

$$(\rho G_L u, v) = (\rho u, G_L v) \quad \forall u,\ \forall v \in \overline{U}_L. \tag{16b}$$

This compact operator is a Hilbert-Schmidt one. This class is made up of integral operators which have a kernel belonging to the product space $L^2(\Omega)\ XL^2(\Omega)$ and which can be developed in series in the basis of the solutions to the eigenproblem associated with the free modes of the structure when no force is exerted along boundaries Γ_i:

$$Ax_{Li} = \omega_L^2 \rho x_{Li} \quad \forall M \in \Omega \tag{17a}$$

$$D_i x_{Li} = 0 \quad \forall M \in S_{1i} \tag{17b}$$

$$F_i T x_{Li} = 0 \quad \forall M \in S_{2i} \tag{17c}$$

$$F_i T x_{Li} = 0 \quad \forall M \in \Gamma_i. \tag{17d}$$

Thus if operator G_L is a Hilbert Schmidt operator, it can be expressed in the following series form:

$$G_L = \sum_{i=1}^{\infty} \gamma_{Li}(.\ ,\ \rho x_{Li}) x_{Li} \tag{18a}$$

with

$$\gamma_{Li} = \omega_{Li}^2. \tag{18b}$$

This series converges absolutely and uniformly if operator G_L is applied to a square-integrable function.

In the case of unbounded domains, the operators are no longer compact, but the notion of singular values allows some substructuring methods to be extended to operators which are bounded. When the substructure has rigid body modes, the compact operator $\tilde{G}_L$, defined by the following equation, should be introduced:

$$\tilde{a}(\tilde{G}_L u, v) = (\rho u, v) \quad \forall u,\ \forall u,\ v \in \tilde{U}_L. \tag{19}$$

This operator possess the same eigenvectors as G_L and it possesses eigenvalues which are directly related to those of G_L. Likewise, in the modal synthesis methods using fixed-interface modes, the compact operator defined below will need to be introduced

$$a(G_E u, v) = (\rho u, v) \quad \forall u,\ \forall v \in \overline{U}_E. \tag{20}$$

The eigenvectors x_{Ei} and eigenvalues ω_{Ei}^{-2} of this operator are obtained by solving the modal problem which corresponds to clamped boundaries Γ_i. Thus

$$Ax_{Ei} = \omega^2 \rho X_{LI} \quad \forall M \in \Omega \tag{21a}$$

$$D_i x_{Ei} = 0 \quad \forall M \in S_{1i} \tag{21b}$$

$$F_i T x_{Ei} = 0 \quad \forall M \in S_{2i} \tag{21c}$$

$$D_i x_{Ei} = 0 \quad \forall M \in \Gamma_i. \tag{21d}$$

The free and fixed modes of the substructure considered can also be obtained from a weak formulation

$$a(x_{Li}, v) = \omega_{Li}^2 (\rho x_{Li}, v) \quad \forall v \in \overline{U}_L \tag{22}$$

$$a(x_{Ei}, v) = \omega_{Ei}^2 (\rho x_{Ei}, v) \quad \forall v \in \overline{U}_E. \tag{23}$$

These normal modes satisfy the classical orthogonality properties

$$(\rho x_{Li}, x_{Lj}) = \delta_{ij} \tag{24a}$$

$$a(x_{Li}, x_{Lj}) = \omega_{Lj}^2 \delta_{ij} \tag{24b}$$

$$(\rho x_{Ei}, x_{Ej}) = \delta_{ij} \tag{24c}$$

$$a(x_{Ei}, x_{Ej}) = \omega_{Eij}^2 \delta_{ij}. \tag{24d}$$

This kinematic expression is directly linked to Hamilton's principle of least action applied to the case of harmonic solutions.

2.2 Formulation in Force. Likewise, by using the canonic decomposition of operator A given in Eq. (5), a *formulation in force* of dynamic equilibrium of the elastic medium can be obtained and will be linked to Toupin's variational principle.

In fact, if harmonic solutions of pulsation ω are sought, the equilibrium Eq. (1) becomes

$$Au = \omega^2 \rho u. \quad \forall M \in \Omega \tag{25}$$

If the canonic decomposition of A is used, one can write

$$\overline{u} = \frac{1}{\rho} T^* \sigma \tag{26a}$$

with

Downloaded 03 May 2010 to 171.66.16.20. Redistribution subject to ASME license or copyright; see http://www.asme.org/terms/Terms_Use.cfm

$$\bar{u} = \omega^2 u \text{ and } \sigma = Tu. \tag{26b}$$

By applying operator T to both members of Eq. (26), we obtain a dynamic equilibrium equation in terms of the stress function

$$B\sigma = \omega^2 \sigma \quad \forall M \in \Omega. \tag{27}$$

This equation shows up the differential operator B of order $2m$ given by

$$B = T \frac{1}{\rho} T^*. \tag{28}$$

In the case where the continuous medium is subjected to a load $\{f_i\}$ along boundaries Γ_i, the following boundary conditions must be included to the equilibrium equation in stress:

$$\forall M \in S_{1i} \quad D_i \frac{1}{\rho} T^* \sigma = 0 \tag{29a}$$

$$\forall M \in S_{2i} \quad F_i \sigma = 0 \tag{29b}$$

$$\forall M \in \Gamma_i \quad F_i \sigma = -f_i. \tag{29c}$$

Let V_E be the space of the functions which are sufficiently differentiable and which satisfy the zero force conditions along boundaries $\{S_{2i}\}$.

As this expression in stress will be linked to modal synthesis methods utilizing fixed-interface modes, it is more interesting to study an associated problem which is obtained by imposing generalized displacements $\{d_i\}$ along boundaries Γ_i. This problem is governed by the following boundary conditions:

$$\forall M \in S_{1i} \quad D_i \frac{1}{\rho} T^* \sigma = 0 \tag{30a}$$

$$\forall M \in S_{2i} \quad F_i \sigma = 0 \tag{30b}$$

$$\forall M \in \Gamma_i \quad D_i \frac{1}{\rho} T^* \sigma = d_i \omega^2 = \bar{d}_i. \tag{30c}$$

From Green's formula, written in the form (8), we obtain the equation

$$t\left(T \frac{1}{\rho} T^* \sigma, \tau\right) = \left(\frac{1}{\rho} T\sigma, T\tau\right) - \langle \bar{d}, \tau \rangle. \tag{31}$$

In order to obtain a comparable variational principle to that obtained in displacement, it appears natural to introduce the following bilinear form:

$$b(\sigma, \tau) = \left(\frac{1}{\rho} T^* \sigma, T^* \tau\right). \tag{32}$$

This form cannot generate a norm in the stress space $\bar{E}$ since the self-equilibrated stress fields would cancel it out. It is thus necessary to introduce the space E_S defined below:

$$E_S = \{\tau / \tau \in \bar{E}, \ T^* \tau = 0\}. \tag{33}$$

This closed space is analogous to that of all of the rigid-body modes L_R in the displacement formulation. Its orthogonal complement with respect to scalar product $t(.\ ,\ .)$ in space $\bar{E}$ is termed $E_S^{\perp}$.

$$E_S^{\perp} = \bar{E} \ominus E_S. \tag{34}$$

The sufficiently differentiable function space which belongs to $E_S^{\perp} \cap V_E$ can be completed with the aid of the scalar product $b(.\ ,\ .)$. In this space, termed $\bar{V}_E$, a weak formulation of the associated problem defined by boundary conditions (30) is obtained:

$$b(\sigma, \tau) = \omega^2 t(\sigma, \tau) + \langle \bar{d}, F\tau \rangle \quad \forall \tau \in \bar{V}_E. \tag{35}$$

In particular, the fixed-interface modes obtained by imposing $\bar{d} = 0$ are weak solutions of

$$b(y_{Ei}, \tau) = \omega_{Ei}^2 t(y_{Ei}, \tau) \quad \forall \tau \in \bar{V}_E. \tag{36}$$

The fixed-interface modes y_{Ei} are linked to the normal modes previously introduced by

$$y_{Ei} = T x_{Ei}. \tag{37}$$

The bilinear form $b(.\ ,\ .)$ induces a compact and self-adjoint operator H_E that satisfies

$$b(H_E \sigma, \tau) = t(\sigma, \tau) \quad \forall \sigma, \ \forall \tau \in \bar{V}_E. \tag{38}$$

So as to make the best use of the force formulation in the modal synthesis methods, it is necessary to introduce the space $\tilde{V}_E$ obtained by completing the space V_E with the scalar product $b(.\ ,\ .)$ defined by

$$\tilde{b}(\sigma, \tau) = b(\sigma, \tau) + t(\sigma, \tau). \tag{39}$$

Since in $\bar{V}_E$ the norms induced by b and $\tilde{b}$ are equivalent, we obtain the relationship

$$\bar{V}_E = \tilde{V}_E \cap E_S^{\perp}. \tag{40}$$

Let $\tilde{V}_L$ be the space engendered by functions of $\tilde{V}_E$ which satisfy the free-edge conditions along boundaries Γ_i

$$\tilde{V}_L = \{\sigma / \sigma \in \tilde{V}_E, \ \forall M \in \Gamma_i : F_i \sigma = 0\}. \tag{41}$$

than is a closed subspace of $\tilde{V}_E$.

$$\tilde{V}_L \subset \tilde{V}_E \tag{42}$$

This inclusion relationship disappears when the intersections of these spaces with $E_S^{\perp}$ are considered. The bilinear form $b(.\ ,\ .)$ induces a self-adjoint operator in space $\tilde{V}_E$.

$$\tilde{b}(\tilde{H}_E \sigma, \tau) = t(\sigma, \tau) \quad \forall \sigma, \ \forall \tau \in \tilde{V}_E \tag{43}$$

This operator has the same eigenvectors as H_E and eigenvalues which are directly linked to those of H_E. It also has the eigenvalue $\tilde{\gamma}_E = 1$ which is generally of infinite multiplicity. However, in the case of beams, this operator is compact for E_S and is then of finite dimension.

The aim of the modal synthesis methods presented in this study is to describe, as well as possible, the dynamic behavior of substructures subjected to loads along connecting boundaries Γ_i. We shall first study an isolated structure in order to obtain its fixed-interface modes from a description based on its free modes, and conversely, its free modes from a description based on its fixed-interface modes like those show in Fig. 2. The method used is based on the introduction of intermediate problems which will be extended in Part II of this paper to the calculation of the modes of an assembly of substructures.

3 Intermediate Problem Definition

3.1 Formulation in Displacement. In accordance with the primal formulation based on displacement field u, we consider the operator $\tilde{G}_L$ defined by Eq. (19). This operator corresponds to the kinematic conditions given in Eq. (2*a*) and its eigenvectors belong to space $\tilde{U}_L$. In order to obtain from $\tilde{G}_L$ a resonance frequencies ω_{Ei} of the substructure that satisfies the additional kinematic conditions (21*d*), the complement orthogonal with respect to scalar product $\tilde{a}(.\ ,\ .)$ of $\tilde{U}_E$, the closed subspace of $\tilde{U}_L$, should be introduced.

$$\tilde{W}_L = \tilde{U}_L \ominus \tilde{U}_E \tag{44}$$

This is the equivalent of

$$\tilde{a}(v, u) = 0 \quad \forall u \in \tilde{W}_L \rightarrow v \in \tilde{U}_L. \tag{45}$$

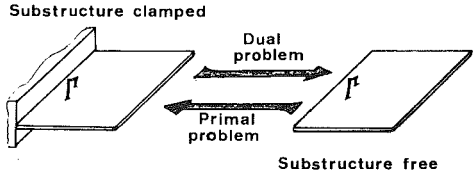


Fig. 2 Definition of basic problems for one isolated substructure

Downloaded 03 May 2010 to 171.66.16.20. Redistribution subject to ASME license or copyright; see http://www.asme.org/terms/Terms_Use.cfm

In order to construct the space $\tilde{W}_L$, functions $\tilde{p}$ that are solutions to the following pseudo-static problems are introduced

$$a(\tilde{p},v) + (\rho\tilde{p},\ v) = \langle f,\ Dv\rangle \quad \forall v \in \tilde{U}_L. \tag{46}$$

Each solution $\tilde{p}$ can be projected onto the previously defined space L_R.

$$\tilde{p} = p_R + \hat{p} \cdot \quad p_R \in L_R \tag{47}$$

This decomposition corresponds to the direct sum in space $\tilde{U}_L$, induced by space $\overline{U}_L$ defined in Eq. (14*a*).

$$\tilde{U}_L = \overline{U} \oplus \overline{L}_R \tag{48}$$

$$p_R \in \overline{L}_R \text{ and } p \in \overline{U}_L \tag{49}$$

where $\overline{L}_R$ is the projection of $\tilde{U}_L$ in L_R.

We consider the space $\tilde{W}_{Lk}$ of finite dimension engendered by k independent solutions $\tilde{p}_i$ and the projection operator $\tilde{P}_k$ on this space. The intermediate problem of order k corresponds to the search for the spectrum of operator G_L projected onto the orthogonal complement of $\tilde{W}_{Lk}$

$$\tilde{Q}_k \tilde{G}_L \tilde{Q}_k u = \tilde{\gamma}^{(k)} u \tag{50a}$$

with

$$\tilde{Q}_k = I - \tilde{P}_k. \tag{50b}$$

The characteristic values $\tilde{\omega}^{2(k)} = \tilde{\gamma}^{-1(k)}$ of this operator lead to lower bounds of the resonance frequencies ω_{Ei} of the fixed-interface modes obtained by imposing kinematic condition (21*d*)

$$\omega_i^{(0)} < \omega_i^{(1)} \leq \ldots \leq \omega_i^{(k)} \leq \ldots < \omega_i^{(\infty)} = \omega_{Ei} \tag{51a}$$

with

$$\omega_i^{(k)} = (\tilde{\omega}_i^{2(k)} - 1)^{1/2}. \tag{51b}$$

This estimation of resonance frequencies can be linked to Weinstein's Max-Min principle (Weinstein and Stenger, 1972), which seems to be the opposite of the Min-Max principle used in the Rayleigh-Ritz method, where the projection spaces of the operators are of increasing dimension.

The eigenvalue problem given in Eq. (50*a*) can be written in the following equivalent form:

$$\tilde{Q}_k \tilde{G}_L u = \tilde{\gamma}^{(k)} u. \tag{52}$$

Consequently we can write

$$\gamma^{(k)} u = G_L u - P_k G_L u, \tag{53}$$

and by multiplying both members of this equation by P_k we obtain

$$\begin{aligned} \tilde{P}_k u &= 0 \\ \tilde{Q}_k u &= u. \end{aligned} \tag{54}$$

Equation (52) corresponds to the *intermediate problem* of the first type, which is written in the form

$$u - \tilde{\omega}^2 \tilde{G}_L u = \sum_{i=1}^{m} \tilde{p}_i \mu_i \tag{55a}$$

with

$$-\tilde{\omega}^2 \tilde{P}_k \tilde{G}_L u = \sum_{i=1}^{m} \tilde{p}_i \mu_i. \tag{55b}$$

Freedom's integral equation (55*a*) gives displacement u as a function of generalized forces μ_i,

$$u = \sum_{i=1}^{m} \tilde{R}_L \tilde{p}_i u_i. \tag{56}$$

The resolvent $\tilde{R}_L$ is the compact operator defined by

$$\tilde{R}_L = (I - \tilde{\omega}^2 \tilde{G}_L)^{-1}. \tag{57}$$

The condition (54) corresponds to a set of k constraint equation

$$\tilde{a}(u,\ \tilde{p}_i) = 0 \quad \forall i \in [1,\ k]. \tag{58}$$

Linked to relation (56), these equations give the following symmetrical and homogeneous system:

$$[\tilde{S}]\{\mu_i\} = 0 \tag{59a}$$

with

$$\tilde{S}_{ji} = \tilde{a}(\tilde{R}_L \tilde{p}_j,\ \tilde{p}_i). \tag{59b}$$

The pseudo-frequencies $\tilde{\omega}_i$ appear to be values which null out Weinstein's determinant, that is,

$$\det \tilde{S}(\tilde{\omega}) = 0. \tag{60}$$

The matrix system (59) suggests the introduction of generalized displacement λ_j associated with generalized forces and defined by

$$\lambda_j = \tilde{a}(u,\ \tilde{p}_j). \tag{61}$$

Thus taking the definition of stress functions p_j given in Eq. (46),

$$\lambda_j = \langle f_j,\ Du\rangle. \tag{62}$$

Terms $\tilde{S}_{ij}$ which are contained in Weinstein's determinant utilize quantities associated with operator $\tilde{G}_L$ which do not represent the actual behavior of the structure. For such a method to be applied experimentally, the resolvent R_L associated with operator G_L and defined in space $\overline{U}_L$ must be introduced,

$$R_L = (I - \omega^2 G_L)^{-1}. \tag{63}$$

It is also useful to introduce new static deformations p_i that are associated with force distributions f_i and that are solutions to the following static problems

$$a(p_i,\ v) = \langle f,\ Dv\rangle \quad \forall v \in \overline{U}_L. \tag{64}$$

By using the relationship between operators G_L and $\tilde{G}_L$ we obtain

$$\tilde{a}(\tilde{R}_L p_i,\ p_j) = a(R_L p_i,\ p_j) \quad \forall i,\ \forall j. \tag{65}$$

By using the decomposition given in Eq. (47) and the scalar product definition $\tilde{a}(.\ ,\ .)$, the coefficients involved in Weinstein's determinant become

$$\tilde{S}_{ji} = a(p_j,\ R_L p_i) - \omega^2(\rho \tilde{R}_L p_{Rj},\ p_{Ri}). \tag{66}$$

Projections p_{Ri} of $\tilde{p}_i$ in space $\overline{L}_R$ are solutions of

$$(\rho p_{Ri},\ v) = \langle f_i,\ Dv\rangle \quad \forall v \in \overline{L}_R. \tag{67}$$

The restriction of resolvent $\tilde{R}_L$ to space $\overline{L}_R$ is easily expressed,

$$R_L v = -\omega^{-2} v \quad \forall v \in L_R. \tag{68}$$

The resonance frequencies of the intermediate problem of order k thus null out the following determinant:

$$\det[S_{ji}(\omega) - \omega^{-2}(\rho p_{Rj},\ p_{Ri})] = 0 \tag{69a}$$

with

$$S_{ji}(\omega) = a(p_j,\ R_L p_i). \tag{69b}$$

We obtain a comparable problem to that of Kron (Sehmi, 1985), and solutions ω_i are obtained by the Wittrick-Williams algorithm (Wittrick and Williams, 1971).

If the structure possess r rigid-body modes, displacement fields p_i are the projection onto $\overline{U}_L$ of static displacements obtained by applying boundary force distributions f_i and by imposing r constraints.

Resolvent R_L satisfies the following equation:

$$R_L = I + \omega^2 G_L R_L. \tag{70}$$

The terms of the dynamic flexibility matrix S can thus be written in the form

$$S_{ji} = a(p_j,\ p_i) + \omega^2(\rho p_j,\ R_L p_i). \tag{71}$$

3.2 Formulation in Force. The dual hybrid formulation which utilizes a stress field is based on the same Min-Max principle as the primal hybrid formulation. The base problem

Downloaded 03 May 2010 to 171.66.16.20. Redistribution subject to ASME license or copyright; see http://www.asme.org/terms/Terms_Use.cfm

corresponds to operator $\tilde{H}_E$ defined in Eq. (43). The projection fields are defined from stress fields which are weak solutions of the following problems:

$$\tilde{b}(\tilde{\tau}, \sigma) = \langle \bar{d}, F\sigma \rangle \quad \forall \sigma \in \tilde{V}_E. \tag{72}$$

The space engendered by the solutions associated with displacements d_i *of* $L^2(\Gamma)$ is dense in the closed subspace $\tilde{W}_E$ defined by

$$\tilde{W}_E = \tilde{V}_E \ominus \tilde{V}_L \tag{73}$$

which also can be written as

$$\tilde{b}(\sigma, \tilde{\tau}) = 0 \quad \forall \tau \in \tilde{W}_E \rightarrow \sigma \in \tilde{V}_L. \tag{74}$$

The intermediate problem of order k is defined from subspace $\tilde{W}_{Ek}$ engendered by k solutions $\tilde{\tau}_i$ and from the projection operator $\tilde{K}_k$ onto this space with respect to scalar product $\tilde{b}(.\ ,\ .)$, say

$$\tilde{J}_k \tilde{H}_E \tilde{J}_k \sigma = \tilde{\gamma}^{(k)} \sigma \tag{75}$$

with

$$\tilde{J}_k = I - \tilde{K}_k.$$

Just as in the primal formulation, the spectrum of operator $\tilde{J}_k\, \tilde{H}_E\, \tilde{J}_k$ can be obtained from Freedolm's equation.

$$\sigma - \tilde{\omega}^2 \tilde{H}_E \sigma = \sum_{i=1}^{m} \lambda_i^* \tilde{\tau}_i \tag{76}$$

with

$$\tilde{\omega}^2 = \tilde{\gamma}^{-1}.$$

By introducing the resolvent in force defined by

$$\tilde{R}_E = (I - \tilde{\omega}^2 \tilde{H}_E)^{-1}, \tag{77}$$

the stress field σ can be expressed as a function of the generalized displacement λ_i^* associated with the stress fields τ_i

$$\sigma = \sum_{i=1}^{m} \tilde{R}_E \tilde{\tau}_i \lambda_i^*. \tag{78}$$

To this equation must be added k constraint equations corresponding to the projection of the operator onto space $\tilde{V}_E \ominus \tilde{W}_{Ek}$

$$\tilde{b}(\sigma, \tilde{\tau}_i) = 0 \quad \forall i \in [1, k]. \tag{79}$$

This formulation, linked to Eq. (72), suggests the introduction of generalized force defined by

$$\mu_i^* = -\omega^{-2} \tilde{b}(\sigma, \tilde{\tau}_i) \tag{80}$$

say

$$\mu_i^* = -\langle d_i, F\sigma \rangle \tag{81}$$

with

$$d_i = \bar{d}_i \omega^{-2} \quad \omega^2 = \tilde{\omega}^2 - 1. \tag{82}$$

Given relation (78), Eq. (79) gives the following homogeneous system:

$$[\tilde{Z}]\{\lambda_j^*\} = 0 \tag{83}$$

with

$$\tilde{Z}_{ij} = -\omega^{-2} \tilde{b}(\tilde{R}_E \tilde{\tau}_j, \tilde{\tau}_i). \tag{84}$$

The resonance frequencies of the intermediate problem thus appear as the values ω which null out the Weinstein determinant

$$\det\, [\tilde{Z}_{ij}(\tilde{\omega})] = 0. \tag{85}$$

In order to use quantities actually measured during vibration tests, the terms of Weinstein's determinant must be related to resolvent R_E of operator H_E defined by

$$R_E = (I - \omega^2 H_E)^{-1}. \tag{86}$$

Such a result is obtained by projecting the stress functions $\tilde{\tau}_i$ onto space E_S, that is,

$$\tilde{\tau}_i = \bar{\tau}_{si} + \hat{\tau}_i. \tag{87}$$

This decomposition corresponds to the direct sum in space $\tilde{V}_E$ induced by space $\bar{V}_E$ defined in Eq. (46).

$$\tilde{V}_E = \bar{V}_E \oplus \bar{E}_S \tag{88}$$

whence

$$\hat{\tau}_i \in \bar{V}_E \text{ and } \bar{\tau}_{si} \in \bar{E}_S. \tag{89}$$

$\bar{E}_S$ is the projection of $\tilde{V}_E$ onto E_S.

The terms of the generalized impedance matrix defined in Eq. (84) are expressed as

$$\tilde{Z}_{ij} = -t(\tilde{R}_E \bar{\tau}_{si}, \bar{\tau}_{sj}) \omega^{-2} + \bar{Z}_{ij} \tag{90}$$

and the terms of matrix $\bar{Z}$ can be related to resolvent R_E by

$$\bar{Z}_{ij} = \omega^2 b(R_E \bar{\tau}_i, \bar{\tau}_j). \tag{91}$$

The stress fields $\bar{\tau}_i$ are defined by relation

$$b(\bar{\tau}_i, \sigma) = \langle \bar{d}_i, F\sigma \rangle \quad \forall \sigma \in \bar{V}_E \tag{92}$$

and the stress fields $\bar{\tau}_{si}$ are solutions of

$$t(\bar{\tau}_{si}, \sigma) = \langle \bar{d}_i, F\sigma \rangle \quad \forall \sigma \in \bar{E}_S \tag{93}$$

Projections of $\bar{\tau}_i$ thus appear as static stress fields obtained by imposing boundary displacements $-\omega^2 d_i$ along boundaries Γ. So if displacements d_i are supposed to be induced by the displacement stress functions p_i used in the primal hybrid formulation, we can write the following relations:

$$\bar{p}_i = \omega^2 p_i \quad \bar{\tau}_{si} = \omega^2 \tau_{si}$$

$$T\, p_i = -\tau_{si}. \tag{94}$$

Likewise, the stress fields τ_i, which belong to $\bar{V}_E$, can be related to the stress fields τ_{si} induced by the static solutions p_i.

$$\forall M \in \Omega \quad : \quad T^* \frac{1}{\rho} \tau_i = p_i \tag{95}$$

In fact, according to Green's relation (31), function $\bar{\tau}_i$ which satisfies relation (92) is the solution of the following differential problem of order m:

$$\forall M \in \Omega \quad B\tau_i = -\tau_{si} \tag{96a}$$

$$\forall M \in S_{1j} \quad D_j \frac{1}{\rho} T^* \tau_i = 0 \tag{96b}$$

$$\forall M \in S_{2j} \quad F_j\, \tau_i = 0 \tag{96c}$$

$$\forall M \in \Gamma_j \quad D_j \frac{1}{\rho} T^*\, \tau_i = d_i \tag{96d}$$

with

$$\tau_i = \bar{\tau}_i / \omega^2.$$

There is a unique solution to this equation in $\bar{V}_E$, but its existence depends on the compatibility conditions between τ_{si} and d_i, which corresponds to Eq. (93). The restriction of resolvent $\tilde{R}_E$ in space E_S is a simple expression

$$\tilde{R}_E \tau_{si} = \tau_{si} \omega^{-2} \quad \forall \tau \in E_S. \tag{97}$$

The generalized impedance matrix $\tilde{Z}$ then takes the following simple form:

$$\tilde{Z}_{ij} = t(\tau_{si}, \tau_{sj}) - \omega^2 \bar{M}_{ij} \tag{98}$$

with

$$\bar{M}_{ij} = b(R_E\, \tau_i, \tau_j). \tag{99}$$

The first term in Eq. (98*a*) can be written as a function of static deformations p_i and p_j as follows:

$$t(\tau_{si}, \tau_{sj}) = a(p_i, p_j). \tag{100}$$

In Jezequel (1985b) it is shown that the frequencies which cancel out Weinstein determinant tend towards the frequencies of free structures.

However, although the process used in the formulation in

Downloaded 03 May 2010 to 171.66.16.20. Redistribution subject to ASME license or copyright; see http://www.asme.org/terms/Terms_Use.cfm

force is based on a Min-Max principle, the calculated values are the upper bounds of free frequencies:

$$\omega_i^{(0)} \geq \omega_i^{(1)} \geq \ldots \geq \omega_i^{(k)} \geq \ldots \omega_i^{(\infty)} = \omega_{Li} \tag{101}$$

This apparent contradiction can be explained by the existence of the eigenvalues 0 to infinite multiplicity (Jezequel, 1985b).

4 Expression of the Resolvent

In formulating a dynamic problem with the aid of flexibilities S_{ij} and impedances Z_{ij}, one comes up against the difficulty of expressing resolvents. In the context of formulation in displacement, the problem is to calculate $R_L p_i$ solutions of the following equation:

$$(I - \omega^2 G_l) R_L p_i = p_i. \tag{102}$$

In accordance with modal synthesis methods, the projection operator P_n, with respect to the scalar product $(\rho \ . \ , \ .)$ onto the first n modes x_{Li}, is introduced. Equation (102) can then be written thus:

$$(I - \omega^2 P_n G_L P_n - \omega^2 Q_n G_L Q_n) R_L p_i = p_i \tag{103a}$$

with

$$Q_n = I - P_n.$$

Likewise, in the formulation in force, the projection operator $\overline{P}_n$ onto the first n modes in force y_{Ei}, is introduced in order to calculate $R_E \tau_j$.

$$(I - \omega^2 P_n H_E P_n + Q_n H_E Q_n) R_E \tau_i = \tau_i \tag{104a}$$

again with

$$Q_n = I - P_n. \tag{104b}$$

The various modal truncation methods correspond to simplification forms of operators $G_O = Q_n G_L Q_n$ and $H_O = \overline{Q}_n H_E \overline{Q}_n$.

4.1 Truncation of Rayleigh-Ritz Type. In this simplification the eigenvalues γ_{Li} or γ_{Ei} of order higher than n are replaced by zero, that is,

$$G_O = 0 \text{ or } H_O = 0.$$

The flexibility matrices utilized in the formulation in displacement are written, given relation (104), as

$$S_{ji} = \left[\sum_{l=1}^{n} \frac{\alpha_{jl}\alpha_{il}}{\omega_{Li}^2 - \omega^2} \omega_{Ll}^4 \right] \tag{105a}$$

with

$$\alpha_{il} = (\rho p_i, x_{Ll}). \tag{105b}$$

This method of truncation leads to a problem of n degrees-of-freedom, which corresponds to a Rayleigh-Ritz description associated to a modal base,

$$u = \sum_{i=1}^{n} q_i x_{Lj}. \tag{106}$$

As canceling out all of G_L's eigenvalues of order greater than n means increasing the stiffness of the substructure, the eigenvalues of the intermediate problem are no longer necessarily lower than those of fixed-interface modes. Also although this type of truncation reduces the effective degrees-of-freedom, it has an advantage in counterbalancing the real connections along boundaries Γ_i which are not taken into account.

In the framework of the formulation in force, this truncation method allows us to approximate the impedance matrix in the following form:

$$\tilde{Z}_{ij} = a(p_i, p_j) - \omega^2 \sum_{l=1}^{n} \frac{\beta_{il}\beta_{jl}}{\omega_{El}^2 - \omega^2} \omega_{El}^2 \tag{107a}$$

with

$$\beta_{il} = (\rho p_i, x_{El}). \tag{107b}$$

This expression is obtained thanks to relation (95a) and to the duality between T and T^*, leading to

$$t(Tx_{El}, \tau_j) = (x_{El}, T^* \tau_j) \tag{108a}$$

with

$$Tx_E = y_E \text{ and } T^* \tau_j = \rho p_j. \tag{108b}$$

The advantage of the Rayleigh-Ritz truncation procedure is that it gives upper bounds of free-mode resonance frequencies. The fact that the impedance matrices can be calculated from displacement solutions explains why most modal synthesis applications in solid mechanics are not presented in the framework of the formulation in force. It is important to note that when formulation in force is used, the modal model obtained using a Rayleigh-Ritz type truncation of the resolvant does not require any constraint modes associated with the boundary degrees-of-freedom to be introduced. Though such a model has often been used in acoustics when calculating pressure fields, it has never, to our knowledge, been introduced into structural dynamics.

4.2 Truncation by Projection. In order to obtain lower bounds of fixed-interface-mode resonance frequencies ω_{Ei} in spite of the modal base truncation, operator G_L can be maximized by attributing to all eigenvectors of order greater than n the eigenvalue γ_{Ln+1}, that is

$$G_0 = \overline{Q}_n G_L \overline{Q}_m = \gamma_{Ln+1} \overline{Q}_n. \tag{109}$$

Solution $R_L p_i$ is therefore approximated in the form

$$R_L p_i = \sum_{l=1}^{n} \frac{\alpha_{il} x_{Li}}{(1 - \omega^2/\omega_{Ll}^2)} + \frac{1}{(1 - \omega^2/\omega_{Ln+1}^2)} \left(p - \sum_{l=1}^{n} \alpha_{il} x_{Ll} \right) \tag{110}$$

Terms S_{ji}, which appear in Weinstein's determinant in Eq. (59), are thus written as

$$S_{ji} = \frac{a(p_i, p_j)}{(1 - \omega^2/\omega_{Ln+1}^2)} + \omega^2 \sum_{l=1}^{n} \alpha_{jl}\alpha_{il} \frac{(1 - \omega^2/\omega_{Ll}^2)}{(1 - \omega^2/\omega_{Ll}^2)(\omega^2/\omega_{Ll}^2)(\omega^2/\omega_{Ll}^2 - \omega_{Ln+1}^2/\omega_{Ll}^2)} \tag{111}$$

When the truncation by projection is utilized, frequencies which null out the Weinstein determinant will always be lower bounds of resonance frequencies of fixed-interface modes.

In the context of the formulation in force, a similar expression of the generalized mass matrix can be obtained

$$\overline{M}_{ij} = \frac{b(\tau_i, \tau_j)}{(1 - \omega^2/\omega_{En+1}^2)} + \omega^2 \sum_{l=1}^{n} \beta_{jl}\beta_{il} \frac{(1 - \omega_{En+1}/\omega_{El}^2)}{(\omega_{El}^2 - \omega^2)(\omega^2/\omega_{El}^2)(\omega^2/\omega_{El}^2 - \omega_{En+1}^2/\omega_{El}^2)} \tag{112}$$

This expression introduces new terms $b(\tau_i, \tau_j)$, which can be expressed as functions of static deformations p_i and p_j if the definition Eq. (32) is used:

$$b(\tau_i, \tau_j) = \left(\frac{1}{\rho} T^* \tau_i, T^* \tau_j \right). \tag{113}$$

That is, given Eq. (95a),

$$b(\tau_i, \tau_j) = (\rho p_i, p_j). \tag{114}$$

When a Rayleigh-Ritz truncation is utilized, frequencies which null out the Weinstein determinant will always be upper bounds of resonance frequencies of free modes. Conversely, utilization of truncation by projection has tendency to decrease the frequencies of the intermediate problem and thus decrease the influence of real force conditions along boundaries Γ_i which are not taken into account.

However, these truncation methods are relatively inefficient,

Downloaded 03 May 2010 to 171.66.16.20. Redistribution subject to ASME license or copyright; see http://www.asme.org/terms/Terms_Use.cfm

for they only use one part of the information given by operator G_L. On the other hand, utilization of a development in ω^2 allows one to obtain an estimation of the resolvent whose quality can be chosen as great as desired.

4.3 Truncation by Development in ω^2. For all ω and all positive integers K, the following identity is satisfied:

$$R_L = (I-\omega^2 G_L)^{-1} = I + \omega^2 G_L + \ldots + \omega^{2(K-1)} G_L^{(K-1)} + \omega^{2K} R_L^K. \quad (115)$$

From this equation, we deduce a new expression for terms S_{ji} which appear in Weinstein's determinant. The advantage of this development is that the influence of the modal truncation is reduced to order n:

$$S_{ji} = a(p_i, p_j) + \omega^2 a(p_j, G_L p_i) + \ldots + \omega^{2(K-1)} a(p_j, G_L^{(K-1)} p_i) + \omega^{2K} \sum_{l=1}^{n} \frac{\alpha_{il}\alpha_{jl}}{(1-\omega^2/\omega_{Ll}^2)} \omega_{Ll}^{2(K-1)} \quad (116)$$

Likewise, a development of resolvent r_E which is analogous to that given in Eq. (115) leads to generalized masses written in the following form:

$$\overline{M}_{ij} = b(\tau_i, \tau_j) + \omega^2 b(\tau_j, H_E \tau_i) + \ldots + \omega^{2(K-1)} b(\tau_j, H_E^{(K-1)} \tau_i) + \omega^{2K} \sum_{l=1}^{n} \frac{\beta_{il}\beta_{jl}}{\omega_{El}^{2(k-1}} (\omega_{El}^2 - \omega^2)^{-1}. \quad (117)$$

The terms which appear in the series in ω^2 introduce the following symmetrical matrices:

$$\text{Even terms} : \quad a(p_j, G_L^{2N} p_i) = a(G_L^N p_j, G_L^N p_i) \quad (118a)$$

$$b(\tau_i, H_E^{2N} \tau_j) = b(H_E^N \tau_i, H_E^N \tau_j) \quad (118b)$$

$$\text{Odd terms} : \quad a(p_j, G_L^{2N+1} p_i) = (\tau G_L^N p_j, G_L^N p_i) \quad (119a)$$

$$b(\tau_i, H_E^{2N+1} \tau_j) = t(H_E^N \tau_i, H_E^N \tau_j). \quad (119b)$$

In the context of the formulation in displacement, the following residual deformations may be introduced:

$$r_i = p_i - \sum_{l=1}^{n} \alpha_{il} x_{Ll}. \quad (120)$$

From this, a new expression of the flexibility matrix is deduced from the expression

$$S_{ji} = \sum_{M=0}^{K} \omega^{2M} S_{Rji}^{(M)} + \sum_{l=1}^{n} \alpha_{jl}\alpha_{il}\omega_{Ll}^2 (1-\omega^2/\omega_{Ll}^2)^{-1}. \quad (121)$$

The residual terms appear as the following symmetrical matrices:

$$\text{Even terms} : \quad S_{Rij}^{(2N)} = a(G_L^N r_j, G_L^N r_i) \quad (122)$$

$$\text{Odd terms} : \quad S_{Riij}^{(2N+1)} = (\rho G_L^N r_j, G_L^N r_i). \quad (123)$$

The latter expressions were obtained by using the following relation:

$$a(p_j, G_L^M r_i) = a(r_j, G_L^M r_i) \quad \forall i, \forall j. \quad (124)$$

In accordance with the mode acceleration method (Hurty and Rubinstein, 1966), good estimation of resonance frequencies of intermediate problems can be obtained even in the case of a development to the first order by introducing static deformations. Thus in most cases the development will be limited to the value $K = 0$, and the residual flexibility terms S_{Rji} can be explicitly expressed by using Eq. (120).

$$S_{Rji} = S_{Rji}^{(0)} = a(p_j, p_i) - \sum_{l=1}^{n} \alpha_{jl}\alpha_{il}\omega_{Ll}^2. \quad (125)$$

Thus the construction of modal synthesis methods based on free modes naturally introduces static deformations which allows one to define generalized coordinates along boundaries and to utilize an optimal truncation procedure.

Likewise, the formulation in force, used to define a modal synthesis method which is based on fixed-interface modes, introduces stress fields associated with static solutions p_i. In order to link the terms given in Eq. (119) to these static deformations, the displacement functions w_i that belong to space $\overline{U}_E$ and that are associated with stress fields τ_i may be introduced.

$$Tw_i = \tau_i \; w_i \in \overline{U}_E \quad (126)$$

As $\overline{\tau}_i = \omega^2 \tau_i$ is the solution to problem (95), the displacement fields w_i are solutions to the following differential system:

$$A w_i = \tau p_i \quad (127a)$$

$$D_j w_i = 0 \quad \forall M \in S_{1j} \quad (127b)$$

$$F_j T w_i = 0 \quad \forall M \in S_{2j} \quad (127c)$$

$$D_j w_i = 0 \quad \forall M \in \Gamma_j. \quad (127d)$$

The solution is obtained by using operator G_E defined in Eq. (20):

$$w_i = G_E p_i. \quad (128)$$

Since H_E is the inverse operator of $T \rho^{-1} T^*$, we have the following identity:

$$1/\rho T^* H_E^{N+1} T u = G_E^N u \quad \forall u \in \overline{U}_L. \quad (129)$$

By associating this relationship to Eqs. (126) and (128), we obtain for $u = w_i$

$$1/\rho T^* H_E^{N+1} \tau_i = G_E^{N+1} p_i \quad (130)$$

In order to obtain the participation of the first n fixed-interface modes, the residual deformations defined as below are introduced:

$$s_i = p_i - \sum_{l=1}^{n} \beta_{il} x_{El}. \quad (131)$$

The series in the second term converges in $L^2(\Omega)$ but not in $\tilde{U}_L$, for it is associated with a development in stress, which converges in the metric defined by scalar product $\tilde{b}(.\,,.)$.

$$T s_i = -\tau_{Si} - \sum_{l=1}^{n} \beta_{il} y_{El} \quad (132)$$

After rearranging the terms that appear in the generalized mass expression given in Eq. (117), we obtain

$$\overline{M}_{ji} = \sum_{M=0}^{K} \omega^{2M} M_{Rji}^{(M)} + \sum_{l=1}^{n} \beta_{jl}\beta_{il}\omega_{El}^2 (1-\omega^2/\sigma_{El}^2)^{-1}. \quad (133)$$

The terms of residual matrices have the following simple expressions:

$$\text{Even terms} : \quad M_{Rij}^{(2N+1)} = (\rho G_E^N s_j, G_E^N s_i) \quad (134a)$$

$$\text{Odd terms} : \quad M_{Rij}^{2N} = a(G_E^N s_j, G_E^N s_i). \quad (134b)$$

In most cases only the residual matrix $M_R^{(0)}$ is used, which can be expressed in the following form:

$$M_{Rij} = M_{Rij}^{(0)} = (\rho p_i, p_j) - \sum_{l=1}^{n} \beta_{il}\beta_{jl}. \quad (135)$$

The model limited to the value $K = 0$ in Eq. (133) is equivalent to the Rayleigh-Ritz model obtained by using the following discrete expression:

$$u = \sum_{i=1}^{n} q_{Ei} x_{Ei} + \sum_{i=1}^{k} \lambda_i^* p_i. \quad (136)$$

Downloaded 03 May 2010 to 171.66.16.20. Redistribution subject to ASME license or copyright; see http://www.asme.org/terms/Terms_Use.cfm

In accordance with the Rayleigh-Ritz method, upper bounds of the resonance frequencies of the free structure are obtained. These upper bounds will therefore be better than those obtained by Rayleigh-Ritz truncation, Eq. (107), but more complex experimental procedures will be needed in order to identify the model. This model, which corresponds to the Craig and Bampton method (Craig and Bampton, 1968), gives a better result than that of Hou which utilizes free modes (Hou, 1969) and which is based on a Rayleigh-Ritz type of truncation (Eq. (105a)). On the other hand, the Craig and Chang free-mode method (Craig and Chang, 1976), which uses a residual flexibility matrix (Eq. (121) with $K = 1$), possesses a similar convergence.

5 Conclusion

In this study, a general theory of modal synthesis applied to continuous structures has been developed. A mathematical formalism based on the definition of compact operator allows one to master the convergence of the various approximation procedures. Such a theory introduces, in a natural manner, generalized boundary degrees-of-freedom associated with static displacement fields. The presentation of the spectral problem presentation in the context of a formulation in displacement and a formulation in force allows one to treat in parallel the procedures based on free modes and those based on fixed-interface modes. This unification would have been practically impossible in the discrete framework, where a description in displacement in the case of structures and a description in force in the case of fluids is routinely chosen. In (Jezequel, 1985b) a more precise mathematical formalism based on the definition of compact operator classes had been proposed to master the convergence of the various approximation procedures.

References

Allen, J. J., "Techniques for Implementing Statically Complete Component Mode Synthesis Forced Response," *Proceedings of the Fifth International Modal Analysis Conference*, London, Apr., pp. 42–48.

Benfield, W. A., and Hruda, R. F., 1971, "Vibration Analysis of Structures by Component Mode Substitution," *AIAA Journal*, Vol. 9, pp. 1255–1261.

Beninghof, J. K., 1987, "Component Mode Iteration for Frequency Calculations," *AIAA Journal*, Vol. 25, No. 7, pp. 996–1002.

Coleman, A. D., et al., 1988, "A Mass-Additive Technique for Modal Testing as Applied to the Space Shuttle Astro-1 Payload," *Proceedings of the 6th International Modal Analysis Conference*, Kissimmee, FL, Feb., pp. 154–159.

Craig, R. R., Jr., 1981, *Structural Dynamics: An Introduction to Computer Methods*, John Wiley and Sons, New York.

Craig, R. R., Jr., 1987, "A Review of Time-Domain and Frequency-Domain Component-Mode Synthesis Methods," *International Journal of Analytical and Experimental Modal Analysis*, Vol. 2, No. 2, Apr., pp. 59–72.

Craig, R. R., Jr., and Bampton, M. C. C., 1968, "Coupling of Substructures for Dynamic Analysis," *AIAA Journal*, Vol. 6, pp. 1313–1321.

Craig, R. R., Jr., and Chang, C. J., 1976, "Free-Interface Methods of Substructure Coupling for Dynamic Analysis," *AIAA Journal*, Vol. 14, pp. 1163–1635.

Craig, R. R., Jr., and Chang, C. J., 1977, "On the Use of Attachment Modes in Substructure Coupling for Dynamic Analysis," AIAA Paper No. 77-405, *AIAA 18th Structures, Structural Dynamics and Materials Conference*, San Diego, Mar., pp. 89–99.

Gladwell, G. M. L., 1964, "Branch Mode Analysis of Vibrating Systems," *Journal of Sound and Vibration*, Vol. 1, pp. 41–59.

Goldenberg, S., and Shapiro, M., 1973, "A Study of Coupling Procedures for the Space Shuttle," NASA CR-112252.

Goldman, R. L., 1968, "Vibration Analysis by Dynamic Partitioning," *AIAA Journal*, Vol. 7, pp. 1152–1154.

Hale, A. L., and Meirovitch, L., 1982, "A Procedure for Improving Discrete Substructure Representation in Dynamic Synthesis," *AIAA Journal*, Vol. 20, pp. 1123–1136.

Hale, A. L., and Meirovitch, L., 1982, "A General Procedure for Improving Discrete Substructures Representation in Dynamic Synthesis," *Journal of Sound and Vibration*, Vol. 84, pp. 269–287.

Hou, S. N., 1969, "Review of Modal Synthesis Techniques and a New Approach," *Shock and Vibration Bulletin*, Vol. 40, pp. 25–30.

Hurty, W. C., 1965, "Dynamic Analysis of Structural Systems Using Component Modes," *AIAA Journal*, Vol. 3, pp. 678–685.

Hurty, W., and Rubinstein, M., 1966, *Dynamics of Structures*, Prentice-Hall, Englewood Cliffs, NJ.

Jezequel, L., 1980, "A Method of Damping Synthesis From Substructure Tests," ASME *Journal of Mechanical Design*, Vol. 102, pp. 286–294.

Jezequel, L., 1985a, "A Hybrid Method of Modal Synthesis Using Vibration Tests," *Journal of Sound and Vibration*, Vol. 100, pp. 191–210.

Jezequel, L., 1985b, "Synthese modale et extensions," These d'Etat, Lyon, France.

Jezequel, L., and Setio, H. D., 1994, "Component Modal Synthesis Methods Based on Hybrid Model, Part II: Numerical Tests and Experimental Identification of Hybrid Models," ASME JOURNAL OF APPLIED MECHANICS, Vol. 61, pp. 109–116.

Kline, K. A., 1986, "Dynamic Analysis Using a Reduced Basis of Exact Modes and Ritz Vectors," *AIAA Journal*, Vol. 24, No. 12, pp. 2022–2029.

Mac Neal, R. H., 1971, "A Hybrid Method of Component Mode Synthesis," *Computers & Structures*, Vol. 1, pp. 581–601.

Rubin, S., 1975, "Improved Component-Mode Representation for Structural Dynamic Analysis," *AIAA Journal*, Vol. 13, pp. 996–1006.

Sehmi, N. S., 1985, "A Newtonian Procedure for the Solution of the Kron Characterishybrid Method of Modal Synthesis Using Vibration Tests," *Journal of Sound and Vibration*, Vol. 100, pp. 191–210.

Weinstein A., and Stenger, W., 1972, *Intermediate Problems for Eigenvalues*, Academic Press, New York.

Wittrick, W. H., and Williams, F. W., 1971, "A General Algorithm for Computing Natural Frequencies of Elastic Structures," *Quarterly Journal of Mechanics and Applied Mathematics*, Vol. 24, pp. 263–284.

Downloaded 03 May 2010 to 171.66.16.20. Redistribution subject to ASME license or copyright; see http://www.asme.org/terms/Terms_Use.cfm

Component Modal Synthesis Methods Based on Hybrid Models, Part II: Numerical Tests and Experimental Identification of Hybrid Models

L. Jezequel

H. D. Setio

Laboratoire de Tribologie et de Dynamique des Systemes, URA CNRS 855, Ecole Centrale de Lyon, 36, av. de Collongue, 69131 Ecully Cedex, France

A double modal synthesis method in which compatibility conditions at substructure interfaces are ensured by the introduction of loaded modes is presented in this study. These loaded modes, which are obtained by introducing mass loading or stiffness loading along the boundaries, are used to define generalized boundary coordinates. Thus the hybrid models presented in the first part of this study are developed so that they can be derived from test data as results of independent modal identifications. Unlike in classical modal synthesis methods, in this double modal synthesis method, it is not necessary to clamp the interfaces, which is always difficult to carry out during vibration tests. By introducing loaded modes, generalized boundary coordinates which represent boundary deformability in the frequency range under study can be defined.

1 Introduction

A general theory of modal synthesis based on new formulation has been proposed in Jezequel and Setio (1994), and the aim of this accompanying paper is to illustrate its application in numerical and experimental contexts. Furthermore, in the framework of the finite element method, the proposed first development consists in constructing hybrid models defined in Jezequel and Setio (1994). Thus it can be observed that certain models lead to those currently used in modal synthesis, but that others appear to be new. Particularly, it can be noted that a truncation by projection technique, which gives lower bounds of natural frequencies in the primal formulation, has never been, to our knowledge, used in the context of component mode synthesis methods. The modal synthesis based on hybrid models is particularly adapted to substrate assembly in an experimental context (Jezequel, 1980, 1985). Thus the most important goal of this study is to define a method for identifying hybrid models from vibration tests. This procedure consists in utilizing a family of loaded modes obtained by fixing known impedances along the connection boundaries. Several numerical simulations are presented to illustrate the proposed identification method and to verify its efficiency. Finally, this double modal synthesis method is applied in the case of substructure assembly. The results obtained for the examples presented in the last part of this paper certify the efficiency of hybrid models in the primal formulation associated with free modes as well as in dual formulation associated with fixed-interface modes.

2 Hybrid Models in the Finite Element Context

In the displacement p_i formulation, hybrid models which are linked to the intermediate problems of Weinstein are associated with a force distribution along free boundaries Γ_i (Jezequel and Setio, 1994). This force distribution produces static displacements which are used in enforcing the compatibility of substructure interface coordinates. It can be obtained by imposing a unit force on one physical boundary coordinate and zero force on the rest. But such a type of loading can be replaced by any other type of force distribution. For example, several continuous forces in triangular form can be applied along boundaries so that the number of static displacement vectors can be reduced. The static modes resulting from this type of force distribution are a generalization of attachment modes used by Craig and Chang in defining residual terms (Craig and Chang, 1976).

If the substructure is unrestrained, rigid-body modes must first be removed by imposing some constraints. The inertia-

Contributed by the Applied Mechanics Division of THE AMERICAN SOCIETY OF MECHANICAL ENGINEERS for publication in the ASME JOURNAL OF APPLIED MECHANICS.

Discussion on this paper should be addressed to the Technical Editor, Professor Lewis T. Wheeler, Department of Mechanical Engineering, University of Houston, Houston, TX 77204-4792, and will be accepted until four months after final publication of the paper itself in the ASME JOURNAL OF APPLIED MECHANICS.

Manuscript received by the ASME Applied Mechanics Division, Jan. 30, 1991; final revision, Dec. 3, 1992. Associate Technical Editor: P. D. Spanos.

Copyright © 1994 by ASME

Downloaded 03 May 2010 to 171.66.16.20. Redistribution subject to ASME license or copyright; see http://www.asme.org/terms/Terms_Use.cfm

relief procedure can then be used to obtain the flexibility matrix for an unconstrained substructure (Craig, 1981).

Intermediate problems in the dual formulation based on stress space are associated with static displacements imposed along the boundaries which corresponds to the constraint modes used by Craig and Bampton to define substructure generalized coordinates (Craig and Bampton, 1968).

A constraint mode is obtained by imposing a unit displacement on one physical boundary coordinate and zero displacement on the rest. But in the theory of hybrid models (Jezequel and Setio, 1994) the static displacement fields p_i can be associated with any boundary displacements.

3 Hybrid Model Associated With Loaded Modes

The static deformations p_i which are associated with the boundary loadings and the normal modes of the fixed interface or free structure, can be approximated by a numerical discretization method. However, when applying modal synthesis methods in an experimental context, there is often difficulty in measuring the static displacement of a structure. If the dual hybrid method is used, we must also measure clamping forces in order to obtain the static stiffness matrix made up of terms $a(p_i, p_j)$. With the primal hybrid method, the residual terms associated with the static deformations which appear in Eq. (I.122) (Part I of this paper) can be identified from a smoothing of the impedance curves, but there are often mistakes in the values obtained. Moreover, in the case of assemblies along continuous boundaries, if a discrete model of the finite element type is not available, a great number of boundary displacements must be measured, thus making the experimental procedure more difficult, especially when rotations are being studied.

To avoid all of these difficulties, static deformations are introduced through the *loaded modes*. These are the modes of a new structure obtained by introducing a load along boundaries Γ_i. This load is obtained by attaching known mass or elastic members along the boundary or by joining the structure to any other structure. If the last procedure is used, one part of the structure can be isolated by using the modes of the assembled structure. Introducing loaded modes also allows the definition of generalized boundary displacements which are representative of the real flexibility of the boundaries in the frequency domain under study. Moreover, the hybrid models will be built from the experimental identification of two families of independently tested modes.

The displacement fields $\tilde{x}_{Bi}$ of the structure under consideration, which are induced by the loaded modes, satisfy:

$$A\tilde{x}_{Bi} = \omega_{Bi}^2 \rho \tilde{x}_{Bi} \quad \forall M \in \Omega \tag{1}$$

The dual hybrid models can be similarly identified by introducing the stress fields $\tilde{y}_{Bi}$ induced by the loaded modes, and which satisfy

$$B\tilde{y}_{Bi} = \omega_{Bi}^2 \tilde{y}_{Bi} \quad \forall M \in \Omega \tag{2a}$$

with

$$\tilde{y}_{Bi} = T\tilde{x}_{Bi}. \tag{2b}$$

By using this equation and Green's formula (I.36), the following relations are obtained:

$$a(\tilde{x}_{Bi}, v) = \omega_{Bi}^2(\rho \tilde{x}_{Bi}, v) + \langle f_i, Dv \rangle \quad \forall v \in \tilde{U}_L \tag{3}$$

$$b(\tilde{y}_{Bi}, \sigma) = \omega_{Bi}^2 t(\tilde{y}_{Bi}, \sigma) + \omega_{Bi}^2 \langle d_i, F\sigma \rangle \quad \forall \sigma \in \tilde{V}_E. \tag{4}$$

The distribution of force f_i correspond to the coupling force applied along the boundaries $\{\Gamma_i\}$, which is induced by the loaded modes, and the boundary displacements d_i are associated with the loaded modes by the equation

$$D\tilde{x}_{Bi} = d_i. \tag{5}$$

The loaded modes may be projected onto space $\overline{L}_R$, which is the projection of space $\tilde{U}_L$ associated with the free structure onto the space generated by rigid-body modes.

$$\tilde{x}_{Bi} = x_{BRi} + x_{Bi} \tag{6a}$$

with

$$x_{BRi} \in \overline{L}_R \text{ and } x_{Bi} \in \overline{U}_L. \tag{6b}$$

Given relation (3), the fields x_{Bi} satisfy the following integral equation:

$$x_{Bi} - \omega_{Bi}^2 G_L x_{Bi} = p_i^1. \tag{7}$$

The static solution p_i^1 introduced in this expression is the weak solution to the following problem:

$$a(p_i^1, v) = \langle f_i, Dv \rangle. \tag{8}$$

Likewise, the dual hybrid models can be identified by projecting the stress fields induced by the loaded modes onto space $\overline{E}_S$.

$$\tilde{y}_{Bi} = y_{BSi} + y_{Bi} \tag{9a}$$

with

$$y_{BSi} \in \overline{E}_S \text{ and } y_{Bi} \in \overline{V}_E. \tag{9b}$$

Given relation (4), the stress fields y_{Bi} satisfy the following integral equation:

$$y_{Bi} - \omega_{Bi}^2 H_E y_{Bi} = \omega_{Bi}^2 \tau_i. \tag{10}$$

The τ_i stress fields are defined by relation

$$b(\tau_i, \sigma) = \langle d_i, F\sigma \rangle \quad \forall \sigma \in \overline{V}_E. \tag{11}$$

These τ_i fields are also solutions to equation system (I.102), where the static deformations associated with boundary displacements d_i and which are obtained by applying force distributions along boundaries Γ_i appear, so

$$T^* \tau_i = \rho p_i^2 \quad \forall M \in \Omega \tag{12}$$

$$F_j \tau_i = 0 \qquad \forall M \in S_{2j} \tag{13}$$

and

$$Dp_i^2 = d_i. \tag{14}$$

Static deformations p_i^2 are different from the static deformation p_i^1 in the primal formulation and are defined in Eq. (8). In fact, the former are associated with the generalized displacement given in Eq. (5), and the latter with force distributions f_i defined by

$$f_i = F\tilde{y}_{Bi}. \tag{15}$$

Where the load applied to the boundaries is simple, these force distributions are directly related to generalized displacements d_i.

Mass Loading.

$$f_i = \{f_j\}_i = \omega_{Bi}^2 \{m_j D_j \tilde{x}_{Bi}\} \tag{16}$$

m_j is the distribution of inertia associated with the generalized displacement defined by operator D_j which appears in the boundary condition along boundary Γ_i. If the boundary load is experimentally obtained by attaching rigid bodies, generalized displacements $D_j \tilde{x}_{Bi}$ become easy to measure.

Stiffness Loading.

$$f_i = \{f_j\}_i = \{-k_j D_j \tilde{x}_{Bi}\} \tag{17}$$

Stiffness distribution k_j corresponds to the blocking of boundary Γ_j by a flexible coupling element.

Any Loading. If the loaded modes originate in a coupling any other structure, the force distributions will be unknown, but they are presumed to be independent.

4 Identification of the Flexibility Matrices

The identification of primal hybrid models is based on the

Downloaded 03 May 2010 to 171.66.16.20. Redistribution subject to ASME license or copyright; see http://www.asme.org/terms/Terms_Use.cfm

displacements associated with the first $k\hat{x}_{Bi}$ loaded modes and with the first nx_{Ll} free modes, as measured during vibration tests. Whatever truncation is used to express $R_L p_i$ in Eq. (I.110) of Jezequel and Setio (1994), the generalized flexibility matrices introduced in Eq. (I.67) can only be determined by calculating the coefficients defined by

$$\alpha_{il} = (\rho p_i^1,\ x_{Ll}) \tag{18}$$

As the static deformations p_i^1 are not measured during the experimental process, these coefficients are calculated using scalar values γ_{il} defined by

$$\gamma_{il} = (\rho \tilde{x}_{Bi},\ x_{Ll}). \tag{19}$$

That is, given the decomposition introduced in Eq. (6),

$$\gamma_{il} = (\rho x_{Bi},\ x_{Ll}). \tag{20}$$

To this end the two members of integral equation are multiplied by x_{Ll} with respect to the scalar product associated with the energy of deformation.

$$a(x_{Bi},\ x_{Ll}) - \omega_{Bi}^2(\rho x_{Bi},\ x_{Ll}) = a(p_i^1,\ x_{Ll}). \tag{21}$$

Moreover, as x_{Bi} and p_i^1 belong to space $\overline{U}_L$, the variational Eq. (I.28*a*) gives

$$a(x_{Bi},\ x_{Ll}) = \omega_{Li}^2(\rho x_{Bi},\ x_{Ll}) \tag{22}$$

$$a(p_i^1,\ x_{Ll}) = \omega_{Li}^2(\rho p_i^1,\ x_{Ll}). \tag{23}$$

These two equations allow the γ_{il} to be introduced into relation (18), so we finally obtain

$$\alpha_{il} = \gamma_{il}(1 - \omega_{Bi}^2/\omega_{Ll}^2). \tag{24}$$

The mass coupling terms γ_{il} can be calculated if we have the M_O mass matrix associated with the m measurement points P_j used during the vibration tests.

$$\gamma_{il} = \tilde{X}_{Bi}^T M_0 X_{Ll} \tag{25}$$

Vectors $\tilde{X}_{Bi}$ and X_{Ll} are made up of the amplitudes at points P_j of the $\tilde{X}_{Bi}$ loaded modes and the X_{Ll} free modes. If the mass matrix is imprecise, it must be corrected using the procedures given in Berman (1979), so that the orthogonality of the free modes is satisifed.

If a truncation of the Rayleigh-Ritz type (I.112) is used, it is sufficient to know the α_{il} in order to build the primal hybrid model. However, if the space $\overline{L}_R$ is not equal to zero, terms $(\rho p_{Rj},\ p_{Ri})$, which appear in the Weinstein determinant given in Eq. (I.74) and which are associated with rigid-body movements, must be identified.

To this end, Green's relation (3) is applied to functions of $\overline{L}_R$, producing

$$-\omega_{Bi}^2(\rho x_{BRi},\ v) = \langle f_i,\ Dv\rangle \quad \forall v \in \overline{L}_R. \tag{26}$$

Given Eq. (I.75), x_{BRi} appears to be proportional to p_{Ri}^1, that is,

$$x_{BRi} = -\omega_{Bi}^{-2} p_{Ri}^1. \tag{27}$$

Thus we obtain

$$(\rho p_{Rj}^1,\ p_{Ri}^1) = \omega_{Bj}^2\omega_{Bi}^2(\rho x_{BRj},\ x_{BRi}). \tag{28}$$

In accordance with the experimental procedure, these terms can be calculated using the displacements induced by the loaded modes and measured at m points P_j. Likewise, if we want to use the flexibility matrices obtained by truncating the resolvent R_L by projection, Eq. (I.121), or by using a development in ω^2, Eq. (I.138), the following terms need to be determined:

$$S_{Sji}^{(1)} = a(p_j^1,\ p_i^1). \tag{29}$$

These coefficients can be related to the quantities which can be measured during vibration tests by using the expression given in Eq. (23), giving

$$S_{Sji}^{(1)} = a(x_{Bj},\ x_{Bi}) - (\omega_{Bj}^2 + \omega_{Bi}^2)(\rho x_{Bj},\ x_{Bi}) + \omega_{Bj}^2\omega_{Bi}^2(\rho G_L \rho x_{Bj},\ x_{Bi}). \tag{30}$$

The last scalar product which enters into this expression is evaluated by means of terms γ_{il} defined in Eq. (20).

$$(\rho G_L \rho x_{Bj},\ x_{Bi}) = \omega_{Bj}^2\omega_{Bi}^2 \sum_{l=1}^{n} \omega_{Ll}^{-2}\gamma_{jl}\gamma_{il} \tag{31}$$

According to the Hilbert-Schmidt theorem, this series converges rapidly (Weinstein and Stenger, 1972), and truncation of order n introduces only slight errors in most cases. The mass terms which appear in relation (30) are obtained by using the mass matrix of the structure.

$$(\rho x_{Bj},\ x_{Bi}) = X_{Bj}^T M_0 X_{Bi} \tag{32}$$

Terms $a(x_{Bj},\ x_{Bi})$ could be obtained in a similar manner by using a stiffness matrix. But, generally modal synthesis methods are applied to structures whose geometry is too complex to allow even approximate stiffness matrices to be built. If the boundary loads are simple, terms $a(x_{Bj},\ x_{Bi})$ are precisely obtained during the experimental identification. In fact, orthogonality of the loaded modes gives the following:

For a mass loading,

$$a(x_{Bj},\ x_{Bi}) = \omega_{Bj}\omega_{Bi}\delta_{ij}. \tag{33}$$

For a stiffness loading,

$$a(x_{Bj},\ x_{Bi}) = \omega_{Bj}\omega_{Bi}\delta_{ij} - \sum_{l=1}^{m} (k_l D_l \tilde{x}_{Bj},\ D_l \tilde{x}_{Bi})_{\Gamma l}. \tag{34}$$

In the case of any loading, terms $a(x_{Bj},\ x_{Bi})$ are obtained using a series development:

$$a(x_{Bj},\ x_{Bi}) = \sum_{l=1}^{N} \omega_{Ll}^2 \gamma_{jl}\gamma_{il}. \tag{35}$$

As this series only converges slowly, this expression requires identification of N free modes, $(N > n)$ which appear explicitly in the definition of primal hybrid models. If a development of a higher order is used to express the flexibility matrices, the following terms must be evaluated:

$$S_{Sji}^{(K)} = a(p_j^1,\ G_L^{K-1} p_i^1). \tag{36}$$

In order to relate them to the modal parameters defined during the tests, p_j^1 and p_i^1 are replaced by their expression as a function of the loaded modes given in Eq. (7):

$$S_{Sji}^{(K)} = (\rho x_{Bj},\ G_L^{K-2}(x_{Bi} - (\omega_{Bj}^2 + \omega_{Bi}^2) G_L x_{Bi} + \omega_{Bj}^2\omega_{Bi}^2 G_L^2 x_{Bi}). \tag{37}$$

These terms can be evaluated using the γ_{il} components of loaded modes in the basis of free modes.

$$S_{(K)}Sji = \sum_{l=1}^{N} \omega_l^{2(2-K)}(1 - (\omega_{Bj}^2 - \omega_{Bi}^2)/\omega_l^2 + \omega_{Bj}^2\omega_{Bi}^2/\omega_l^4)\gamma_{jl}\gamma_{il} \tag{38}$$

These series must use a number of modes greater than n. It is easy to show that where $n = N$ the introduction of terms $S_{Sji}^{(K)}$ does not improve the definition of the flexibility matrices. However, terms of second order bring out the generalized masses of the loaded modes

$$S_{Sji}^{(2)} = (\rho x_{Bj},\ x_{Bi}) - (\omega_{Bj}^2 + \omega_{Bi}^2)(\rho x_{Bj},\ G_L x_{Bi}) + \omega_{Bj}^2\omega_{Bi}^2(\rho G_L x_{Bj},\ G_L x_{Bi}). \tag{39}$$

As terms $(\rho x_{Bj},\ x_{Bi})$ are calculated using relation (32), a development based on the first n free modes is enough to evaluate the other two terms.

$$S_{Sji}^{(2)} = X_{Bj}^T M_0 X_{Bi} + \sum_{l=1}^{n} ((\omega_{Bj}^2\omega_{Bi}^2)/\omega_l^4 - (\omega_{Bj}^2 + \omega_{Bi}^2)/\omega_l^2)\gamma_{jl}\gamma_{il} \tag{40}$$

Thus if a mass or stiffness load is used, a primal hybrid model of the second order may be obtained by only identifying the modes used to define it. However, if the boundary displacements are imprecise, Eq. (35) instead of Eq. (34) must be used to calculate terms $S_{Sji}^{(1)}$ in the case of stiffness load, which

Downloaded 03 May 2010 to 171.66.16.20. Redistribution subject to ASME license or copyright; see http://www.asme.org/terms/Terms_Use.cfm

means that a number of free modes that is greater than n must be identified. Moreover, in an experimental context it is much easier to fix masses along boundaries Γ_i than to introduce an elastic link with a fixed reference, which is always difficult to define. In most cases it is therefore preferable to attach rigid bodies in order to define the loaded modes.

5 Identification of Impedance Matrices

A knowledge of the displacements associated with the first nx_{Ei} fixed-interface modes and the first kx_{Bi} loaded modes is necessary to identify dual hybrid models. The process is similar to that used to build the models defined in the primal formulation. However, the essential terms of the impedance matrix shown in Eq. (I.105) of Jezequel and Setio (1994) are associated with the stress fields τ_{Si} generated by the static deformations p_i^2.

$$K_{Sji} = t(\tau_{si}, \tau_{sj}) \tag{41}$$

These static stiffness terms can also be expressed using the deformation energy expression used in the primal formulation.

$$K_{Sji} = a(p_j^2, p_i^2) \tag{42}$$

Fields τ_{Si} can be related to the stress fields y_{Bsi} defined in Eq. (15) by using Green's relation (4) applied to functions of E_S.

$$-t(y_{Bsi}, \sigma) = \langle d_i, F\sigma \rangle \quad \forall \sigma \epsilon \overline{E}_S \tag{43}$$

For, given the variational Eq. (I.100), the following simple result is obtained:

$$\tau_{si} = -y_{Bsi} \tag{44}$$

This equation and relation (41) finally produce

$$K_{Sji} = a(x_{Bj}, x_{Bi}). \tag{45}$$

In order to identify these terms from modal characteristics, a simple boundary load must be used. This is because these terms, which in the primal formulation were approximated by a development over the free modes in Eq. (35), cannot be approximated in dual formulation, for the series

$$\tilde{x}_{Bi} = \sum_{l=1}^{\infty} \theta_{il} x_{El} \tag{46}$$

with

$$\theta_{ij} = (\rho \tilde{x}_{Bi}, x_{El}) \tag{47}$$

converges in $\overline{L}$ but not in $\tilde{U}_L$. However, if a mass load is used, terms K_{Sji} will be obtained directly by Eq. (33), and if a stiffness load is used, by Eq. (34).

Components θ_{il} are linked to β_{il}, which appear in the expression of generalized masses by multiplying the two members of the integral Eq. (10) by the stress fields y_{El} with respect to scalar product $b(.,.)$.

$$b(y_{Bi}, y_{El}) - \omega_{Bi}^2 b(H_E y_{Bi}, y_{El}) = \omega_{Bi}^2 b(\tau_i, y_{El}) \tag{48}$$

Given the decomposition defined in Eqs. (6) and (9), fields x_{Bi} and y_{Bi} are related to fields $\tilde{x}_{Bi}$ and $\tilde{y}_{Bi}$ by the following relation:

$$Tx_{Bi} = \tilde{y}_{Bi} \tag{49}$$

and

$$T^* y_{Bi} = \omega_{Bi}^2 \tilde{x}_{Bi}. \tag{50}$$

Moreover, by using the definition of the scalar product $b(.,.)$ and Eqs. (I.41), (I.102a), (I.118b), and (49), we may write

$$b(y_{Bi}, y_{El}) = \omega_{Bi}^2 \omega_{El}^2 \theta_{il} \tag{51}$$

$$b(\tau_i, y_{El}) = \omega_{El}^2 \beta_{il}. \tag{52}$$

Finally, as y_{El} is an eigenvector of operator H_E, coefficient β_{il} can be obtained by integrating these equations with relation (46), in the following form:

$$\beta_{il} = \theta_{il}(1 - \omega_{Bi}^2/\omega_{El}^2). \tag{53}$$

The similarity of this expression to that obtained in the primal formulation from the integral Eq. (7) means that the relation between the static deformations p_i^2 and the loaded modes can be shown clearly.

$$\tilde{x}_{Bi} - \omega_{Bi}^2 G_E \tilde{x}_{Bi} = p_i^2 \tag{54}$$

By using the eigenvectors of G_E, the following expression is deduced:

$$\tilde{x}_{Bi} - p_i^2 = \omega_{Bi}^2 \sum_{l=i}^{\infty} \omega_{El}^2 x_{El}. \tag{55}$$

According to the Hilbert-Schmidt theorem, this series converges absolutely and strongly (Weinstein and Stenger (1972)).

If a truncation by projection or a development in ω^2 of resolvent R_E is used, the following terms must be calculated in order to build the generalized mass matrices given in Eq. (I.123) or (I.134):

$$M_{Sij}^{(1)} = b(\tau_i, \tau_j). \tag{56}$$

These terms can be calculated from measured modes by using the expression of τ_i given in Eq. (10),

$$M_{Sij}^{(1)} = \frac{b(y_{Bi}, y_{Bj})}{\omega_{Bi}^2 \omega_{Bj}^2} - (\omega_{Bi}^{-2} + \omega_{Bj}^{-2}) t(y_{Bi}, y_{Bj}) + t(y_{Bi}, H_E y_{Bj}). \tag{57}$$

Given relation (50), the first term of this expression is written:

$$\frac{b(y_{Bi}, y_{Bj})}{\omega_{Bi}^2 \omega_{Bj}^2} = (\rho \tilde{x}_{Bi}, \tilde{x}_{Bj}). \tag{58}$$

These scalar products can easily be calculated using the mass matrix of the structure associated with the measurement points. The other terms which appear in expression (57) require the y_{Bi} to be known which, thanks to Eqs. (I.101), (9), (12), (44), (49) and (54), is expressed in the form

$$y_{Bi} = T(x_{Bi} - p_i^2) = \omega_{Bi}^2 \sum_{l=1}^{\infty} \omega_{El}^{-2} y_{El}. \tag{59}$$

Terms $M_{Sji}^{(1)}$ will therefore be approximated by the following relation:

$$M_{Sij}^{(1)} = \tilde{X}_{Bi}^T M_O \tilde{X}_{Bj} - (\omega_{Bi}^2 + \omega_{Bj}^2) \sum_{l=1}^{n} \frac{\theta_{il}\theta_{jl}}{\omega_{EL}^2} + \omega_{Bi}^2 \omega_{Bj}^2 \sum_{l=1}^{n} \frac{\theta_{il}\theta_{jl}}{\omega_{El}^4}. \tag{60}$$

As the series converge so well, the truncation of order n leads in most cases to very slight errors only. The terms of higher order that appear in the generalized mass expression given in Eq. (I.151) are calculated using Eqs. (59) and (10).

$$M_{Sij}^{(K)} = \sum_{l=1}^{N} \omega_l^{2(1-K)} (1 - (\omega_{Bj}^2 + \omega_{Bi}^2)/\omega_l^2 + \omega_{Bj}^2 \omega_{Bi}^2/\omega_l^4) \theta_{jl} \theta_{il}. \tag{61}$$

For a development of a higher order than one to be efficient, a number of N fixed-interface modes greater than n must be used. Thus for fixed k and n, a greater number of modes must be identified in order to build second-order hybrid models in the dual formulation than in the primal formulation. Moreover, comparing Eqs. (39) and (61) shows that terms $S_{Sji}^{(2)}$ and $M_{Sji}^{(1)}$ are estimated with the same degree of precision.

6 Simulation of the Experimental Procedure

The efficiency of the identification methods presented in this part of the study is tested by using the finite element approach to simulate the experimental procedure. A rectangular cantilever thin plate measuring 60 × 40 × 0.5 cm is chosen for constructing the base model (Fig. 1). The fixed-interface structure corresponds to the plate which is clamped along boundary

Downloaded 03 May 2010 to 171.66.16.20. Redistribution subject to ASME license or copyright; see http://www.asme.org/terms/Terms_Use.cfm

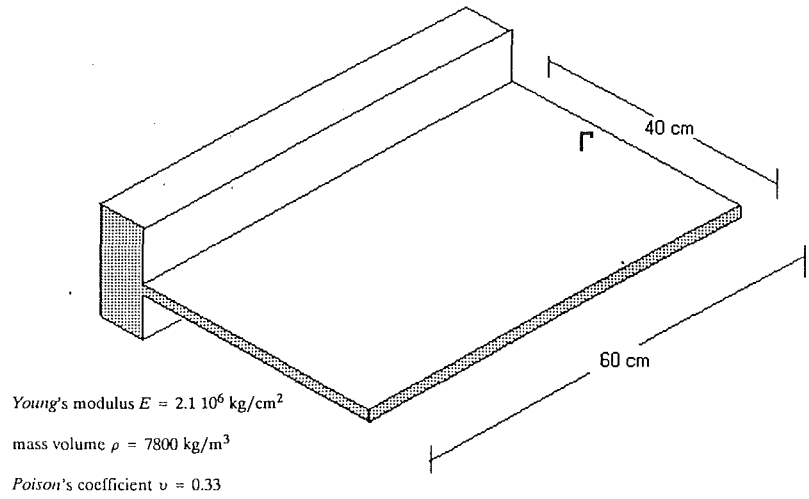


Fig. 1 Rectangular cantilever thin plate model

Table 1 Resonance frequencies of loaded modes used in the experimental simulations

loading C1	loading C2	loading C3
18.671	29.972	38.848
35.174	55.043	100.570
61.743	117.990	183.227
72.937	175.988	212.300
100.490	208.625	258.456
123.586	250.256	347.071
137.572	304.848	381.142
145.417	445.391	502.111
172.122	448.671	527.413

Table 2 Resonance frequencies of fixed-interface modes of the plate obtained by synthesis with $n = 9$ and $k = 6$

loading type	model 1	model 2	model 3	model 4	exact values
C1	44.221	38.842	39.878	39.851	39.112
	140.163	101.238	104.645	104.225	104.399
	185.021	179.700	180.812	180.732	184.869
	NC	231.433	237.133	237.126	237.540
			268.817	268.086	267.687
C2	45.971	39.041	39.179	39.098	39.112
	148.913	99.078	101.916	101.914	104.399
	178.365	169.827	185.012	184.352	184.869
	NC	227.471	NC	235.206	237.540
		247.395	256.200	256.171	267.687
C3	43.843	39.035	39.072	39.067	39.112
	138.002	102.829	104.885	104.485	104.399
	188.197	183.614	185.399	184.451	184.869
	NC	220.960	237.950	237.639	237.540
				280.954	267.687

NC : Not Calculated

Γ (the side AB of the plate). So as to construct the hybrid models which correspond to various truncation methods presented in this study, the first n free modes and fixed-interface modes have been calculated. The structure has been meshed into 32 rectangular plate elements measuring 7.5 × 10, with three degrees-of-freedom for each node: one translation in the nodal z-direction and two rotations about the nodal x and y-axes. The loaded modes were obtained by introducing load distribution along the boundary.

The influence of the choice of loaded modes is evaluated by using three types of loading: one mass loading and two stiffness loadings. The efficiency of the proposed methods will be made clear by using two stiffness loadings which correspond to two extreme values. The first gives natural frequencies which are close to those of free modes and the second gives the natural frequencies of a structure that is nearly clamped. The frequencies of these various loaded modes are given in Table 1.

6.1 Primal Formulation. Using the first n free modes and the first k loaded modes obtained by introducing successively the three types of load, four hybrid models which correspond to the various truncation methods presented previously have been constructed. They are identified by using Eqs. (24) and (30) for the three first models and by using Eq. (39) for model 4.

Solving for the roots of Weinstein's determinant gives approximate values of the resonance frequencies of the fixed-interface modes obtained by clamping boundary Γ. Table 2 shows the fixed-interface frequencies calculated using the first nine free modes and the first six loaded modes.

It can be shown that the calculated frequencies are close to the exact resonance frequencies of fixed-interface modes obtained by a finite element calculation. Model 1 gives resonance frequencies which are greater than exact values. This is because a truncation of the Rayleigh-Ritz type makes the structure more rigid, as predicted by the theory. Again, it can be stated that this truncation produces low accuracy so that a great number of modes must be identified. Model 2, which corresponds to a truncation by projection, gives lower bounds of fixed-interface modes, which are very interesting for experimental application. By using this model, the values obtained by a truncation of the Rayleigh-Ritz type can be considerably improved.

It can also be stated that model 3, which corresponds to a development in ω^2 of the first order improves values calculated by model 1 and that a development of the second order (model 4) modifies the results, but this modification is not very significant.

The influence of truncations can be made clear by reducing the free modes taken into account. Table 3 gives the results of calculation carried out with six free modes and three loaded modes. It can be shown that resonance frequencies which are close to the exact values can be obtained even if the number of loaded modes used is limited.

6.2 Dual Formulation. The plate used in primal formulation tests and which is clamped along boundary Γ has been used to test the efficiency of hybrid models in the dual formulation. Thus the free modes which are calculated correspond to the resonance frequencies of the structure with free boundary, and are obtained by solving for the rooth of Weinstein's determinant.

With the aid of the first nine free modes and the first six

Downloaded 03 May 2010 to 171.66.16.20. Redistribution subject to ASME license or copyright; see http://www.asme.org/terms/Terms_Use.cfm

Table 3 Resonance frequencies of fixed-interface modes of the plate obtained by synthesis with $n = 6$ and $k = 3$

loading type	model 1	model 2	model 3	model 4	exact values
C1	42.454	39.065	39.076	39.068	39.112
	123.842	103.583	104.984	104.976	104.399
	188.275	183.939	184.158	184.156	184.869
	245.277	231.197	237.937	237.632	237.540
	291.735	260.974	267.918	267.721	267.687
		401.350	401.931	401.930	409.668
C2	43.190	38.994	39.206	39.195	39.112
	128.017	103.088	104.494	104.464	104.399
	92.4781	183.931	184.412	184.352	184.869
	NC	228.099	237.652	237.551	237.540
	290.943	258.957	262.759	262.751	267.687
		386.060	393.862	393.825	409.668
C3	42.240	39.058	39.129	39.118	39.112
	123.481	103.602	104.416	104.406	104.399
	189.169	184.166	184.424	184.419	184.869
	NC	230.414	237.906	237.733	237.540
	293.784	260.400	264.938	264.282	267.687
		394.300	398.999	398.806	409.668

NC : Not Calculated

Table 4 Resonance frequencies of free modes of the plate obtained by synthesis with $n = 9$ and $k = 6$

loading type	model 1	model 2	model 3	model 4	exact values
C1	30.750	28.945	28.954	28.868	27.485
	60.404	50.052	50.149	50.100	50.052
	154.553	116.669	117.979	116.560	113.976
		183.066	183.346	182.102	174.651
		213.871	222.774	221.555	205.956
C2	29.425	28.466	28.469	28.001	27.485
	55.600	51.373	51.464	50.859	50.052
	143.789	123.575	125.008	123.326	113.976
		184.957	184.987	183.145	174.651
		NC	NC	216.402	205.651

NC : Not Calculated

loaded modes, four hybrid models in the dual formulation have been built. Equations (30), (31), and (40) can be used to identify the models.

The resonance frequencies obtained by synthesis are reported in Table 4. Good approximations of free modes are obtained. Just like in the primal formulation, the efficiency of models in this formulation is proved. The mass loading *C*1 gives resonance frequencies which are closer to exact values than those of the stiffness loading. We can thus conclude that mass loadings are more convenient to use than stiffness loadings. Furthermore, this type of loading is very easy to apply and allows hybrid models to be built with only a few loaded modes. Model 2 produces accurate results because a truncation by projection has a tendency to decrease the resonance frequencies of intermediate problems.

Table 5 gives the resonance frequencies by using the same models and the same type of loading as previous models but with $n = 6$ and $k = 3$. Good estimations are obtained even when the free modes used in building the modal base and the loaded modes used in defining boundary generalized coordinates are limited.

7 Method of Substructure Coupling

7.1 Hybrid Assembly Procedure. In order to extend modal synthesis methods as well as possible to the assembly of two substructures along boundaries Γ_i (Fig. 2), the following notations are introduced:

Table 5 Resonance frequencies of free modes of the plate obtained by synthesis with $n = 6$ and $k = 3$

loading type	model 1	model 2	model 3	model 4	exact values
C1	29.070	27.843	27.846	27.665	27.485
	57.507	50.088	50.104	50.086	50.052
	141.525	114.201	114.799	114.223	113.976
	183.821	181.404	181.682	180.016	174.651
		213.148	217.473	215.524	205.956
		252.067	256.462	255.012	247.205
		297.408.	310.731	309.055	302.653
C2	30.051	28.258	28.261	27.985	27.485
	59.312	50.675	50.733	50.723	50.052
	143.325	120.146	120.713	118.258	113.976
	185.601	180.904	181.165	180.953	174.651
		218.417	222.153	221.201	205.651
		258.952	263.645	260.125	247.205
		311.035	324.216	320.020	302.653

NC : Not Calculated

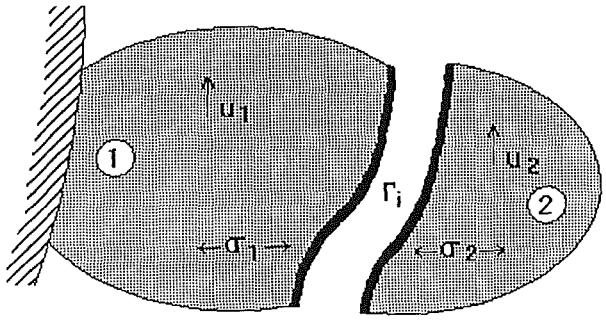


Fig. 2 Modelization of substructure assembly

$$u^T = \{u^1, u^2\} \tag{62}$$

$$\sigma^T = \{\sigma^1, \sigma^2\}. \tag{63}$$

Indices 1 and 2 correspond to the numbers of the two substructures. The scalar product associated with displacement fields u^T and stress fields σ^T are defined by

$$\tilde{a}_T(u^T, v^T) = \tilde{a}_1(u^1, v^1) + \tilde{a}_2(u^2, v^2) \quad \forall u^T, \forall v^T \in \tilde{U}_L^1 \times \tilde{U}_L^2 \tag{64}$$

$$\tilde{b}_T(u^T, \tau^T) = \tilde{b}_1(u^1, \tau^1) + \tilde{b}_2(\sigma^2, \tau^2) \quad \forall \sigma^T, \forall \tau^T \in \tilde{V}_E^1 \times \tilde{V}_E^2 \tag{65}$$

Depending on which formulation is chosen, the assembly methods are obtained from the clamped or the free substructures.

7.2 Primal Formulation. In the displacement formulation, the coupling condition between the two substructures is written thus:

$$\langle f, D_T u^T \rangle = 0 \quad \forall f \in \tilde{U}_\Gamma \tag{66}$$

with

$$D_T u^T = D_1 u^1 - D_2 u^2. \tag{67}$$

Using the scalar product introduced in Eq. (64), a family of adjoint operators can be associated with D_T:

$$\langle f, D_T u^T \rangle = \tilde{a}_T(u^T, D_T^* f) \forall u^T, \forall v^T \in \tilde{U}_L^1 \times \tilde{U}_L^2 \forall f \in \tilde{U}_\Gamma. \tag{68}$$

In accordance with the notations of the preceding chapters, the following pseudo-static deformations associated with each coupling force distribution f_i:

$$D_T^* f_i = \tilde{p}_i^T \tag{69a}$$

with

$$\tilde{p}_i^T = \{\tilde{p}_i^1, \tilde{p}_i^2\}. \tag{69b}$$

By applying the same procedure as when clamping a simple

Downloaded 03 May 2010 to 171.66.16.20. Redistribution subject to ASME license or copyright; see http://www.asme.org/terms/Terms_Use.cfm

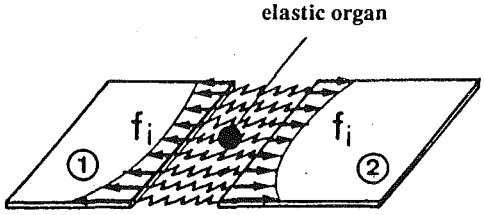


Fig. 3 Experimental substructure coupling in primal formulation

structure, the following intermediate problem of order k associated with a set of k functions p_i^T is obtained:

$$u^T - \omega^2 \tilde{G}_L^T u^T = \sum_{i=1}^{k} \tilde{p}_i^T u_i \tag{70}$$

$$\tilde{a}_T(u^T, \tilde{p}_i^T) = 0 \quad \forall i \in [1, k] \tag{71}$$

with

$$\tilde{G}_L^T u^T = \{\tilde{G}_L^1 u^1, \tilde{G}_L^2 u^2\}. \tag{72}$$

If resolvent $\tilde{R}_L^1$ and $\tilde{R}_L^2$ associated with operators $\tilde{G}_L^1$ and $\tilde{G}_L^2$ are known, the resonance frequencies of the coupled problem can be approached by calculating the roots of the following equation:

$$\det \tilde{a}_T(\tilde{R}_L^T \tilde{p}_i^T, \tilde{p}_j^T) = 0 \tag{73a}$$

with

$$\tilde{R}_L^T \tilde{p}_i^T = \{\tilde{R}_L^1 \tilde{p}_i^1, \tilde{R}_L^2 \tilde{p}_i^2\}. \tag{73b}$$

Decomposing the displacements as defined in Eqs. (I.53) and (I.54) gives a more easily exploitable expression given in relation (I.74):

$$\det(S_{ji}^T(\omega) - \omega^{-2}(\,(\rho^1 p_{Rj}^1, p_{Ri}^1) + (\rho^2 p_{Rj}^2, p_{Ri}^2))) = 0 \tag{74a}$$

with

$$S_{ji}^T(\omega) = a_1(p_j^1, R_L^1 p_i^1) + a_2(p_j^2, R_L^2 p_i^2). \tag{74b}$$

The expressions of resolvent R_L^1 and R_L^2 associated with the primal hybrid models and which correspond to different types of truncation can be used to calculate the resonance frequencies of the intermediate problems.

7.3 Dual Formulation. The coupling condition in dual formulation is written in the following form:

$$\langle d, F_T \sigma^T \rangle = 0 \quad \forall f \in \tilde{U}_\Gamma \tag{75a}$$

with

$$F_T \sigma^T = F_1 \sigma^1 - F_2 \sigma^2. \tag{75b}$$

We associate with this formal operator an adjoint operator defined by

$$\langle d, F_T \sigma^T \rangle = \tilde{b}_T(\sigma^T, F_T^* d) \quad \forall \sigma^T, \forall \tau^T \in \tilde{V}_E^1 \times \tilde{V}_E^2 \forall d \in \tilde{U}_\Gamma. \tag{76}$$

k stress fields $\tilde{\tau}_i^T$ associated with k boundary deformation d_i are introduced:

$$F_T^* f_i = \tilde{\tau}_i^T. \tag{77}$$

The intermediate problems of order k are defined by:

$$\sigma^T - \omega^2 \tilde{H}_E^T \sigma^T = \sum_{i=1}^{k} \tilde{\tau}_i^T \lambda_i^* \tag{78a}$$

with

$$\tilde{H}_E^T \sigma^T = \{\tilde{H}_E^1 \sigma^1, \tilde{H}_E^2 \sigma^2\}. \tag{78b}$$

Given relations (I.80) and (75), the coupling equations are written as

$$\tilde{b}^T(\sigma_i^T, \tilde{\tau}_i^T) = 0 \quad \forall i \in [1, k] \tag{79a}$$

with

$$\tilde{\tau}_i^T = \{\tilde{\tau}_i^1, \tilde{\tau}_i^2\}. \tag{79b}$$

The resonance frequencies of the intermediate problems cancel out Weinstein's determinant

$$\det \tilde{b}_T(\tilde{R}_E^T \tilde{\tau}_i^T, \tilde{\tau}_j^T) = 0 \tag{80a}$$

with

$$\tilde{R}_E^T \tilde{\tau}_i^T = \{\tilde{R}_E^1 \tilde{\tau}_i^1, \tilde{R}_E^2 \tilde{\tau}_i^2\}. \tag{80b}$$

If the decomposition of the stress fields given in Eq. (I.94) is used, a simpler expression of the determinant is obtained:

$$\det(-\omega^2 M_{ij}^T(\omega) + t_1(\tau_{Si}^1, \tau_{Sj}^1) + t_2(\tau_{Si}^2, \tau_{Sj}^2)) = 0 \tag{81a}$$

with

$$M_{ij}^T(\omega) = b_1(\tau_i^1, R_E^1 \tau_j^1) + b_2(\tau_i^2, R_E^2 \tau_j^2). \tag{81b}$$

The stress fields which appear in these equations are the solutions to the following variational problems:

$$b_1(\tau_i^1, \sigma^1) = \langle d_i, F_1 \sigma^1 \rangle \quad \forall \sigma^1 \in \overline{V}_E^1 \tag{82}$$

$$b_2(\tau_i^2, \sigma^2) = \langle d_i, F_2 \sigma^2 \rangle \quad \forall \sigma^2 \in \overline{V}_E^2 \tag{83}$$

$$t_1(\tau_{si}^1, \sigma^1) = \langle d_i, F_1 \sigma^1 \rangle \quad \forall \sigma^1 \in \overline{E}_S^1 \tag{84}$$

$$t_2(\tau_{si}^2, \sigma^2) = \langle d_i, F_2 \sigma^2 \rangle \quad \forall \sigma^2 \in \overline{E}_S^2. \tag{85}$$

The various types of truncation of resolvent R_E^1 and R_E^2 used to define the dual hybrids models allow the approximate resonance frequencies of the coupled structures to be calculated. In an experimental context, these models are identified by the methods explained above.

In order to assemble two substructures using hybrid modal synthesis methods, a family of force or displacement distributions along interface boundaries Γ_i must be introduced. These distributions must be applied to both of the substructures under study. In the context of the finite element method, it is easy to generate them by imposing displacements or forces to the junction nodes. In the experimental context, force distributions can be generated by introducing an elastic element between the two structures (Fig. 3). The loaded modes used to identify the models are, then, the modes of the assembly.

By applying the coupling methods presented above in the primal formulation, the dynamic behavior of the two substructures can then be approximated.

In most cases, the loaded modes of each of the two substructures must be identified separately, and the force or displacement distributions applied to one substructure must be expressed as a function of those applied to the other (Jezequel, 1985b).

7.4 Numerical Tests. The two identical thin plates shown in Fig. 4 have been chosen to test the validity of hybrid models in the case of substructure coupling. Four models which correspond to a truncation of the Rayleigh-Ritz type, truncation by projection and a development in ω^2 of first and second orders have been used in order to evaluate the effect of the various truncation procedures presented. Two types of loading $C1$ and $C2$ which are, respectively, mass loading and stiffness loading have been used in these numerical tests.

The resonance frequencies of the assembled structure obtained by primal formulation modal synthesis are reported in Table 6. These values have been calculated with $n = 12$ and $k = 6$. It can be shown that the eigenvalues which cancel out Weinstein's determinant are close to the resonance frequencies of the whole structure obtained by the finite element approach, which are considered as exact values. It can be stated that the results obtained by model 2 (truncation by projection) are the lower bounds of the resonance pulsations of the assembled structure.

Table 7 shows the resonance frequencies of intermediate problems in dual formulation with $n = 12$ and $k = 6$. A better approximation of the assembled modes than that of the primal formulation is obtained for the same number of free modes taken into account in generating the models. It can be shown

Downloaded 03 May 2010 to 171.66.16.20. Redistribution subject to ASME license or copyright; see http://www.asme.org/terms/Terms_Use.cfm

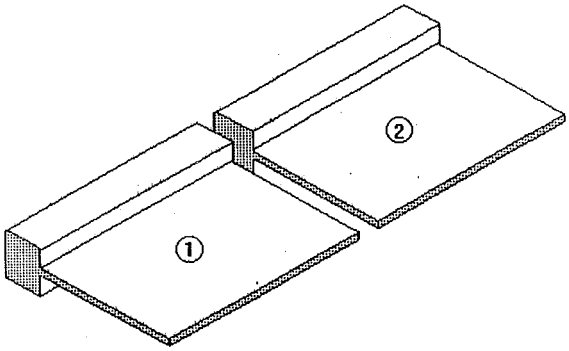


Fig. 4 Assembly of two identical cantilever plates

Table 6 Resonance frequencies of the assembled structure obtained by the proposed hybrid models in primal formulation

loading type	model 1	model 2	model 3	model 4	exact values
	35.666	27.575	27.645	27.641	27.628
	42.589	34.107	34.110	34.110	34.563
	87.300	52.947	53.962	53.549	53.577
mass	122.087	81.021	81.867	81.857	85.573
	179.273	128.092	133.710	133.702	133.692
loading	181.381	172.704	174.791	174.782	174.784
		181.204.	182.213	182.011	. 181.650
		NC	NC	NC	202.149
		208.830	209.462	209.130	. 210.459
		27.325	27.649	27.542	27.628
		34.353	34.355	34.354	34.563
		53.016	54.031	53.639	53.577
stiffness		82.322	82.426	82.421	85.573
	NC	131.031	133.729	133.551	133.692
loading		174.636	174.690	174.685	174.784
		180.600.	181.720	181.652	. 181.650
		NC	202.146	202.132	202.149
		209.557.	209.920	209.912	. 210.459

NC : Not Calculated

that model 1 and 3 give the upper bounds of the resonance frequencies of the assembled structure as predicted by the theory.

8 Conclusion

A general theory for identifying hybrid models experimentally has been presented in this study. Loaded modes which can be relatively easily obtained during vibration tests, are introduced when defining the generalized boundary coordinates. Various numerical tests have also been carried out in order to evaluate the efficiency of the proposed methods. Loaded modes have been proved to be highly representative of the boundary deformability in the frequency range under study so that this identification procedure can be used effectively in substructure connection along continuous boundaries.

Table 7 Resonance frequencies of the assembled structure obtained by the proposed hybrid models in dual formulation

loading type	model 1	model 2	model 3	model 4	exact values
	27.988	27.525	27.904	27.831	27.628
	37.198	34.203	34.599	34.598	34.563
	55.914	53.200	54.051	54.026	53.577
mass	111.722	85.628	89.799	89.602	85.573
	149.195	135.140	139.204	136.365	133.692
loading	174.794	175.221	175.622	175.325	174.784
	193.005	181.203	184.620	184.532	181.650
	NC	NC	207.504	NC	202.149
	30.244	27.630	27.926	27.896	27.628
	35.966	34.331	34.603	34.568	34.563
	61.600	54.005	54.192	54.126	53.577
stiffness	97.543	85.193	86.342	86.168	85.573
	155.593	135.206	137.921	136.234	133.692
loading	179.429	172.633	174.952	174.865	174.784
	191.256	182.941	184.026	183.989	181.650
		NC	205.431	204.356	202.149

NC : Not Calculated

References

Berman, A., 1979, "Mass Matrix Correction Using a Set of Measured Modes," *AIAA Journal*, Vol. 17, pp. 1147–1148.

Craig, R. R., Jr., 1981, *Structural Dynamics: An Introduction to Computer Methods*, John Wiley and Sons, New York, 1981.

Craig, R., Jr., and Bampton, M. C. C., 1968, "Coupling of Substructures for Dynamic Analysis," *AIAA Journal*, Vol. 6, pp. 1313–1321.

Craig, R. R., Jr., and Chang, C. J., 1976, "Free-Interface Methods of Substructure Coupling for Dynamic Analysis," *AIAA Journal*, Vol. 14, pp. 1163–1635.

Jezequel, L., 1980, "A Method of Damping Synthesis From Substructure Test," ASME *Journal of Mechanical Design*, Vol. 102, pp. 286–294.

Jezequel, L., 1985a, "A Hybrid Method of Modal Synthesis Using Vibration Tests," *Journal of Sound and Vibration*, Vol. 100, pp.. 191–210.

Jezequel, L., 1985b, "Synthese Modale Theorie et Extensions," These d'Etat, Lyon, France.

Jezequel, L., and Setio, H. D., 1994, "Component Modal Synthesis Methods Based on Hybrid Models, Part I: Theory of Hybrid Models and Modal Truncation Methods," ASME JOURNAL OF APPLIED MECHANICS, Vol. 61, pp. 100–108.

Weinstein, A., and Stenger, W., 1972, *Intermediate Problems for Eigenvalues*, Academic Press, New York.

Downloaded 03 May 2010 to 171.66.16.20. Redistribution subject to ASME license or copyright; see http://www.asme.org/terms/Terms_Use.cfm

Angular Momentum of a Torque-Free Deforming Axisymmetric Gyro

F. P. J. Rimrott
Professor of Mechanical Engineering,
Fellow ASME.

F. Janabi-Sharifi
Graduate Student.

University of Toronto,
Five King's College Road,
Toronto, ON M5S 1A4, Canada

Attitude drift and attitude stability studies of torque-free gyros involve an angular momentum that is constant in magnitude and direction. The problem is to find suitable coordinates to describe the gyro's behavior, and then to express the (constant) angular momentum in these coordinates. Expressions for small deformation are available. In the present paper the expression, in floating coordinates, for the angular momentum of a torque-free deforming axisymmetric gyro in terms of inertia moments and angular velocity components is extended to beyond small deformations. The angular momentum expression is written first in its general form. Then the angular momentum is expressed in matrix form for the calculation of angular momentum components for arbitrarily large deformation. Finally, three models are presented to illustrate the application of the angular momentum expression obtained.

1 Introduction

The establishment of an angular momentum expression in suitable terms for deforming bodies is of great importance for a study of the behavior of such bodies.

The key to the establishment of a suitable angular momentum expression is the selection of an appropriate coordinate frame. Floating reference frames have shown an advantage. The advantage of these frames is that they can follow the body in an optimal manner (De Veubeke, 1976). The majority of floating coordinate frames employed so far have been for rigid bodies and for bodies with small deformations (Canavin and Likins, 1977; Rimrott, 1988).

The present paper concentrates on the development of an angular momentum expression for torque-free, deforming, originally axisymmetric bodies by the use of an appropriate floating coordinate frame. In the present study not only the case of small, but also of large deformations is considered, and in order to demonstrate the feasibility of the angular momentum expressions obtained, three cases are studied in some detail.

2 Formulation

2.1 General Case. The angular momentum $\mathbf{H}$ of a gyro of mass m is defined as

$$\mathbf{H} = \int_m \mathbf{r} \times \dot{\mathbf{r}}\, dm \tag{1}$$

where $\mathbf{r}$ is the position vector of the mass element m and $\dot{\mathbf{r}}$ is the absolute velocity of the same mass element (Fig. 1). Any mass element dm that is located at a position $\boldsymbol{\rho}$ in the gyro in its undeformed state will be displaced by a distance $\boldsymbol{\delta}$ in the deformed state, which is brought about by the inertial forces acting within the gyro such that

$$\mathbf{r} = \boldsymbol{\rho} + \boldsymbol{\delta}. \tag{2}$$

Let the angular velocity of the body (more specifically of the $Cxyz$ coordinate system attached to three separate points of the rotating gyro) be $\boldsymbol{\omega}$, and the angular velocity of a suitable chosen floating $Cuvz$ frame be $\boldsymbol{\Omega}$. Thus the velocity of a mass element dm will be

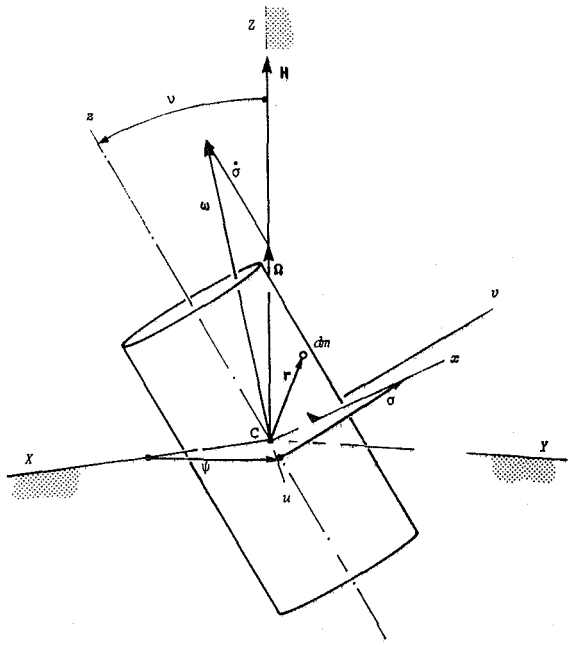


Fig. 1 Position of mass element *dm*, and Euler angles in gyro

Contributed by the Applied Mechanics Division of THE AMERICAN SOCIETY OF MECHANICAL ENGINEERS for publication in the ASME JOURNAL OF APPLIED MECHANICS.

Discussion on this paper should be addressed to the Technical Editor, Professor Lewis T. Wheeler, Department of Mechanical Engineering, University of Houston, Houston, TX 77204-4792, and will be accepted until four months after final publication of the paper itself in the ASME JOURNAL OF APPLIED MECHANICS.

Manuscript received by the ASME Applied Mechanics Division, Nov. 10, 1990; final revision, Aug. 5, 1991. Associate Technical Editor: R. L. Huston.

Copyright © 1994 by ASME
Downloaded 03 May 2010 to 171.66.16.20. Redistribution subject to ASME license or copyright; see http://www.asme.org/terms/Terms_Use.cfm

$$\dot{\mathbf{r}} = \mathring{\mathbf{r}} + \Omega \times \mathbf{r} \tag{3}$$

or, replacing from Eq. (2),

$$\dot{\mathbf{r}} = \mathring{\rho} + \mathring{\delta} + \Omega \times (\rho + \delta). \tag{4}$$

When an in its undeformed shape axisymmetric body is involved (Rimrott, 1988), then

$$\dot{\rho} = \omega \times \rho = \mathring{\rho} + \Omega \times \rho, \tag{5}$$

thus,

$$\mathring{\rho} = (\omega - \Omega) \times \rho. \tag{6}$$

Following common practice (Rimrott, 1988), we place the Z-axis of a space-fixed $CXYZ$ coordinate system such that it coincides with the constant angular momentum vector $\mathbf{H}$, and use Euler angles with ψ as precession angle, ν as nutation angle, and σ as spin angle, such that

$$\omega = \Omega + \dot{\sigma}\mathbf{e}_z, \tag{7}$$

and obtain

$$\mathring{\rho} = \dot{\sigma}\mathbf{e}_z \times \rho. \tag{8}$$

Using Eqs. (2), (4), and (8), one can write Eq. (1) as

$$\begin{aligned}\mathbf{H} = &\int_m \rho \times (\Omega \times \rho) dm + \int_m \rho \times (\Omega \times \delta) dm \\ &+ \int_m \delta \times (\Omega \times \rho) dm + \int_m \delta \times (\Omega \times \delta) dm \\ &+ \int_m \rho \times (\dot{\sigma}\mathbf{e}_z \times \rho) dm + \int_m \delta \times (\dot{\sigma}\mathbf{e}_z \times \rho) dm \\ &+ \int_m \rho \times \mathring{\delta} dm + \int_m \delta \times \mathring{\delta} dm. \end{aligned} \tag{9}$$

For attitude drift studies, it typically suffices to ignore transient vibrations terms since they die out in a relatively short time due to internal damping. After they have died out, the internal damping is no longer active and a gyro can be looked upon as purely elastic. Its deformation will then follow the inertial loading without phase shift, or in other words its deformation will be "constant" in a coordinate frame that follows the loading.

For such deforming bodies of constant configuration in the floating $Cuvz$ coordinate frame, we can write

$$\int_m \rho \times \delta dm = \text{constant}$$

and

$$\frac{d}{dt} \int_m \rho \times \delta dm = 0$$

in the $Cuvz$ frame, or

$$\int_m \mathring{\rho} \times \delta dm + \int_m \rho \times \mathring{\delta} dm = 0$$

or

$$\int_m \rho \times \mathring{\delta} dm = \int_m \delta \times \mathring{\rho} dm. \tag{10}$$

Using Eqs. (7) and (10), one can combine the fifth and first terms and the sixth and seventh terms in Eq. (9). The combination of the fifth and first terms leads to

$$\begin{aligned}&\int_m \rho \times (\Omega \times \rho) dm + \int_m \rho \times (\dot{\sigma}\mathbf{e}_z \times \rho) dm \\ &\quad = [\mathbf{e}_u\ \mathbf{e}_v\ \mathbf{e}_z] \begin{bmatrix} A_0 & 0 & 0 \\ 0 & A_0 & 0 \\ 0 & 0 & C_0 \end{bmatrix} \begin{bmatrix} \omega_u \\ \omega_v \\ \omega_z \end{bmatrix} \end{aligned} \tag{11}$$

where A_0, $B_0 = A_0$ and C_0 are the principal inertia moments when the gyro is undeformed.

The combination of the second, third, sixth, and seventh terms gives

$$\begin{aligned}&\int_m \rho \times (\Omega \times \delta) dm + \int_m \delta \times (\Omega \times \rho) dm \\ &\quad + \int_m \delta \times (\dot{\sigma}\mathbf{e}_z \times \rho) dm + \int_m \rho \times \mathring{\delta} dm \\ &\quad = [\mathbf{e}_u\ \mathbf{e}_v\ \mathbf{e}_z] \begin{bmatrix} J_{uu} & J_{uv} & J_{uz} \\ J_{vu} & J_{vv} & J_{vz} \\ J_{zu} & J_{zv} & J_{zz} \end{bmatrix} \begin{bmatrix} \omega_u \\ \omega_v \\ \omega_z + \dot{\sigma} \end{bmatrix} \\ &\quad + [\mathbf{e}_u\ \mathbf{e}_v\ \mathbf{e}_z] \begin{bmatrix} J_{uu} & J_{vu} & J_{zu} \\ J_{uv} & J_{vv} & J_{zv} \\ J_{uz} & J_{vz} & J_{zz} \end{bmatrix} \begin{bmatrix} \omega_u \\ \omega_v \\ \omega_z - \dot{\sigma} \end{bmatrix} \end{aligned} \tag{12}$$

where the elements of the two *primary partial inertia matrices* appearing in Eq. (12) consist of the primary partial inertia moments

$$J_{uu} = \int_m (\rho_v \delta_v + \rho_z \delta_z) dm \tag{13a}$$

$$J_{vv} = \int_m (\rho_z \delta_z + \rho_u \delta_u) dm \tag{13b}$$

$$J_{zz} = \int_m (\rho_u \delta_u + \rho_v \delta_v) dm \tag{13c}$$

and primary partial inertia products

$$J_{uv} = -\int_m \rho_u \delta_v dm \tag{13d}$$

$$J_{uz} = -\int_m \rho_u \delta_z dm \tag{13e}$$

$$J_{vu} = -\int_m \rho_v \delta_u dm \tag{13f}$$

$$J_{vz} = -\int_m \rho_v \delta_z dm \tag{13g}$$

$$J_{zu} = -\int_m \rho_z \delta u dm \tag{13h}$$

$$J_{zv} = -\int_m \rho_z \delta_v dm. \tag{13i}$$

The fourth term in Eq. (9) can be expanded and written as

$$\int_m \delta \times (\Omega \times \delta) dm = [\mathbf{e}_u\ \mathbf{e}_v\ \mathbf{e}_z] \begin{bmatrix} K_{uu} & K_{uv} & K_{uz} \\ K_{vu} & K_{vv} & K_{vz} \\ K_{zu} & K_{zv} & K_{zz} \end{bmatrix} \begin{bmatrix} \Omega_u \\ \Omega_v \\ \Omega_z \end{bmatrix} \tag{14}$$

where $[K]$ is the *secondary inertia matrix* and its elements consist of the secondary inertia moments

$$K_{uu} = \int_m (\delta_v^2 + \delta_z^2) dm \tag{15a}$$

Downloaded 03 May 2010 to 171.66.16.20. Redistribution subject to ASME license or copyright; see http://www.asme.org/terms/Terms_Use.cfm

$$K_{vv}=\int_m(\delta_u^2+\delta_z^2)dm \tag{15b}$$

$$K_{zz}=\int_m(\delta_u^2+\delta_v^2)dm \tag{15c}$$

and the secondary inertia products

$$K_{uv}=K_{vu}=-\int_m\delta_u\delta_v dm \tag{15d}$$

$$K_{uz}=K_{zu}=-\int_m\delta_u\delta_z dm \tag{15e}$$

$$K_{vz}=K_{zv}=-\int_m\delta_v\delta_z dm \tag{15f}$$

Finally, substitution from Eqs. (11), (12), and (14) into Eq. (9) will result in

$$\begin{aligned}\mathbf{H}=[\mathbf{e}_u\ \mathbf{e}_v\ \mathbf{e}_z]&\begin{bmatrix}A_0&0&0\\0&A_0&0\\0&0&C_0\end{bmatrix}\begin{bmatrix}\omega_u\\\omega_v\\\omega_z\end{bmatrix}\\&+[\mathbf{e}_u\ \mathbf{e}_v\ \mathbf{e}_z]\begin{bmatrix}J_{uu}&J_{uv}&J_{uz}\\J_{vu}&J_{vv}&J_{vz}\\J_{zu}&J_{zv}&J_{zz}\end{bmatrix}\begin{bmatrix}\omega_u\\\omega_v\\\omega_z+\dot\sigma\end{bmatrix}\\&+[\mathbf{e}_u\ \mathbf{e}_v\ \mathbf{e}_z]\begin{bmatrix}J_{uu}&J_{vu}&J_{zu}\\J_{uv}&J_{vv}&J_{zv}\\J_{uz}&J_{vz}&J_{zz}\end{bmatrix}\begin{bmatrix}\omega_u\\\omega_v\\\omega_z-\dot\sigma\end{bmatrix}\\&+[\mathbf{e}_u\ \mathbf{e}_v\ \mathbf{e}_z]\begin{bmatrix}K_{uu}&K_{uv}&K_{uz}\\K_{vu}&K_{vv}&K_{vz}\\K_{zu}&K_{zv}&K_{zz}\end{bmatrix}\begin{bmatrix}\omega_u\\\omega_v\\\omega_z-\dot\sigma\end{bmatrix}+\int_m\boldsymbol{\delta}\times\mathring{\boldsymbol{\delta}}dm\end{aligned} \tag{16}$$

with $\omega_z+\dot\sigma=2\omega_z-\Omega_z$, and $\omega_z-\dot\sigma=\Omega_z$.

Or we can write the angular momentum vector of a deforming axisymmetric gyro in a more compact form as

$$\begin{aligned}\mathbf{H}=[\mathbf{e}_u\ \mathbf{e}_v\ \mathbf{e}_z]\{&[I]\{\omega\}+[J]\{2\omega-\Omega\}\\&+[J]^T\{\Omega\}+[K]\{\Omega\}\}+\int_m\boldsymbol{\delta}\times\mathring{\boldsymbol{\delta}}dm.\end{aligned} \tag{17}$$

For small displacements $|\boldsymbol{\delta}|$ and small velocities $|\mathring{\boldsymbol{\delta}}|$, the last two terms of Eq. (16) become negligible, such that (Rimrott, 1988)

$$\begin{aligned}\mathbf{H}=[\mathbf{e}_u\ \mathbf{e}_v\ \mathbf{e}_z]&\begin{bmatrix}A_0&0&0\\0&A_0&0\\0&0&C_0\end{bmatrix}\begin{bmatrix}\omega_u\\\omega_v\\\omega_z\end{bmatrix}\\&+[\mathbf{e}_u\ \mathbf{e}_v\ \mathbf{e}_z]\begin{bmatrix}J_{uu}&J_{uv}&J_{uz}\\J_{vu}&J_{vv}&J_{vz}\\J_{zu}&J_{zv}&J_{zz}\end{bmatrix}\begin{bmatrix}\omega_u\\\omega_v\\\omega_z+\dot\sigma\end{bmatrix}\\&+[\mathbf{e}_u\ \mathbf{e}_v\ \mathbf{e}_z]\begin{bmatrix}J_{uu}&J_{vu}&J_{zu}\\J_{uv}&J_{vv}&J_{zu}\\J_{uz}&J_{vz}&J_{zz}\end{bmatrix}\begin{bmatrix}\omega_u\\\omega_v\\\omega_z-\dot\sigma\end{bmatrix}\end{aligned} \tag{18}$$

with $\omega_z+\dot\sigma=2\omega_z-\Omega_z$, and $\omega_z-\dot\sigma=\Omega_z$.

Or, in a more compact form,

$$\mathbf{H}=[\mathbf{e}_u\ \mathbf{e}_v\ \mathbf{e}_z]\{[I]\{\omega\}+[J]\{2\omega-\Omega\}+[J]^T\{\Omega\}\}. \tag{19}$$

In the beginning we assumed that the angular velocity of a suitable floating coordinate frame $Cuvz$ is $\boldsymbol{\Omega}$. Now we put a constraint on the definition of our coordinate frame.

Since any vector can be resolved into two components, we can always select (Rimrott, 1981) the $Cuvz$ coordinate frame such that the angular momentum component

$$H_u=0. \tag{20}$$

The constraint (20) means that $\boldsymbol{\Omega}$ now also represents the angular velocity of the inertial force field of a rigid gyro (Rimrott, 1988), with the inertia moments A_0, A_0, C_0.

Selecting the floating coordinate systems in this fashion turns out to be highly suitable for attitude drift and attitude stability studies. With $H_u=0$ the angular momentum now becomes

$$\mathbf{H}=[\mathbf{e}_u\ \mathbf{e}_v\ \mathbf{e}_z]\begin{bmatrix}0\\H_v\\H_z\end{bmatrix}=[\mathbf{e}_u\ \mathbf{e}_v\ \mathbf{e}_z]\begin{bmatrix}0\\H\ \sin\nu\\H\ \cos\nu\end{bmatrix}. \tag{21}$$

With the u-axis constrained in this fashion, however, it can no longer be expected to represent a principal axis of the deformed gyro.

No special conditions have been specified so far for the v and z-axes, other than that $Cuvz$ shall form a right-handed orthogonal coordinate system, and that it represents a principal coordinate system of the gyro when undeformed. Not being a principal coordinate system of the deforming gyro means that the inertia tensor for the deforming gyro must contain inertia products in addition to inertia moments.

2.2 On Terminology. For example, the inertia moment about the u-axis in a $Cuvz$ coordinate system is defined as

$$I_{uu}=\int_m(v^2+z^2)dm. \tag{22}$$

For

$$\mathbf{r}=[\mathbf{e}_u\ \mathbf{e}_v\ \mathbf{e}_z]\begin{bmatrix}u\\v\\z\end{bmatrix} \tag{23}$$

$$\boldsymbol{\rho}=[\mathbf{e}_u\ \mathbf{e}_v\ \mathbf{e}_z]\begin{bmatrix}\rho_u\\\rho_v\\\rho_z\end{bmatrix} \tag{24}$$

$$\boldsymbol{\delta}=[\mathbf{e}_u\ \mathbf{e}_v\ \mathbf{e}_z]\begin{bmatrix}\delta_u\\\delta_v\\\delta_z\end{bmatrix} \tag{25}$$

and Eq. (2), the inertia moment (22) becomes

$$I_{uu}=\int_m((\rho_v+\delta_v)^2+(\rho_z+\delta_z)^2)dm \tag{26}$$

or

$$I_{uu}=\int_m(\rho_v^2+\rho_z^2)dm+2\int_m(\rho_v\delta_v+\rho_z\delta_z)dm+\int_m(\delta_v^2+\delta_z^2)dm, \tag{27}$$

which we shall rewrite as

$$I_{uu}=A_0+2J_{uu}+K_{uu}, \tag{28}$$

with J_{uu} as given by Eq. (13a) and K_{uu} as given by Eq. (15a).

The inertia moment I_{uu} of Eq. (28) is seen to be made up of several parts, viz. the *rigid-body inertia moment* A_0, *the primary partial inertia moment* J_{uu} due to deformation, and the *secondary inertia moment* K_{uu} due to deformation. The primary partial inertia moment J_{uu} contains first-power terms of the displacement $\boldsymbol{\delta}$. The secondary inertia moment K_{uu} contains second-power terms of the displacement $\boldsymbol{\delta}$ and will be negligibly small when the displacements are small. Similar results are obtained for I_{vv} and I_{zz}.

Downloaded 03 May 2010 to 171.66.16.20. Redistribution subject to ASME license or copyright; see http://www.asme.org/terms/Terms_Use.cfm

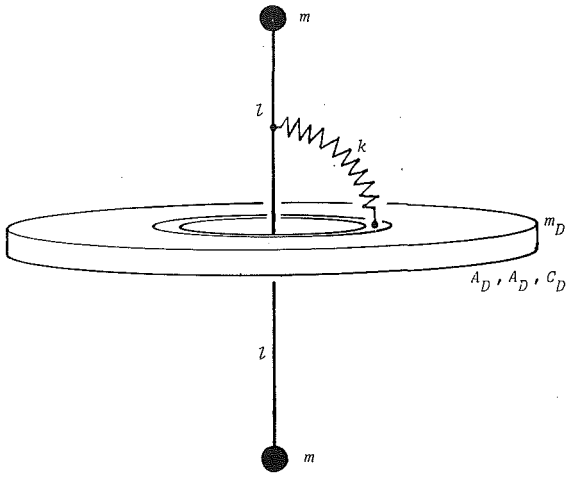


Fig. 2 Model gyro I

For inertia products let us pick for an example

$$I_{uv} = -\int_m uv\,dm. \tag{29}$$

By using equations (13*d*), (13*f*), and (15*d*) for the originally axisymmetric body, Eq. (29) reduces to

$$I_{uv} = J_{uv} + J_{vu} + K_{uv}. \tag{30}$$

The inertia product of Eq. (30) is made up of the *primary partial inertia products* J_{uv} and J_{vu}, and the *secondary inertia product* K_{uv}. The secondary inertial product will be negligibly small when the displacements are small. Similar results are obtained for I_{uz} and I_{vz}. When

$$\int_m \delta \times \mathring{\delta}\, dm = 0, \tag{31}$$

the last term in Eqs. (16) and (17) vanishes. Condition (31) occurs, e.g., when δ and $\mathring{\delta}$ are collinear. It also is approximately true when $|\delta|$ and $|\mathring{\delta}|$ are both small. Condition (31) turns out to be very common.

3 Model Gyros

3.1 Model Gyro I. This model gyro consists of a rigid axisymmetric oblate massive disk and a rigid axial massless rod with point masses at each tip, mounted in a ball and socket joint at the disk's center and connected to the disk by a torsion spring (Fig. 2). This model gyro was used by Janabi-Sharifi (1990) to demonstrate the occurrence of trap states in energy troughs at some attitude $0 < \nu < 90$ deg. The rod is free to spin with respect to the disk. The inertia moments of the gyro at rest, i.e., when the spring is undeformed, are

$$B_0 = A_0 = A_D + 2ml^2 \tag{32}$$

$$C_0 = C_D \tag{33}$$

where A_D, B_D, and C_D are the principal inertia moments of the disk and $2l$ is the length of the rod. The floating coordinate frame, $Cuvz$, is chosen such that $H_u = 0$, and such that z is the axis of symmetry of the disk, and v such that $Cuvz$ forms a right-handed orthogonal system. The $Cuvz$ frame is rotating with Ω around the space-fixed Z-axis, while the disk's angular velocity is ω (Fig. 2). There are no displacement rates in the gyro, i.e., $\mathring{\delta} = 0$. Also it is assumed that there is no vibration, i.e., $\dot{\phi} = \ddot{\phi} = \dot{\nu} = \ddot{\nu} = 0$. For this model gyro (Fig. 3), with $m_1 = m_2 = m$, $\rho_u = 0$, $\rho_v = 0$, $\rho_z = l$, $\dot{\rho}_u = \dot{\rho}_v = \dot{\rho}_z = 0$, $\delta_u = 0$, $\delta_v = -l\sin\phi$, $\delta_z = -l(1-\cos\phi)$, $\dot{\delta}_u = \dot{\delta}_v = \dot{\delta}_z = 0$ the elements of the primary partial inertia matrices are obtained as

$$J_{uu} = -2ml^2(1-\cos\phi) \tag{34a}$$

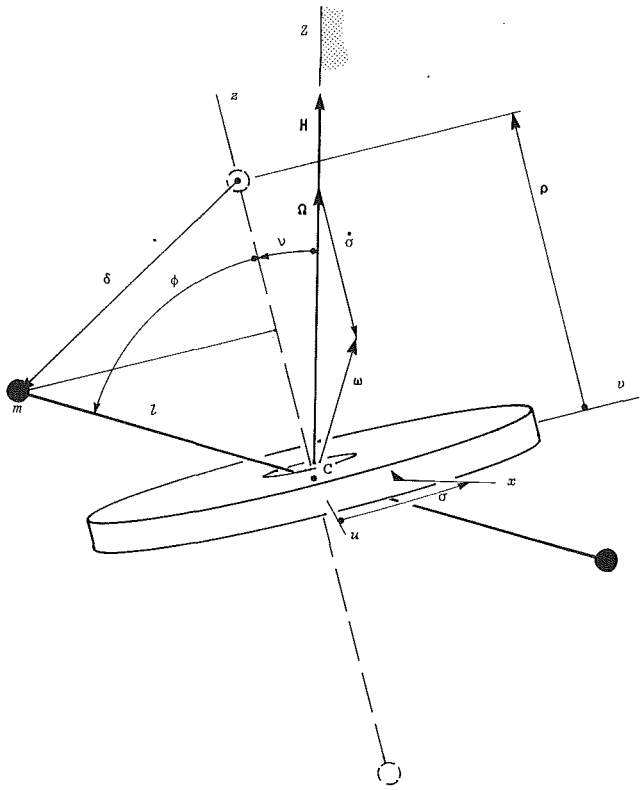


Fig. 3 Rigid body (= original) position ρ and displacement δ of a tip mass m

$$J_{vv} = -2ml^2(1-\cos\phi) \tag{34b}$$

$$J_{zz} = 0 \tag{34c}$$

$$J_{uv} = 0 \tag{34d}$$

$$J_{vu} = 0 \tag{34e}$$

$$J_{zv} = 2ml^2\sin\phi \tag{34f}$$

$$J_{uz} = J_{zu} = 0 \tag{34g}$$

$$J_{vz} = 0. \tag{34h}$$

The elements of the secondary partial inertial matrix for our model gyro are obtained as

$$K_{uu} = 2ml^2(1-\cos\phi) \tag{35a}$$

$$K_{vv} = 2ml^2(1-\cos\phi)^2 \tag{35b}$$

$$K_{zz} = 2ml^2\sin^2\phi \tag{35c}$$

$$K_{zv} = K_{vz} = -2ml^2\sin\phi(1-\cos\phi) \tag{35d}$$

$$K_{uv} = K_{vu} = 0 \tag{35e}$$

$$K_{uz} = K_{zu} = 0. \tag{35f}$$

Having chosen the $Cuvz$ coordinate frame such that H_u is eliminated, and noting that using equations (16), (34), and (35), the angular momentum components of our model gyro can be arranged as

$$H_u = 0 \tag{36a}$$

$$H_v = A_0\omega_v + (2ml^2\sin\phi - 2ml^2\sin\phi(1-\cos\phi))(\omega_z - \dot{\sigma}) - 2ml^2(1-\cos^2\phi)\omega_v \tag{36b}$$

$$H_z = C_0\omega_z + 2ml^2\sin\phi\cos\phi\omega_v + 2ml^2\sin\phi\ \omega_v - 2ml^2\sin\phi\omega_v + 2ml^2\sin^2\phi(\omega_z - \dot{\sigma}\,t) \tag{36c}$$

with (Fig. 3)

$$\omega_v = \Omega_v = \Omega\sin\nu \tag{37}$$

$$\omega_z - \dot{\sigma} = \Omega_z = \Omega\cos\nu. \tag{38}$$

Downloaded 03 May 2010 to 171.66.16.20. Redistribution subject to ASME license or copyright; see http://www.asme.org/terms/Terms_Use.cfm

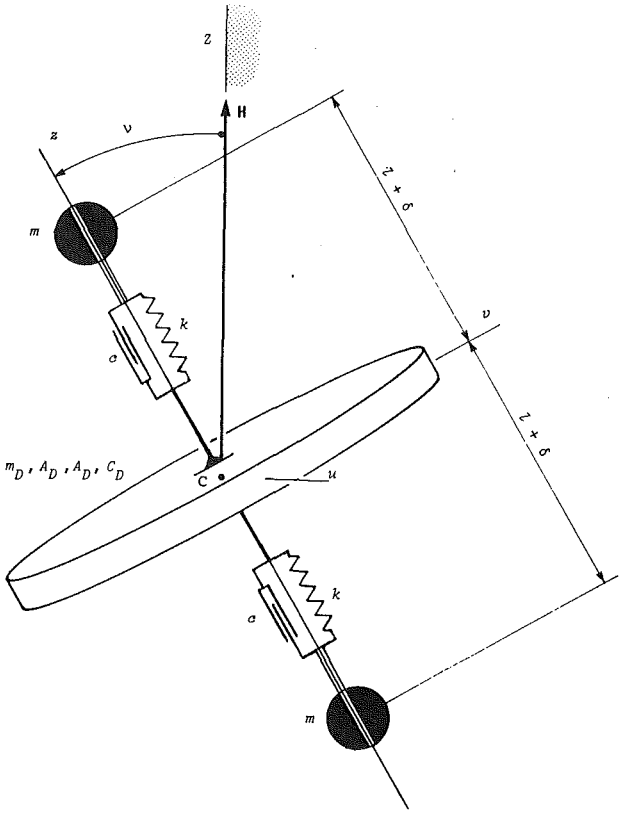


Fig. 4 Model gyro II

Substituting from Eqs. (37) and (38) into Eqs. (36) it follows that

$$H_u = 0 \tag{39a}$$

$$H_v = A_D\omega_v + 2ml^2\Omega\sin(\nu+\phi)\cos\phi \tag{39b}$$

$$H_z = C_D\omega_z + 2ml^2\Omega\sin(\nu+\phi)\sin\phi. \tag{39c}$$

Equations (39) can also be obtained directly as is done in Janabi-Sharifi (1990).

At first sight, the steady-state (i.e., $\dot{\phi} = \dot{\nu} = 0$) gyro model described here appears as being unjustifiably singled out. The steady-state case, however, does represent a possible state, and when one searches for energy troughs of gyros with internal damping, it represents the only possible state in a trough. In an energy trough all vibrations have died out, and any damping mechanism has ceased to function. Note that for the present gyro model, ω is the angular velocity of the disk, while Ω is the angular velocity of the floating coordinate system, of the rod with tip masses, and of the system's steady-state inertial force field.

3.2 Model Gyro II. This model gyro (Fig. 4) has two equal point masses m at the tip of each rigid massless rod connected by springs and dashpots to the rigid central disk of mass m_D. It can deform along its axis of symmetry, but $C = C_0 = C_D$ remains constant. Opposing tip masses are assumed connected such that their δ, $\dot{\delta}$, and $\ddot{\delta}$ are the same, one consequence of this is that the mass center C of the whole gyro remains at one and the same location within the model gyro. The principal inertia moments of the model gyro at rest are

$$B_0 = A_0 = A_D + 2ml^2 \tag{40}$$

$$C_0 = C_D \tag{41}$$

where A_D, $B_D = A_D$ and C_D are the principal inertia moments of the disk and l is the unstrained distance of each mass from the mass center of the gyro. The floating coordinate frame, $Cuvz$, is chosen such that its u and v-axes spin within the disk with respect to the body-fixed x and y-axes. The u and v-axes as well as the z-axis represent the principal axes of the disk, as do the body-fixed x-y-z-axes. The primary partial inertia products for this model (Fig. 4) are

$$J_{uu} = 2ml\delta \tag{42a}$$

$$J_{vv} = 2ml\delta \tag{42b}$$

$$J_{zz} = 0 \tag{42c}$$

$$J_{uv} = J_{vu} = 0 \tag{42d}$$

$$J_{zv} = J_{vz} = 0 \tag{42e}$$

$$J_{zu} = J_{uz} = 0 \tag{42f}$$

where δ is the deformation along the z-axis. It should be noted that the term $\delta \times \mathring{\delta}$ for each mass becomes zero because of collinearity.

The elements of the secondary inertia matrix are

$$K_{uu} = 2m\delta^2 \tag{43a}$$

$$K_{vv} = 2m\delta^2 \tag{43b}$$

$$K_{zz} = 0 \tag{43c}$$

$$K_{vz} = K_{zv} = 0 \tag{43d}$$

$$K_{uv} = K_{vu} = 0 \tag{43e}$$

$$K_{uz} = K_{zu} = 0. \tag{43f}$$

Choosing a proper floating coordinate frame with

$$\omega_v = \sqrt{\omega_x^2 + \omega_y^2} \tag{44}$$

will eliminate ω_u and H_u, and we will have only H_v and H_z. For such a coordinate frame the spin rate (Rimrott, 1988) becomes

$$\dot{\sigma} = \frac{A_D + 2m(l+\delta)^2 - C_D}{A_D}\,\omega_z. \tag{45}$$

Finally, substituting from Eqs. (40), (41), (42), and (43) into Eq. (16) will give

$$H_u = 0 \tag{46a}$$

$$H_v = [A_D + 2m(l+\delta)^2]\omega_v \tag{46b}$$

$$H_z = C_D\omega_z. \tag{46c}$$

Displacement δ and attitude angle ν will then be related by

$$k\delta = m(l+\delta)\Omega^2\sin^2\nu, \tag{47}$$

where the term $m(l+\delta)\Omega^2\sin^2\nu$ is the component of the centrifugal force along the rod, which is compensated by the spring force. For a given angle ν in the steady-state solution,

$$\delta = \frac{ml\Omega^2\sin^2\nu}{k - ml\Omega^2\sin^2\nu} \tag{48}$$

which can remain constant, thus the system is in equilibrium at the displacement δ of the masses given by Eq. (48) and the associated attitude angle ν. Whether this equilibrium is stable or unstable is a question not considered here. Note that ω is the gyro's angular velocity, while Ω is the angular velocity of the floating coordinate system and of the gyro's steady-state inertial force field.

In contradistinction to model gyro's I and III, the equations of motion for model gyro II are relatively short, and it may be instructive to derive them here. Using Euler angles, model gyro II's kinetic co-energy is

$$T^* = \frac{1}{2}\left((A_D + 2m(l+\delta)^2)(\dot{\psi}^2\sin^2\nu + \dot{\nu}^2) + C_D(\dot{\psi}\cos\nu + \dot{\sigma})^2 + 2m\dot{\delta}^2\right). \tag{49}$$

Its potential energy is

Downloaded 03 May 2010 to 171.66.16.20. Redistribution subject to ASME license or copyright; see http://www.asme.org/terms/Terms_Use.cfm

$$V=\frac{1}{2}2k\delta^2, \tag{50}$$

the Lagrangian

$$\mathbf{L}=T^*-V \tag{51}$$

and the Lagrange equation

$$\frac{d}{dt}\frac{\partial L}{\partial q_i}-\frac{\partial L}{\partial q_i}=Q_i'. \tag{52}$$

With $q_1=\psi$, $q_2=\nu$, $q_3=\sigma$, $q_4=\delta$, $Q_1'=Q_2'=Q_3'=0$, $Q_4'=-2c\dot{\delta}$, the four equations of motion emerge as

$$\frac{d}{dt}((A_D+2m(l+\delta)^2)\dot{\psi}\sin^2\nu+C_D(\dot{\psi}\cos\nu+\dot{\sigma})\cos\nu)=0 \tag{53a}$$

$$\frac{d}{dt}((A_D+2m(l+\delta)^2)\dot{\nu})-(A_D+2m(l+\delta)^2 - C_D)\dot{\psi}^2\sin\nu\cos\nu+C_D\dot{\psi}\dot{\sigma}\sin\nu=0 \tag{53b}$$

$$\frac{d}{dt}(C_D(\dot{\psi}\cos\nu+\dot{\sigma}))=0 \tag{53c}$$

$$m\ddot{\delta}+c\dot{\delta}+k\delta=m(l+\delta)(\dot{\psi}^2\sin^2\nu+\dot{\nu}^2). \tag{53d}$$

Equation (53d) for the steady-state, i.e., for $\ddot{\delta}=\dot{\delta}=\dot{\nu}=0$, is seen to give the same results as Eq. (47).

The generalized momenta p_i are defined by

$$p_i=\frac{\partial T^*}{\partial\dot{q}_i}. \tag{54}$$

For the generalized angular momenta we thus find from Eqs. (49) and (54)

$$p_\psi=\frac{\partial T^*}{\partial\dot{\psi}}=(A_D+2m(l+\delta)^2)\dot{\psi}\sin^2\nu - C_D(\dot{\psi}\cos\nu+\dot{\sigma})\cos\nu \tag{55a}$$

$$p_\nu=\frac{\partial T^*}{\partial\dot{\nu}}=(A_D+2m(l+\delta)^2)\dot{\nu} \tag{55b}$$

$$p_\sigma=\frac{\partial T^*}{\partial\dot{\sigma}}=C_D(\dot{\psi}\cos\nu+\dot{\sigma}). \tag{55c}$$

Angular momentum components in $Cuvz$ coordinates and covariant generalized angular momenta can be shown (Rimrott, 1988) to be related by

$$\begin{bmatrix}H_u\\H_v\\H_z\end{bmatrix}=\begin{bmatrix}0&1&0\\\frac{1}{\sin\nu}&0&\frac{1}{\tan\nu}\\0&0&1\end{bmatrix}\begin{bmatrix}p_\psi\\p_\nu\\p_\sigma\end{bmatrix} \tag{56}$$

such that Eqs. (55) and (56) can be combined to give

$$H_u=(A_D+m(l+\delta)^2)\dot{\nu} \tag{57a}$$

$$H_v=(A_D+2m(l+\delta)^2)\dot{\psi}\sin\nu \tag{57b}$$

$$H_z=C_D(\dot{\psi}\cos\nu+\dot{\sigma}). \tag{57c}$$

For the steady-state case, with $\dot{\nu}=0$, $\dot{\psi}\sin\nu=\omega_v$, and $\dot{\psi}\cos\nu+\dot{\sigma}=\omega_z$, Eqs. (57) are seen to equal Eqs. (46).

3.3 Model Gyro III. This model gyro (Fig. 5) has four equal point masses m at the tip of each of four rigid massless rods which in turn are connected by rotational springs and dashpots to the rigid central body of mass m_D. The rods are mounted such that the tip masses are displaceable in the z-direction only, assuming small displacements. This simple model resembles a spacecraft with radial antennas. Again, like in the previous cases, the mass center of the system remains at one and the same location within the model gyro. The present example is a case where it suffices to assume small deformations

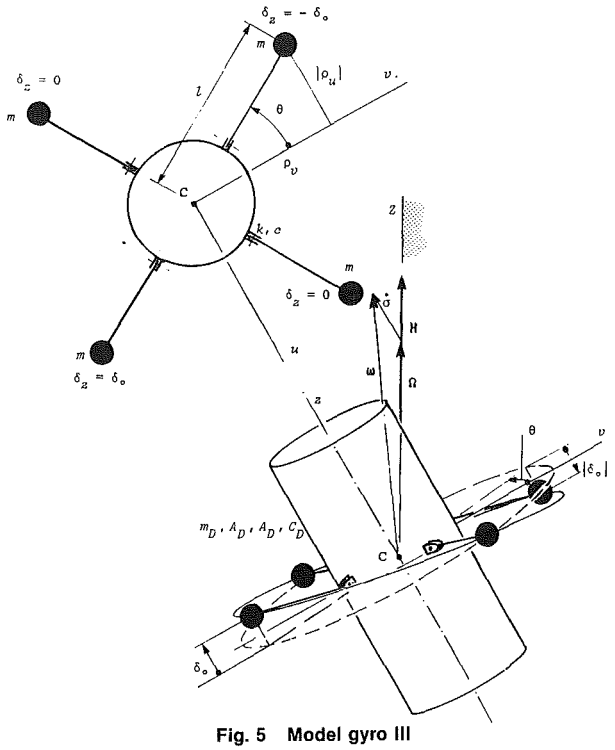


Fig. 5 Model gyro III

in order to describe the behaviour of the system. The principal inertia moments of the model gyro at rest are

$$B_0=A_0=A_D+2ml^2 \tag{58}$$

$$C_0=C_D+4ml^2 \tag{59}$$

where A_D, $B_D=A_D$ and C_D are the principal inertia moments of the disk and l is the undeformed distance of each tip mass from the mass center of the gyro. The floating coordinate frame, $Cuvz$, is chosen such that its axes are coincident with the central body's principal axes. During motion at some attitude angle ν (Fig. 5), the masses will be displaced as shown, by the inertial force field present. Because of the dampers there will be a phase difference (either lag or lead) θ between the v-axis and the location of maximum deflection (Fig. 5). With $\rho_u=-l\sin\theta$, $\rho_v=l\cos\theta$, $\rho_z=0$, $\delta_u=\delta_v=0$, $\delta_z=-\delta_o$, the elements of the primary inertia matrices for this model will be

$$J_{uu}=0 \tag{60a}$$

$$J_{vv}=0 \tag{60b}$$

$$J_{zz}=0 \tag{60c}$$

$$J_{uv}=0 \tag{60d}$$

$$J_{uz}=-2ml\delta_o\sin\theta \tag{60e}$$

$$J_{vu}=0 \tag{60f}$$

$$J_{vz}=2ml\delta_o\cos\theta \tag{60g}$$

$$J_{zu}=0 \tag{60h}$$

$$J_{zv}=0. \tag{60i}$$

The elements of the secondary inertia matrix will be

$$K_{uu}=2m\delta_o^2\approx 0 \quad \text{for small } \delta_o \tag{61a}$$

$$K_{vv}=2m\delta_o^2\approx 0 \tag{61b}$$

$$K_{zz}=0 \tag{61c}$$

$$K_{uv}=K_{vu}=0 \tag{61d}$$

$$K_{uz}=K_{zu}=0 \tag{61e}$$

$$K_{vz}=K_{zv}=0. \tag{61f}$$

Downloaded 03 May 2010 to 171.66.16.20. Redistribution subject to ASME license or copyright; see http://www.asme.org/terms/Terms_Use.cfm

With $\delta_u = \delta_v = \dot{\delta}_u = \dot{\delta}_v = 0$, $\delta_z = \delta_o$ and $\dot{\delta}_z = \dot{\delta}_o$ the term $\int_m \delta \times \mathring{\delta} dm$ vanishes, even if $\dot{\delta}_o \neq 0$.

The quantity δ_o is the maximum displacement value and θ is the phase angle. Then using an appropriate floating coordinate frame (i.e., $H_u = 0$), and from Eqs. (18), (58), (59), (60), and (61) we can write the angular momentum components as

$$H_u \approx [A_D + 2ml^2]\omega_u - [2ml\delta_o \sin\theta](2\omega_z - \Omega_z) = 0 \quad (61a)$$

$$H_v \approx [A_D + 2ml^2]\omega_v - [2ml\delta_o \cos\theta](2\omega_z - \Omega_z) = H\sin\nu \quad (61b)$$

$$H_z \approx [2ml\delta_o \sin\theta]\omega_u - [2ml\delta_o \cos\theta]\omega_v + [C_D + 4ml^2]\omega_z = H\cos\nu. \quad (61c)$$

The drift rate $\omega_u = \dot{\nu}$ can be found from (61a), and is

$$\dot{\nu} = \omega_u = \frac{2ml\delta_o \sin\theta}{A_o}(2\omega_z - \Omega_z) \quad (62)$$

where $\sin\theta$ is a measure of internal damping, with $\theta = 0$ for a gyro without internal damping, with $\theta \neq 0$ for gyros with internal damping, and $0 < \theta < 180$ deg for prolate gyros (Fig. 5), and $0 > \theta > -180$ deg for oblate gyros (Rimrott, 1988).

4 Conclusions

Using a floating coordinate frame, chosen such that one angular momentum component vanishes, the general expression for the constant angular momentum of a torque-free deforming axisymmetric gyro in terms of inertia moments and inertia products, and angular velocities of gyro and inertial force field was obtained. It is concluded that when a gyro is deforming, the deformation can be displayed in the angular momentum expression by inertia moments and inertia products. Consequently, new types of inertia moments and products, viz. primary and secondary partial inertia moments and products, have been defined.

The engineer's interest in such studies involves either the search for an energy trough, or the description of the (slow) attitude drift towards an energy trough, such that it typically suffices to study a steady-state system without transient vibration terms.

References

Canavin, J. R., and Likins, P. W., 1977, "Floating Reference Frame for Flexible Spacecraft," *AIAA Journal of Spacecraft and Rockets*, Vol. 14, No. 12, pp. 724–732.

De Veubeke, B. F., 1976, "Nonlinear Dynamics of Flexible Bodies," *Dynamics and Control of Non-Rigid Spacecraft*, European Space Agency, Neuilly, France, Special Rept. 117, pp. 11–19.

Janabi-Sharifi, F., 1990, "A Torque-Free Flexible Model Gyro," M.A.Sc. Thesis, University of Toronto, Toronto, Canada.

Rimrott, F. P. J., 1988, *Introductory Attitude Dynamics*, Springer-Verlag, New York.

Rimrott, F. P. J., 1981, "Energy Dissipation in Gyrodynamics Through the Concept of Intervalwise Rigidity," *Journal of Mechanical Engineering Science*, Vol. 23, No. 2, pp. 93–101.

Downloaded 03 May 2010 to 171.66.16.20. Redistribution subject to ASME license or copyright; see http://www.asme.org/terms/Terms_Use.cfm

Theoretical Simulation of an Anomalous Response in a Torsional Oscillator

M. Negahban
Department of Engineering Mechanics and the Center for Materials Research and Analysis, University of Nebraska, Lincoln, NE 68588-0347
Assoc. Mem. ASME

In a torsional oscillator, constructed by stretching a hollow cylindrical natural rubber member and connecting one end to a fly wheel and the other end to a fixed support, an anomalous behavior has been experimentally observed which is attributed to crystallization in the rubber. The anomalous behavior is observed when the rubber is stretched to more than 3.5 times its initial length and is characterized by a reduction in the period of the oscillator during stress relaxation. This indicates a gradual increase in the torsional rigidity of the rubber which can be explained by crystallization. Analyzing the response of the oscillator based on modeling the rubber as an incompressible isotropic elastic or viscoelastic material predicts a behavior opposite to that observed in the experiments. Using a model developed for characterizing mechanical response during crystallization in polymers, the anomalous behavior of the oscillator is reproduced.

1 Introduction

This paper is motivated by the work of Rosen, Kolsky, and Pipkin (1975), Min (1976), and Kolsky and Pipkin (1980) on the anomalous behavior of a torsional oscillator made with a stretched natural rubber torsional spring. These researchers observed that the response of the torsional oscillator violates the theoretical predictions based on assuming elastic or viscoelastic response in the rubber spring. They attributed the anomalous response to crystallization in the natural rubber. Using a constitutive equation developed by Negahban and Wineman (1992) and Negahban, Wineman, and Ma (1993) for predicting the mechanical response of polymers undergoing crystallization, the anomalous response of the oscillator is reproduced in this article.

Figure 1 shows a schematic drawing of the torsional spring, which is a hollow cylindrical member made from natural rubber, and a cross-section of the oscillator, which is made from extending the rubber spring and connecting one end to a fly wheel and the other to a fixed constraint. It is assumed that the deformation of the torsional spring is represented by a deformation of the form

$$\begin{aligned} r &= f(R), \\ \phi &= \Phi + \lambda Z\psi, \\ z &= \lambda Z, \end{aligned} \tag{1}$$

where (r, ϕ, z) are the current cylindrical coordinates of a particle in location (R, Φ, Z) in the undeformed configuration, f is a function of R, λ is the ratio of the current length of the cylinder to its initial length, and ψ is the twist per unit current length of the cylinder. Assuming such a deformation, Rivlin (1949) has shown that for all incompressible isotropic elastic materials one has the relation

$$\left.\frac{M}{\psi}\right|_{\psi=0} = \frac{(R_i^2 + R_o^2)\lambda F}{2(\lambda^3 - 1)}, \tag{2}$$

where M is the torsional moment in the cylindrical member, F is the axial load in the cylindrical member, and R_i and R_o are the inner and outer radii, respectively, of the member in its undeformed configuration. The relation obtained by Rivlin (1949) is universal in the sense that it must hold for all incompressible isotropic elastic materials which undergo the deformation described in (1). It is also important to note that this relation does not contain any explicit material constants or functions. That is, material specific functions will always ap-

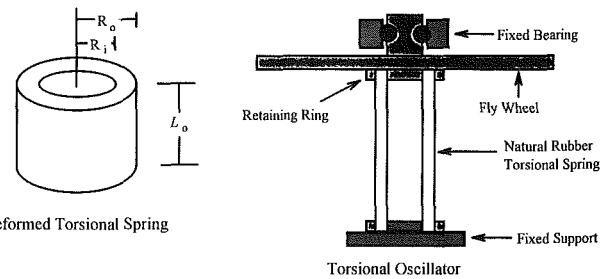


Fig. 1 Schematic drawings of the torsional spring and a cross-section of the torsional oscillator. The oscillator consists of a stretched cylindrical natural rubber spring connected to a fly wheel at one end and to a fixed support at the other end.

Contributed by the Applied Mechanics Division of THE AMERICAN SOCIETY OF MECHANICAL ENGINEERS for presentation at the ASME Winter Annual Meeting, New Orleans, LA, Nov. 28–Dec. 3, 1993.

Discussion on this paper should be addressed to the Technical Editor, Professor Lewis T. Wheeler, Department of Mechanical Engineering, University of Houston, Houston, TX 77204-4792, and will be accepted until four months after final publication of the paper itself in the ASME JOURNAL OF APPLIED MECHANICS.

Manuscript received by the ASME Applied Mechanics Division, Sept. 3, 1992; final revision, Feb. 24, 1993. Associate Technical Editor: W. N. Sharpe, Jr.

Paper No. 93-WA/APM-22.

Copyright © 1994 by ASME
Downloaded 03 May 2010 to 171.66.16.20. Redistribution subject to ASME license or copyright; see http://www.asme.org/terms/Terms_Use.cfm

pear in an appropriate combination to yield the expressions for the axial force and torsional moment. If the rotation of the fly wheel in the torsional pendulum is denoted by Ψ and the initial unstretched length of the sample is given by L_o, one will have $\Psi = \lambda L_o \psi$, and the free response of the pendulum for small oscillations can be represented by the expression

$$\ddot{\Psi} + \frac{k}{I}\Psi = 0, \tag{3}$$

where I is the moment of inertia of the fly wheel, and

$$k = \frac{(R_i^2 + R_o^2)\lambda F}{2L_o(\lambda^3 - 1)} \tag{4}$$

is the torsional rigidity of the rubber at $\Psi = 0$. Therefore, the period of free vibration of this oscillator, τ, is given by

$$\tau = \sqrt{\frac{8\pi^2 L_o I}{R_i^2 + R_o^2}}\sqrt{\frac{\lambda^3 - I}{\lambda F}}. \tag{5}$$

This result suggested to Kolsky and his co-workers that the plot of $\sqrt{(\lambda^3 - 1)/\lambda F}$ as a function of the period of oscillation in the torsional oscillator should yield a linear relation with a positive slope equal to $\sqrt{(R_i^2 + R_o^2)/8\pi^2 L_o I}$ and which is only a function of the undeformed shape of the torsional spring and the moment of inertia of the fly wheel and not a function of the particular material used in the torsional spring (as long as the spring is isotropic, elastic, and incompressible, and the oscillations are small). Figure 2 shows experimental results obtained by Rosen, Kolsky, and Pipkin (1975) for stretch ratios λ up to 3 in the natural rubber torsional spring at room temperature. These experimental results seem to validate the theoretical relation given in (5).[1] For λ larger than about 3.5, these researchers observed an anomalous behavior at room temperature, which is shown in Fig. 3 for $\lambda = 5.059$. This anomalous behavior is characterized by the reversal of the slope of the plot of $\sqrt{(\lambda^3 - 1)/\lambda F}$ as a function of τ from positive to negative. An additional difference between the behavior at stretch ratios below 3 and above 3.5 is the appearance of a substantial stress relaxation in the natural rubber for stretch ratios above 3.5, which makes it possible to make plots for many different loads and periods at the same stretch ratio. As noted by these researchers, normal viscoelastic response would not account for this reversal of slope. Rosen, Kolsky, and Pipkin (1975) suggest that this behavior is due to gradual crystallization in the rubber, which results in the gradual increase of the torsional rigidity with stress relaxation.

To observe the effects of crystallization in the rubber on the behavior of the pendulum, a theoretical model developed by Negahban and Wineman (1992) and Negahban, Wineman, and Ma (1993) will be used in this article. In Section 2 the model used to follow mechanical response during crystallization is described, and the instantaneous elastic response of the rubber is fit to experimental results obtained by Min et al. (1976, 1977). In Section 3 the torsional response during crystallization is predicted and compared to the anomalous experimental results obtained by Min (1976) and presented by Kolsky and Pipkin (1980). Special comments and conclusions are presented in Section 4.

2 Definitions, Notation, and the Constitutive Equation

A constitutive theory has been developed by Negahban and Wineman (1992) to model crystallization in polymers. This theory is a microstructurally motivated one. It assumes that

[1] Due to a lack of information on the moment of inertia of the fly wheel and the inner and outer radii of the undistorted spring, it is not possible to exactly validate this relation using the experimental results given by Rosen, Kolsky, and Pipkin (1975).

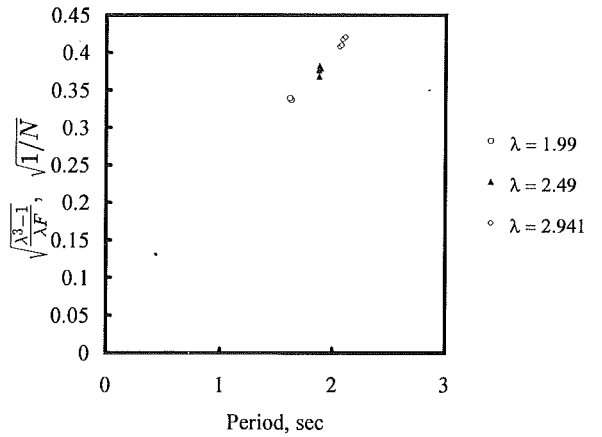


Fig. 2 Experimental results of Rosen, Kolsky, and Pipkin (1975) on the behavior of a torsional oscillator consisting of a stretched natural rubber torsional spring connected to a fly wheel

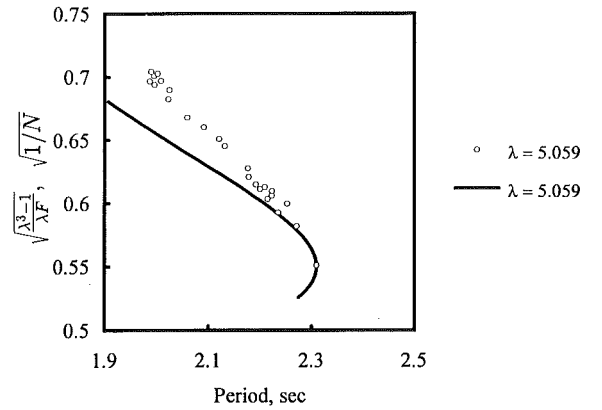


Fig. 3 An anomalous behavior is seen in the torsional oscillator for stretch ratios larger than about $\lambda = 3.5$. Experimental results of Rosen, Kolsky, and Pipkin (1975) and theoretical predictions for a stretch ratio of $\lambda = 5.059$.

crystals are continuously being generated and that the response of these crystals will change as the conditions of crystallization change. The mechanism for including this effect is the assumption that the macroscopic value of the Cauchy stress is the mass weighted average of the effective stress in the amorphous (uncrystallized) material and the stresses in the different crystals. The constitutive equation for the Cauchy stress $\mathbf{T}$ at the current time t has the form

$$\mathbf{T}(t) = b(t)\mathbf{T}^A(t) + \int_{t_s}^{t} a(s)\mathbf{T}^C(t,s)ds, \tag{6}$$

where $b(t)$ is the current ratio of amorphous matter to total matter at the particular material point, $a(s)$ is the normalized rate of mass transfer from amorphous matter to crystalline matter at time s, $\mathbf{T}^A(t)$ is the current value of the effective stress in the amorphous portion of the material, $\mathbf{T}^C(t,s)$ is the current value of the effective stress in the crystal created at time s, and t_s is the starting time of crystallization. In this expression time s is used as a marker to distinguish between crystals formed at different times, under different conditions, and which have different mechanical properties.

The rate of crystallization $a(s)$ is the rate of mass transfer per unit total mass (amorphous plus crystallized mass) at any particular material point. Conservation of mass requires that

$$b(t) = 1 - \int_{t_s}^{t} a(s)ds. \tag{7}$$

Downloaded 03 May 2010 to 171.66.16.20. Redistribution subject to ASME license or copyright; see http://www.asme.org/terms/Terms_Use.cfm

2.1 Kinematics. The location of a particle X in the initial configuration will be denoted by $\mathbf{X}$, and its location in the configuration at time s will be denoted by $\mathbf{x}(s)$. The components of $\mathbf{X}$ in a cylindrical coordinate system are given by R, Φ, and Z, and the components of $\mathbf{x}(s)$ in this same coordinate system are given by $r(s)$, $\phi(s)$, and $z(s)$. The deformation gradient comparing the configuration at time s to the initial configuration will be denoted by $\mathbf{F}(s)$. The deformation gradient comparing the configuration at the current time t to the configuration at time s will be denoted by $\mathbf{F}_s(t)$ and defined as $\mathbf{F}_s(t) = \mathbf{F}(t)\mathbf{F}^{-1}(s)$. The two left Cauchy strain tensors created by $\mathbf{F}(t)$ and $\mathbf{F}_s(t)$ will be given by $\mathbf{B}(t) = \mathbf{F}(t)\mathbf{F}^T(t)$ and $\mathbf{B}_s(t) = \mathbf{F}_s(t)\mathbf{F}_s^T(t)$, respectively. The volume ratio, the ratio of current volume to initial volume at any material point, will be denoted by $J(t)$ and is given by $J(t) = \det(\mathbf{F}(t))$, where $\det(\cdot)$ denotes the determinant operation.

2.2 Description of the Specific Model Used. For the purpose of illustrating the predictions of the model and for the purpose of reproducing the behavior of natural rubber, the special form of the constitutive equation proposed by Negahban, Wineman, and Ma (1993) will be used in this article. This model is given as

$$\mathbf{T}(t) = p\mathbf{I} + \frac{mJ(t)-1}{m-1} q(t)\mathbf{B}(t) + \frac{m}{m-1}\int_{J(t)}^{1} w(s)\mathbf{B}_s(t)\,dJ(s), \quad (8)$$

where p is an indeterminate constant, $q(t)$ can be a function of the volume ratio $J(t)$, and $w(s)$ can be a function of the three isotropic invariants of $\mathbf{B}(s)$, $m = \rho_C/\rho_A$, ρ_C is the density for the crystal, and ρ_A is the density for the amorphous polymer. In essence, it is assumed that the equation for the effective stress in the amorphous part is given by $\mathbf{T}^A(t) = q(t)\mathbf{B}(t)$ and in the crystals is given by $\mathbf{T}^C(t,s) = w(s)\mathbf{B}_s(t)$. In this form it is assumed that each phase is incompressible, allowing volume change only due to transformation of matter from the amorphous to crystalline phase. In this case, the ratio of amorphous matter and the rate of crystallization are given by

$$b(t) = \frac{mJ(t)-1}{m-1} \quad \text{and} \quad a(s) = -\frac{m}{m-1}\frac{dJ(s)}{ds}. \quad (9)$$

Negahban, Wineman, and Ma (1993) have fit this model using $q(t) = Q_1 + Q_2(1-J(t))$ and $w(s) = W_1 + W_2(1-J(s))$ to experimental results on the change of elastic modulus in unconstrained natural rubber at 0°C given by Leitner (1955). In this case Q_1, Q_2, W_1, and W_2 are taken to be constants given as

$$Q_1 = 0.327\,\text{MPa},\quad Q_2 = -31.9\,\text{MPa},\quad W_1 = 5.19\,\text{MPa},$$
$$W_2 = 119\times 10^2\,\text{MPa},\quad \text{and}\quad m = 1.10. \quad (10)$$

Figure 4 shows the theoretical curve and the experimental results of Lietner (1955).

In this article only Q_1 will be adjusted to fit experimental results obtained by Min (1976) for the instantaneous response of rubber under tension at room temperature. For this model, in the absence of crystallization, $J(t) = 1$, the mechanical response is that of a Neo-Hookian material. That is

$$\mathbf{T}(t) = p\mathbf{I} + Q_1\mathbf{B}(t). \quad (11)$$

This results in an expression for the true stress, σ, in uniaxial extension of the form

$$\sigma = Q_1\left(\lambda^2 - \frac{1}{\lambda}\right), \quad (12)$$

where λ is the stretch ratio. *A least-square fit of this expression to the experimental results of Min (1976) yields a value of* $Q_1 = 0.405$ MPa. Figure 5 shows Eq. (12) for $Q_1 = 0.405$ MPa and the experimental results of Min (1976).

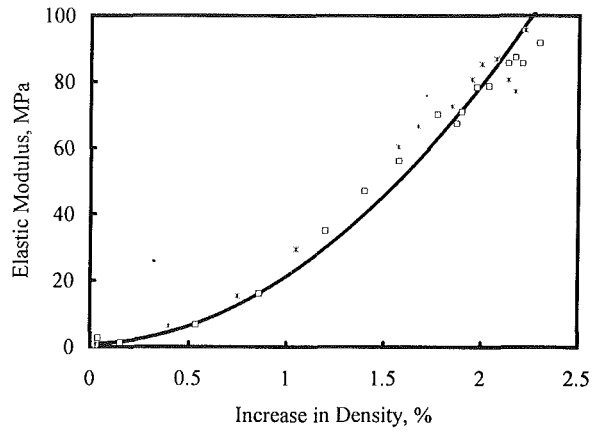


Fig. 4 Theoretical fit to experimental results of Lietner (1955) on the elastic modulus at 0°C during unconstrained crystallization. — Theoretical; ∗ Leitner sample A; □ Leitner sample B.

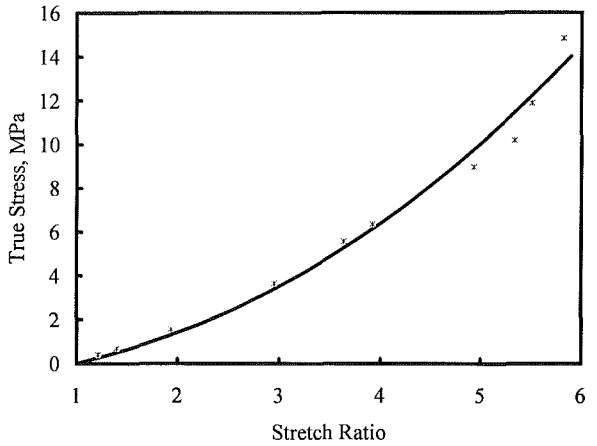


Fig. 5 Theoretical fit to experimental results of Min (1976) on the instantaneous response (1 sec after loading) in uniaxial extension of natural rubber at room temperature (22°C). — Theoretical; ∗ Experimental results of Min.

3 Response During Crystallization in the Torsional Oscillator

The experimental results presented on the response of the torsional oscillator in the works of Rosen, Kolsky, and Pipkin (1975), Min (1976), and Kolsky and Pipkin (1980) were conducted in the following manner. The torsional rubber spring was extended and allowed to relax in the stationary oscillator for an initial period of time, then the oscillator was slightly perturbed and the period of 15 to 40 oscillations was measured. By adjusting the initial period of stationary stress relaxation, the period of free oscillation of the torsional oscillator was obtained at different points in the load relaxation.

As is suggested by the aforementioned experimental procedure, most of the crystallization occurs in the initial interval of load relaxation. Therefore, it will be assumed that the rubber will crystallize under uniaxial extension ($\psi = 0$), and negligible crystallization occurs during the oscillations (J is constant). If s is a time in the initial interval of load relaxation, the deformation of the rubber can be represented by

$$r(s) = \sqrt{\frac{I(s)}{\lambda}}R,\qquad \phi(s) = \Phi,\qquad z(s) = \lambda Z. \quad (13)$$

Downloaded 03 May 2010 to 171.66.16.20. Redistribution subject to ASME license or copyright; see http://www.asme.org/terms/Terms_Use.cfm

The components of the deformation gradient at time s and in cylindrical coordinates will be given by

$$\mathbf{F}(s)=\begin{bmatrix} \frac{\partial r(s)}{\partial R} & \frac{1}{R}\frac{\partial r(s)}{\partial \Phi} & \frac{\partial r(s)}{\partial Z} \\ r(s)\frac{\partial \phi(s)}{\partial R} & \frac{r(s)}{R}\frac{\partial \phi(s)}{\partial \Phi} & r(s)\frac{\partial \phi(s)}{\partial Z} \\ \frac{\partial z(s)}{\partial R} & \frac{1}{R}\frac{\partial z(s)}{\partial \Phi} & \frac{\partial z(s)}{\partial Z} \end{bmatrix}$$

$$=\begin{bmatrix} \sqrt{\frac{J(s)}{\lambda}} & 0 & 0 \\ 0 & \sqrt{\frac{J(s)}{\lambda}} & 0 \\ 0 & 0 & \lambda \end{bmatrix}. \quad (14)$$

During stress relaxation, assuming no torsion, the axial stretch λ is held constant and one will get the expression

$$\mathbf{F}_s(t)=\mathbf{F}(t)\mathbf{F}^{-1}(s)=\begin{bmatrix} \sqrt{\frac{J(t)}{J(s)}} & 0 & 0 \\ 0 & \sqrt{\frac{J(t)}{J(s)}} & 0 \\ 0 & 0 & 1 \end{bmatrix}. \quad (15)$$

Expressions (14) and (15) result in

$$\mathbf{B}(t)=\begin{bmatrix} \frac{J(t)}{\lambda} & 0 & 0 \\ 0 & \frac{J(t)}{\lambda} & 0 \\ 0 & 0 & \lambda^2 \end{bmatrix}, \quad (16)$$

and

$$\mathbf{B}_s(t)=\begin{bmatrix} \frac{J(t)}{J(s)} & 0 & 0 \\ 0 & \frac{J(t)}{J(s)} & 0 \\ 0 & 0 & 1 \end{bmatrix}. \quad (17)$$

Substitution of these expressions into (8) results in the two independent equations

$$T_{rr}(t)=p+\frac{mJ(t)-1}{m-1}q(t)\frac{J(t)}{\lambda}+\frac{m}{m-1}\int_{J(t)}^{1} w(s)\frac{J(t)}{J(s)}dJ(s),$$

$$T_{zz}(t)=p+\frac{mJ(t)-1}{m-1}q(t)\lambda^2+\frac{m}{m-1}\int_{J(t)}^{1} w(s)dJ(s), \quad (18)$$

where T_{rr} and T_{zz} are the components of the Cauchy stress in cylindrical coordinates. Substitution of the condition $T_{rr}(t)=0$, to satisfy the stress-free boundary condition on the lateral surfaces and elimination of p from these equations results in the expression for the axial stress as

$$T_{zz}(t)=\frac{mJ(t)-1}{m-1}q(t)\left[\lambda^2-\frac{J(t)}{\lambda}\right]+\frac{m}{m-1}\int_{J(t)}^{1} w(s)\left[1-\frac{J(t)}{J(s)}\right]dJ(s). \quad (19)$$

Integration over the cross-section, one obtains the expression for the axial load as

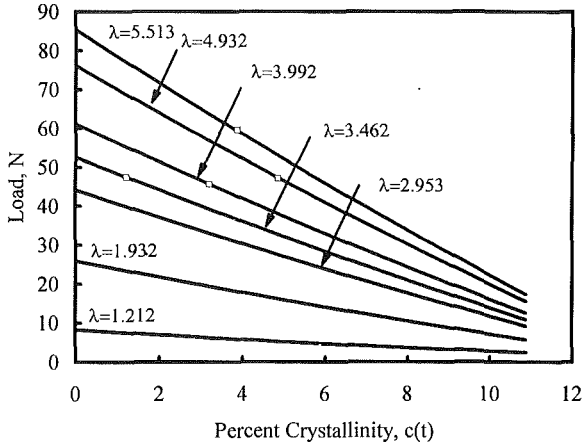


Fig. 6 Theoretical plots of load relaxation as a function of percent crystallinity. Final loads after relaxation obtained by Min (1976) are marked using a □.

$$F=2\pi\int_{r_i(t)}^{r_o(t)} T_{zz}(t)r(t)dr$$

$$=\frac{\pi[R_o^2-R_i^2]J(t)}{\lambda}\left[\frac{mJ(t)-1}{m-1}q(t)\left[\lambda^2-\frac{J(t)}{\lambda}\right]+\frac{m}{m-1}\int_{J(t)}^{1} w(s)\left[1-\frac{J(t)}{J(s)}\right]dJ(s)\right], \quad (20)$$

where $r_i(t)=\sqrt{J(t)/\lambda}\,R_i$ and $r_o(t)=\sqrt{J(t)/\lambda}\,R_o$ are the current values of the inner and outer radii, respectively. Figure 6 shows the relaxation of load as a function of percent crystallization, $c(t)$, which is given as

$$c(t)=\frac{100m[1-J(t)]}{m-1}. \quad (21)$$

Comparison of Fig. 6 and the load relaxation data of Min (1976) shows that there is between one and five percent crystallization in samples which show the anomalous behavior. The final load after relaxation obtained by Min (1976) is superimposed on Fig. 6. These results are consistent with the X-ray diffraction studies of Wildschut (1946) and the calorimetric studies of Göritz and Müller (1973) for natural rubber at room temperature.

After crystallization under uniaxial extension, it is assumed that there is negligible crystallization during the torsional oscillation (J is constant). A deformation of the form given in (1) is assumed to represent the stretched and twisted cylindrical member. The current value of the deformation gradient will be given by

$$\mathbf{F}(t)=\begin{bmatrix} \frac{J(t)R}{\lambda r(t)} & 0 & 0 \\ 0 & \frac{r(t)}{R} & r(t)\lambda\psi(t) \\ 0 & 0 & \lambda \end{bmatrix}, \quad (22)$$

where use has been made of the relation $J(t)=(\partial r(t)/\partial R)(r(t)/R)\lambda$. This results in

$$\mathbf{B}(t)=\begin{bmatrix} \frac{J^2(t)R^2}{\lambda^2 r^2(t)} & 0 & 0 \\ 0 & \frac{r^2(t)}{R^2}+r^2(t)\lambda^2\psi^2(t) & r(t)\lambda^2\psi(t) \\ 0 & r(t)\lambda^2\psi(t) & \lambda^2 \end{bmatrix}. \quad (23)$$

Downloaded 03 May 2010 to 171.66.16.20. Redistribution subject to ASME license or copyright; see http://www.asme.org/terms/Terms_Use.cfm

If s is a time in the interval of crystallization (uniaxial extension), then using Eqs. (14) and (22) one gets

$$\mathbf{F}_s(t)=\mathbf{F}(t)\mathbf{F}^{-1}(s)$$
$$=\begin{bmatrix} \dfrac{J(t)R}{r(t)\sqrt{\lambda J(s)}} & 0 & 0 \\ 0 & \dfrac{r(t)}{R}\sqrt{\dfrac{\lambda}{J(s)}} & r(t)\lambda\psi(t) \\ 0 & 0 & 1 \end{bmatrix}, \quad (24)$$

and

$$\mathbf{B}_s(t)=\begin{bmatrix} \dfrac{J^2(t)R^2}{r^2(t)\lambda J(s)} & 0 & 0 \\ 0 & \dfrac{r^2(t)\lambda}{R^2J(s)}+r^2(t)\lambda^2\psi^2(t) & r(t)\lambda\psi(t) \\ 0 & r(t)\lambda\psi(t) & 1 \end{bmatrix}. \quad (25)$$

Substitution of (23) and (25) into (8) results in the equation

$$T_{\phi z}(t)=\frac{mJ(t)-1}{m-1}q(t)r(t)\lambda^2\psi(t)+\frac{m}{m-1}\int_{J(t)}^{1}w(s)r(t)\lambda\psi(t)dJ(s). \quad (26)$$

The torsional moment, M, is then obtained from

$$M(t)=2\pi\int_{r_j(t)}^{r_o(t)}T_{\phi z}r^2(t)dr$$
$$=\frac{\pi[r_o^4(t)-r_i^4(t)]}{2}\left[\frac{mJ(t)-1}{m-1}q(t)\lambda+\frac{m}{(m-1)}\int_{J(t)}^{1}w(s)dJ(s)\right]\lambda\psi(t). \quad (27)$$

Substituting for $\psi(t)$ from the relation $\Psi(t)=\lambda L_o\psi(t)$, dividing by $\Psi(t)$, taking the limit as $\Psi(t)$ goes to zero, and substituting from $r_i(t)=\sqrt{J(t)/\lambda}\,R_i$ and $r_o(t)=\sqrt{J(t)/\lambda}\,R_o$ at $\Psi(t)=0$, one gets

$$k=\left.\frac{M(t)}{\Psi(t)}\right|_{\Psi(t)=0}=\frac{\pi[R_o^4-R_i^4]J^2(t)}{2\lambda^2L_o}\left[\frac{mJ(t)-1}{m-1}q(t)\lambda+\frac{m}{(m-1)}\int_{J(t)}^{1}w(s)dJ(s)\right], \quad (28)$$

where k is the torsional rigidity of the torsional spring. Figure 7 shows the plot of k as a function of percent crystallization $c(t)$ for different stretch ratios λ assuming a torsional spring of unit initial length, inner radius of 0.318-cm, and thickness of 0.159-cm.[2] As can be seen, the torsional rigidity shows a slight initial decrease before increasing.

For small oscillations, the period of free oscillation of the fly wheel in the torsional oscillator is given by

$$\tau=2\pi\sqrt{\frac{I}{k}}. \quad (29)$$

To reproduce the available experimental results it is necessary to know the moment of inertia I. A study of the experimental results presented by Rosen, Kolsky, and Pipkin (1975)

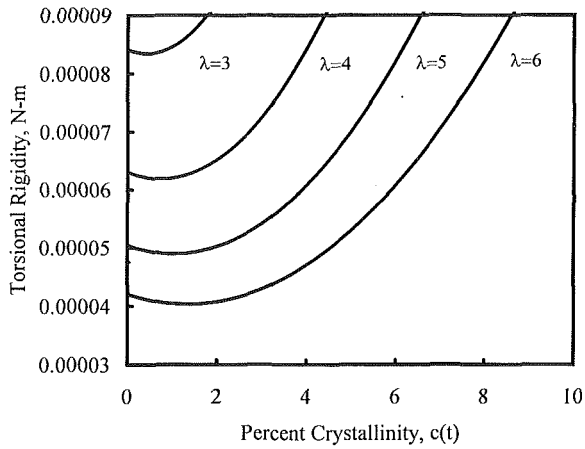


Fig. 7 Theoretical plots of torsional rigidity k as a function of percent crystallinity for several different stretch ratios λ. It is assumed that the sample has an initial length of unity and inner radius of 0.318 cm and thickness of 0.159 cm.

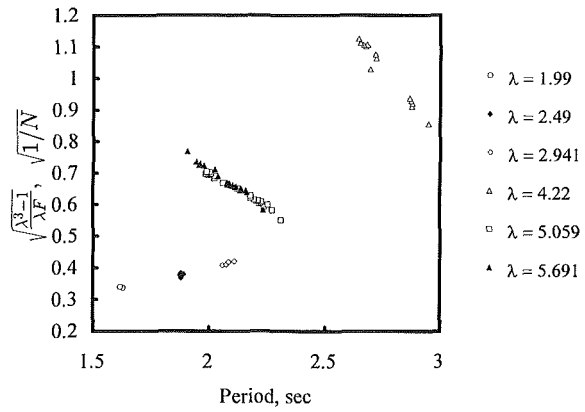


Fig. 8 Composite of experimental results of Rosen, Kolsky, and Pipkin (1975) for the response of a natural rubber torsional oscillator at room temperature. The data for λ less than three have been adjusted based on Eq. (5) to account for the difference in length between the rubber specimens used for these stretch ratios.

shows that there is some variation between the conditions existing in the different experiments. These differences can be attributed to variations in I and the rubber specimens. This variation is immediately obvious from plotting all the results they present on a single graph of $\sqrt{(\lambda^3-1)/\lambda F}$ as a function of period, as shown in Fig. 8 (adjustment has been made for the difference between the length of the samples below and above $\lambda=2$). The response of the oscillator before crystallization should be elastic, and, therefore, a straight line passing through the origin should connect the lowest points (initial unrelaxed response) of all results. In addition, the plots show that the load for $\lambda=4.22$ is much smaller than that for $\lambda=1.99$, 2.49, and 2.941, suggesting a difference between the sample cross-sectional areas. Accepting the possibility of variation between the experimental conditions, a fitting of one point, point of maximum τ of the theoretical response to the experimental data, was used to reproduce the response for $\lambda=5.059$. The results of the predicted and observed response of the oscillator are shown in Fig. 3.

There seems to be "less" variation between the experimental results of Min (1976), which are presented by Kolsky and Pipkin (1980), for λ between 3.462 and 3.992 at 22°C. In this case, the moment of inertia I is obtained by fitting the instantaneous response (lowest experimental points) to Eq. (5) by a least-square procedure. The moment of inertia obtained

[2] The specimens used by Rosen, Kolsky and Pipkin (1975) had a length of 3.75 in. for $\lambda=1.99$, 2.49, and 2.941, and had a length of 2.5 in. for $\lambda=4.22$, 5.059, and 5.691. The experiments of Min (1976) were conducted with specimens of length 2.5 in. and inner radius of 1/8 in. and thickness 1/16 in.

Downloaded 03 May 2010 to 171.66.16.20. Redistribution subject to ASME license or copyright; see http://www.asme.org/terms/Terms_Use.cfm

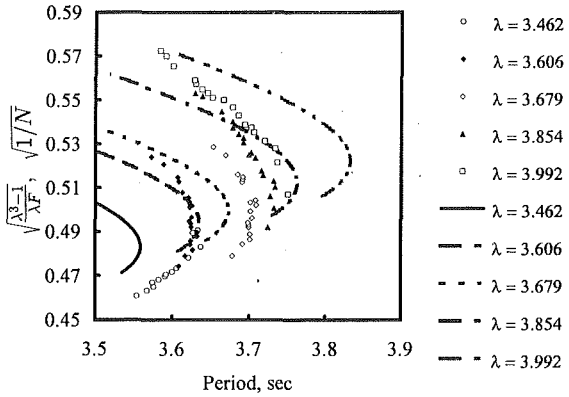


Fig. 9 Theoretical predictions and experimental results of Min (1976) for the response of a natural rubber torsional oscillator at room temperature

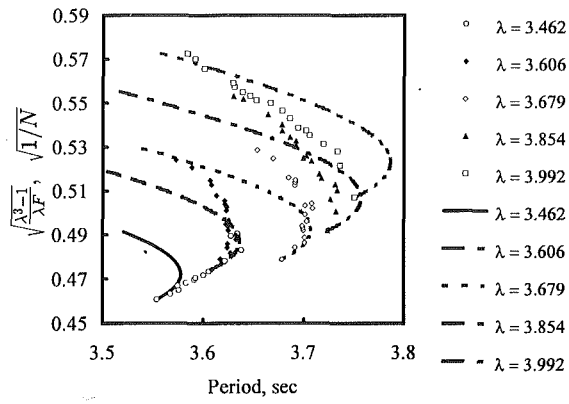


Fig. 10 Theoretical predictions and experimental results of Min (1976) for the response of a natural rubber torsional oscillator at room temperature. The theoretical plots are fit to the initial response of the oscillator, assuming the initial response is the elastic response.

using this procedure is $I = 0.376 \times 10^{-3}$ kg m^2.[3] Figure 9 shows the experimental and predicted values of the response of the oscillator. As can be seen, the experimental results show a gradual transition from the so called normal to anomalous behavior at these stretch ratios. The data do not seem to follow a very regular pattern, which might be an indication of the difficulty in conducting these experiments. In spite of this, the theoretical model can capture the general behavior of the oscillator. The ability of the theoretical model to capture the initial increase and later decrease of the period of oscillation is a result of the slight dip observed in the torsional rigidity as a function of crystallization, as shown in Fig. 7. Assuming that the geometric shape of the samples used or the moment of inertia of the fly wheel can be slightly different for the different experiments, the theoretical results were fit to the initial response of the oscillator, assuming this represents elastic response. Figure 10 shows the result of this operation. As can be seen, the stress relaxes at a slower rate in the theoretical model. This can be either an indication of normal viscoelastic stress relaxation in addition to relaxation due to crystallization, or the material relaxes more rapidly due to crystallization at room temperature than it relaxes at -26°C (the originally proposed material constants for the model, Eq. (13), assume full stress relaxation at approximately ten percent crystallization as suggested by data presented by Gent (1954) for natural rubber at -26°C). Without access to other information it would not be appropriate to make any further changes in the material properties. Figure 11 shows the general response theoretically predicted for the oscillator using parameters similar to those used in Fig. 9.

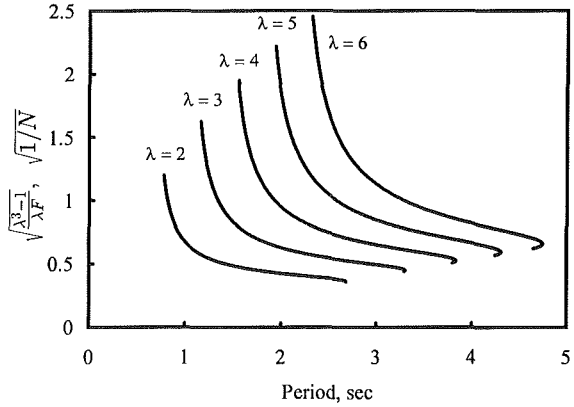


Fig. 11 Theoretical predictions of the response of the torsional oscillator for different stretch ratios

4 Summary and Conclusion

As has been shown, the constitutive equation developed for modeling mechanical response during crystallization can be used to predict qualitatively the anomalous behavior seen in the torsional oscillator at large stretch ratios. The lack of information on some of the parameters of the experimental setup required a fitting of the theoretical results to the instantaneous (initially unrelaxed) response of the oscillator, but the shape and behavior during the portion that involves crystallization is totally predicted based on fitting the model to other experimental results. One source of difference between the predicted and observed results might be due to the fact that most material parameters are fit to experimental results of Lietner (1955) which were conducted at 0°C (the current results are for room temperature).

In the work of Min (1976) and Kolsky and Pipkin (1980), there is a set of plots obtained at temperatures between 23°C and 37°C which indicate that the anomalous response will stop at the higher temperatures and an S-shaped plot results. This response, which shows a transition from normal to anomalous and back to normal behavior, cannot be predicted by the model proposed in this article. At these temperatures it is reasonable to assume that crystallization is occurring in conjunction with normal viscoelastic relaxation. A replacement of the model for the behavior of the amorphous part of the rubber from elastic to viscoelastic should result in a model which is able to predict these S-shaped response curves.

Acknowledgment

This work was partially supported by the Air Force through the Air Force Engineering Foundation Grant RI-B-90-12. The author would like to thank Mr. Farrell Calcaterra and Ms. Ruo-Juan Ma for the help they provided.

References

Gent, A. N., 1954, "Crystallization and the Relaxation of Stress in Stretched Natural Rubber Vulcanizates," *Trans. Faraday Soc.*, Vol. 50, pp. 521–533.

Göritz, V. D., and Müller, F. H., 1973, "Zustandsänderungen von polymeren Netzwerken bei Orientierung II. Analyse der Dehnungskristallisation auf der Grundlage kalorimetrischer Untersuchungen," *Kolloid-Z. U. Z. Polymere*, Vol. 25, pp. 892–900.

Kolsky, H., and Pipkin, A. C., 1980, "The Viscoelastic Response of Highly-

[3] A similar procedure for find I for the data of Rosen, Kolsky and Pipkin (1975) resulted in $I = 0.322 \times 10^{-3}$ Kg m^2, based on using two torsional springs as is suggested in their description. Therefore, there seems to be up to 17 percent difference in I between the results of Rosen, Kolsky, and Pipkin (1975) and Min (1976), assuming all other parameters are equal.

Downloaded 03 May 2010 to 171.66.16.20. Redistribution subject to ASME license or copyright; see http://www.asme.org/terms/Terms_Use.cfm

Stretched Rubber Specimens to Superposed Torsional Deformation," *Ingenieur-Archiv*, Vol. 49, pp. 337–345.

Leitner, M., 1955, "Young's Modulus of Crystalline, Unstretched Rubber," *Trans. Faraday Soc.*, Vol. 51, p. 1015.

Min, B. K., 1976, "Dynamic Behavior of Some Solids and Liquids," Doctoral dissertation, Brown University, Providence, RI.

Min, B. K., Kolsky, H., and Pipkin, A. C., 1977, "Viscoelastic Response to Small Deformations Superimposed on a Large Stretch," *Int. J. Solids Structures*, Vol. 13, pp. 771–781.

Negahban, M., and Wineman, A. S., 1992, "Modeling the Mechanical Response of a Material Undergoing Continuous Isothermal Crystallization," *International Journal of Engineering Science*, Vol. 30, No. 7, pp. 953–962.

Negahban, M., Wineman, A. S., and Ma, R. J., 1993, "Simulation of Mechanical Response in Polymer Crystallization," *International Journal of Engineering Science*, Vol. 31, No. 1, pp. 93–113.

Rivlin, R. S., 1949, "Large Elastic Deformation of Isotropic Materials—VI. Further Results in the Theory of Torsion, Shear and Flexure," *Phil. Trans. Royal Soc. London*, Vol. A242, pp. 173–195.

Rosen, R. H., Kolsky, H., Pipkin, A. C., 1975, "Anomalous Torsional Dynamic Response of Axially Stretched Rubber While Stress Relaxation is Taking Place," *Journal of Applied Physics*, Vol. 46, No. 10, pp. 4441–4444.

Wildschut, A. J., 1946, "On the Proportion of Crystalline and Amorphous Components in Stretched Vulcanized Rubber," *Journal of Applied Physics*, Vol. 17, pp. 51–60.

Downloaded 03 May 2010 to 171.66.16.20. Redistribution subject to ASME license or copyright; see http://www.asme.org/terms/Terms_Use.cfm

Mode-Locking and Chaos in a Jeffcott Rotor With Bearing Clearances

Sang-Kyu Choi
Graduate Student.

Sherif T. Noah
Professor,
Mem. ASME.

Department of Mechanical Engineering,
Texas A&M University,
College Station, TX 77843-3123

A complex mode-locking (or entrainment) structure underlying the nonlinear whirling phenomenon of a horizontal Jeffcott rotor with a discontinuous nonlinearity (bearing clearance) was identified. A winding number is introduced as a measure of the ratio between two frequencies involved in the aperiodic whirling motions of the rotor system considered. Utilizing the winding number map, it was revealed that the alternating periodic and quasi-periodic responses take place according to the Farey number tree. The winding number varies in the form of the so-called "Devil's staircase" as a certain system parameter varies.

From the mode-locking pattern in the parameter space of the forcing amplitude and frequency, it was observed that as the forcing amplitude increases, the size of each locking interval increases so that its growth takes place in the form of "Arnol'd tongues," where the winding number remains a rational number. Moreover, inside each locking zone, i.e., each "Arnol'd tongue," there exist many smaller tongues similar to the main tongue, in which a sequence of period-doubling bifurcations leading to chaos occurred. The boundaries of each locking zone was obtained using a fixed-point algorithm along with the Floquet theory for checking the stability of the periodic solutions. The winding numbers were estimated utilizing a fixed-point algorithm modified to obtain quasi-periodic responses. A jump phenomenon was also observed by tracking multiple periodic solutions for several parameters of the rotor system.

1 Introduction

It is well known that general rotor systems exhibit nonlinear behavior due to bearing clearances, squeeze film dampers, seals and fluid-dynamic effects, and other sources. Recently, several investigators have paid particular attention to understand nonsynchronous whirling behavior of nonlinear rotor systems involving bearing clearances. A jump phenomenon, which typically occurs in nonlinear systems, was first observed by Yamamoto (1960). The existence of subharmonic whirling motions in a simple experimental rotor system with a bearing clearance was reported by Bently (1974). Childs (1982) used a perturbation technique to study the occurrence of subharmonics, assuming small nonlinearity for the bearing clearance. Choi and Noah (1987) showed the occurrence of super and subharmonics in a rotor model involving a bearing clearance using a harmonic balance method (HBM) along with a discrete Fourier transform (DFT) procedure, which was originally used by Yamauchi (1983) and Saito (1985). Ehrich (1988) used numerical integration to show the presence of higher subharmonics (up to ninth order) in a high-speed rotor system with a bearing clearance.

In addition to the super and subharmonic whirling motions, it was reported that a nonlinear rotor system could show aperiodic whirling motion (Child, 1983). An attempt to explain the occurrence of this aperiodic motion in a Jeffcott rotor model was made by Day (1987) using the multiple scale method. Day's analysis, however, failed to yield an adequate explanation for the aperiodic whirling motions. This stems from the fact that the multiple scale method has a limitation in its application to highly nonlinear, nonanalytic functions, such as that describing a bearing clearance. Beatty and Hine (1989) also reported their experimental observation of subsynchronous (aperiodic) whirls at about 90 percent of shaft speed in the High Pressure Oxygen Turbopump (HPOTP) of the Space Shuttle Main Engine (SSME). Kim and Noah (1990) used a modified Jeffcott model to determine the onset of aperiodic whirling motion using bifurcation theory. Nevertheless, the understanding of the underlying structure of the quasi-periodic whirling behavior of rotor systems is far from being complete.

In this paper, by introducing the winding number as a measure of the ratio between two frequencies involved in the aperiodic whirling responses, an attempt is made to reveal a partial picture of the underlying structure of the dynamic behavior

Contributed by the Applied Mechanics Division of THE AMERICAN SOCIETY OF MECHANICAL ENGINEERS for publication in the ASME JOURNAL OF APPLIED MECHANICS.

Discussion on this paper should be addressed to the Technical Editor, Professor Lewis T. Wheeler, Department of Mechanical Engineering, University of Houston, Houston, TX 77204-4792, and will be accepted until four months after final publication of the paper itself in the ASME JOURNAL OF APPLIED MECHANICS.

Manuscript received by the ASME Applied Mechanics Division, Mar. 17, 1992; final revision, Dec. 10, 1992. Associate Technical Editor: D. J. Inman.

Copyright © 1994 by ASME
Downloaded 03 May 2010 to 171.66.16.20. Redistribution subject to ASME license or copyright; see http://www.asme.org/terms/Terms_Use.cfm

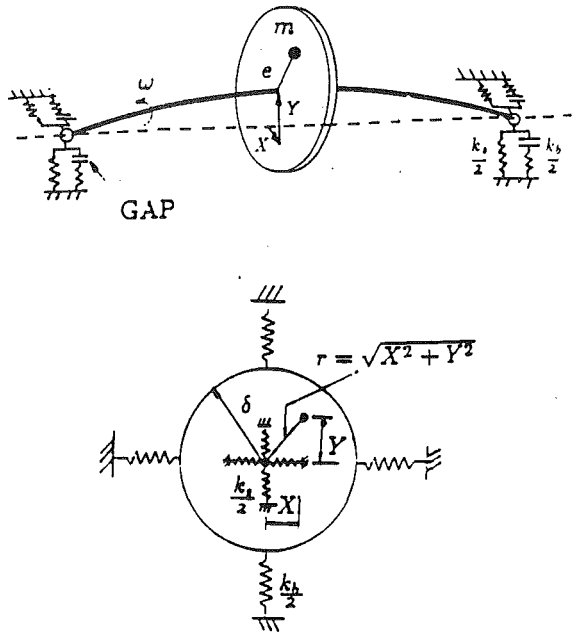


Fig. 1 Jeffcott rotor with bearing clearances

of a modified Jeffcott rotor. The paper consists of two parts. First, a modified fixed-point algorithm (FPA) for quasi-periodic solutions is introduced which explicitly calculates analytical derivatives directly to get an exact Jacobian matrix necessary for a robust iterative procedure. Second, a procedure to estimate an approximate winding number is presented and applied to search for any underlying rule dominating the system behavior.

2 Equations of Motion

For the linear analysis of a rotor which has a relatively flexible shaft, compared to the bearing support, operating below the second critical flexural mode, a simple flexible rotor model is used widely and is called the Jeffcott rotor. The Jeffcott rotor model consists of a massive unbalanced disk mounted midway between the bearing supports on a flexible shaft of negligible mass. The gyroscopic moments associated with the spinning disk is neglected. The bearings are rigidly supported and viscous damping acts to oppose absolute motion of the disk (Vance, 1988). Nonlinearities due to bearing clearances, or contacts between rotor and stator, have been incorporated into the conventional Jeffcott rotor model as in Fig. 1 (Childs, 1982; Saito, 1985; Day, 1987; Ehrich, 1988). The equations of motion for a horizontal Jeffcott rotor with bearing clearances can be written as

$$mX'' + cX' + k_sX + Q_sY + \Phi k_bX\left(1-\frac{\delta}{R}\right) - \mu\Phi k_bY\left(1-\frac{\delta}{R}\right) = me\omega^2\cos\omega t \quad (1a)$$

$$mY'' + cY' + k_sY - Q_sX + \Phi k_bY\left(1-\frac{\delta}{R}\right) + \mu\Phi k_bX\left(1-\frac{\delta}{R}\right) = me\omega^2\sin\omega t - mg \quad (1b)$$

where k_s represents the shaft stiffness including the linear bearing stiffness and k_b is the nonlinear bearing stiffness, respectively; e is the mass imbalance radius, Q_s is the cross-coupling stiffness, c is the system damping, μ is the friction coefficient, δ is the radial clearance of the bearing, R is the whirling radius ($\sqrt{X^2+Y^2}$), and ω is the forcing frequency, mg is the weight of the disk. A prime denotes a derivative with respect to time t and

$$\Phi = \begin{cases} 1 & \text{if } R \geq \delta, \\ 0 & \text{otherwise.} \end{cases}$$

Equation (1) can also be written as

$$\ddot{x} + \frac{2\zeta\nu}{\Omega}\dot{x} + \frac{\beta\nu^2}{\Omega^2}x + \frac{\gamma\nu^2}{\Omega^2}y + T(\tau) - \mu F(\tau) = \frac{\epsilon\nu^2}{\Omega^2}\cos\tau \quad (2a)$$

$$\ddot{y} + \frac{2\zeta\nu}{\Omega}\dot{y} + \frac{\beta\nu^2}{\Omega^2}y - \frac{\gamma\nu^2}{\Omega^2}x + F(\tau) + \mu T(\tau) = \frac{\epsilon\nu^2}{\Omega^2}\sin\tau - \frac{\phi\nu^2}{\Omega^2}, \quad (2b)$$

using the following nondimensional groups: $\omega_n = \sqrt{K/m}$, $K = 4k_sk_b/(\sqrt{k_s}+\sqrt{k_b})^2$, $x = X/\delta$, $y = Y/\delta$, $\Omega = \omega/\omega_n$, $\zeta = c/2m\omega_n$, $\gamma = Q_s/K$, $\alpha = k_b/k_s$, $\epsilon = e/\delta$, $\phi = g/\omega_n^2\delta$, $r = \sqrt{x^2+y^2}$, and $\nu\tau = \omega t$; ν represents the subharmonic ratio. In Eq. (2), a dot denotes a derivative with respect to time τ. Also, β, $T(\tau)$, $F(\tau)$ are given by

$$\beta = \frac{(1+\sqrt{\alpha})^2}{4\alpha},$$

$$T(\tau) = \Phi\frac{\alpha\beta\nu^2}{\Omega^2}x\left(1-\frac{1}{r}\right),$$

$$F(\tau) = \Phi\frac{\alpha\beta\nu^2}{\Omega^2}y\left(1-\frac{1}{r}\right).$$

3 Method of Analysis

3.1 Fixed-Point Algorithm. The fixed-point algorithm (FPA) has been previously used, as a shooting method, to obtain periodic solutions (Chua and Lin, 1975; Parker and Chua, 1989). The FPA algorithm is based on the utilization of the Poincaré map in which the flow of an nth-order continuous time system is replaced with an $(n-1)$th-order discrete time system. Kaas-Petersen (1985) reformulated the problem of finding aperiodic (almost periodic and quasi-periodic) solutions of a forced system with two forcing frequencies as a fixed point problem of the second-order Poincaré map. An interpolation technique was utilized to locate a fixed point in the second-order Poincaré map. Choi and Noah (1991) applied the FPA to a piecewise linear oscillator under multifrequency excitation to obtain torus solutions and locate corresponding bifurcation thresholds. For details, refer to the aforementioned references.

The fixed-point algorithm was extended to apply to quasi-periodic solutions resulting from a Hopf bifurcation of a periodically forced system by Kaas-Petersen (1987). An interpolation technique was used to determine a fixed point in a priori assumed second-order Poincaré section in the state space. A forward difference approximation was used to estimate the Jacobian matrix for an iterative process, which may often lead to poor estimates of the Jacobian matrix, which in turn caused nonconvergence due to improper choice of increments.

More recently, Ling (1991) presented a modified version of Kaas-Petersen's method (1985), for bi-periodically forced systems, by using analytical derivatives instead of the difference approximation and by using all, rather than few as in Kaas-Petersen's formulation, iterative points in the interpolation. For quasi-periodic solutions resulting from a Hopf bifurcation, Ling (1991) utilized a minimization technique which solves the indeterminate (i.e., more unknowns than number of equations) systems involved. In the system, an extra unknown is the winding number. The minimization technique, however, has its own drawbacks such as its use of numerical differentiation. Moreover, Ling (1991) did not describe how to analyze the stability

Downloaded 03 May 2010 to 171.66.16.20. Redistribution subject to ASME license or copyright; see http://www.asme.org/terms/Terms_Use.cfm

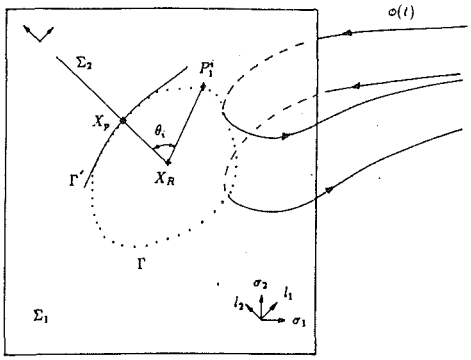


Fig. 2 Schematic diagram of a torus solution with first and second order Poincaré spaces (Σ_1, first-order Poincaré space; Σ_2, second-order Poincaré space; θ_i, phase angle for the circle map; Γ, solution circle in Σ_1)

of aperiodic solutions from a Hopf bifurcation using his method.

This paper presents a method which uses analytical, rather than numerical, derivatives for the bifurcating quasi-periodic solutions and for checking the stability of the solutions.

A brief exposition of the FPA, utilizing analytical derivatives for elements of the Jacobian matrix, for bifurcating aperiodic (almost-periodic and quasi-periodic) solutions is presented in what follows.

Consider a system described by the following equation:

$$\dot{\mathbf{x}} = f(\mathbf{x}, \omega_f, t) = f(\mathbf{x}, \omega_f, t + T_f);$$
$$\mathbf{x} = \{x_1, x_2, \ldots, x_n\}, \tag{3}$$

where f is a periodic function with period $T_f = 2\pi/\omega_f$, and ω_f is the forcing frequency. Let $X(t)$ be an aperiodic solution of Eq. (3) with two frequencies involved, ω_f and ω_h, the forcing frequency and a newly generated frequency resulting from a Hopf bifurcation, respectively. By sampling $X(t)$ stroboscopically at $t = 0, T_f, 2T_f, \ldots$, a first-order Poincaré map representation of $X(t)$ is obtained as

$$\Gamma(X) = \{X, P_1(X), P_1^2(X), \ldots, P_1^i(X), \ldots\} \in \Sigma_1(\mathbf{x}) \tag{4}$$

where $i = 0, 1, 2, \ldots$. The discrete points in the first order Poincaré space $\Sigma_1(\mathbf{x})$ ($\mathbf{x} \in R^n$) are winding around a closed curve Γ with the unknown frequency ω_h.

Figure 2 shows a schematic diagram of the second-order Poincaré space and the interpolation scheme for the iterates to locate a fixed point X_p. The torus solution Γ crosses the second-order Poincaré space Σ_2 at X_p. In the figure, Γ' represents an interpolated curve of the iterates close to the second-order Poincaré space, Σ_2.

Assume there is a point X_p such that

$$P_1^{T_h}(X_p) = X_p \in \Sigma_2(\mathbf{x}), \tag{5}$$

so that X_p is a fixed point to be obtained in the second-order Poincaré space $\Sigma_2(\mathbf{x})$ ($\mathbf{x} \in R^{n-1}$). In practice, it is difficult to determine $T_h (= 2\pi/\omega_h)$ for a quasi-periodic solution due to T_h/T_f being irrational, thus an interpolation technique is utilized.

Through a coordinate transformation, Σ_1 can be expressed in terms of an orthonormal basis $\{l_1, l_2, l_3, \ldots, l_n\}$ rather than a normal cartesian coordinates, $\{\sigma_1, \sigma_2, \sigma_3, \ldots, \sigma_n\}$. Let l_1 be a unit tangent vector of $\Sigma_1(\mathbf{x})$, then $\Sigma_2(\mathbf{x})$, the second-order Poincaré space, is defined as

$$\Sigma_2(\mathbf{x}) = span\{l_2, l_3, \ldots, l_n\} \tag{6}$$

which is orthogonal to l_1.

With a prescribed tolerance angle ϵ, chosen larger than zero, a set of the iterates S in the first-order Poincaré space will be composed of those points $P_1^i(X)$ where i satisfies

$$\theta_i = \cos^{-1}(\Delta) < \epsilon \tag{7}$$

where

$$\Delta = \frac{(P_1^i(X_p) - X_R) * (X_p - X_R)}{\|P_1^i(X_p) - X_R\| \cdot \|X_p - X_R\|}.$$

Here, "$*$" represents a vector product and $\|\cdot\|$ an Euclidean norm. Therefore, S is a set of points where θ_i satisfies condition (7). Clearly, as ϵ goes to zero, θ_i tends to zero. Using this property, the fixed point X_p satisfying the condition (5) can be estimated by interpolating each coordinate of $S(\theta_i)$ as a function of θ_i. The interpolated point at $\theta_i = 0$ will be the solution X_p. Hence the problem of finding the bifurcating quasi-periodic solution is thereby reduced to the problem of finding a fixed point of the system, given by Eq. (3), in the second-order Poincaré space. The Newton-Raphson procedure is utilized to find a fixed point iteratively which takes the form

$$z_p^{(n+1)} = z_p^{(n)} - J^{-1} \cdot H \tag{8}$$

where

$$H = P_2(z_p^n) - z_p^n,$$
$$J = (n-1) \text{ by } (n-1) \text{ Jacobian matrix of } H$$
$$= \frac{\partial H}{\partial z}\bigg|_{z=z_p}$$
$$= \frac{\partial P_2}{\partial z}\bigg|_{z=z_p} - I. \tag{9}$$

Here P_2 represents the second-order Poincaré map, z_p is X_p expressed in $\{l_2, l_3, \ldots, l_n\}$ basis (Σ_2), and z is $\mathbf{x}$ in $\{l_1, l_2, l_3, \ldots, l_n\}$ basis (Σ_1).

The derivative $\partial P_2/\partial z$ can be estimated as follows. Consider the following periodically forced nth-order system

$$\dot{x} = f(x, t) = f(x, t + T_f), \quad x(0) = x_0 \tag{10}$$

for a quasi-periodic solution $\phi(t)$ of (10) for which

$$\dot{\phi}(t) = f(\phi(t), t), \quad \phi(0) = x_0. \tag{11}$$

The variational equation, representing a small perturbation about $\phi(t)$, can be obtained by differentiating both sides of Eq. (11) with respect to x_0, so that

$$\frac{\partial \dot{\phi}(t)}{\partial x_0} = \frac{\partial f}{\partial \phi(t)} \cdot \frac{\partial \phi(t)}{\partial x_0}, \quad \frac{\partial \phi(0)}{\partial x_0} = I. \tag{12}$$

Rewrite Eq. (10) in $\{l_1, l_2, l_3, \ldots, l_n\}$ basis as

$$E\dot{x} = f(Ex, t), \quad Ex(0) = Ex_0 \tag{13}$$

where E is a coordinate transformation matrix. Let $Ex = z$, then Eq. (13) becomes

$$\dot{z} = f(z, t), \quad z(0) = z_0. \tag{14}$$

The variational equation for Eq. (14) is

$$\frac{\partial \dot{\psi}(t)}{\partial z_0} = \frac{\partial f}{\partial \psi(t)} \cdot \frac{\partial \psi(t)}{\partial z_0}, \quad \frac{\partial \psi(0)}{\partial z_0} = I, \tag{15}$$

where $\psi(t)$ is the solution of Eq. (14). Note that $\phi(t)$ and $\psi(t)$ are the same solutions of Eq. (10) but are expressed in different bases.

The fundamental solution matrix $\Psi(t)$ is

$$\Psi(t) = \frac{\partial \psi(t)}{\partial z_0}. \tag{16}$$

Thus

$$\dot{\Psi}(t) = \frac{\partial f}{\partial \psi(t)} \cdot \Psi(t), \quad \Psi(0) = I. \tag{17}$$

In order to calculate $\Psi(t)$ matrix, $\partial f/\partial \psi(t)$ must be known prior to any operation. It is not, however, easy to compute $\partial f/\partial \psi(t)$ in the $\{l_1, l_2, \ldots, l_n\}$ basis.

Downloaded 03 May 2010 to 171.66.16.20. Redistribution subject to ASME license or copyright; see http://www.asme.org/terms/Terms_Use.cfm

Differentiating both sides of Eq. (14) with respect to x_0, and after some manipulation, the following simple expression for $\partial f/\partial\psi(t)$ is obtained:

$$\frac{\partial f}{\partial \psi(t)} = E \frac{\partial f}{\partial \phi(t)} E^{-1}. \tag{18}$$

Thus $\Psi(t)$ can be readily obtained using (18) with Eq. (17).

Since each column of $\Psi(t)$ represents a time evolution of a unit perturbation about $\psi(t)$ in each orthogonal direction of z, an $(n-1)$ by $(n-1)$ partial matrix of $\Psi(t)$, corresponding to the second-order Poincaré space, becomes the derivative $\partial P_2/\partial z$. Again, $\Psi(t)$ for the fixed point X_p is obtained through interpolation.

Now the stability of the quasi-periodic solutions of the present harmonically forced system can be determined from the eigenvalues of $\partial P_2/\partial z$ (the Floquet multipliers). If the norm of the largest eigenvalue is less than unity, a solution is stable, otherwise it is unstable. When a Floquet multiplier has a magnitude equal to one, the system being studied is often considered to be marginally stable rather than unstable.

3.2 Circle Maps and Calculation of Winding Number. For the last two decades, it has been widely recognized that circle maps can produce very simple, yet complete, descriptions of complex nonlinear behavior of high-dimensional coupled nonlinear systems. Due to their simplicity and ability to provide visible forms of transitions from quasi-periodic regimes to chaos as well as quasi-periodic behavior and mode-locking, circle maps have been used to facilitate the understanding of the dynamic behavior of a broad range of nonlinear dynamical systems (see, for example, Matsumoto et al., 1987; Stavans et al., 1985; Haucke and Ecke, 1987).

In general, circle maps are

$$\theta_{n+1} = \bar{f}(\theta_n) = \theta_n + \Omega' + g(\theta_n, \epsilon) \tag{19}$$

where the nonlinear part is taken as

$$g(\theta_n, \epsilon) = g(\theta_n + 1, \epsilon) \pmod 1.$$

Here θ_n represents the phase of a first-order Poincaré point P_1^n with respect to a reference axis, Ω' is a bias term representing the frequency of the system in the absence of the nonlinear coupling g (Jensen et al., 1984) and ϵ is a nonlinear parameter. Usually the iterates fall into two regions, an upper branch and a lower branch separated by the unit slope line, $\theta_{n+1} = \theta_n$. For the specific rotor system considered here, where $g(\theta_n, \epsilon)$ is not known explicitly, the two branches are determined numerically.

The winding, or rotation, number ρ of a circle map $\bar{f}$ is defined as

$$\rho(\theta_0) = \lim_{n\to\infty} \frac{F^n(\theta_0) - \theta_0}{n}. \tag{20}$$

Here $F^n(\theta_0)$ represents an accumulated rotation from θ_0 without the condition of (mod 1). If ρ is rational, i.e., $\rho = p/q$, where p and q are positive integers, the trajectory is q-periodic and winding around a circle Γ, p times before completing one periodic orbit. If ρ is irrational, then the orbit is quasi-periodic and the iterates will fill up the circle without ending or repeating themselves. If the nonlinear coupling g comes into play, there might exist a zone called mode locking (or frequency, phase locking or entrainment) tongue or Arnol'd tongue where an irrational winding number locks into a rational number.

For the Jeffcott rotor model considered, the phase angle θ is defined as in Eq. (7) (refer to Fig. 2). Here an unstable periodic solution is used as a reference point X_R inside a torus solution. Once a fixed point X_p in the second-order Poincaré map is obtained utilizing the fixed-point algorithm, a winding (rotation) number, defined as

$$\rho = \frac{\omega_h}{\omega_f}, \tag{21}$$

is estimated numerically (via the fourth-order Runge-Kutta integration scheme) employing a modified definition of ρ,

$$\rho = \lim_{n\to\infty} \frac{m}{n}, \tag{22}$$

where n is the total number of iterates of P_1^j starting from X_p and m is the number of iterates located on the lower branch of the circle map represented by Eq. (19). In fact, if the map is order preserving or orientation preserving, where the slope $d\bar{f}/d\theta$ remains positive, the order of visits along the unit circle is the same as that of the circle without the nonlinearity g, with the same winding number (Hao, 1989).

For the calculation of winding numbers, up to 1000 Poincaré points were used starting at the point X_p.

4 Numerical Results and Discussion

4.1 Mode-Locking and Chaos. In many periodically driven coupled nonlinear oscillators, it has been observed that complex mode-locking behavior of quasi-periodic responses leading to chaos take place in addition to the well-known period-doubling of periodic responses (Franceschini, 1983; Bohr et al., 1984; Stavans et al., 1985; Haucke and Ecke, 1987; Matsumoto et al., 1987).

In recent years, aperiodic responses of rotor systems have been observed numerically (Childs, 1984; Day, 1987) and experimentally (Beatty and Hine, 1989). These observations pointed to the possibility that general rotor systems could go through a Hopf bifurcation due to the cross-coupling effects resulting from seals or other fluid-rotor interactions along with nonlinear effects of the rotor supports (Kim and Noah, 1990). With explanations using a Hopf bifurcation alone, it is difficult to conceive manners in which the aperiodic responses are related to periodic (harmonic, subharmonics) responses observed in rotor systems.

The nonlinear Jeffcott rotor model considered here is subject to a periodic external force due to shaft imbalance and is capable of synchronous and nonsynchronous response due to fluid cross-coupling forces. An attempt is made to reveal any underlying rule for periodic and aperiodic motions to occur. As a result, a complex mode-locking structure of the system behavior is uncovered in the parameter space of forcing amplitude and forcing frequency of the system (Fig. 3). Regions of mode locking separate parameter domains of periodic responses from those of quasi-periodic responses.

As the normalized forcing frequency Ω is varied (Fig. 3), the system shows various order of subharmonic responses—2, 3, 5, 7, 8, 9, 11, 12, 13, . . .—as well as quasi-periodic responses.

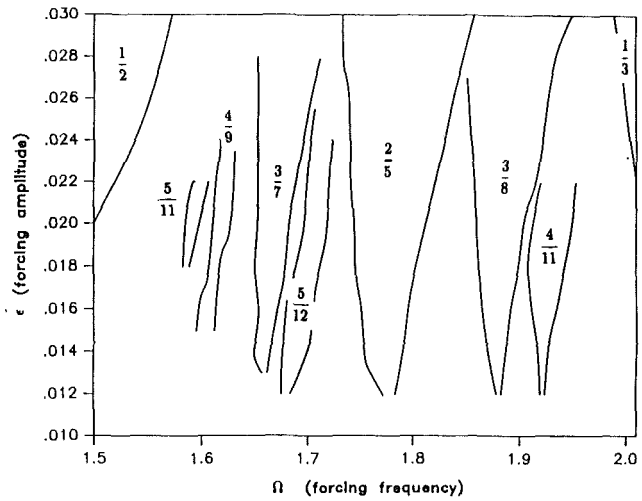


Fig. 3 Mode-locking tongues with rational winding numbers in ϵ-Ω parameter space (α = 20, ζ = 0.1, γ = 0.2)

Downloaded 03 May 2010 to 171.66.16.20. Redistribution subject to ASME license or copyright; see http://www.asme.org/terms/Terms_Use.cfm

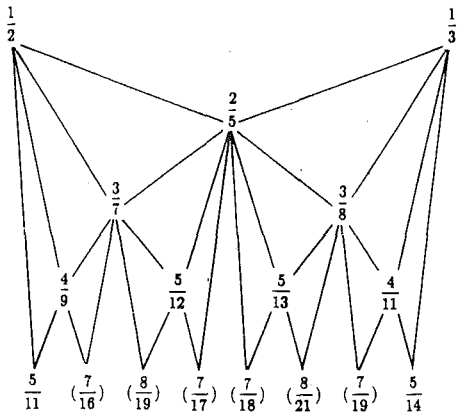


Fig. 4 Mode-locking tongues positioned in a Farey number tree. Cases in parenthesis were not identified ($\alpha = 20$, $\zeta = 0.1$, $\gamma = 0.2$).

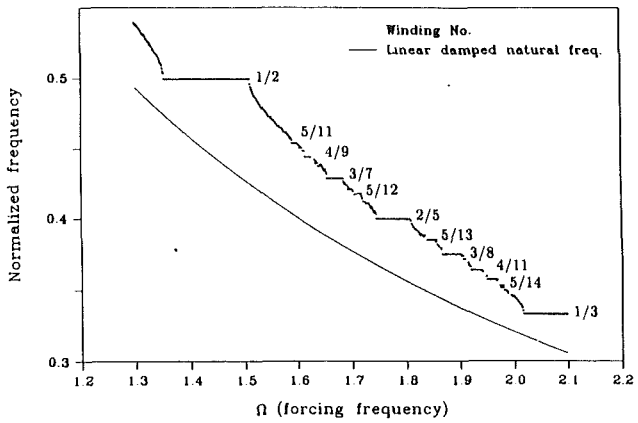


Fig. 5 Devil's staircase with rational winding numbers compared with linear damped natural frequency ω_d ($\alpha = 20$, $\zeta = 0.1$, $\gamma = 0.2$)

Each subharmonic response has its own V-shaped territory and these territories begin to overlap above a certain value of the normalized forcing amplitude (about $\epsilon = 0.023$). Beyond that critical value, in the overlapped regions, various order of subharmonic, quasi-periodic and chaotic motions were observed (not shown in Fig. 3). The chaos occurring in this overlapped region is called a "frustrated" response since the orbit jumps between harmonic and subharmonic resonances in an erratic way (Jensen et al., 1984).

The observed pattern in the two-parameter space is known as the mode or frequency locking, phase locking, or entrainment phenomena. Each mode-locked zone is called an "Arnol'd tongue."

By examining the structure of mode locking, it was also observed that the mode-locking order could be organized according to the Farey tree. The Farey tree is a hierarchical arrangement of all the rational numbers on the unit interval. In between two mode-locked regimes, described by rational fractions p/q and p'/q', respectively, the most easily observable period (i.e., the widest in the parameter space), would be given by the Farey composition (Hao, 1989)

$$\frac{p}{q}\oplus\frac{p'}{q'}=\frac{p+p'}{q+q'}. \tag{23}$$

Therefore, each successive level contains all possible "daughter" ratios obtainable from Eq. (23) using "parent" ratios in previous levels as shown in Fig. 4. Although only few generations were identified, due to some locking intervals being too narrow to be detected, they were sufficient to construct a visibly developed Farey tree.

Winding numbers were estimated and are presented in Fig. 5 over the range $1.43 < \Omega < 2.13$ with a fixed value of $\epsilon = 0.02$. The winding number as a function of Ω forms a "Devil's staircase" which has been found in different nonlinear systems (Jensen et al., 1983; 1984). The plateaus of rational winding numbers display a fractal distribution. In Fig. 5, the normalized linear damped natural frequency is also compared to the winding number. The normalized linear damped natural frequency is obtained from a linear and homogeneous version of Eq. (2) as

$$\omega_d^2=\frac{(\beta-\zeta^2)}{2\Omega^2}\pm\frac{1}{2\Omega^2}\left[(\zeta^2-\beta)^2+\gamma^2\right]^{1/2}. \tag{24}$$

As seen in Fig. 5, the winding number can be considered as a modified linear damped natural frequency, i.e., the "nonlinear resonant frequency" of the rotor system considered here. In reality, the nonlinear resonant frequency can be roughly observed in a FFT spectra by picking up a major peak component other than the forcing frequency. Since the FFT spectra might contain frequency components of higher amplitude, which are sums and differences of the nonlinear resonant frequency and the forcing frequency, an error in estimating the system nonlinear resonant frequency might occur. Thus a nonlinear resonant frequency of the system deduced from the FFT spectra could be confirmed through comparison with a measured winding number from experimental data.

As the torus solutions approach the mode-locking boundaries, it was observed that the torus solutions go through a tangent bifurcation, which can be clearly distinguishable in the circle maps, as shown in Fig. 6. The phase angle θ_n was obtained using Eq. (7). Subharmonic solutions of order two and three are about to be generated from the torus solutions.

Further investigation of the bifurcation pattern inside each mode-locking tongue was performed and revealed that there are many smaller tongues where period-doubling bifurcations occur. A mode-locked periodic motion eventually led to chaos by a sequence of period-doubling bifurcation within the boundary of its own mode-locked zone (Fig. 7).

To check the stability of the torus solutions between mode-locked tongues, the fixed-point algorithm was used. The largest eigenvalue was found to approach $+1$ as the torus solutions gets closer to the mode-locking boundaries. In the vicinity of bifurcation boundaries, however, the fixed-point algorithm (FPA) was found to be very much dependent on the location of the second-order Poincaré space in estimating the Floquet multipliers. With different Poincaré sections, the FPA gives quite different values of the largest eigenvalue making it difficult to determine the type of bifurcation involved. According to the authors' experience, this seems to be stemming from the fact that the FPA currently utilizes an interpolation scheme to locate a fixed point as well as the Jacobian matrix. In the vicinity of a bifurcation boundary, folding and stretching associated with the torus solutions occur, preventing the interpolation from yielding a correct Jacobian matrix. Thus for a better estimation of the eigenvalues, it is desired to use carefully chosen second-order Poincaré space so as not to contain folding and stretching sectors.

4.2 Amplitude-Frequency Response and Bifurcations. A jump phenomenon, which is one of the typical characteristics of nonlinear systems, was detected and multiple harmonic (p_1) and subharmonic (p_2, p_3) solutions were found using the fixed-point algorithm for periodic solutions. An amplitude-frequency response plot is shown in Fig. 8. As can be seen, there are stable and unstable harmonic and subharmonic solutions undergoing various kinds of bifurcations; i.e., period-doubling, Hopf, and saddle-node bifurcations.

Solution p_1^1, a higher solution branch of the amplitude-frequency response plot, has two unstable ranges ($0.732 < \Omega < 0.826$ and $0.911 < \Omega < 0.963$) within which torus solutions

Downloaded 03 May 2010 to 171.66.16.20. Redistribution subject to ASME license or copyright; see http://www.asme.org/terms/Terms_Use.cfm

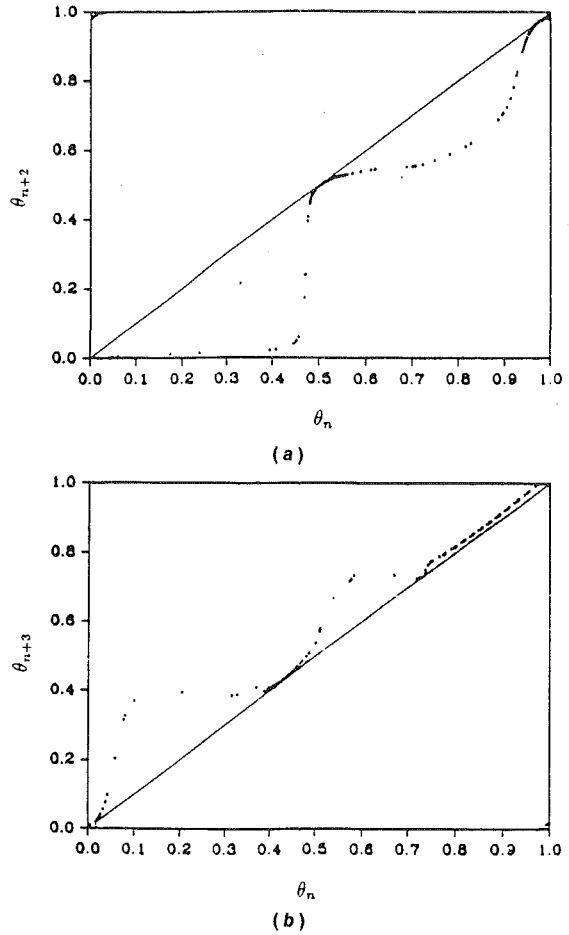


Fig. 6 Examples of tangent bifurcations (α = 20, ζ = 0.1, γ = 0.2, ϵ = 0.02). (top) circle map near a period 2 tongue (two channels close to the unit slope line exist) for Ω = 1.515; (bottom) circle map near a period 3 tongue (three channels close to the unit slope line exist) for Ω = 2.01.

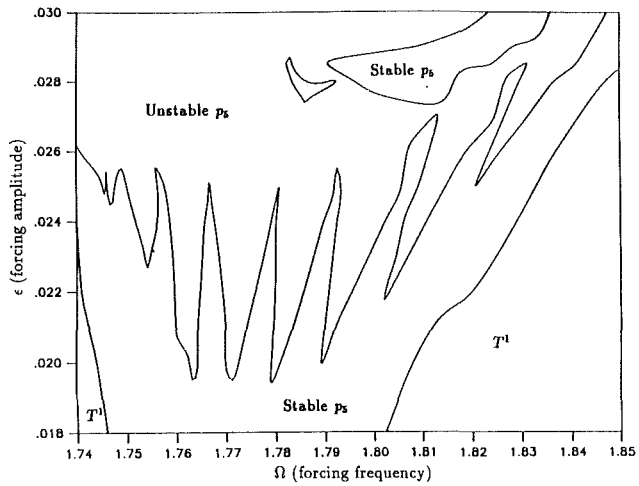


Fig. 7 Stability boundary of period 5 (p_5) solution inside p_5 mode-locking tongue. The boundary is also of a period-doubling bifurcation sequence (α = 20, ζ = 0.1, γ = 0.2). T^1 represents a torus solution.

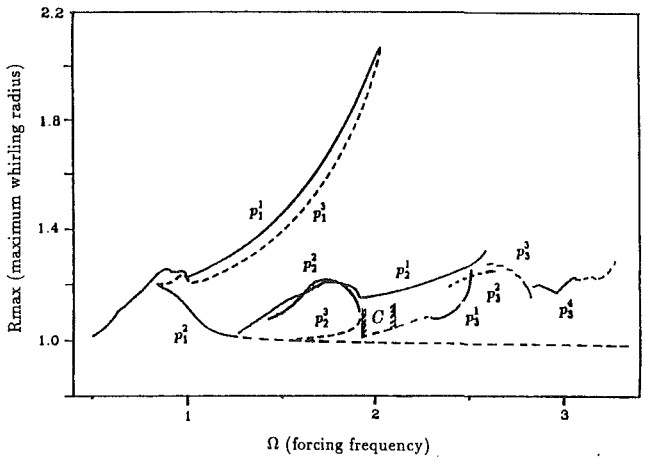


Fig. 8 Amplitude-frequency response (—·, stable solution; · · ·, unstable solution). p represents periodic and C the chaotic solution. Subscript of p indicates subharmonic order of periodic solutions, and superscript, type of periodic solutions (α = 20, ζ = 0.1, γ = 0.2).

occur via Hopf bifurcations. The newly generated frequency in these ranges are corresponding to a nonlinear resonant frequency of the system which is higher than the forcing frequency. Thus the system response is supersynchronous (see Fig. 9(*a*) and (*b*)). In this case, the normalized nonlinear system frequency is equal to 1 + ρ(winding number). On the other hand, as shown in Fig. 9(*c*) and (*d*), a subsynchronous response could be observed for the forcing frequency above the system nonlinear resonant frequency. The normalized nonlinear resonant frequency, for the subsynchronous case, is equivalent to the winding number.

In Fig. 8, p_1^2 is a stable harmonic solution bifurcating into a stable subharmonic 2 solution, p_2^1, at Ω = 1.254, and p_1^3 is an unstable solution of which bifurcation is characterized by a saddle-node bifurcation at Ω = 0.841 and 2.036.

A subharmonic order 2 solution, p_2^1, also shows Hopf bifurcation phenomena at Ω = 1.459, 1.766 (supercritical) and Ω = 1.554, 1.847 (subcritical), and a period-doubling bifurcation over the range of 1.915 < Ω < 1.997. A bifurcation plot for the range of 1.76 < Ω < 1.86 is shown in Fig. 10 which shows alternating periodic, quasi-periodic, and chaotic responses. There are subharmonic responses of order 10 and 8 involved where it is conjectured that the sequence is following a mode-locking rule discussed in the previous section. It is observed that the chaotic attractors in this range, developed from subharmonic responses through period doubling, are following the pattern of the folding, stretching, and breaking behavior of a torus solution.

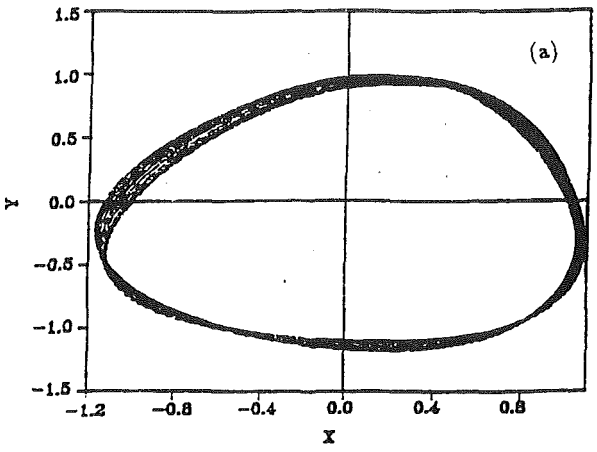
Other subharmonic order-two solutions, stable p_2^2 and saddle type p_2^3, are generated by a saddle-node bifurcation at Ω = 1.9166.

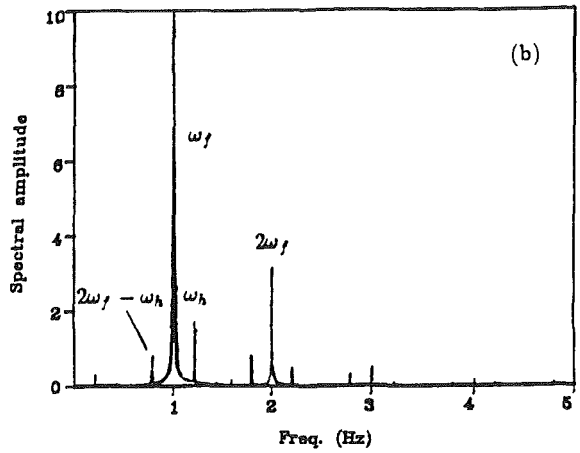
Subharmonic order-three solutions p_3^1, p_3^2, and p_3^3 were also found. Starting from Ω = 2.5061, solution p_3^1 undergoes period-doubling bifurcation at Ω = 2.294, leading to chaos as Ω decreases (see Figure 8). This chaotic attractor, however, disappears suddenly by encountering the unstable p_2^3 solution around Ω = 1.9163. The Poincaré map shows a coexistence of an unstable p_2 solution (p_2^3) and a chaotic solution at Ω = 1.9164. This is clearly a boundary crisis (Grebogi et al., 1983). The p_3^2 solution, which also goes through a period-doubling bifurcation at Ω = 2.448, appeared at Ω = 2.661. The birth of p_3^2 and death of its chaotic attractor was not clearly identified. However, it is assumed that there exists an unidentified, unstable p_3 solution born through a saddle-node bifurcation with the p_3^2 solution around Ω = 2.661, with which the chaotic attractor collides and consequently is annihilated.

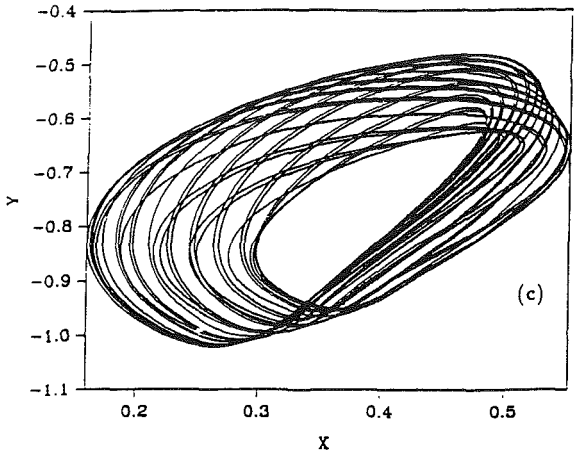
Over the range of 2.4 < Ω < 2.9, again, a very complex pattern of periodic, aperiodic, and chaotic responses were observed numerically (p_5, p_8, and p_{11} responses) (Fig. 11). Here it was difficult to identify detailed bifurcation phenomena involved in this parameter range. Its bifurcation pattern also seems to follow the mode-locking rule discussed in the previous section.

Finally, Figs. 12 and 13 show the effect of other parameters, cross-coupling stiffness γ, and the bilinear stiffness ratio α on

Downloaded 03 May 2010 to 171.66.16.20. Redistribution subject to ASME license or copyright; see http://www.asme.org/terms/Terms_Use.cfm







the amplitude-frequency response of the rotor system considered. As the cross-coupling stiffness increases above a critical value (about $\gamma = 0.13$), a jump phenomenon could be observed (Fig. 12). The effect of α is shown in Fig. 13, in which the forcing frequency is renormalized as $\Omega^* = \Omega/\sqrt{\beta}$ which is then proportional to the forcing frequency ω only. Note that, as the bilinear stiffness ratio α increases, the hardening-type jump phenomenon becomes clear. It could also be observed that, as the forcing amplitude ϵ decreases from 0.1, the frequency range for the larger amplitude p_1 solution (p_1^1) decreases and the smaller p_1 response (p_1^2) encounters a change of bifurcation type from a period-doubling to a Hopf bifurcation. Thus it could be speculated that there is a critical value at which a p_1 tongue and a p_2 tongue start to overlap.

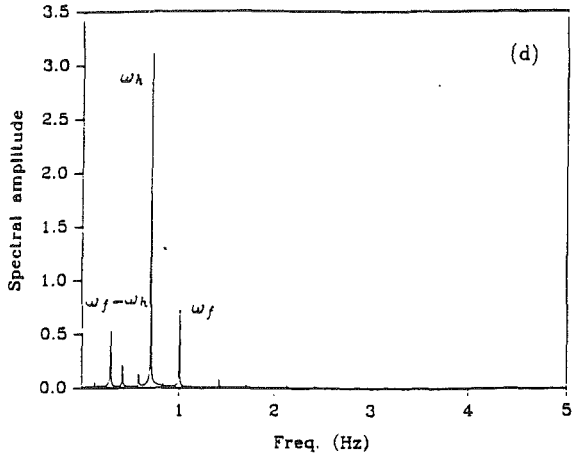


Fig. 9 Examples of sub and supersynchronous responses ($\alpha = 20$, $\zeta = 0.1$, $\gamma = 0.2$). (*a*) supersynchronous whirling response of the rotor and (*b*) FFT spectra ($\rho = 0.21108$); $\Omega = 0.95$, $\epsilon = 0.1$; (*c*) subsynchronous whirling response of the rotor, and (*d*) FFT spectra ($\rho = 0.71927$); $\Omega = 1$, $\epsilon = 0.02$.

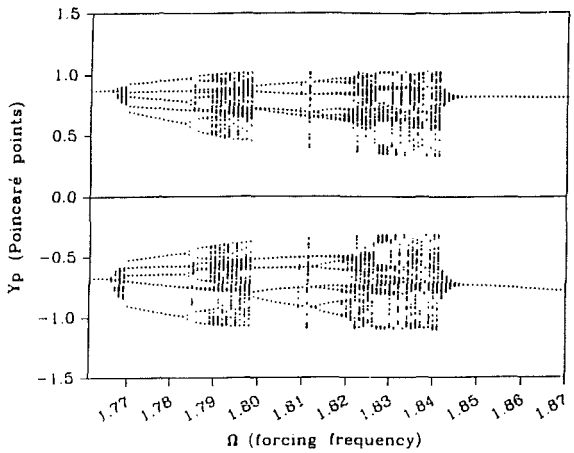


Fig. 10 Bifurcation behavior for $1.76 < \Omega < 1.87$ ($\alpha = 20$, $\zeta = 0.1$, $\gamma = 0.2$, $\epsilon = 0.1$). Hopf bifurcations at $\Omega = 1.766$ (supercritical) and 1.847 (subcritical).

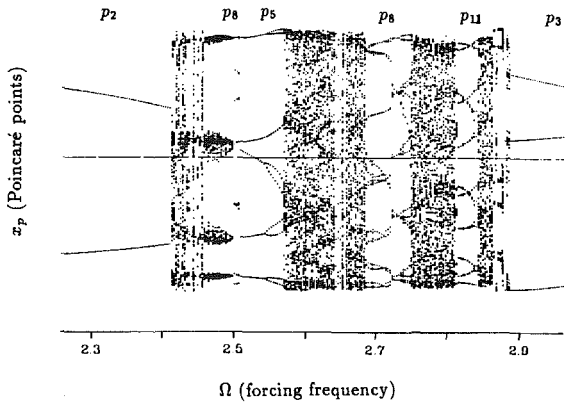


Fig. 11 Bifurcation plot with periodic windows ($\alpha = 20$, $\zeta = 0.1$, $\gamma = 0.2$, $\epsilon = 0.1$)

5 Conclusions

In this study, modern dynamical system theory is used to examine the complex dynamic behavior of a simple horizontal Jeffcott rotor with bearing clearances. A modified fixed-point algorithm was developed by which quasi-periodic solutions can be determined. Using the modified algorithm, relationships between quasi-periodic solutions and periodic solutions of the

Downloaded 03 May 2010 to 171.66.16.20. Redistribution subject to ASME license or copyright; see http://www.asme.org/terms/Terms_Use.cfm

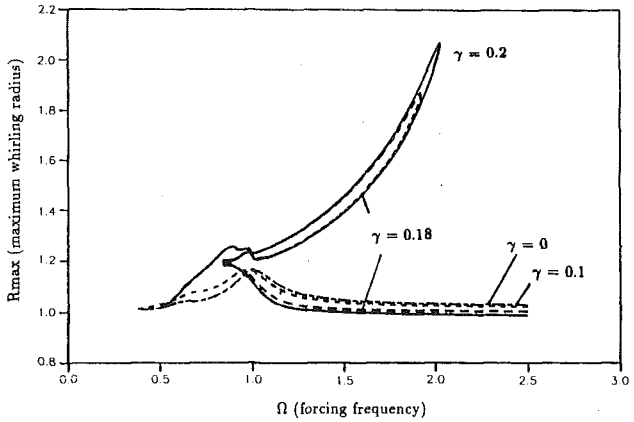


Fig. 12 Effect of the cross-coupling stiffness, γ, on the amplitude-frequency response (only the p_1 solutions are considered) (α = 20, ζ = 0.1, ϵ = 0.1)

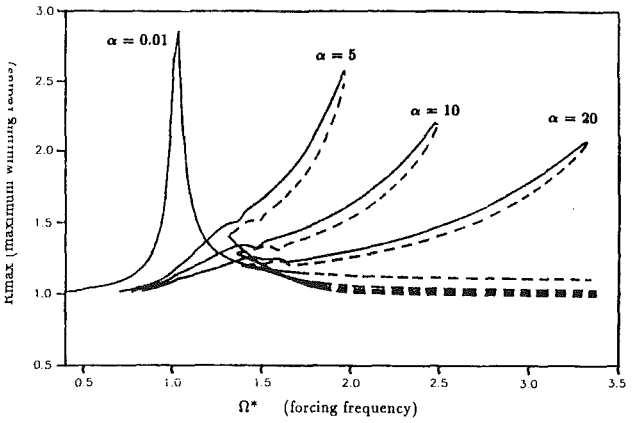


Fig. 13 Effect of the bi-linear stiffness ratio, α, on the amplitude-frequency response (ζ = 0.1, γ = 0.2, ϵ = 0.1). —, stable; · · ·, unstable solutions

Jeffcott rotor were sought. Based on the results obtained in the present study, the following conclusions can be made.

1 Alternating periodic, aperiodic, and chaotic responses is governed by the rule of the Farey number tree.

2 There are mode-locking tongues at which forcing and system frequencies lock to yield periodic responses in the parameter space of the forcing amplitude and forcing frequency.

3 Within each mode-locking tongue, a number of smaller tongues exist where a sequence of period-doubling bifurcations leading to chaos takes place.

4 As the cross-coupling stiffness increases, the possibility of observing a jump phenomenon increases and the system behavior becomes much more complex.

5 The hardening-type jump phenomenon is due to the bi-linear stiffness ratio being larger than unity.

6 In a general nonlinear rotor system, a subsynchronous vibration observed at about, say, 70 to 90 percent of synchronous speed is a modified linear natural frequency; i.e., a nonlinear resonant frequency of the system. The winding number could be used to estimate this nonlinear resonant frequency more accurately and uniquely than through FFT spectra.

References

Beatty, R. F., and Hine, M. J., 1989, "Improved Rotor Response of the Updated High Pressure Oxygen Turbopump for the Space Shuttle Main Engine," ASME *Journal of Vibration, Acoustics, Stress, and Reliability in Design*, Vol. 111, pp. 163–169.

Bently, D., 1974, "Forced Subrotative Speed Dynamic Action of Rotating Machinery," ASME Paper No. 74-PET-16, Petroleum Mechanical Engineering Conference, Dallas, Texas.

Bohr, T., Bak, P., and Jensen, M. H., 1984, "Transition to Chaos by Interaction of Resonances in Dissipative Systems II. Josephson Junctions, Charge-density Waves, and Standard Maps," *Phys. Rev. A*, Vol. 30, No. 4, pp. 1960–1969.

Childs, D. W., 1982, "Fractional-frequency Rotor Motion due to Nonsymmetric Clearance Effects," ASME *Journal of Energy and Power*, Vol. 104, pp. 533–541.

Childs, D. W., 1984, "Rotordynamic Characteristics of the HPOTP (High Pressure Oxygen Turbopump) of the SSME (Space Shuttle Main Engine)," Turbomachinery Laboratories Report (Texas A&M Univ.), FD-1-84.

Choi, Y. S., and Noah, S. T., 1987, "Nonlinear Steady-state Response of a Rotor Support System," ASME *Journal of Vibration, Acoustics, Stress, and Reliability in Design*, Vol. 109, pp. 255–261.

Choi, S. K., and Noah, S. T., 1992, "Response and Stability Analysis of Piecewise-Linear Oscillators Under Multi-Forcing Frequencies," *Nonlinear Dynamics*, Vol. 3, pp. 105–121.

Chua, L. O., and Lin, P. M., 1975, *Computer-aided Analysis of Electronic Circuits: Algorithms and Computational Techniques*, Prentice-Hall, Englewood Cliffs, N.J.

Day, W. B., 1987, "Asymptotic Expansions in Nonlinear Rotordynamics," *Quarterly of Applied Mechanics*, Vol. 44, pp. 779–792.

Ehrich, F. F., 1988, "High Order Subharmonic Response of High Speed Rotors in Bearing Clearance," ASME *Journal of Vibration, Acoustics, Stress, and Reliability in Design*, Vol. 110, pp. 9–16.

Franceschini, V., 1983, "Bifurcation of Tori and Phase Locking in a Dissipative System of Differential Equations," *Physica*, Vol. 60, pp. 285–304.

Grebogi, C., Ott, E., and Yorke, J. A., 1983, "Crisis, Sudden Changes in Chaotic Attractors, and Transient Chaos," *Physica D*, Vol. 7, pp. 181–200.

Hao, B., 1989, *Elementary Symbolic Dynamics and Chaos in Dissipative Systems*, World Scientific Publishing Co., Singapore.

Haucke, H., and Ecke, R., 1987, "Mode-Locking and Chaos in Rayleigh-Bénard Convection," *Physica D*, Vol. 25, pp. 307–329.

Jensen, M. H., Bak, P., and Bohr, T., 1983, "Complete Devil's Staircase, Fractal Dimension, and Universality of Mode-Locking Structure in the Circle Map," *Phys. Rev. Lett.*, Vol. 50, No. 21, pp. 1630–1639.

Jensen, M. H., Bak, P., and Bohr, T., 1984, "Transition to Chaos by Interaction of Resonances in Dissipative Systems I. Circle Maps," *Phys. Rev. A*, Vol. 30, No. 4, pp. 1960–1969.

Kaas-Petersen, C., 1985, "Computation of Quasi-Periodic Solutions of Forced Dissipative Systems," *Physics*, Vol. 58, pp. 395–403.

Kaas-Petersen, C., 1987, "Computation, Continuation, and Bifurcation of Torus Solutions for Dissipative Maps and Ordinary Differential Equations," *Physica D*, Vol. 25, pp. 288–306.

Kim, Y. B., and Noah, S. T., 1990, "Bifurcation Analysis for a Modified Jeffcott Rotor with Bearing Clearances," *Nonlinear Dynamics*, Vol. 1, pp. 221–241.

Ling, F. H., 1991, "Quasi-Periodic Solutions Calculated with the Simple Shooting Technique," *Journal of Sound and Vibration*, Vol. 144, No. 2, pp. 293–304.

Matsumoto, T., Chua, L. O., and Tokunaga, R., 1987, "Chaos via Torus Breakdown," *IEEE Transactions on Circuits and Systems*, Vol. CAS-34, No. 3, pp. 240–253.

Parker, T. S., and Chua, L. O., 1989, *Practical Numerical Algorithms for Chaotic Systems*, Springer-Verlag, New York.

Saito, S., 1985, "Calculation of Nonlinear Unbalance Response of Horizontal Jeffcott Rotors Supported by Ball Bearings with Radial Clearances," ASME Paper No. 85-DET-33.

Stavans, J., Heslot, F., and Libchaber, A., 1985, "Fixed Winding Number and the Quasi-Periodic Route to Chaos in a Convective Fluid," *Phys. Rev. Lett.*, Vol. 55, No. 6, pp. 596–599.

Vance, J. M., 1988, *Rotordynamics of Turbomachinery*, John Wiley and Sons, New York.

Yamamoto, T. T., 1954, "On Critical Speeds of a Shaft," *Memoirs of the Faculty of Engineering, Nagoya (Japan) University*, Vol. 6, No. 2.

Yamauchi, S., 1983, "The Nonlinear Vibration of Flexible Rotors, 1st Report, Development of a New Analysis Technique," *JSME*, Vol. 49, No. 446, Series C, pp. 1862–1868.

Downloaded 03 May 2010 to 171.66.16.20. Redistribution subject to ASME license or copyright; see http://www.asme.org/terms/Terms_Use.cfm

A Rotation Rate Sensor Based Upon a Rayleigh Resonator

N. S. Clarke
Department of Engineering Mechanics.

J. S. Burdess
Department of Mechanical, Materials and Manufacturing Engineering.

University of Newcastle upon Tyne, Newcastle upon Tyne, NE1 7RU England

Rayleigh waves generated by line loads on the surface of an elastic half-space experience a change in both amplitude and wave number if the medium undergoes rotation. Use is to be made of this to form the basis of a rotation sensor. The relative changes are, however, extremely small. It is the purpose of this paper to show how, by use of the properties of Rayleigh waves, the changes induced by rotation may be amplified while the basic wave is not. This is achieved by use of a Rayleigh resonator with carefully chosen characteristics. The basic theory of such a resonator has been worked out in Clarke et al. (1989) and Clarke and Burdess (1991) and is here extended to account for rotational effects. It is shown that it should be possible to construct a practicably sized device, based upon this theory, to act as a robust rotation rate sensor.

1 Introduction

When an elastic medium with a free surface rotates, then the Rayleigh waves propagating along the surface are perturbed away from their nonrotating (i.e., static) form. Lao (1980) suggested that this perturbation could form the basis of a design for a robust rotation rate sensor and proceeded to calculate the approximate shift in the wave number due to rotation. This idea was taken a little further in Wren and Burdess (1987) and again the wave number shift was deduced, this time by means of singular perturbation theory. In both papers it was shown that rotation causes right and left moving waves to have different wave speeds.

The stumbling block to further development was that, for most situations likely to be encountered in practice, the relative shift in wave number was $0(10^{-6})$. This implies that fairly sophisticated measuring equipment would be required and hence would be inappropriate for use in the "field"; i.e., it would not be robust. We believe that we have overcome this difficulty by employing a Rayleigh resonator with selected characteristics, so that the perturbed field is amplified while the static field is not, so that they may become of comparable magnitude.

In Clarke and Burdess (1991) we have described a Rayleigh resonator in some detail and shown how to derive expressions for the displacement fields for a nonrotating medium. The present paper extends the analysis of Clarke and Burdess (1991) to include the effects of rotation and proceeds to exploit the flexibility of choice of resonator parameters to achieve the required response amplification.

Contributed by the Applied Mechanics Division of THE AMERICAN SOCIETY OF MECHANICAL ENGINEERS for publication in the ASME JOURNAL OF APPLIED MECHANICS.

Discussion on this paper should be addressed to the Technical Editor, Professor Lewis T. Wheeler, Department of Mechanical Engineering, University of Houston, Houston, TX 77204-4792, and will be accepted until four months after final publication of the paper itself in the ASME JOURNAL OF APPLIED MECHANICS.

Manuscript received by the ASME Applied Mechanics Division, Mar. 23, 1992; final revision, Jan. 20, 1993. Associate Technical Editor: S. K. Datta.

The progress towards this ultimate goal is taken in several stages. First, in Section 2, the displacements associated with the Rayleigh waves on a plane surface generated by a given time-harmonic line load are derived. These are found accurate to the first order in a small parameter, which is the ratio of the rotation rate of the medium to the frequency of the imposed loads. As in practice this parameter can be expected to be $0(10^{-6})$ or thereabouts, it is truly small. It is in fact possible to determine the wave number valid for all values of this parameter, but, as it is of no relevance in the present context, it will be published separately.

In the resonator the Rayleigh waves generated by the surface loads are repeatedly reflected from a pair of regions etched in the surface on either side of a plane "cavity" wherein the loads are applied. The basic analysis for the reflection from such regions has been achieved in Clarke et al. (1989) and Clarke and Burdess (1991), and in Section 3 we extend this work to cover the rotation effects. The displacements anywhere on the surface within the cavity of the resonator are found.

Finally, in Section 4, we examine the expressions for these displacements in order to exploit their possibilities. There are several parameters which at this stage are still arbitrary, and are now selected so that the solutions have a form which will be advantageous when the resonator is used as a rotation sensor. We here show one way in which this may be satisfactorily achieved, but readily admit that there may well be other choices of parameters which confer equal if not greater virtue.

2 The Rayleigh Waves due to Surface Loading

In this section we determine the effect of rotation upon Rayleigh waves propagating in the vicinity of a plane surface. These waves are generated by a time-dependent line surface load with both normal and shear components. The method employed is similar to that described in Clarke and Burdess (1991), where the "static" problem was treated.

Consider the half-space, denoted by $y' < 0$, occupied by an

Copyright © 1994 by ASME
Downloaded 03 May 2010 to 171.66.16.20. Redistribution subject to ASME license or copyright; see http://www.asme.org/terms/Terms_Use.cfm

isotropic homogeneous linearly elastic material and bounded by the plane surface $y'=0$. We take the origin to lie on the surface and consider the space to be rotating about an axis lying in the surface, and denoted as the z'-axis, with constant angular speed Ω. A line load, coincident with the z'-axis, is applied so that the displacements caused by the resulting Rayleigh waves have components in the x' and y' directions only, that is the displacement vector may be written as

$$\mathbf{u}' = u_1' \mathbf{i} + u_2' \mathbf{j}.$$

The field equations to be satisfied in $y'<0$ are

$$(\lambda+2\mu)\text{grad}(\text{div}\,\mathbf{u}') - \mu\,\text{curl}\,\text{curl}\,\mathbf{u}' = \rho\left(\frac{\partial}{\partial t'} + \Omega\mathbf{k}\wedge\right)\left(\frac{\partial \mathbf{u}'}{\partial t'} + \Omega\mathbf{k}\wedge\mathbf{u}'\right), \quad (1)$$

where λ, μ are the Lamé constants and ρ the density of the material and t' is time. Notice that the usual time derivative has been adapted to account for the moving reference frame.

The conditions to be satisfied on the plane surface are that there should be no traction except at $x'=0$, where the load is applied. These conditions, in component form, are

$$\mu\left(\frac{\partial u_1'}{\partial y'} + \frac{\partial u_2'}{\partial x'}\right) = (\mu^3/\rho\omega^2)^{1/2} S\delta(x')e^{-i\omega t'},$$

$$\lambda\frac{\partial u_1'}{\partial x'} + (\lambda+2\mu)\frac{\partial u_2'}{\partial y'} = (\mu^3/\rho\omega^2)^{1/2} N\delta(x')e^{-i\omega t'}, \quad (2)$$

where S and N are the dimensionless amplitudes of the shear and normal loads (not necessarily real), and ω is the frequency of imposed loads (see Fig. 1).

As in Clarke et al. (1989) and Clarke and Burdess (1991) we define dimensionless variables by

$$t' = \omega^{-1}t, \quad (x', y', u_1', u_2') = (\mu/\rho\omega^2)^{1/2}(x, y, u_1, u_2), \quad (3)$$

and introduce the material parameter α $(0\le\alpha\le 0.5)$ by

$$\alpha = \mu/(\lambda+2\mu), \quad = (1-2\sigma)/(2-2\sigma), \quad (4)$$

where σ is Poisson's ratio. We also introduce the dimensionless rotation parameter δ by

$$2\Omega/\omega = (1-\alpha)\delta. \quad (5)$$

The factor $(1-\alpha)$ is used purely for future algebraic convenience. In terms of the dimensionless variables the field equations, in $y<0$, are

$$\frac{\partial^2 u_1}{\partial x^2} + \alpha\frac{\partial^2 u_1}{\partial y^2} + (1-\alpha)\frac{\partial^2 u_2}{\partial x\partial y} = \alpha\frac{\partial^2 u_1}{\partial t^2} - \delta\alpha(1-\alpha)\frac{\partial u_2}{\partial t} - \frac{1}{4}\delta^2\alpha(1-\alpha)^2 u_1,$$

$$(1-\alpha)\frac{\partial^2 u_1}{\partial x\partial y} + \alpha\frac{\partial^2 u_2}{\partial x^2} + \frac{\partial^2 u_2}{\partial y^2} = \alpha\frac{\partial^2 u_2}{\partial t^2} + \delta\alpha(1-\alpha)\frac{\partial u_1}{\partial t} - \frac{1}{4}\delta^2\alpha(1-\alpha)^2 u_2, \quad (6)$$

while on $y=0$

$$\frac{\partial u_1}{\partial y} + \frac{\partial u_2}{\partial x} = S\delta(x)e^{-it},$$

$$(1-2\alpha)\frac{\partial u_1}{\partial x} + \frac{\partial u_2}{\partial y} = \alpha N\delta(x)e^{-it}. \quad (7)$$

For the purposes of this work the information which is required for later use is the value on the surface of the displacements, caused by the surface loads, in the form of Rayleigh waves (we may, as argued in Clarke and Burdess (1991), ignore any bulk waves generated).

In practice δ will be very small, typically of order 10^{-6}. It follows that it is necessary only to calculate the displacement accurate to the first order in δ. This may readily be achieved by the method used in Clarke and Burdess (1991), namely by Fourier transforms. We shall be content to state the results here as there is little difference, save for increased algebraic complexity, between the present work and that described in Clarke and Burdess (1991).

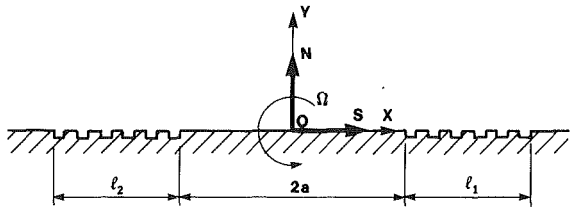


Fig. 1 Configuration of the resonator

For $x>0$,

$$u_1 = Ve^{i\kappa x - it}, \quad u_2 = i\xi Ve^{i\kappa x - it},$$

while for $x<0$,

$$u_1 = \overline{V}e^{-i\overline{\kappa}x - it}, \quad u_2 = -i\overline{\xi}\,\overline{V}e^{-i\overline{\kappa}x - it}, \quad (8)$$

where

$$V = \{i[(\kappa^2-1)^{1/2} + \delta(k^2-pq)/k]S + [(2\kappa^2-1)/2\kappa + \delta(\alpha k^2+pq)/2k^2q]N\}/g'(\kappa),$$

$$\overline{V} = \{-i[(\overline{\kappa}^2-1)^{1/2} - \delta(k^2-pq)/k]S + [(2\overline{\kappa}^2-1)/2\overline{\kappa} - \delta(\alpha k^2+pq)/2k^2q]N\}/g'(-\overline{\kappa}), \quad (9)$$

$$\xi = (2\kappa^2-1)/2\kappa(\kappa^2-1)^{1/2} - \delta[2(1-\alpha)k^2-1]/4k^2q^2,$$

$$\overline{\xi} = (2\overline{\kappa}^2-1)/2\overline{\kappa}(\overline{\kappa}^2-1)^{1/2} + \delta[2(1-\alpha)k^2-1]/4k^2q^2. \quad (10)$$

Note that Eqs. (8) represent the solutions on the surface for any right-moving $(x>0)$ and left-moving $(x<0)$ Rayleigh wave with amplitude V and $\overline{V}$, respectively. Here the wave number κ, for a right-moving wave, satisfies the equation

$$g(\kappa) = 4\kappa^2(\kappa^2-\alpha)^{1/2}(\kappa^2-1)^{1/2} - (2\kappa^2-1)^2 - \delta[\alpha\kappa(\kappa^2-1)^{-1/2} - (\kappa^2-\alpha)^{1/2}\kappa^{-1}] = 0, \quad (11)$$

and is given by

$$\kappa = k + \delta k_1, \quad (12)$$

where k satisfies the static equation

$$f(k) = 4k^2(k^2-\alpha)^{1/2}(k^2-1)^{1/2} - (2k^2-1)^2 = 0. \quad (13)$$

Also

$$k_1 = (\alpha k^2 - pq)/kqf'(k), \quad (14)$$

where

$$p = (k^2-\alpha)^{1/2} \quad \text{and} \quad q = (k^2-1)^{1/2}. \quad (15)$$

The parameters k and k_1 are functions only of α (and hence of Poisson's ratio) and are shown in Fig. 2.

The wave number for a left-moving wave is

$$\overline{\kappa} = k - \delta k_1, \quad (16)$$

as $-\overline{\kappa}$ is also a root of (11). Notice that rotation has altered the wave number and, not unexpectedly, the effect differs for left and right moving waves. We note also that the amplitudes of the waves have also been altered. The shift in the wave number is identical to that reported in Lao (1980), though that for the amplitudes is not as in Lao (1980) which is in error on this point.

3 The Reflection From the Etched Region

In Clarke et al. (1989) we considered the static case and found that if the surface etchings were periodic with a wave

Downloaded 03 May 2010 to 171.66.16.20. Redistribution subject to ASME license or copyright; see http://www.asme.org/terms/Terms_Use.cfm

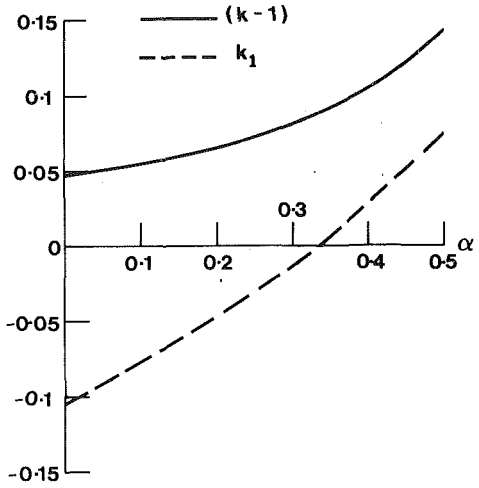


Fig. 2 k and k_1 as functions of α

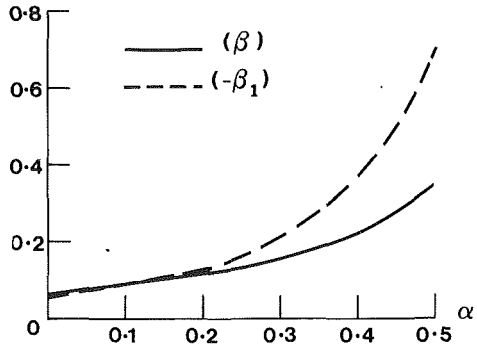


Fig. 3 β and β_1 as functions of α

number twice that of the incoming wave, i.e., they were "matched," then an appreciable part of the incoming wave would be reflected. Indeed, it could be arranged for virtually all of it to be reflected, that is the reflection coefficient R could be made to have magnitude close to unity.

For the rotating case the geometry of the etchings is maintained exactly as for the static case, that is the Fourier representation of the surface for $a<x<a+l$, in dimensionless form, is

$$y=H(x)=\epsilon\{h\,e^{i2k(x-a)}+h^*\,e^{-i2k(x-a)}+\hat{H}\}, \qquad (17)$$

where ϵ is the small dimensionless amplitude of the etchings, h and its complex conjugate h^* the relevant Fourier coefficients, and $\hat{H}$ represents all irrelevant (for our case) Fourier components.

For the static case, the first term in H combines with a left-moving wave to form a right-moving wave and thereby sets up a form of internal resonance within the etching. In the rotating case the same occurs due to the fact that $e^{i2k(x-a)}\cdot e^{-i\bar{\kappa}(x-a)}=e^{i\kappa(x-a)}$. The second term in (17) combines with the expression for the right-moving wave and shows that left-moving waves are generated within the right-hand etching.

The procedure for finding the solution within $a<x<a+l$ is exactly the same as in Clarke et al. (1989) for the static case. A perturbation scheme based upon the smallness of ϵ is employed, and multiple scales techniques are used to overcome the ensuing singular nature. During this process the other small parameter δ plays a passive role.

The arbitrary constants appearing in this solution are found by matching this solution to the solution in $x<a$ and to that in $x>a+l$, as in Clarke et al. (1989). These solutions consist of an incoming wave plus a reflected wave (of relative amplitude R) in $x<a$ and a transmitted wave in $x>a+l$ of unknown amplitude. This matching at $x=a$ and at $x=a+l$ provides the reflection coefficient R and the transmission coefficient if required. The basic Rayleigh wave solutions valid either side of the etched region may either be deduced from (8) or derived *ab initio* as in Clarke et al. (1989) but with rotation effects included.

As there is essentially nothing of a novel nature in the procedure but a mere repetition of Clarke et al. (1989) with more complicated algebra, we will be content to quote the expression for the reflection coefficient. This is

$$R=i(\kappa/\bar{\kappa})(1-\delta\beta_1/\beta)\{1-\delta(2k^2-1)/2k^3q\}(h^*/|h|)\tau, \qquad (18)$$

where $\tau=\tanh(\beta|h|\epsilon l)$ and β and β_1 are material parameters. β is given in Clarke et al. (1989) and β_1, though known explicitly in terms of k and α, is sufficiently complicated to be shown only in Fig. 3 along with β.

It should be noted that for $\tau\to 1$, $|R|$ may exceed unity. This seeming paradox may be accounted for by the fact that the reflected wave has a slightly different wave number to that of the incoming wave and to that of the transmitted wave.

Similarly if we have an etched region in $-a-\bar{l}<x<-a$ whose surface has a Fourier representation,

$$y=\bar{H}(x)=\epsilon\{\bar{h}e^{i2k(x+a)}+\bar{h}^*e^{-i2k(x+a)}+\dot{\bar{H}}\}, \qquad (19)$$

(i.e., we admit the possibility of small differences in the two etched regions) then a left-moving wave will be partially reflected from the etched region with a reflection coefficient

$$\bar{R}=i(\bar{\kappa}/\kappa)(1+\delta\beta_1/\beta)\{1+\delta(2k^2-1)/2k^3q\}(\bar{h}/|\bar{h}|)\bar{\tau}, \qquad (20)$$

where $\bar{\tau}=\tanh(\beta|\bar{h}|\epsilon\bar{l})$.

It follows from the above and from (8) that the basic wave generated by the surface load moves to the right and then encounters the etched region in $a<x<a+l$. The amplitude for u_1 at $x=a$ is $Ve^{i\kappa a}$ and that of the reflected wave $RVe^{i\kappa a}$. Similarly for u_2, the incoming amplitude is $i\xi Ve^{i\kappa a}$ and for its reflection $-i\bar{\xi}\,VRe^{i\kappa a}$. For the left-moving wave u_1 has amplitude $\bar{V}e^{i\kappa a}$ at $x=-a$ when it encounters the etched region in $-a-\bar{l}<x<-a$, and its reflection has amplitude $\bar{R}\bar{V}e^{i\kappa a}$, whereas for u_2 its incident and reflected amplitudes are $-i\bar{\xi}\bar{V}e^{i\kappa a}$ and $i\bar{\xi}\bar{V}\bar{R}e^{i\kappa a}$.

The reflected waves will re-traverse the cavity and be partially reflected from the other etched region, and so on. The actual displacements at any point in the cavity will then have contributions from each of these multiple reflections. As in Clarke and Burdess (1991) these contributions may be summed and we find that for $x<0$,

$$u_1=e^{i\bar{\kappa}a-it}\{\bar{V}+VRe^{i2ka}\}\{e^{-i\bar{\kappa}(x+a)}+\bar{R}e^{i\kappa(x+a)}\}\{1-R\bar{R}e^{i4ka}\}^{-1},$$

$$u_2=-ie^{i\bar{\kappa}a-it}\{\bar{V}+VRe^{i2ka}\}\{\bar{\xi}e^{-i\bar{\kappa}(x+a)}-\xi\bar{R}e^{i\kappa(x+a)}\}\{1-R\bar{R}e^{i4ka}\}^{-1},$$

while for $x>0$,

$$u_1=e^{i\kappa a-it}\{V+\bar{V}\bar{R}e^{i2ka}\}\{e^{-i\kappa(x-a)}+Re^{-i\bar{\kappa}(x-a)}\}\{1-R\bar{R}e^{i4ka}\}^{-1},$$

$$u_2=ie^{i\kappa a-it}\{V+\bar{V}\bar{R}e^{i2ka}\}\{\xi e^{i\kappa(x-a)}-\bar{\xi}Re^{-i\bar{\kappa}(x-a)}\}\{1-R\bar{R}e^{i4ka}\}^{-1}. \qquad (21)$$

4 The Design Parameters for the Resonator

The displacements given by (21) are valid for unrestricted values of some of the parameters. So far we have insisted that the wavelength of the induced Rayleigh wave should be matched to that of the etchings. For convenience, but not necessity, we have chosen to place the loads at the midpoint of the resonator cavity, and have taken the etched regions to be similar but not necessarily identical.

Downloaded 03 May 2010 to 171.66.16.20. Redistribution subject to ASME license or copyright; see http://www.asme.org/terms/Terms_Use.cfm

We now wish to examine how we can choose the free parameters so that the performance of our device will be enhanced. These parameters are the cavity width $2a$, the extent of the etched regions l and $\bar{l}$, the applied loads S and N, and also the position(s) x at which the displacements are measured.

Again for convenience alone we shall choose the lengths of the etched regions to be the same $\bar{l}=l$, and to choose a specific etching profile. This is taken to be such that the etched regions are the mirror images of each other and to be of rectangular cross-section so that (see Clarke and Burdess (1991))

$$h=i/\pi \quad \text{and} \quad \bar{h}=-i/\pi.$$

This means that $\bar{\tau}=\tau$ and we shall envisage l to be sufficiently large so that τ is close to unity which means that the reflection will be almost total.

It follows that

$$R=\tau(1-\delta\zeta),$$

and

$$\bar{R}=\tau(1+\delta\zeta), \tag{22}$$

where

$$\zeta=(2k^2-1)/2k^3q+\beta_1/\beta-2k_1/k, \tag{23}$$

and so $R\bar{R}=\tau^2+0(\delta^2)$.

The denominator D of each of the displacements, given by (21) is then

$$D=1-\tau^2e^{i4ka}$$

and so does not depend upon δ. Hence the cavity width $2a$ may be chosen to maximize the displacements (i.e., for resonance). In what follows we take

$$2a=M\pi/k, \tag{24}$$

for some integer M, and note that as this does not depend upon δ then the cavity width is set as for the static case. Since the shape of the resonator is symmetric about the y-axis, a rotation about the z-axis is not expected to produce first-order changes in the value of the resonant frequency. Because of this symmetry a view taken from the "other side" of the resonator allows the situation caused by a rotation Ω about the z-axis to be interpreted as being the same as that caused by a rotation $-\Omega$ about the z-axis. The denominator is now

$$D=1-\tau^2. \tag{25}$$

Next we consider the effect of a judicious choice of loading. This manifests itself in the displacements, (21), in the factors

$$A^{(+)}(\delta)=(V+\overline{VR}\,e^{i2ka})/D,$$

and

$$A^{(-)}(\delta)=(\bar{V}+VR\,e^{i2ka})/D, \tag{26}$$

where V and $\bar{V}$ are given in (9). For $\delta=0$ these are

$$A^{(\pm)}(0)=\{iqS(1+(-1)^M\tau) \pm(pq)^{1/2}N(1-(-1)^M\tau)\}/(1-\tau^2)f'(k) \tag{27}$$

and we would like these to be as small as possible so that the contribution due to rotation will "stand out." There are (at least) two such possibilities here but the one we choose to pursue here is to set

$$S=0,$$

i.e., purely a normal load, and to insist that

$$M=2m$$

for integer m. This means that the cavity width must now be of the form

$$2a=2m\pi/k. \tag{28}$$

It follows that with these values for a and S that

$$A^{(\pm)}(\delta)=\{\pm(pq)^{1/2}(1+\tau)^{-1} +\delta[B(1-\tau)^{-1}+(pq)^{1/2}\zeta(1+\tau)^{-1}]\}N/f'(k), \tag{29}$$

where

$$B=(2k^2+1)k_1/2k^2+\{\alpha k^2+pq)/2k^2q-(2k^2-1)(C+\zeta)/2k. \tag{30}$$

The quantity

$$C=k_1f''(k)/f'(k)+\alpha(q^{-3}+k^{-2}p^{-1})/f'(k), \tag{31}$$

arises from the terms $g'(\kappa)$ and $g'(-\bar{\kappa})$.

In the absence of rotation a cavity with width defined by (28) does not produce a resonant response when excited by the normal force N. This behavior is determined by the spatial characteristics of the exciting forces and is discussed in detail by Clarke and Burdess (1991). When rotation occurs resonance appears and the term $B(1-\tau)^{-1}$ becomes large as $\tau\to1$. This unexpected result may be explained in terms of the excitation caused by the Coriolis inertia forces generated as a result of the coupling between the "stationary" response and the rotation Ω. These forces will further excite the cavity and their distribution within the cavity is such as to cause resonance.

Consider finally the positional terms in (21) namely

$$\Phi_1^{(-)}(\delta)=e^{-i\bar{\kappa}(x+a)}+\bar{R}e^{i\kappa(x+a)},$$
$$\Phi_2^{(-)}(\delta)=\bar{\xi}e^{-i\bar{\kappa}(x+a)}-\xi\bar{R}e^{i\kappa(x+a)}, \tag{32}$$

for $-a<x<0$, and similar expressions valid in $0<x<a$. Now when $\delta\equiv0$

$$\Phi_1^{(-)}(0)=e^{-ik(x+a)}+\tau e^{ik(x+a)},$$
$$\Phi_2^{(-)}(0)=(p/q)^{1/2}\{e^{-ik(x+a)}-\tau e^{ik(x+a)}\}. \tag{33}$$

For the ideal resonator, i.e., $\tau=1$, Eqs. (33) show that at a position determined from $2k(x+a)=2n\pi$, for integer n, the displacement u_1 has an antinode and u_2 a node, and vice versa for $2k(x+a)=(2n+1)\pi$. The same occurs for $0<x<a$ with $(x+a)$ replaced by $(a-x)$. Although no true node exists when $\tau<1$, the displacement at this point is expected to be small and could show significant changes due to the effects of rotation.

Therefore, if $-a<x<0$, we will choose

$$x=-a+n\pi/k, \tag{34}$$

and similarly if $0<x<a$, the choice will be

$$x=a-n\pi/k, \tag{35}$$

where n is an integer such that $0<n<ka/\pi$. These are then the positions at which we measure the displacements.

The corresponding rotation-dependent terms at these positions are given by

$$\Phi_1^{(-)}(\delta)=(-1)^ne^{i\delta n\pi k_1/k}\{1+\tau+\delta\tau\zeta\},$$
$$\Phi_2^{(-)}(\delta)=(-1)^ne^{i\delta n\pi k_1/k}(p/q)^{1/2}\{1 -\tau+\delta[(q/p)^{1/2}(1+\tau)Z-\tau\zeta]\}, \tag{36}$$

and $\Phi_{1,2}^{(+)}(\delta)=\Phi_{1,2}^{(-)}(-\delta)$, where

$$Z=k_1/2k^2q^3+\{2(1-\alpha)k^2-1\}/4k^2q^2. \tag{37}$$

We may now display the displacements at the prescribed positions as, for $x<0$,

$$u_1=(-1)^{n+m}e^{i\delta(n-m)\pi k_1/k-it}\{-(pq)^{1/2}+\delta[B(1+\tau)/(1-\tau) +(pq)^{1/2}\zeta/(1+\tau)]\}N/f'(k),$$
$$u_2=i(-1)^{n+m}e^{i\delta(n-m)\pi k_1/k-it}\{(pq)^{1/2}(1-\tau)/(1+\tau) -\delta[B-qZ+(pq)^{1/2}\zeta/(1+\tau)]\}\left(\frac{p}{q}\right)^{1/2}N/f'(k), \tag{38}$$

while for $x>0$,

Downloaded 03 May 2010 to 171.66.16.20. Redistribution subject to ASME license or copyright; see http://www.asme.org/terms/Terms_Use.cfm

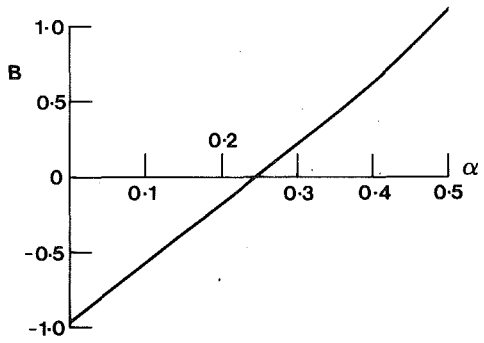


Fig. 4 B as a function of α

$$u_1 = (-1)^{n+m} e^{-i\delta(n-m)\pi k_1/k - it}\{(pq)^{1/2} + \delta[B(1+\tau)/(1-\tau) + (pq)^{1/2}\zeta/(1+\tau)]\}N/f'(k),$$

$$u_2 = i(-1)^{n+m} e^{-i\delta(n-m)\pi k_1/k - it}\{(pq)^{1/2}(1-\tau)/(1+\tau) + \delta[B - qZ + (pq)^{1/2}\zeta/(1+\tau)]\}\left(\frac{p}{q}\right)^{1/2} N/f'(k).$$

There may be many ways of interpreting these solutions for practical advantage, such as combining the signals from the mirror image positions in $x>0$ and $x<0$ in order to eliminate the static terms along with any vagaries associated with their measurements. However, if we restrain such flights of fancy and consider the basic signal from a chosen position in either $x>0$ (or in $x<0$) then an inspection of (38) reveals that while u_2 remain small under rotation, u_1 may suffer a substantial change due to rotation if $(1-\tau)=0(\delta)$. If we let θ be the ratio of the perturbed terms (due to rotation) to the static terms, then

$$\theta = \delta B(1+\tau)(1-\tau)^{-1}(pq)^{-1/2}. \tag{39}$$

B has been calculated numerically as a function of α and is shown in Fig. 4. When $\alpha=0.24986$, $B=0$ and, for values of α less than this, B is virtually a straight line given by

$$B = 3.9813(\alpha - 0.24986). \tag{40}$$

For larger values of α it deviates away slightly from this line.

Obviously, for practical reasons the resonator should not be constructed from a material for which α is close to the value 0.24986.

By altering the length of the etched region we change τ and hence θ. This length, in dimensional form, is given by (for a rectangular sectioned etching profile, see Clarke and Burdess, 1991)

$$l' = (\mu/\rho\omega^2)^{1/2}(\pi/2\beta\epsilon)\ln\{(pq)^{1/2}\theta/B\delta\}. \tag{41}$$

As an example, if the resonator material was stainless steel then $\alpha \simeq 0.303$, and if we choose $\omega = 10^6$ herz, the rotation rate 1 herz, i.e., $\delta = 10^{-6}$, and choose the small etching depth parameter $\epsilon = 10^{-2}$, then $L = 0.051$ m for $\theta = 1$. It would seem from this that the foregoing analysis could form the basis for the construction of a rotation sensor of a practicable size.

References

Clarke, N. S., Davies, C., and Burdess, J. S., 1989, "On the Multiple Scattering of Rayleigh Waves by Surface Roughness," *Wave Motion*, Vol. 11, pp. 371-381.

Clarke, N. S., and Burdess, J. S., 1991, "A Rayleigh Resonator," *Wave Motion*, Vol. 13, pp. 193-200.

Lao, B. Y., 1980, "Gyroscopic Effect in Surface Acoustic Waves," *Ultrasonic Symposium Proceedings*, IEEE Cat. No. 80 Ch 1602 2, Institute of Electrical and Electronic Engineers, New York, p. 687.

Wren, T., and Burdess, J. S., 1987, "Surface Waves Perturbed by Rotation," ASME Journal of Applied Mechanics, Vol. 54, pp. 464-466.

Downloaded 03 May 2010 to 171.66.16.20. Redistribution subject to ASME license or copyright; see http://www.asme.org/terms/Terms_Use.cfm

Domains of Attraction of a Forced Beam by Interpolated Mapping

W. K. Lee
Associate Professor,
Department of Mechanical Engineering,
Mem. ASME.

M. R. Ghang
Researcher,
Institute of Industrial Technology.

Yeungnam University,
Gyongsan 712-749, Korea

A nonlinear dissipative dynamical system can often have multiple attractors. In this case it is important to study the global behavior of the system by determining the global domain of attraction of each attractor. In this paper we study the global behavior of a forced beam with two-mode interaction. The governing equation of motion is reduced to two second-order nonlinear nonautonomous ordinary differential equations. When $\omega_2 \approx 3\omega_1$ and $\Omega \approx \omega_1$, the system can have two asymptotically stable steady-state periodic solutions, where ω_1, ω_2 and Ω denote natural frequencies of the first and second modes and the excitation frequency, respectively. Both solutions have the same period as the excitation period. Therefore, each of them shows up as a period-1 solution in Poincaré map. We show how interpolated mapping method can be used to determine the two four-dimensional domains of attraction of the two solutions in a very effective way. The results are compared with the ones obtained by direct numerical integration.

1 Introduction

A nonlinear dissipative dynamical system can have multiple attractors. In this case, the asymptotic behavior of the system depends on the initial condition. A set of initial states, which is called the domain of attraction, is attracted to one of attractors. Consider a mechanical system with multiple asymptotically stable steady-state responses. From the engineering point of view, in some circumstances, only one of these responses may be desirable for the sake of the reliable performance of the system. Then one might ask what initial disturbances can change the asymptotic behavior from the desirable response to the others. Therefore, it can be said that to find the domains of attraction is the ultimate aim of any complete analysis of a nonlinear system.

However, not much attention has been paid to domains of attraction, especially for multi-degree-of-freedom systems. Since the state space of an N-degree-of-freedom system is $2N$-dimensional, it is very difficult to find domains of attraction of the system. If we use a computer, it may take the Nth power times as much as the computation time required for a single-degree-of-freedom system.

In order to reduce the computation time Hsu (1980, 1981) invented cell mapping methods, which have been used to analyze many kinds of engineering problems (Polchai and Hsu, 1985; Xu et al., 1985; Hsu and Chiu, 1986, 1987; Hsu, 1987; Lee, 1992). Tongue (1987) and Tongue and Gu (1988) proposed the interpolated cell mapping method to find the domains of attraction of a forced Duffing oscillator having a strange attractor and a third-order subharmonic solution. They obtained the interpolated image by solving a system of linear equations. Instead of solving a system of linear equations, Lee (1988) and Lee and Hsu (1994) presented the method in a compact form so that it can be applied to systems with dimension higher than two. They called the method the interpolated mapping method because it is not based upon the cell-state space concept.

Nayfeh et al. (1974) and Lee and Soh (1994) found that a harmonically excited hinged-clamped beam can have two asymptotically stable steady-state solutions when certain resonance conditions are satisfied. In this paper, two four-dimensional domains of attraction of two solutions are determined by the interpolated mapping method.

2 Interpolated Mapping Method

In this section we shall give a brief description of the interpolated mapping method to be used to determine the domains of attraction of the two steady-state solutions for the forced beam system.

Consider a point mapping system governed by

$$\mathbf{x}(n+1) = \mathbf{G}(\mathbf{x}(n)), \quad \mathbf{x} \in \mathbf{R}^4, \tag{1}$$

where $\mathbf{x}$ is a four-dimensional state vector, n is an integer, and $\mathbf{G} : \mathbf{R}^4 \rightarrow \mathbf{R}^4$. The basic idea of the interpolated mapping method is to find the image $\mathbf{x}(n+1)$ by using an interpolation procedure instead of system (1). We present the method in the following procedure.

The first step is to discretize the state space of interest. Let us assume that the system is defined merely over a proper subset of $\mathbf{R}^4$ rather than $\mathbf{R}^4$ itself. The subset will be specified by a cartesian product $[x_{1(\min)}, x_{1(\max)}] \times [x_{2(\min)}, x_{2(\max)}] \times$

Contributed by the Applied Mechanics Division of THE AMERICAN SOCIETY OF MECHANICAL ENGINEERS for publication in the ASME JOURNAL OF APPLIED MECHANICS.

Discussion on this paper should be addressed to the Technical Editor, Professor Lewis T. Wheeler, Department of Mechanical Engineering, University of Houston, Houston, TX 77204-4792, and will be accepted until four months after final publication of the paper itself in the ASME JOURNAL OF APPLIED MECHANICS.

Manuscript received by the ASME Applied Mechanics Division, Apr. 13, 1992; final revision, Feb. 3, 1993. Associate Technical Editor: D. J. Inman.

Copyright © 1994 by ASME
Downloaded 03 May 2010 to 171.66.16.20. Redistribution subject to ASME license or copyright; see http://www.asme.org/terms/Terms_Use.cfm

$[x_{3(\min)}, x_{3(\max)}] \times [x_{4(\min)}, x_{4(\max)}]$, denoted by D_x. The subset D_x is assumed to include all attractors whose domains of attraction are to be determined. Now let us cut it into a large number of four-dimensional parallelepipeds. The cuts are made parallel to the x_1, x_2, x_3, and x_4 axes. Let i_j be the number of intervals in the x_j-direction. Every parallelepiped has a uniform size, say $h_1 \times h_2 \times h_3 \times h_4$, where $h_j = (x_{j(\max)} \times x_{j(\min)})/i_j$, $j = 1, 2, 3, 4$. Then D_x includes $\Pi_{j=1}^4 (i_j + 1)$ grid points. The second step is to find the image of every grid point by using system (1). The third step is to pick a point in D_x whose long-term behavior is to be determined, and is to find the subsequent trajectory by using the following interpolation procedure. Let $\{\mathbf{e}_1, \mathbf{e}_2, \mathbf{e}_3, \mathbf{e}_4\}$ be the usual basis of $\mathbf{R}^4$. Suppose that a point $\mathbf{x}_0 = \Sigma_{m=1}^4 x_{0m}\mathbf{e}_m$ belongs to a parallelepiped whose corner points are $\mathbf{x}_{ijkl}$, $i, j, k, l = 1, 2$. Here we locate the corner points (or corresponding grid points) of the parallelepiped as follows:

$$\mathbf{x}_{2jkl} - \mathbf{x}_{1jkl} = h_1\mathbf{e}_1,$$

$$\mathbf{x}_{i2kl} - \mathbf{x}_{i1kl} = h_2\mathbf{e}_2,$$

$$\mathbf{x}_{ij2l} - \mathbf{x}_{ij1l} = h_3\mathbf{e}_3,$$

$$\mathbf{x}_{ijk2} - \mathbf{x}_{ijk1} = h_4\mathbf{e}_4, \tag{2}$$

where $i, j, k, l = 1, 2$.

Let x_{ijklm} be the component of $\mathbf{x}_{ijkl}$ associated with the x_m-direction. Then $\mathbf{x}_{ijkl} = \Sigma_{m=1}^4 x_{ijklm}\mathbf{e}_m$. The point $\mathbf{x}_0$ can then be expressed as

$$\mathbf{x}_0 = \sum_{i,j,k,l=1}^{2} t_{1i}t_{2j}t_{3k}t_{4l}\mathbf{x}_{ijkl}, \tag{3}$$

where

$$t_{m1} = 1 - b_m, \quad t_{m2} = b_m, \quad b_m = (x_{0m} - x_{1111m})/h_m, \quad m = 1, 2, 3, 4.$$

The approximate image $\mathbf{x}_0'$ of the point $\mathbf{x}_0$ can be obtained from the linear interpolation as follows:

$$\mathbf{x}_0' = \sum_{i,j,k,l=1}^{2} t_{1i}t_{2j}t_{3k}t_{4l}\mathbf{x}_{ijkl}', \tag{4}$$

where $\mathbf{x}_{ijkl}'$ is the true image of $\mathbf{x}_{ijkl}$, that is, $\mathbf{x}_{ijkl}' \equiv \mathbf{G}(\mathbf{x}_{ijkl})$. The case of a two-dimensional state space is shown in Fig. 1 where

$$\mathbf{y}_j = (1 - b_1)\mathbf{x}_{1j} + b_1\mathbf{x}_{2j} = \sum_{i=1}^{2} t_{1i}\mathbf{x}_{ij},$$

$$\mathbf{x}_0 = (1 - b_2)\mathbf{y}_1 + b_2\mathbf{y}_2 = \sum_{j=1}^{2} t_{2j}\mathbf{y}_j = \sum_{i,j=1}^{2} t_{1i}t_{2j}\mathbf{x}_{ij},$$

$$\mathbf{y}_j' = (1 - b_1)\mathbf{x}_{1j}' + b_1\mathbf{x}_{2j}' = \sum_{i=1}^{2} t_{1i}\mathbf{x}_{ij}',$$

$$\mathbf{x}_0' = (1 - b_2)\mathbf{y}_1' + b_2\mathbf{y}_2' = \sum_{j=1}^{2} t_{2j}\mathbf{y}_j' = \sum_{i,j=1}^{2} t_{1i}t_{2j}\mathbf{x}_{ij}'.$$

The truncation error e_t between the interpolated image $\mathbf{x}_0'$ and the true image $\mathbf{G}(\mathbf{x}_0)$ can be expressed as

$$e_t = \mathbf{x}_0' - \mathbf{G}(\mathbf{x}_0) = \sum_{i,j,k,l=1}^{2} t_{1i}t_{2j}t_{3k}t_{4l}\mathbf{G}(\mathbf{x}_{ijkl}) - \mathbf{G}(\mathbf{x}_0).$$

By the Taylor's expansion of $\mathbf{x}_{ijkl}'$ about $\mathbf{x}_0$, we have

$$\mathbf{x}_{ijkl}' = \mathbf{G}(\mathbf{x}_{ijkl}) = \mathbf{G}(\mathbf{x}_0) + \left.\frac{\partial \mathbf{G}(\mathbf{x})}{\partial \mathbf{x}}\right|_{\mathbf{x}=\mathbf{x}_0} (\mathbf{x}_{ijkl} - \mathbf{x}_0) + O(|\mathbf{x}_{ijkl} - \mathbf{x}_0|^2). \tag{6}$$

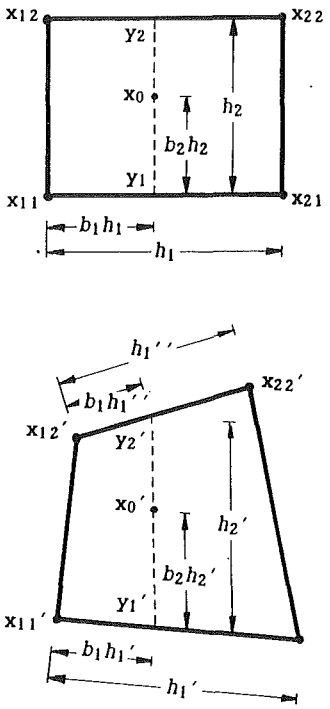


Fig. 1 The interpolated mapping for the case of a two-dimensional state space

Using the relation $\Sigma_{i,j,k,l=1}^2 t_{1i}t_{2j}t_{3k}t_{4l} = 1$ and substituting Eq. (6) into Eq. (5), we can write

$$e_t = \left.\frac{\partial \mathbf{G}(\mathbf{x})}{\partial \mathbf{x}}\right|_{\mathbf{x}=\mathbf{x}_0} \sum_{i,j,k,l=1}^{2} t_{1i}t_{2j}t_{3k}t_{4l}(\mathbf{x}_{ijkl} - \mathbf{x}_0) + O(h^2), \tag{7}$$

where $h^2 = \Sigma_{m=1}^4 h_m^2$. By Eq. (3), (7) becomes

$$e_t = O(h^2). \tag{8}$$

This is a contrast to the truncation error $O(h)$ for the simple cell mapping (Hsu, 1980).

In order to proceed to the next step, we have to find a parallelepiped which includes the point $\mathbf{x}_0'$. Then we can find the image of $\mathbf{x}_0'$ by using Eq. (4). In this manner we can obtain the trajectory of the system with $\mathbf{x}_0$ as an initial state by applying repeatedly the interpolation procedure.

Before leaving this section we would like to make some remarks about the interpolated mapping method. Once images of all grid points in the discretization of the state space of interest are obtained, within the context of approximation by discretizing the state space, these contain all the dynamics information of the system. Now the interpolation procedure is used to extract the information from the images of the finite number of uniformly distributed grid points (Lee, 1988; Lee and Hsu, 1994).

3 Equations of Motion and Steady-State Solutions

A straight beam with fixed ends experiences midplane stretching when deflected. The influence of this stretching on the dynamic response increases with the amplitude of the solution. This situation can be described with nonlinear strain-displacement equations and a linear stress-strain law which give us the nonlinear beam equation. Consider a slender, initially straight hinged-clamped beam, which is shown in Fig. 2. For such a beam, the partial differential equation of motion and boundary conditions can be represented as (Nayfeh, Mook, and Sridhar, 1974; Lee and Soh, 1991).

$$EI\frac{\partial^4 \overline{w}}{\partial \overline{x}^4} + m\frac{\partial^2 \overline{w}}{\partial \overline{t}^2} = -2\overline{c}\frac{\partial \overline{w}}{\partial \overline{t}} + \overline{H}\frac{\partial^2 \overline{w}}{\partial \overline{x}^2} + \overline{p}(\overline{x}, \overline{t}) \tag{9a}$$

Downloaded 03 May 2010 to 171.66.16.20. Redistribution subject to ASME license or copyright; see http://www.asme.org/terms/Terms_Use.cfm

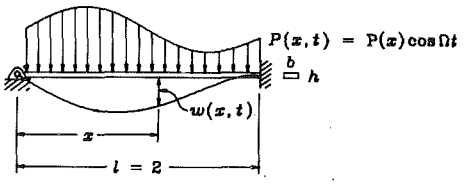


Fig. 2 A schematic diagram of a hinged-clamped beam

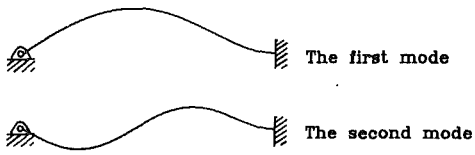


Fig. 3 Eigenfunctions of the beam vibration

$$\overline{w}(0, \bar{t}) = 0, \quad \frac{\partial^2 \overline{w}(0, \bar{t})}{\partial \bar{x}^2} = 0 \qquad (9b, c)$$

$$\overline{w}(\bar{l}, \bar{t}) = 0, \quad \frac{\partial \overline{w}(\bar{l}, \bar{t})}{\partial \bar{x}} = 0 \qquad (9d, e)$$

where m = mass per unit length; $I = bh^3/12$ = area moment of inertia; E = Young's modulus; b = width of beam; h = thickness of beam; $\bar{c}$ = damping coefficient; $\overline{p}$ = exciting force; $\bar{l}$ = length of beam; $\overline{H} = EA/2\bar{l}\int_0^{\bar{l}} (\partial \overline{w}/\partial \bar{x})^2 d\bar{x}$ = tension due to midplane stretching; $\overline{w}$ = deflection of beam; $\bar{t}$ = time in second; $\bar{x}$ = longitudinal axis; A = cross-section of beam.

Rewriting the equations in terms of dimensionless variables, we have

$$\frac{\partial^4 w}{\partial x^4} + \frac{\partial^2 w}{\partial t^2} = \epsilon\left(-2c\frac{\partial w}{\partial t} + H\frac{\partial^2 w}{\partial x^2} + p\right) \qquad (10a)$$

$$w(0, t) = 0, \quad \frac{\partial^2 w(0, t)}{\partial x^2} = 0, \qquad (10b, c)$$

$$w(l, t) = 0, \quad \frac{\partial w(l, t)}{\partial x} = 0 \qquad (10d, e)$$

where

$$H = \nu \int_0^l \left(\frac{\partial w}{\partial x}\right)^2 dx$$

$\bar{x} = xL$, $L = \bar{l}/2$, $l = \bar{l}/L = 2$, $\bar{c} = 2cr^3A(mE)^{1/2}/L^4$, $\overline{p} = (r^6EA/L^7)p$, $r = (I/A)^{1/2}$ = radius of gyration, $\epsilon = r^2/L^2 = (h/L)^{1/2}/12$, $\overline{w} = r^2w/L$, $\bar{t} = (mL^4/Er^2)^{1/2}t$, $\overline{H} = EAH(r/L)^4$.

Equation (10) can be solved approximately by the Galerkin's method. The deflection is approximated by

$$w(x, t) = \sum_{m=1}^{\infty} u_m(t)\varphi_m(x) \qquad (11)$$

where u_m are generalized coordinates and φ_m are eigenfunctions of the following eigenvalue problem:

$$\frac{d^4\varphi_m}{dx^4} - \omega_m^2\varphi_m = 0 \text{ and} \qquad (12a)$$

$$\varphi_m(0) = 0, \quad \frac{d^2\varphi_m(0)}{dx^2} = 0, \qquad (12b, c)$$

$$\varphi_m(l) = 0, \quad \frac{d\varphi_m(l)}{dx} = 0, \qquad (12d, e)$$

where ω_m are natural frequencies.

The eigenfunction of the eigenvalue problem (12) is

$$\varphi_n = E_n[\sin(\alpha_n x) - R_n \sinh(\alpha_n x)]$$

where

$$E_n = \left[\frac{1}{2}l(1 - R_n^2) + (R_n^2 \sinh 2\,\alpha_n l - \sin 2\,\alpha_n l)/4\alpha_n\right]^{-1/2}$$

$$R_n = \sin\alpha_n l/\sinh\alpha_n l, \quad \alpha_n = (\omega_n)^{1/2}/l$$

and the α_n are the roots of $\tan \alpha_n l = \tanh \alpha_n l$. The first two eigenfunctions are shown in Fig. 3. Since $l = 2$, the first two roots and frequencies are

$$\alpha_1 l = 3.927 \text{ and } \omega_1 = 15.421$$

$$\alpha_2 l = 7.069 \text{ and } \omega_2 = 49.970.$$

From the observation of these natural frequencies, we can see the relations $\omega_2 \approx 3\omega_1$, which is the condition of the internal resonance.

Substituting Eq. (11) into Eq. (10), multiplying by φ_n, integrating over the length, and using the orthogonality of the eigenfunctions we obtain a set of nonlinear ordinary differential equations.

$$\frac{d^2u_n}{dt^2} + \omega_n^2 u_n = \epsilon\left[-2c_n\frac{du_n}{dt} + f_n\cos\Omega t + \sum_{m,p,q=1}^{\infty}\alpha_{nmpq}u_m u_p u_q\right], \quad n = 1, 2, \ldots \qquad (13)$$

where

$$c_n = \int_0^l c\varphi_n^2 dx = \text{modal damping coefficient},$$

$$\alpha_{nmpq} = \nu\int_0^l \varphi_n\frac{d^2\varphi_q}{dx^2}dx\int_0^l \frac{d\varphi_m}{dx}\frac{d\varphi_p}{dx}dx,$$

$$\nu = 1/2l = 1/4$$

$$f_n = \int_0^l P(x)\varphi_n \nu dx = \text{excitation amplitude},$$

$$p(x, t) = P(x)\cos\Omega t = \text{harmonic exciting force},$$

$$\Omega = \text{excitation frequency}.$$

Nayfeh et al. (1974) and Lee and Soh (1994) found that the first two modes are dominant when $\Omega \approx \omega_1$. Thus the Eqs. (13) can be reduced to the equations of a two-degree-of-freedom system as follows:

$$\frac{d^2u_n}{dt^2} + \omega_n^2 u_n = \epsilon\left[-2c_n\frac{du_n}{dt} + f_n\cos\Omega t + \sum_{m,p,q=1}^{2}\alpha_{nmpq}u_m u_p u_q\right], \quad n = 1, 2. \qquad (14)$$

The damping is assumed to be modal and the exciting force is assumed to be harmonic.

Using the eigenfunctions φ_n, we can obtain the coefficients α_{nmpq} as follows:

$$\alpha_{1111} = -2.071, \quad \alpha_{1112} = -0.770$$
$$\alpha_{1121} = -0.770, \quad \alpha_{1122} = -7.716$$
$$\alpha_{1211} = -0.770, \quad \alpha_{1212} = -0.286$$
$$\alpha_{1221} = -0.286, \quad \alpha_{1222} = -2.870$$
$$\alpha_{2111} = -0.770, \quad \alpha_{2112} = -0.286$$
$$\alpha_{2121} = -0.286, \quad \alpha_{2122} = -2.870$$
$$\alpha_{2211} = -7.716, \quad \alpha_{2212} = -2.870$$
$$\alpha_{2221} = -2.870, \quad \alpha_{2222} = -28.751.$$

Nayfeh et al., (1974) and Lee and Soh (1994) found that the system can have two asymptotically stable steady-state solutions when the excitation frequency Ω is near the natural fre-

Downloaded 03 May 2010 to 171.66.16.20. Redistribution subject to ASME license or copyright; see http://www.asme.org/terms/Terms_Use.cfm

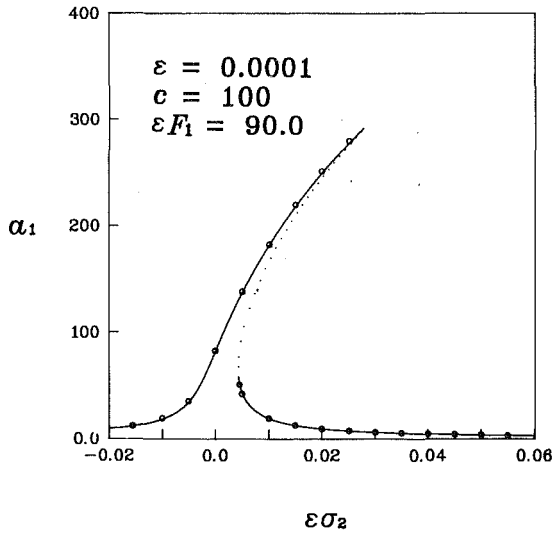


Fig. 4 Variation of amplitude a_1 of the first mode with the detuning parameter σ_2

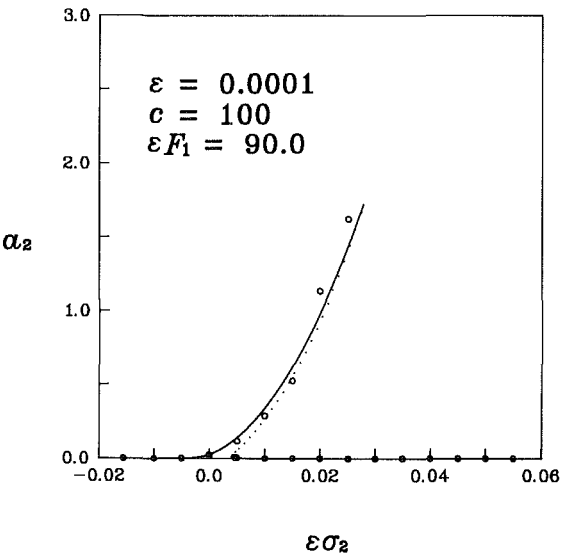


Fig. 5 Variation of amplitude a_2 of the second mode with the detuning parameter σ_2

quency of the first mode ω_1. Using the detuning parameter, we can represent the excitation frequency as follows:

$$\Omega = \omega_1(1 + \epsilon\sigma_2),$$

where a detuning parameter σ_2 is 140. In the case, the frequency response curves are in Figs. 4 and 5. The results are similar to the frequency response curve of a Duffing oscillator for a hardening spring. The results obtained by numerical integration (circles) are in agreement with the ones obtained analytically. The solid and dotted lines denote the stable and unstable solutions, respectively. The large amplitude solution is called the upper branch solution. The other solution (small amplitude) is called the lower branch solution.

For the subsequent discussion, it is convenient to write the equations of motion (14) as a system of four first-order nonautonomous equations. Letting

$$x_1 = u_1, \quad x_2 = \dot{u}_1, \quad x_3 = u_2, \quad x_4 = \dot{u}_2 \tag{15}$$

we have

$$\dot{\mathbf{x}} = \mathbf{F}(\mathbf{x}, t), \quad \mathbf{x} \in \mathbf{R}^4, \tag{16}$$

where $\mathbf{x} = \{x_1, x_2, x_3, x_4\}^T$ and $\mathbf{F}(\mathbf{x}, t) = \{F_1, F_2, F_3, F_4\}^T$, with components

$$F_1 = x_2$$

$$F_2 = -\omega_2^2 x_1 + \epsilon[-2c_1 x_2 + \alpha_{1111}x_1^3 + (\alpha_{1112} + \alpha_{1121} + \alpha_{1211})x_1^2 x_3 + (\alpha_{1122} + \alpha_{1212} + \alpha_{1221})x_1 x_3^2 + \alpha_{1222}x_3^3 + f_1 \cos \Omega t]$$

$$F_3 = x_4$$

$$F_4 = -\omega_2^2 x_3 + \epsilon[-2c_2 x_4 + \alpha_{2111}x_1^3 + (\alpha_{2112} + \alpha_{2121} + \alpha_{2211})x_1^2 x_3 + (\alpha_{2122} + \alpha_{2212} + \alpha_{2221})x_1 x_3^2 + \alpha_{2222}x_3^3 + f_2 \cos \Omega t]. \tag{17}$$

In order to investigate the global behavior of the system (16) given by nonautonomous ordinary differential equation, it is convenient to construct the point mapping system (1).

Since the system (16) is periodic with the period $T = 2\pi/\Omega$, we can generate numerically a Poincaré map by inspecting the phase projection only at the specific times, $t = mT$ (m, integer). In the Poincaré section, each of the upper and lower branch solutions shows up as a periodic solution of period 1, which consists of one point in the four-dimensional state space. For numerical integration, we employ the Runge-Kutta fourth-order method with the time-step size of integration, $\Delta t = T/30$.

Among combinations of parameter values for which two asymptotically stable solutions exist, we consider the case of

$$\{\epsilon, c_1, c_2, \omega_1, \omega_2, f_1, f_2, \sigma_2\} = \{0.0001, 100, 100, 15.421, 49.970, 900{,}000, 0.01, 140\}. \tag{18}$$

The projections of phase trajectories of two solutions are shown in Fig. 6.

Corresponding periodic solutions in Poincaré section are as follows:

the upper branch solution,

$$\{x_1, x_2, x_3, x_4\} = \{141.59, 2552.62, 0.36, -18.59\} \tag{19}$$

and

the lower branch solution,

$$\{x_1, x_2, x_3, x_4\} = \{-13.96, 13.89, 0.00, 0.00\}, \tag{20}$$

which are shown in Fig. 6.

4 Domains of Attraction

In this section the interpolated mapping method will be used to determine the domains of attraction of two solutions (the upper and lower branch solutions) in a four-dimensional space. First of all,

$$D_x = [x_{1(\min)}, x_{1(\max)}] \times [x_{2(\min)}, x_{2(\max)}] \times [x_{3(\min)}, x_{3(\max)}] \times [x_{4(\min)}, x_{4(\max)}] = [-247.28, 374.910] \times [-3794.20, 6360.7] \times [-2.5426, 2.90630] \times [-148.75, 130.15]$$

is divided into 19^4 cubes, where 19 is the number of intervals in each x_m-direction. Then 20^4 (= 160,000) grid points are in D_x. Replacing the point mapping system (1) by the Poincaré map described earlier, we can locate the image of every grid point by integrating numerically Eq. (16) over the period T.

Now we can examine the long-term behavior of the system starting from any initial state in D_x by applying repeatedly the interpolation procedure until the trajectory leads to any attractor. In this study the set $\overline{D}_x = \{\mathbf{x} | \mathbf{x} \notin D_x \text{ and } \mathbf{x} \in \mathbf{R}^4\}$ is considered as an attractor. Since D_x includes both the upper and lower branch solutions, each trajectory will either leave D_x, lead to the upper branch solution, or lead to the lower branch solution. Because of the truncation error introduced by interpolating the image, a long-term trajectory by the interpolated mapping method which doesn't leave D_x does not

Downloaded 03 May 2010 to 171.66.16.20. Redistribution subject to ASME license or copyright; see http://www.asme.org/terms/Terms_Use.cfm

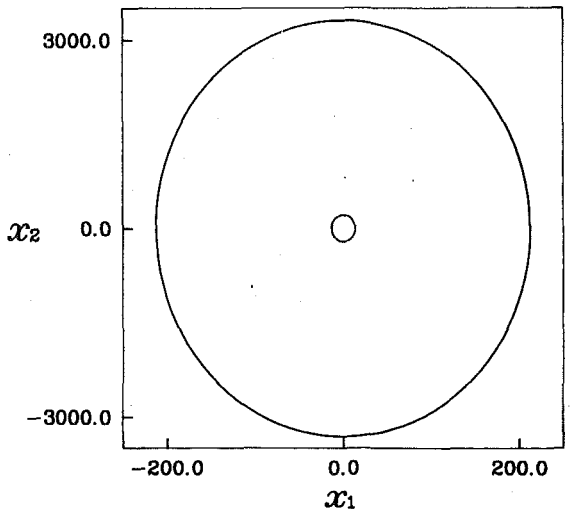


Fig. 6(*a*)

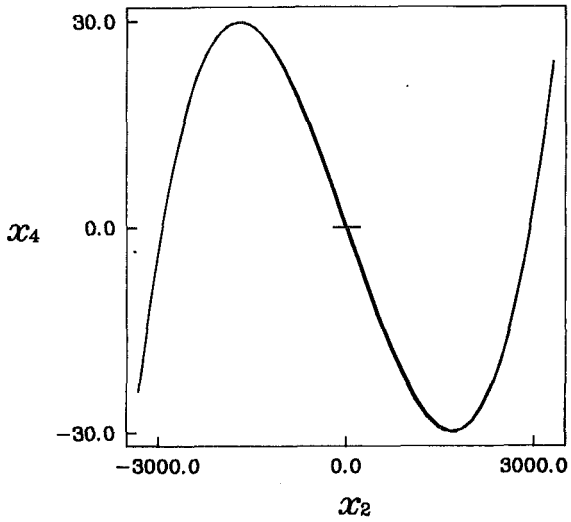


Fig. 6(*c*)

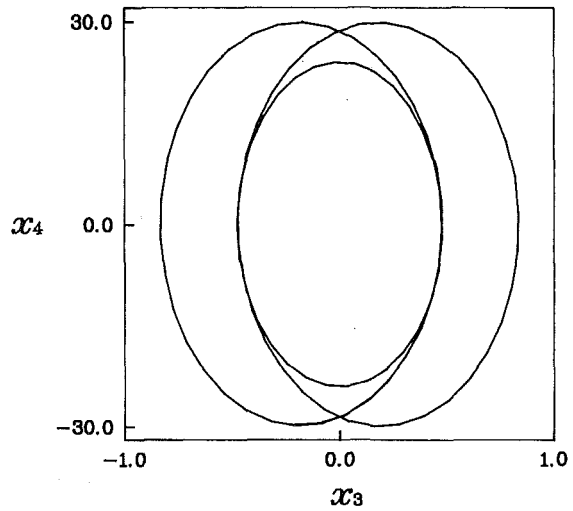


Fig. 6(*b*)

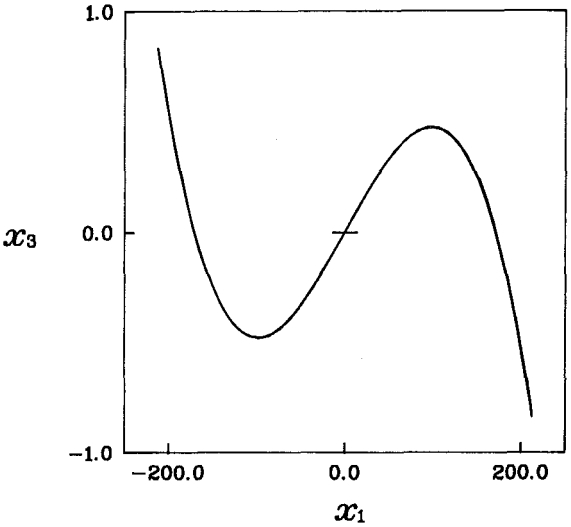


Fig. 6(*d*)

Fig. 6 Projections of two stable steady-state solutions; • • • , the lower branch solution; —, the upper branch solution. (*a*) on the $x_1 - x_2$ plane; (*b*) on the $x_3 - x_4$ plane; (*c*) on the $x_2 - x_4$ plane; (*d*) on the $x_1 - x_3$ plane.

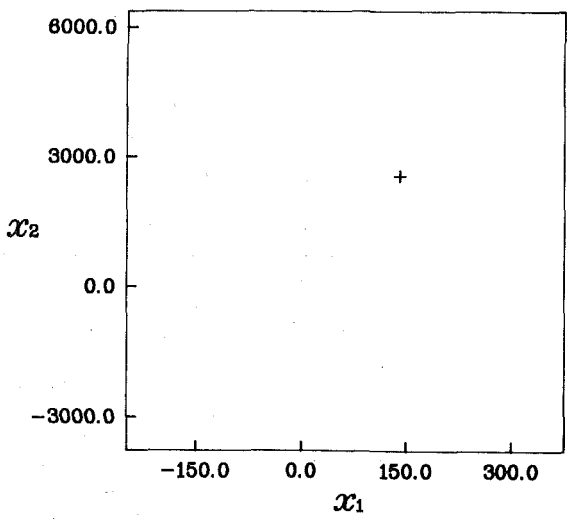


Fig. 7(*a*)

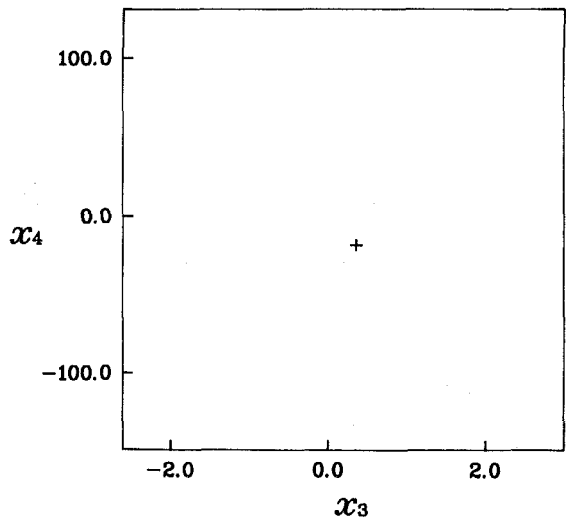


Fig. 7(*b*)

Fig. 7 Projections of Poincaré maps of two stable steady-state solutions, the upper branch solution; +, the lower branch solution; •. (*a*) on the $x_1 - x_2$ plane; (*b*) on the $x_3 - x_4$ plane.

Downloaded 03 May 2010 to 171.66.16.20. Redistribution subject to ASME license or copyright; see http://www.asme.org/terms/Terms_Use.cfm

necessarily converge to a periodic solution but may wander around the solution. Thus once a trajectory is in a small neighborhood of a periodic solution, the trajectory is assumed to lead to the solution. In this study a parallelepiped having the size $h_1 \times h_2 \times h_3 \times h_4$ and the center at the corresponding periodic solution is considered as the neighborhood. Taking 5^4 (= 625) uniformly distributed points in the cube as initial states and integrating numerically Eq. (16), we check the validity of the assumption.

It is difficult to represent graphically domains of attraction in a four-dimensional space. In this study we show the domains in some two-dimensional sections. Taking each of 39 × 39 points in a two-dimensional section as an initial state, we determine the attractor to which the trajectory eventually approaches. The two-dimensional sections chosen are as follows:

in Fig. 7,

(*a*) $x_1 - x_2$ plane at $z_3 = 19$, $z_4 = 19$

(*b*) $x_2 - x_4$ plane at $z_1 = 15$, $z_3 = 21$

(*c*) $x_3 - x_4$ plane at $z_1 = 25$, $z_2 = 15$

(*d*) $x_1 - x_3$ plane at $z_2 = 25$, $z_4 = 21$

where $z_m = n$ implies $x_m = x_{m(\min)} + (n - 1)h_m/2$. For instance, $z_m = 1$ and 39 imply $x_m = x_{x(\min)}$ and $x_{m(\max)}$, respectively. In these figures points belonging to the domains of attraction of the *P*-1 and *P*-2 solutions are indicated by "•" and "+", respectively. A blank indicates a point which is mapped out of D_x in its evolution.

To check the validity of the domains of attraction obtained by the interpolated mapping method, we have also obtained the domains for some sections by numerical integration. Figure 8(*a–d*) shows the results for the same sections as in Figure 7(*a–d*). We can see that the results obtained by the two methods agree remarkably well. There are a few points whose domains of attraction are not predicted correctly by the interpolated mapping method. Because of the truncation error introduced by the interpolation this is to be expected.

All the computations reported here were carried out on an IBM PC 386. The computation time required to find images

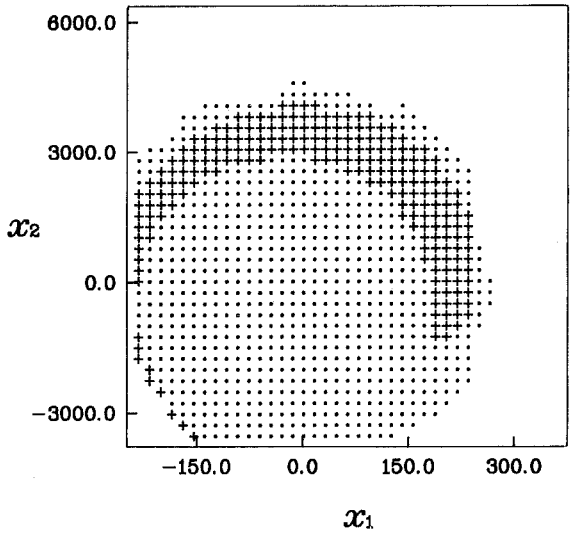


Fig. 8(*a*)

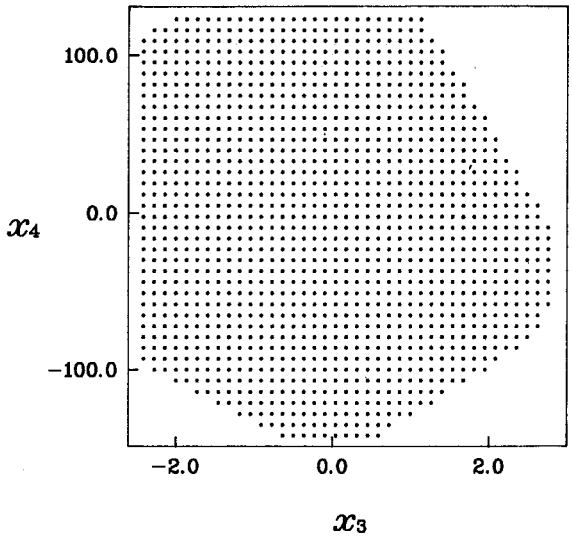


Fig. 8(*c*)

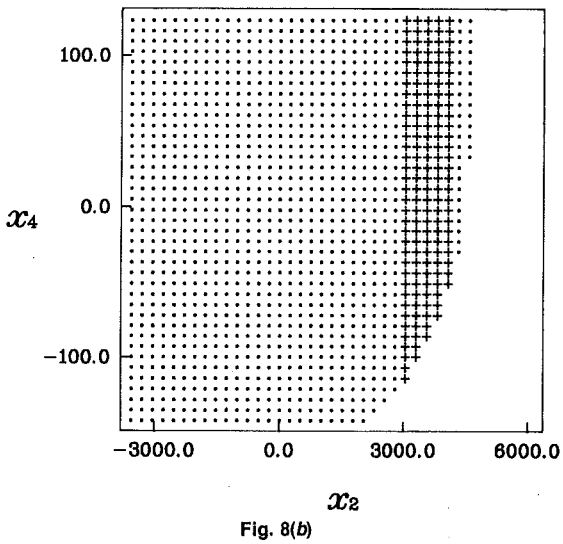


Fig. 8(*b*)

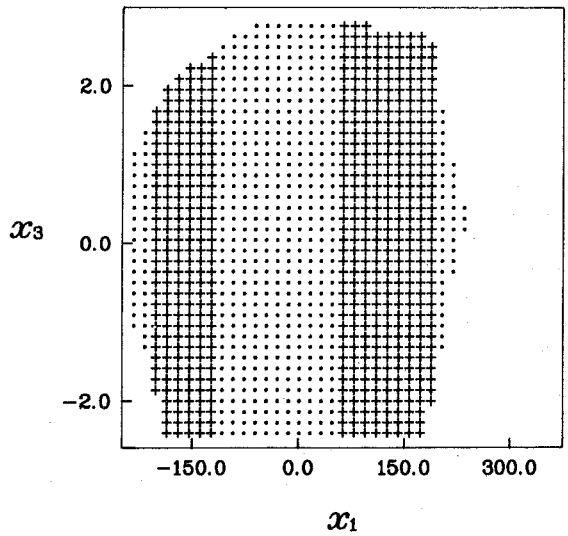


Fig. 8(*d*)

Fig. 8 The domains of attraction obtained by the interpolated mapping method for $\{\epsilon, c_1, c_2, \omega_1, \omega_2, f_1, f_2, \sigma_2\}$ = {0.0001, 100, 100, 15.421, 49.970, 900000, 0.01, 140}, the upper branch solution: +, the lower branch solution: •. (*a*) the $x_1 - x_2$ plane at $z_3 = 19$, $z_4 = 19$; (*b*) the $x_2 - x_4$ plane at $z_1 = 15$, $z_3 = 21$; (*c*) the $x_3 - x_4$ plane at $z_1 = 25$, $z_2 = 15$; (*d*) the $x_1 - x_3$ plane at $z_2 = 25$, $z_4 = 21$.

Downloaded 03 May 2010 to 171.66.16.20. Redistribution subject to ASME license or copyright; see http://www.asme.org/terms/Terms_Use.cfm

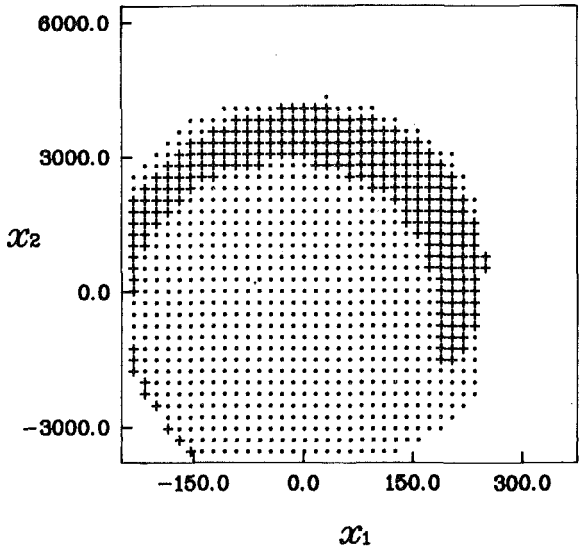


Fig. 9(a)

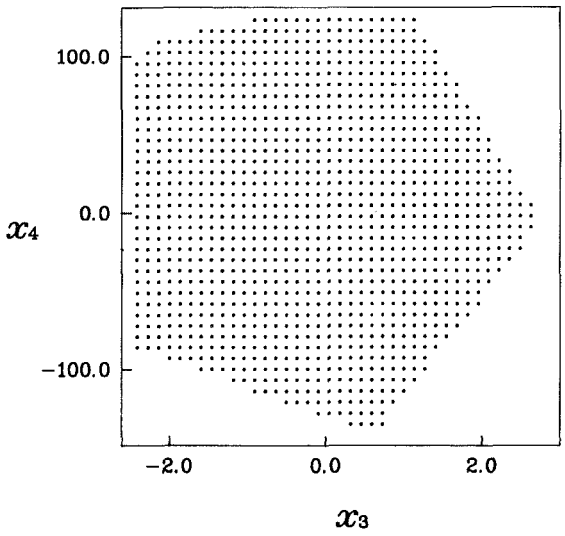


Fig. 9(c)

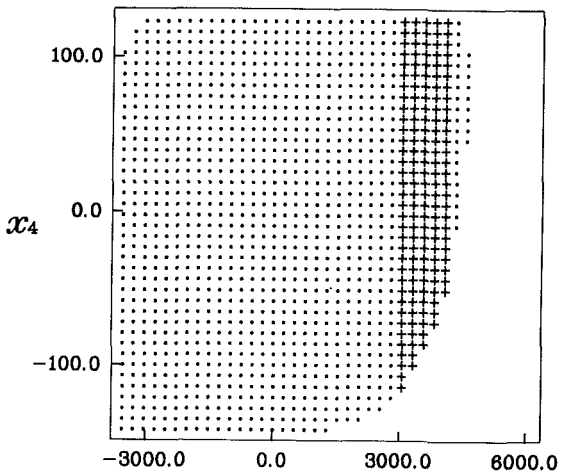


Fig. 9(b)

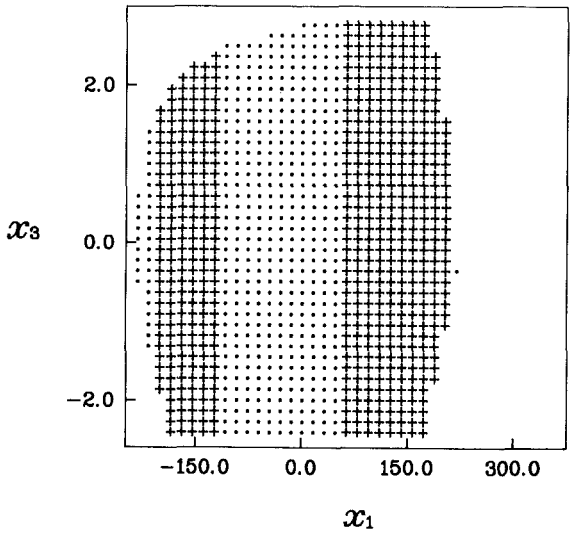


Fig. 9(d)

Fig. 9 The domains of attraction obtained by the direct numerical integration for $\{\epsilon, c_1, c_2, \omega_1, \omega_2, f_1, f_2, \sigma_2\}$ = {0.0001, 100, 100, 15.421, 49.970, 900000, 0.01, 140}, the upper branch solution: +, the lower branch solution: •. (*a*) the $x_1 - x_2$ plane at $z_3 = 19$, $z_4 = 19$; (*b*) the $x_2 - x_4$ plane at $z_1 = 15$, $z_3 = 21$; (*c*) the $x_3 - x_4$ plane at $z_1 = 25$, $z_2 = 15$; (*d*) the $x_1 - x_3$ plane at $z_2 = 25$, $z_4 = 21$.

of all grid points in D_x is 0.2599×20^4 seconds (≈ 11.55 hours). The average computation time used to obtain the interpolated mapping method result for a two-dimensional section is about 5.6 minutes (335.8 s) while the time used for the numerical integration result is about 17 h. Table 1 shows the computation time for the interpolated mapping and numerical integration methods. When the overhead of computing images of all the grid points is included in the computing time for the interpolated mapping, the average computation time would be about 6 min ($=5.6 + 11.56 \times 60/(39)^2$). Taking the numerical integration results as exact ones, we also calculated the correctness of the results predicted by using the interpolated mapping method. The results show that once images of all grid points are found, the interpolated mapping method yields a very good prediction of global domains of attraction but only requires about one 170th of the computation time for numerical integration.

Table 1 Computation time and correctness

	(a)	(b)	(c)	(d)	average
Interpolated Mapping(sec)	253.9	287.7	396.6	394.3	335.8
Exact(sec)	43825	66764	82092	55110	61031
Correctness(%)	97.50	98.95	90.20	96.45	95.83

5 Conclusions

The global behavior of a continuous system has been studied. The specific system investigated is a forced beam which can be reduced to a two-degree-of-freedom system. The system can have two asymptotically stable periodic solutions (the upper and lower branch solutions). By using the interpolated mapping method, the approximate domains of attraction in a four-dimensional state space are obtained. In order to check the validity of the domains of attraction, we also obtained the results by direct numerical integration. The interpolated mapping algorithm achieves an approximate 170 folds improvement in computing efficiency for this problem.

Downloaded 03 May 2010 to 171.66.16.20. Redistribution subject to ASME license or copyright; see http://www.asme.org/terms/Terms_Use.cfm

Acknowledgment

The authors would like to thank the Korea Science and Engineering Foundation for supporting this study.

References

Hsu, C. S., 1980, "A Theory of Cell-to-Cell Mapping Dynamical Systems," ASME JOURNAL OF APPLIED MECHANICS, Vol. 47, pp. 931–939.

Hsu, C. S., 1981, "A Generalized Theory of Cell-to-Cell Mapping for Nonlinear Dynamical Systems," ASME JOURNAL OF APPLIED MECHANICS, Vol. 48, pp. 634–642.

Hsu, C. S., 1987, *Cell-to-Cell Mapping: A Method of Global Analysis for Nonlinear Systems*, Springer-Verlag; New York.

Hsu, C. S., and Chiu, H. M., 1986, "A Cell Mapping Method for Nonlinear Deterministic and Stochastic System, Part I: The Method of Analysis," ASME JOURNAL OF APPLIED MECHANICS, Vol. 53, pp. 695–701.

Hsu, C. S., and Chiu, H. M., 1987, "Global Analysis of a System with Multiple Responses Including a Strange Attractor," *Journal of Sound and Vibration*, Vol. 114, No. 2, pp. 203–218.

Lee, W. K., 1988, "A Global Analysis of a Forced Spring-Pendulum System," University of California, Berkeley, CA, Ph.D. dissertation.

Lee, W. K., and Soh, K. Y., 1994, "Nonlinear Analysis of the Forced Response of a Beam with Three Mode Interactions," to appear in *Nonlinear Dynamics*.

Lee, W. K., 1992, "Domains of Attraction of System of Nonlinearly Coupled Ship Motions by Simple Cell Mapping," ASME *Journal of Offshore Mechanics and Arctic Engineering*, Vol. 114, No. 1, pp. 22–27.

Lee, W. K., and Hsu, C. S., 1994, "A Global Analysis of a Harmonically Excited Spring-Pendulum System with Internal Resonance," to appear in *Journal of Sound and Vibration*.

Nayfeh, A. H., Mook, D. T., and Sridhar, S., 1974, "Nonlinear Analysis of the Forced Responses of Structural Elements," *Journal of Acoustical Society of America*, Vol. 55, No. 2, pp. 281–291.

Polchai, A., and Hsu, C. S., 1985, "Domain of Stability of Synchronous Generators by Cell Mapping Approach," *International Journal of Control*, Vol. 41, pp. 1253–1271.

Tongue, B. H., 1987, "On Obtaining Global Nonlinear System Characteristics through Interpolated Cell Mapping," *Physica D*, Vol. 28, pp. 401–408.

Tongue, B. H., and Gu, K., 1988, "Interpolated Cell Mapping of Dynamical Systems," ASME JOURNAL OF APPLIED MECHANICS, Vol. 55, pp. 461–466.

Xu, J. X., Guttalu, R. S., and Hsu, C. S., 1985, "Domains of Attraction for Multiple Limit Cycles of Coupled van der Pol Equations by Simple Cell Mapping," *International Journal of Non-Linear Mechanics*, Vol. 20, pp. 507–517.

Downloaded 03 May 2010 to 171.66.16.20. Redistribution subject to ASME license or copyright; see http://www.asme.org/terms/Terms_Use.cfm

Dynamic Response of a Spinning Timoshenko Beam With General Boundary Conditions and Subjected to a Moving Load

J. W.-Z. Zu

R. P. S. Han
Mem. ASME

Department of Mechanical and Industrial Engineering,
University of Manitoba,
Winnipeg, Manitoba, R3T 2N2
Canada

The dynamic response of a spinning Timoshenko beam with general boundary conditions and subjected to a moving load is solved analytically for the first time. Solution of the problem is achieved by formulating the spinning Timoshenko beams as a non-self-adjoint system. To compute the system dynamic response using the modal analysis technique, it is necessary to determine the eigenquantities of both the original and adjoint systems. In order to fix the adjoint eigenvectors relative to the eigenvectors of the original system, the biorthonormality conditions are invoked. Responses for the four classical boundary conditions which do not involve rigid-body motions are illustrated. To ensure the validity of the method, these results are compared with those from Euler-Bernoulli and Rayleigh beam theories. Numerical simulations are performed to study the influence of the four boundary conditions on selected system parameters.

1 Introduction

The dynamic analysis of spinning Timoshenko beams is of great interest to many researchers because of its wide applications in engineering problems. A number of practical structures such as spinning bodies in space applications, rotating workpieces in machining operation, and rotating shafts in rotordynamics can be modeled by such a system. A very systematic and comprehensive investigation on the vibrations of rotating shafts based on the Euler-Bernoulli beam theory can be found in the book by Dimentberg (1961). Using this theory, Bauer (1980) carried out both free and forced vibration analyses on spinning shafts for all possible combinations of the classical boundary conditions. When a structure is short and thick, it is imperative that higher order beam theories such as the Rayleigh and Timoshenko beam theories be employed in the modeling so that the shear and rotary inertia effects are captured for an accurate dynamic analysis. This has been done by several researchers using both numerical and theoretical methods. Hashish and Sankar (1984) solved a spinning Timoshenko beam system under stochastic loading conditions via a finite element procedure. They analyzed a flexible rotor bearing system, taking into account the linear and nonlinear stiffnesses, and bearing support flexibility. Using modal analysis, Lee et al. (1988) proposed a theoretical solution to solve a spinning *Rayleigh* beam. They also presented a Galerkin's approach to analyze the forced response of an undamped gyroscopic system. In another paper by the same researches (Katz et al., 1988), a finite integral transform technique was employed to calculate transient response for spinning Rayleigh and Timoshenko beams with the simply supported boundary condition and subjected to a moving load. An alternative method for solving this problem was provided by Han and Zu (1991). Unlike the approach of Katz et al., Han and Zu used a modal analysis technique which provided a better physical understanding of the problem. This procedure yielded, in addition to transient response, eigenquantities such as natural frequencies and mode shapes. A highly accurate simplified analysis for frequency calculations was also suggested in their work. In a subsequent paper, Zu and Han (1991) obtained for the first time, closed-form solutions for the free-vibration analysis of spinning Timoshenko beams for all the six classical boundary conditions, namely, simply supported or hinged-hinged, hinged-free, free-free, fixed-fixed, fixed-free and fixed-hinged. The introduction of the nonsimply supported boundary condition required a different approach as the situation now involves complex arguments.

In this paper, the work of Zu and Han (1991) for free-vibration analysis is extended to handle the response analysis of spinning Timoshenko beams with general boundary conditions and subjected to a moving load. Unfortunately, in the

Contributed by the Applied Mechanics Division of THE AMERICAN SOCIETY OF MECHANICAL ENGINEERS for presentation at the ASME Winter Annual Meeting, New Orleans, LA, Nov. 28-Dec. 3, 1993.

Discussion on this paper should be addressed to the Technical Editor, Professor Lewis T. Wheeler, Department of Mechanical Engineering, University of Houston, Houston, TX 77204-4792, and will be accepted until four months after final publication of the paper itself in the ASME JOURNAL OF APPLIED MECHANICS.

Manuscript received by the ASME Applied Mechanics Division, Dec. 16, 1991; final revision, Mar. 8, 1993. Associate Technical Editor: D.J. Inman.

Paper No. 93-WA/APM-26.

Copyright © 1994 by ASME
Downloaded 03 May 2010 to 171.66.16.20. Redistribution subject to ASME license or copyright; see http://www.asme.org/terms/Terms_Use.cfm

modeling of a spinning Timoshenko beam system, it manifests itself naturally as a *non*-self-adjoint. To convert it into a self-adjoint system, one method is to derive the appropriate transformation relationship. The relationship for our spinning system is given here and it involves a complex transformation of the time variable. In general, the additional effort in obtaining the transformation relationship for a problem, if it exists, may overwhelm the slightly more tedious task of solving it as a non-self-adjoint system. Also as Lanczos (1964) has pointed out, handling in this non-self-adjoint manner results in the canonical scheme for the problem. Hence we will treat our problem here as a non-self-adjoint system and solve it as such. In his book Meirovitch (1980) gave a brief introduction for non-self-adjoint systems and applied the theory to the flutter analysis of a cantilever aircraft wing. Later he and Silverberg (1985) used the concept for controlling non-self-adjoint distributed systems, even though the problem is actually a self-adjoint systems. Afagh and Leipholz (1990) showed that a spatially one-dimensional elastic system under follower forces is a typical example of a non-self-adjoint system.

Using the concepts of adjoint differential matrix operators and the biorthonormality conditions for a non-self-adjoint system, the response analysis of a spinning Timoshenko beam with general boundary conditions and subjected to a moving load is computed. It is found that the eigenquantities of the original system computed here are identical to those given in Zu and Han (1991) using a different starting procedure. As a further check, comparison of the response analysis computed for the Rayleigh and Euler-Bernoulli beams are also presented. A parametric study of the influence of some selected parameters pertaining to the problem for different boundary conditions is given. Having obtained these closed-form solutions for the response analysis, the dynamics of a spinning Timoshenko beam in terms of both its free and forced vibrations are now complete.

2 Formulation

2.1 Differential Matrix Operator. The system comprising a spinning beam with general boundary conditions and subjected to a constant moving load is shown in Fig. 1. The coupled equations of motion based on an inertial frame *oxyz*, for a spinning uniform Timoshenko beam of a finite length l is given in Han and Zu (1991) as

$$[M]\{\dot{w}\} = [K]\{w\} + \{p\} \tag{1}$$

in which the state vector $\{w\}$ is given by

$$\{w\} = \langle \dot{u}\ u\ \dot{\psi}\ \psi \rangle^T. \tag{2}$$

The complex variables u and ψ are defined as

$$u = u_x + i\,u_y$$
$$\psi = \psi_x + i\psi_y$$

where u_x, u_y are the transverse deflections along *ox*, *oy* directions, and ψ_x and ψ_y are their corresponding bending angles. The mass and stiffness matrices $[M]$, $[K]$, and the load vector $\{p\}$, are calculated from

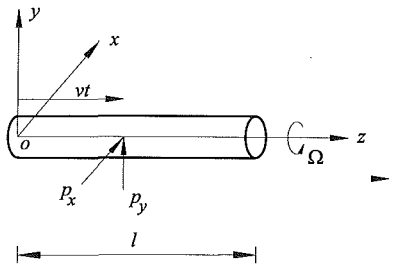


Fig. 1 A spinning shaft and its frame of reference

$$[M] = \begin{bmatrix} 0 & -A/I & 0 & 0 \\ -A/I & 0 & 0 & 0 \\ 0 & 0 & 0 & 1 \\ 0 & 0 & 1 & -i\Omega\dfrac{J_z}{\rho I} \end{bmatrix} \tag{3}$$

$$[K] = \begin{bmatrix} -A/I & 0 & 0 & 0 \\ 0 & -\dfrac{\kappa AG}{\rho I l^2}\dfrac{\partial^2}{\partial\zeta^2} & 0 & \dfrac{\kappa AG}{\rho\, Il}\dfrac{\partial}{\partial\zeta} \\ 0 & 0 & 1 & 0 \\ 0 & \dfrac{\kappa AG}{\rho Il}\dfrac{\partial}{\partial\zeta} & 0 & \dfrac{E}{\rho l^2}\dfrac{\partial^2}{\partial\zeta^2} - \dfrac{\kappa AG}{\rho I} \end{bmatrix} \tag{4}$$

$$\{p\} = \langle 0 \quad -\frac{\bar{p}}{\rho I} \quad 0 \quad 0 \rangle^T. \tag{5}$$

Note that $[K]$ is a differential matrix operator. In these expressions, ρ is the mass density, A is the cross-sectional area, I is the transverse moment of inertia of an axisymmetric cross-section, J_z is the polar mass moment of inertia, and E, G, and κ are the Young's modulus, shear modulus, and shear coefficient, respectively. The term in the load vector $\bar{p}$ consists of the forces p_x, p_y acting in the *ox*, *oy* directions, respectively. That is, $\bar{p} = p_x + ip_y$.

2.2 Adjoint Differential Matrix Operator. It can be shown that the adjoint differential matrix operator comprises a differential matrix operator and some boundary terms. This differential matrix operator of the adjoint system is called the formal adjoint to the differential matrix operator of the original system. If the formal adjoint differential matrix operator and the differential matrix operator for the original system are the same, they are said to be *formally self-adjoint*. If, in addition, they define the same linear manifold, meaning they satisfy the same boundary conditions, they are said to be *self-adjoint* or *Hermitian*. The formal adjoint differential matrix operator to $[M]$ and $[K]$, are

$$[M^*] = \begin{bmatrix} 0 & -A/I & 0 & 0 \\ -A/I & 0 & 0 & 0 \\ 0 & 0 & 0 & 1 \\ 0 & 0 & 1 & i\Omega\dfrac{J_z}{\rho I} \end{bmatrix} \tag{6}$$

$$[K^*] = \begin{bmatrix} -A/I & 0 & 0 & 0 \\ 0 & -\dfrac{\kappa AG}{\rho I l^2}\dfrac{\partial^2}{\partial\zeta^2} & 0 & -\dfrac{\kappa\, AG}{\rho\, Il}\dfrac{\partial}{\partial\zeta} \\ 0 & 0 & 1 & 0 \\ 0 & -\dfrac{\kappa\, AG}{\rho\, Il}\dfrac{\partial}{\partial\zeta} & 0 & \dfrac{E}{\rho l^2}\dfrac{\partial^2}{\partial\zeta^2} - \dfrac{\kappa AG}{\rho I} \end{bmatrix}. \tag{7}$$

Observe that $[M] \neq [M^*]$ and $[K] \neq [K^*]$, and hence a spinning Timoshenko beam when modeled in this fashion, appears naturally to be a non-self-adjoint system. To convert it into the self-adjoint system, the following transformation relation is proposed:

$$\tau = it. \tag{8}$$

However, to demonstrate a general technique for solving structural dynamics problems, we would like to retain the non-self adjointness form of our problem and solve it as such.

2.3 Response Analysis. Let $\{W\}_m$ denote the mth eigenvector of the original system defined by Eq. (1) and $\{V\}_n$ represent the nth eigenvector of the adjoint system. The eigenvalue problems associated with these two systems are

Downloaded 03 May 2010 to 171.66.16.20. Redistribution subject to ASME license or copyright; see http://www.asme.org/terms/Terms_Use.cfm

$$\lambda_m[M]\{W\}_m=[K]\{W\}_m,\ m=\pm1,\ \pm2,\ \ldots \quad (9)$$

$$\lambda_n^*[M^*]\{V\}_m=[K]\{V\}_n,\ n=1,\ \pm2,\ \ldots \quad (10)$$

in which λ_m and λ_n^* are the mth and nth eigenvalues of the original and adjoint systems, respectively. Applying mode superposition, let

$$\{w\}=\sum_{m=-\infty}^{\infty}\{W\}_m q_m \quad (11)$$

where q_m are the generalized coordinates. Substituting Eq. (11) into Eq. (1) and taking the inner product with $\{V\}_n$ yields

$$\sum_{m=-\infty}^{\infty}\langle[M]\{W\}_m,\ \{V\}_n\rangle\dot{q}_m=\sum_{m=-\infty}^{\infty}\langle[K]\{W\}_m,\ \{V\}_n\rangle q_m+\sum_{m=-\infty}^{\infty}\langle\{p\}_m,\ \{V\}_n\rangle \quad (12)$$

where $\langle,\rangle$ denotes inner product. The eigenvector $\{W\}_m$ and the adjoint eigenvector $\{V\}_m$ are biorthogonal and can be normalized so as to satisfy

$$\langle[M]\{W\}_m,\ \{V\}_n\rangle=\delta_{mn},\ m,\ n=\pm1,\ \pm2,\ \ldots \quad (13)$$

$$\langle[K]\{W\}_m,\ \{V\}_n\rangle=\lambda_m\delta_{mn},\ m,\ n=\pm1,\ \pm2,\ \ldots \quad (14)$$

where δ_{mn} is the kronecker delta, namely,

$$\delta_{mn}=\begin{cases}0 & (m\neq n)\\ 1 & (m=n).\end{cases}$$

Equation (1) becomes

$$\dot{q}_m=\lambda_m q_m+Q_m,\ m=\pm1,\ \pm2,\ \ldots \quad (15)$$

in which

$$Q_m=\langle\{p\}^T,\ \{V\}_m\rangle. \quad (16)$$

Equation (15) is now a set of decoupled first-order ordinary differential equations and can be easily solved. For convenience, let

$$\{W\}_m=\langle\tilde{W}_{um}\ W_{um}\ \tilde{W}_{\psi m}\ W_{\psi m}\rangle^T \quad (17)$$

$$\{V\}_m=\langle\tilde{V}_{um}\ V_{um}\ \tilde{V}_{\psi m}\ V_{\psi m}\ V_{\psi m}\rangle^T \quad (18)$$

where the tilded variables are those associated with time derivatives, while the untilded variables pertain to nontime derivative variables. In view of Eq. (18), Eq. (16) now becomes

$$Q_m=-\frac{A}{I}\int_0^1\overline{V}_{um}\,\overline{p}\,d\zeta \quad (19)$$

where $\overline{V}_{um}$ is the complex conjugate of the mth eigenvector of the adjoint system associated with the u variable. Substituting Eq. (17) into Eq. (11) and from Eq. (2), the dynamic response u is obtained, that is

$$u=\sum_{m=-\infty}^{\infty}W_{um}q_m. \quad (20)$$

Now consider a special loading situation, namely that of a load moving at a constant speed v along the oz direction. For simplicity and without loss of generality, assume that the load acts in the ox direction and of magnitude P. Mathematically, this is described by

$$\overline{p}=P\delta\left(\zeta-\frac{v}{l}t\right). \quad (21)$$

Substituting Eq. (21) into Eq. (19) and performing the integration, we get

$$Q_m=-\frac{P}{\rho I}\overline{V}_{um}\left(\frac{v}{l}t\right). \quad (22)$$

In view of Eq. (22), Eq. (15) can now be solved for q_m by introducing appropriate initial conditions. Assuming zero initial conditions, we get

$$q_m=\int_0^t Q_m(s)e^{\lambda_m(t-s)}ds$$

$$q_m=-\frac{P}{\rho I}\int_0^t\overline{V}_{um}\left(\frac{v}{l}s\right)e^{\lambda_m(t-s)}ds. \quad (23)$$

Substituting Eq. (23) into Eq. (20), the dynamic response u can be computed, provided that the eigenvalue λ_m and the eigenvector W_{um} of the original system, and the complex conjugate eigenvector of the adjoint system $\overline{V}_{um}$ are known. Hence solution of the eigenproblem as defined by Eqs. (9)–(10), for both the original and the adjoint systems is outlined next. Also since it is necessary to delete rigid-body motions in response calculations, only the four classical boundary conditions are considered here: hinged-hinged (or simply supported), fixed-hinged, fixed-fixed, and fixed-free.

3 Eigenvalue Solutions

3.1 Original System. The eigenproblem of the original system is defined by Eq. (9). Expanding this set of equations results in

$$-\lambda_m\frac{A}{I}W_{um}=-\frac{A}{I}\tilde{W}_{um} \quad (24)$$

$$-\lambda_m\frac{A}{I}\tilde{W}_{um}=-\frac{\kappa}{\rho}\frac{AG}{Il^2}W''_{um}+\frac{\kappa AG}{\rho Il}W'_{\psi m} \quad (25)$$

$$\lambda_m W_{\psi m}=\tilde{W}_{\psi m} \quad (26)$$

$$\lambda_m\left(\tilde{W}_{\psi m}-i\frac{\Omega J_z}{\rho I}W_{\psi m}\right)=\frac{\kappa AG}{\rho Il}W'_{um}+\frac{E}{\rho l^2}W''_{\psi m}-\frac{\kappa AG}{\rho Il}W_{\psi m}. \quad (27)$$

From Eqs. (24) and (26), the following relationships hold true:

$$\lambda_m W_{um}=\tilde{W}_{um} \quad (28)$$

$$\lambda_m W_{\psi m}=\tilde{W}_{\psi m}. \quad (29)$$

As for Eqs. (25) and (27), they can be arranged as

$$e_2W''_{um}-e_1W'_{\psi m}+e_0\ W_{um}=0 \quad (30)$$

$$f_2W''_{\psi m}+f_1W'_{um}+f_0\ W_{\psi m}=0 \quad (31)$$

where

$$e_0=-\lambda_m^2\frac{A}{I},\quad f_0=-\left(\lambda_m^2-i\lambda_m\frac{\Omega J_z}{\rho I}+\frac{\kappa AG}{\rho I}\right)$$

$$e_1=\frac{\kappa AG}{\rho Il},\qquad f_1=e_1=\frac{\kappa AG}{\rho Il}$$

$$e_2=\frac{\kappa AG}{\rho Il^2},\qquad f_2=\frac{E}{\rho l^2}. \quad (32)$$

Observe that Eqs. (30) and (31) are coupled differential equations and to decouple them requires into higher order derivatives. That is,

$$l_2W^{(4)}_{um}+l_1W''_{um}+l_0W_{um}=0 \quad (33)$$

$$l^2W^{(4)}_{\psi m}+l_1W''_{\psi m}+l_0W_{\psi m}=0 \quad (34)$$

where

$$l_0=e_0f_0,\ l_1=e_2f_0+e_0f_2+e_1^2,\ l_2=e_2f_2.$$

Since damping is neglected in the system, we can assume $\lambda_m=i\omega_m$. Substituting this solution into Eq. (32) and then the result into Eq. (35), the coefficients l_0, l_1, and l_2 can be evaluated:

Downloaded 03 May 2010 to 171.66.16.20. Redistribution subject to ASME license or copyright; see http://www.asme.org/terms/Terms_Use.cfm

$$l_0=\frac{\rho I}{\kappa AG}\,\omega_m^4-\frac{\Omega J_z}{\kappa AG}\omega_m^3-\omega_m^2$$

$$l_1=\frac{I}{l^2A}\left(1+\frac{E}{\kappa G}\right)\omega_m^2-\frac{\Omega J_z}{l^2\rho A}\,\omega_m$$

$$l_2=\frac{EI}{\rho Al^4}. \tag{36}$$

Solving Eq. (33), the following solution is obtained for the case of $\sqrt{l_1^2-4l_2l_0}>l_1$:

$$W_{um}(\zeta)=A_1\cosh(s_1\zeta)+A_2\sinh(s_1\zeta)+A_3\cos(s_2\zeta)+A_4\sin(s_2\zeta). \tag{37}$$

Similarly, from Eq. (34) we can solve for $W_{\psi m}$.

$$W_{\psi m}(\zeta)=A_1'\sinh(s_1\zeta)+A_1'2\cosh(s_1\zeta)+A_3'\sin(s_2\zeta)+A_4'\cos(s_2\zeta)$$

in which

$$s_1=\sqrt{\frac{-l_1+\sqrt{l_1^2-4l_2l_0}}{2l_2}},\quad s_2=\sqrt{\frac{l_1+\sqrt{l_1^2-4l_2l_0}}{2l_2}}. \tag{39}$$

The coefficients $A_1\sim A_4$ and $A_1'\sim A_4'$ are not independent but related by

$$A_1'=c_1A_1,\qquad A_3'=c_2A_3$$
$$A_2'=c_1A_2,\qquad A_4'=-c_2A_4 \tag{40}$$

where

$$c_1=\frac{1}{s_1}\left(\frac{\rho l}{\kappa G}\,\omega_\omega^2+\frac{1}{l}\,s_1^2\right),\quad c_2=\frac{1}{s_2}\left(\frac{\rho l}{\kappa G}\,\omega_m^2-\frac{1}{l}\,s_2^2\right). \tag{41}$$

For the case of $\sqrt{l_1^2-4l_2l_0}<l_1$, the solutions for W_{um} and $W_{\psi m}$, can be derived in the same fashion. The results are

$$W_{um}(\zeta)=A_1\cos(s_1'\zeta)+A_2\sin(s_1'\zeta)+A_3\cos(s_2\zeta)+A_4\sin(s_2\zeta) \tag{42}$$

$$W_{\psi m}(\zeta)=A_1'\sin(s_1'\zeta)+A_2'\cos(s_1'\zeta)+A_3'\sin(s_2\zeta)+A_4'\cos(s_2\zeta) \tag{43}$$

in which s_1' is defined as

$$s_1'=is_1=\sqrt{\frac{l_1-\sqrt{l_1^2-4l_2l_0}}{2l_2}}. \tag{44}$$

As before, the coefficients here $A_1\sim A_4$ and $A_1'\sim A_4'$ are related by

$$A_1'=c_1'A_1,\qquad A_3'=c_2A_3$$
$$A_2'=c_1'A_2,\qquad A_4'=-c_2A_4 \tag{45}$$

where

$$c_1'=\frac{1}{s_1'}\left(\frac{\rho l}{\kappa G}\,\omega_m^2-\frac{1}{l}\,s_1'^2\right). \tag{46}$$

Comparing the results given here and those derived in Zu and Han (1991) based on a different starting approach, it is clear that these two methods give an identical answer. Thus, the eigensolutions for the various boundary solutions listed in that paper will be used directly as the eigensolutions of the original system Eq. (9) in this paper.

3.2 Adjoint System. In this section, the eigenproblem of the adjoint system as defined by Eq. (10) is solved. Expanding this set of equations leads to

$$-\lambda_n^*\frac{A}{I}\,V_{un}=-\frac{A}{I}\,\tilde V_{un} \tag{47}$$

$$-\lambda_n^*\frac{A}{I}\,\tilde V_{un}=-\frac{\kappa AG}{\rho\, Il^2}\,V_{un}''-\frac{\kappa AG}{\rho Il}\,V_{\psi n}' \tag{48}$$

$$\lambda_n^*\,V_{\psi n}=\tilde V_{\psi n} \tag{49}$$

$$\lambda_n^*(\tilde V_{\psi n}+i\frac{\Omega J_z}{\rho I}\,V_{\psi n})=-\frac{\kappa AG}{\rho\, Il}\,V_{ui}'+\frac{E}{\rho l^2}\,v_{\psi n}''-\frac{\kappa AG}{\rho\, Il}\,V_{\psi n}. \tag{50}$$

Taking the complex conjugate we have, from Eqs. (47) and (49),

$$\bar\lambda_n^*\,\bar V_{un}=\bar{\tilde V}_{un} \tag{51}$$
$$\bar\lambda_n^*\,\bar V_{\psi n}=\bar{\tilde V}_{\psi n}. \tag{52}$$

Further, from the complex conjugate of Equations (48) and (50) we have

$$e_2^*\bar V_{un}''+e_1^*\bar V_{\psi n}'+e_0^*\bar V_{un}=0 \tag{53}$$
$$f_2^*\bar V_{\psi n}''-f_1^*\bar V_{un}'+f_0^*\bar V_{\psi n}=0 \tag{54}$$

where

$$e_0^*=-\bar\lambda_n^{*2}\frac{A}{I},\quad f_0^*=-\left(\bar\lambda_n^{*2}-i\bar\lambda_n^*\frac{\Omega J_z}{\rho I}+\frac{\kappa AG}{\rho I}\right)$$

$$e_1^*=-\frac{\kappa AG}{\rho Il},\quad f_1^*=e_1^*=\frac{\kappa AG}{\rho\, Il},$$

$$e_2^*=\frac{\kappa AG}{\rho Il^2},\qquad f_2^*=\frac{E}{\rho l^2}. \tag{55}$$

Except for the sign difference in the second term, Eqs. (53)–(54) and Eqs. (30)–(31) are similar. Hence e_i^* and f_i^* ($i=0$, 1, 2) of the adjoint system are the exact counterparts of e_i and f_i of the original system. Letting $\bar\lambda_n^*=i\omega_n^*$, the following decoupled equations are obtained:

$$l_2^*\,\bar V_{un}^{(4)}+l_1^*\,\bar V_{un}''+l_0^*\,\bar V_{un}=0 \tag{56}$$
$$l_2^*\,\bar V_{\psi n}^{(4)}+l_1^*\bar V_{\psi n}''+l_0^*\bar V_{\psi n}=0 \tag{57}$$

where

$$l_0^*=\frac{\rho I}{\kappa AG}\,\omega_n^{*4}-\frac{\omega_n^*J_z}{\kappa AG}\,\omega_n^{*3}-\omega_n^{*2}$$

$$l_1^*=\frac{I}{l^2A}\left(1+\frac{E}{\kappa G}\right)\omega_n^{*2}-\frac{\Omega^*J_z}{l^2\rho A}\,\omega_n^*$$

$$l_2^*=\frac{EI}{\rho Al^4}. \tag{58}$$

Once again, in solving Eqs. (56)–(57) for $\bar V_{un}$ and $\bar V_{\psi n}$, it is necessary to consider two cases, namely: $\sqrt{l_1^{*2}-4l_2^*l_0^*}>l_1^*$ and $\sqrt{l_1^{*2}-4l_2^*l_0^*}<l_1^*$. However, only the results for the first case, that is $\sqrt{l_1^{*2}-4l_2^*l_0^*}>l_1^*$, are shown here as it is quite easy to deduce the corresponding expressions for the second case which have the same form as those of the original system. Thus solving for the case of $\sqrt{l_1^{*2}-4l_2^*l_0^*}>l_1^*$, we have

$$\bar V_{un}(\zeta)=B_1\cosh(d_1\zeta)+B_2\sinh(d_1\zeta)+B_3\cos(d_2\zeta)+B_4\sin(d_2\zeta) \tag{59}$$

$$\bar V_{\psi n}(\zeta)=B_1'\sinh(d_1\zeta)+B_2'\cosh(d_1\zeta)+B_3'\sin(d_2\zeta)+B_4'\cos(d_2\zeta) \tag{60}$$

in which

$$d_1=\sqrt{\frac{-l_1'+\sqrt{l_1'^2-4l_2'l_0'}}{2l_2'}},$$

$$d_2=\sqrt{\frac{l_1'+\sqrt{l_1'^2-4l_2'l_0'}}{2l_2'}}. \tag{61}$$

Downloaded 03 May 2010 to 171.66.16.20. Redistribution subject to ASME license or copyright; see http://www.asme.org/terms/Terms_Use.cfm

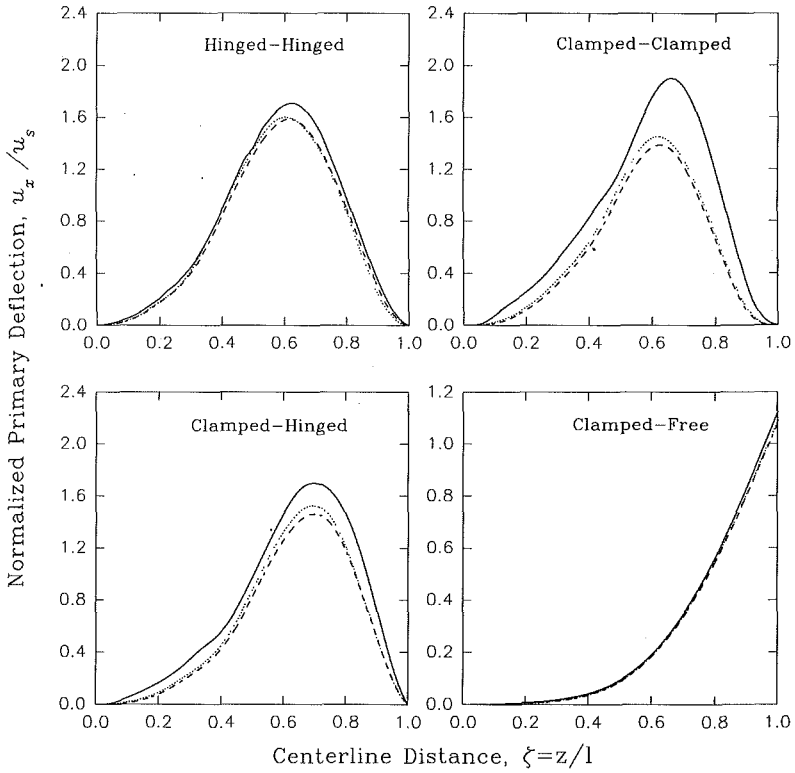


Fig. 2 Primary deflection u_x/u_s using different beam theories at $\bar{\Omega} = 2.5$, $\alpha = 0.5$, and $\beta = 0.15$ (——— Timoshenko, · · · Rayleigh, ... Euler-Bernoulli)

The coefficients $B_1 \sim B_4$ and $B_1' \sim B_4'$ are related by

$$\begin{aligned} B_1' &= c_1^* B, \qquad B_3' = c_2^* B_3 \\ B_2' &= c_1^* B, \qquad B_4' = -c_2^* B_4 \end{aligned} \tag{62}$$

where

$$c_1^* = -\frac{1}{d_1}\left(\frac{\rho l}{\kappa G}\omega_n^{*2} + \frac{1}{l}d_1^2\right), \quad c_2^* = -\frac{1}{d_2}\left(\frac{\rho l}{\kappa G}\omega_n^{*2} - \frac{1}{l}d_2^2\right). \tag{63}$$

Note that if the boundary conditions for computing the adjoint eigenvectors are the same as those for calculating the eigenvectors of the original system, then it is possible to deduce $\bar{\lambda}_m^*$ and $\bar{V}_{un}$, $\bar{V}_{\psi n}$ of the adjoint system from λ_m and W_{ui}, $W_{\psi m}$ of the original system without any additional work. This situation is only true for the three boundary conditions of simply supported, fixed-hinged and fixed-fixed. There will, however, be a minor adjustment to account for the difference in sign between Eqs. (63) and (41). Unfortunately, the fourth boundary condition, namely the fixed-free case does not belong to this situation and therefore the adjoint frequency equation and the adjoint eigenvectors must be calculated.

Although the eigenvectors W_{um}, $W_{\psi m}$, $\bar{V}_{un}$, and $\bar{V}_{\psi n}$ are determined from the above discussion, each set is still not fixed relative to each other. In order to fix the adjoint eigenvectors relative to the eigenvectors of the original system, it is necessary to impose the satisfaction of either one of the biorthonormality conditions depicted in (Eqs. (13)–(14). Setting $m = n$ yields

$$(\lambda_m + \bar{\lambda}_m^*)\left(-\frac{A}{I}\int_0^1 \bar{V}_{um}W_{um} + \int_0^1 \bar{V}_{\psi m}W_{\psi m}\right) - i\Omega\frac{J_z}{\rho I}\int_0^1 \bar{V}_{\psi m}W_{\psi m} = 1. \tag{64}$$

The problem is now completely solved.

4 Numerical Examples and Discussion

Numerical simulations to demonstrate the computation of dynamic response of a spinning Timoshenko beam with general boundary conditions and subjected to a constant moving load are presented here. From our numerical experimentation, we found that summation to five terms yields sufficiently good accuracy. To avoid rigid-body motions in the response calculations, only four types of boundary conditions are considered: simply supported, fixed-hinged, fixed-fixed, and fixed-free. These boundary conditions are physically realizable. For example, a rotating workpiece for machining operation is held fixed at one end by the chuck and pinned at the other end. Thus, it represents the fixed-hinged boundary condition. A drill is an example of the fixed-free boundary condition. The proposed formulation is then verified by checking its limiting case results with responses from an Euler-Bernoulli beam and a Rayleigh beam. Finally, parametric studies depicting the influence of the four boundary conditions on some selected systems parameters are also given.

The basic data employed for the simulation are the same as those from the free vibration analysis outlined in Zu and Han (1991):

$l = 1.0$ m, $\quad G = 77.6$ GPa

$\rho = 7700$ kg/m^3, $\quad \kappa = 0.09$

$E = 207$ GPa

The following three nondimensional variables which represent the moving load speed α, the spin rate Ω, and the slenderness ratio β are also used here. They are defined by

$\alpha = v/v_{cr}$ nondimensional load speed

Downloaded 03 May 2010 to 171.66.16.20. Redistribution subject to ASME license or copyright; see http://www.asme.org/terms/Terms_Use.cfm

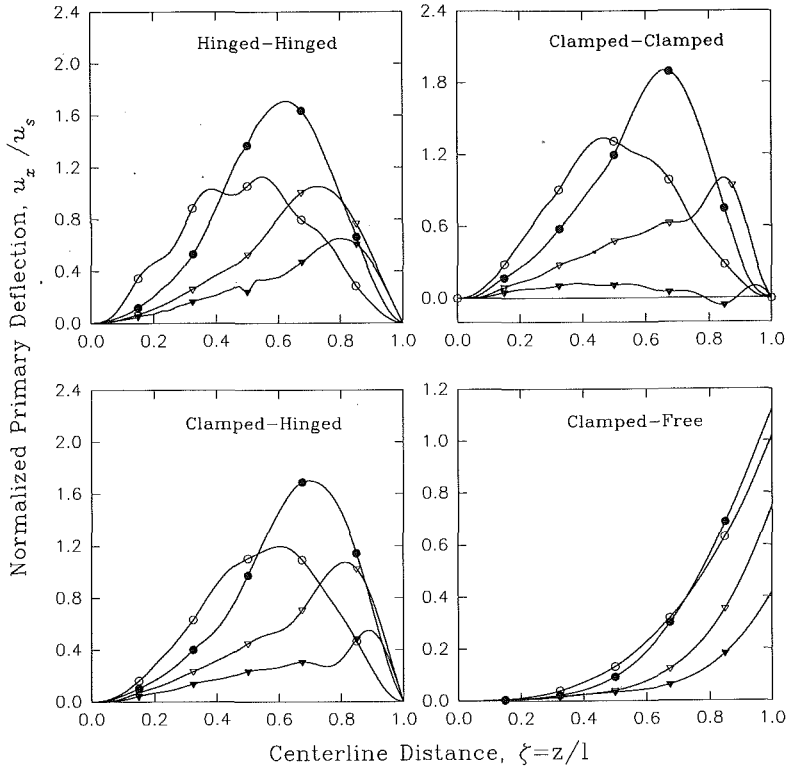


Fig. 3 Primary deflection u_x/u_s for varying speed parameter α at $\bar{\Omega} = 2.5$, and $\beta = 0.15$ ($\circ\ \alpha = 0.1$, $\bullet\ \alpha = 0.5$, $\triangleleft\ \alpha = 1.0$, $\triangleright\ \alpha = 1.5$)

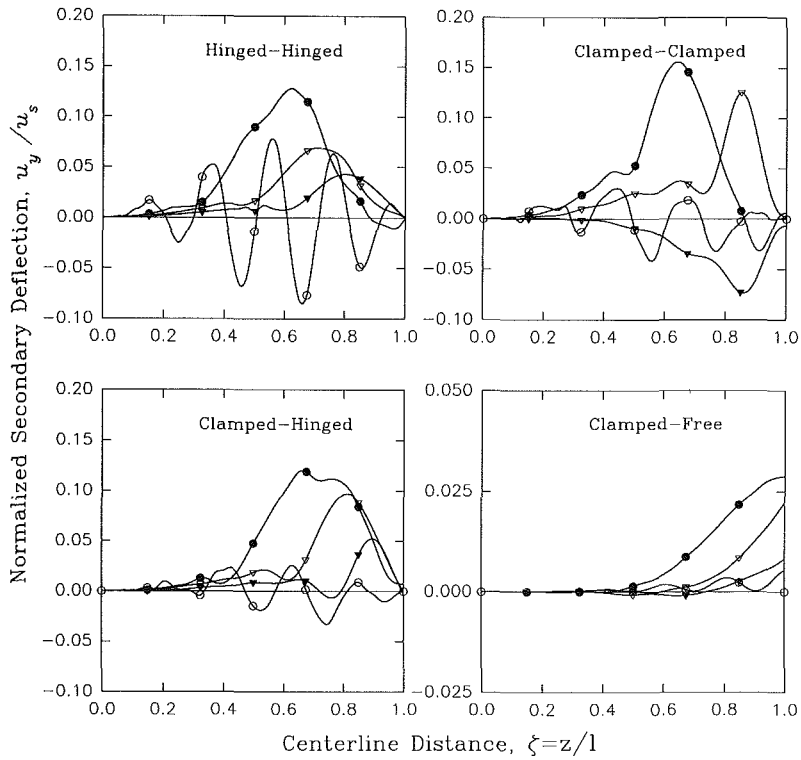


Fig. 4 Secondary deflection u_y/u_s for varying speed parameter α at $\bar{\Omega} = 2.5$ and $\beta = 0.15$ ($\circ\ \alpha = 0.1$, $\bullet\ \alpha = 0.5$, $\triangleleft\ \alpha = 1.0$, $\triangleright\ \alpha = 1.5$)

$\bar{\Omega} = \Omega/\omega_{10}$ nondimensional rotational speed

$\beta = \pi r_0/l$ Rayleigh beam coefficient

where v_{cr} is the critical speed of the load, ω_{10} is the at-rest fundamental natural frequency, and r_0 is the radius of gyration of a circular cross-section. The critical speed v_{cr} is the speed when the frequency of the load is equal to the fundamental natural frequency of an Euler-Bernoulli beam with corresponding boundary conditions. For a circular cross-section, β is proportional to the ratio of the diameter and the length of the beam. Therefore, β characterizes the stubbiness of a beam.

There are two transverse displacements in a spinning

Downloaded 03 May 2010 to 171.66.16.20. Redistribution subject to ASME license or copyright; see http://www.asme.org/terms/Terms_Use.cfm

Timoshenko beam: u_x is the deflection in the plane of the loading and since it is the predominant deflection, it is called the primary deflection, and u_y, which occurs in the plane perpendicular to the plane of loading, is the secondary deflection. In all the plots given here, the transverse displacements u_x and u_y are measured at the location of the moving load. Both u_x and u_y are normalized with respect to the maximum static deflection u_s of a stationary Euler-Bernoulli beam loaded by a concentrated force positioned at the location of the maximum static deflection. Since u_s depends on the type of boundary conditions, the following expressions are used:

$u_s = Pl^3/48EI$ simply supported
$u_s = Pl^3/192EI$ clamped clamped
$u_s = 0.0098Pl^3/EI$ clamped hinged
$u_s = Pl^3/3EI$ clamped free.

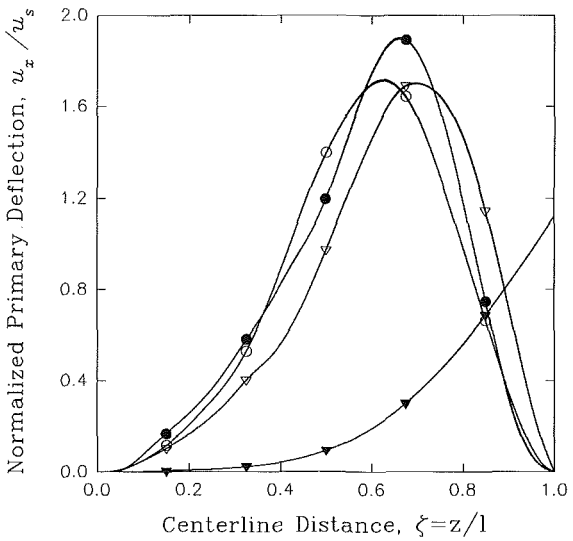


Fig. 5 Primary deflection u_x/u_s for varying spin-rate parameter $\bar{\Omega} = 0.5$, 1.0, 1.5, 2.0 at $\alpha = 0.5$, $\beta = 0.15$ ($\circ$ S – S, $\bullet$ C – C, $\triangleleft$ C – H, $\triangleright$ C – F)

In order to provide a check of the solutions obtained here, the normalized primary deflections of the spinning Timoshenko beam under a moving load are plotted together with the well-known results from the Euler-Bernoulli beam theory and those obtained using Rayleigh beam theory by Lee et al. (1988). This is given in Fig. 2, where solutions for all four boundary conditions at $\Omega = 2.5$, $\alpha = 0.5$, $\beta = 0.15$ (i.e., slenderness ratio of 1/5) are depicted. Although the tendency of the curves remains the same, the results from the Euler-Bernoulli and Rayleigh beam theories are very close to each other, while the deflections based on the Timoshenko beam theory are noticeably larger. This can be attributed to shear effects in the Timoshenko beam model, causing the structure to be more flexible. Recall that neither the Euler-Bernoulli beam theory nor the Rayleigh beam theory is able to capture shear effects in its model. It is also observed that the discrepancy between the Timoshenko beam solutions and the results from the other two beams theories is the largest for the clamped-clamped boundary condition, while the clamped-free boundary condition exhibits the smallest difference. This is attributed to the degree of fixity at the support. Hence the more restraint the support has, the larger will be the relative difference in the response.

The next few graphs investigate the influence of the three system parameters α, Ω, and β on the dynamic responses for the four boundary conditions. In Figs. 3 and 4, the normalized primary and secondary deflections are plotted for different load speed parameters α ($0.1 \leq \alpha \leq 1.5$) at $\bar{\Omega} = 2.5$ and $\beta = 0.15$. It is clear from Fig. 3 that the normalized deflections are the largest at $\alpha = 0.5$ and smallest at $\alpha = 1.5$ for all four boundary conditions. This is related to the proximity of the excitation, which in this case is in the form of the moving speed of the force to the resonant condition of the structure. Another interesting observation is the little "dip" below the vertical axis in the clamped-clamped curve for the case of $\alpha = 1.5$. Physically, it implies that the beam is deflecting in a direction opposite to the direction of loading. This is not surprising as it reflects the inability of the propagating response waves to "catch-up" with the force which is moving at such

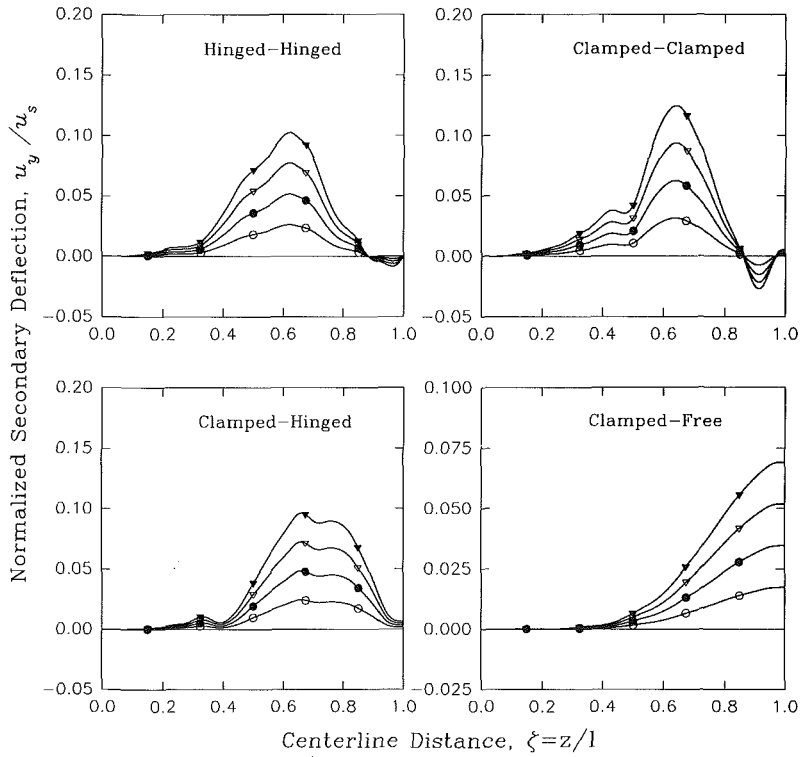


Fig. 6 Secondary deflection u_y/u_s for varying spin-rate parameter $\bar{\Omega}$ at $\alpha = 0.5$, $\beta = 0.15$ ($\circ \bar{\Omega} = 0.5$, $\bullet \bar{\Omega} = 1.0$, $\triangleleft \bar{\Omega} = 1.5$, $\triangleright \bar{\Omega} = 2.0$)

Downloaded 03 May 2010 to 171.66.16.20. Redistribution subject to ASME license or copyright; see http://www.asme.org/terms/Terms_Use.cfm

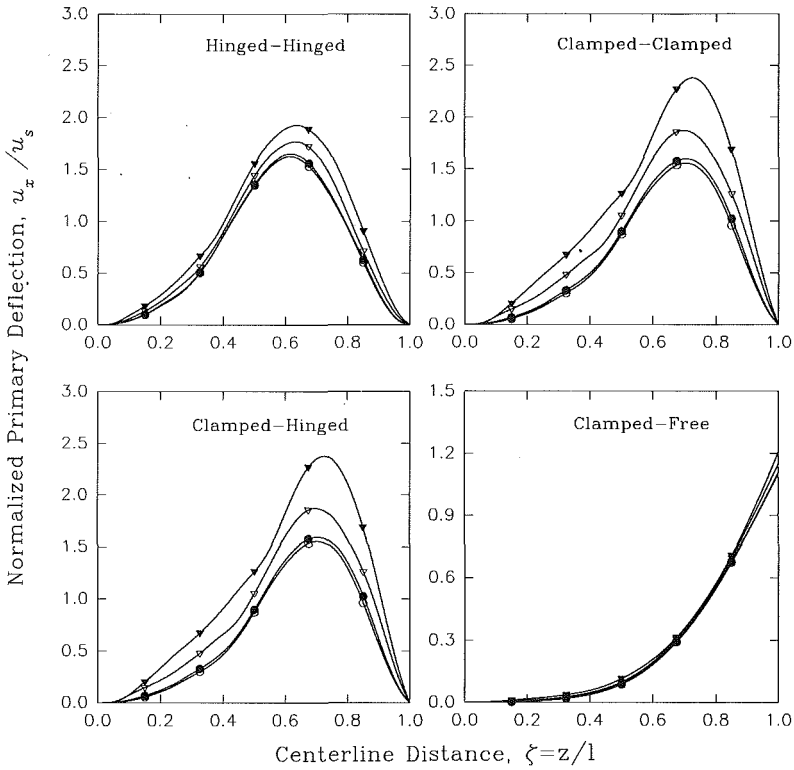


Fig. 7 Primary deflection u_x/u_s for varying Rayleigh beam coefficient beam coefficient β at $\bar{\Omega} = 0.5$, $\alpha = 0.5$ ($\circ\beta = 0.07$, $\bullet\beta = 0.1$, $\triangleleft\beta = 0.1$, $\beta = 0.2$, $\triangleright\beta = 0.3$)

a high speed. Figure 4 shows the normalized secondary deflections which are of an order-of-magnitude smaller than the primary deflections. Their presence here are due to the combination of the spinning motion of the beam and the shear and rotary inertia effects. Thus, this phenomenon is not observed in a spinning Euler-Bernoulli beam.

The normalized primary deflection for varying spin-rate parameter $\bar{\Omega}(0.5 \le \bar{\Omega} \le 2.0)$ are given in Fig. 5 at $\alpha = 0.5$ and $\beta = 0.15$. As shown, the dynamic response for each boundary condition type appears to be independent of the spin rate of the beam. This seems to conform to the response of a spinning Euler-Bernoulli beam where its equations of motion, when formulated in an inertial reference frame, do not contain the spin-rate term, i.e., the primary deflections are independent of the spin rate. However, this comment is not valid for the secondary deflections as they do exhibit a strong dependency on the spin rate.

The influence of the Rayleigh beam coefficient $\beta(0.07 \le \beta \le 0.3)$ on the primary deflections at $\bar{\Omega} = 0.5$ and $\alpha = 0.5$ is sketched in Fig. 7. This range of β values corresponds to slenderness ratios varying from 1/12 to 1/2.6, representing slender-to-stubby beams. Since deflections are normalized with respect to the maximum static deflections of a stationary Euler-Bernoulli beam with the *same* Rayleigh coefficient, the normalized deflections as presented here are larger for stubby beams than for slender beams. Also, for the same reason as given in Fig. 2, the results for the clamped-free boundary condition exhibit the smallest difference in the responses between stubby and slender beams.

5 Summary and Conclusions

The dynamic response of a spinning Timoshenko beam with general boundary conditions and subjected to a moving load is solved analytically for the first time. To demonstrate a general technique for computing the solutions, the spinning Timoshenko beam is formulated as a non-self-adjoint system. Unlike the concepts of adjoint differential matrix operators and the biorthonormality conditions, the modal analysis technique is employed to compute the dynamic response from the eigenquantities of the original and adjoint systems. Response calculations for the four types of boundary conditions that do not involve rigid-body motions are shown. Comparison with limiting case solutions obtained using Euler-Bernoulli and Rayleigh beam models are also given. Numerical simulations depicting the effects of the four boundary conditions on some selected system parameters are presented and discussed. It is shown that when the speeds of the moving load are sufficiently high, the primary deflection of the beam can actually be in a direction opposite to that of the loading. Also, the influence of the spin rate on the primary deflections is negligible whereas it is not so on the secondary deflections.

Acknowledgments

This work was supported by an operating grant from the Natural Sciences and Engineering Research Council of Canada.

References

Afagh, F. F., and Leipholz, H. H. E., 1990, "Dynamic Response of Elastic Rods Subjected to Uniformly Distributed, Tangential Follower Forces," *Ingenieur-Archive*, Vol. 60, pp. 165–175.

Bauer, H. F., 1980, "Vibration of a Rotating Uniform Beam, Part I: Orientation in the Axis of Rotation," *Journal of Sound and Vibration*, Vol. 72, pp. 177–189.

Dimentberg, F. M., 1961, *Flexural Vibrations of Rotating Shafts*, Butterworths, London.

Han, R. P. S., and Zu, J. W. Z., 1992, "Modal Analysis of Rotating Shafts—A Body-Fixed Axis Formulation Approach," *Journal of Sound and Vibration*, Vol. 156, pp. 1–16.

Hashish, E., and Sankar, T. S., 1984, "Finite Element and Modal Analyses of Rotor-Bearing Systems Under Stochastic Loading Conditions," ASME *Journal of Vibration, Acoustics, Stress and Reliability in Design*, Vol. 106, pp. 80–89.

Downloaded 03 May 2010 to 171.66.16.20. Redistribution subject to ASME license or copyright; see http://www.asme.org/terms/Terms_Use.cfm

Katz, R., Lee, C. W., Ulsoy, A. G., and Scott, R. A., 1988, "The Dynamic Response of a Rotating Shaft Subject to a Moving Load," *Journal of Sound and Vibration*, Vol. 122, pp. 131–148.

Lanczos, C. 1964, *Linear Differential Operators*, D. Van Nostrand Co., London.

Lee, C. W., Katz, R., Ulsoy, A. G., and Scott, R. A., 1988, "Modal Analysis of a Distributed Parameter Rotating Shaft," *Journal of Sound and Vibration*, Vol. 122, pp. 119–130.

Meirovitch, L., 1980, *Computational Methods in Structural Dynamics*, Sijthoff and Noordjoff, Maryland.

Meirovitch, L., and Silverberg, L. M., 1985, "Control of Non-Self-Adjoint Distributed-Parameter Systems," *Journal of Optimization Theory and Applications*, Vol. 47, pp. 77–90.

Zu, J. W. Z. and Han, R. P. S., 1992, "Natural Frequencies and Normal Modes of a Spinning Timoshenko Beam with General Boundary Conditions," ASME JOURNAL OF APPLIED MECHANICS, Vol. 59, pp. S197–S204.

Downloaded 03 May 2010 to 171.66.16.20. Redistribution subject to ASME license or copyright; see http://www.asme.org/terms/Terms_Use.cfm

Boundary Layer Transient Hygroscopic Stresses in Orthotropic Thick Shells Under External Pressure

G. A. Kardomateas
Associate Professor.

C. B. Chung
Graduate Research Assistant.

School of Aerospace Engineering,
Georgia Institute of Technology,
Atlanta, GA 30332-0150

An exact elasticity solution is obtained for the stresses and displacements in an orthotropic cylindrical shell loaded by an external pressure under imposed constant moisture concentrations on the inner and outer surfaces. The material properties are assumed moisture independent and a displacement approach is used. Since the moisture diffusion process is relatively slow, the hygroscopic stresses are confined for practical time values to a boundary layer region near the surfaces. Illustrative results are presented for graphite-epoxy material regarding the boundary layer hygroscopic effect on the stress field with respect to time and the coupling of mechanical loading (external pressure) and moisture diffusion. For this material, it is shown that this effect is more pronounced for the axial component of stress.

Introduction

The understanding of the stresses induced by moisture in a composite structure is essential for the design and the comprehensive study of its response during service in severe hygroscopic environments. It is well known that a polymeric resin absorbs moisture from its environment. Whitney and Husman (1978) showed that the absorption of moisture from severely hygroscopic environments reduces the modulus and the strength of a resin-based composite. Wang and Choi (1982) suggested that an unanticipated failure of a composite structure, frequently initiated at the edges, can be a result of hygroscopic stresses near the edges.

The hygroscopic stress field in the vicinity of laminate plate boundaries, i.e., the so-called hygroscopic boundary layer stresses, which might be primarily responsible for strength degradation and failure of composites, has been investigated by several researchers using different approximate methods (e.g., Farley and Herakovich, 1978; Crossman and Wang, 1978). The high hygroscopic stresses are also reported to be confined within a localized region of several laminar thicknesses from the edge, and in the boundary layer region they cannot be assessed accurately with classical lamination theory.

The behavior of this highly stressed boundary layer region is of great importance in controlling the complex failure modes and performance of the composite. Accurate quantitative assessment of the hygroscopic boundary layer stresses is essential to the design, failure analysis, and serviceability of composite structures.

Although the majority of hygroelastic analyses have been performed in plate structures, some studies have also been reported in thin shell geometries. In particular, Lee and Yen (1988) showed that the moisture absorption can degrade the buckling load in a composite shell structure subjected to compression. Doxee and Springer (1989) analyzed hygrothermal stresses and strains in an axisymmetric composite shell according to their higher order shell theory.

In view of the fairly thick construction envisioned for composite shells in marine applications, there is a need to investigate the stress and strain fields induced by the joint action of moisture absorption and mechanical (pressure) loading in a thick composite shell structure. To this extent, an elasticity solution would provide accurate results for certain simple configurations, but, more importantly, would form a basis for comparing various shell theories that could be potentially used for more complex geometries.

In this work, the problem of transient hygroscopic stresses in a hollow orthotropic circular cylinder loaded by external pressure is examined. It is assumed that both the inner and outer surfaces are at constant (but different) concentrations of moisture. The material properties are assumed independent of the concentration of moisture. It is also assumed that there is only radial dependence of the moisture concentration field. In a related study, Kardomateas (1989, 1990) used a displacement approach and a series expansion technique to solve the transient thermal stress problem in composite cylinders. In this paper, the displacement approach will be used to analyze the coupled transient moisture diffusion and mechanical loading

Contributed by the Applied Mechanics Division of THE AMERICAN SOCIETY OF MECHANICAL ENGINEERS for publication in the ASME JOURNAL OF APPLIED MECHANICS.

Discussion on this paper should be addressed to the Technical Editor, Professor Lewis T. Wheeler, Department of Mechanical Engineering, University of Houston, Houston, TX 77204-4792, and will be accepted until four months after final publication of the paper itself in the ASME JOURNAL OF APPLIED MECHANICS.

Manuscript received by the ASME Applied Mechanics Division, June 23, 1992; final revision, Feb. 4, 1993. Associate Technical Editor: R. M. Bowen.

Copyright © 1994 by ASME
Downloaded 03 May 2010 to 171.66.16.20. Redistribution subject to ASME license or copyright; see http://www.asme.org/terms/Terms_Use.cfm

(external pressure) problem. Numerical results are presented for the stresses with respect to time and the radial coordinates for an example case of graphite/epoxy material. The results illustrate clearly the nature of the transient hygroscopic boundary stress layer.

Mathematical Formulation

Consider a hollow cylinder, in general under external pressure p, as shown in Fig. 1. The cylinder has an inner radius, r_1 and an outer radius, r_2. The radial, circumferential, and axial coordinates are denoted by r, θ, and z, respectively. It is assumed that the initial concentration (at $t = 0$) is C_0. For $t > 0$, the boundaries $r = r_1$ and $r = r_2$ are kept at constant concentrations C_1 and C_2, respectively. The reference concentration is taken as zero. The moisture problem is solved by the Fickian diffusion equation

$$\frac{\partial C(r,\,t)}{\partial t} = D\,\frac{1}{r}\,\frac{\partial}{\partial r}\left(r\,\frac{\partial C}{\partial r}\right) \quad r_1 \le r \le r_2, \tag{1a}$$

where $C(r, t)$ is the moisture concentration and D is the moisture diffusivity of the composite in the r direction. The initial and boundary conditions are

$$C(r,\,t=0) = C_0 \quad r_1 \le r \le r_2, \tag{1b}$$

$$C(r_1,\,r) = C_1 \quad \text{and} \quad C(r_2,\,t) = C_2 \quad t > 0, \tag{1c}$$

where C_0, C_1, and C_2 are constants. Crank (1975) gives the general solution for the distribution of the concentration of moisture $C(r, t)$ to Eq. (1) in terms of the Bessel functions of the first and second kind J_n and Y_n, as follows:

$$C(r,\,t) = b_1 \ln\,(r/r_1) + b_2 \ln\,(r_2/r) + \sum_{n=1}^{\infty} [c_n J_0(r\alpha_n) + d_n Y_0(r\alpha_n)]e^{-D\alpha_n^2 t}, \tag{2a}$$

where

$$b_1 = \frac{C_2}{\ln\,(r_2/r_1)}; \quad b_2 = \frac{C_1}{\ln\,(r_2/r_1)}, \tag{2b}$$

$$c_n = \pi C_0\,\frac{J_0(r_1\alpha_n)\,Y_0(r_2\alpha_n)}{J_0(r_1\alpha_n) + J_0(r_2\alpha_n)} - \pi J_0(r_1\alpha_n)\,Y_0(r_2\alpha_n)\,\frac{C_2 J_0(r_1\alpha_n) - C_1 J_0(r_2\alpha_n)}{J_0^2(r_1\alpha_n) - J_0^2(r_2\alpha_n)}, \tag{2c}$$

$$d_n = -\pi C_0\,\frac{J_0(r_1\alpha_n)\,J_0(r_2 a_n)}{J_0(r_1\alpha_n) + J_0(r_2\alpha_n)} + \pi J_0(r_1\alpha_n)\,J_0(r_2\alpha_n)\,\frac{C_2 J_0(r_1\alpha_n) - C_1 J_0(r_2\alpha_n)}{J_0^2(r_1\alpha_n) - J_0^2(r_2\alpha_n)}, \tag{2d}$$

and α_n are the positive roots of

$$J_0(r_1\alpha_n)\,Y_0(r_2\alpha_n) - J_0(r_2\alpha_n)\,Y_0(r_1\alpha_n) = 0. \tag{2e}$$

The hygroscopic stress-strain relations for the orthotropic body are

$$\begin{bmatrix} \sigma_{rr} \\ \sigma_{\theta\theta} \\ \sigma_{zz} \\ \tau_{\theta z} \\ \tau_{rz} \\ \tau_{r\theta} \end{bmatrix} = \begin{bmatrix} c_{11} & c_{12} & c_{13} & 0 & 0 & 0 \\ c_{12} & c_{22} & c_{23} & 0 & 0 & 0 \\ c_{13} & c_{23} & c_{33} & 0 & 0 & 0 \\ 0 & 0 & 0 & c_{44} & 0 & 0 \\ 0 & 0 & 0 & 0 & c_{55} & 0 \\ 0 & 0 & 0 & 0 & 0 & c_{66} \end{bmatrix} \begin{bmatrix} \epsilon_{rr} - \beta_r \Delta C \\ \epsilon_{\theta\theta} - \beta_\theta \Delta C \\ \epsilon_{zz} - \beta_z \Delta C \\ \gamma_{\theta z} \\ \gamma_{rz} \\ \gamma_{r\theta} \end{bmatrix}, \tag{3}$$

where c_{ij} are the elastic constants and β_i the swelling coefficients (1, 2, and 3 represent r, θ, and z, respectively). The geometry (Fig. 1) is axisymmetric. Since the moisture concentration is assumed to depend only on the r direction, the stresses are independent of θ and z and the hoop displacement is zero. In addition to the constitutive Eq. (3), the equilibrium equations have to be satisfied; since $\tau_{r\theta} = \tau_{rz} = \tau_{\theta z} = 0$, only one equilibrium equation remains:

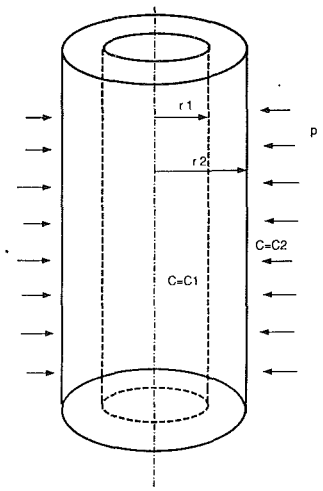


Fig. 1 Thick cylindrical shell under constant boundary concentrations of moisture

$$\frac{\partial \sigma_{rr}}{\partial r} + \frac{\sigma_{rr} - \sigma_{\theta\theta}}{r} = 0. \tag{4}$$

In this work the displacement field derived by Lekhnitskii (1981) for time-independent problems and modified by Kardomateas (1989) for time-dependent thermal stress problems (which are analogous to the time-dependent moisture-induced stress problems) is used:

$$u_r = U(r,\,t) + z(w_y \cos\theta - w_x \sin\theta) + u_0 \cos\theta + v_0 \sin\theta,$$
$$u_\theta = -z(w_y \sin\theta + w_x \cos\theta) + w_z r - u_0 \sin\theta + v_0 \cos\theta,$$
$$u_z = zf(t) - r(w_j \cos\theta - w_x \sin\theta) + w_0, \tag{5}$$

where the function $U(r, t)$ represents the radial displacement accompanied by deformation. The constants u_0, v_0, and w_0 denote the rigid-body translation along the x, y, and z directions in the Cartesian coordinate system, respectively, and w_x, w_y, and w_z denote the rigid-body rotation in the x, y, and z directions (these may also be functions of time, but since they do not appear in the strain expressions, such a dependence would not affect the expressions that follow in this section).

The parameter $f(t)$ is obtained from boundary conditions, as discussed later. The strains are expressed in terms of the displacements as follows:

$$\epsilon_{rr} = \frac{\partial U(r,\,t)}{\partial r}, \quad \epsilon_{\theta\theta} = \frac{U(r,\,t)}{r}, \quad \epsilon_{zz} = f(t),$$
$$\gamma_{\theta z} = \gamma_{zr} = \gamma_{r\theta} = 0. \tag{6}$$

Substituting Eqs. (6) and (3) into the equilibrium Eq. (4) gives the following differential equation for $U(r, t)$:

$$c_{11}\left[\frac{\partial^2 U(r,\,t)}{\partial r^2} + \frac{1}{r}\,\frac{\partial U(r,\,t)}{\partial r}\right] - \frac{c_{22}}{r^2}\,U(r,\,t) = q_1\,\frac{\partial C(r,\,t)}{\partial r} + q_2\,\frac{C(r,\,t)}{r} + (c_{23} - c_{13})\,\frac{f(t)}{r}, \tag{7a}$$

where

$$q_1 = c_{11}\beta_r + c_{12}\beta_\theta + c_{13}\beta_z, \tag{7b}$$

$$q_2 = (c_{11} - c_{12})\beta_r + (c_{12} - c_{22})\beta_\theta + (c_{13} - c_{23})\beta_z. \tag{7c}$$

Now set $f(t)$ in the form

$$f(t) = f_0 + \sum_{n=1}^{\infty} f_n e^{-D\alpha_n^2 t}. \tag{8}$$

Downloaded 03 May 2010 to 171.66.16.20. Redistribution subject to ASME license or copyright; see http://www.asme.org/terms/Terms_Use.cfm

Moreover, to solve Eq. (7), set

$$U(r, t) = U_0(r) + \sum_{n=1}^{\infty} R_n(r) e^{-D\alpha_n^2 t}. \quad (9)$$

Substituting Eqs. (2), (8), and (9) into Eq. (7*a*) yields the following equations to be satisfied for U_0, and R_n for $n = 1, 2, \ldots, \infty$:

$$c_{11}U_0''(r) + \frac{c_{11}}{r}U_0'(r) - \frac{c_{22}}{r^2}U_0(r) = \frac{c_{23}-c_{13}}{r}f_0 + q_1\frac{b_1-b_2}{r} + q_2 b_1\frac{\ln(r/r_1)}{r} + q_2 b_2\frac{\ln(r_2/r)}{r}, \quad (10a)$$

$$c_{11}R_n''(r) + \frac{c_{11}}{r}R_n'(r) - \frac{c_{22}}{r^2}R_n(r) = \frac{c_{23}-c_{13}}{r}f_n + c_n\left[q_2\frac{J_0(r\alpha_n)}{r} - q_1\alpha_n J_1(r\alpha_n)\right] + d_n\left[q_2\frac{Y_0(r\alpha_n)}{r} - q_1\alpha_n Y_1(r\alpha_n)\right] \quad n = 1, \ldots, \infty. \quad (10b)$$

For each of the previous equations, the solution is the sum of a homogeneous solution and a particular one. The solution of the homogeneous equation is in the form $G_1(t)r^{\lambda_1} + G_2(t)r^{\lambda_2}$ with

$$\lambda_{1,2} = \pm\sqrt{c_{22}/c_{11}}. \quad (10c)$$

In a similar fashion to the parameter $f(t)$, set $G_i(t)$ in the form: $G_i(t) = G_{i0} + \Sigma G_{in}e^{-D\alpha_n^2 t}$, $i = 1, 2$.

Since the constants f_n and G_{ij} are yet unknown, we shall indicate the places where they enter in the expressions that follow (these constants are found later from the boundary conditions). For $c_{11} \neq c_{22}$, the solution of (10*a*) for $U_0(r)$ is

$$U_0(r) = G_{10}r^{\lambda_1} + G_{20}r^{\lambda_2} + \frac{c_{23}-c_{13}}{c_{11}-c_{22}}f_0 r + U_0^*(r), \quad (11a)$$

where

$$U_0^*(r) = \frac{q_2 b_1}{c_{11}-c_{22}}r\ln(r/r_1) + \frac{q_2 b_2}{c_{11}-c_{22}}r\ln(r_2/r) + \frac{[q_1(c_{11}-c_{22}) - 2q_2c_{11}]}{(c_{11}-c_{22})^2}(b_1-b_2)r. \quad (11b)$$

For $c_{11} = c_{22}$, the corresponding solution of (10*a*) is

$$U_0(r) = G_{10}r + \frac{G_{20}}{r} + \frac{c_{23}-c_{13}}{2c_{11}}f_0 r\ln(r/r_1) + U_0^*(r), \quad (12a)$$

where

$$U_0^*(r) = \frac{q_2 b_1}{4c_{11}}r\ln^2(r/r_1) - \frac{q_2 b_2}{4c_{11}}r\ln^2(r_2/r) + \frac{(2q_1-q_2)(b_1-b_2)}{4c_{11}}r\ln(r/r_1). \quad (12b)$$

To solve (10*b*) we use the series expansions of the Bessel functions to obtain a series expansion of the right-hand side, as given in Appendix A. In the following, γ stands for the Euler's constant ($\simeq 0.577215\ldots$).

For $c_{11} \neq c_{22}$, the resulting Eq. (A3) in Appendix A leads to the solution of (10*b*) for R_n, $n = 1, \ldots, \infty$, as follows:

$$R_n(r) = G_{1n}r^{\lambda_1} + G_{2n}r^{\lambda_2} + \frac{c_{23}-c_{13}}{c_{11}-c_{22}}f_n r + R_n^*(r), \quad (13a)$$

$$R_n^*(r) = B_{0n}r + \frac{2q_2 d_n}{\pi(c_{11}-c_{22})}r\ln(r\alpha_n/2) + \sum_{k=0}^{\infty} B_{1nk}r^{2k+3}\ln(r\alpha_n/2) + B_{2nk}r^{2k+3}, \quad (13b)$$

where

$$B_{0n} = \frac{c_n q_2 + d_n(2/\pi)(q_1+\gamma q_2)}{c_{11}-c_{22}} - \frac{4c_{11}q_2 d_n}{\pi(c_{11}-c_{22})^2}. \quad (13c)$$

The coefficients in the sum over k are given in terms of

$$f_{kn} = \left[c_n - \frac{2d_n}{\pi}\left(1 + \frac{1}{2} + \ldots + \frac{1}{k+1} - \gamma\right)\right] \times [q_2 + 2q_1(k+1)] + \frac{2d_n q_1}{\pi}, \quad (13d)$$

as follows:

$$B_{1nk} = \frac{2d_n(-1)^{k+1}\alpha_n^{2k+2}[q_2+2q_1(k+1)]}{\pi 2^{2k+2}[(k+1)!]^2[c_{11}(2k+3)^2 - c_{22}]}, \quad (14a)$$

$$B_{2nk}[c_{11}(2k+3)^2 - c_{22}] = \frac{(-1)^{k+1}\alpha_n^{2k+2}}{2^{2k+2}[(k+1)!]^2}f_{kn} - B_{1nk}2c_{11}(2k+3). \quad (14b)$$

In the (unlikely) event that for a certain k, $c_{11}(2k+3)^2 = c_{22}$, the term in the sum for this k is replaced by the one in Appendix B.

For $c_{11} = c_{22}$ the solution of (10*b*) for R_n is

$$R_n(r) = G_{1n}r + \frac{G_{2n}}{r} + \frac{c_{23}-c_{13}}{2c_{11}}f_n r\ln(r/r_1) + R_n^*(r), \quad (15a)$$

$$R_n^*(r) = B_{0n}r\ln(r\alpha_n/2) + \frac{d_n q_2}{2\pi c_{11}}r\ln^2(r\alpha_n/2) + \sum_{k=0}^{\infty} B_{1nk}r^{2k+3}\ln(r\alpha_n/2) + B_{2nk}r^{2k+3}, \quad (15b)$$

where

$$B_{0n} = \frac{\pi c_n q_2 + d_n(2q_1 + 2\gamma q_2 - q_2)}{2\pi c_{11}}. \quad (15c)$$

The series expansion for the Bessel functions cannot be used for large arguments; hence, the requirement of including an increasing number of terms and therefore large arguments necessitates finding a particular solution for the "large arguments" domain. This is achieved by using the Hankel asymptotic expansions of the Bessel functions of the first and second kind (see Appendix A). Employing the substitution

$$\rho = r\alpha_n; \quad R_n^{**}(\rho) = R_n^*(r), \quad (16)$$

gives the following equation for $R_n^{**}(\rho)$

$$c_{11}\alpha_n^2\left(R_n^{**\prime\prime}(\rho) + \frac{R_n^{**\prime}(\rho)}{\rho}\right) - c_{22}\alpha_n^2\frac{R_n^{**}(\rho)}{\rho^2} = \sum_{k=0}^{\infty}\frac{(-1)^k\alpha_n\psi_1(k)}{(2k)!(8\rho)^{2k}\rho\sqrt{\pi\rho}} \times \{(c_n+d_n)(q_2\sin\rho - a_{1,k}\rho\cos\rho + a_{2,k}\rho^2\sin\rho) + (c_n-d_n)(q_2\cos\rho + a_{1,k}\rho\sin\rho + a_{2,k}\rho^2\cos\rho)\}, \quad (17)$$

where

$$a_{1,k} = q_1\frac{4k+1}{4k-1} - q_2\frac{16k}{(4k-1)^2}; \quad a_{2,k} = \frac{16kq_1}{(4k-1)(4k-3)}. \quad (18)$$

and $\psi_1(k)$ is defined in Appendix A.

The solution of the above equation for the function $R_n^{**}(\rho)$ is found to be

$$R_n^{**}(\rho) = \sum_{k=0}^{\infty} p_{k,1}^n\rho^{-2k-1/2}\cos\rho + s_{k,1}^n\rho^{-2k-1/2}\sin\rho + p_{k,2}^n\rho^{-2k-3/2}\cos\rho + s_{k,2}^n\rho^{-2k-3/2}\sin\rho. \quad (19a)$$

The coefficients $p_{k,1}^n$, $s_{k,1}^n$, $p_{k,2}^n$, $s_{k,2}^n$ are determined by considering the terms in the sum that contribute to the terms $\rho^{-2k-1/2}\cos\rho$, $\rho^{-2k-1/2}\sin\rho$, $\rho^{-2k-3/2}\cos\rho$, $\rho^{-2k-3/2}\sin\rho$ in the right-hand side of (17). Define

Downloaded 03 May 2010 to 171.66.16.20. Redistribution subject to ASME license or copyright; see http://www.asme.org/terms/Terms_Use.cfm

$$D_k = \frac{(-1)^k \psi_1(k)}{(2k)!\, 8^{2k} \alpha_n \sqrt{\pi}}. \quad (19b)$$

We obtain the following recursive formulas for $p^n_{k,1}$, $s^n_{k,1}$:

$$p^n_{k,1}c_{11} = p^n_{k-1,1}[c_{11}(2k-3/2)^2 - c_{22}] - s^n_{k-1,2}c_{11}(4k-2) + D_k a_{1,k}(c_n + d_n), \quad (20a)$$

$$s^n_{k,1}c_{11} = s^n_{k-1,1}[c_{11}(2k-3/2)^2 - c_{22}] + p^n_{k-1,2}c_{11}(4k-2) - D_k a_{1,k}(c_n - d_n), \quad (20b)$$

and for $p^n_{k,2}$, $s^n_{k,2}$:

$$p^n_{k,2}c_{11} = p^n_{k-1,2}[c_{11}(2k-1/2)^2 - c_{22}] - s^n_{k,1}c_{11}4k - (D_k q_2 + D_{k+1}a_{2,k+1})(c_n - d_n), \quad (20c)$$

$$s^n_{k,2}c_{11} = s^n_{k-1,2}[c_{11}(2k-1/2)^2 - c_{22}] + p^n_{k,1}c_{11}4k - (D_k q_2 + D_{k+1}a_{2,k+1})(c_n + d_n). \quad (20d)$$

The process starts from $k = 1$ and the starting values for $k = 0$ are from (17) and (18) as follows:

$$p^n_{0,1} = -\frac{q_1(c_n + d_n)}{c_{11}\alpha_n\sqrt{\pi}}; \quad s^n_{0,1} = \frac{q_1(c_n - d_n)}{c_{11}\alpha_n\sqrt{\pi}}, \quad (21a)$$

$$p^n_{0,2} = (-8q_2 + 3q_1)\frac{(c_n - d_n)}{8c_{11}\alpha_n\sqrt{\pi}};$$

$$s^n_{0,2} = (-8q_2 + 3q_1)\frac{(c_n + d_n)}{8c_{11}\alpha_n\sqrt{\pi}}. \quad (21b)$$

An important issue regarding this analysis will be discussed now. The solution (19) is a particular solution of Eq. (17) derived by considering the Hankel asymptotic expansions of the Bessel functions for values of the argument $\rho = r\alpha_n \geq \rho_{tr} = 18.0$ (see Appendix A), whereas the solution (13*b*), which will be denoted by $R^*_{nS}(r)$, had been derived based on a series expansion for the Bessel functions, for values of the argument $\rho \leq \rho_{tr}$. Since for a given root α_n the argument ρ ranges from $r_1\alpha_n$ to $r_2\alpha_n$, there may be a transition point from one solution to the other for $R^*_n(r)$ in the expression (15*a*). Both solutions are particular ones and may be different. Therefore, at that transition point a homogeneous solution term should be added to (19) so that

$$R^{**}_{nL}(\rho_{tr}) = R^*_{nS}(\rho_{tr}/\alpha_n); \quad R^{**\prime}_{nL}(\rho_{tr})\alpha_n = R^{*\prime}_{nS}(\rho_{tr}/\alpha_n). \quad (22b)$$

where h_{1n} and h_{2n} are determined from the condition of equal value and slope at the transition point

$$R^{**}_{nL}(\rho_{tr}) = R^*_{nS}(\rho_{tr}/\alpha_n); \quad R^{**}_{nL\prime}(\rho_{tr})\alpha_n = R^*_{nS\prime}(\rho_{tr}/\alpha_n). \quad (22b)$$

Thus, the expression for $U(r, t)$ satisfying the equilibrium equations is obtained with the unknown coefficients G_{10}, G_{20}, f_0; G_{1n}, G_{2n} and f_n for $n = 1, 2 \ldots$. These coefficients are determined from the following boundary conditions:

$$\sigma_{rr}(r_1, t) = 0, \quad \sigma_{rr}(r_2, t) = -p;$$
$$\tau_{r\theta}(r_i, t) = \tau_{rz}(r_i, t) = 0, \quad i = 1, 2 \quad (23)$$

where p is the external pressure. Only those for the stress σ_{rr} are not identically satisfied. The stress σ_{rr} on the boundaries is written in terms of the displacement field:

$$\sigma_{rr}(r_i, t) = c_{11}U_{,r}(r_i, t) + c_{12}\frac{U(r_i, t)}{r} + c_{13}f(t) - q_1 C(r_i, t), \quad i = 1, 2. \quad (24)$$

Substituting Eqs. (2), (8), (9) into (24) for $U_0(r)$ gives the following two linear equations for G_{10}, G_{20}, and f_0:

$$(c_{11}\lambda_1 + c_{12})r_i^{\lambda_1 - 1}G_{10} + (c_{11}\lambda_2 + c_{12})r_i^{\lambda_2 - 1}G_{20} + A_0 f_0 = -c_{11}U_0^{*\prime}(r_i) - c_{12}\frac{U_0^*(r_i)}{r_i} + q_1[b_1 \ln(r_i/r_1) + b_2 \ln(r_2/r_1)] + p_i \quad i = 1, 2, \quad (25a)$$

where

$$A_0 = \frac{c_{11} + c_{12}}{c_{11} - c_{22}}(c_{23} - c_{13}) + c_{13} \quad \text{for } c_{11} \neq c_{22}$$

$$= \frac{c_{23} - c_{13}}{2c_{11}}[c_{11} + (c_{11} + c_{12}) \ln(r_i/r_1)] + c_{13} \quad \text{for } c_{11} = c_{22} \quad (25b)$$

and $p_i = 0$, at $i = 1$; $p_i = -p$ at $i = 2$.

In a similar fashion, by substituting the expressions for $R_n(r)$, there correspond two linear equations for G_{1n}, G_{2n}, f_n, for $n = 1, \ldots, \infty$, as follows:

$$(c_{11}\lambda_1 + c_{12})r_i^{\lambda_1 - 1}G_{1n} + (c_{11}\lambda_2 + c_{12})r_i^{\lambda_2 - 1}G_{2n} + A_0 f_n = -c_{11}R^{*\prime}_n(r_i) - c_{12}\frac{R^*_n(r_i)}{r_i} + q_1[c_n J_0(r_i\alpha_n) + d_n Y_0(r_i\alpha_n)]; \quad i = 1, 2. \quad (25c)$$

Now let us consider the conditions of resultant forces and moments. Since the stresses do not depend on z, these conditions exist in any cross-section. It can be proved (e.g., Lekhnitskii, 1963, although hygroscopic effects are not included) that the conditions of zero resultant forces along the x and y-axes of a Cartesian coordinate system are satisfied identically. The conditions of zero resultant moment along x and y-axes (and that of zero twisting moment) are also satisfied by the symmetry of the problem. Therefore, it remains only the condition of resultant axial force, P_z, arising in a hydrostatic field:

$$\int_{r_1}^{r_2} \sigma_{zz}(r, t)2\pi r dr = P_z(t) = -p\pi(r_2^2 - r_1^2). \quad (26)$$

This gives the last set of equations that are needed to determine the constants G_{ij}, f_j. In terms of

$$q_3 = c_{13}\beta_r + c_{23}\beta_\theta + c_{33}\beta_z, \quad (27)$$

Eq. (26) gives

$$\left(\frac{c_{13}\lambda_1 + c_{23}}{\lambda_1 + 1}\right)(r_2^{\lambda_1 + 1} - r_1^{\lambda_1 + 1})G_{10} + A_1 G_{20} + A_2 f_0 = (c_{13} - c_{23})I_0 + \frac{q_3}{2}\left[\frac{(r_2^2 - r_1^2)}{2}(b_2 - b_1) + (r_2^2 b_1 - r_1^2 b_2)\ln(r_2/r_1)\right] - \frac{p}{2}(r_2^2 - r_1^2) + c_{13}\sum_{i=1,2}(-1)^{i+1}r_i U_0^*(r_i), \quad (28a)$$

and for $n = 1, \ldots \infty$,

$$\left(\frac{c_{13}\lambda_1 + c_{23}}{\lambda_1 + 1}\right)(r_2^{\lambda_1 + 1} - r_1^{\lambda_1 + 1})G_{1n} + A_1 G_{2n} + A_2 f_n = (c_{13} - c_{23})I_n + c_{13}\sum_{i=1,2}(-1)^{i+1}r_i R^*_n(r_i) + (q_3/\alpha_n)(-1)^i[c_n r_i J_1(r_i\alpha_n) + d_n r_i Y_1(r_i\alpha_n)], \quad (28b)$$

where I_0 and I_n are given in Appendix C. The coefficients A_1, A_2 are defined as

$$A_1 = \left(\frac{c_{13}\lambda_2 + c_{23}}{\lambda_2 + 1}\right)(r_2^{\lambda_2 + 1} - r_1^{\lambda_2 + 1}) \quad \text{for } c_{11} \neq c_{22}$$
$$= (c_{23} - c_{13}) \ln(r_2/r_1) \quad \text{for } c_{11} = c_{22} \quad (29a)$$

$$A_2 = \frac{r_2^2 - r_1^2}{2}\left(c_{33} + \frac{c_{23}^2 - c_{13}^2}{c_{11} - c_{22}}\right) \quad \text{for } c_{11} \neq c_{22}$$
$$= \frac{(r_2^2 - r_1^2)}{8c_{11}}[4c_{33}c_{11} - (c_{23} - c_{13})^2] + \frac{c_{23}^2 - c_{13}^2}{4c_{11}}r_2^2 \ln(r_2/r_1) \quad \text{for } c_{11} = c_{22}. \quad (29b)$$

Therefore, the constants f_j, G_{ij} and hence the displacement U

Downloaded 03 May 2010 to 171.66.16.20. Redistribution subject to ASME license or copyright; see http://www.asme.org/terms/Terms_Use.cfm

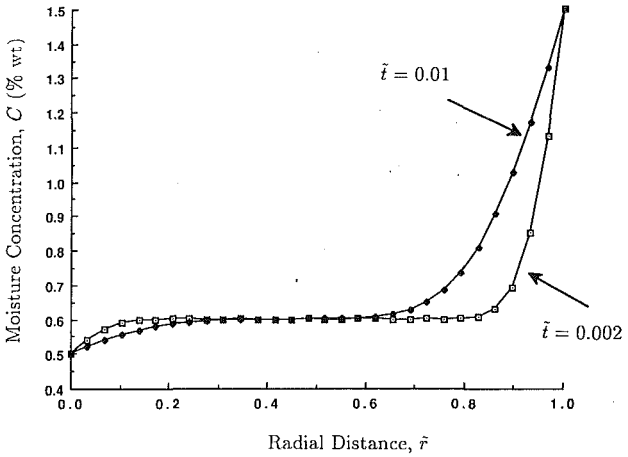


Fig. 2 Radial distribution of the concentration $C(r, t)$ at different times. The nondimensional time is defined by $\tilde{t} = Dt/(r_2 - r_1)^2$. The nondimensional radial distance is defined by $\tilde{r} = (r - r_1)/(r_2 - r_1)$.

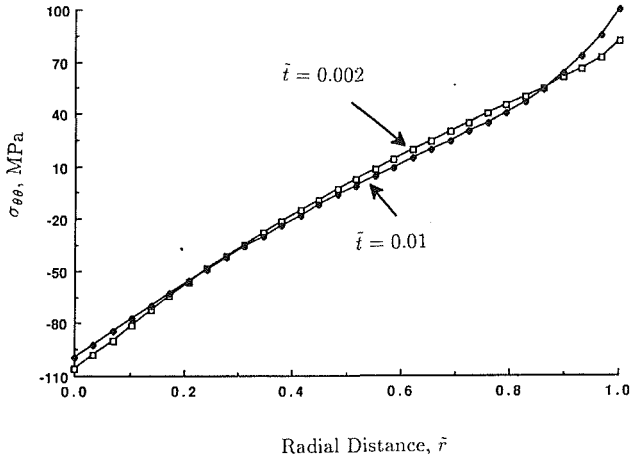


Fig. 3 Distribution of the hoop stress $\sigma_{\theta\theta}$ (no mechanical loading)

can be found by solving (25) and (28). After obtaining the displacement field, the stresses can be found by substituting in (6) and (3).

Results and Discussion

First, a significant observation is that due to the slow rate of moisture diffusion, many terms, i.e., roots α_n of the characteristic Eq. (2*c*), are needed, which makes the Hankel asymptotic regime very important. In the results presented in this section, 15 terms were used.

As an illustrative example, a T300/5208 Gr/Ep circular cylinder of inner radius $r_1 = 20$ mm and radii ratio $r_2/r_1 = 1.50$ was considered. The fibers are oriented along the circumferential direction. The typical values of moduli in GN/m^2 and Poisson's ratios are as follows: $E_1 = 9.9$, $E_2 = 140$, $E_3 = 9.1$, $G_{23} = 4.3$, $G_{12} = 4.7$, $G_{31} = 5.9$, $\nu_{12} = 0.020$, $\nu_{23} = 0.30$, $\nu_{31} = 0.49$, where 1 is the radial (r), 2 is the circumferential (θ), and 3 is the axial (z) direction. The typical values of hygroscopic expansion coefficients (e.g., Hahn, 1976) are $\beta_r = \beta_z = 6.67 \times 10^{-3}$/wt percent, $\beta_\theta = 0$. For this material, the moisture diffusivity in the radial direction is $D = 2.145 \times 10^{-13}$ m^2/sec. This value was obtained by substituting a temperature of 50°C to the equation for the temperature-dependent moisture diffusivity in Hahn (1976).

To illustrate the results, the nondimensional radial distance $\tilde{r} = (r - r_1)/(r_2 - r_1)$, and normalized time $\tilde{t} = Dt/(r_2 - r_1)^2$ are used. The initial concentration (at $t = 0$) is taken $C_0 = 0.1$, whereas the concentrations at the ends for $t > 0$ are $C_1 = 0.5$ and $C_2 = 1.5$.

Figure 2 shows the spatial distribution of the concentration. Two time values, $\tilde{t} = 0.002$ (corresponding to about 10 days) and $\tilde{t} = 0.01$ (corresponding to about 50 days), are used. The major stresses are the hoop, $\sigma_{\theta\theta}$, and the axial one σ_{zz}, and these are shown in Figs. 3 and 4. The boundary layer effect is more clearly shown in the axial stress. Notice that these plots illustrate the cases with no mechanical load present, i.e., these stresses are induced purely from the hygroscopic effects. Although a normalization of the stresses would be generally desirable in presenting the results, it is our opinion that for this particular hygroelastic problem, absolute values give a more clear description of the resulting effects. It should also be mentioned that longer time scales are used because the equilibrium process of moisture absorption or desorption takes much longer than that of temperature.

The coupling of mechanical loading and hygroscopic effects is illustrated in Figs. 5 and 6 which show the hoop stress, $\sigma_{\theta\theta}$, and the axial one, σ_{zz}, for (a) applied external pressure only

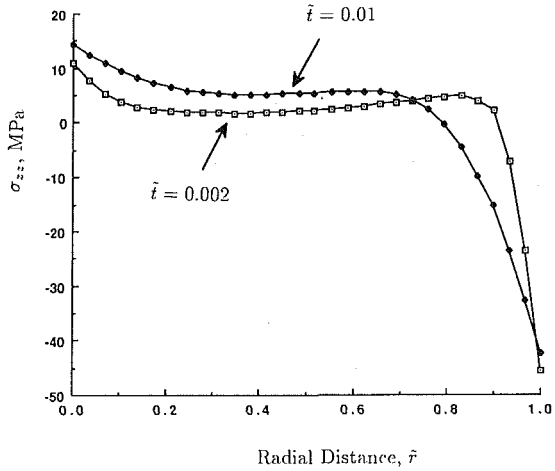


Fig. 4 Distribution of the axial stress σ_{zz} (no mechanical loading)

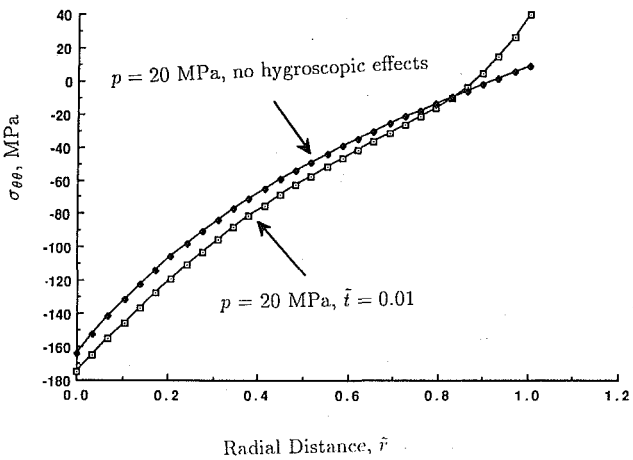


Fig. 5 Distribution of the hoop stress $\sigma_{\theta\theta}$, illustrating the coupling of mechanical loading (external pressure) and hygroscopic effects

and (b) applied external pressure with consideration of the hygroscopic effects at time $\tilde{t} = 0.01$. The stress distribution for hydrostatic pressure only is taken from Lekhnitskii (1981). It is seen that the hygroscopic effects result in an increase in the absolute value of the hoop stress at both the inner and outer boundaries. Again, the hygroscopic boundary layer is

Downloaded 03 May 2010 to 171.66.16.20. Redistribution subject to ASME license or copyright; see http://www.asme.org/terms/Terms_Use.cfm

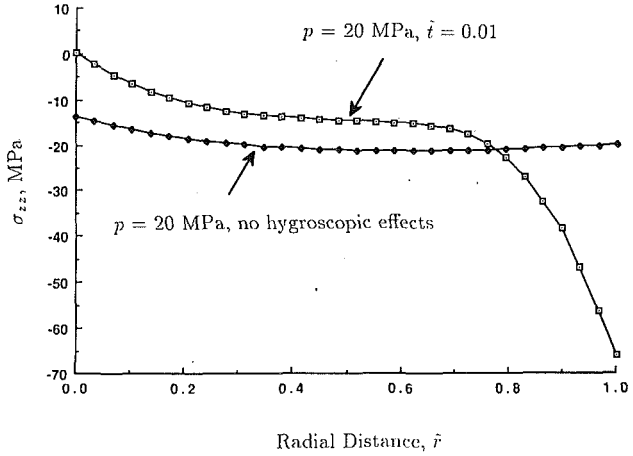


Fig. 6 Distribution of the axial stress σ_{zz}, illustrating the coupling of mechanical loading (external pressure) and hygroscopic effects

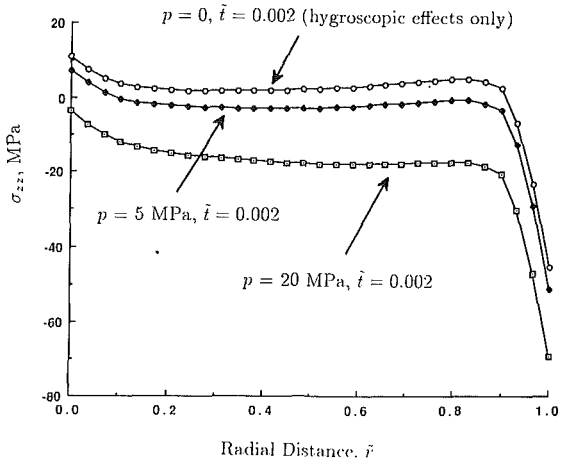


Fig. 7 Distribution of the axial stress σ_{zz}, illustrating the effect of variable mechanical loading (external pressure) coupled with the hygroscopic effects

more clearly seen in the axial stress σ_{zz}, which shows a large increase near the outer surface. In this example, a value of the external pressure $p = 20$ MPa was taken. Other values of the hydrostatic pressure would affect mainly the mean value and not the existence of the boundary stress layer. More specifically, Fig. 7 shows the effect of coupled applied pressure p, and hygroscopic fields, on the axial stress, for $p = 0$ (only hygroscopic effects), $p = 5$ and $p = 20$ MPa at time $\tilde{t} = 0.002$.

Notice also that for the example considered the reinforcement is along the periphery, thus the axial direction is a direction of weakness. Therefore, the boundary layer effect on the axial stress may have more important implications for failure initiation than a similar one on the hoop component.

Applications of thick composite shells in marine environments may actually involve a larger size than the one considered in these examples. For an insight into these size effects, the results for the transient stress profiles were derived for a shell made out of the same material with the same fiber orientation, and of inner radius $r_1 = 4$ m and radii ratio $r_2/r_1 = 1.25$. A time value of 50 days with no mechanical loading and the same initial and boundary moisture concentrations were used. It turns out that the same boundary layer effect on the axial stress σ_{zz} appears (as in the present, smaller size example, Fig. 4, $\tilde{t} = 0.01$) with a similar range of negative values; however, the boundary layer was confined to a smaller $\tilde{r}$ range near the outer surface. A much smaller effect exists for the hoop stress $\sigma_{\theta\theta}$, with smaller positive and less negative values than in the small size example, Fig. 3.

A noteworthy observation is that the classical shell theory, in which the radial displacement $U(r)$ is assumed constant, would not be capable of capturing these boundary layer stresses. Finally, it should be mentioned that in this paper moisture-independent material constants (stiffness) were assumed, but the moisture absorption may affect these constants as well. Moreover, the moisture diffusion process is accelerated or decelerated by temperature. In the future, it is desirable to consider these additional effects caused by coupled moisture and temperature fields. It is also desirable to examine the extent to which higher-order shell theories (e.g., Whitney and Sun, 1974; Librescu, 1975; Reddy and Liu, 1985) can predict this boundary layer stress field.

Acknowledgment

The financial support of the Office of Naval Research, Mechanics Division, Grant N00014-91-J-1892, and the interest and encouragement of the Project Monitor, Dr. Y. Rajapakse, are both gratefully acknowledged.

References

Abramowitz, M., and Stegun, I. A., 1970, *Handbook of Mathematical Functions with Formulas, Graphs, and Mathematical Tables*, National Bureau of Standards Applied Mathematics Series No. 55, 9th Printing, Washington, D.C.

Crank, J., 1975, *The Mathematics of Diffusion*, 2nd ed., Clarendon Press.

Crossman, F. W., and Wang, A. S. D., 1978, "Stress Field Induced by Transient Moisture Sorptions in Finite-Width Composite Laminates," *Journal of Composite Materials*, Vol. 12, pp. 2–18.

Doxee, L. E. Jr., and Springer, G. S., 1989, "Hygrothermal Stresses and Strains in Axisymmetric Composite Shells," *Computers and Structures*, Vol. 32, No. 2, pp. 395–407.

Farley, G. L., and Herakovich, C. T., 1978, "Influence of Two Dimensional Hygrothermal Gradients on Interlaminar Stresses Near Free-Edges," *Advanced Composite Materials—Environmental Effects*, ASTM STP 658, J. Vinson, ed., ASTM, Philadelphia, PA, pp. 143–159.

Hahn, H. T., 1976, "Residual Stresses in Polymer Matrix Composite Laminates," *J. Composite Materials*, Vol. 10, pp. 266–277.

Kardomateas, G. A., 1989, "Transient Thermal Stresses in Cylindrically Orthotropic Composite Tubes," ASME JOURNAL OF APPLIED MECHANICS, Vol. 56, pp. 411–417; also Errata, Ibid., 1991, Vol. 58, p. 909.

Kardomateas, G. A., 1990, "The Initial Phase of Transient Thermal Stresses due to General Boundary Thermal Loads in Orthotropic Hollow Cylinders," ASME JOURNAL OF APPLIED MECHANICS, Vol. 57, pp. 719–724; also Errata, Ibid., 1991, Vol. 58, p. 909.

Lee, S. Y., and Yen, W. J., 1988, "Hygrothermal Effects on the Stability of a Cylindrical Composite Shell Panel," ASME Aerospace Division AD, Vol. 13, ASME, New York, pp. 21–31.

Lekhnitskii, S. G., 1981, *Theory of Elasticity of an Anisotropy Body*, Mir Publishers, Moscow, pp. 124–128.

Librescu, L., 1975, *Elastostatics and Kinetics of Anisotropic and Heterogeneous Shell-Type Structures*, Nordhoff International, Leyden.

Reddy, J. N., and Liu, C. F., 1985, "A Higher-Order Shear Deformation Theory of Laminated Elastic Shells," *Int. J. Eng. Sci.*, Vol. 23, No. 3, pp. 319–330.

Wang, S. S., and Choi, I., 1982, "Boundary-Layer Hygroscopic Stresses in Angle-Ply Composite Laminates," *AIAA Journal*, Vol. 20, No. 11, pp. 1592–1598.

Whitney, J. M., and Husman, G. E., 1978, "Use of the Flexure Test for Determining Environmental Behavior of Fibrous Composites," *Experimental Mechanics*, Vol. 8, No. 5, pp. 185–190.

Whitney, J. M., and Sun, C. T., 1974, "A Refined Theory for Laminated Anisotropic Cylindrical Shells," ASME JOURNAL OF APPLIED MECHANICS, Vol. 41, No. 2, pp. 471–476.

Wylie, C. Ray, 1975, *Advanced Engineering Mathematics*, 4th ed., McGraw-Hill, New York.

APPENDIX A

The Bessel functions of first and second kind of order zero and one have a series expansion of the form (see, e.g., Wylie, 1975)

$$J_0(x) = \sum_{k=0}^{\infty} \frac{(-1)^k x^{2k}}{2^{2k}(k!)^2}; \quad J_1(x) = \sum_{k=0}^{\infty} \frac{(-1)^k x^{2k+1}}{2^{2k+1} k!(k+1)!}, \tag{A1}$$

$$Y_0(x) = \frac{2}{\pi}\left(\ln\frac{x}{2} + \gamma\right) J_0(x) - \frac{2}{\pi}\sum_{k=1}^{\infty} \frac{(-1)^k x^{2k}}{2^{2k}(k!)^2}\,\psi(k), \tag{A2a}$$

Downloaded 03 May 2010 to 171.66.16.20. Redistribution subject to ASME license or copyright; see http://www.asme.org/terms/Terms_Use.cfm

$$Y_1(x)=\frac{2}{\pi}\left(\ln\frac{x}{2}+\gamma\right)J_1(x)-\frac{2}{\pi}\frac{1}{x}$$
$$-\frac{1}{\pi}\sum_{k=0}^{\infty}\frac{(-1)^k x^{2k+1}}{2^{2k+1}(k!)(k+1)!}\left(2\psi(k+1)-\frac{1}{k+1}\right). \quad \text{(A2}b\text{)}$$

In the above expressions $\gamma = 0.577215\ldots$ is the Euler's constant and $\psi(k)$ is defined as

$$\psi(k)=1+\frac{1}{2}+\ldots+\frac{1}{k}. \quad \text{(A2}c\text{)}$$

The above series expansions can be used to calculate the Bessel's functions up to a value of the argument of about $x = 18$. They are rapidly convergent especially for small values of the argument.

Using the series expansion, we obtain the following equation in place of (10*b*):

$$c_{11}\left(R_n''(r)+\frac{R_n'(r)}{r}\right)-\frac{c_{22}}{r^2}R_n(r)=\frac{(c_{23}-c_{13})f_n}{r}$$
$$+\frac{c_nq_2+(2/\pi)(q_1+\gamma q_2)d_n}{r}+\frac{2d_nq_2}{\pi}\frac{\ln(r\alpha_n/2)}{r}$$
$$+\frac{2d_n}{\pi}\sum_{k=0}^{\infty}\frac{(-1)^{k+1}\alpha_n^{2k+2}[q_2+2q_1(k+1)]}{2^{2k+2}[(k+1)!]^2}r^{2k+1}\ln(r\alpha_n/2)$$
$$+\sum_{k=0}^{\infty}\frac{(-1)^{k+1}\alpha_n^{2k+2}f_{kn}}{2^{2k+2}[(k+1)!]^2}r^{2k+1}, \quad \text{(A3)}$$

where f_{kn} is defined in (13*d*).

For *large arguments* we can use the Hankel asymptotic expansions for the Bessel functions (see, e.g., Abramowitz and Stegun, 1970) to obtain the following expressions:

$$J_0(x)=A_0(x)\sin x+B_0(x)\cos x;$$
$$J_1(x)=B_1(x)\sin x-A_1(x)\cos x, \quad \text{(A4}a\text{)}$$
$$Y_0(x)=B_0(x)\sin x-A_0(x)\cos x;$$
$$Y_1(x)=-A_1(x)\sin x-B_1(x)\cos x. \quad \text{(A4}b\text{)}$$

The functions $A_0(x)$, $A_1(x)$, $B_0(x)$, $B_1(x)$ are given in terms of

$$\psi_1(k)=1^2.3^2.5^2\ldots(4k-1)^2,\quad k=1,\infty;\quad \psi_1(0)=1, \quad \text{(A5)}$$

as follows:

$$(\pi x)^{1/2}A_0(x)=\sum_{k=0}^{\infty}\frac{(-1)^k\psi_1(k)}{(2k)!(8x)^{2k}}\left[1-\frac{16kx}{(4k-1)^2}\right], \quad \text{(A6}a\text{)}$$

$$(\pi x)^{1/2}A_1(x)=\sum_{k=0}^{\infty}\frac{(-1)^{k+1}\psi_1(k)(4k+1)}{(2k)!(8x)^{2k}(4k-1)}\times\left[1-\frac{16kx}{(4k-3)(4k+1)}\right], \quad \text{(A6}b\text{)}$$

$$(\pi x)^{1/2}B_0(x)=\sum_{k=0}^{\infty}\frac{(-1)^k\psi_1(k)}{(2k)!(8x)^{2k}}\left[1+\frac{16kx}{(4k-1)^2}\right], \quad \text{(A6}c\text{)}$$

$$(\pi x)^{1/2}B_1(x)=\sum_{k=0}^{\infty}\frac{(-1)^{k+1}\psi_1(k)(4k+1)}{(2k)!(8x)^{2k}(4k-1)}\times\left[1+\frac{16kx}{(4k-3)(4k+1)}\right]. \quad \text{(A6}d\text{)}$$

In this way, the above series of the Hankel asymptotic expansion can be used to calculate the Bessel functions for values of the argument $x \geq 18$. The series converges rapidly and the number of terms required in the summation over k is at most 13 at $x = 18.0$, being smaller for larger values of the argument.

APPENDIX B

In the event that for a certain k, $c_{11}(2k+3)^2 = c_{22}$, the term in the sum in (13*b*) and (15*b*) for this k is

$$B_{1nk}r^{2k+3}\ln^2(r\alpha_n/2)+B_{2nk}r^{2k+3}\ln(r\alpha_n/2), \quad \text{(B1)}$$

where now

$$B_{1nk}=\frac{2d_n(-1)^{k+1}\alpha_n^{2k+2}[q_2+2q_1(k+1)]}{\pi 2^{2k+2}[(k+1)!]^2 4c_{11}(2k+3)}, \quad \text{(B2}a\text{)}$$

$$B_{2nk}=\frac{(-1)^{k+1}\alpha_n^{2k+2}}{2^{2k+2}[(k+1)!]^2 2c_{11}(2k+3)}\times\left\{f_{kn}-\frac{2d_n[q_2+2q_1(k+1)]}{2\pi(2k+3)}\right\}. \quad \text{(B2}b\text{)}$$

APPENDIX C

For $c_{11} \neq c_{22}$, the expression for I_0 in (28*a*) is

$$I_0=\frac{q_2(b_1r_2^2-b_2r_1^2)}{2(c_{11}-c_{22})}\ln(r_2/r_1)$$
$$+\left[\frac{(2q_1-q_2)}{4(c_{11}-c_{22})}-\frac{q_2c_{11}}{(c_{11}-c_{22})^2}\right](b_1-b_2)(r_2^2-r_1^2), \quad \text{(C1)}$$

and the expressions for I_n, $n = 1, \ldots, \infty$, in (28*b*), for the small arguments domain, are

$$I_n=\sum_{i=1,2}(-1)^i\frac{r_i^2}{2}\left(B_{0n}-\frac{d_nq_2}{\pi(c_{11}-c_{22})}\right)$$
$$+(-1)^i\frac{d_nq_2}{\pi(c_{11}-c_{22})}r_i^2\ln(r_i\alpha_n/2)+S_n, \quad \text{(C2}a\text{)}$$

$$S_n=\sum_{i=1}^{2}\sum_{k=0}^{\infty}(-1)^iB_{1nk}\frac{r_i^{2k+4}}{2k+4}\ln(r_i\alpha_n/2)$$
$$+(-1)^i\left(B_{2nk}-\frac{B_{1nk}}{2k+4}\right)\frac{r_i^{2k+4}}{2k+4}. \quad \text{(C2}b\text{)}$$

For $c_{11} = c_{22}$, the expression for I_0 is

$$8I_0c_{11}=q_2(b_1r_2^2+b_2r_1^2)\ln^2(r_2/r_1)$$
$$+(q_2-q_1)(b_1-b_2)(r_2^2-r_1^2)+[(2q_1-q_2)(b_1-b_2)r_2^2$$
$$+q_2(b_2r_1^2-b_1r_2^2)]\ln(r_2/r_1), \quad \text{(C3}a\text{)}$$

and the expressions for I_n, $n = 1, \ldots \infty$, again in the small arguments domain, are

$$I_n=\sum_{i=1,2}(-1)^i\frac{d_nq_2}{\pi 4c_{11}}r_i^2\ln^2(r_i\alpha_n/2)$$
$$+(-1)^i\left(\frac{B_{0n}}{2}-\frac{d_nq_2}{\pi 4c_{11}}\right)r_i^2\ln(r_i\alpha_n/2)$$
$$+(-1)^{i+1}\left(\frac{B_{0n}}{2}-\frac{d_nq_2}{\pi 4c_{11}}\right)\frac{r_i^2}{2}+S_n. \quad \text{(C3}b\text{)}$$

For large arguments with $\rho_i = r_i\alpha_n$,

$$\alpha_nI_n=\sum_{i=1,2}(-1)^i\sum_{k=0}^{\infty}\left(p_{k,1}^n+\frac{s_{k,2}^n}{2k+1/2}\right)I_{c,k}(\rho_i)$$
$$+\left(s_{k,1}^n-\frac{p_{k,2}^n}{2k+1/2}\right)I_{s,k}(\rho_i)-\frac{p_{k,2}^n}{2k+1/2}\rho_i^{-2k-1/2}\cos\rho_i$$
$$-\frac{s_{k,2}^n}{2k+1/2}\rho_i^{-2k-1/2}\sin\rho_i, \quad \text{(C4)}$$

where $I_{c,k}(\rho)$ and $I_{s,k}(\rho)$ are defined by the recursive formulas

Downloaded 03 May 2010 to 171.66.16.20. Redistribution subject to ASME license or copyright; see http://www.asme.org/terms/Terms_Use.cfm

$$(2k-1/2)(2k-3/2)I_{c,k} = -(2k-3/2)\rho^{-2k+1/2}\cos\rho + \rho^{-2k+3/2}\sin\rho - I_{c,k-1}, \quad \text{(C5}a\text{)}$$

$$(2k-1/2)(2k-3/2)I_{s,k} = -(2k-3/2)\rho^{-2k+1/2}\sin\rho - \rho^{-2k+3/2}\cos\rho - I_{s,k-1}. \quad \text{(C5}b\text{)}$$

The process starts from $k = 0$, and initially;

$$I_{c,0}(\rho) = \int \rho^{-1/2}\cos\rho d\rho; \quad I_{s,0}(\rho) = \int \rho^{-1/2}\sin\rho d\rho. \quad \text{(C5}c\text{)}$$

Notice that the integral of the homogeneous solution (22*a*) (due to continuity requirements at the transition point of the two partial solutions) should be added to I_n, i.e., for $c_{11} \neq c_{22}$, the following term should be added:

$$\sum_{i=1,2}(-1)^i\left(h_1\frac{\rho_i^{\lambda_1+1}}{\lambda_1+1} + h_2\frac{\rho_i^{\lambda_2+1}}{\lambda_2+1}\right). \quad \text{(C6)}$$

For $c_{11} = c_{22}$, the term multiplying h_2 in the previous relation (C6) is $\ln \rho_i$.

Downloaded 03 May 2010 to 171.66.16.20. Redistribution subject to ASME license or copyright; see http://www.asme.org/terms/Terms_Use.cfm

G. J. Simitses
Professor and Head,
Aerospace Engineering and
Engineering Mechanics,
University of Cincinnati,
Cincinnati, OH 45211
Fellow ASME

Y. Song[1]
Engineering Technology
Associates, Inc.
Madison Heights, MI 48071

Thermo-Elastoviscoplastic Buckling Behavior of Plates

The thermo-elastoviscoplastic buckling behavior of plates is investigated. The analysis is based on nonlinear kinematic relations and nonlinear rate-dependent unified constitutive equations which include both Bodner-Partom's and Walker's material models. A finite element approach is employed to predict the inelastic buckling behavior. Numerical examples are given to demonstrate the effects of several parameters, which include temperature, small initial imperfections, and the thickness of the plate. Comparisons of buckling responses for the two models, Bodner-Partom's and Walker's, are also presented.

Introduction

The post-buckling behavior of rectangular plates has been studied extensively using elastic material models. Numerous analytical and computational results have been reported in the literature (see Chia, 1979). The study of plastic buckling of plates started in the late 1940s with the investigation of Illyshin (1947), Stowell (1948), and Bijlaard (1949) on the basis of deformation theory and Handelman and Prager (1948) on the basis of the incremental theory of plasticity. Pride and Heimerl (1949) made experiments on the rectangular shaped aluminum tubes and showed that the deformation theory gives buckling loads which are in reasonable agreement with the experimental results, while the incremental theory gives buckling loads which are sometimes much higher than the experimental ones. It appeared to be a paradox since incremental theory is a widely accepted theory in plasticity, while some postulates of the deformation theory are not well fulfilled in the buckling calculations. Following the initial works, Pearson (1950) improved the incremental results using the assumption that no unloading takes places over the entire thickness of the plate. Shrivastava (1979) considered the transverse shear effects on the critical stress, which were neglected in the previous investigations, and showed that the decrease in the buckling stress for the incremental theory is larger than that for the deformation theory. The effects of initial imperfections on the plastic buckling were investigated by Neale (1975), who showed that the buckling load is highly imperfection sensitive. Neale also pointed out that the buckling load based on the incremental theory can be reduced considerably in the presence of small initial geometric imperfections, so a proper consideration of imperfections provides an explanation for the plastic buckling paradox. The buckling behavior including small initial imperfections was also studied by Needleman and Tvergaard (1976) who used the asymptotic analysis approach to compute the buckling stresses for the case for which the critical stress is higher than the yielding stress of the material. With regard to rate-dependent constitutive models, Tvergaard (1985) studied the rate-dependent buckling behavior and imperfection sensitivity of plates reinforced by stiffeners on one side. Column theory is used in the investigation to simplify the problem. Examples were given to evaluate the effects of strain rate. The results showed that the strain rate has strong influence on the bifurcation load, while the classical elastic-plastic buckling predictions remain good approximations if reasonable initial imperfections and relatively low strain rates are given.

Creep buckling of plates has been discussed by Hoff (1973). Some assumptions, such as cubic form of the constitutive equation, were used in the investigation for sandwich construction. Tvergaard (1979) studied the creep buckling behavior by employing the perturbation method in the prebuckling stage and numerical scheme in the post-buckling stage. The creep behavior of the material is taken to be the steady creep and is described by Norton's law. Elastic and plastic deformations were accounted for. However, the time-dependent and time-independent deformations were considered as independent processes. This means that the interactions between the two processes are neglected.

Even though plastic analysis with deformation theory could accurately predict buckling stresses for plates, it is not quite appropriate for the post-buckling analysis. Theoretically, the path-independent deformation theory requires simple loading to guarantee its validity. In other words, the conditions such as small deformation, proportional loading, incompressible material behavior, and power form of constitutive equations need to be satisfied. However, these conditions could not be generally fulfilled in the post-buckling calculations. Moreover, most of the discussions involved, both in the deformation theory and incremental theory in the common literature, are for the cases in which the buckling stress is beyond the yield stress of the material. Actually, this situation can occur only when the ratio of the thickness to length of a plate is greater than $(1/\pi)\sqrt{3(1-\nu^2)}\sigma_y/E$, where σ_y is the yield stress of the

[1] Formerly, Graduate Research Assistant, Aerospace Engineering Department, Georgia Institute of Technology, Atlanta, GA 30332.

Contributed by the Applied Mechanics Division of THE AMERICAN SOCIETY OF MECHANICAL ENGINEERS for publication in the ASME JOURNAL OF APPLIED MECHANICS.

Discussion on this paper should be addressed to the Technical Editor, Professor Lewis T. Wheeler, Department of Mechanical Engineering, University of Houston, Houston, TX 77204-4792, and will be accepted until four months after final publication of the paper itself in the ASME JOURNAL OF APPLIED MECHANICS.

Manuscript received by the ASME Applied Mechanics Division, Apr. 10, 1991; final revision, July 26, 1991. Associate Technical Editor: A. K. Noor.

Copyright © 1994 by ASME
Downloaded 03 May 2010 to 171.66.16.20. Redistribution subject to ASME license or copyright; see http://www.asme.org/terms/Terms_Use.cfm

material. For the commonly used engineering materials, this ratio is greater than 0.03 and for the common discussions given by Shrivastava (1979), Neale (1975), and Needleman and Tvergaard (1976), the ratios employed are from 0.031 to 0.1. Obviously, these cases represent the buckling behavior of rather thick plates. For the thinner plates, both an elastic buckling load and a post-buckling plastic limit point load exist. So the problems are more complicated.

In the classical creep buckling analysis, the separation of time-dependent and time-independent deformations can simplify both the formulation and the computations. However, it is not always a reasonable approximation to separate these two types of deformation, especially at high temperatures and complex thermomechanical loading cycles. Actually, the deformation is not only determined by the current loading situation but also by the whole loading history.

The unified constitutive equations developed in recent years can serve as a material model in the buckling analysis of plates for various loading and temperature conditions. The model can cover elastic and inelastic material behavior and temperature effects, simultaneously. Unlike the traditional approach, it does not separate the inelastic deformation into time-dependent (creep) and time-independent (plastic) deformations. Instead, it describes the deformation in terms of not only current mechanical quantities but also in terms of several state variables. The state variables are employed to characterize the deformation history. Thus, the path-dependent behavior of material can be better represented.

There have been several unified constitutive models (see Miller, 1987). Among them Bodner-Partom's model (Chan et al., 1984) (Lindholm et al., 1985) and Walker's model (Lindholm et al., 1985) are applicable over a wide range of strain rates and of temperatures. The kinematic equations for these two material models are expressed in exponential form, which has the desirable feature that the strain rate is small, essentially negligible, at low stress levels until a threshold value is reached and it then increases with a slope determined by a parameter. In the Bodner-Partom's model, both scalar and tensor-valued internal variables are introduced into the constitutive equation to represent the isotropic hardening and directional hardening. In Walker's model two sets of state variables, back stress and drag stress, are employed. The back stress represents nonlinear kinematic hardening to account for the Bauschinger effect while the drag stress represents isotropic hardening to account for cyclic hardening or softening of the material. Both Bodner-Partom's model and Walker's model are in good agreement with experimental tests (James et al., 1987).

Recently Paley and Aboudi (1991) studied the viscoplastic bifurcation buckling behavior of plates using Bodner-Partom's constitutive model. With the method they proposed, the buckling load of inelastic rate-sensitive plates can be deduced from the solution of the corresponding elastic problem under the same boundary conditions. In their investigations, time-dependent instantaneous moduli are used, which are calculated from constitutive equations and updated in every loading step. The effects of both shear deformation and rate sensitivity were discussed for simply-supported rectangular plates under different loading rates and thermal conditions.

The general difficulty with using unified constitutive equations is the increase in complexity. The constitutive equations are a group of strongly coupled nonlinear differential equations. In order to avoid the large number of subiterations in the calculations of a finite element procedure, Tanaka and Miller (1988) proposed a unified numerical method to integrate the stiff time-dependent constitutive equations. The asset of the method is that it eliminates the need to integrate the constitutive equations iteratively. Two phases, the process phase and the solution phase, are introduced in the overall procedure. In the process phase, the stiffness matrix and initial stress vector are produced and then the displacement increments are solved for, globally. In the solution phase, the strain increments are substituted back, so the increments in stresses and state variables as well as other quantities can be solved for, locally.

In this paper, the finite element method is used to predict the buckling behavior of simply-supported rectangular plates. Both Bodner-Partom's and Walker's models are employed to represent the thermo-elastoviscoplastic material behavior. Comparisons of the results for the two types of material models are given. The material used is B1900+Hf, which is a commonly utilized alloy in high temperature environments. The effects of several parameters are assessed. The parameters include temperature, small initial imperfections, and the ratio of the thickness to the length of the plates. Creep failure behavior is given as an example to show the time-dependent deformation process. The plates studied in this paper cover a wide range of thicknesses.

Constitutive Equations

Bodner-Partom's Model. Bodner-Partom's constitutive equations are based on the assumption of additive decomposition of the total strain rate into elastic and plastic parts. The kinematic equation in multidimensional cases can be derived as

$$\dot{\epsilon}_{ij}^{p}=\frac{s_{ij}}{J_2^{1/2}}D_0\exp\left\{-\left[\frac{Z^2}{3J_2}\right]^n\right\}$$

where $\dot{\epsilon}_{ij}^{p}$, s_{ij}, J_2, and Z are plastic strain rate, stress deviator, second invariant of stress deviator, and state variable, respectively. The state variable Z can be interpreted as a load history-dependent parameter which represents the hardened state of the material with respect to resistance to plastic flow. The variable Z consists of both isotropic and directional components which are denoted as Z^I and Z^D. The temperature effects in the constitutive equations are given by the temperature-dependent variables. The whole set of equations is

(1) flow law

$$\dot{\epsilon}_{ij}=\dot{\epsilon}_{ij}^{e}+\dot{\epsilon}_{ij}^{p};\quad \dot{\epsilon}_{ij}^{p}=\lambda s_{ij}$$

$$\dot{\epsilon}_{kk}^{p}=0;\quad s_{ij}=\sigma_{ij}-\frac{1}{3}\delta_{ij}\sigma_{kk}.$$

(2) kinematic equation

$$D_2^p=D_0^2\exp\left\{-\left[\frac{Z^2}{3J_2}\right]^n\right\} \tag{1}$$

$$Z=Z^I+Z^D;\quad D_2^p=\frac{1}{2}\dot{\epsilon}_{ij}^{p}\dot{\epsilon}_{ij}^{p}$$

$$J_2=\frac{1}{2}s_{ij}s_{ij};\quad \lambda^2=D_2^p/J_2.$$

(3) isotropic hardening

$$\dot{Z}^I=m_1[Z_1+\alpha Z_3-Z^I]\dot{W}^p-A_1Z_1\left[\frac{Z^I-Z_2}{Z_1}\right]^{r_1} \tag{2}$$

where

$$\dot{\alpha}=m_2(\alpha_1-\alpha)\dot{W}^p\sin\theta;\quad \theta=\cos^{-1}(v_{ij}\bar{v}_{ij})$$

$$v_{ij}=\beta_{ij}/(\beta_{kl}\beta_{kl})^{1/2};\quad \bar{v}_{ij}=\dot{\beta}_{ij}/(\dot{\beta}_{kl}\dot{\beta}_{kl})^{1/2}$$

$$u_{ij}=\sigma_{ij}/(\sigma_{kl}\sigma_{kl})^{1/2};\quad \bar{u}_{ij}=\dot{\sigma}_{ij}/(\dot{\sigma}_{kl}\dot{\sigma}_{kl})^{1/2}$$

with the initial conditions

$$Z^I(0)=Z_0;\quad \dot{W}_p=\sigma_{ij}\dot{\epsilon}_{ij}^{p};\quad W_p(0)=0;\quad \alpha(0)=0.$$

(4) directional hardening

$$\dot{\beta}_{ij}=m_2(Z_3u_{ij}-\beta_{ij})\dot{W}_p-A_2Z_1\left[\frac{(\beta_{kl}\beta_{kl})^{1/2}}{Z_1}\right]^{r_2}v_{ij} \tag{3}$$

with the initial conditions

Downloaded 03 May 2010 to 171.66.16.20. Redistribution subject to ASME license or copyright; see http://www.asme.org/terms/Terms_Use.cfm

$$Z^D=\beta_{ij}u_{ij};\quad Z^D(0)=0;\quad \beta_{ij}(0)=0.$$

In the above equations, D_0, Z_0, Z_1, Z_2, Z_3, m_1, m_2, α_1, A_1, A_2, r_1, r_2, n are material constants. Among them, n, A_1, A_2, Z_0, Z_2 are temperature dependent (for more detail see Lindholm et al., 1985).

Walker's Model. The basic form of Walker's constitutive equation is

$$\dot{\epsilon}^p=\dot{\epsilon}-\frac{\dot{\sigma}}{E}=f^{-1}\left(\frac{\sigma-\Omega}{\Psi}\right) \tag{4}$$

where ϵ^p, ϵ, σ, Ω, and Ψ represent the inelastic strain, the total strain, the current stress, the back stress, and the drag stress, respectively. The back stress is used to represent directional hardening. It consists of three components Ω_{ij0}, Ω_{ij1}, and Ω_{ij2}. The drag stress Ψ is used to represent isotropic hardening. The value of Ψ is initially $\Psi_1-\Psi_2$ and will saturate at a value Ψ_1 with increasing plastic strain. The whole set of Walker's constitutive equations is given as

(1) kinematic equation

$$\dot{\epsilon}^p_{ij}=\frac{\left(\frac{3}{2}\epsilon_{ij}-\Omega_{ij}\right)}{\sqrt{\frac{2}{3}\left(\frac{3}{2}s_{ij}-\Omega_{ij}\right)\left(\frac{3}{2}s_{ij}-\Omega_{ij}\right)}}\times\left[\exp\left(\frac{\sqrt{\frac{2}{3}\left(\frac{3}{2}s_{ij}-\Omega_{ij}\right)\left(\frac{3}{2}s_{ij}-\Omega_{ij}\right)}}{\Psi}\right)-1\right]/\beta. \tag{5}$$

(2) the internal variables

$$\Psi=\Psi_1-\Psi_2e^{-n_7R}-\Psi_3e^{-n_8L}\quad \dot{L}=\left\|\sqrt{\frac{2}{3}\dot{\epsilon}^p_{ij}\dot{\epsilon}^p_{ij}}\right\|-\left\|\sqrt{\frac{2}{3}\dot{\epsilon}_{ij}\epsilon_{ij}}\right\|$$

$$\Omega_{ij}=\Omega_{ij0}+\Omega_{ij1}+\Omega_{ij2}\quad \dot{R}=\sqrt{\frac{2}{3}\dot{\epsilon}^p_{ij}\dot{\epsilon}^p_{ij}}$$

$$\dot{\Omega}_{ij0}=3\dot{\Omega}_0\left[\frac{\dot{\epsilon}^p_{ik}\epsilon^p_{kj}}{\epsilon^p_{pq}\epsilon^p_{pq}}+\frac{\epsilon^p_{ik}\dot{\epsilon}^p_{kj}}{\epsilon^p_{pq}\epsilon^p_{pq}}-\left(\frac{2\epsilon^p_{ik}\epsilon^p_{kj}}{\epsilon^p_{pq}\epsilon^p_{pq}}\right)\left(\frac{\epsilon^p_{rt}\dot{\epsilon}^p_{rt}}{\epsilon^p_{uv}\epsilon^p_{uv}}\right)\right]+\left[3\frac{\epsilon^p_{ik}\epsilon^p_{kj}}{\epsilon^p_{pq}\epsilon^p_{pq}}-\delta_{ij}\right]\frac{\partial\dot{\Omega}}{\partial\theta}$$

$$\dot{\Omega}_{ij1}=n_2\dot{\epsilon}^p_{ij}-\Omega_{ij1}\left(\left[n_3+n_4e^{-n_5\left\|\log\frac{\dot{R}}{\dot{R}_0}\right\|}\right]\dot{R}+n_6+\frac{1}{n_2}\frac{\partial n_2}{\partial\theta}\dot{\theta}\right)+\Omega_{ij1}\frac{1}{n_3}\frac{\partial n_3}{\partial\theta}\dot{\theta}+\left(\frac{n_2}{n_3}-\Omega_{ij1}\right)\frac{\partial n_3}{\partial\theta}\epsilon^p_{ij}\dot{\theta}$$

$$\dot{\Omega}_{ij2}=n_{11}\dot{\epsilon}^p_{ij}-\Omega_{ij2}\left(n_9\dot{R}+n_{10}+\frac{1}{n_{11}}\frac{\partial n_{11}}{\partial\theta}\dot{\theta}-\frac{1}{n_9}\frac{\partial n_9}{\partial\theta}\dot{\theta}\right)+\left(\frac{n_{11}}{n_9}-\Omega_{ij2}\right)\frac{\partial n_9}{\partial\theta}\epsilon^p_{ij}\dot{\theta}.$$

The material constants are λ, μ, Ω_0, β, n_2, n_2, n_3, n_4, n_5, n_6, n_7, n_8, n_9, n_{10}, n_{11}, Ψ_1, Ψ_2, Ψ_3 (for more detail see Lindholm et al., 1985).

Finite Element Formulation

The virtual power equation in incremental form can be written as

$$\int_\Omega(T_{iA}+\Delta T_{iA})\delta\left(\frac{\partial\Delta u_i}{\partial X_A}\right)d\Omega=\int_s(T_i-\Delta T_i)\delta\Delta u_i ds \tag{6}$$

where T_{iA} and u_i are the first Piola-Kirchhoff stress elements and displacement components, respectively. Let D_{ij} and W_{ij} be the deformation and spin increments, then

$$D_{ij}=\frac{1}{2}\left(\frac{d\Delta u_i}{dx_j}+\frac{d\Delta u_j}{dx_i}\right);\quad W_{ij}=\frac{1}{2}\left(\frac{d\Delta u_i}{dx_j}-\frac{d\Delta u_j}{dx_i}\right).$$

Using the expression for the Jaumann rate tensor

$$\hat{\sigma}_{ij}=\dot{\sigma}_{ij}+\sigma_{ik}\omega_{kj}+\sigma_{jk}\omega_{ki}, \tag{7}$$

and the relation between Kirchhoff and first Piola-Kirchhoff stress tensors

$$\sigma_{ij}=T_{iA}g_{jA},$$

the increment of the first Piola-Kirchhoff stress elements can be expressed as

$$\Delta T_{ij}=\Delta\hat{\sigma}_{ij}+\sigma_{jk}\Delta u_{i,k}-(\sigma_{ik}D_{jk}+\sigma_{jk}D_{ik}). \tag{8}$$

Substitution of Eq. (8) into Eq. (6) yields

$$\int_\Omega\left[\Delta\hat{\sigma}_{ij}\delta D_{ij}-\frac{1}{2}\sigma_{ij}\delta\left(2D_{ik}D_{kj}-\frac{\partial(\Delta u_k)}{\partial x_i}\frac{\partial(\Delta u_k)}{\partial x_j}\right)\right]d\Omega=\int_s(T_i+\Delta T_i)\delta(\Delta u_i)ds-\int_\Omega\sigma_{ij}\delta D_{ij}d\Omega \tag{9}$$

Bodner-Partom's constitutive equation at any instant can be expressed in incremental form

$$\Delta\hat{\sigma}_{ij}=C^*_{ijkl}D_{kl}-\sigma^*_{ij}\quad\text{or}\quad\{\Delta\hat{\sigma}\}=[C^*]\{\Delta\epsilon\}-\{\sigma^*\}$$

where C^*_{ijkl} and σ^*_{ij} are functions of strain, strain rate, loading history and temperature and they are formed in every step. The algorithm to obtain C^*_{ijkl} and σ^*_{ij} will be illustrated later. Equation (9) is given below in incremental form:

$$\sum_n\int_{el}([B_1]^T[C^*][B_1]-2[B_2]^T[\sigma][B_2]+[B_3]^T[\sigma][B_3])\{\Delta u^k\}d\Omega=\sum_n\int_{el}[N]^T\{T+\Delta T\}ds-\sum_n\int_{el}[B_1]^T\{\sigma\}d\Omega+\sum_n\int_{el}[B_1]^T\{\sigma^*\}d\Omega \tag{10}$$

where the corresponding relations from Eq. (9) to Eq. (10) are

$$\int C^*_{ijkl}D_{kl}\delta D_{ij}d\Omega\rightarrow\int[B_1]^T[C^*][B_1]\{\Delta u^k\}d\Omega$$

$$\int\sigma_{ij}\delta(D_{ik}D_{kl})d\Omega\rightarrow 2\int[B_2]^T[\sigma][B_2]\{\Delta u^k\}d\Omega$$

$$\int\frac{1}{2}\sigma_{ij}\delta(\Delta u_{k,i}\Delta u_{k,j})d\Omega\rightarrow\int[B_3]^T[\sigma][B_3]\{\Delta u^k\}d\Omega$$

where the strain-displacement transformation matrices $[B_1]$, $[B_2]$, and $[B_3]$ can be derived from the derivative of shape functions (Bathe, 1982; Song, 1991). Using the notation

$$[K^*]=\sum_n\int_{el}[B_1]^T[C^*][B_1]d\Omega \tag{11}$$

$$[K_n]=\sum_n\int_{el}([B_3]^T[\sigma][B_3]-2[B_2]^T[\sigma][B_2])d\Omega \tag{12}$$

$$\{\Delta p\}=\sum_n\int_{el}[N]^T\{T+\Delta T\}ds-\sum_n\int_{el}[B_1]^T\{\sigma\}d\Omega \tag{13}$$

$$\{\Delta p^*\}=\sum_n\int_{el}[B_1]^T\{\sigma^*\}d\Omega, \tag{14}$$

Eq. (10) becomes

$$([K^*]+[K_n])\{\Delta u^g\}=\{\Delta p\}+\{\Delta p^*\}. \tag{15}$$

Downloaded 03 May 2010 to 171.66.16.20. Redistribution subject to ASME license or copyright; see http://www.asme.org/terms/Terms_Use.cfm

This is the equation used in solving the nodal displacements in the finite element method.

The two-phase solution method of Tanaka and Miller (1988) is used to capture the material parameters $[C^*]$ and $\{\sigma^*\}$ at any instant. Bodner-Partom's constitutive equations have the form

$$\dot{\sigma} = \mathbf{C}(\dot{\epsilon} - \dot{\epsilon}^N); \quad \dot{\epsilon}^N = \mathbf{f}(\sigma, \mathbf{x}, T); \quad \dot{\mathbf{x}} = \mathbf{g}(\sigma, \dot{\epsilon}^N, \mathbf{x}, T)$$

where $\dot{\epsilon}$, $\dot{\epsilon}^N$, $\mathbf{x}$, and $\dot{\mathbf{x}}$ are the total strain rate, the inelastic strain rate, the state variable and the rate of state variable, respectively. These expressions can be linealized by the Taylor expansion

$$\begin{aligned} \dot{\epsilon}^{Nb} &= \mathbf{f}^a + \mathbf{f}^a_{,\sigma}\Delta\sigma + \mathbf{f}^a_{,\mathbf{x}}\Delta\mathbf{x} \\ \dot{\mathbf{x}}^b &= \mathbf{g}^a + \mathbf{g}^a_{,\sigma}\Delta\sigma + \mathbf{g}^a_{,\dot{\epsilon}^N}\Delta\dot{\epsilon}^N + \mathbf{g}^a_{,\mathbf{x}}\Delta\mathbf{x} \\ \dot{\sigma}^b &= C(\dot{\epsilon}^b - \dot{\epsilon}^{Nb}) \end{aligned} \tag{16}$$

where the superscripts a and b represent the starting and ending time for an arbitrary time interval $\Delta t = t^b - t^a$. With the implicit time stepping scheme, the increments for the stress, strain, and the state variables (let $\mathbf{y}$ represent any one of them) can be expressed as

$$\Delta\mathbf{y} = \Delta t\{(1-\eta)\dot{\mathbf{y}}^a + \eta\dot{\mathbf{y}}^b\} \tag{17}$$

where η is a weighting coefficient.

Use of Eq. (17) to eliminate the quantities with the superscript b in Eq. (16) gives

$$\begin{bmatrix} -\eta\Delta t\mathbf{f}^a_{,\sigma} & \mathbf{I} & -\eta\Delta t\mathbf{f}^a_{,\mathbf{x}} & 0 \\ -\eta\Delta t\mathbf{g}^a_{,\sigma} & -\mathbf{g}^a_{,\dot{\epsilon}^N}\mathbf{I} & -\eta\Delta t\mathbf{g}^a_{,\mathbf{x}} & 0 \\ \mathbf{I} & \mathbf{C} & 0 & -\mathbf{C} \end{bmatrix} \begin{Bmatrix} \Delta\sigma \\ \Delta\epsilon^N \\ \Delta\mathbf{x} \\ \Delta\epsilon \end{Bmatrix}$$

$$= \begin{Bmatrix} \Delta t(\dot{\epsilon}^{Na} - \eta(\dot{\epsilon}^{Na} - \mathbf{f}^a)) \\ \Delta t((\dot{\mathbf{x}}^a - \mathbf{g}_{,\dot{\epsilon}^{Na}}\dot{\epsilon}^{Na}) - \eta(\dot{\mathbf{x}}^a - \mathbf{g}^a)) \\ 0 \end{Bmatrix}. \tag{18}$$

Partially diagonalizing the coefficient matrix of the equations yields

$$\begin{bmatrix} \mathbf{I} & 0 & 0 & -\mathbf{C}^* \\ 0 & \mathbf{I} & 0 & -\mathbf{C}^* \\ 0 & 0 & \mathbf{I} & -\mathbf{C}^* \end{bmatrix} \begin{Bmatrix} \Delta\sigma \\ \Delta\epsilon^N \\ \Delta\mathbf{x} \\ \Delta\epsilon \end{Bmatrix} = \begin{Bmatrix} -\Delta\zeta_1 \\ -\Delta\zeta_2 \\ -\Delta\zeta_3 \end{Bmatrix}. \tag{19}$$

The first group of equations gives

$$\{\Delta\sigma\} = [C^*]\{\Delta\epsilon\} - \{\Delta\zeta_1\}. \tag{20}$$

So $[C^*]$ and $\{\sigma^*\} = \{\Delta\zeta_1\}$ are the quantities used to build the stiffness matrix and the pseudo-load vector, i.e.,

$$[K^*] = \sum_n \int_{el} [B_1]^T[C^*][B_1]d\Omega \quad \{\Delta p^*\} = \sum_n \int_{el} [B_1]^T\{\Delta\zeta_1\}d\Omega$$

which are the stiffness matrix and the load vector in Eqs. (11) and (14).

A finite element computer program has been written to solve the necessary field equations (incremental form).

Numerical Results

The "degenerated" three-dimensional isoparametric shell element (see Bathe, 1982) is employed in the investigation. There are eight nodes in an element. For each node, there are five degrees-of-freedom (three translations and two rotations). The basic assumptions of this type of finite element formulation is that the lines originally normal to the shell midsurface remain straight and the transverse normal stress is zero, which is equivalent to using a general nonlinear shell theory. In order to obtain the post-buckling behavior, Crisfield's arc-length

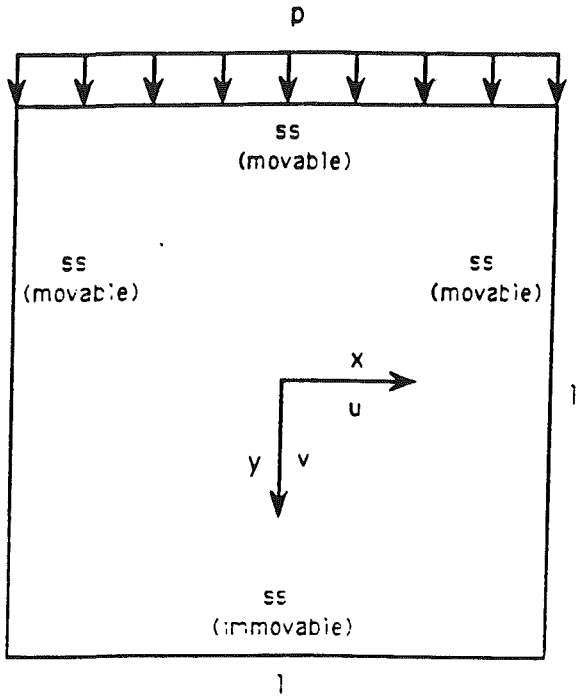


Fig. 1 Simply supported square plate

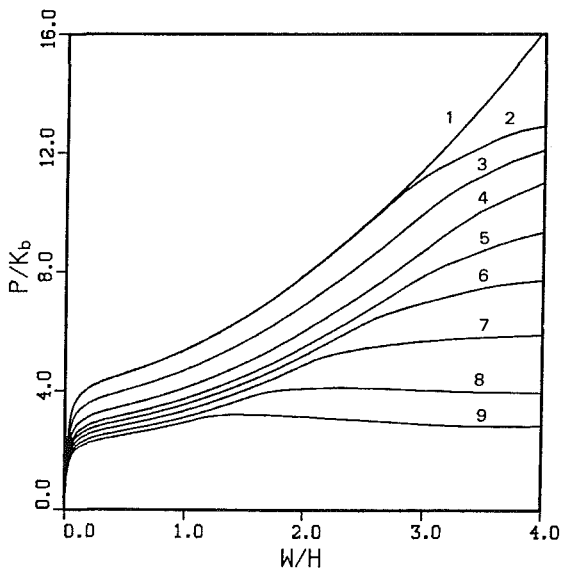


Fig. 2 Load deflection response using Bodner-Partom's model

method (Crisfield, 1983) is used in the equilibrium iterations. The program has been checked by comparing the nonlinear elastic response of a thin plate with that predicted by a series solution. Good agreement was found. The same program has also been used to predict the buckling stresses of cylindrical shells under axial compression. The validity of the results has been proven through comparison with experimental tests (Song, 1991). The material used in this paper is nickel-based superalloy B1900+hf. Although the employed material constants are limited to the small strain regime (less than two percent) (Lindholm et al., 1985), the formulation and the finite element program are for much wider application in which moderate strains may be involved.

The simply-supported plate is loaded uniformly as shown in Fig. 1. The unloaded edges are movable in the original plane. Square plates are employed in the calculations. The length, thickness, and imperfection amplitude (sine sine curve) at the

Downloaded 03 May 2010 to 171.66.16.20. Redistribution subject to ASME license or copyright; see http://www.asme.org/terms/Terms_Use.cfm

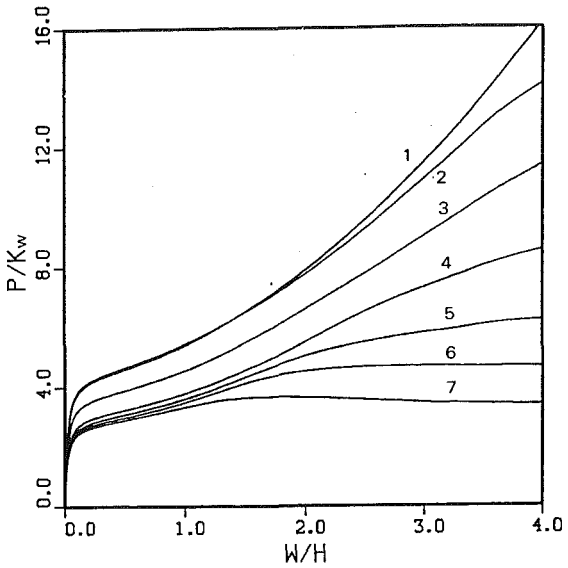


Fig. 3 Load deflection response using Walker's model

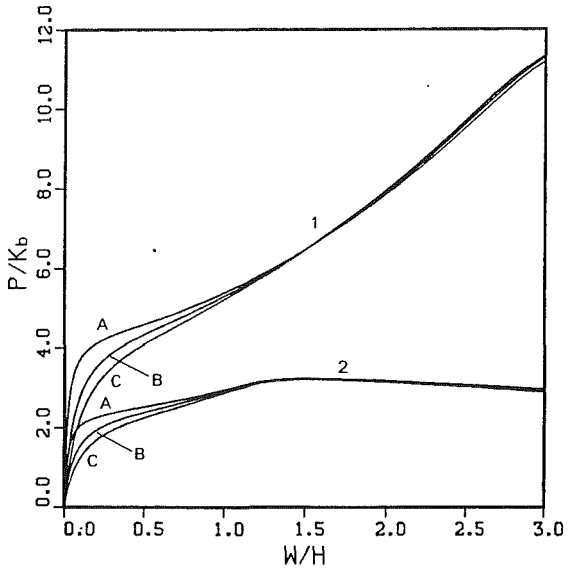


Fig. 6 The effect of small initial imperfections (thin plate)

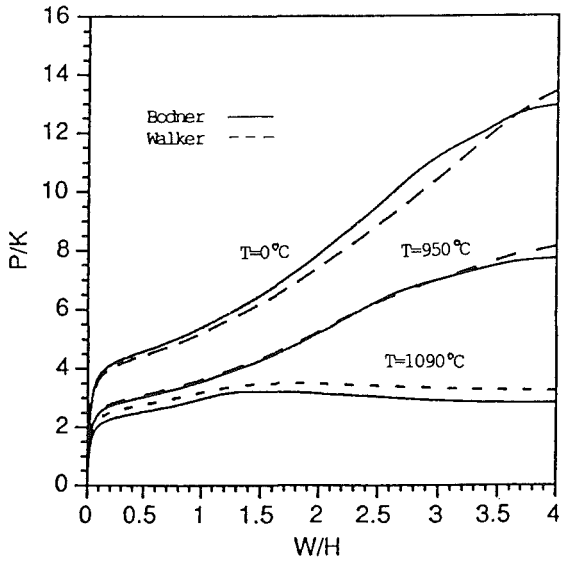


Fig. 4 Comparison of Bodner-Partom's and Walker's models

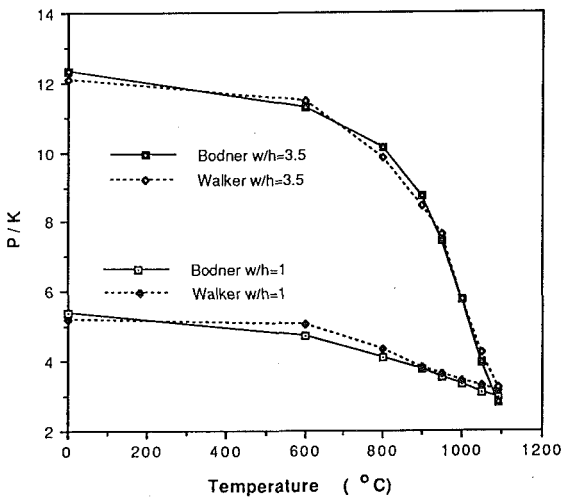


Fig. 5 Effect of temperature

midpoint of the plates are denoted by l, h, and δ, respectively. The boundary conditions of the plate are

$$w=0;\ M_{yy}=0;\ N_{xy}=0;\ v=0;\ \text{at } y=\frac{l}{2}$$

$$w=0;\ M_{yy}=0;\ N_{yy}=-p;\ N_{xy}=0;\ \text{at } y=-\frac{l}{2}$$

$$w=0;\ M_{xx}=0;\ N_{xx}=0;\ N_{xy}=0;\ \text{at } x=\pm\frac{l}{2}.$$

It is assumed that the plate is at uniform temperature. The total loading time, if not specified, is around 800 seconds with equal loading steps (approximately 80 steps). Figure 2 shows the buckling response at different temperatures using Bodner-Partom's material model. The ratio of the thickness to the length of the plate is 0.01. The horizontal coordinate is the nondimensional deflection of the midpoint of the plate w/h and the vertical coordinate is the nondimensional load, where $K_b=(\pi^2Eh^3/12l^2)$ and E is the Young's modulus at room temperature. The initial imperfection at midpoint of the plate (δ/h) is 0.02. Since the elastic modulus is slightly different for the two models (Bodner-Partom's and Walker's), a subscript is used with K to denote the modulus employed in the nondimensional process. Curve 1 in Fig. 2 represents the elastic response. Curves 2, 3, 4, 5, 6, 7, 8, 9 represent the elastoviscoplastic response at temperatures 0, 600, 800, 900, 950, 1000, 1050, and 1090°C, respectively. Since the plate is quite thin in this example, elastic buckling takes place first. As the load increases, the inelastic deformation develops. Note that curve 1 assumes elastic response throughout, while curve 2 allows for plastic response. From the figure, not only the load carrying capability at high temperature is lower, but plastic response occurs early on. Because primarily of plastic deformation, a limit point, beyond which the load carrying capability decreases, exists in the post-buckling region. On the figure, the limit point load for 1050°C and 1090°C can clearly be seen. For other curves (lower temperatures), it appears that a limit point exists but the corresponding w/h value is greater than four. Figure 3 is the same as Fig. 2 except that Walker's model is employed. On this figure, curve 1 represents elastic response and curves 2, 3, 4, 5, 6, 7 represent inelastic response for 0, 800, 950, 1000, 1050, and 1090°C, respectively. Figure 4 gives a comparison of the postbuckling curves between Bodner-Partom's and Walker's models. On this figure, the solid lines

Downloaded 03 May 2010 to 171.66.16.20. Redistribution subject to ASME license or copyright; see http://www.asme.org/terms/Terms_Use.cfm

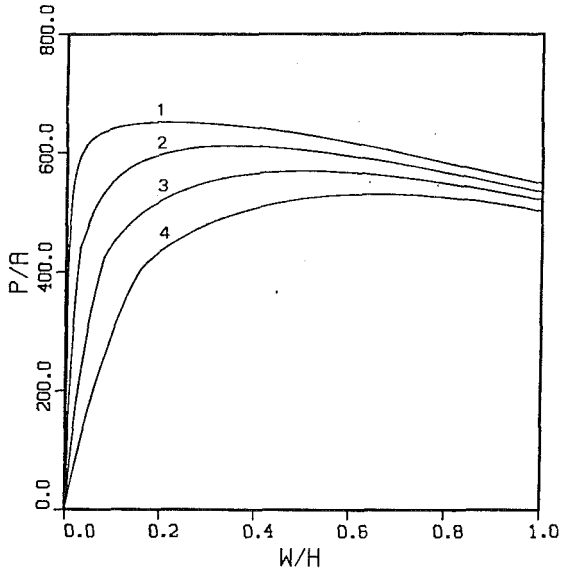


Fig. 7 The effect of small initial imperfections (thick plate)

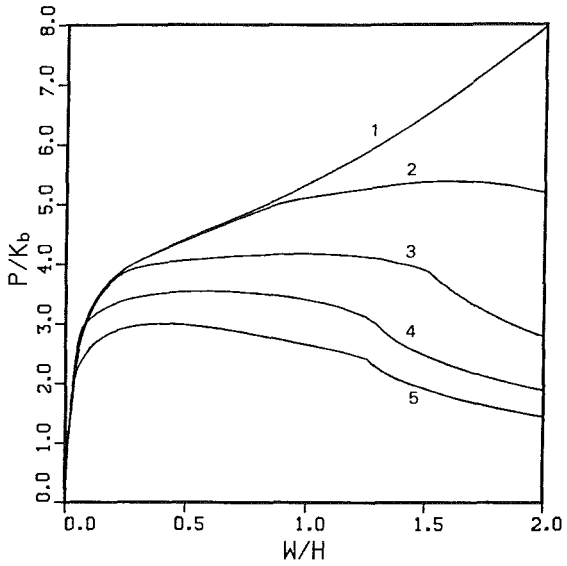


Fig. 8 The effect of plate thickness on the deflection response

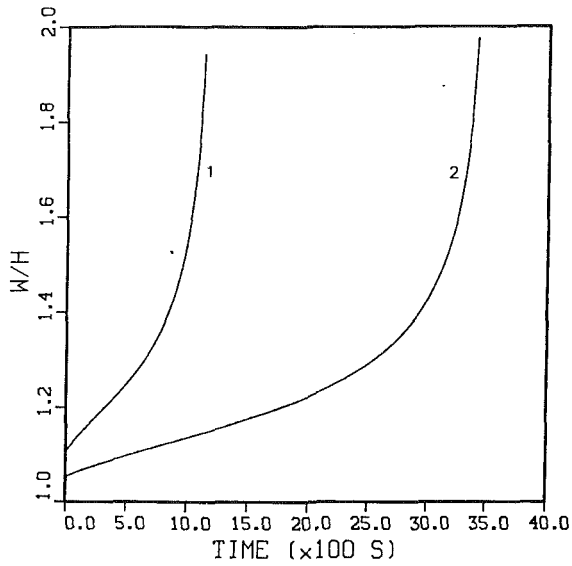


Fig. 9 The creep failure behavior of plates

represent Bodner's model and the dashed lines represent Walker's model. The same value for Young's modulus has been used in this comparison. It seems that at low temperatures, Bodner's model gives higher estimation of the load for the same deflection than Walker's. At 950°C, the two curves are quite close in most of the range considered. Figure 5 shows the temperature effect for both Bodner-Partom's and Walker's models at fixed deflections. Different curves here represent the nondimensional loads at different deflections. It can be seen that in the inelastic range ($w/h = 3.5$), the load drops significantly after 600°C. In the elastic range ($w/h = 1$), the change, when the temperature increases, is not as big as that in the inelastic range.

Figure 6 shows the effect of small initial imperfections for the thin plate $h/l = 0.01$. The first group of curves corresponds to room temperature. The second group of curves corresponds to a higher temperature (1090°C). Curves A, B, and C correspond to the cases with initial imperfections $\delta/h = 0.02$, 0.06, and 0.08, respectively. From the figure, the initial imperfections influence the elastic buckling load and the load carrying capability in a range of small deflections. However, this influence decreases quickly as the deflection increases in either low or high temperature cases. This means that failure (plastic) of thin plates is independent of small initial imperfections. Figure 7 gives the effect of small initial imperfections for a thicker plate. In this case, the thickness ratio (h/l) is 0.035. The values of δ/h for curves 1, 2, 3, and 4 are 0.0057, 0.0285, 0.857, and 0.2 respectively. The results show that thick plates are initial imperfection sensitive. In this example, the limit point stress in curve 4 is 18.6 percent smaller than that in curve 1. Figure 8 shows the response of plates with different thicknesses. The h/l values of curves 1, 2, 3, 4, and 5 are 0.01, 0.02, 0.025, 0.03, 0.035, respectively. The P/K_b value corresponding to the same deflection is lower for thicker plates, since K_b is cubic in the thickness. It is seen that, when the plate goes into the plastic range, a limit point will eventually exist. Interestingly, the curves are not smooth, which indicates that there exist mode changes. A mode change due to large deformation has been observed by Stein (1960).

With the unified constitutive equations, creep buckling or creep failure can be calculated. Figure 9 is an example of creep behavior of thin plates ($h/l = 0.01$) at high temperature (1090°C). The plate is loaded to a load level in 360 seconds and then the load is kept constant. The load level is defined as p/p_{cr}, where p_{cr} is the limit point load. The time spent in loading is not plotted on the figure, so the origin of the horizontal coordinate is the real start time of creep. The load levels for curve 1 and curve 2 are 0.9506 and 0.9335, which are higher than the buckling load and lower than the limit point load. From the figure, the slope of the curve is nearly constant in the first stage of creep and increases quickly in the second stage. When it is close to 1135 and 3435 seconds, the slope of the curve tends to be very large, which corresponds to failure.

Conclusions

Unified constitutive equations have been employed to study the elastoviscoplastic post-buckling behavior of plates. From the generated results, the following conclusions and observations may be listed:

(1) A limit point exists mainly because of elastoplastic material behavior. The limit point load is higher than the buckling load when the plate is thin.

(2) Both the buckling load and the limit point load decrease when temperature increases. The reduction of the limit point load is especially significant.

(3) The response curves for Bodner-Partom's model and Walker's model for the material employed, B1900+Hf, are

Downloaded 03 May 2010 to 171.66.16.20. Redistribution subject to ASME license or copyright; see http://www.asme.org/terms/Terms_Use.cfm

very close. Either one of the constitutive models, for this material, can be used in elastoviscoplastic buckling analysis.

(4) Thick plates (plastic behavior) are imperfection sensitive.

(5) Thin plates are not imperfection sensitive.

(6) The unified constitutive equations, as a viscoplastic material model, can be employed to calculate stability problems which include elastic, time-independent inelastic (plastic) and time-dependent inelastic (creep) deformations at elevated temperatures.

Acknowledgment

The work reported herein was supported by the NASA-Lewis Research Center under Grant NAG3-534. The financial support provided by NASA is gratefully acknowledged. The authors wish to thank Dr. Chris C. Chamis for his support, encouragement, and patience.

References

Bathe, K. J., 1982, *Finite Element Procedures in Engineering Analysis*, Prentice-Hall, Englewood Cliffs, NJ.

Bijlaard, P. P., 1949, "Theory and Tests on the Plastic Stability of Plates and Shells," *Journal of Aeronautical Sciences*, Vol. 9, pp. 529–541.

Chan, K. S., et al., 1984, "A Survey of Unified Constitutive Theories," NASA Contractor's Report, NASA CR 23925, Cleveland, OH.

Chia, Y., 1979, *Nonlinear Analysis of Plates*, McGraw-Hill Co., New York.

Crisfield, M. A., 1983, "An Arc-Length Method Including Line Searches and Accelerations," *International Journal of Numerical Methods in Engineering*, Vol. 19, pp. 1269–1289.

Handelman, G. H., and Prager, W., 1948, "Plastic Buckling of Rectangular Plates under Edge Thrusts," NACA TN 1530.

Hoff, J. N., 1973, "Creep Buckling of Plates and Shells," *Proceedings 13th International Congress of Applied Mechanics*, pp. 124–140.

Illyshin, A. A., 1947, "The Elastic Plastic Stability of Plates," NACA TM 1188.

James, G. H., et al., 1987, "An Experimental Comparison of Several Current Viscoplastic Constitutive Models at Elevated Temperature," ASME *Journal of Engineering Materials Technology*, Vol. 109, pp. 130–139.

Lindholm, U. S., et al., 1985, "Constitutive Modeling for Isotropic Materials (HOST)," NASA CR-174980, Cleveland, OH.

Miller, A. K., 1987, *Unified Constitutive Equations for Creep and Plasticity*, Elsevier, New York.

Neale, K. W., 1975, "Effect of Imperfections on the Plastic Buckling of Rectangular Plates," ASME JOURNAL OF APPLIED MECHANICS, Vol. 42, pp. 115–120.

Needleman, A., and Tvergaard, V., 1976, "An Analysis of the Imperfection Sensitivity of Square Elastic-Plastic Plates under Axial Compression," *International Journal of Solids and Structures*, Vol. 12, pp. 185–201.

Paley, M., and Aboudi, J., 1991, "Viscoplastic Bifurcation Buckling of Plates," *AIAA Journal*, Vol. 29, pp. 627–632.

Pearson, C. E., 1950, "Bifurcation Criterion and Plastic Buckling of Plates and Columns," *Journal of Aeronautical Sciences*, Vol. 7, pp. 417–424.

Pride, R. A., and Heimerl, G. J., 1949, "Plastic Buckling of Simply-Supported Compressed Plates," NACA TN 1817.

Shrivastava, S. C., 1979, "Inelastic Buckling of Plates Including Shear Effects," *International Journal Solids and Structures*, Vol. 15, pp. 567–575.

Song, Y., 1991, "Thermo-elastoviscoplastic Postbuckling Behavior of Shell-like Structures," Ph.D. Dissertation, Aerospace Engineering, Georgia Institute of Technology, Atlanta, GA.

Stein M., 1960, "Behavior of Buckled Rectangular Plates," *Journal of the Engineering Mechanics Division*, ASCE, Vol. 86, pp. 59–76.

Stowell, E. Z., 1948, "A Unified Theory of Plastic Buckling of Columns and Plates," NACA TN 1156.

Tanaka, T. G., and Miller, A. K., 1988, "Development of a Method for Integrating Time-Dependent Constitutive Equations with Large, Small or Negative Strain Rate Sensitivity," *International Journal of Numerical Methods in Engineering*, Vol. 26, pp. 2457–2485.

Tvergaard, V., 1979, "Creep Buckling of Rectangular Plates under Axial Compression," *International Journal of Solids and Structures*, Vol. 15, pp. 441–456.

Tvergaard, V., 1985, "Rate-Sensitivity in Elastic-Plastic Panel Buckling," *Aspects of the Analysis of Plate Structures*, D. J. Sawe et al., eds., Clarendon Press, Oxford, pp. 293–308.

Downloaded 03 May 2010 to 171.66.16.20. Redistribution subject to ASME license or copyright; see http://www.asme.org/terms/Terms_Use.cfm

The Mechanics of Ideal Forming

K. Chung
Assoc. Mem. ASME.

O. Richmond

Alcoa Laboratories,
Alcoa Technical Center,
Alcoa Center, PA 15069

In this paper, the mechanics of ideal forming theory are summarized for general, three-dimensional, nonsteady processes. This theory has been developed for the initial stages of designing deformation processes. The objectives is to directly determine configurations, both initial and intermediate, that are required to ideally form a specified final shape. In the proposed theory, material elements are prescribed to deform along minimum plastic work paths, assuming that the materials have optimum formabilities in such paths. Then, the ideal forming processes are obtained so as to have the most uniform strain distributions in final products without shear tractions. As solutions, the theory provides the evolution of intermediate shapes of products and external forces as well as optimum strain distributions. Since the requirement of ideal forming to follow minimum work paths involves an over determination of the field equations, the theory places constraints on constitutive and boundary conditions. For example, tool interfaces must be frictionless and yield conditions must have vertices to achieve self-equilibrating three-dimensional deformations in most cases. Despite these constraints, the theory is believed to provide a useful starting point for deformation process design.

1 Introduction

Conventional practices for optimizing forming processes are based on trial and error during which various combinations of process parameters are tried out experimentally and analytically. Because of the indirect nature of the experimental and analytical methods, a significant number of iterations are usually required before optimum processes are obtained. In order to overcome the indirect nature of these analytical methods, a direct design theory for obtaining ideal (or optimum) forming processes has been developed. The objective is to directly determine ideal configurations for both the initial and intermediate stages in order to form a specified final shape. This theory provides direct information regarding optimum process parameters in the initial design stage.

A major difference between design theory and analytical theory is that some aspects of the deformation of material elements are prescribed in advance in design theory. In the present case, material elements are prescribed to deform along minimum plastic work paths, assuming that materials have optimum formabilities in such paths. Then, ideal forming processes are obtained so as to have the most uniform strain distributions in final products without having shear tractions at surfaces or body forces in the interior. As solutions, besides the optimum strain distributions, the design theory provides intermediate shapes and boundary traction histories, which are the ideal forming process parameters. When applied for sheet forming, the theory also provides optimum initial blank shape as part of the solution.

In this paper, the mechanics of ideal forming theory are summarized for general, three-dimensional, nonsteady forming processes: kinematics of minimum work paths, constitutive relations based on minimum work paths, formulations to achieve optimum strain distributions, theory for evolution of intermediate shapes, and external forces for achieving these shapes. For illustration purposes, sample solutions are shown for three-dimensional membrane sheet forming. Discussions are limited to rigid-(visco)plastic materials.

2 Minimum Plastic Work Paths

It has been found that the minimum work path is achieved if materials deform in such a way as to satisfy two conditions (Nadai, 1963; Hill, 1986): first, the set of three principal axes of stretching is fixed with respect to the material; second, the logarithms of the stretches remain in a fixed ratio. The fixed material lines in the first condition may be chosen arbitrarily for isotropic materials, but they are more restrictive for anisotropic materials.

These two conditions are valid for any convex yield condition with isotropic hardening. However, Chung and Richmond (1992a) have shown that both of the conditions are required only when the yield surface is smooth enough to have a unique normal direction; in such a case, the minimum path is uniquely defined. When there is a pointed vertex on the yield surface at a desired stress state, no unique normal direction is defined at the vertex, so that only some parts of the two conditions are required; in such a case, multiple minimum work paths are possible. For example, for the Tresca yield condition, only

Contributed by the Applied Mechanics Division of THE AMERICAN SOCIETY OF MECHANICAL ENGINEERS for presentation at the ASME Winter Annual Meeting, New Orleans, LA, Nov. 28–Dec. 3, 1993.

Discussion on this paper should be addressed to the Technical Editor, Professor Lewis T. Wheeler, Department of Mechanical Engineering, University of Houston, Houston, TX 77204-4792, and will be accepted until four months after final publication of the paper itself in the ASME JOURNAL OF APPLIED MECHANICS.

Manuscript received by the ASME Applied Mechanics Division, Dec. 26, 1991; final revision, Mar. 15, 1993. Associate Technical Editor: R. M. McMeeking.

Paper No. 93-WA/APM-19.

Copyright © 1994 by ASME
Downloaded 03 May 2010 to 171.66.16.20. Redistribution subject to ASME license or copyright; see http://www.asme.org/terms/Terms_Use.cfm

the axis having the absolute maximum stretch is required to be fixed with respect to the material, and there are no other major additional conditions[1].

The minimum plastic work paths can be expressed mathematically. The deformation gradient tensor $\mathbf{F}$ describes a deformation between a final shape and an initial shape. $\mathbf{F}$ is defined, by polar decomposition, as

$$\mathbf{F}(t)=\mathbf{R}(t)\cdot\mathbf{U}(t) \tag{1}$$

where $\mathbf{U}$ is the right stretch tensor which is symmetric, $\mathbf{R}$ is the orthogonal rotation tensor, and t is time. The three principal directions of $\mathbf{U}$, because of its Lagrangian nature, refer to three material lines which are perpendicular to each other in the original configuration. Equation (1) represents a physical deformation process which is composed of an initial stretch of principal material lines, $\mathbf{U}$, followed by a rigid-body rotation, $\mathbf{R}$. It is a description of the total amount of deformation and the total rigid-body rotation required by two prescribed geometries, but the history of deformation (or deformation path) is only implicit.

When decomposed into principal values and directions, $\mathbf{U}$ and the logarithmic strain tensor $\boldsymbol{\epsilon}_L$ are defined as

$$\mathbf{U}(t)=\mathbf{Q}(t)\cdot\boldsymbol{\lambda}(t)\cdot\mathbf{Q}^t(t),\quad \boldsymbol{\epsilon}_L(t)=\mathbf{Q}(t)\cdot\boldsymbol{\xi}(t)\cdot\mathbf{Q}^t(t) \tag{2}$$

where

$$\lambda_i=\frac{l_i}{l_{io}},\quad \xi_i=\ln(\lambda_i). \tag{3}$$

In Eq. (2), $\boldsymbol{\lambda}$ and $\boldsymbol{\xi}$ are diagonal tensors consisting of principal values (λ_i and ξ_i), and $\mathbf{Q}$ is an orthogonal rotation tensor consisting of the principal directions of $\mathbf{U}$. The superscript t stands for transpose. In Eq. (3), l_i is the length of the principal material line for $i=1, 2, 3$; the subscript "io" and "i" stand for the values at the initial and current time, respectively. Note that $\boldsymbol{\epsilon}_L$ is also a Lagrangian quantity.

When the same principal material lines are kept constant during deformation, the principal material lines of $\dot{\mathbf{U}}$ and $\dot{\boldsymbol{\epsilon}}_L$ coincide with those of $\mathbf{U}$ obtained for a final shape at a time t_f; i.e.,

$$\dot{\mathbf{U}}(t)=\mathbf{Q}(t_f)\cdot\dot{\boldsymbol{\lambda}}(t)\cdot\mathbf{Q}^t(t_f),$$

$$\mathbf{U}(t)=\mathbf{Q}(t_f)\cdot\boldsymbol{\lambda}(t)\cdot\mathbf{Q}^t(t_f)\quad 0<t<t_f \tag{4}$$

$$\dot{\boldsymbol{\epsilon}}(t)=\mathbf{Q}(t_f)\cdot\dot{\boldsymbol{\xi}}(t)\cdot\mathbf{Q}^t(t_f),$$

$$\boldsymbol{\epsilon}_L(t)=\mathbf{Q}(t_f)\cdot\boldsymbol{\xi}(t)\cdot\mathbf{Q}^t(t_f)\quad 0<t<t_f \tag{5}$$

Let us consider a strain rate $\dot{\boldsymbol{\epsilon}}$ which is defined as

$$\dot{\boldsymbol{\epsilon}}=\mathbf{R}^t\cdot\mathbf{D}\cdot\mathbf{R}=(\dot{\mathbf{U}}\cdot\mathbf{U}^{-1})_s \tag{6}$$

where $\mathbf{D}$ is the rate of deformation tensor and the subscript s stands for the symmetric part of a tensor. The quantity $\dot{\boldsymbol{\epsilon}}$ is considered to be the value of $\mathbf{D}$ measured with respect to the coordinate system which rotates by $\mathbf{R}(t)$, so that the values are invariant with respect to $\mathbf{R}$. For this reason, $\dot{\boldsymbol{\epsilon}}$ is called the "rotationless" strain rate (Stören and Rice, 1975). When the same principal material lines are kept constant during deformation, the principal material lines of $\dot{\mathbf{U}}$ and $\mathbf{U}$ coincide as shown in Eq. (4). Consequently, in such cases the principal directions of $\dot{\boldsymbol{\epsilon}}$ are stationary and are aligned with the principal material lines of $\mathbf{U}(t_f)$, regardless of arbitrary rotation $\mathbf{R}(t)$, while the principal directions of $\mathbf{D}$ vary continuously; i.e.,

$$\dot{\boldsymbol{\epsilon}}(t)=\dot{\boldsymbol{\epsilon}}_L(t)=\mathbf{Q}(t_f)\cdot\dot{\boldsymbol{\xi}}(t)\cdot\mathbf{Q}^t(t_f). \tag{7}$$

In fact, when the same principal material lines are kept constant, $\dot{\boldsymbol{\epsilon}}$ also becomes a Lagrangian quantity whose principal directions refer to the fixed principal material lines and whose principal values are the logarithmic (or true) strain rates of the principal material lines.

The minimum work path for a smooth yield function is achieved if deformation follows the description

$$\dot{\boldsymbol{\epsilon}}(t)=\dot{\alpha}(t)\cdot\boldsymbol{\epsilon}_L(t_f)=\mathbf{Q}(t_f)\cdot(\dot{\alpha}(t)\cdot\boldsymbol{\xi}(t_f))\cdot\mathbf{Q}^t(t_f),$$

$$\boldsymbol{\epsilon}(t)=\mathbf{Q}(t_f)\cdot(\alpha(t)\cdot\boldsymbol{\xi}(t_f))\cdot\mathbf{Q}^t(t_f), \tag{8}$$

or, equivalently,

$$\mathbf{U}(t)=\mathbf{Q}(t_f)\cdot\boldsymbol{\lambda}(t)\cdot\mathbf{Q}^t(t_f) \tag{9}$$

where

$$\lambda_i(t)=\lambda_i^{\alpha(t)}(t_f). \tag{10}$$

In Eqs. (8) and (10), $\alpha(t)$ is a function of time t, satisfying

$$\int_0^{t_f}\dot{\alpha}dt=1,$$

and $\dot{\alpha}$ is always positive. In Eqs. (8) and (9), the principal material lines are fixed, and the ratios of the principal true strain rates are fixed during deformation. Note that the condition $\dot{\boldsymbol{\epsilon}}=\dot{\alpha}(t)\,\boldsymbol{\epsilon}$ is not sufficient to describe the minimum work path because $\mathbf{Q}$ can be time dependent. Also, the condition in Eq. (7) alone is not sufficient because the condition of fixed ratios of the principal true strain rates is not imposed. The minimum work path described in Eqs. (8) and (9) allows arbitrary rotations, $\mathbf{R}(t)$, of the principal material lines in Eq. (1). Also, this is not inconsistent with the concept of incompressible deformations usually assumed in rigid-plastic materials.

Of these two equivalent representations of minimum work paths, Eq. (8) is useful for deriving the deformation theory of plasticity described in Section 3, and Eq. (9) is convenient for discussing the geometric compatibility of intermediate shapes in Section 5. When a yield surface is smooth so that normal directions are uniquely defined on the surface, $\boldsymbol{\epsilon}(t)$ in Eq. (9) and $\mathbf{U}(t)$ in Eq. (9) are fully prescribed for a given $\alpha(t)$.

When a yield surface has a pointed vertex at a desired stress state, $\boldsymbol{\epsilon}(t)$ and $\mathbf{U}(t)$ are not prescribed completely. With a Tresca yield condition, for example $\mathbf{Q}(t)$ is prescribed in such a way that the principal material line having the absolute maximum principal stretch is fixed; therefore, among the three degrees-of-freedom of $\mathbf{Q}$, which describe rotations in a three-dimensional space, only one is prescribed. For principal values, the condition in Eq. (10) is applied only for the absolute maximum principal stretch, and the only requirement on the other two principal values is

$$|d(\ln\lambda_i)/dt| \text{ or } |d(\ln\lambda_j)/dt| \le |d(\ln\lambda_{\max})/dt| \tag{11}$$

where i and j refer to the other two principal values. With the condition in Eq. (11), the absolute maximum stretch is guaranteed to occur along the material line prescribed in $\mathbf{Q}$.

3 Deformation Theory Based on Minimum Plastic Work Paths

When deformation paths of materials are specified, the plastic work becomes dependent only on total deformation. In such cases, a constitutive law for the deformation theory can be derived from the flow theory using the assumed deformation path. Here, a deformation theory based on minimum plastic work paths is derived.

The effective yield stress, $\bar{\sigma}$, and the associated effective strain rate, $\bar{\dot{\delta}}$, are defined in the Cauchy stress space, $\boldsymbol{\sigma}$, and in the rate of plastic deformation space, $\mathbf{D}$, respectively. Since $\bar{\sigma}$ and $\bar{\dot{\delta}}$ are materially embedded properties, they are invariant with respect to any rotation. Therefore, they can be written in terms of $\dot{\boldsymbol{\epsilon}}$ and its conjugate stress, $\boldsymbol{\tau}$ (defined as $\boldsymbol{\tau}=\mathbf{R}^t\cdot\boldsymbol{\sigma}\cdot\mathbf{R}$), simply by replacing $\mathbf{D}$ and $\boldsymbol{\sigma}$ with $\dot{\boldsymbol{\epsilon}}$ and $\boldsymbol{\tau}$, respectively; i.e.,

$$\bar{\sigma}(\boldsymbol{\sigma})=\bar{\tau}(\boldsymbol{\tau}),\quad \bar{\dot{\delta}}(\mathbf{D})=\bar{\dot{\epsilon}}(\dot{\boldsymbol{\epsilon}}) \tag{12}$$

where $\bar{\tau}$ and $\bar{\dot{\epsilon}}$ are the effective stress and the associated effective strain rate defined in the $\boldsymbol{\tau}$ and $\dot{\boldsymbol{\epsilon}}$ spaces, respectively. Equation (12) expresses "objectivity," but not "isotropy." The definitions of $\bar{\tau}$ and $\bar{\dot{\epsilon}}$ are considered first-order homogeneous functions, and isotropic hardening is assumed.

[1] There is one minor additional requirement, and that is discussed in Eq. (11).

Downloaded 03 May 2010 to 171.66.16.20. Redistribution subject to ASME license or copyright; see http://www.asme.org/terms/Terms_Use.cfm

By applying the minimum work path in Eq. (8), the minimum effective strain is obtained as

$$\bar{\epsilon}(t_f) = \int_0^{t_f} \dot{\bar{\epsilon}}(\dot{\epsilon})dt = \bar{\epsilon}(\epsilon_L)\int_0^{t_f} \dot{\alpha}dt = \bar{\epsilon}(\epsilon_L(t_f)) \tag{13}$$

if materials harden isotropically. Equation (13) shows that the total effective strain $\bar{\epsilon}$ in the minimum work path is obtained from $d\bar{\epsilon}/dt$ in Eq. (12) simply by replacing $\dot{\epsilon}$ with $\epsilon_L(t_f)$. Equation (13) is equivalent to

$$d\bar{\epsilon}/dt = \dot{\alpha}(t)\bullet\bar{\epsilon}(t_f), \quad \bar{\epsilon}(t) = \alpha(t)\bullet\bar{\epsilon}(t_f). \tag{14}$$

The deformation theory is derived by applying the relations in Eqs. (8) and (14) to the flow theory.

The constitutive equation for the flow theory of incompressible rigid-plastic materials is obtained from the normality rule, which is

$$\mathbf{D} = \dot{\bar{\delta}}\frac{\partial\bar{\sigma}(\sigma)}{\partial\sigma} = \dot{\bar{\delta}}\frac{\partial\bar{\sigma}'(\sigma')}{\partial\sigma'}, \quad \sigma' = \bar{\sigma}'\frac{\partial\dot{\bar{\delta}}}{\partial\mathbf{D}} \tag{15}$$

where σ' is the deviatoric part of σ. By "objectivity," Eqs. (15) are equivalent to

$$\dot{\epsilon} = \dot{\bar{\epsilon}}\frac{\partial\bar{\tau}}{\partial\tau} = \dot{\bar{\epsilon}}\frac{\partial\bar{\tau}}{\partial\tau'}, \quad \tau' = \bar{\tau}'\frac{\partial\dot{\bar{\epsilon}}}{\partial\dot{\epsilon}} \tag{16}$$

where τ' is the deviatoric part of τ.

Explicit representations of the constitutive relations for deformation plasticity, which are valid when materials deform in minimum work paths, are obtained from Eq. (16) by applying Eqs. (8) and (14); i.e.,

$$\epsilon = \bar{\epsilon}\frac{\partial\bar{\tau}}{\partial\tau} = \bar{\epsilon}\frac{\partial\bar{\tau}'}{\partial\tau'}, \quad \tau' = \bar{\tau}'\frac{\partial\bar{\epsilon}}{\partial\epsilon} \tag{17}$$

or

$$\mathbf{R}\bullet\frac{\epsilon}{\bar{\epsilon}}\bullet\mathbf{R}^t = \frac{\partial\bar{\sigma}}{\partial\sigma} = \frac{\partial\bar{\sigma}'}{\partial\sigma'}, \quad \sigma' = \mathbf{R}\bullet\bar{\tau}'\frac{\partial\bar{\epsilon}}{\partial\epsilon}\bullet\mathbf{R}^t. \tag{18}$$

The relations in Eqs. (17) and (18) have been found valid for faceted yield surfaces as well as smooth yield surfaces (Chung and Richmond, 1993). τ' is in a fixed direction with respect to the material lines when the material hardens isotropically, while σ' is in an arbitrary direction depending on $\mathbf{R}$: proportional loading of τ'. τ is obtained by adding arbitrary hydrostatic pressure to τ', so that τ is not in the fixed direction.

Equations (17) and (18) represent constitutive relations for deformation theory of plasticity when minimum work paths are assumed. Not only do these equations satisfy the objectivity rule, but also $\mathbf{R}$ is arbitrary, which allows arbitrary rigid-body rotations during deformation. The equations describe a deformation theory for large deformations and arbitrary anisotropic materials which harden isotropically. Even though the original deformation theory proposed by Hencky (1924) for Mises materials and small deformations is path independent, the equation is known to comply with the flow theory only for proportional loading of σ'. Since τ' is proportional in the theory based on minimum work path, while σ' is arbitrary, there is a difference between the equations of the two deformation theories. Also the new deformation theory is based on an implicit path, while the original theory is independent of path. This is the major difference between these two theories.

4 Optimum Inhomogeneous Deformation

In the previous two sections, the ways to describe the deformation of a material element along the minimum work path and the constitutive relation under such a deformation have been discussed, assuming that the total stretch, $\mathbf{U}(t_f)$, is provided. If deformation from an initial to a final configuration can be homogeneous, then the ideal stretch $\mathbf{U}(t_f)$ is determined directly from those configurations. If inhomogeneous deformation is required, then the final configuration of material elements, $\mathbf{x}$, is prescribed and the initial configuration, $\mathbf{X}$, is obtained so as to have the most uniform deformation in the final configuration without shear tractions at the boundaries or body forces inside. In fact, it has been found that such an optimum deformation distribution is obtained when the plastic work is a relative maximum (Chung and Richmond, 1992b). The optimum $\mathbf{U}(t_f)$ is then calculated from $\mathbf{x}$ and $\mathbf{X}$. The procedure is discussed in this section.

The plastic work, W, for a process involving inhomogeneous deformation is given by

$$W = \int\left(\int \mathbf{f}\bullet d\mathbf{u}\right)ds + \int\left(\int \rho\mathbf{b}\bullet d\mathbf{u}\right)dV \tag{19}$$

$$= \int\left(\int (\operatorname{div}\sigma + \rho\mathbf{b})\bullet d\mathbf{u}\right)dV + \int\left(\int \sigma\bullet\mathbf{D}\,dt\right)dV \tag{20}$$

where $\mathbf{f}$, $\mathbf{b}$, and $\mathbf{u}$ are the surface traction per unit area, body force per unit mass, and displacement, respectively. Also, ρ, S, and V are the mass density, surface area, and volume at time t. When materials are in a static condition, the first term in Eq. (20) vanishes, so that the following relations are obtained for isochoric deformations:

$$W = \int\left(\int \sigma\bullet\mathbf{D}\,dt\right)dV_o = \int\left(\int \bar{\sigma}\,d\bar{\epsilon}\right)dV_o \tag{21}$$

$$= \int\left(\int \mathbf{f}\bullet d\mathbf{u}\right)dS + \int\left(\int \rho\mathbf{b}\bullet d\mathbf{u}\right)dV_o \tag{22}$$

where V_o is the initial volume of incompressible materials.

In Eqs. (21) and (22), the global plastic work, W, depends on the deformation histories of the individual material elements as well as on the displacements $\mathbf{u}$, of the individual elements. When the deformation history of each material element is prescribed, however, the plastic work of an element is determined by $\mathbf{u}$ only, i.e., by $\bar{\epsilon}(\mathbf{u})$.[2] Therefore, the global plastic work, W, depends on displacements only; i.e.,

$$W = W(\mathbf{u}) \quad \text{or} \quad W = W(\mathbf{X}) \tag{23}$$

when $\mathbf{x}$ is prescribed.

The optimum deformation distribution defined above for ideal forming has been found to have the global plastic work in a relative maximum value—an extreme value. When a deformation path is prescribed for each material element, a necessary condition for the global plastic work, W, to be an extreme value is

$$\frac{dW(\mathbf{u})}{d\mathbf{u}} = \mathbf{0} \quad \text{or} \quad \frac{dW(\mathbf{X})}{d\mathbf{X}} = \mathbf{0}. \tag{24}$$

In the ideal forming theory, the condition in Eq. (24) is formulated for a final shape at $t = t_f$, with each element undergoing a minimum work path. Among the multiple solutions of Eq. (24), the deformation which has a relative maximum value for W (or equivalently, which has the most uniform strain distribution) is chosen as the optimum solution $\mathbf{u}(\mathbf{X}, t_f)$. When applied for membrane sheet-forming, the solution $\mathbf{u}(\mathbf{X}, t_f)$ provides an optimum initial blank shape. A sample solution obtained for an isotropic aluminum membrane sheet is shown in Fig. 1 where (a) shows the optimum initial blank shape calculated when the final rectangular cup (f) is prescribed.

The optimum strain distribution, $\mathbf{U}(t_f)$, is easily derived from this $\mathbf{u}(\mathbf{X}, t_f)$, considering the following relation:

$$\mathbf{U}^2(\mathbf{X}, t_f) = \left\{\mathbf{I} + \left(\frac{\partial\mathbf{u}}{\partial\mathbf{X}}\right) + \left(\frac{\partial\mathbf{u}}{\partial\mathbf{X}}\right)^t + \left(\frac{\partial\mathbf{u}}{\partial\mathbf{X}}\right)^t\bullet\left(\frac{\partial\mathbf{u}}{\partial\mathbf{X}}\right)\right\} \tag{25}$$

where $\mathbf{I}$ is an identity tensor.

[2] In a strict sense, $\bar{\epsilon}$ is a functional of $\mathbf{u}$ as partially suggested by the relationship in Eq. (25). However, after shape functions are introduced as practiced in the finite element method, $\bar{\epsilon}$ becomes a function of $\mathbf{u}$.

Downloaded 03 May 2010 to 171.66.16.20. Redistribution subject to ASME license or copyright; see http://www.asme.org/terms/Terms_Use.cfm

5 Intermediate Shapes and Geometrical Compatibility Conditions

In ideal forming theory, material elements are prescribed to deform along minimum work paths individually. For smooth yield functions this implies that the right stretch tensors, $\mathbf{U}(\mathbf{X}, t)$, of material elements are prescribed by Eq. (9). Then, optimum deformation distributions in final products, $\mathbf{U}(\mathbf{X}, t_f)$, which are also necessary to describe $\mathbf{U}(\mathbf{X}, t)$, are obtained from the condition in Eq. (24). However, minimum work paths might not be possible for material elements without violating compatibility of displacement in intermediate configurations. That is, in what is called geometric incompatibility, the minimum work path of each material element might interfere with the paths of neighboring elements. In fact, the plastic work, W, in Eq. (23) was obtained mathematically, but without considering geometric compatibility. The compatibility of intermediate shapes when material elements deform in minimum work paths is discussed in this section. It will be shown that rotation distributions, $\mathbf{R}(\mathbf{X}, t)$, are obtained by considering compatibility, so that $\mathbf{F}(\mathbf{X}, t)$ is completely determined for ideal forming. Then, the evolution of intermediate shapes is obtained from $\mathbf{F}(\mathbf{X}, t)$ by integrating it.

The conditions for intermediate shapes $\mathbf{x}(\mathbf{X}, t)$ to be geometrically compatible are obtained from the condition for the deformation gradient tensor, $\mathbf{F}$, to be integrable and to have a continuous $\mathbf{x}(\mathbf{X}, t)$, where $\mathbf{F}$ is defined as

$$\mathbf{F}(\mathbf{X}, t) = \frac{\partial \mathbf{x}}{\partial \mathbf{X}} = \mathbf{R}(\mathbf{X}, t) \cdot \mathbf{U}(\mathbf{X}, t). \tag{26}$$

Here, $\mathbf{F}$, whose determinant is positive, is assumed to be continuous. These assumptions guarantee smooth mapping between $\mathbf{x}$ and $\mathbf{X}$ without sharp points, edges, cuttings. From the definition in Eq. (26), the integrability conditions are obtained as

$$H_1 = \frac{\partial F_{11}}{\partial X_2} - \frac{\partial F_{12}}{\partial X_1} = 0, \quad H_2 = \frac{\partial F_{12}}{\partial X_3} - \frac{\partial F_{13}}{\partial X_2} = 0,$$
$$H_3 = \frac{\partial F_{13}}{\partial X_1} - \frac{\partial F_{11}}{\partial X_3} = 0 \quad \text{for } x_1(\mathbf{X}) \tag{27}$$

$$H_4 = \frac{\partial F_{21}}{\partial X_2} - \frac{\partial F_{22}}{\partial X_1} = 0, \quad H_5 = \frac{\partial F_{22}}{\partial X_3} - \frac{\partial F_{23}}{\partial X_2} = 0,$$
$$H_6 = \frac{\partial F_{23}}{\partial X_1} - \frac{\partial F_{21}}{\partial X_3} = 0 \quad \text{for } x_2(\mathbf{X}) \tag{28}$$

$$H_7 = \frac{\partial F_{31}}{\partial X_2} - \frac{\partial F_{32}}{\partial X_1} = 0, \quad H_8 = \frac{\partial F_{32}}{\partial X_3} - \frac{\partial F_{33}}{\partial X_2} = 0,$$
$$H_9 = \frac{\partial F_{33}}{\partial X_1} - \frac{\partial F_{31}}{\partial X_3} = 0 \quad \text{for } x_3(\mathbf{X}) \tag{29}$$

using the Cartesian coordinate system, or equivalently,

$$\nabla \times \mathbf{F} = \mathbf{0}. \tag{30}$$

There are three conditions for each component $x_i(\mathbf{X})$ in these equations. However, these three conditions are dependent; i.e.,

$$-\frac{\partial H_1}{\partial X_3} = \frac{\partial H_2}{\partial X_1} + \frac{\partial H_3}{\partial X_2} \quad \text{for } x_1(\mathbf{X}) \tag{31}$$

$$-\frac{\partial H_4}{\partial X_3} = \frac{\partial H_5}{\partial X_1} + \frac{\partial H_6}{\partial X_2} \quad \text{for } x_2(\mathbf{X}) \tag{32}$$

$$-\frac{\partial H_7}{\partial X_3} = \frac{\partial H_8}{\partial X_1} + \frac{\partial H_9}{\partial X_2} \quad \text{for } x_3(\mathbf{X}) \tag{33}$$

Therefore, there are two independent conditions for each component $x_i(\mathbf{X})$, and there are six conditions as a whole for geometric compatibility.

In Eq. (26), the components of the deformation gradient tensor for intermediate shape are made of $\mathbf{R}(\mathbf{X}, t)$ and $\mathbf{U}(\mathbf{X}, t)$ such that

$$F_{ij}(\mathbf{X}, t) = F_{ij}(\theta_k(\mathbf{X}, t), \phi_k(\mathbf{X}, t), \lambda_k(\mathbf{X}, t)), \tag{34}$$

where θ_k and ϕ_k refer to three independent rotation angles defined in $\mathbf{R}(\mathbf{X}, t)$ and the principal directions of $\mathbf{U}(\mathbf{X}, t)$, respectively, and λ_k are three principal values of $\mathbf{U}(\mathbf{X}, t)$. In Eq. (34), nine components F_{ij} are determined by nine independent variables, while there are six compatibility conditions for F_{ij} to satisfy. Therefore, three among nine independent variables might be prescribed in advance at every moment. Then six compatibility conditions will determine the other six variables, which satisfy geometric compatibility. For isochoric deformation, the condition $(\det(\mathbf{F}) = \lambda_1\lambda_2\lambda_3 = 1)$ is required in addition to those six compatibility conditions: therefore, only two variables may be prescribed.

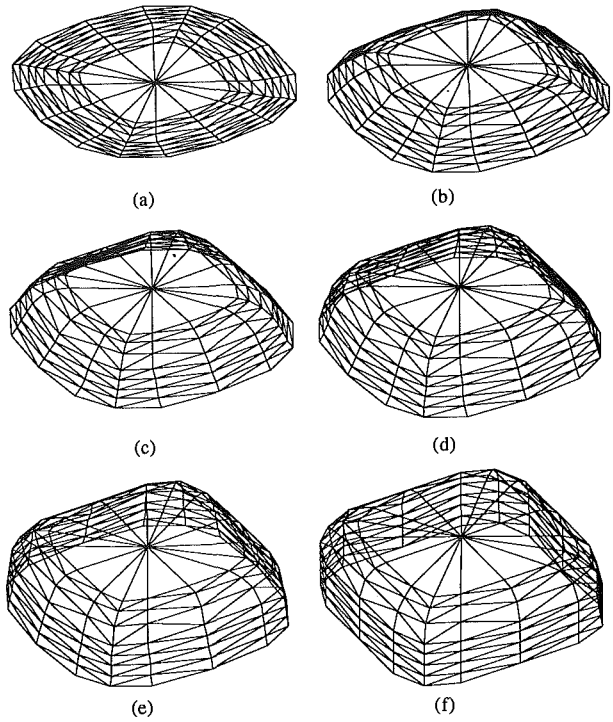


Fig. 1 *(a)* Initial cutout shape; *(b)*-*(e)* intermediate shapes at 20 percent, 40 percent, 60 percent, and 80 percent completion, respectively; *(f)* final rectangular cup with round corners

5.1 Three-Dimensional Bulk Forming. If compatibility conditions are considered for materials having smooth yield functions, six variables defining $\mathbf{U}(\mathbf{X}, t)$ are completely prescribed for intermediate configurations; i.e., for a given $\alpha(t)$. Note that $\alpha(t)$ is assumed to be uniform for all material elements in order to ensure that most uniform strain distribution even for intermediate configurations. Therefore, $\mathbf{F}(\mathbf{X}, t)$ are overly constrained, and intermediate shapes are not compatible in general.

If the Tresca yield condition is considered, the absolute maximum principal stretch $\lambda_{\max}(\mathbf{X}, t)$ and the associated principal material line $\phi_{\max}(\mathbf{X}, t)$ are prescribed for the intermediate shape; therefore, geometric compatibility should be achievable in most cases. However, attention must be paid to nonabsolute maximum principal stretches, $\lambda_i(\mathbf{X}, t)$, because they should also satisfy the condition described in Eq. (11).

5.2 Three-Dimensional Membrane Sheet-Forming. In the membrane sheet-forming process, consider for simplicity the case when an initial configuration is flat as shown in Fig. 1. Also intermediate and final configurations of the sheet are in a three-dimensional space; i.e.,

Downloaded 03 May 2010 to 171.66.16.20. Redistribution subject to ASME license or copyright; see http://www.asme.org/terms/Terms_Use.cfm

$$x_{i=1,2,3} = x_i(X_1, X_2, t) \tag{35}$$

where $\mathbf{x} = (x_1, x_2, x_3)$ and $\mathbf{X} = (X_1, X_2, X_3 = 0)$ with respect to the Cartesian coordinate system fixed on the initial flat surface. From Eq. (35), $F_{i3} = 0$, so that $\mathbf{F}$ has only six nonvanishing components. The compatibility conditions in Eqs. (27)–(29) provide only three conditions; i.e.,

$$H_1 = 0, \quad H_4 = 0, \quad H_7 = 0. \tag{36}$$

The rest of the compatibility conditions and the relations in Eqs. (31)–(33) are satisfied trivially. In fact, the derivation of Eq. (36), as shown in Eqs. (27)–(29), proves that the relations are necessary conditions for compatibility. However, it is simple to prove that the conditions in Eq. (36) are also sufficient conditions for compatibility of membrane sheet (see the Appendix).

For a membrane sheet, $\mathbf{U}(\mathbf{X}, t)$ becomes

$$\mathbf{U}(\mathbf{X}, t) = \begin{pmatrix} \cos\phi & \sin\phi & 0 \\ -\sin\phi & \cos\phi & 0 \\ 0 & 0 & 1 \end{pmatrix} \cdot \begin{pmatrix} \lambda_1 & 0 & 0 \\ 0 & \lambda_2 & 0 \\ 0 & 0 & 0 \end{pmatrix} \cdot \begin{pmatrix} \cos\phi & -\sin\phi & 0 \\ \sin\phi & \cos\phi & 0 \\ 0 & 0 & 1 \end{pmatrix}. \tag{37}$$

Note that $\lambda_3 = 0$ because there is no thickness in a membrane model. Thickness changes of the real sheet, however, can be obtained from $\lambda_3 = (\lambda_1\lambda_2)^{-1}$ using incompressibility. This is possible because incompatibility in a thickness direction occurring by this practice is not a concern in the membrane theory. Equation (37) shows that there are three independent variables: $\phi(\mathbf{X}, t)$, $\lambda_{i=1,2}(\mathbf{X}, t)$. In $\mathbf{R}(\mathbf{X}, t)$, however, there are three independent variables, $\theta_{i=1,2,3}(\mathbf{X}, t)$, because intermediate shapes are in a three-dimensional space. Therefore, in general membrane cases, six nonvanishing components F_{ij} are made of six independent variables, and there are three compatibility conditions. So, three independent variables may be prescribed in advance.

When compatibility conditions are considered for materials having smooth yield functions, three variables defining $\mathbf{U}(\mathbf{X}, t)$ are completely prescribed for intermediate configurations. Therefore, there are no geometric incompatibility problems for intermediate configurations. Therefore, there are no geometric incompatibility problems for intermediate configurations of membrane sheet forming, even for materials having smooth yield functions. This is generally true even when the initial blank sheet is curved. The compatibility conditions in Eqs. (36) are convenient for confirming the geometric compatibility of intermediate configurations. However, solving Eqs. (36) to construct intermediate shapes is difficult because the equations eventually become the Gauss and Mainardi-Codazzi compatibility conditions, which are one order higher than Eqs. (36) (Lipschutz, 1969).

Calculation of intermediate shapes is possible using the nonlinear least squares method. In the least square method, the intermediate shape is obtained using the Newton-Raphson iteration until the resulting strain has the least difference from the prescribed strain, $\mathbf{U}$. Under this scheme, a compatible surface is obtained if such a surface exists for a prescribed strain distribution. The numerical scheme is formulated so that the difference is the minimum between the trial and the prescribed (or target) strains of a whole body; i.e.,

$$\frac{\partial f}{\partial \mathbf{x}} = \mathbf{0} \tag{38}$$

where

$$f = (\mathbf{U}^* - \mathbf{U}) \cdot (\mathbf{U}^* - \mathbf{U})/2. \tag{39}$$

In Eq. (38), $\mathbf{x}$ is an intermediate shape and in Eq. (39) $\mathbf{U}^*$ is a target quantity of a whole body. Sample intermediate shapes obtained for $\alpha = 0.2, 0.4, 0.6, 0.8$ are shown in Fig. 1.

6 History of External Forces

In the previous section, intermediate shapes were obtained with individual deformations occurring along minimum work paths and with compatibility occurring between individual deformations. The intermediate shapes thus can be obtained by applying proper external forces taking into account static equilibrium.

The static equilibrium equation, when the deformation path of a material element is prescribed, is obtained from Eqs. (21) and (22) as

$$\frac{dW(\mathbf{u})}{d\mathbf{u}} = \int \bar{\sigma} \frac{d\bar{\epsilon}}{d\mathbf{u}} dV_o = d\mathbf{F}_s(\mathbf{X}) \quad \text{or} \quad d\mathbf{F}_b(\mathbf{X}) \tag{40}$$

where

$$d\mathbf{F}_s = \mathbf{f} dS = \mathbf{f}_o dS_o \quad \text{for} \quad \mathbf{X} \text{ on a surface,} \tag{41}$$

$$d\mathbf{F}_b = (\rho \mathbf{b}) dV_o = (-\operatorname{div}\sigma) dV_o \quad \text{for} \quad \mathbf{X} \text{ inside a body.} \tag{42}$$

In Eq. (41), S_o is the initial surface area and $\mathbf{f}_o$ is the surface traction per initial unit area. Equation (40) shows that external forces at a surface and inside a body can be applied to balance a deformation distribution throughout a whole body which is in a static state. The relation in Eq. (40) differs for different prescribed paths because $\bar{\epsilon}(\mathbf{u})$ depends upon a deformation history; therefore, Eq. (40) is formulated assuming the minimum work path for ideal forming. When any displacement $\mathbf{u}$ which satisfies the assumed deformation in $\bar{\epsilon}(\mathbf{u})$ is plugged into the left-hand side, the external force associated with that displacement is obtained from the right-hand side of Eq. (40). Therefore, the history of external forces is obtained from Eq. (40) by plugging in the $\mathbf{u}$ of intermediate shapes.

When compared with the equilibrium equation in Eq. (40), the necessary condition in Eq. (24) looks like a special case of Eq. (40) having vanished external forces. In fact, this is not true, and there is a major difference between these two equations. When Eq. (24) is formulated in the ideal forming theory, a final shape of a product is specified in advance and material elements on a surface are prescribed to stay on that surface; therefore, the positions of material elements at a surface have only two independent components. Equation (24) is formulated with respect to these independent components only. Equation (40) is a general description without such restrictions, so that Eq. (40) is valid when it is formulated with all three components of $\mathbf{u}$. In fact, the condition in Eq. (24) is satisfied when all external surface forces are normal to a surface, while all body forces inside a body vanish (Chung and Richmond, 1992b). Note that the condition in Eq. (24) is imposed on a final configuration, so that the conditions of external forces described in Eq. (24) are only for a final configuration, but not for intermediate configurations during the process. The magnitudes of external forces at final configurations are not explicit in the solutions of Eq. (24). Those are obtained from Eq. (40) when whole components of $\mathbf{u}$ are plugged in after $\mathbf{u}$ are obtained from the solution of Eq. (24) and the surface description.

For a final configuration, all body forces inside a body vanish; however, they do not vanish in general for intermediate configurations of bulk forming processes since $\operatorname{div}\sigma$ in Eq. (42) does not generally vanish. In such cases, it might be impractical to impose the required internal body forces. However, Wienecke and Richmond (1992) have shown that internal body forces are not generally required for the Tresca yield condition. Consequently, for ideal bulk forming design, the nonhardening Tresca yield condition assures geometric compatibility and stress equilibrium without body forces for intermediate shapes. For ideal sheet-forming, material elements in a membrane model do not have internal body forces. Therefore, smooth yield conditions with hardening can be used for ideal sheet

Downloaded 03 May 2010 to 171.66.16.20. Redistribution subject to ASME license or copyright; see http://www.asme.org/terms/Terms_Use.cfm

forming design because there are no restrictions resulting from geometric compatibility nor required internal body forces.

7 Summary

An ideal forming theory has been developed in order to obtain direct information regarding optimum process parameters in the design stage of processes. In the proposed theory, material elements are prescribed to deform along minimum plastic work paths, assuming that materials have optimum formabilities in such paths. Then the ideal forming processes are obtained so as to have the most uniform strain distributions in final products without shear tractions at boundaries nor body forces inside. As solutions, the theory provides the evolution of intermediate shapes and external forces during processing as well as optimum final strain distributions.

The ideal forming theory might provide useful design information which is needed in process design as well as in product design. In the product design stage, the optimum strain distributions are evaluated for proposed product shapes. Then, it is judged whether the proposed shapes are formable or not, by comparing the optimum strains with forming limit strains: a "feasibility" test. If the proposed product shapes fail the test, the shapes require modification. When the product shapes pass the test, optimum processes to achieve those products are designed considering the evolution of intermediate shapes and external forces. In practice, optimum process design might take several trials before a realistic process is achieved; however, the ideal forming theory will contribute to guide the direction of such trials, and minimize the cost of trials.

References

Chung, K., and Richmond, O., 1992a, "Ideal Forming, Part I: Homogeneous Deformation with Minimum Plastic Work," *International Journal of Mechanical Science*, Vol. 34, No. 7, pp. 575–591.

Chung, K., and Richmond, O., 1993, "A Deformation Theory of Plasticity Based on Minimum Work Paths," *International Journal of Plasticity*, accepted for publication.

Chung, K., and Richmond, O., 1992b, "Ideal Forming, Part II: Sheet Forming with Optimum Deformation," *International Journal of Mechanical Science*, Vol. 34, No. 8, pp. 617–633.

Hencky, H., 1924, "Zur Theorie Plastischer Deformationen und der hierdurch hervorgerufenen Nachspannunger," *Zeits. angew. Math. u. Mech.*, Vol. 4, pp. 323–334.

Hill, R., 1986, "Extremal Paths of Plastic Work and Deformation," *Journal of the Mechanics and Physics of Solids*, Vol. 34, pp. 511–523.

Lipschutz, M. M., 1969, *Differential Geometry*, McGraw-Hill, New York, pp. 201–226.

Nadai, A., 1963, *Theory of Flow and Fracture of Solids*, Vol. 2, McGraw-Hill, New York, pp. 96–105.

Stören, S., and Rice, J. R., 1975, "Localized Necking in Thin Sheets," *Journal of the Mechanics and Physics of Solids*, Vol. 23, pp. 421–441.

Wienecke, H. A., and Richmond, O., 1992, "Ideal Flow of Isotropic Solids," ASME JOURNAL OF APPLIED MECHANICS, accepted for publication.

APPENDIX

It is as summarized here, simple to prove that the conditions in Eqs. (36) are also sufficient conditions for compatibility of membrane sheet. Considering the definitions

$$F_{11}=\frac{\partial x_1(X_1, X_2)}{\partial X_1} \quad \text{and} \quad F_{12}=\frac{\partial x_1(X_1, X_2)}{\partial X_2},$$

the relation $x_1=x_1(X_1, X_2)$ are obtained, respectively, as

$$x_1=\int F_{11}dX_1+\int F_{12}dX_2 - \int\left(\int\frac{\partial F_{11}}{\partial X_2}dX_1\right)dX_2+\text{constant} \quad \text{(A1)}$$

and

$$x_1=\int F_{11}dX_1+\int F_{12}dX_2 - \int\left(\int\frac{\partial F_{12}}{\partial X_1}dX_2\right)dX_1+\text{constant}. \quad \text{(A2)}$$

These two relations become equivalent when the condition $H_1=0$ is satisfied; therefore, compatibility of $x_1=x_1(X_1, X_2)$ is assured. Compatibility of $x_2=x_2(X_1, X_2)$ and $x_3=x_3(X_1, X_2)$ are also assured similarly by the conditions $H_4=0$ and $H_7=0$, respectively.

Downloaded 03 May 2010 to 171.66.16.20. Redistribution subject to ASME license or copyright; see http://www.asme.org/terms/Terms_Use.cfm

J. K. Good
Professor,
Mem. ASME.

Z. Wu
Research Assistant.

M. W. R. Fikes
Research Assistant.

School of Mechanical and
Aerospace Engineering, EN 218,
Oklahoma State University,
Stillwater, OK 74078

The Internal Stresses in Wound Rolls With the Presence of a Nip Roller

Models which can be used to calculate the internal stresses within wound rolls of web material have all been confined to the center winding technique to date. In this publication, a new boundary condition is presented which will allow existing models to calculate the internal stresses within a wound roll which has been center wound with an undriven nip roller impinged upon the outside of the roll. Experimental verification of the new boundary condition is presented.

Introduction

Web handling is a manufacturing process which pervades almost every manufacturing industry in one way or another. A web is a continuous, flexible strip of material such as paper, plastic film, metal foil, textiles, and nonwoven materials which are stored at least on an intermediate basis in wound rolls to accommodate high speed, automated manufacturing operations. Web handling is the science involving the mechanics and dynamics of transporting webs from unwind stations, through process machinery, to rewind stations.

Winding is an integral operation in almost every web handling process. During the course of a web becoming a final converted product, it may be unwound and rewound several times depending upon the number of web processes which must be performed. Winding exerts stresses and curvatures upon webs which often can degrade the web quality but the wound roll form is the most efficient and opportune storage format for high-speed automated manufacturing processes. It is desirable to wind just enough stress into a wound roll that a stable package is wound, which has as few defects as possible, which can result from too little or too much stress being wound into the roll.

Much of the winding which is currently performed is accomplished via a technique which is known as center winding with an undriven nip roll, refer to Fig. 1. This technique requires that the winding torque be provided to the center (called the core) of the winding roll. An undriven nip roll follows the outside radius of the winding roll with a dual purpose. One purpose is to help exude wound-in air from the wound roll which could lead to an unstable, loosely wound roll package which is apt to sustain web defects during web storage or transport. The second purpose is to provide an increased tension in the web, above the web line tension, for the web winding process. This increased tension is due to a nip mechanics mechanism which has been understood empirically for quite some time (Pfeiffer, 1968). Recently Good and Wu (1992) determined the mechanism of the nip-induced tension via an investigation composed of finite element and experimental analyses. The mechanism is an elongating machine direction strain which exists beneath the nip roll location on the lower side of the web which is in intimate contact with the wound roll. This elongating strain is due to the compressive Hertzian-like contact stresses which exist through the depth of the web beneath the nip roller. As this elongating strain advances with the moving nip roll, web material attempts to advance in front of the nip and contract in towards the nip in back of the rolling nip. If the web material in back of the nip is constrained, a net increase in tension will result due to the nip. The nip-induced tension cannot exceed the kinetic coefficient of traction between the outer wrap and the wrap beneath it multiplied by the nip loading.

There are several wound roll stress models in existence which differ mainly in the manner in which the web material properties are allowed to vary. All of these models apply only to the center winding technique without a nip roll. This publication will show that with the basic understanding of the nip-

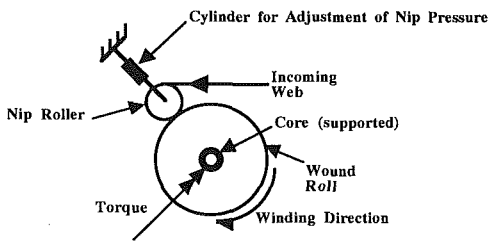


Fig. 1 A center winder with an impinging nip roller

Contributed by the Applied Mechanics Division of THE AMERICAN SOCIETY OF MECHANICAL ENGINEERS for publication in the ASME JOURNAL OF APPLIED MECHANICS.

Discussion on this paper should be addressed to the Technical Editor, Professor Lewis T. Wheeler, Department of Mechanical Engineering, University of Houston, Houston, TX 77204-4792, and will be accepted until four months after final publication of the paper itself in the ASME JOURNAL OF APPLIED MECHANICS.

Manuscript received by the ASME Applied Mechanics Division, Mar. 14, 1991; final revision, July 7, 1992. Associate Technical Editor: M. E. Fourney.

Copyright © 1994 by ASME
Downloaded 03 May 2010 to 171.66.16.20. Redistribution subject to ASME license or copyright; see http://www.asme.org/terms/Terms_Use.cfm

induced tension mechanism that new boundary conditions can be developed for use with the existing wound roll models to model center winding with an undriven nip roll. Experimental results have been included to confirm that the new modeling technique is valid.

Some reference will be made to a machine direction. The machine direction in a web line is the direction in which the web travels through the web line.

Internal Stress Models for Center Wound Rolls

As mentioned in the Introduction, several models exist which differ mainly in the way which the material parameters are included. The first models, Gutterman (1959) and Catlow et al. (1962), assumed that a wound roll could be modeled as a linear isotropic material, where the radial modulus was equivalent to the circumferential modulus of elasticity ($E_r = E_\theta$). The next generation of models, Altmann (1968) and Yagoda (1980), assumed the wound roll could be modeled as a linear anisotropic material, where E_r is unequal to E_θ although both parameters are assumed to be constants. In reality the radial modulus of a wound roll is a parameter which encompasses both structural and material nonlinearities. Paper, plastic film, and other webs have asperities upon their surfaces and when the web is wound or stacked asperities from one surface contact asperities upon the next surface. Thus, upon compression, the contact area becomes a function of radial or normal pressure and the measured radial modulus, E_r, is a function, typically nonlinear, of radial pressure. Thus the most realistic models of Pfeiffer (1968), Hakiel (1987), and Willett and Poesch (1988) allow for nonlinear anisotropic properties.

Hakiel combined equilibrium, compatibility, and material relationships to yield a second order differential equation in radial pressure:

$$r^2\frac{d^2\sigma_r}{dr^2}+3r\frac{d\sigma_r}{dr}-\left[\frac{E_\theta}{E_r}-1\right]\sigma_r=0 \tag{1}$$

where r denotes a radial location in the wound roll, E_θ and E_r denote the respective circumferential and radial Young's moduli and σ_r denotes the radial pressure. Equation (1) requires two boundary conditions for solution. The second-order differential equation must be solved several times for the wound roll as the geometry, boundary conditions, and material parameters are continually changing throughout the winding process. Restating, Eq. (1) in a slightly different form:

$$r^2\frac{d^2[\delta\sigma_r]}{dr^2}+3r\frac{d[\delta\sigma_r]}{dr}-\left[\frac{E_\theta}{E_r}-1\right][\delta\sigma_r]=0. \tag{2}$$

Hakiel implemented a finite difference technique to solve Eq. (2). The radial modulus E_r is a function of the radial pressure σ_r and is measured using a material testing system, the procedure for which has been documented by Pfeiffer (1981). Each time the equation is solved, the radial stress distribution obtained must be added to the sum of all the previous radial stress distributions which resulted from previous solutions of the equation or

$$\sigma_{ri}=\sigma_{ri}+\sum_{j=i+1}^{n}\delta\sigma_{rij}, \tag{3}$$

where $\delta\sigma_{rij}$ denotes the radial stress in the ith layer due to the winding on of the jth layer. This procedure is continued until the total n layers have been wound onto the roll. With a known radial stress distribution the tangential stresses can be calculated from the equilibrium expression

$$r\frac{\partial\sigma_r}{\partial r}+\sigma_r-\sigma_\theta=0. \tag{4}$$

The boundary conditions for center winding are obtained by considering both the inner and outermost layers of the wound roll. At the inner layer, the radial deformation of the first wound on layer should be equal to the radial deformation of the core. Mathematically this is stated as

$$u(1)=-\frac{\delta\sigma_r(1)}{E_c} \tag{5}$$

where E_c represents the radial stiffness of the core and u represents the normalized deformation (by dividing by the outside radius of the core) of the first layer. After use of compatibility and material expressions, the radial deformation can be eliminated yielding the following relationship:

$$\left.\frac{d\delta\sigma_r}{dr}\right|_{r=1}=\left[\frac{E_\theta}{E_c}-1+\nu_{r\theta}\right]\delta\sigma_r|_{r=1} \tag{6}$$

in which $\nu_{r\theta}$ is Poisson's ratio which governs deformation in the r direction due to a stress in a θ direction. The second boundary condition involves the outer layer. The circumferential stress, σ_θ, is equivalent to the incoming web tensile stress, T_w, in the outer layer. Treating the outer wrap of the wound roll as a thin wall pressure vessel the radial stress can be related to the circumferential stress via the relationship

$$\delta\sigma_r|_{r=s}=\{T_w|_{r=s}\}\frac{h}{s} \tag{7}$$

where h is the web thickness and s is the radial location of the current outer wrap of the winding roll.

Modifications of Hakiel's Model to Incorporate an Undriven Nip

The modification consists of altering the second boundary condition for the center winding model (7). It was noted in the earlier work, Good and Wu (1992), that the nip-induced tension had reached its saturated value after the nip had rolled five to ten centimeters for the aluminum web strip tested. The nip-induced tensions in the upper five sheets in a stack composed of eight sheets of newsprint were experimentally determined using a modified version of the apparatus described in the previous work, which is shown in Fig. 2. Note in the plot of the nip-induced tensions in Fig. 3 that the phenomena resides mainly in the first or uppermost sheet. The result of averaging five such tests, with the exception that a normal pressure was applied to the top of the stack to simulate the radial pressure in a wound roll, is shown in Fig. 4. It is clear that the nip-induced tension phenomena resides mainly in the first layer. Note that the saturated value of the nip-induced tension is approached at approximately 38.1 cm in Fig. 3. Tests upon lightweight coated papers and upon polypropylene films have

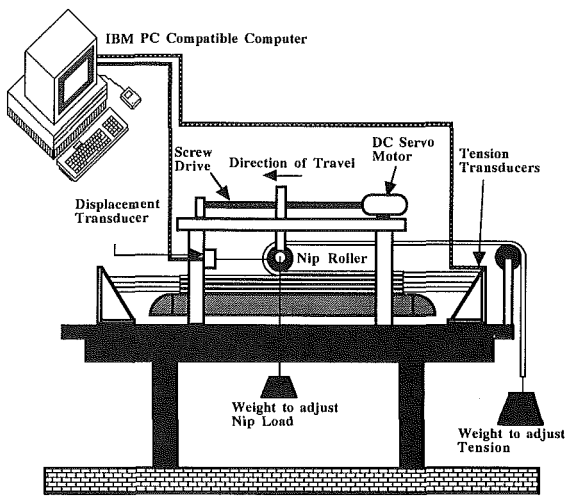


Fig. 2 Experimental apparatus

Downloaded 03 May 2010 to 171.66.16.20. Redistribution subject to ASME license or copyright; see http://www.asme.org/terms/Terms_Use.cfm

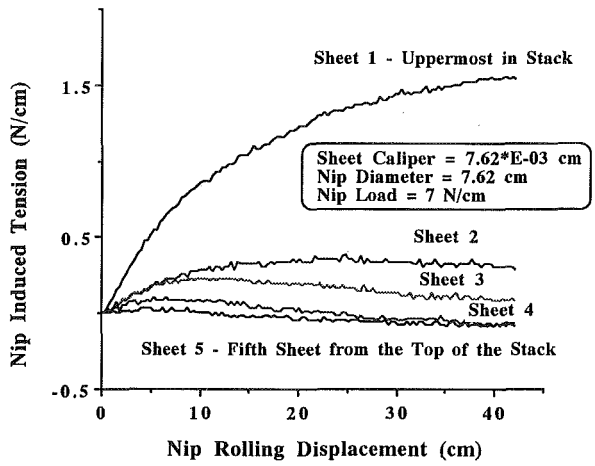


Fig. 3 Nip-induced tensions in an eight-sheet stack of newsprint

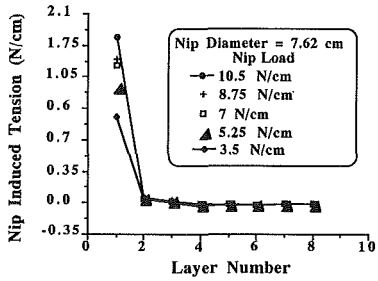


Fig. 4 Saturated nip-induced tensions in an eight-sheet stack with simulated radial pressure

shown similar results. Webs are wound upon cores of various diameters but typically not less than 7.62 cm in inside diameter or 8.89 cm in outside diameter. The first wrap would have a circumference of approximately 27.9 cm. Thus, for almost the entire winding process which typically consists of thousands of layers, the nip-induced tension has reached its saturated value. Thus, the new boundary condition, which relies principally on the coefficient of friction and the nip loading, may be presented as

$$\sigma_r|_{r=s} = \left[(T_w|_{r=s}) + \frac{\mu N}{h} \right] \frac{h}{s} \tag{8}$$

where N is the nip loading which may vary through the winding process and μ is the coefficient of friction. After the nip-induced tension has saturated, gross slippage of the web has begun to occur on the lower surface of the outer wrap which is in contact with the wrap beneath. Thus the coefficient of friction μ must be the kinetic value of the coefficient of friction.

Experimental Verification of the Modified Model

Tests were performed upon lightweight coated paper and polypropylene film webs. The web and core properties pertinent to the model input are shown in Table 1. The tests were performed upon a pilot unwind/rewind facility in the mechanics laboratory of the Web Handling Research Center.[1] The interlayer radial pressures in the wound roll were measured using Force Sensitive Resistors[2] by Good and Fikes (1991). The winding velocity for these tests was 15 m/min. This velocity was chosen such that the effects of air entrainment into the winding roll could be neglected. The radial pressure profiles for the light weight coated paper web is shown in Figs. 5 and 6. In each figure the experimental data, the output from Hakiel's model neglecting the nip, and the output from a modified version of Hakiel's model which incorporates the new nip boundary condition is shown. Each experimental data point shown in these figures represents the average pressure obtained from nine winding tests. The error bar which is overlaid upon each data point is the standard deviation of the pressure measured at that radius throughout the nine windings. Note in each figure how well the modified model matches the experimental data. A radial pressure profile for a polypropylene web is shown in Fig. 7 and again the modified model matches the experimental data nicely.

[1] The Web Handling Research Center, An NSF-IUCRC Program, EN 218, Oklahoma State University, Stillwater, OK 74078.

[2] Force Sensitive Resistors (FSRs™), Interlink Electronics, P.O. Box 40760, Santa Barbara, CA 93103.

Table 1 Web Properties and Winding Parameters

	Lightweight Coated Paper	Polypropylene
thickness (cm)	5.08E-03	2.54E-03
width (cm)	15.24	15.24
Poisson's ratio ($\nu_{r\theta}$)	0.0[1]	0.0[1]
E_r (kPa)	72.8*σ_r	260.*σ_r
E_θ (GPa)	8.268	3.101
coefficient of traction	0.30[2]	0.22[2]
core i.d. (cm)	7.71	7.71
core o.d. (cm)	8.75	8.75
core stiffness-steel (GPa)	27.1	27.1
final roll diameter (cm)	17.78	17.78
winding velocity (m/min)	15.0	15.0

[1] Poisson's ratio as a stack property was assumed to be zero as assumed by Hakiel (1987)

[2] Kinetic values of the coefficient of friction

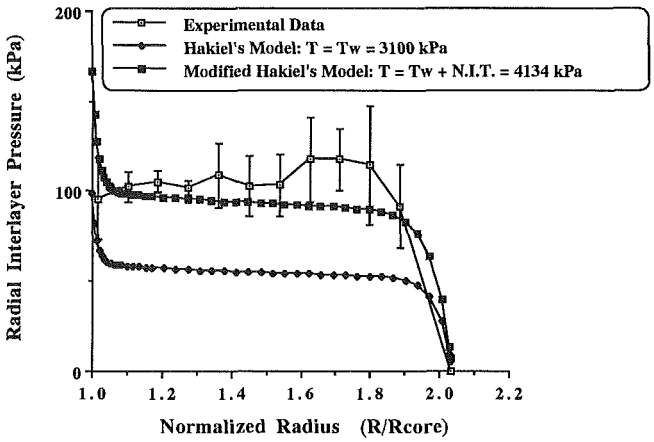


Fig. 5 Results for lightweight coated paper, nip load = 1.75 N/cm

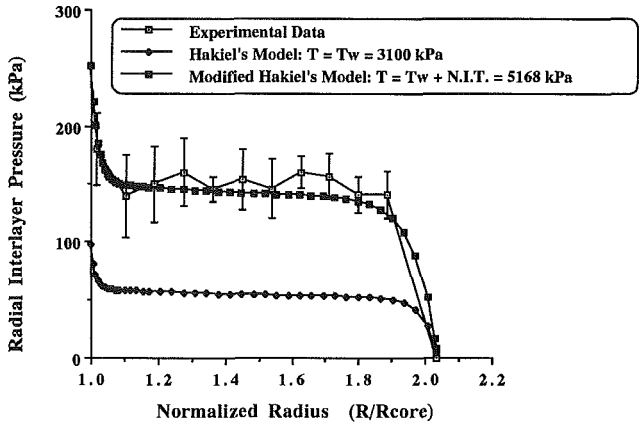


Fig. 6 Results for lightweight coated paper, nip load = 3.5 N/cm

Downloaded 03 May 2010 to 171.66.16.20. Redistribution subject to ASME license or copyright; see http://www.asme.org/terms/Terms_Use.cfm

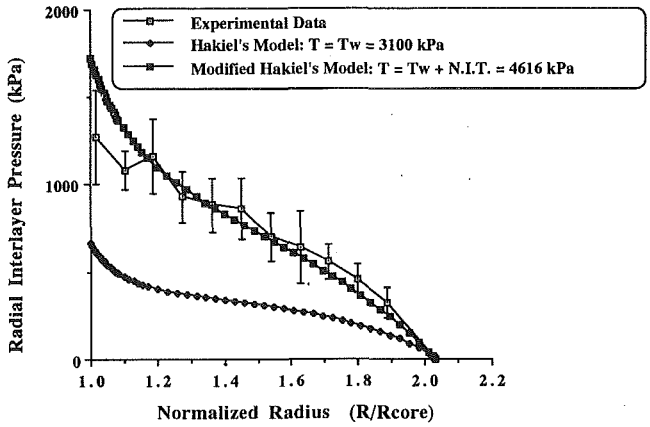


Fig. 7 Results for Polypropylene, nip load = 1.75 N/cm

Conclusions

The mechanism which is responsible for nip-induced tension in wound rolls has been incorporated into a new wound roll boundary condition. The nip-induced tension cannot exceed the kinetic coefficient of traction between the outer wrap and the wrap beneath it multiplied by the nip loading, and when summed with the web line tension this is defined as the saturated value of the nip-induced tension. It has been found that the saturated value of the nip-induced tension occurs after short nip rolling distances when compared to the roll circumference. A new boundary condition was formulated for wound roll stress models in which the tension in the outer wrap was set equal to the sum of the incoming web stress and the saturated value of the nip induced tension. This new boundary condition was incorporated into a model which performs very well when compared to experimental data.

The mechanism of nip-induced tension described by Good and Wu (1992) applies a broad domain of web materials. The effects of entrained air into wound rolls can, however, drastically alter the radial pressure profiles within wound rolls. The technique for modeling the radial pressures described herein is applicable as long as the nip loading is high enough such that little or no air is allowed to be entrained into the wound roll. Currently no model exists from which the amount of entrained air can be calculated for the winding geometry shown in Fig. 1 and should be a topic of future research.

Acknowledgments

This publication is a result of research which was funded by the Web Handling Research Center of Oklahoma State University. The authors would like to thank the sponsors of the WHRC for supporting this research. The sponsors include the National Science Foundation, the Noble Foundation, the State of Oklahoma and an industrial consortium of which Beloit Corp., Eastman Kodak Co., E.I.Dupont de Nemours & Co. (Inc.), Fife Corp., Hoescht-Celanese Corp., ICI Americas, James River Corp., Kimberly-Clark Corp., 3M Co., Mead Corp., Mobil Chemical Co., Polaroid Corp., Reliance Electric Co., Rexham Corp. Sonoco Products Co., Specialty Coatings Group (Inc.), Union Camp Corp., Valmet-Appleton Inc., and Worldwide Process Technologies are members.

References

Altmann, H. C., 1968, "Formulas for Computing the Stresses in Center Wound Rolls," *TAPPI Journal*, Vol. 51, No. 4, pp. 176–179.

Catlow, M. G., and Walls, G. W., 1962, "A Study of Stress Distribution in Pirns," *Journal of Textile Institute*, Part 3, pp. T410–429.

Good, J. K., and Fikes, M. W. R., 1991, "Predicting Internal Stresses in Centerwound Rolls with an Undriven Nip Roller," *TAPPI Journal*, Vol. 74, No. 6, pp. 101–109.

Good, J. K., and Wu, Z., 1992, "The Mechanism of Nip Induced Tension in Wound Rolls," ASME JOURNAL OF APPLIED MECHANICS, accepted for publication.

Gutterman, R. P., 1959, "Theoretical and Practical Studies of Magnetic Tape Winding Tensions and of Environmental Roll Stability," US Contract No. DA-18-119-SC-42.

Hakiel, Z., 1987, "Nonlinear Model for Wound Roll Stress," *TAPPI Journal*, Vol. 70, No. 5, pp. 113–117.

Pfeiffer, J. D., 1981, "Measurement of the K2 Factor for Paper," *TAPPI Journal*, Vol. 64, No. 4, pp. 105–106.

Pfeiffer, J. D., 1968, "Mechanics of a Rolling Nip on Paper Webs," *TAPPI Journal*, Vol. 51, No. 8, pp. 77A–85A.

Pfeiffer, J. D., 1966, "Internal Pressures in a Wound Roll of Paper," *TAPPI Journal*, Vol. 49, No. 8, pp. 342–347.

Willett, M. S., and Poesch, W. L., 1988, "Determining the Stress Distributions in Wound Rolls of Magnetic Tape using a Nonlinear Finite Difference Approach," ASME JOURNAL OF APPLIED MECHANICS, Vol. 55, pp. 365–371.

Yagoda, H. P., 1980, "Integral Formulas for Wound Rolls," *Mechanics Research Communications*, Vol. 7, No. 2, pp. 103–112.

Downloaded 03 May 2010 to 171.66.16.20. Redistribution subject to ASME license or copyright; see http://www.asme.org/terms/Terms_Use.cfm

Kai-Yuan Yeh
Visiting Professor.

R. P. S. Han
Assoc. Professor,
Mem. ASME.

Department of Mechanical Engineering,
University of Manitoba,
Winnipeg, Manitoba R3T 2N2, Canada

Analysis of High-Speed Rotating Disks With Variable Thickness and Inhomogeneity

A rotating disk with varying thickness and inhomogeneity, and subjected to a steady, inhomogeneous temperature field is analyzed. To handle the arbitrary profile, the disk is discretized into a series of uniform annular disks possessing constant material properties and then solved by the step-reduction method. Analytic expressions for thermoelastic stresses are given, and based on these results, the formulation is extended to include the calculation of shrink fit, the solving of the inverse problem for equistrength rotating disks, and the computations of plastic stresses and creep at elevated temperatures.

1 Introduction

This paper is concerned with the analysis of a rotating disk with a temperature gradient using an analytical method. There are many applications of such temperature loaded-rotating disks, such as in turbines, rotors and, with the advent of computers, disk drives. Naturally, with all these applications and interest, there has been much research in this field. The analytical procedures presently available are restricted to problems with the simplest configurations, possessing constant material properties and thickness. To take into account variations of material properties and thickness, it is usual to resort to numerical techniques. While this approach is straightforward and the stress distribution can be easily computed, there are situations where it would be desirable to be able to perform the analysis with the aid of closed form analytical solutions. One such situation involves solving the inverse problem where it desired to compute the profile of a disk from a given dynamic performance and/or strength characteristics. It is much easier to perform the inverse analysis using analytical solutions than to do it numerically. Our motivation for this study is to obtain an analytical procedure that is applicable to rotating disks with inhomogeneity and variable thickness, subjected to a steady inhomogeneous temperature field so that the results can be used in the development of the inverse analysis.

The analytical solution of a homogeneous, constant thickness rotating disk possessing axisymmetry is already a standard technique, available in textbooks such as in Mendelson (1970). To handle disks of any arbitrary thickness, Leopold (1948) introduced a semigraphical procedure for computing the elastic stresses. With the widespread computer usage, various numerical methods have also been employed to solve this problem: the finite difference method of Manson (1947), and Mendelson (1970), the method of second iteration of Shilizki (1958), the finite element method of Genta et al. (1982), the successive solution method of Mendelson et al. (1959), and the boundary element method of Abdul-Mihsein et al. (1985). Analytical studies of vibrations in spinning disks have also been conducted by Ghosh (1975, 1985). With the exception of the work of Mendelson and co-workers, most of the studies conducted so far are concerned with the computations of elastic stresses.

In this paper, a systematic formulation to handle an inhomogeneous, rotating disk with an arbitrary varying thickness under thermal loading is presented. The methodology involves approximating a physical disk by a system of discrete annular disks possessing constant material and thickness properties, in which closed-form solutions are derived. The conventional method of discretization such as that suggested by Leopold (1948) and many others, results in a system of algebraic equations and thereby necessitating a numerical technique for the solution. In this procedure (Yu and Yeh, 1984), the continuity conditions at the junctions of any two discrete annular disks are expressed in terms of the boundary conditions for the overall problem, and this is done successively for all the junctions. Hence, instead of getting a system of algebraic equations, only a single equation is produced, regardless of how many annular disks are employed in the discretization scheme. This very useful concept implies that an analytical treatment for handling the problem of inhomogeneity and variable thickness in rotating disks can now be formulated. The accuracy of the step-reduction method depends on the number of annular disks employed in the discretization. As this number increases to infinity, the approximate solution approaches the exact solution. Analytic expressions for thermoelastic stresses are given, and based on these results, procedures for calculating shrink-fit and for solving the inverse problem of an equistrength

Contributed by the Applied Mechanics Division of THE AMERICAN SOCIETY OF MECHANICAL ENGINEERS for publication in the ASME JOURNAL OF APPLIED MECHANICS.

Discussion on this paper should be addressed to the Technical Editor, Professor Lewis T. Wheeler, Department of Mechanical Engineering, University of Houston, Houston, TX 77204-4792, and will be accepted until four months after final publication of the paper itself in the ASME JOURNAL OF APPLIED MECHANICS.

Manuscript received by the ASME Applied Mechanics Division, Aug. 6, 1991; final revision, Oct. 22, 1992. Associate Technical Editor: D. J. Inman.

Copyright © 1994 by ASME
Downloaded 03 May 2010 to 171.66.16.20. Redistribution subject to ASME license or copyright; see http://www.asme.org/terms/Terms_Use.cfm

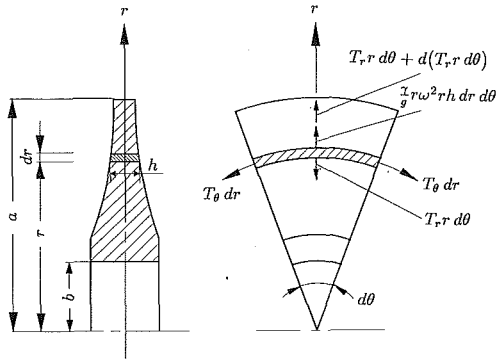


Fig. 1 Profile of the rotating disk and the forces acting on an element

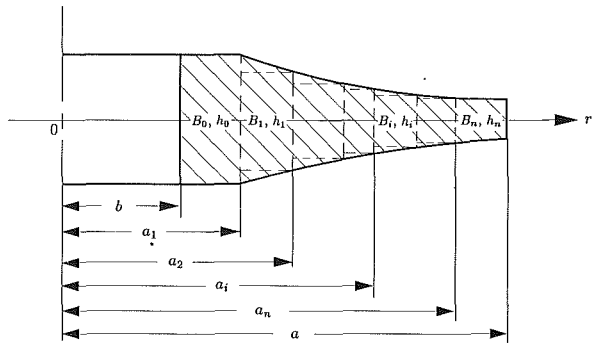


Fig. 2 Discretization by a system of step-annular disks

rotating disk are discussed. The computations of plastic stresses and creep at elevated temperatures are then formulated using Ilyushin's method of successive elastic solutions (Ilyushin, 1946) and Wahl's creep rule (Wahl et al., 1954).

2 Governing Equations for Thermoelastic Analysis

The governing equations for thermoelastic analysis of an inhomogeneous, rotating disk with arbitrary varying thickness are given here. Small deformations and rotational symmetry are assumed. If the thickness of the disk is small compared to its radius, the axial stress is negligible and the disk is then in a state of plane stress. The material is assumed to be isotropic but inhomogeneous along the radial direction. That is, the Young's modulus $E = E(r)$, the density of the disk material $\gamma = \gamma(r)$, the coefficient of linear expansion $\alpha = \alpha(r)$, and the Poisson's ratio $\nu = \nu(r)$. The temperature field is steady, axisymmetric but inhomogeneous. That is, $T = T(r)$ where T is the temperature. Let T_r represent the radial component of the tensile force per unit length and T_θ be its tangential component per unit length as depicted in Fig. 1. From equilibrium consideration of an element, the following equation is derived:

$$\frac{dT_r}{dr}+\frac{T_r-T_\theta}{r}+\frac{h\gamma}{g}\omega^2 r=0 \tag{1}$$

where $h = h(r)$ is the thickness of the disk at distance r, g is the gravitational acceleration, and ω is the angular velocity of the disk. The stress-strain relationships are

$$\epsilon_r=\frac{du}{dr}=\frac{1}{Eh}(T_r-\nu T_\theta)+\alpha(r)T(r)$$

$$\epsilon_\theta=\frac{u}{r}=\frac{1}{Eh}(T_\theta-\nu T_r)+\alpha(r)T(r) \tag{2}$$

in which u is the radial displacement and ϵ_r, ϵ_θ are the radial and tangential strain components. Defining

$$B=(1-\nu^2)/E \tag{3}$$

and

$$\Theta=\alpha(r)T(r) \tag{4}$$

the tensile force components T_r, T_θ are given by

$$T_r=\frac{h}{B}\left[\frac{du}{dr}+\nu\frac{u}{r}-(1+\nu)\Theta\right]$$

$$T_\theta=\frac{h}{B}\left[\frac{u}{r}+\nu\frac{du}{dr}-(1+\nu)\Theta\right]. \tag{5}$$

These tensile forces can be eliminated by substituting Eq. (5) into Eq. (1), and this yields the governing equation for a rotating disk with inhomogeneity and variable thickness loaded by an inhomogeneous, steady temperature field:

$$\frac{d^2u}{dr^2}+\frac{1}{r}\frac{du}{dr}-\frac{u}{r^2}+\frac{d\nu}{dr}\frac{u}{r}+\left(\frac{du}{dr}+\nu\frac{u}{r}\right)\frac{d}{dr}\left(\ln\frac{h}{B}\right)$$

$$=\frac{d}{dr}[(1+\nu)\Theta]-\frac{B}{g}\gamma\omega^2 r+(1+\nu)\Theta\frac{d}{dr}\left(\ln\frac{h}{B}\right). \tag{6}$$

In the case of a constant thickness and homogeneous disk, namely, ν, h, B, E, γ are constants, the solution of the above equation in the initial parameter form is

$$u(r)=\frac{1}{2}u(b)\left[\left(\frac{r}{b}+\frac{b}{r}\right)-\nu\left(\frac{r}{b}-\frac{b}{r}\right)\right]+\frac{1}{2}\frac{B}{h}T_r(b)\left(r-\frac{b^2}{r}\right)$$

$$+(1+\nu)\frac{1}{r}\int_b^r \xi\Theta d\xi-\frac{B}{8g}\frac{\gamma\omega^2}{r}(r^2-b^2)^2, \tag{7}$$

where b is the inner radius of the disk, $u(b)$ and $T_r(b)$ are the radial displacement and the radial tensile force per unit length at $r = b$, in which one of them is known and the other can be determined by the boundary condition at the outer radius of the disk, $r = a$. Note that Eq. (7) will be used as the basic solution to solve Eq. (6) for a variable thickness, inhomogeneous disk by means of a system of step-annular disks.

3 Elastic Stress Calculation

Exact solution of Eq. (6) is possible only for the simplest configurations, with constant material properties and thickness. For an arbitrary varying thickness disk with inhomogeneous property, an approximate method is employed. This involves discretizing the disk into a finite number of annular disks with constant B and h as illustrated in Fig. 2. At each annular disk, the governing equation in Eq. (6) becomes

$$\frac{d^2u}{dr^2}+\frac{1}{r}\frac{du}{dr}-\frac{u}{r^2}=(1+\nu)\frac{d\Theta}{dr}-\frac{B_0}{g}H_n(r)\gamma\omega^2 r \tag{8}$$

in which

$$H_n(r)=1+\sum_{i=1}^{n}\{r-a_i\}^0(\delta_i-\delta_{i-1}). \tag{9}$$

$\{r - a_i\}^0$ is the unit step function defined as

$$\{r-a_i\}^0=\begin{cases}0, & \text{for } r<a_i\\ 1, & \text{for } r\geq a_i\end{cases} \tag{10}$$

and

$$\delta_i=\frac{B_i}{B_0},\quad (i=1, 2, \ldots, n) \tag{11}$$

where n is the number of annular disk employed in the discretization scheme. Observe that the Poisson's ratio ν is assumed constant as its variation is minimal (Holms and Faldetta, 1947) in stress computations. To ensure the solutions are continuous at the junction between any two annular disk, the continuity conditions are

Downloaded 03 May 2010 to 171.66.16.20. Redistribution subject to ASME license or copyright; see http://www.asme.org/terms/Terms_Use.cfm

$$u(a_i-\epsilon)=u(a_i),\qquad T_r(a_i-\epsilon)=T_r(a_i),\qquad (i=1,\,2,\,\ldots,\,n) \tag{12}$$

where ϵ is an infinitesimal quantity. The boundary conditions for the disk are

$$u(b)=\lambda+\beta T_r(b)\quad \text{at } r=b,\qquad T_r(a)=\zeta\quad \text{at } r=a \tag{13}$$

Note that λ, β, ζ are constants. The problem now is changed to: solve Eq. (8) subject to the continuity and boundary conditions depicted in Eqs. (12)–(13). In accordance to Eq. (7), the solution can be expressed in the following form:

$$u(r)=\frac{1}{2}u(b)\left[\left(\frac{r}{b}+\frac{b}{r}\right)-\nu\left(\frac{r}{b}-\frac{b}{r}\right)\right]+\frac{1}{2}\frac{B_0}{h_0}T_r(b)\left(r-\frac{b^2}{r}\right)+(1+\nu)\frac{1}{r}\int_b^r\xi\Theta d\xi-\frac{B_0}{g}\frac{\omega^2}{r}\int_b^r\xi d\xi\int_b^\xi\gamma H_n(\rho)\rho d\rho+\frac{1}{2}\sum_{i=1}^{n}\{r-a_i\}^0 f_i\left(r-\frac{a_i^2}{r}\right) \tag{14}$$

where f_i is an arbitrary constant evaluated by satisfying Eq. (12b). Note that the continuity condition of Eq. (12a) is automatically satisfied in Eq. (14). For convenience, the solution for f_i can be expressed as

$$f_i=\frac{1}{2}u(b)f_i^{(1)}+\frac{1}{2}\frac{B_0}{h_0}T_r(b)f_i^{(2)}-f_i^{(3)} \tag{15}$$

in which $f_i^{(1)}$, $f_i^{(2)}$, $f_i^{(3)}$ are associated with respect to terms containing $u(b)$, $T_r(b)$ and the particular solution, respectively. They are given by

$$f_i^{(1)}=\left\{(1-\nu^2)\left(\frac{1}{b}-\frac{b}{\alpha_i^2}\right)+\frac{1}{2}\sum_{j=1}^{i-1}f_j^{(1)}\left[\left(1+\frac{a_j^2}{a_i^2}\right)+\nu\left(1-\frac{a_j^2}{a_i^2}\right)\right]\right\}\psi_i \tag{16}$$

$$f_i^{(2)}=\left\{\left(1+\frac{b^2}{a_i^2}\right)+\nu\left(1-\frac{b^2}{a_i^2}\right)+\frac{1}{2}\sum_{j=1}^{i-1}f_j^{(2)}\left[\left(1+\frac{a_j^2}{a_i^2}\right)+\nu\left(1-\frac{a_j^2}{a_i^2}\right)\right]\right\}\psi_i \tag{17}$$

$$f_i^{(3)}=\left\{\frac{1-\nu^2}{a_i^2}\int_b^{a_i}r\Theta dr+\frac{B_0}{g}\omega^2\left[\int_b^{a_i}\gamma H_{i-1}(r)rdr-\frac{1-\nu}{a_i^2}\int_b^{a_i}rdr\int_b^r\gamma H_{i-1}(\xi)\xi d\xi\right]+\frac{1}{2}\sum_{j=1}^{i-1}f_j^{(3)}\left[\left(1+\frac{a_j^2}{a_i^2}\right)+\nu\left(1-\frac{a_j^2}{a_i^2}\right)\right]\right\}\psi_i \tag{18}$$

where

$$H_{i-1}(r)=1+\sum_{j=1}^{i-1}\{r-a_j\}^0\left(\frac{B_j-B_{j-1}}{B_0}\right) \tag{19}$$

$$\psi_i=\frac{B_i}{h_i}\frac{h_{i-1}}{B_{i-1}}-1. \tag{20}$$

Substitute Eq. (15) into Eq. (14), and after some algebraic manipulations get

$$u(r)=\frac{\lambda}{2}\left\{\left(\frac{r}{b}+\frac{b}{r}\right)-\nu\left(\frac{r}{b}-\frac{b}{r}\right)+\frac{1}{2}\sum_{i=1}^{n}\{r-a_i\}^0 f_i^{(1)}\left(r-\frac{a_i^2}{r}\right)\right\}+\frac{1}{2}T_r(b)\left\{\beta\left[\left(\frac{r}{b}+\frac{b}{r}\right)-\nu\left(\frac{r}{b}-\frac{b}{r}\right)\right]+\frac{B_0}{h_0}\left(r-\frac{b^2}{r}\right)+\frac{1}{2}\sum_{i=1}^{n}\times\{r-a_i\}^0\left[\beta f_i^{(1)}+\frac{B_0}{h_0}f_i^{(2)}\right]\left(r-\frac{a_i^2}{r}\right)\right\}+(1+\nu)\frac{1}{r}\int_b^r\xi\Theta d\xi-\frac{B_0\omega^2}{rg}\int_b^r\xi d\xi\int_b^\xi\gamma H_n(\rho)\rho d\rho+\frac{1}{2}\sum_{i=1}^{n}\{r-a_i\}^0 f_i^{(3)}\left(r-\frac{a_i^2}{r}\right). \tag{21}$$

Both radial and tangential components of the tensile force are given by substituting Eq. (21) into Eq. (5). The results are

$$T_r(r)=\frac{1}{2}\lambda k_n(r)\left\{(1-\nu^2)\left(\frac{1}{b}-\frac{b}{r^2}\right)+\frac{1}{2}\sum_{i=1}^{n}\{r-a_i\}^0 f_i^{(1)}\times\left[\left(1+\frac{a_i^2}{r^2}\right)+\nu\left(1-\frac{a_i^2}{r^2}\right)\right]\right\}+\frac{1}{2}T_r(b)k_n(r)\left\{\beta(1-\nu^2)\left(\frac{1}{b}-\frac{b}{r^2}\right)+\frac{B_0}{h_0}\left[\left(1+\frac{b^2}{r^2}\right)+\nu\left(1-\frac{b^2}{r^2}\right)\right]+\frac{1}{2}\sum_{i=1}^{n}\{r-a_i\}^0\left[\beta f_i^{(1)}+\frac{B_0}{h_0}f_i^{(2)}\right]\times\left[\left(1+\frac{a_i^2}{r^2}\right)+\nu\left(1-\frac{a_i^2}{r^2}\right)\right]\right\}-(1-\nu^2)\frac{k_n(r)}{r^2}\int_b^r\xi\Theta d\xi-\frac{B_0}{g}\times\omega^2k_n(r)\left\{\int_b^r\gamma H_n(\xi)\xi d\xi-\left(\frac{1-\nu}{r^2}\right)\int_b^r\xi d\xi\int_b^\xi\gamma H_n(\rho)\rho d\rho\right\}-\frac{1}{2}k_n(r)\sum_{i=1}^{n}\{r-a_i\}^0 f_i^{(3)}\left[\left(1+\frac{a_i^2}{r^2}\right)+\nu\left(1-\frac{a_i^2}{r^2}\right)\right] \tag{22}$$

and

$$T_\theta(r)=\frac{1}{2}\lambda k_n(r)\left\{(1-\nu^2)\left(\frac{1}{b}+\frac{b}{r^2}\right)+\frac{1}{2}\sum_{i=1}^{n}\{r-a_i\}^0 f_i^{(1)}\times\left[\left(1-\frac{a_i^2}{r^2}\right)+\nu\left(1+\frac{a_i^2}{r^2}\right)\right]\right\}+\frac{1}{2}T_r(b)k_n(r)\left\{\beta(1-\nu^2)\left(\frac{1}{b}+\frac{b}{r^2}\right)+\frac{B_0}{h_0}\left[\left(1-\frac{b^2}{r^2}\right)+\nu\left(1+\frac{b^2}{r^2}\right)\right]+\frac{1}{2}\sum_{i=1}^{n}\{r-a_i\}^0\left[\beta f_i^{(1)}+\frac{B_0}{h_0}f_i^{(2)}\right]\times\left[\left(1-\frac{a_i^2}{r^2}\right)+\nu\left(1+\frac{a_i^2}{r^2}\right)\right]\right\}+(1-\nu^2)k_n(r)\left(\frac{1}{r^2}\int_b^r\xi\Theta d\xi-\Theta\right)-\frac{B_0}{g}\omega^2k_n(r)\left\{\nu\int_b^r\gamma H_n(\xi)\xi d\xi+\frac{1-\nu}{r^2}\int_b^r\xi d\xi\int_b^\xi\gamma H_n(\rho)\rho d\rho\right\}-\frac{1}{2}k_n(r)\sum_{i=1}^{n}\{r-\alpha_i\}^0 f_i^{(3)}\left[\left(1-\frac{a_i^2}{r^2}\right)+\nu\left(1+\frac{a_i^2}{r^2}\right)\right] \tag{23}$$

where

Downloaded 03 May 2010 to 171.66.16.20. Redistribution subject to ASME license or copyright; see http://www.asme.org/terms/Terms_Use.cfm

$$k_n(r)=\frac{h_0}{B_0}\left[1+\sum_{i=1}^{n}\{r-a_i\}^0\left(\frac{h_i}{B_i}\frac{B_0}{h_0}-\frac{h_{i-1}}{B_{i-1}}\frac{B_0}{h_0}\right)\right]. \quad (24)$$

Observe that Eqs. (21)–(23) are all expressed in terms of $T_r(b)$ which is given by

$$T_r(b)=\frac{1}{\Delta}\left\{\zeta-\frac{1}{2}\lambda\frac{h_n}{B_n}\left\{(1-\nu^2)\left(\frac{1}{b}-\frac{b}{a^2}\right)+\frac{1}{2}\sum_{i=1}^{n}f_i^{(1)}\left[\left(1+\frac{a_i^2}{a^2}\right)+\nu\left(1-\frac{a_i^2}{a^2}\right)\right]\right\}+(1-\nu^2)\frac{h_n}{B_n a^2}\int_b^a r\Theta dr+\frac{B_0\omega^2}{g}\frac{h_n}{B_n}\times\left\{\int_b^a\gamma H_n(r)rdr-\frac{1-\nu}{a^2}\int_b^a rdr\int_b^r\gamma H_n(\xi)\xi d\xi\right\}+\frac{1}{2}\frac{h_n}{B_n}\sum_{i=1}^{n}f_i^{(3)}\left[\left(1+\frac{a_i^2}{a^2}\right)+\nu\left(1-\frac{a_i^2}{a^2}\right)\right]\right\} \quad (25)$$

in which

$$\Delta=\frac{1}{2}\frac{h_n}{B_n}\left\{\beta(1-\nu^2)\left(\frac{1}{b}-\frac{b}{a^2}\right)+\frac{B_0}{h_0}\left[\left(1+\frac{b^2}{a^2}\right)+\nu\left(1-\frac{b^2}{a^2}\right)\right]+\frac{1}{2}\sum_{i=1}^{n}\left[\beta f_i^{(1)}+\frac{B_0}{h_0}f_i^{(2)}\right]\left[\left(1+\frac{a_i^2}{a^2}\right)+\nu\left(1-\frac{a_i^2}{a^2}\right)\right]\right\}. \quad (26)$$

The radial and tangential stress components are then obtained as follows:

$$\sigma_r(r)=T_r(r)/G_n(r) \quad (26)$$

$$\sigma_\theta(r)=T_\theta(r)/G_n(r) \quad (27)$$

where

$$G_n(r)=h_0\left[1+\sum_{i=1}^{n}\{r-a_i\}^0\left(\frac{h_i}{h_0}-\frac{h_{i-1}}{h_0}\right)\right]. \quad (28)$$

4 Discussion

Unlike the conventional method of discretization which results in a system of algebraic equations and thus requires a numerical approach for solution, this technique produces only a single algebraic equation, regardless of the number of discrete annular disks used in the model. This is achieved by expressing the continuity conditions between any two annular disks in terms of the boundary conditions for the overall problem using the unit step function, and this is done successively for all the junctions. The main advantage of the step reduction method is that it permits an analytical formulation for handling the problem of inhomogeneity and variable thickness in rotating disks. The accuracy of using this procedure depends on the discretization scheme used: as the number of annular disks increases to infinity, the discretized disk tends towards the continuous disk and the approximate solution approaches the exact solution. Fortunately for problems of practical interest, the profile of a disk is usually quite smooth and this method will generally yield very good results. Also, since the physical disk can either be inscribed or circumscribed by a series of discrete annular disks, it is relatively easy to make an estimate of the error caused by this process. An example is now solved to illustrate accuracy of the step reduction method. Consider the rotating disk shown in Fig. 2. The following data are used:

$$b=5\text{ cm},\quad \nu=0.3,\quad \gamma(r)=0.0681r^{0.1}\text{ N/cm}^3,$$

$$a=30\text{ cm},\quad \omega=837.76\frac{1}{\text{sec}},\quad E(r)=1.5\times10^8 r^{0.1}\text{ N/cm}^2,$$

$$h=100r^{-0.1}. \quad (29)$$

In view of Eq. (29), the governing equation in Eq. (6) becomes

$$\frac{d^2u}{dr^2}+\frac{1}{r}\frac{du}{dr}-\frac{u}{r^2}=(1+\nu)\frac{d\Theta}{dr}-\frac{B}{g}\gamma\omega^2 r \quad (30)$$

where $B(r) = 0.6067 \times 10^{-8}r^{-0.1}$. The general solution of Eq. (30) is

$$u(r)=C_1r+\frac{C_2}{r}-\frac{1}{2r}\int_b^r f(\xi)\xi^2d\xi+\frac{r}{2}\int_b^r f(\xi)d\xi, \quad (31)$$

where C_1, C_2 are integration constants and

$$f(r)=(1+\nu)\frac{d\Theta}{dr}-\frac{B}{g}\gamma\omega^2 r. \quad (32)$$

For simplicity, assume $\Theta = 0$, that is, ignore thermal loads. The boundary conditions are

$$u(b)=0,\quad T_r(a)=0. \quad (33)$$

Solving for the integration constants, the exact elastic displacement and radial and tangential force components are

$$u(r)=\left(83.26r+\frac{2058.11}{r}-0.037r^3\right)\times10^{-4}\text{ cm} \quad (34)$$

$$T_r(r)=1.6484\left(1.0824+14.40\frac{1}{r^2}-1.2205\times10^{-3}r^2\right)\times10^8\text{ N/cm} \quad (35)$$

$$T_\theta(r)=1.6484\left(1.0824+14.40\frac{1}{r^2}-7.027\times10^{-4}r^2\right)\times10^8\text{ N/cm}. \quad (36)$$

Figures 3 and 4 give a comparison of the displacement and stresses between the step-annular disk method and the exact solutions given by Eqs. (34)–(36). As observed, excellent agreement is obtained using only $n = 6$ annular disks.

As further applications of the results from the formulations are developed thus far, the calculation of shrink fit, the solution of the inverse problem of an equi-strength design, and the computations of plastic stresses and the analysis of creep at elevated temperatures will now be presented.

4.1 Calculation of Shrink Fit. As depicted in Fig. 5, a variable thickness, inhomogeneous disk of inner radius b, is to be fitted into a shaft of radius r_w. Mathematically, this involves computing the λ, β expressions listed in the boundary conditions of Eq. (13a). For simplicity, the Young's modulus of the shaft will be assumed to be constant, denoted by E^*. The boundary condition on the shaft, in terms of the radial component of the tensile force, is now given by

$$T_r(b)=-\eta h_0 p,\quad \text{when } r=r_w \quad (38)$$

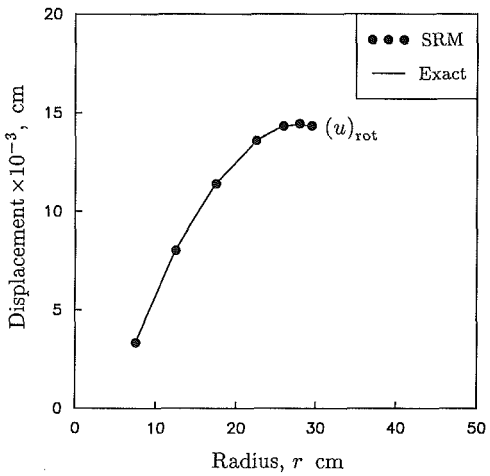


Fig. 3 Comparison of displacement predictions by the exact method and the step reduction method for $n = 6$ discrete disks

Downloaded 03 May 2010 to 171.66.16.20. Redistribution subject to ASME license or copyright; see http://www.asme.org/terms/Terms_Use.cfm

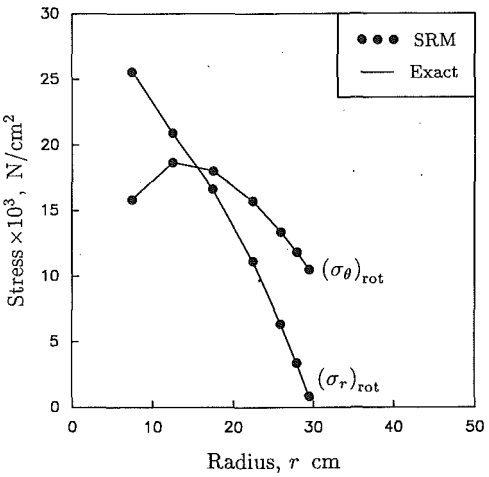


Fig. 4 Comparison of stresses predictions by the exact method and the step reduction method for n = 6 discrete disks

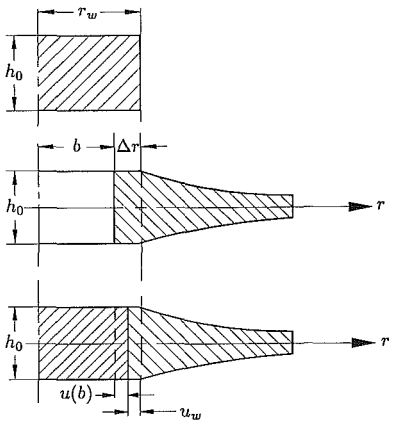


Fig. 5 Shrink fit between shaft and disk

in which p denotes the contact pressure. An empirical factor $\eta(0 < \eta \leq 1)$ is used here to assist in the computation of an effective contact area between the hub of the disk and the shaft. If L is the length of the shaft, Chien (1962) showed that for $L \gg h_0$ and $h_0/r_w = 0.5 \sim 1.5$, $\eta \approx 0.7 \sim 0.9$ and for $L \sim h_0$, $\eta = h_0/L$. The solution here is

$$u(r) = \left\{(1-\nu)\frac{1}{r_w^2}\int_b^{r_w} \xi\Theta d\xi + \frac{1}{1+\nu}\frac{B^*\omega^2}{g} \times \left[\int_0^{r_w} \gamma\xi d\xi - \frac{(1-\nu)}{r_w^2}\int_0^{r_w} \xi d\xi \int_0^{\xi} \gamma\rho d\rho\right] - \frac{\eta B^* p}{1+\nu}\right\} r + (1+\nu)\frac{1}{r}\int_0^{r} \xi\Theta d\xi - \frac{B^*\omega^2}{rg}\int_0^{r} \xi d\xi \int_0^{\xi} \gamma\rho d\rho. \quad (39)$$

At $r = r_w$, we have

$$u(r_w) = u_w = \frac{2}{r_w}\int_0^{r_w} \xi\Theta d\xi + \frac{1}{1+\nu}\frac{B^*\omega^2}{g} \times \left[r_w\int_0^{r_w} \gamma\xi d\xi - \frac{2}{r_w}\int_0^{r_w} \xi d\xi \int_0^{\xi} \gamma\rho d\rho\right] - \frac{\eta B^* p r_w}{1+\nu}. \quad (40)$$

Note that $B^* = (1 - \nu^2)/E^*$. The condition at the shaft-disk interface is

$$\Delta r = u(b) - u_w, \quad (41)$$

or substituting from Eq. (40) and rearranging leads to

$$u(b) = \Delta r - \frac{\eta B^* p r_w}{1+\nu} + \frac{2}{r_w}\int_0^{r_w} \xi\Theta d\xi + \frac{1}{1+\nu}\frac{B^*\omega^2}{g}\left[r_w\int_0^{r_w} \gamma\xi d\xi - \frac{2}{r_w}\int_0^{r_w} \xi d\xi \int_0^{\xi} \gamma\rho d\rho\right]. \quad (42)$$

Eliminating the pressure p by using Eq. (37) yields

$$u(b) = \Delta r + \frac{B^* r_w}{(1+\nu)h_0} T_r(b) + \frac{2}{r_w}\int_0^{r_w} \xi\Theta d\xi + \frac{1}{1+\nu}\frac{B^*\omega^2}{g}\left[r_w\int_0^{r_w} \gamma\xi d\xi - \frac{2}{r_w}\int_0^{r_w} \xi d\xi \int_0^{\xi} \gamma\rho d\rho\right] \quad (43)$$

For the rotating disk $\eta = 1$, and thus $T_r(b) = -h_0 p$. Comparing with Eq. (13a)

$$\lambda = \Delta r + \frac{2}{r_w}\int_0^{r_w} \xi\Theta d\xi + \frac{1}{1+\nu}\frac{B^*\omega^2}{g} \times \left[r_w\int_0^{r_w} \gamma\xi d\xi - \frac{2}{r_w}\int_0^{r_w} \xi d\xi \int_0^{\xi} \gamma\rho d\rho\right]$$

which, after integrating the second term for the constant γ of the shaft here, get

$$\lambda = \Delta r + \frac{2}{r_w}\int_0^{r_w} \xi\Theta d\xi + \frac{1}{4(1+\nu)}\frac{B^*\omega^2 r_w^3\gamma}{g}, \quad (44)$$

and for β in Eq. (13a), we have

$$\beta = \frac{B^* r_w}{(1+\nu)h_0}. \quad (45)$$

Substituting Eqs. (44)–(45) into the results obtained previously produces the required solution for shrink fit.

4.2 Equi-Strength Design for Rotating Disk. In this section, it will be of interest to develop the criterion for equi-strength design of a variable thickness, inhomogeneous disk rotating at a high speed loaded by an inhomogeneous steady temperature field. The motivation here is to compute the varying thickness of the disk such that its strength is constant everywhere in the disk. Assume the criterion of strength is described by

$$f(T_r(r), T_\theta(r)) = C(r). \quad (46)$$

Substituting Eqs. (22)–(23) to Eq. (46) yields

$$f(T_r(b), \Psi(b), h_0, h_1, \ldots, h_n, r) = C(r) \quad (47)$$

where

$$T_r(b) = \varphi_1(h_0, h_1, \ldots, h_n)$$
$$\Psi(b) = \varphi_2(h_0, h_1, \ldots, h_n). \quad (48)$$

Note that $\Psi(b)$ is obtained by solving the equation of heat conduction of arbitrary thickness disk whose property is similar to $T_r(b)$. Further details can be obtained by referring to Yeh and Lieu (1984). It should be pointed out that Eq. (47) relates the thickness h and the radius vector r of an equi-strength rotating disk. To solve this equation, the following procedure is used. Assume that $T_r(b)$ and $\Psi(b)$ are known, namely

$$T_r(b) = T_r^*(b), \quad \Psi(b) = \Psi^*(b). \quad (49)$$

It is possible to solve for h_0 from Eq. (47) at $r = a_1 - \epsilon$, that is

$$f(T_r^*(b), \Psi^*(b), h_0, a_1) = C(a_1). \quad (50)$$

Next, solve for h_1 at $r = a_2 - \epsilon$ from

$$f(T_r^*(b), \Psi^*(b), h_0, h_1, a_1, a_2) = C(a_2). \quad (51)$$

This process is repeated for k-iterations until a converged solution of the complete result for the disk, for $(T_r^*(b))_k$, $(\Psi^*(b))_k$, $(h_0)_k$, $(h_1)_k$, ..., $(h_n)_k$ is obtained. It should be noted that this procedure for the inverse problem here does

Downloaded 03 May 2010 to 171.66.16.20. Redistribution subject to ASME license or copyright; see http://www.asme.org/terms/Terms_Use.cfm

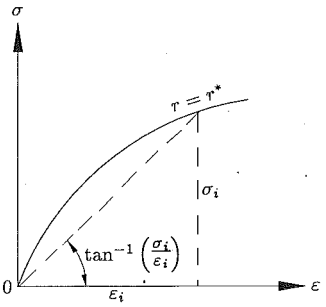


Fig. 6 Typical stress-strain curve

not produce unique solutions and a further discussion of this problem is given in Yeh and Lieu (1986).

4.3 Plastic Stress and Elevated Temperature Creep Calculations. To facilitate the computation of plastic stresses, Ilyushin's method of successive elastic solutions is adopted. In addition to assuming rotational symmetry and the plane stress situation, it is also assumed that the material is incompressible. The stress-strain relationships are

$$\epsilon_r = \frac{du}{dr} = \frac{\epsilon_i}{\sigma_i}\left(\sigma_r - \frac{1}{2}\sigma_\theta\right) + \Theta$$

$$\epsilon_\theta = \frac{u}{r} = \frac{\epsilon_i}{\sigma_i}\left(\sigma_\theta - \frac{1}{2}\sigma_r\right) + \Theta \tag{52}$$

where

$$\epsilon_i = f(\sigma_i)$$

and

$$\sigma_i = \sqrt{\sigma_r^2 + \sigma_\theta^2 - \sigma_r\sigma_\theta}. \tag{53}$$

Comparing Eq. (52) with Eq. (2) results in

$$E(r) = \sigma_i/\epsilon_i, \quad \nu = \frac{1}{2}. \tag{54}$$

Using the results gained in elastic analysis of the previous section with $\nu = 1/2$, the first approximation of the plastic stresses are given by

$$\sigma_r = (\sigma_r)_1, \quad \sigma_\theta = (\sigma_\theta)_1. \tag{55}$$

Substituting into Eq. (53) we get

$$(\sigma_i)_1 = \sqrt{(\sigma_r^2)_1 + (\sigma_\theta^2)_1 - (\sigma_r)_1(\sigma_\theta)_1}. \tag{56}$$

Having determined σ_i, the ratio σ_i/ϵ_i can be obtained from a uniaxial tensile stress-strain curve such as shown in Fig. 6. This produces a new $E(r)$ for the next iteration. As before, from the results of the elastic analysis, a second approximation of the plastic stresses can be computed:

$$\sigma_r = (\sigma_r)_2, \quad \sigma_\theta = (\sigma_\theta)_2. \tag{57}$$

This procedure is repeated until convergence is attained. In the calculation of elevated temperature creep, Wahl's creep rule is adopted. Using the von Mises yield criterion, this rule can be written in the following form:

$$\frac{d\dot{u}}{dr} = \dot{\epsilon}_r = k(\sigma_r^2 + \sigma_\theta^2 - \sigma_r\sigma_\theta)^{1/2}\left(\sigma_r - \frac{1}{2}\sigma_\theta\right)f(t)$$

and

$$\frac{\dot{u}}{r} = \dot{\epsilon}_\theta = k(\sigma_r^2 + \sigma_\theta^2 - \sigma_r\sigma_\theta)^{1/2}\left(\sigma_\theta - \frac{1}{2}\sigma_r\right)f(t) \tag{58}$$

where "$\cdot$" $= d/dt$, k is a constant and $f(t)$ is a given function. It should be noted that $\sigma_r = \sigma_r(r)$, $\sigma_\theta = \sigma_\theta(r)$. By means of the same algorithm as employed in the plastic stress calculations, the required results can be computed. However, the use of a stress-strain curve is now not necessary.

Acknowledgments

Financial support via a Professional Associateship for the first author from the University of Manitoba is gratefully acknowledged. The authors also wish to thank Dr. P. Lieu and Mr. C. Y. Hsu for their contributions in this work.

References

Abdul-Mihsein, M. J., Bakr, A. A., and Packer, A. P., 1985, "Stresses in Axisymmetric Rotating Bodies Determined by the Boundary Equation Method," *J. Strain Anal.*, Vol. 20, pp. 79–86.

Chien, W. Z., 1962, *Lectures on Strength of Materials*, Tsinghua University, Beijing.

Genta, G., Gola, M., and Gugliotta, A., 1982, "Axisymmetric Computation of the Stress Distribution in Orthotropic Rotating Disks," *Int. J. Mech. Sci.*, Vol. 24, pp. 21–26.

Ghosh, N. C., 1975, "Thermal Effect on the Transverse Vibration of Spinning Disk of Variable Thickness," ASME JOURNAL OF APPLIED MECHANICS, Vol. 42, pp. 358–362.

Ghosh, N. C., 1985, "Thermal Effect on the Transverse Vibration of High-Speed Rotating Anisotropic Disk," ASME JOURNAL OF APPLIED MECHANICS, Vol. 52, pp. 543–548.

Holms, A. C., and Faldetta, R. D., 1947, "Effects of Temperature Distribution and Elastic Properties on Gas Turbine Disk Stresses," NACA TN-864.

Ilyushin, A. A., 1943, "Some Problems in the Theory of Plastic Deformation," *RMB-12, Prikl. Math. Mech.*, Vol. 7, pp. 245–272.

Leopold, W. R., 1948, "Centrifugal and Thermal Stresses in Rotating Disks," ASME JOURNAL OF APPLIED MECHANICS, Vol. 15, pp. 322–326.

Mendelson, A., Hirschberg, M. H., and Manson, S. S., 1959, "A General Approach to the Practical Solution of Creep Problems," *Transactions of the ASME*, Vol. 81D, pp. 585–598.

Mendelson, A., 1970, *Plasticity: Theory and Application*, Macmillan, New York.

Millenson, M. B., and Manson, S. S., 1948, "Determination of Stresses in Gas Turbine Disks Subjected to Plastic Flow and Creep," NACA TR-906.

Shilizki, G. S., 1958, *The Calculation of Structure and Strength of Machine Elements of Steam Turbines*, Mechanical Engineering Publishers (in Russian).

Wahl, A. M., Sankey, G. A., Manjoine, M. J., and Shoemaker, E., 1954, "Creep Tests of Rotating Disks at Elevated Temperature and Comparison with Theory," ASME JOURNAL OF APPLIED MECHANICS, Vol. 21, pp. 222–235.

Yu, H. R., and Yeh, K. Y., 1984, "Optimal Design of Thin Elastic Solid Annular Plate under Arbitrary Distributed Load," *16th Int. Congr. Theoretical and Appl. Mech.*, Lyngby, Denmark.

Yeh, K. Y., and Lieu, P., 1984, "Steady Heat Conduction of a Disk with Nonhomogeneity and Variable Thickness," *Appl. Math. Mech.*, (English ed.), Vol. 5, pp. 1587–1593.

Yeh, K. Y., and Lieu, P., 1986, "Equi-strength Design of Nonhomogeneous, Variable Thickness High-Speed Rotating Disk under a Steady Temperature Field," *Appl. Math. Mech.*, (English ed.), Vol. 7, pp. 825–834.

Downloaded 03 May 2010 to 171.66.16.20. Redistribution subject to ASME license or copyright; see http://www.asme.org/terms/Terms_Use.cfm

D. Post
Fellow ASME

J. D. Wood

B. Han

Engineering Science and Mechanics Department, Virginia Polytechnic Institute and State University, Blacksburg, VA 24061

V. J. Parks
Civil Engineering Department, The Catholic University of Arizona, Washington, DC 20064
Fellow ASME

F. P. Gerstle, Jr.
Sandia National Laboratories, Albuquerque, NM 87185

Thermal Stresses in a Bimaterial Joint: An Experimental Analysis

An experimental analysis was conducted on a bimaterial plate subjected to a uniform change of temperature. Whole-field displacement measurements U *and* V *were made on the free surface by means of high-sensitivity moiré interferometry, and stresses were calculated from these data. Stresses resembled those of stress singularities, but they reached finite tensile and compressive peaks on opposite sides of the interface. The peaks and a severe stress gradient between them occurred in a narrow zone of about* ± 25 *μm from the interface. The results pertain to an elastic three-dimensional body.*

Specimen, Experimental Method

The complex state of elastic strains and stresses in a bimaterial joint subjected to a uniform change of temperature was investigated. The specimen configuration illustrated in Fig. 1 was studied. The steel and brass plates were joined by a very thin (<15 μm), continuous, high-temperature, high-strength, silver-solder film along the mating surfaces. It was a commercial alloy of 50 percent silver, 34 percent copper, and 16 percent zinc, with tensile strength approximately equal to that of the adherends in butt joints of steel or brass. In the soldering operation, the plates and solder were clamped together and heated with an oxyacetylene torch. The specimen was then machined on all surfaces to its final size.

The experimental analysis utilized high-sensitivity moiré interferometry (Post, 1987) to measure the deformations caused by a change of temperature of -133°C. A special implementation (Post and Wood, 1989) was used for the thermal stress analysis. In this case, a crossed line diffraction grating of 1200 lines/mm (30,480 lines/in.) was replicated on the specimen at an elevated temperature of 157°C. The procedure is illustrated in Fig. 2, where the mold is a cross-line diffraction grating (i.e., with furrows in orthogonal x and y directions) on an ultra-low expansion (ULE) glass substrate; the thermal expansion of the mold is negligible compared to that of the metals. The epoxy cement was squeezed to a thin film, about 25 μm (0.001 in.) thick. After the cement solidified and cured,

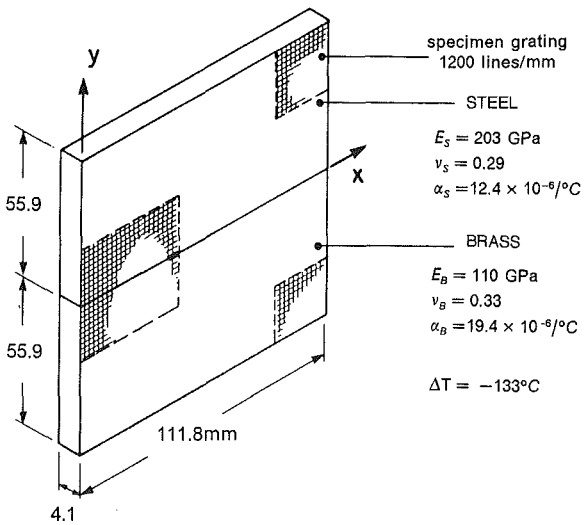


Fig. 1 Bimetal specimen with specimen gratings

Contributed by the Applied Mechanics Division of THE AMERICAN SOCIETY OF MECHANICAL ENGINEERS for publication in the ASME JOURNAL OF APPLIED MECHANICS.

Discussion on this paper should be addressed to the Technical Editor, Professor Lewis T. Wheeler, Department of Mechanical Engineering, University of Houston, Houston, TX 77204-4792, and will be accepted until four months after final publication of the paper itself in the ASME JOURNAL OF APPLIED MECHANICS.

Manuscript received by the ASME Applied Mechanics Division, Feb. 3, 1992; final revision, Dec. 21, 1992. Associate Technical Editor: W. N. Sharpe, Jr.

Copyright © 1994 by ASME
Downloaded 03 May 2010 to 171.66.16.20. Redistribution subject to ASME license or copyright; see http://www.asme.org/terms/Terms_Use.cfm

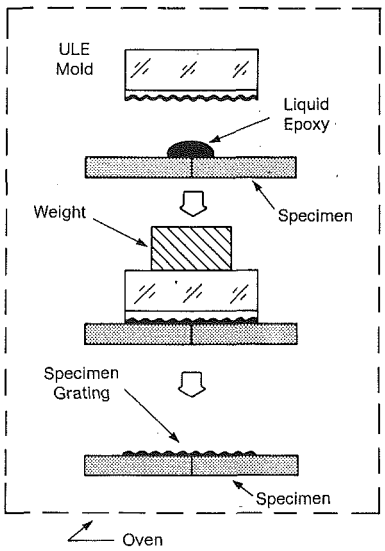


Fig. 2 Procedure to produce the specimen grating at elevated temperature. ULE glass is an ultra-low expansion substrate.

the mold was separated at the elevated temperature. This left a cross-line grating imprinted in the epoxy on the specimen. At that temperature the lines of the specimen grating were uniformly spaced. When cooled to room temperature (24°C), the specimen and overlying grating deformed as a result of (a) the free thermal contraction of the steel and brass and (b) the state of stress caused by the mutual constraint along the joint interface. The grating that crossed the interface (Fig. 1) deformed as a result of both effects, while the gratings near the traction-free corners experienced only the thermal contractions; the latter were used for measurements of the coefficients of thermal expansion of the steel and brass.

Moiré interferometry was used to record the U and V displacement at each point in the gratings, i.e., the displacement components in the x and y directions, respectively. The experimental data were received as fringe patterns that represented whole-field contour maps of the displacement fields. The contour interval was 0.417 μm (16.4 μin.) per fringe order, corresponding to moire with 2400 lines/mm (60,960 lines/in.), i.e., twice the initial specimen grating frequency (Post, 1987). In the course of the experiments, carrier fringes (Guo et al., 1989) were used to emphasize features of the deformation field. In addition, a special technique (whereby carrier fringes canceled the uniform deformation fringes of free thermal contraction) was applied to produce patterns that represented the stress-induced displacements alone (Post and Wood, 1989).

The measurements are independent of the state of residual stresses in the specimen (except to the extent that the residual stresses might influence the mechanical and thermal properties of the material). The experiments measure the deformations incurred between the application of the diffraction grating to the specimen and the subsequent observation of the deformed grating. In this analysis the material properties were assumed to be constant throughout each element, brass and steel, although the residual stresses from fabrication of the specimen were concentrated near the interface.

Relationships and Notation

The following equations of moiré interferometry and elastic thermal stress analysis were used to analyze the experimental results. The results are described in terms of the notation defined here. Additional notation is defined in subsequent sections.

$$U=\frac{1}{f}N_x^t \quad V=\frac{1}{f}N_y^t \tag{1}$$

$$\epsilon^t=\epsilon^\sigma+\epsilon^\alpha=\epsilon^\sigma+\alpha\Delta T \tag{2}$$

$$\epsilon_x^\sigma=\frac{\partial U}{\partial x}-\epsilon^\alpha=\frac{1}{f}\frac{\partial N_x^t}{\partial x}-\epsilon^\alpha=\frac{1}{f}\frac{\partial N_x^\sigma}{\partial x} \tag{3}$$

$$\epsilon_y^\sigma=\frac{\partial V}{\partial y}-\epsilon^\alpha=\frac{1}{f}\frac{\partial N_y^t}{\partial y}-\epsilon^\alpha=\frac{1}{f}\frac{\partial N_y^\sigma}{\partial y} \tag{4}$$

$$\gamma_{xy}=\gamma_{xy}^\sigma=\frac{\partial U}{\partial y}+\frac{\partial V}{\partial x}=\frac{1}{f}\left[\frac{\partial N_x^t}{\partial y}+\frac{\partial N_y^t}{\partial x}\right]=\frac{1}{f}\left[\frac{\partial N_x^\sigma}{\partial y}+\frac{\partial N_y^\sigma}{\partial x}\right] \tag{5}$$

$$\sigma_x=\frac{E}{1-\nu^2}(\epsilon_x^\sigma+\nu\epsilon_y^\sigma) \quad \sigma_y=\frac{E}{1-\nu^2}(\epsilon_y^\sigma+\nu\epsilon_x^\sigma) \tag{6}$$

$$\tau_{xy}=G\gamma_{xy}=\frac{E\gamma_{xy}}{2(1+\nu)} \tag{7}$$

where

N_x^t and N_y^t are fringe orders in the patterns of total displacements,
N_x^σ and N_y^σ are fringe orders in the patterns of stress-induced displacements,
f is 2400 lines/mm (60,960 lines/in.) for the macroscopic analysis,
ϵ and γ are normal and shear strains,
superscripts t, σ, and α represent the total strain, the stress-induced part of the strain, and the free thermal expansion part of the strain, respectively;
α is coefficient of thermal expansion, listed in Fig. 1 for the steel and brass;
ΔT is the temperature increment;
σ and τ are normal stress and shear stress;
E is modulus of elasticity, listed in Fig. 1;
ν is Poisson's ratio, listed in Fig. 1; and
G is shear modulus of elasticity (or modulus of rigidity).

Equations (2)–(4) and (6), (7) pertain to the steel and brass portions separately, inasmuch as α, E, and ν are different in the two materials. Equations (6) are used for the surface of the specimen since there are no normal tractions on the surface. Shear stresses and shear strains are independent of the uniform thermal contraction, so either N^t or N^σ can be used in (5).

Results: Moiré Interferometry

The direct results of moiré interferometry are shown in Figs. 3 and 4. Figure 3(a) is the total V displacement field, i.e., the N_y^t pattern. It is dominated by the thermal contraction of each part, steel, and brass; thus the gradient $\partial N_y^t/\partial y$ is negative everywhere. Of course, the total displacements are continuous across the steel/brass interface. The stress-induced deformations combine with the free thermal contractions to produce a sharp change of fringe gradient across the interface. This change is emphasized in Fig. 3(b), where carrier fringes of extension were introduced. They have the effect of subtracting off a uniform strain equal to the average (approximately) of the thermal contractions. The change across the interface is rather abrupt.

In Fig. 3(c), the carrier fringes introduced a uniform apparent strain equal and opposite to the experimentally determined ϵ^α (or $\alpha\Delta T$), which had the effect of canceling the free thermal contraction part of the fringe pattern. The result is the pattern of the stress-induced displacements, namely the contour map of the N_y^σ. The procedure was carried out separately for the upper and lower regions since the magnitudes of α are different for steel and brass.

Corresponding U displacement fields are shown in Fig. 4, where carrier fringes were used in (a) to subtract a strain approximately equal to the average of the thermal contractions; (b) is the stress-induced part of the U field, depicted by contours of N_x^σ. Pattern (a) proves that the ϵ_x^t strains in the steel and

Downloaded 03 May 2010 to 171.66.16.20. Redistribution subject to ASME license or copyright; see http://www.asme.org/terms/Terms_Use.cfm

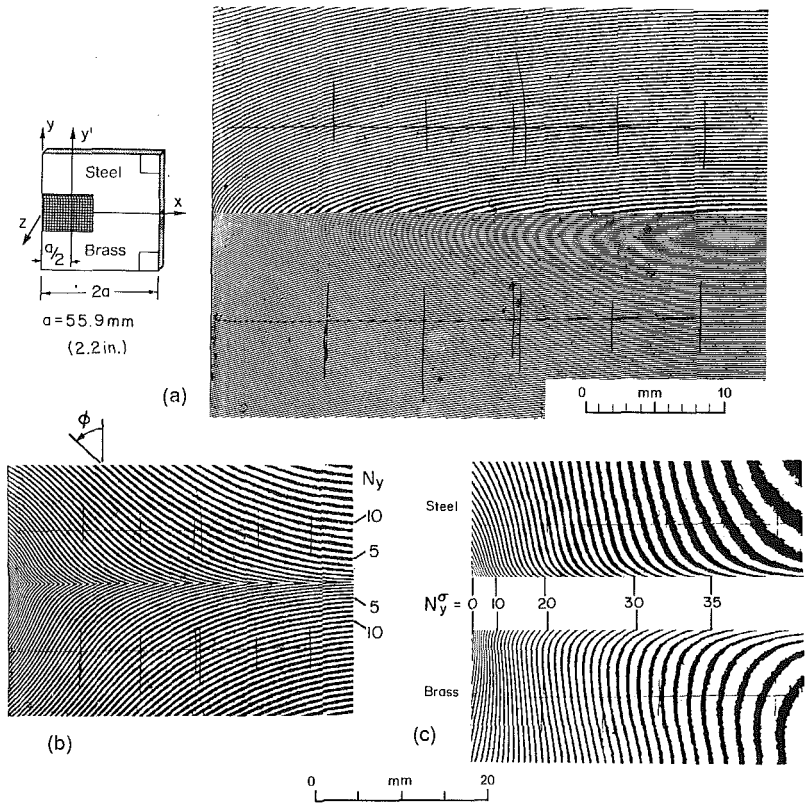


Fig. 3 *V* displacement fields in shaded region for $\Delta T = -133°C$. (*a*) contours of N_y^t, depicting the total displacements. (*b*) N_y field modified by carrier fringes of extension. (*c*) contours of N_y^σ, depicting the stress-induced displacements in steel and brass.

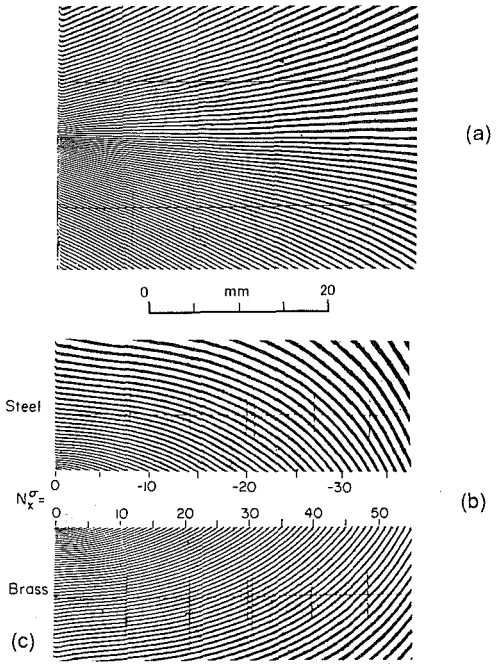


Fig. 4 *U* displacement fields for $\Delta T = -133°C$. (*a*) N_x field with carrier of extension, (*b*) contours of N_x^σ.

brass are constant along the interface and identical in the two materials. The fringe orders marked in (b) indicate that the stress-induced strain ϵ_x^σ along the interface is compressive in the steel and tensile in the brass. This is consistent with the greater thermal contraction of the brass and the opposing restraint by steel.

Results: Mechanical Differentiation

Figure 5 introduces another kind of fringe pattern, the pattern of mechanical differentiation (Duncan and Sabin, 1965; Post, 1987). Using (a) as an example, the pattern was constructed by superimposing two photographic images of the fringe pattern of N_x^t, with a shift of one image relative to the other by a finite increment Δx. When shifted, the dark lines of the two patterns interweave and create a moire effect. The effect is known as geometric moiré, which is distinct from the interferometric moiré of Figs. 3 and 4. At any point in the pattern, the fringe order N_{xx}^* equals the difference, ΔN_x^t, of fringe orders N_x^t in the two superimposed transparencies. Thus,

$$N_{xx}^* = \Delta N_x^t = \Delta x \frac{\partial N_x^t}{\Delta x} \approx \Delta x \frac{\partial N_x^t}{\partial x} \tag{8}$$

The double subscript refers, first, to the displacement component of the fringe pattern and, second, to the direction of the shift.

Accordingly, N_{xx}^* is proportional to the finite-increment approximation of the differential. By (3),

$$\epsilon_x^\sigma \approx \frac{1}{f\Delta x} N_{xx}^* - \epsilon^\alpha \tag{9}$$

The finite increment approximation must exactly equal the derivative at one point in the interval and it is very accurate in regions where the strain gradient in the interval Δx is either linear or small. In this case, it is a useful means of extracting the derivatives on a whole-field basis everywhere except in the immediate vicinity of the interface.

Although two fields are shown, the same procedure was used to portray all four derivative fields, i.e., shifting each pattern N_x^t and N_y^t by increments Δx and Δy. The increments were 2.5 mm (0.1 in.) in all cases, and the data pertains to the

Downloaded 03 May 2010 to 171.66.16.20. Redistribution subject to ASME license or copyright; see http://www.asme.org/terms/Terms_Use.cfm

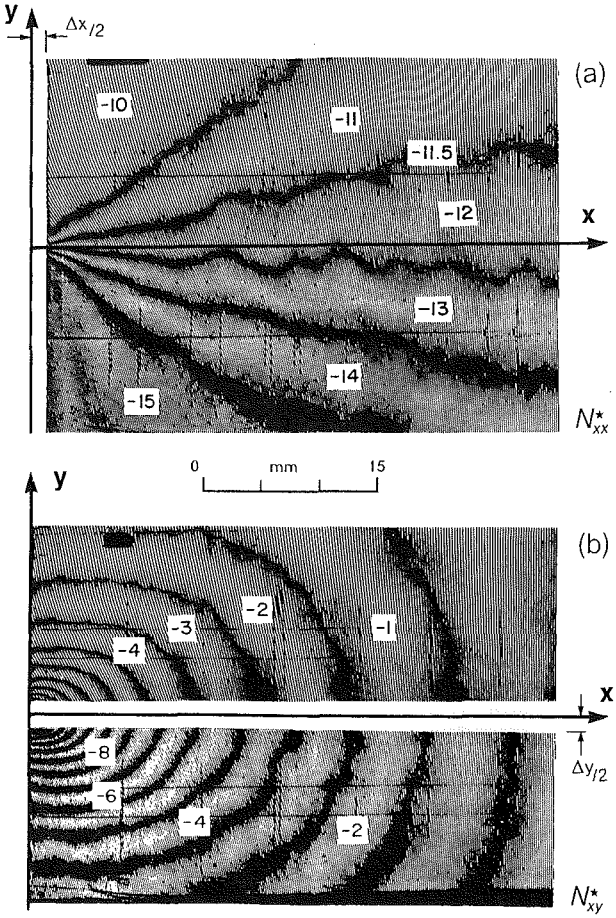


Fig. 5 Contours of displacement derivatives by mechanical differentiation. $\Delta x = \Delta y = 2.5$ mm (0.1 in.). (*a*) N^*_{xx} fringe orders are proportional to $\partial U/\partial x$. (*b*) N^*_{xy} fringe orders are proportional to $\partial U/\partial y$.

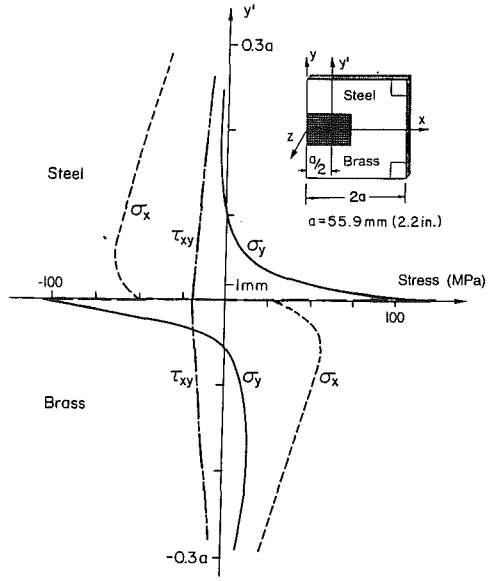


Fig. 6 The distribution of stresses on the y' axis

midpoint of each increment. Therefore, zones of width $\Delta x/2$ and $\pm\Delta y/2$ are blank in the figures because the parent patterns did not overlap in these zones and no data exist there. These blank zones are only 1.25 mm wide (or about one percent of the specimen length) and, in this case, the gradients were large in these zones.

An obvious feature of the strain distribution is the irregular nature of fringes in Fig. 5(*a*). A theoretical elasticity solution would prescribe smooth contours, so the irregularities must be associated with some facet of the experiment. We cannot develop a consistent argument that attributes the fringe irregularities to features of the experimental technique. It is tempting to attribute them to gaps or cracks in the silver-solder joint, but cracks would induce out-of-phase fluctuations on opposite sides of the interface in Fig. 5(*a*). The observed in-phase fluctuations indicate ϵ_x continuity across the interface. We believe that there are no gaps or cracks in the joint, but instead, one or both of the materials exhibits small variations of (one or more) physical properties, namely thermal coefficient of expansion, modulus of elasticity, and Poisson's ratio. These variations might be heightened in a heat-affected zone near the silver-soldered interface, where the fringe irregularities are most severe. This is the zone of largest residual stresses, too. Such anomalies illustrate the vagaries of real materials.

The largest departure from a smooth N^*_{xx} fringe occurs near the interface in the brass, where the departure is 1/4 fringe order. If a variation of thermal coefficient of expansion in the brass was fully responsible for this irregularity, the local value of α would have changed by $3\times10^{-7}/°C$, or by 1.5 percent of its global value.

The fringes were smoothed for data interpretation. Then, the total strains were determined from fringe orders by $\epsilon^t_x = N^*_{xx}/f\Delta x = 164\times10^{-6}\,N^*_{xx}$, and the stress-induced strains by $\epsilon^\sigma_x = 164\times10^{-6}\,N^*_{xx} - \epsilon^\alpha$. Note that ϵ^α is negative for both materials. Similar relationships apply for all four derivatives. The numbers shown on the fringe patterns are N^* values for each derivative field.

Results: Graphs and Contour Maps

The displacement patterns of Figs. 3 and 4 were analyzed in accordance with (3)–(5). A detailed analysis was performed along the y'-axis at the quarter width of the specimen. The ϵ^σ_x and γ_{xy} curves were nearly linear and data extraction was relatively easy. Special attention was given to the determination of ϵ^σ_y near the interface. The data were extracted from Fig. 3(*a*) by (a) measuring fringe positions on an enlarged pattern using a digitizing tablet, (b) calculating the incremental derivative $\Delta N^t_y/\Delta y$ between fringes, and (c) calculating the best fit of a second-order polynomial curve to the high gradient portion of the data. The ϵ_y strains were not extrapolated to the interface, but remain undetermined, for now, in the narrow zone bounded by $y \approx \pm 100$ μm (0.004 in.), which will be called the *interface zone*.

The corresponding stresses were calculated from the strains by (6), (7), which are valid over the free surface of the specimen, where $\sigma_z = 0$. These stresses are plotted in Fig. 6. The stress distributions are remarkably similar in the steel and brass. The shear stresses are nearly symmetrical and exhibit equal magnitudes at the interface. Normal stresses σ_x have similar distributions, but opposite signs. The difference between interface values does not violate equilibrium. Normal stresses σ_y exhibit similar distributions, but with opposite signs. These stresses were not extrapolated to the interface; if they were, a violation of σ_y equilibrium would appear. The σ_y stresses in the interface zone will be discussed in the next section.

A detailed analysis of the fringe patterns, Figs. 3 and 4, was also performed within the interface zone. The stresses plotted in Fig. 7 represent σ_x and τ_{xy} at the interface and the peak values of σ_y, which occur *near* the interface. They illustrate that the stress disturbance at the specimen corner is highly localized—within about one percent of the specimen length for the normal stresses and three percent for the shear stress. Elsewhere, the normal stresses are constant and the shear stresses vary linearly along the interface length. Of course,

Downloaded 03 May 2010 to 171.66.16.20. Redistribution subject to ASME license or copyright; see http://www.asme.org/terms/Terms_Use.cfm

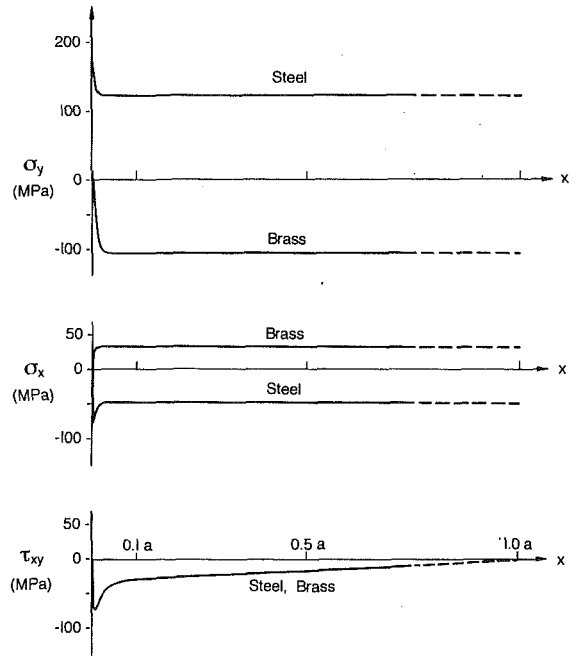


Fig. 7 The distribution of peak stresses near the interface along the free surface

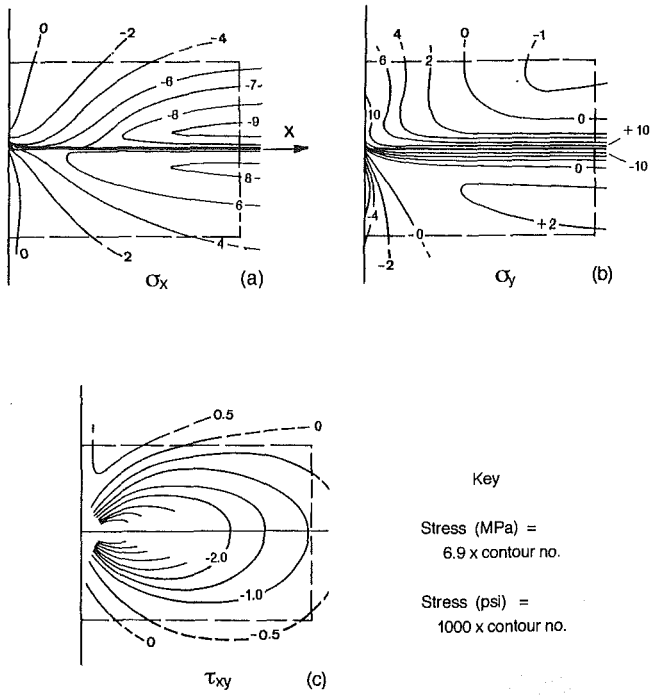


Fig. 8 Contour maps of surface stress distributions in 30 x 40 mm portion of the specimen

these represent stresses at the surface of the specimen and they are not proposed as representative of the interior stresses.

Whole-field contour maps of the surface stress fields are shown in Fig. 8. The mechanical differentiation data were used for the portion of the specimen covered by the specimen grating (except in the high gradient region). For the shear stress determination, the special graphical process in Post et al. (1985) was used to add the cross-derivatives and construct the map of shear strains. Equations (6), (7), were used to calculate the stresses. In the high gradient region, stresses were calculated using data from the moiré patterns of Figs. 3 and 4. Figure 8(b) illustrates that σ_y is very small except near the interface. The σ_y distribution is essentially independent of x near the interface, except close to the free corner of the specimen.

σ_y Within the Interface Zone

In order to assess the distribution of σ_y in the immediate vicinity of the interface, the sharpness of the chevron-like fringes of Fig. 3(b) must be evaluated. The fringes are clearly delineated outside the interface zone; within the tiny interface zone, however, the paths of the fringes are inconclusive. If the clearly delineated fringes in the steel and brass are extrapolated to the interface with a monotonically increasing inclination (i.e., increasing $|\phi|$), or else with a constant inclination, then the peak values of σ_y in both materials would occur at the interface, $y=0$. A physically inadmissible condition would result, where σ_y at each interface point would have two distinct values and where vertical equilibrium would be violated.

On the other hand, if the fringes change their course and bend toward the interface, the curve of σ_y versus y' would reach peak positive and negative values at some small distance from the interface. The σ_y curve would then turn sharply away from the peaks and progress in the interface zone with finite slopes between the peak values. The analysis that relates the fringe inclination ϕ (Fig. 3b) to σ_y is given by Wood (1992), which shows that σ_y is proportional to $\tan\phi$ minus a constant.

Supplementary Experiment. Since σ_y depends critically upon ϕ in the narrow interface zone of Fig. 3(b), and the shape of the fringes in that zone remains uncertain, additional experimental evidence was sought by the method of microscopic moiré interferometry (Han and Post, 1992; Han, 1992). With this method, an immersion interferometer provided a twofold increase of basic sensitivity, utilizing a virtual reference grating of 4800 lines/mm (122,000 lines/in.). Phase shifting and optical/digital fringe sharpening and multiplication provided contour maps of displacements with contour intervals of 52 nm/fringe contour. Microscopic fields of view of 540 and 310 μm (0.021 and 0.012 in.) widths were observed, spanning the interface region.

The same specimen as that of Fig. 1 was used, except its width and height were cut to half the previous dimensions. The specimen grating was applied at elevated temperature, as before, and observed at room temperature to reveal the thermal deformation. The specimen grating was applied at the center as depicted in Fig. 9. This change from the quarter-width position of y' is permissible since σ_y is independent of x in these regions. Replication of the specimen grating in this small region of interest was achieved with a much smaller grating thickness, approximately 2 μm thickness in this case. Accordingly, the shear lag that occurs through the grating thickness in the vicinity of high strain gradients is now expected to affect a zone of about $y=\pm 5$ μm (± 0.0002 in.). Authentic results can be expected at locations ten times closer to the interface than in the previous macroscopic experiment.

The resulting fringe contours are shown in Fig. 9, which represent the thermal deformations plus carrier fringes. The carrier fringes were applied again to emphasize the changes near the interface. Carrier fringes of extension subtracted off the average (approximately) of the fringe gradients in the steel and brass, as before. Carrier fringes of rotation were applied to create a vertical bias in the pattern and thereby delineate the fringe contours across the interface. Note that the carrier of extension adds a constant apparent strain to ϵ_y^σ, and that the carrier fringes of rotation are parallel to the y-axis and have no influence on $\partial N_y/\partial y$ and no influence on ϵ_y^σ. The interface is indicated by the broken line in Fig. 9; its location relative to the contour map was determined by microscopic inspection.

The patterns show a distinct decrease of $|\phi|$ in a 50 μm (0.002 in.) zone, which proves that the curves of ϵ_y^σ for the

Downloaded 03 May 2010 to 171.66.16.20. Redistribution subject to ASME license or copyright; see http://www.asme.org/terms/Terms_Use.cfm

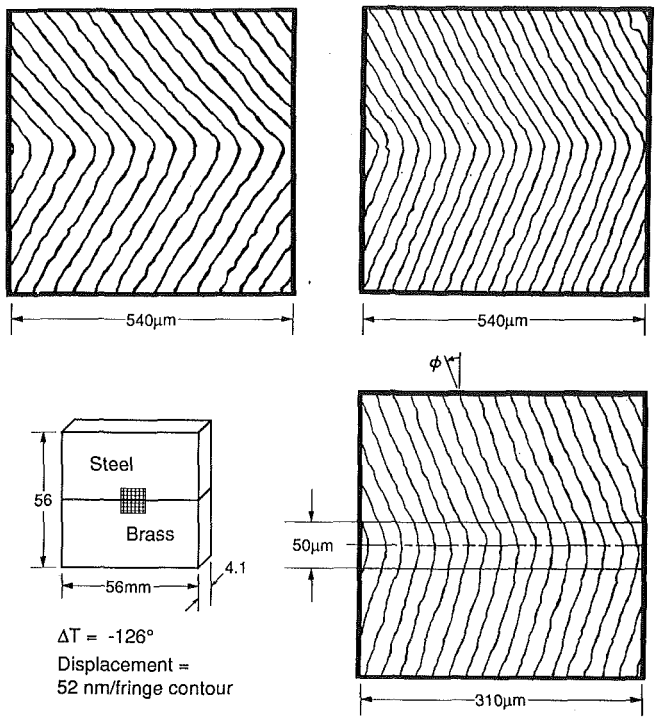


Fig. 9 Patterns corresponding to Fig. 3(*b*), but with higher sensitivity and higher spatial resolution, produced by microscopic moiré interferometry. The patterns differ by the amount of carrier of rotation and magnification.

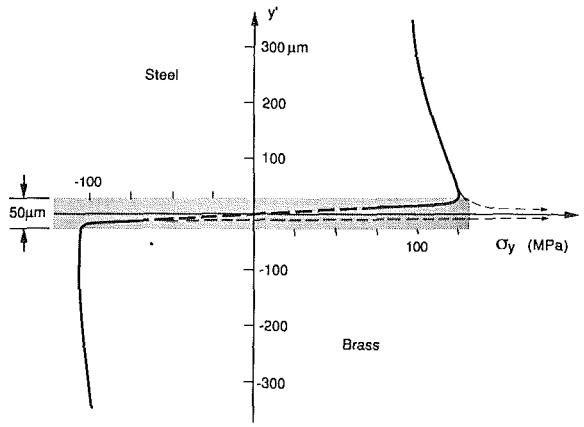


Fig. 10 Magnified view of σ_y across the interface. The bold curve shows experimental results.

steel and brass turn around from their peak values and move towards each other in a very narrow zone of extremely high strain gradients. By Eq. (6), and knowledge that ϵ_x is essentially constant in this zone, σ_y must follow the same trend. The distribution of σ_y is illustrated in Fig. 10, where the vertical scale is greatly magnified relative to Fig. 6. The axis is marked y', but the results apply for most of the interface zone as indicated in Fig. 7 and discussed above. The bold dashed line recognizes the remaining uncertainty in the high gradient region. The region of uncertainty is now diminished by an order of magnitude, and a monotonic variation of σ_y within the region can be rationalized with substantial confidence. The microscopic analysis indicates a σ_y curve near the interface that is always single valued, i.e., the curve has finite slope, and the potential equilibrium imbalance is eliminated. The stress gradients are high, but finite.

The fringe contours in Fig. 9 clarified the local field. The peak value of σ_y in the steel obtained from Fig. 3 was slightly lower than that obtained from Fig. 9, but the result of the microscopic analysis has been incorporated into the curves of Figs. 6 and 7.

Discussion

Note that $\partial N_y/\partial x$ is not affected by the fringe curvature in the interface zone. Note, too, that there is no corresponding uncertainty for the N_x fringes. Accordingly, the σ_x and τ_{xy} curves in Fig. 6 extend to the interface, $y' = 0$.

The behavior of σ_y along y' is considered the most important finding; we will focus on that result. Related elasticity solutions appear in the literature, although none match the experimental parameters. Thus, quantitative comparisons are not contemplated, but qualitative comparisons seem significant.

Williams (1952), Hein and Erdogan (1971), Kuo and Bogy (1974), Wang and Choi (1982), Zwiers et al. (1982), Blanchard and Ghoniem (1989), and Kuo (1989) developed analytical elasticity solutions to examine stresses at the end of the bonded interface. Singular stresses were predicted at the junction of the bimaterial interface and the free surface for most combinations of material and geometry. These analyses are typified as plane solutions with assumptions of two dimensionality, whereas the experimental analysis investigated stresses in a three-dimensional body.

Analytical solutions with simplifying assumptions provided results more amenable to engineering practice. Papers in this category include Hess (Apr. 1969, Oct. 1969), Chen and Nelson (1979), Suhir (1986, 1989), and Pionke and Wempner (1991). Again, high σ_y stresses were predicted at the interface/free boundary junction for most cases. The solutions were two dimensional, except for a three-dimensional finite element analysis included in the last paper.

Numerical elasticity solutions include Gerstle and Chambers (1987), Seo et al. (1989), Wood et al. (1989), Tsai (1990), Tsai and Morton (1991), and Pionke and Wempner (1991). Seo et al. showed families of curves for σ_y similar to the experimental result of Fig. 6. Wood et al., Tsai, and Tsai and Morton studied steel/brass models of various geometries. They showed distributions similar to σ_y in Fig. 6; a clear stress minima appeared in the brass near the interface, whereupon σ_y increased as the interface was approached. These results represented plane, axisymmetric, and three-dimensional models.

Suganuma et al. (1987) performed experimental studies of residual stresses on bimaterial joints with rectangular and circular interfaces. They applied small electrical strain gages on the specimen and used a cutting process to relieve the residual stresses. Although their spatial resolution was relatively low, they reported continuous curves for σ_y with a tensile peak near the interface on one side of the joint and a compressive peak near the interface on the other side, akin to Fig. 10.

By synthesis of all these results, we conclude that an exact elasticity solution for the steel/brass thermal stress specimen (Fig. 1) would show asymptotic curves for σ_y. Their general shape would be that illustrated in Fig. 10 by the solid lines blending into the thin dashed lines. A tensile singularity is envisioned, with extremely large stress gradients in narrow zones above and below the interface.

On the other hand, the results of the microscopic moiré experiment appear to be definitive in prescribing turnarounds of the σ_y curve in both the steel and brass (Fig. 10). In order to indicate an asymptotic rise of σ_y in the steel, the fringe contours in Fig. 9 must exhibit convex curvature (increasing ϕ) as they approach the interface; instead they are concave. If local yielding occurred, the strains would increase near the interface and the fringes would become more convex. That doesn't occur.

Based on St. Venant's principle, the presence of the solder as a third material does not seem to be significant. The turnaround points of the σ_y curve (Fig. 10) are at least three times

Downloaded 03 May 2010 to 171.66.16.20. Redistribution subject to ASME license or copyright; see http://www.asme.org/terms/Terms_Use.cfm

more distant from the centerline of the solder material than the boundary of the solder. Therefore, essentially the same results would be expected in the turnaround region for a theoretical bonding agent of zero thickness.

The experimental analysis must be viewed as an elasticity solution, since the largest stresses along y' were well below the yield points of the materials. There is a conflict. The asymptotic field is not found in the experiments, even though the consensus of the analytical and numerical results suggests its existence. The importance of experimental mechanics is highlighted. The conflict is expected to stimulate further theoretical and experimental investigations.

Thermal loading was used in the tests reported here. However, the stresses near a bimaterial interface under mechanical loading exhibit concentrations of the same nature. In many cases, the stresses in thermal and mechanical loading differ merely by a uniform stress field.

Conclusions

The surface stresses in a bimaterial metal joint subjected to a uniform temperature change were determined experimentally. Surface strains ϵ_x, ϵ_y, and γ_{xy} were determined on a whole-field basis and stresses were calculated using known mechanical properties. Large tensile and compressive stresses, directed normal to the interface, were documented on opposite sides of the interface. They reached finite peak values of opposite signs, whereupon their magnitudes decreased precipitously in an extremely narrow zone extending about ± 25 μm from the interface. This very strong tension-compression stress system occurred along the entire length of the interface and it can be assumed to prevail along the entire perimeter of the joint.

A localized but strong disturbance was observed in the corner region where two free edges intersected. The experiments represent an analysis of a fully three-dimensional, elastic bimaterial thermal stress problem. Both macroscopic and microscopic moiré interferometry were required to extract the stress distribution.

Acknowledgments

This work was sponsored by Sandia National Laboratories under Contract No. 75-8962 and by the Office of Naval Research under Grant N00014-86-K0799. The support and encouragement are gratefully acknowledged.

References

Blanchard, J. P., and Ghoniem, N. M., 1989, "Relaxation of Thermal Stress Singularities in Bonded Viscoelastic Quarter Planes," ASME JOURNAL OF APPLIED MECHANICS, Vol. 56, pp. 756–762.

Chen, W. T., and Nelson, C. W., 1979, "Thermal Stresses in Bonded Joints," *IBM J. of Research and Development*, Vol. 23, No. 2, pp. 179–188.

Duncan, J. P., and Sabin, P. G., 1965, "An Experimental Method for Recording Curvature Contours in Flexed Elastic Plates," *Experimental Mechanics*, Vol. 5, pp. 22–28.

Gerstle, Jr., F. P., and Chambers, R. S., 1987, "Analysis of End Stresses in Glass-Metal Bimaterial Strips," ASME WAM, Dec., Boston, MA.

Guo, Y., Post, D., and Czarnek, R., 1989, "The Magic of Carrier Fringes in Moiré Interferometry," *Experimental Mechanics*, Vol. 29, pp. 169–173.

Han, B., and Post, D., 1992, "Immersion Interferometer for Microscopic Moiré Interferometry," *Experimental Mechanics*, Vol. 32, No. 1, pp. 38–41.

Han, B., 1992, "Higher Sensitivity Moiré Interferometry for Micromechanics Studies," *Optical Engineering*, Vol. 31, No. 7, pp. 1517–1526.

Hein, V. L., and Erdogan, F., 1971, "Stress Singularities in a Two-Material Wedge," *Int. J. of Fracture Mechanics*, Vol. 7, pp. 317–330.

Hess, M. S., Apr. 1969, "The End Problem for a Laminated Elastic Strip—I. The General Solution," *J. Composite Materials*, Vol. 3, pp. 262–280.

Hess, M. S., Oct. 1969, "The End Problem for a Laminated Elastic Strip—II. Differential Expansion Stresses," *J. Composite Materials*, Vol. 3, pp. 630–641.

Kuo, A.-Y., 1989, "Thermal Stresses at the End of a Bimetallic Thermostat," ASME JOURNAL OF APPLIED MECHANICS, Vol. 56, pp. 585–589.

Kuo, M. C., and Bogy, D. B., 1974, "Plane Solutions for the Displacement and Traction-Displacement Problems for Anisotropic Elastic Wedges," ASME JOURNAL OF APPLIED MECHANICS, Vol. 41, pp. 197–202.

Pionke, C. D., and Wempner, G., 1991, "The Various Approximations of the Bimetallic Thermostatic Strips," ASME JOURNAL OF APPLIED MECHANICS, Vol. 58, pp. 1015–1020.

Post, D., Czarnek, R., and Joh, D., 1985, "Shear-Strain Contours by Moiré Interferometry," *Experimental Mechanics*, Vol. 25, pp. 282–287.

Post, D., 1987, "Moiré Interferometry," *Handbook of Experimental Mechanics*, A. S. Kobayashi, ed., Prentice-Hall, Englewood Cliffs, NJ, pp. 314–387.

Post, D., and Wood, J. D., 1989, "Determination of Thermal Strains by Moiré Interferometry," *Experimental Mechanics*, Vol. 29, pp. 318–322.

Seo, K., Kusaka, M., Nogata, F., Terasaki, T., Nakao, Y., and Saida, K., 1989, "Study on the Thermal Stress at Ceramics-Metal Joint," *Proc. Japan Soc. Mech. Engrs.*, (in Japanese), Vol. 55, No. 510, pp. 312–317.

Suganuma, K., Okamoto, T., Koizumi, M., and Kamachi, K., 1987, "Influence of Shape and Size on Residual Stress in Ceramic/Metal Joint," *J. Mat'l. Science*, Vol. 22, pp. 3561–3565.

Suhir, E., 1986, "Stresses in Bimetal Thermostats," ASME JOURNAL OF APPLIED MECHANICS, Vol. 53, pp. 657–660.

Suhir, E., 1989, "Interfacial Stresses in Bimetal Thermostats," ASME JOURNAL OF APPLIED MECHANICS, Vol. 56, pp. 595–600.

Tsai, M.-Y., 1990, "Application of Localized Hybrid Methods of Stress Analysis to Some Problems in the Mechanics of Composites," Ph.D. Dissertation, Virginia Polytechnic Institute and State University, Blacksburg, VA.

Tsai, M.-Y., and Morton, J., 1991, "The Stresses in a Thermally Loaded Bimaterial Interface," *Int. J. of Solids and Structures*, Vol. 28, No. 8, pp. 1053–1075.

Williams, M. L., 1952, "Stress Singularities Resulting from Various Boundary Conditions in Angular Corners of Plates in Extension," ASME JOURNAL OF APPLIED MECHANICS, Vol. 19, pp. 526–528.

Wang, S. S., and Choi, I., 1982, "Boundary-Layer Effects in Composite Laminates; Part I: Free-Edge Stress Singularities," ASME JOURNAL OF APPLIED MECHANICS, Vol. 49, pp. 541–548; "Part 2: Free-Edge Stress Solutions and Basic Characteristics," Ibid, pp. 549–560.

Wood, J. D., Tsai, M.-Y., Post, D., Morton, J., Parks, V. J., and Gerstle, Jr., F. P., 1989, "Thermal Strains in a Bimaterial Joint: An Experimental and Numerical Analysis," *Proc. 1989 Spring Conference of the Society for Experimental Mechanics*, Cambridge, MA, pp. 543–551.

Wood, J. D., 1992, "Determination of Thermal Strains in a Bimaterial Joint," Ph.D. Dissertation, Virginia Polytechnic Institute and State University, Blacksburg, VA.

Zwiers, R. I., Ting, T. C. T., and Spilker, R. L., 1982, "On the Logarithmic Singularity of Free-Edge Stress in Laminated Composites Under Uniform Extension," ASME JOURNAL OF APPLIED MECHANICS, Vol. 49, pp. 561–569.

Downloaded 03 May 2010 to 171.66.16.20. Redistribution subject to ASME license or copyright; see http://www.asme.org/terms/Terms_Use.cfm

Journal of Applied Mechanics

Brief Notes

A Brief Note is a short paper that presents a specific solution of technical interest in mechanics but which does not necessarily contain new general methods or results. A Brief Note should not exceed 1,500 words *or equivalent* (a typical one-column figure or table is equivalent to 250 words; a one line equation to 30 words). Brief Notes will be subject to the usual review procedures prior to publication. After approval such Notes will be published as soon as possible. The Notes should be submitted to the Technical Editor of the JOURNAL OF APPLIED MECHANICS. Discussions on the Brief Notes should be addressed to the Editorial Department, ASME, United Engineering Center, 345 East 47th Street, New York, N. Y. 10017, or to the Technical Editor of the JOURNAL OF APPLIED MECHANICS. Discussions on Brief Notes appearing in this issue will be accepted until two months after publication. Readers who need more time to prepare a Discussion should request an extension of the deadline from the Editorial Department.

On the Permanent Rotation of a Torque-Free Two-Body System With a Flexible Connection

Y. Z. Liu[1] and F. P. J. Rimrott[2,3]

1 Introduction

The motion of a torque-free two-body system with a spherical joint is proposed as a model for the behavior of a dual-spin spacecraft with flexible connections. It has been proven (Liu, 1989) that the normal permanent rotation of a two-body system about coincident common symmetrical axes is always stable when the system has no flexible elements and no energy dissipation. In practice, internal damping effects are unavoidable, therefore the stability of normal permanent rotations is conditioned, and there exist other states of permanent rotation deviating from the principal axes of the bodies. In this paper the various states of permanent rotation and their condition of existence are discussed. The energy-sink method is used in the analysis of the stability of each permanent rotation.

2 Dynamical Equations

Consider a torque-free system composed of two axisymmetric rigid bodies $B_i (i=1,2)$ with a flexible connection, which is modeled as a spherical joint with spring (Fig. 1).

The symbols O_i, m_i, A_i, C_i, represent the mass center, mass, transverse, and polar central inertia moment of B_i, while O_c and m are the mass center and mass of the whole system. We establish the following reference frames:

(O_cXYZ)—inertial reference frame, where O_cZ is parallel to the angular momentum $\mathbf{H}$ of system about O_c

$(O_iX_iY_iZ_i)$—a reference frame with axes parallel to (O_cXYZ)

$(O_ix_iy_iz_i)$—semi-fixed coordinate frame of B_i, with axis of symmetry O_iz_i, and O_ix_i perpendicular to O_iZ_i and O_iz_i

Let ψ_i, θ_i, ϕ_i be the Euler angles of B_i relative to $(O_iX_iY_iZ_i)$ as shown in Fig. 2.

The angular momentum $\mathbf{H}$ of the system about O_c can be written by use of the general expression (Hooker and Margulies, 1965; Liu, 1989)

$$\mathbf{H} = \sum_{i=1}^{2} \mathbf{I}_i \cdot \omega_i \tag{1}$$

where $\mathbf{I}_i$ is the equivalent inertia tensor of the body B_i with respect to O_c. While ω_i is the angular velocity of B_i.

Since the system is torque-free, the angular momentum $\mathbf{H}$ must be constant. Projecting $\mathbf{H}$ onto the axes of (O_cXYZ), we obtain

$$\sum_{i=1}^{2} \{[A_i c\psi_i - \mu(c\theta_i c\theta_j c\psi_i - s\theta_i s\theta_j c\psi_j)]\dot{\theta}_i + [(C_i - A_i)c\theta_i - \mu c\theta_j]s\theta_i s\psi_i \dot{\psi}_i + C_i s\theta_i s\psi_i \dot{\phi}_i\} = 0 \tag{2a}$$

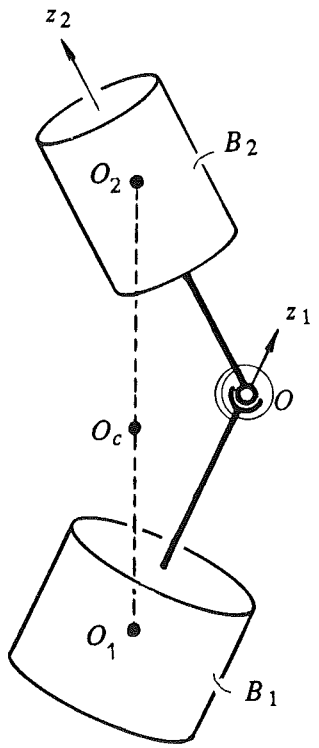


Fig. 1 Two-body system with flexible connection

[1]Department of Engineering Mechanics, Shanghai Jiao Tong University, 1954 Hua Shan Road, Shanghai 200 030, China.

[2]Department of Mechanical Engineering, University of Toronto, Toronto, Ontario MS5 1A4, Canada. Fellow ASME.

[3]To whom correspondence should be addressed.

Manuscript received by the ASME Applied Mechanics Division, Jan. 13, 1992; final revision, June 15, 1992. Associate Technical Editor: P. D. Spanos.

Copyright © 1994 by ASME
Downloaded 03 May 2010 to 171.66.16.20. Redistribution subject to ASME license or copyright; see http://www.asme.org/terms/Terms_Use.cfm

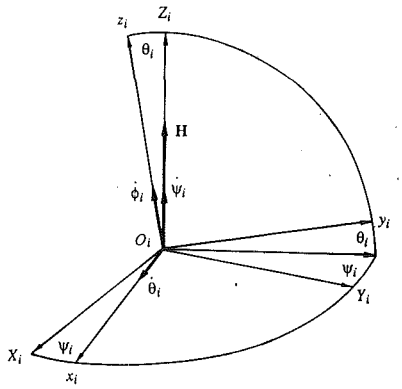


Fig. 2 Coordinates systems ($O_iX_iY_iZ_i$) and ($O_ix_iy_iz_i$)

$$\sum_{i=1}^{2}\{[2A_ic^2\psi_is\psi_i-\mu(c\theta_ic\theta_js\psi_i-s\theta_is\theta_js\psi_j)]\dot{\theta}_i$$

$$-[(C_i-A_i)c\theta_i-\mu c\theta_j]s\theta_ic\psi_i\dot{\psi}_i-C_is\theta_ic\dot{\psi}_i\dot{\phi}_i\}=0 \quad (2b)$$

$$\sum_{i=1}^{2}\{-\mu c\theta_is\theta_js(\psi_i-\psi_j)\dot{\theta}_i+[A_is^2\theta_i+C_ic^2\theta_i$$

$$+\mu s\theta_is\theta_jc(\psi_i-\psi_j)]\dot{\psi}_i+C_ic\theta_i\dot{\phi}_i\}=H \quad (2c)$$

where c,s are the abbreviations for cosine and sine, and $j=1,2$ ($j\neq i$). The torque applied to B_1 by B_2 at joint 0 is composed of an elastic torque $\mathbf{M}^e$ and a drive torque $\mathbf{M}^a$, where $\mathbf{M}^e$ is a linear function of the deformation angle δ of joint 0 and perpendicular to the deformation plane, while $\mathbf{M}^a$ is along the axis of symmetry of B_1.

$$\mathbf{M}=K\delta(\sin\delta)^{-1}(\mathbf{z}_1^o\times\mathbf{z}_2^o)+M^a\mathbf{z}_1^o \quad (3)$$

where $\mathbf{z}_i^o$ is the unit vector of axis O_iz_i.

Applying Euler's equations for body B_i in frame $(O_1x_1y_1z_1)$, we obtain

$$A_1\ddot{\theta}_1+C_1\dot{\phi}_1\dot{\psi}_1s\theta_1+(C_1-A_1)\dot{\psi}_1^2c\theta_1s\theta_1$$

$$+\mu\{\ddot{\theta}_2[c\theta_1c\theta_2c(\psi_1-\psi_2)+s\theta_1s\theta_2]+\ddot{\psi}_2c\theta_1s\theta_2s(\psi_1-\psi_2)$$

$$-(\dot{\theta}_2^2+\dot{\psi}_2^2)c\theta_1s\theta_2c(\psi_1-\psi_2)+\dot{\theta}_2^2s\theta_1c\theta_2-2\dot{\theta}_2\dot{\psi}_2c\theta_1c\theta_2c\psi_1s\psi_2\}$$

$$=K\delta(\sin\delta)^{-1}[c\theta_1s\theta_2c(\psi_1-\psi_2)-s\theta_1c\theta_2] \quad (4a)$$

$$A_1(\ddot{\psi}_1s\theta_1+\dot{\psi}_1\dot{\theta}_1c\theta_1)-C_1\dot{\phi}_1\dot{\theta}_1-(C_1-A_1)\dot{\psi}_1\dot{\theta}_1c\theta_1$$

$$+\mu[-\ddot{\theta}_2c\theta_2s(\psi_1-\psi_2)+\ddot{\psi}_2s\theta_2c(\psi_1-\psi_2)+(\dot{\theta}_2^2+\dot{\psi}_2^2)s\theta_2s(\psi_1-\psi_2)$$

$$+2\dot{\theta}_2\dot{\psi}_2c\theta_2s\psi_1s\psi_2]=K\delta(\sin\delta)^{-1}s\theta_2s(\psi_2-\psi_1) \quad (4b)$$

$$C_1\frac{d}{dt}(\dot{\phi}_1+\dot{\psi}_1c\theta_1)=M^a \quad (4c)$$

where

$$\mu=m_1m_2l_1l_2/m,$$

$$\delta=\sin^{-1}\{[c\theta_1s\theta_2c(\psi_1-\psi_2)-s\theta_1c\theta_2]^2+s^2\theta_2s^2(\psi_2-\psi_1)\}^{1/2}$$

and l_i is the distance from mass center O_1 to joint O, $(i=1,2)$.

3 Permanent Rotation

Let us discuss a stationary state of motion at which each body of the system rotates with one and the same angular velocity ω_o, which is fixed in space and collinear with the angular momentum vector **H**.

Let $\dot{\theta}_i=\dot{\phi}_i=0$, $\dot{\psi}_1=\omega_o$ $(i=1,2)$, then Eqs. (2) and (4) are simplified to

$$\sum_{i=1}^{2}[(C_i-A_i)c\theta_i-\mu c\theta_j]s\theta_is\psi_i=0 \quad (5a)$$

$$\sum_{i=1}^{2}[(C_i-A_i)c\theta_i-\mu c\theta_j]s\theta_ic\psi_i=0 \quad (5b)$$

$$\omega_o=H\left[\sum_{i=1}^{2}(A_is^2\theta_i+C_ic^2\theta_i)+2\mu s\theta_1s\theta_2c(\psi_1-\psi_2)\right]^{-1} \quad (5c)$$

$$(C_1-A_1)\omega_o^2c\theta_1s\theta_1-\mu\omega_o^2c\theta_1s\theta_2c(\psi_1-\psi_2)$$

$$+K\delta(\sin\delta)^{-1}[s\theta_1c\theta_2-c\theta_1s\theta_2c(\psi_1-\psi_2)]=0 \quad (5d)$$

$$[\mu\omega_o^2+K\delta(\sin\delta)^{-2}]s\theta_2s(\psi_1-\psi_2)=0 \quad (5e)$$

$$M^a=0. \quad (5f)$$

Equation (5*e*) requires $\psi_1=\psi_2$, and Eq. (5*c*) determines the angular velocity ω_o as a function of the body's attitude, then Eqs. (5*a*), (5*b*), and (5*d*) become

$$(C_1-A_1)\sin 2\theta_1+(C_2-A_2)\sin 2\theta_2-2\mu\sin(\theta_1+\theta_2)=0 \quad (6)$$

$$(C_1-A_1)\sin 2\theta_1-2\mu c\theta_1s\theta_2$$

$$+2\nu(\theta_1-\theta_2)\left[\sum_{i=1}^{2}(A_is^2\theta_i+C_ic^2\theta_i)+2\mu s\theta_1s\theta_2\right]^2=0 \quad (7)$$

where $\nu=K/H^2$. Equations (6) and (7) permit two special solutions

$$\theta_1=\theta_2=0 \quad (8)$$

$$\theta_1=\theta_2=\pi/2. \quad (9)$$

Solution (8) describes a normal state when the permanent rotation axis O_cZ is along the coaxial symmetry axes O_1z_1 and O_2z_2. Solution (9) corresponds to an overturned state when O_cZ is perpendicular to O_1z_1 and O_2z_2.

4 Trap States

Under certain circumstances, the axis of permanent rotation can deviate from the principal axes of the body. Consider two special cases:

Case 1: System of two identical bodies. Let

$$C_1=C_2, \quad A_1=A_2. \quad (10)$$

Equation (6) permits two possible solutions, different from the trivial solutions (8) and (9)

$$\theta_2=-\theta_1 \quad (11)$$

$$\theta_1=\frac{\pi}{2}+\gamma, \quad \theta_2=\frac{\pi}{2}-\gamma. \quad (12)$$

Substituting Eq. (11) into (7), we obtain

$$F(\theta_1)=(C_1-A_1+\mu)\sin 2\theta_1$$

$$+16\nu\theta_1[C_1+(A_1-C_1-\mu)\sin^2\theta_1]^2=0. \quad (13)$$

Since $F(0)=0$, $F(\pi/2)>0$, if $F'(0)<0$, there should exist at least one root of θ_1, different from zero or $\pi/2$. Consequently, a sufficient condition of existence of a nontrivial solution is

$$A_1>C_1+\mu+8\nu C_1^2. \quad (15)$$

Substituting Eq. (12) into (7) leads to

$$G(\gamma)=(A_1-C_1+\mu)\sin 2\gamma$$

$$+16\nu\gamma[C_1+(A_1-C_1+\mu)\cos^2\gamma]^2=0. \quad (15)$$

Since $G(0)=0$, $G(\pi/2)>0$, a sufficient condition of existence of a nontrivial solution is derived from the condition $G'(0)<0$, and results in

$$C_1>A_1+\mu+8\nu(A_1+\mu)^2. \quad (16)$$

The numerical calculation shows that a bifurcation in the number and position of the axes of permanent rotation can occur when the parameters ν and μ are sufficiently small, i.e., the elastic joint is sufficiently soft and the joint center is sufficiently close to the mass center of one body of the system. As an example, two sets of curves in the plane C_1/A_1 versus θ_1 are given in Fig. 3 to express the bifurcation with $\mu/A_1=0.1$ and different values of $\rho=\omega_e/\omega_n$, where $\omega_e=K/H$ and $\omega_n=H/A_1$ are the eigenfrequency of the elastic oscillation and the

Downloaded 03 May 2010 to 171.66.16.20. Redistribution subject to ASME license or copyright; see http://www.asme.org/terms/Terms_Use.cfm

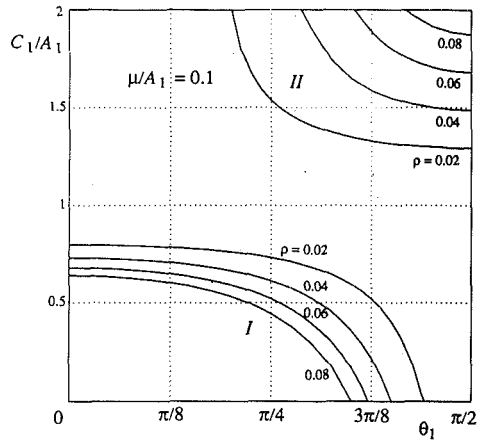


Fig. 3 Bifurcation of the axes of permanent rotation

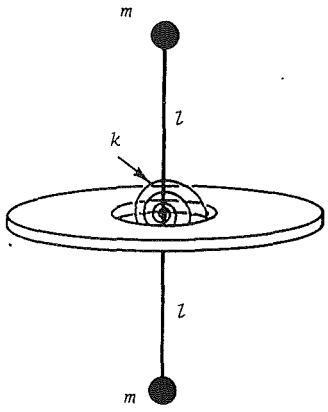


Fig. 4 Disk-dumbbell system

nutational frequency respectively. The curves I, bifurcation from the normal state, and the curves II, bifurcated from the overturned state, correspond to the nontrivial solutions (11) and (12), respectively, and a clear distinction of the trap state for the system composed of prolate bodies or oblate bodies can be observed.

Case 2: Disk-Dumbbell system. Assume that B_1 is a disk and B_2 is a dumbbell, composed of a massless bar and two mass points (see Fig. 4). Let m be the mass and l the half-length of the bar, then

$$A_2 = 2ml^2, \quad C_2 = 0, \quad \mu = 0. \tag{17}$$

We obtain from Eq. (6) a relationship between θ_1 and θ_2

$$(C_1 - A_1)\sin 2\theta_1 - 2ml^2 \sin 2\theta_2 = 0. \tag{18}$$

Equation (7) offers another relationship:

$$F(\theta_1,\theta_2) = (C_1 - A_1)\sin 2\theta_1 + 2\nu(\theta_1 - \theta_2)(A_1 s^2\theta_1 + C_1 c^2\theta_1 + 2ml^2 s^2\theta_2)^2 = 0. \tag{19}$$

Since $F(0,0) = 0$, $F(\pi/2, -\pi/2) > 0$, if $(dF/d\theta_1)|_{0,0} < 0$, there should exist at least one root of θ_1, different from zero or $\pm\pi/2$, thus a sufficient condition for the existence of a nontrivial solution is derived as (Rimrott and Janabi-Sharifi, 1992)

$$A_1 > C_1 + \frac{\nu C_1^2 2ml^2}{2ml^2 - \nu C_1^2}. \tag{20}$$

5 Energy Analysis

Internal damping, which is unavoidable in practice, conditions the stability of different states of permanent rotation. The energy-sink method (e.g., Rimrott, 1985) can be used for discussion. The total mechanical energy of the system during permanent rotation is

$$E = T + V = \frac{H^2}{2\left[\sum_{i=1}^{2}(A_i s^2\theta_i + C_i c^2\theta_i) + 2\mu s\theta_1 s\theta_2\right]} + \frac{K}{2}(\theta_2 - \theta_1)^2. \tag{21}$$

The necessary conditions for the extremum of E of the system in permanent rotation ($\theta_1 = \theta_{10}$, $\theta_2 = \theta_{20}$) are

$$\left(\frac{\partial E}{\partial \theta_1}\right)_{(\theta_{10},\theta_{20})} = \left(\frac{\partial E}{\partial \theta_2}\right)_{(\theta_{10},\theta_{20})} = 0 \tag{22}$$

$$\left[\left(\frac{\partial^2 E}{\partial \theta_2^2}\right)\left(\frac{\partial^2 E}{\partial \theta_2^2}\right) - \left(\frac{\partial^2 E}{\partial \theta_1 \partial \theta_2}\right)\right]_{(\theta_{10},\theta_{20})} > 0. \tag{23}$$

The sufficient condition for a maximum or minimum of the function E is

$$\left(\frac{\partial^2 E}{\partial \theta_1^2}\right)_{(\theta_{10},\theta_{20})} \begin{cases} < 0 & \text{(maximum)} \quad (24a) \\ > 0 & \text{(minimum).} \quad (24b) \end{cases}$$

For the normal state, let $\theta_{10} = \theta_{20} = 0$, Eq. (22) is satisfied automatically, and Eqs. (23) and (24) become

$$(A_1 - C_1)[A_2 - C_2 - \nu(C_1 + C_2)^2] - \nu(C_1 + C_2)^2(A_2 - C_2) - 2\nu\mu(C_1 + C_2)^2 - \mu^2 > 0 \tag{25}$$

$$C_1 - A_1 + \nu(C_1 + C_2)^2 \begin{cases} < 0 & \text{(maximum)} \quad (26a) \\ > 0 & \text{(minimum).} \quad (26b) \end{cases}$$

Substituting Eqs. (10) and (17) into (25) and (26), respectively, it is possible to derive following condition to ensure that conditions (25) and (26*a*) are satisfied at the same time.

Case 1:

$$A_1 > C_1 + \mu + 8\nu C_1^2. \tag{27}$$

Case 2:

$$A_1 > C_1 + \frac{\nu C_1^2 2ml^2}{2ml^2 - \nu C_1^2}. \tag{28}$$

Comparing relations (27) and (28) with (14) and (20), we find that the condition for the existence of an energy trough is also the condition of maximal energy of the normal state of permanent rotation. It means that, as result of the influence of the energy dissipation caused by the small internal damping, the normal permanent rotation transfers to the trap state, as the total mechanical energy decreases over a (long) period of time.

For the overturned state, let $\theta_{10} = \theta_{20} = \pi/2$, then condition (22) is satisfied automatically, and conditions (23) and (24) become

$$(A_1 - C_1 + \mu)[A_2 - C_2 + \mu + \nu(A_1 + A_2 + 2\mu)^2] + \nu(A_1 + A_2 + 2\mu)^2(A_2 - C_2 + \mu) > 0 \tag{29}$$

$$A_1 - C_1 + \mu + \nu(A_1 + A_2 + 2\mu)^2 \begin{cases} < 0 & \text{(maximum)} \quad (30a) \\ > 0 & \text{(minimum).} \quad (30b) \end{cases}$$

Substituting from Eq. (10) into conditions (29) and (30) leads to the result, that condition (27) as well is the sufficient condition of the minimal energy of the overturned state, which is the final state after a (long) period of energy dissipation.

The sufficient condition of the maximum energy of the overturned state is the same as condition (16):

$$C_1 > A_1 + \mu + 8\nu(A_1 + \mu)^2. \tag{31}$$

Condition (31) is also the sufficient condition of the minimal energy of the normal state. It means that when condition (31)

Downloaded 03 May 2010 to 171.66.16.20. Redistribution subject to ASME license or copyright; see http://www.asme.org/terms/Terms_Use.cfm

is satisfied, the overturned state transfers to the trap state due to small energy dissipation, and the final state after a (long) period is the normal state.

Conclusions

The effects of flexibility and internal damping have been discussed, and two special cases have been considered, indicating that there may be energy troughs in which the two-body system will be permanently trapped.

References

Hooker, W. W., and Margulies, G., 1965, "The Dynamical Attitude Equations for an n-Body-Satellite," *J. of Astronautical Science*, Vol. 12, pp. 123–128.

Liu, Y. Z., 1989, "The Stability of the Permanent Rotation of a Free Multibody System," *Acta Mechanica*, Vol. 79, pp. 43–51.

Rimrott, F. P. J., 1985, "Dissipative Rigids in Gyrodynamics," *ZAMM*, Vol. 65, No. 7, pp. 287–300.

Rimrott, F. P. J., and Janabi-Sharifi, F., 1992, "A Torque-free Flexible Model Gyro," ASME JOURNAL OF APPLIED MECHANICS, Vol. 59, No. 1, pp. 7–15.

The Study on Mechanical Parameters of Finite Deformation of Membranes

Gao Yongxiang[4] and Luo Jisheng[4]

1 Introduction

More and more problems arising from the industrial application of elastic materials, such as rubber membranes, need to be solved by solving the finite deformation of membranes. The key to the solution is to first know the mechanical parameters of the membrane and then to choose a suitable method to determine these parameters.

Some of the conventional methods had been proposed by Rivlin and Saunders (1951). One of the methods is by homogeneous deformation and the other is by the inflation of a plane circular membrane. However, both of them have their own disadvantages. The disadvantage of the former is its complexity in testing and presence of edge effect of the material. The latter is simple and easy, but the modern equipment for such tests is not available. The authors of this paper present a new method to deal with the tensile deformation of ring membranes.

The approach to determining the mechanical parameters by a set of data obtained in the tensile experiment, that is, the total displacement due to each loading and the corresponding total tensile force, is virtually in the category of nonlinear regression.

In order to calculate the total displacement of ring membranes under the action of tensile force, Yang and Feng (1970), as well as Tielking and Feng (1974), proposed a mathematical model. But some of their equations are rather complicated to fit in with regressive calculation. For this reason the authors of this paper propose a simplified model. Based on geometrical relations, the first step of this model is to establish a set of geometrical equations for all finite deformation of axisymmetrical membranes, and then to establish balance and constitution equations. As constitution equation of material is taken out of the numerical computation, and no approximation is made for balance equations, the calculation accuracy of the deformation of membranes is entirely dependent upon the accuracy of the constitution equation of material.

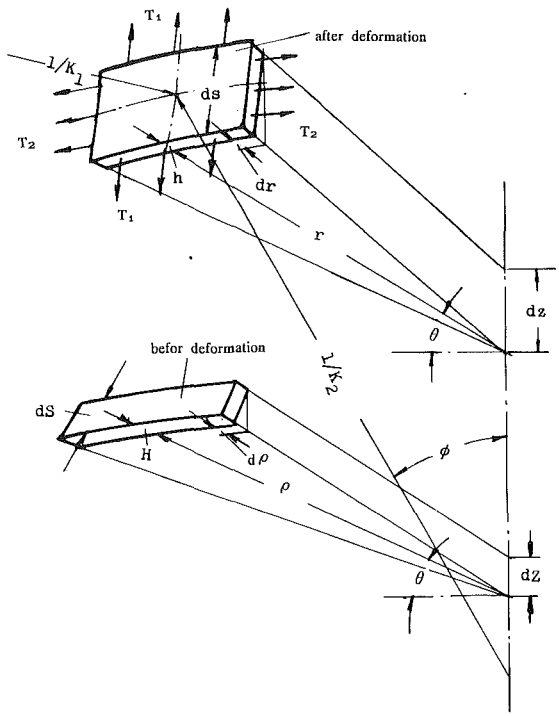


Fig. 1 The used symbols on an element before and after deformation of membrane

2 Experiments and Their Setup

The membrane to be tested is fixed between two concentric rings with different diameters. An axial force is applied to the inner ring at the center of the membrane, pulling the membrane up, with the outer ring fastened on the testing machine. The experiment was carried out automatically on the Universal Testing Machine model 4301 made by Insstron International Ltd. in London.

3 Mathematical Formulae

The symbols used are the conventional ones, as shown in Fig. 1. Take an infinitesimal element and its volume as constant before and after the deformation. The three extension ratios are defined as follows:

$$\lambda_1 = (ds/d\rho)\left(1/\sqrt{1+Z'^2}\right) \tag{1}$$

$$\lambda_2 = r/\rho \tag{2}$$

$$\lambda_3 = h(r,z)/H(\rho,Z) \tag{3}$$

$$\lambda_1\lambda_2\lambda_3 = 1. \tag{4}$$

The principal curvatures of the membrane are

$$K_1 = \pm (d^2r/ds^2)\left[1/\sqrt{1-(dr/ds)^2}\right] \tag{5}$$

$$K_2 = (1/r)\sqrt{1-(dr/ds)^2}. \tag{6}$$

From the preceding relation we have

$$dr/ds = \sqrt{1-(k_2 r)^2},\ dK_2/ds = (dr/ds)(K_1 - K_2)/r.$$

[4]Applied Mechanics Division, Department of Mechanics, Tianjin University, Tianjin 300072, China.

Manuscript received by the ASME Applied Mechanics Division, May 15, 1992; final revision, Oct. 22, 1992. Associate Technical Editor: R. Abeyaratne.

Downloaded 03 May 2010 to 171.66.16.20. Redistribution subject to ASME license or copyright; see http://www.asme.org/terms/Terms_Use.cfm

is satisfied, the overturned state transfers to the trap state due to small energy dissipation, and the final state after a (long) period is the normal state.

Conclusions

The effects of flexibility and internal damping have been discussed, and two special cases have been considered, indicating that there may be energy troughs in which the two-body system will be permanently trapped.

References

Hooker, W. W., and Margulies, G., 1965, "The Dynamical Attitude Equations for an n-Body-Satellite," *J. of Astronautical Science*, Vol. 12, pp. 123–128.

Liu, Y. Z., 1989, "The Stability of the Permanent Rotation of a Free Multibody System," *Acta Mechanica*, Vol. 79, pp. 43–51.

Rimrott, F. P. J., 1985, "Dissipative Rigids in Gyrodynamics," *ZAMM*, Vol. 65, No. 7, pp. 287–300.

Rimrott, F. P. J., and Janabi-Sharifi, F., 1992, "A Torque-free Flexible Model Gyro," ASME JOURNAL OF APPLIED MECHANICS, Vol. 59, No. 1, pp. 7–15.

The Study on Mechanical Parameters of Finite Deformation of Membranes

Gao Yongxiang[4] and Luo Jisheng[4]

1 Introduction

More and more problems arising from the industrial application of elastic materials, such as rubber membranes, need to be solved by solving the finite deformation of membranes. The key to the solution is to first know the mechanical parameters of the membrane and then to choose a suitable method to determine these parameters.

Some of the conventional methods had been proposed by Rivlin and Saunders (1951). One of the methods is by homogeneous deformation and the other is by the inflation of a plane circular membrane. However, both of them have their own disadvantages. The disadvantage of the former is its complexity in testing and presence of edge effect of the material. The latter is simple and easy, but the modern equipment for such tests is not available. The authors of this paper present a new method to deal with the tensile deformation of ring membranes.

The approach to determining the mechanical parameters by a set of data obtained in the tensile experiment, that is, the total displacement due to each loading and the corresponding total tensile force, is virtually in the category of nonlinear regression.

In order to calculate the total displacement of ring membranes under the action of tensile force, Yang and Feng (1970), as well as Tielking and Feng (1974), proposed a mathematical model. But some of their equations are rather complicated to fit in with regressive calculation. For this reason the authors of this paper propose a simplified model. Based on geometrical relations, the first step of this model is to establish a set of geometrical equations for all finite deformation of axisymmetrical membranes, and then to establish balance and constitution equations. As constitution equation of material is taken out of the numerical computation, and no approximation is made for balance equations, the calculation accuracy of the deformation of membranes is entirely dependent upon the accuracy of the constitution equation of material.

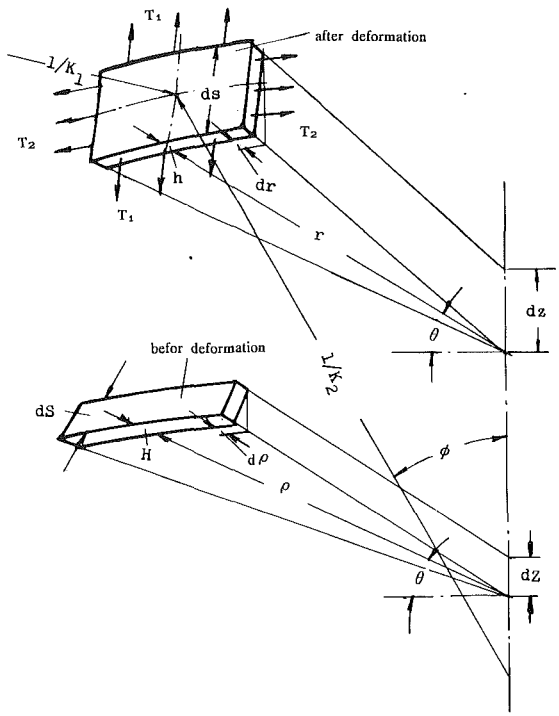


Fig. 1 The used symbols on an element before and after deformation of membrane

2 Experiments and Their Setup

The membrane to be tested is fixed between two concentric rings with different diameters. An axial force is applied to the inner ring at the center of the membrane, pulling the membrane up, with the outer ring fastened on the testing machine. The experiment was carried out automatically on the Universal Testing Machine model 4301 made by Insstron International Ltd. in London.

3 Mathematical Formulae

The symbols used are the conventional ones, as shown in Fig. 1. Take an infinitesimal element and its volume as constant before and after the deformation. The three extension ratios are defined as follows:

$$\lambda_1 = (ds/d\rho)\left(1/\sqrt{1+Z'^2}\right) \tag{1}$$

$$\lambda_2 = r/\rho \tag{2}$$

$$\lambda_3 = h(r,z)/H(\rho,Z) \tag{3}$$

$$\lambda_1\lambda_2\lambda_3 = 1. \tag{4}$$

The principal curvatures of the membrane are

$$K_1 = \pm (d^2r/ds^2)\left[1/\sqrt{1-(dr/ds)^2}\right] \tag{5}$$

$$K_2 = (1/r)\sqrt{1-(dr/ds)^2}. \tag{6}$$

From the preceding relation we have

$$dr/ds = \sqrt{1-(k_2 r)^2},\ dK_2/ds = (dr/ds)(K_1 - K_2)/r.$$

[4]Applied Mechanics Division, Department of Mechanics, Tianjin University, Tianjin 300072, China.

Manuscript received by the ASME Applied Mechanics Division, May 15, 1992; final revision, Oct. 22, 1992. Associate Technical Editor: R. Abeyaratne.

Copyright © 1994 by ASME
Downloaded 03 May 2010 to 171.66.16.20. Redistribution subject to ASME license or copyright; see http://www.asme.org/terms/Terms_Use.cfm

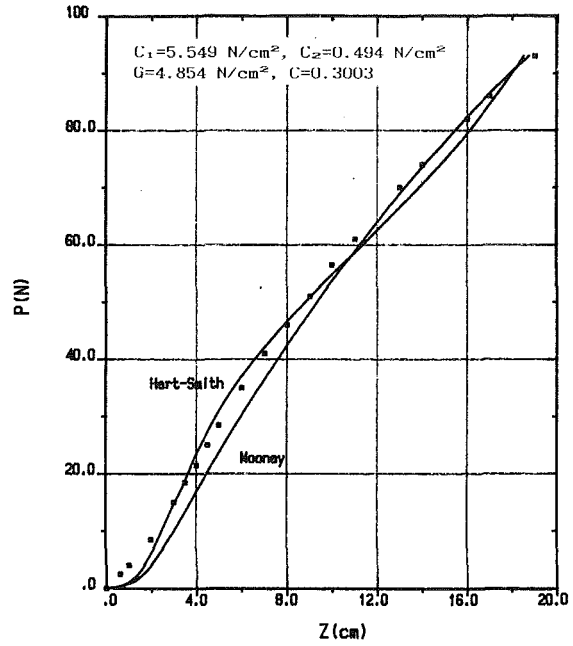


Fig. 2(*a*) Thin emulsion membrane with R_{in} = 3 cm, R_{out} = 7 cm, thickness H = 0.063 cm

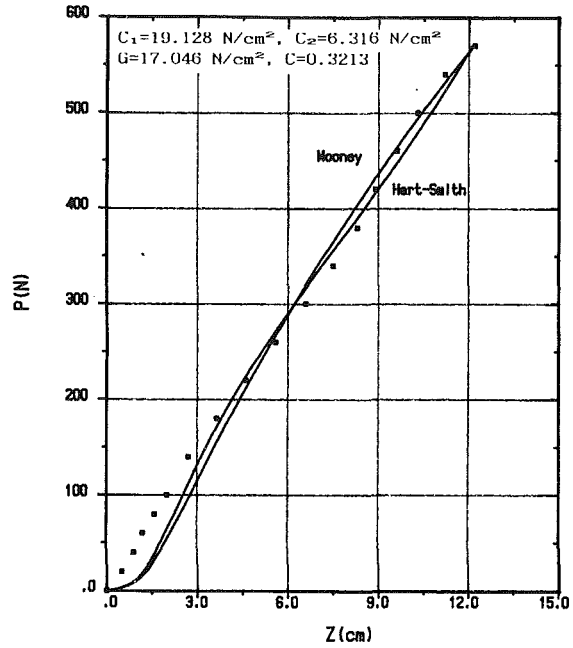


Fig. 2(*c*) Thick emulsion membrane with R_{in} = 3 cm, R_{out} = 7 cm, thickness H = 0.19 cm

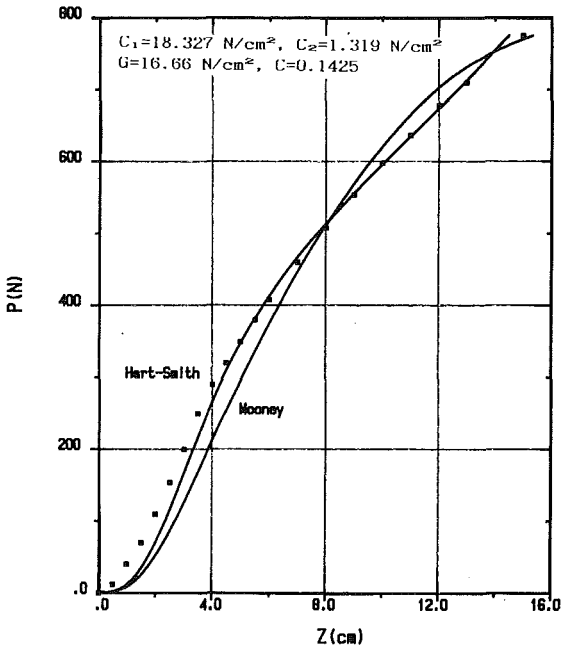


Fig. 2(*b*) Thick emulsion membrane with R_{in} = 2 cm, R_{out} = 5 cm, thickness H = 0.19 cm

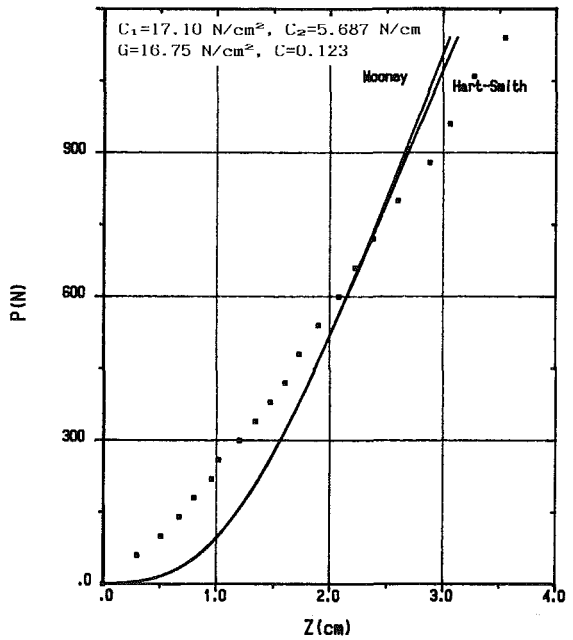


Fig. 2(*d*) Inner rubber membrane with R_{in} = 2 cm, R_{out} = 5 cm, thickness H = 0.16 cm for rubber tube

Fig. 2 Plots of concentrated force P_i against total displacement z_i from experiment on tensile deformation of membrane and its comparisons with theoretical calculation on the *M* model and the *H-S* model

After conversion, a set of ordinary equations with independent variables is derived:

$$dz/d\rho = rK_2\lambda_1\sqrt{1+Z'^2} \tag{7}$$

$$dr/d\rho = \lambda_1\sqrt{1-(K_2r)^2}\sqrt{1+Z'^2} \tag{8}$$

$$dK_2/d\rho = \lambda_1\sqrt{1-(K_2r)^2}\,[(K_1-K_2)/r]\sqrt{1+Z'^2}. \tag{9}$$

The balance equations of two directions and constitution equation can be written as

$$K_1T_1 + K_2T_2 = 0 \tag{10}$$

$$2\pi r^2K_2T_1 = P \tag{11}$$

$$T_1 = (\lambda_1^2-\lambda_3^2)[\partial W/\partial I_1 + \lambda_2^2\partial W/\partial I_2]2H/\lambda_1 \tag{12}$$

$$T_2 = (\lambda_2^2-\lambda_3^2)[\partial W/\partial I_1 + \lambda_1^2\partial W/\partial I_2]2H/\lambda_2. \tag{13}$$

The Mooney-Rivlin model and the Hart-Smith model are

$$\partial W/\partial I_1 = C_1,\ \partial W/\partial I_2 = C_2$$

$$\partial W/\partial I_1 = G\exp[b(I_1-3)^2],\ \partial W/\partial I_2 = GC/I_2,$$

respectively.

To sum up, these are nine independent equations: (2), (4),

Downloaded 03 May 2010 to 171.66.16.20. Redistribution subject to ASME license or copyright; see http://www.asme.org/terms/Terms_Use.cfm

(7), (8), (9), (10), (11), (12), and (13) with nine unknowns T_1, T_2, K_1, K_2, r, z, λ_1, λ_2, and λ_3.

4 Nonlinear Regressive Theory of Least Square Approximation

The method of finding the mechanical parameters C_1 and C_2 or G and C, or rather, is to define the curve of the mathematical model in this paper by successive optimum approximation, i.e., nonlinear regression method of least square approximation. The derivative method and direct calculated method are used.

5 Results and Conclusions

In addition to the tensile experiments on many elastic membranes, regressive analyses of emulsion and rubber membranes are made. Their results and comparisons are plotted in Fig. 2. In the figure the longitudinal coordinates are P_i in Newton (N), and abscissas are z_i in cm. The small square points stand for experimental values and the two solid lines are drawn on the basis of the mechanical parameters C_1, C_2, and G, C, indicated separately in Fig. 2, obtained by regression with the theoretical model formulated in this paper.

(1) The calculation results agree with the experimental data in the main. This shows the correctness of our mathematical model.

(2) The fact that the theoretical curves do not coincide with the test points indicates the imperfection of the constitution equation. Nevertheless, discrepancy does not limit the use of this model in engineering practice to essentially satisfy the requirement of approximation.

It can be seen that for a range of small deformation, the Mooney model and the Hart-Smith model have almost the same accuracy as shown in Fig. 2(d), while for a range of large deformation, the accuracy of the Hart-Smith model is slightly higher than that of the Mooney model.

References

Rivlin, R. S., and Saunders, D. W., 1951, "Large Elastic Deformations of Isotropic Materials, VII. Experiments on the Deformation of Rubber," *Phi. Trans. Roy. Soc. Lond.*, Vol. 243, A865, pp. 251–288.

Tielking, J. T., and Feng, W. W., 1974, "The Application of the Minimum Potential Energy Principle to Nonlinear Axisymmetric Membrane Problems," ASME JOURNAL OF APPLIED MECHANICS, Vol. 41, pp. 491–496.

Yang, W. H., and Feng, W. W., 1970, "On Axisymmetrical Deformation of Nonlinear Membrane," ASME JOURNAL OF APPLIED MECHANICS, Vol. 37, pp. 1002–1011.

A Numerical Solution of Two-Dimensional Torsional Waves in an Elastic/Viscoplastic Cylinder

Kaishin Liu[5] and Takashi Yokoyama[6]

Introduction

This study deals with the numerical solution for two-dimensional torsional waves in an elastic/viscoplastic cylinder.

[5]Associate Professor, Research Institute of Engineering Mechanics, Dalian University of Technology, Dalian 116024, China.

[6]Professor, Department of Mechanical Engineering, Okayama University of Science, Okayama 700, Japan.

Manuscript received by the ASME Applied Mechanics Division, Sept. 14, 1992; final revision, Nov. 18, 1992. Associate Technical Editor: S. K. Datta.

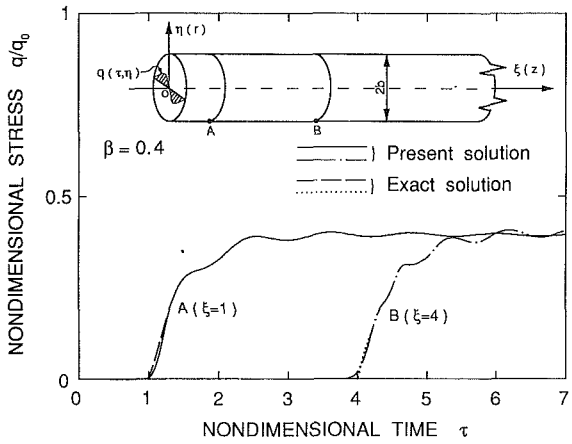


Fig. 1 Comparison between present results and exact solutions; time histories of shear stress on outer surface at two stations $\xi = 1$ and $\xi = 4$

The equations governing the dynamic torsional deformation of the cylinder are solved by the method of finite difference along bi-characteristics, which was first applied by Clifton (1967) to solve the plane problems in elastodynamics. In order to evaluate the accuracy of the method, the numerical solutions obtained for transient torsional elastic waves in the cylinder are compared with the available exact solutions. It is shown through numerical examples that a check on the error in the total energy of the difference solution is very effective for examining the stability and convergence of the method.

Governing Equations

We consider a semi-infinite circular cylinder of diameter $2b$, which is subjected to a suddenly applied shear stress with nonlinear radial variation at its end surface $z = 0$ (see inset Fig. 1). It is assumed that the cylinder is made of an isotropic, homogeneous, elastic/viscoplastic material (Perzyna, 1963); the deformations and rotations are small. The equations governing the dynamic torsional deformation of the elastic/viscoplastic cylinder can be written in the dimensionless form

$$L[\mathbf{W}] \equiv A^{\tau}\mathbf{W}_{\tau} + A^{\xi}\mathbf{W}_{\xi} + A^{\eta}\mathbf{W}_{\eta} + \mathbf{B} = \mathbf{0} \tag{1}$$

where A^{τ} is a unit matrix; A^{ξ} and A^{η} are symmetric matrices with the following nonzero entries: $A^{\xi}_{13} = A^{\xi}_{31} = A^{\eta}_{12} = A^{\eta}_{21} = -1$, in which the subscripts stand for the respective row and column of the entry. $\mathbf{W}$ and $\mathbf{B}$ denote the following vectors:

$$\mathbf{W}^T = [v,\ p,\ q],\ \mathbf{B}^T = \left(-\frac{2}{\eta},\ \frac{1}{\eta} + 2pD,\ 2qD\right).$$

Here the subscripts of $\mathbf{W}$ refer to partial differentiation with respect to the subscript variable. The dimensionless velocity, shear stresses, time, polar coordinates, and elastic/viscoplastic term are defined in terms of their dimensional counterparts by

$$v = \frac{v_\theta}{c_2},\ p = \frac{\sigma_{r\theta}}{\rho c_2^2},\ q = \frac{\sigma_{\theta z}}{\rho c_2^2},\ \tau = \frac{c_2}{b}t,\ \eta = \frac{r}{b},\ \xi = \frac{z}{b},$$

$$D = \begin{cases} \dfrac{\rho b c_2 \gamma_0}{\sqrt{J_2}}\,\phi(F) & \text{for } F > 0 \\ 0 & \text{for } F \leqq 0 \end{cases} \tag{2}$$

where v_θ is the particle velocity in the θ direction, $\sigma_{r\theta}$ and $\sigma_{\theta z}$ the shear stress components, ρ the mass density, $c_2 = \sqrt{\mu/\rho}$ the shear wave velocity, t the time, γ_0 the viscosity coefficient, J_2 the second invariant of the deviatoric stress tensor, and μ

Downloaded 03 May 2010 to 171.66.16.20. Redistribution subject to ASME license or copyright; see http://www.asme.org/terms/Terms_Use.cfm

(7), (8), (9), (10), (11), (12), and (13) with nine unknowns T_1, T_2, K_1, K_2, r, z, λ_1, λ_2, and λ_3.

4 Nonlinear Regressive Theory of Least Square Approximation

The method of finding the mechanical parameters C_1 and C_2 or G and C, or rather, is to define the curve of the mathematical model in this paper by successive optimum approximation, i.e., nonlinear regression method of least square approximation. The derivative method and direct calculated method are used.

5 Results and Conclusions

In addition to the tensile experiments on many elastic membranes, regressive analyses of emulsion and rubber membranes are made. Their results and comparisons are plotted in Fig. 2. In the figure the longitudinal coordinates are P_i in Newton (N), and abscissas are z_i in cm. The small square points stand for experimental values and the two solid lines are drawn on the basis of the mechanical parameters C_1, C_2, and G, C, indicated separately in Fig. 2, obtained by regression with the theoretical model formulated in this paper.

(1) The calculation results agree with the experimental data in the main. This shows the correctness of our mathematical model.

(2) The fact that the theoretical curves do not coincide with the test points indicates the imperfection of the constitution equation. Nevertheless, discrepancy does not limit the use of this model in engineering practice to essentially satisfy the requirement of approximation.

It can be seen that for a range of small deformation, the Mooney model and the Hart-Smith model have almost the same accuracy as shown in Fig. 2(d), while for a range of large deformation, the accuracy of the Hart-Smith model is slightly higher than that of the Mooney model.

References

Rivlin, R. S., and Saunders, D. W., 1951, "Large Elastic Deformations of Isotropic Materials, VII. Experiments on the Deformation of Rubber," *Phi. Trans. Roy. Soc. Lond.*, Vol. 243, A865, pp. 251–288.

Tielking, J. T., and Feng, W. W., 1974, "The Application of the Minimum Potential Energy Principle to Nonlinear Axisymmetric Membrane Problems," ASME JOURNAL OF APPLIED MECHANICS, Vol. 41, pp. 491–496.

Yang, W. H., and Feng, W. W., 1970, "On Axisymmetrical Deformation of Nonlinear Membrane," ASME JOURNAL OF APPLIED MECHANICS, Vol. 37, pp. 1002–1011.

A Numerical Solution of Two-Dimensional Torsional Waves in an Elastic/Viscoplastic Cylinder

Kaishin Liu[5] and Takashi Yokoyama[6]

Introduction

This study deals with the numerical solution for two-dimensional torsional waves in an elastic/viscoplastic cylinder.

[5]Associate Professor, Research Institute of Engineering Mechanics, Dalian University of Technology, Dalian 116024, China.

[6]Professor, Department of Mechanical Engineering, Okayama University of Science, Okayama 700, Japan.

Manuscript received by the ASME Applied Mechanics Division, Sept. 14, 1992; final revision, Nov. 18, 1992. Associate Technical Editor: S. K. Datta.

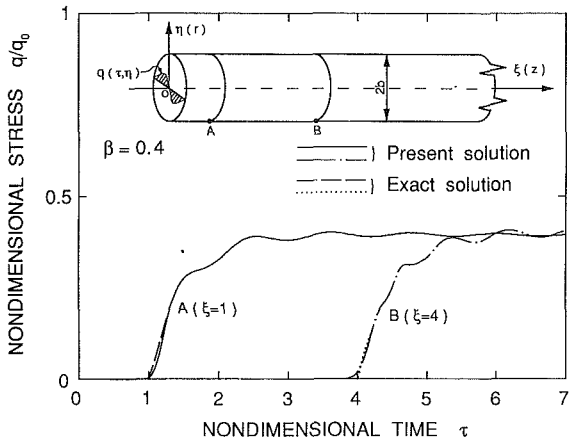


Fig. 1 Comparison between present results and exact solutions; time histories of shear stress on outer surface at two stations $\xi = 1$ and $\xi = 4$

The equations governing the dynamic torsional deformation of the cylinder are solved by the method of finite difference along bi-characteristics, which was first applied by Clifton (1967) to solve the plane problems in elastodynamics. In order to evaluate the accuracy of the method, the numerical solutions obtained for transient torsional elastic waves in the cylinder are compared with the available exact solutions. It is shown through numerical examples that a check on the error in the total energy of the difference solution is very effective for examining the stability and convergence of the method.

Governing Equations

We consider a semi-infinite circular cylinder of diameter $2b$, which is subjected to a suddenly applied shear stress with nonlinear radial variation at its end surface $z = 0$ (see inset Fig. 1). It is assumed that the cylinder is made of an isotropic, homogeneous, elastic/viscoplastic material (Perzyna, 1963); the deformations and rotations are small. The equations governing the dynamic torsional deformation of the elastic/viscoplastic cylinder can be written in the dimensionless form

$$L[\mathbf{W}] \equiv A^{\tau}\mathbf{W}_{\tau} + A^{\xi}\mathbf{W}_{\xi} + A^{\eta}\mathbf{W}_{\eta} + \mathbf{B} = \mathbf{0} \tag{1}$$

where A^{τ} is a unit matrix; A^{ξ} and A^{η} are symmetric matrices with the following nonzero entries: $A^{\xi}_{13} = A^{\xi}_{31} = A^{\eta}_{12} = A^{\eta}_{21} = -1$, in which the subscripts stand for the respective row and column of the entry. $\mathbf{W}$ and $\mathbf{B}$ denote the following vectors:

$$\mathbf{W}^T = [v,\ p,\ q],\ \mathbf{B}^T = \left(-\frac{2}{\eta},\ \frac{1}{\eta} + 2pD,\ 2qD\right).$$

Here the subscripts of $\mathbf{W}$ refer to partial differentiation with respect to the subscript variable. The dimensionless velocity, shear stresses, time, polar coordinates, and elastic/viscoplastic term are defined in terms of their dimensional counterparts by

$$v = \frac{v_\theta}{c_2},\ p = \frac{\sigma_{r\theta}}{\rho c_2^2},\ q = \frac{\sigma_{\theta z}}{\rho c_2^2},\ \tau = \frac{c_2}{b}t,\ \eta = \frac{r}{b},\ \xi = \frac{z}{b},$$

$$D = \begin{cases} \dfrac{\rho b c_2 \gamma_0}{\sqrt{J_2}}\,\phi(F) & \text{for } F > 0 \\ 0 & \text{for } F \leqq 0 \end{cases} \tag{2}$$

where v_θ is the particle velocity in the θ direction, $\sigma_{r\theta}$ and $\sigma_{\theta z}$ the shear stress components, ρ the mass density, $c_2 = \sqrt{\mu/\rho}$ the shear wave velocity, t the time, γ_0 the viscosity coefficient, J_2 the second invariant of the deviatoric stress tensor, and μ

Copyright © 1994 by ASME

Downloaded 03 May 2010 to 171.66.16.20. Redistribution subject to ASME license or copyright; see http://www.asme.org/terms/Terms_Use.cfm

the shear modulus. Note that $D = 0$ corresponds to the elastic cylinder. Following Fyfe (1975), the explicit form of the function ϕ (F) is taken as

$$\phi(F) = e^{2F-1}, \quad \text{where } F = (\sqrt{J_2} - \tau^*)/\tau_0^* \tag{3}$$

where τ^* is the static strain hardening parameter, and τ_0^* is the initial yield stress in simple shear.

Numerical Integration

The characteristic cone for Eq. (1) can be written as

$$c^2(\tau - \tau_0)^2 = (\xi - \xi_0)^2 + (\eta - \eta_0)^2 \quad (c = 1) \tag{4}$$

where the point (τ_0, ξ_0, η_0) is the vertex of the cone, and c is the dimensionless shear wave velocity. Generators of the cone which are the bi-characteristics for Eq. (1) are given by

$$\left.\begin{aligned} \xi - \xi_0 + c(\tau - \tau_0)\sin\alpha = 0 \\ \eta - \eta_0 + c(\tau - \tau_0)\cos\alpha = 0 \end{aligned}\right\} \quad (c = 1). \tag{5}$$

Here, α is the angle with respect to the dimensionless radial coordinate η. The bi-characteristics corresponding to $\alpha = 0$, $\pi/2$, π, $3\pi/2$ are employed. By using the method of numerical integration along bi-characteristics, we finally obtain the following expressions for three unknown increments δv, δp, δq with an accuracy of order k^3 (k is the dimensionless time step):

$$\delta v = k\{-kv_0 + 4\eta_0 p_0 + k\eta_0 v_{\eta 0} + \eta_0^2(p_{\eta 0} + q_{\xi 0}) + k\eta_0^2(v_{\eta\eta 0} + v_{\xi\xi 0}) + 2k\eta_0(D - D_0)[p_0 + \eta_0(p_{\eta 0} + q_{\xi 0})] - 2k\eta_0^2(p_0 D_\eta + q_0 D_\xi)\}/E$$

$$\delta p = k[-2(\eta_0 v_0 + 2kp_0) + k\eta_0(p_{\eta 0} - q_{\xi 0}) + \eta_0^2(2v_{\eta 0} + kp_{\eta\eta 0} + kq_{\eta\xi 0}) - 2\eta_0^2 p_0(D_0 + D^0)]/E$$

$$\delta q = k[2\eta_0 v_{\xi 0} + 2kq_{\xi 0} + k\eta_0(p_{\eta\xi 0} + q_{\xi\xi 0}) + q_0(D_0 + D^0)]/[2\eta_0(kD^0 + 1)]$$

where $E = 2k\eta_0^2 D^0 - k^2 + 2\eta_0^2$, and the subscript 0 refers to the associated function evaluated at the point ($\tau_0 - k$, ξ_0, η_0). The partial differences f_ξ, f_η, $f_{\xi\xi}$, $f_{\eta\eta}$, $f_{\xi\eta}$ at the point (ξ_0, η_0) are replaced by central differences. The unknown quantity D^0, which is a function of $\mathbf{W}$ (τ_0, ξ_0, η_0), is determined by using the iterative procedure. When the point ($\tau_0 - k$, ξ_0, η_0) is located on the boundary, we can make use of admissible boundary conditions instead of unused relations along bi-characteristics which are outside the region of interest.

Numerical Examples

The following material constants for 1100 – O aluminum (Fyfe, 1975) were used for all the computations: $\tau_0^* = 8.84$ MPa, $\rho = 2.71 \times 10^3$ kg/m^3, $\gamma_0 = 100$/s, $\mu = 2.566 \times 10^4$ MPa. The static strain-hardening parameter is expressed as a function of equivalent plastic strain $\bar{\epsilon}_p$ as

$$\tau^* = \tau_0^* + 4\times 10^3\,\bar{\epsilon}_p - 8.1\times 10^5\,\bar{\epsilon}_p^2 + 1.15\times 10^8\,\bar{\epsilon}_p^3 - 7.54\times 10^9\,\bar{\epsilon}_p^4 + 1.79\times 10^{11}\,\bar{\epsilon}_p^5 \quad \text{(MPa)}; \quad (0 < \bar{\epsilon}_p < 0.015).$$

The initial and boundary conditions are given by

$$\begin{cases} \mathbf{W} = \mathbf{0} & \text{for } \tau = 0 \\ q(\tau, \xi, \eta) = \beta q_0 \bar{F}_1(\tau)\bar{F}_2(\eta) = \beta q_0[1 - e^{-2\tau}]\left[\eta - \dfrac{J_1(r_1\eta)}{J_1(r_1)}\right] & \text{for } \xi = 0 \\ p(\tau, \xi, \eta) = 0 & \text{for } \eta = 1 \end{cases}$$

where J_1 denotes the first-order Bessel function of the first kind, r_1 the positive root of the second-order Bessel function of the first kind, and $q_0 = \tau^*/(\rho c_2^2)$. Note that when the magnification factor $\beta > 0.5$, the viscoplastic deformations take place in the cylinder.

Figure 1 depicts a comparison between the present results and the exact solutions obtained by Takeuchi et al. (1967) using the Laplace transform technique for the shear stress-time variation on outer surface at two stations. The present results are in close agreement with the exact solutions. In an effort to investigate the stability and convergence of the numerical solutions, the relative energy error for various values of the grid spacing h and the mesh ratio k/h was evaluated by comparing the total energy imparted to the cylinder E_{total} with the total energy input E_{input}. The relative energy error E_{rr} is defined as

$$E_{rr} = \frac{E_{\text{input}} - E_{\text{total}}}{E_{\text{input}}} \times 100 \text{ (percent)}.$$

Figures 2 and 3, respectively, indicate the relative energy error as a function of time for two values of β. It is seen that for the mesh ratio $k/h \leqq 0.5$, the error remains small at increasing time, whereas for $k/h \geqq 0.6$, the error soon becomes excessively large within $\tau = 2$. In addition, for $k/h \leqq 0.5$, the error generally increases with an increase in the grid spacing h for the same value of k/h. It should be noticed that as time elapses, the error becomes smaller for $\beta = 1.2$ (elastic/viscoplastic solutions) than for $\beta = 0.4$ (elastic solutions). A check on the relative energy error shows that the present method is always stable for $k/h < 0.6$, while for $k/h \geqq 0.6$, the

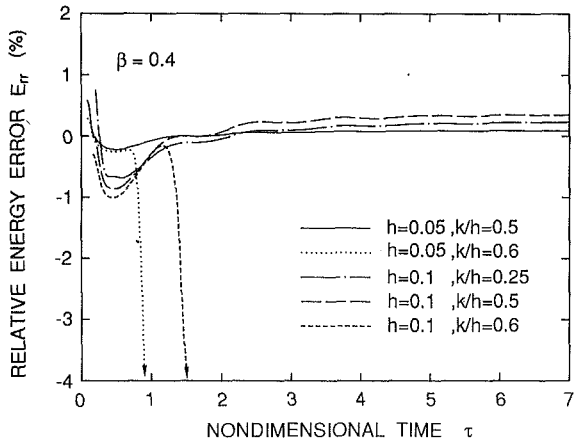


Fig. 2 Time histories of relative energy error in the difference solution (elastic solutions)

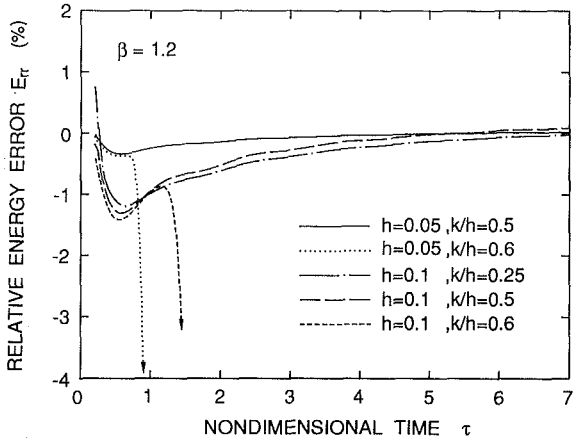


Fig. 3 Time histories of relative energy error in the difference solution (elastic/viscoplastic solutions)

Downloaded 03 May 2010 to 171.66.16.20. Redistribution subject to ASME license or copyright; see http://www.asme.org/terms/Terms_Use.cfm

numerical solutions diverge from the exact solutions, regardless of the value of β.

Acknowledgments

The authors wish to acknowledge the financial support of INOUE Foundation for Science, Tokyo, and the National Natural Science Foundation of China, Beijing.

References

Clifton, R. J., 1967, "A Difference Method for Plane Problems in Dynamic Elasticity," *Quarterly of Applied Mathematics*, Vol. 25, No. 1, pp. 97–116.

Fyfe, I. M., 1975, "The Applicability of Elastic/Viscoplastic Theory in Stress Wave Propagation," ASME JOURNAL OF APPLIED MECHANICS, Vol. 42, pp. 141–146.

Perzyna, P., 1963, "The Constitutive Equations for Rate Sensitive Plastic Materials," *Quarterly of Applied Mathematics*, Vol. 20, No. 4, pp. 321–332.

Takeuchi, K., Matsumoto, H., and Nakahara, I., 1967, "Propagation of Torsional Stress Waves in a Circular Cylinder," *Transactions of the Japan Society of Mechanical Engineers*, Vol. 33, No. 251, pp. 1018–1026, (in Japanese).

On a Class of Planar Motions of Flexible Rods

H. Cohen[7] and M. Epstein[8]

Introduction

Bend a metal measuring tape to form a small loop and see the loop propagate undisturbed along the tape. Or wrap a bungee rope around a wooden disk and stretch it; the disk will start rolling. Our curiosity thus having been aroused, we set out to translate these observations into analytical terms. It soon became apparent that the relevant problem is the following: What are the most general shape-steady motions of flexible rods? In such motions, the rod appears to be at rest, but on closer inspection, its particles are actually moving at a constant speed along the rod, thus creating the illusion of rest. The inertia forces should, therefore, be responsible for possible shapes which are in principle different from the so-called "elastica" (for which indeed there is no motion) and for extra axial forces ("hoop" stresses balancing the "centrifugal" force).

It was a pleasant surprise to discover in a recent article by Healey and Papadopoulos (1990) a revived interest in the steady motion of strings, a problem already tackled by Routh in the last century. Our present work meshes nicely with theirs and throws light on the essentially difference between the two problems brought about by the bending stiffness. We mention also the work of Konno et al. (1981) on the existence of soliton loops. It seems, however, that their basic equation contains certain approximations and would not be directly comparable to ours. It is also worth mentioning related work by Ross (1977) and by Fosdick and Villaggio (1986). Finally, after the preliminary acceptance of this Note, an article by Coleman and Dill (1992) dealing with a similar problem was published.

1 Equations of Motion

In the absence of external body forces, the planar motion of an inextensible flexible rod satisfies the dynamic equations

$$(N\mathbf{t}+Q\mathbf{n})'=\rho\ddot{\mathbf{r}}, \tag{1}$$

$$M'+Q=I\ddot{\psi}, \tag{2}$$

where N, Q, and M are axial force, shear force and bending moment, respectively, $\mathbf{t}$ and $\mathbf{n}$ are the unit tangent and unit normal at a point in the present configuration, $\mathbf{r}$ is the present position vector, ψ is the present slope, ρ is the constant mass density per unit length, I is the centroidal mass moment of inertia of the constant cross-section, dots denote time derivatives, and primes denote derivatives with respect to the length coordinate s of the beam axis. A thorough discussion of these equations from either a *derived* or *direct* approach, the former based on three-dimensional elasticity theory and the latter on the concept of an elastic directed curve, can be found in Cohen and Whitman (1977) and Cohen (1978), respectively, and for the case of constraints in Epstein (1979) and Cohen and Epstein (1979). In the following, the simplest form of the equations relevant to the analysis are presented. Since the rod has been assumed to be axially inextensible, there is no need to make a distinction between lengths of the axis before or during the deformation process, thus avoiding considerable algebraic manipulations and additional nonlinearities. From the definition of curvature κ of a plane curve it follows that

$$\mathbf{t}'=\kappa\mathbf{n}, \tag{3}$$

$$\mathbf{n}'=-\kappa\mathbf{t}. \tag{4}$$

Also, noting that

$$\mathbf{t}=\cos\psi\mathbf{e}_1+\sin\psi\mathbf{e}_2, \tag{5}$$

$$\mathbf{n}=-\sin\psi\mathbf{e}_1+\cos\psi\mathbf{e}_2, \tag{6}$$

where $\mathbf{e}_1$ and $\mathbf{e}_2$ are Cartesian unit vectors, we obtain

$$\dot{\mathbf{t}}=\dot{\psi}\mathbf{n}, \tag{7}$$

$$\dot{\mathbf{n}}=\dot{\psi}\mathbf{t}, \tag{8}$$

$$\ddot{\mathbf{t}}=\ddot{\psi}\mathbf{n}-\dot{\psi}^2\mathbf{t}, \tag{9}$$

and

$$\ddot{\psi}=\ddot{\mathbf{t}}\cdot\mathbf{n}. \tag{10}$$

Since s measures length, we have

$$\mathbf{t}=\mathbf{r}', \tag{11}$$

so that from (10) and (3) we finally obtain

$$\ddot{\psi}=\frac{\ddot{\mathbf{r}}'\cdot\mathbf{r}''}{\kappa}. \tag{12}$$

Returning to the dynamic Eqs. (1) and (2), we combine them so as to eliminate N and Q, which being constraint forces (by virtue of inextensibility and normality hypothesis, respectively) are not determined by the motion through constitutive equations. Plugging (2) into (1) yields

$$[N\mathbf{t}+(I\ddot{\psi}-M')\mathbf{n}]'=\rho\ddot{\mathbf{r}}. \tag{13}$$

On the other hand, projecting this equation onto $\mathbf{t}$ and $\mathbf{n}$, we get

$$N'-\kappa(I\ddot{\psi}-M')=\rho\ddot{\mathbf{r}}\cdot\mathbf{r}', \tag{14}$$

$$\kappa N=(I\ddot{\psi}-M')'=\rho\ddot{\mathbf{r}}\cdot\frac{\mathbf{r}''}{\kappa}, \tag{15}$$

and, reading off N from (15), we finally obtain

$$\left(\frac{1}{\kappa}\left(-(I\ddot{\psi}-M')'+\rho\ddot{\mathbf{r}}\cdot\frac{\mathbf{r}''}{\kappa}\right)\right)'-\kappa(I\ddot{\psi}-M')=\rho\ddot{\mathbf{r}}\cdot\mathbf{r}'. \tag{16}$$

Since the curvature is given in terms of the motion explicitly as

$$\kappa=(\mathbf{r}''\cdot\mathbf{r}'')^{1/2}, \tag{17}$$

and ψ is also specified in (12), and since the bending moment is given by a constitutive law of the form

$$M=M(\kappa), \tag{18}$$

[7]Faculty of Science, University of Manitoba, Winnipeg, Manitoba, Canada.

[8]Department of Mechanical Engineering, University of Calgary, Calgary, Alberta, Canada.

Contributed by the Applied Mechanics Division for publication in the ASME JOURNAL OF APPLIED MECHANICS. Manuscript received by the ASME Applied Mechanics Division, Sept. 10, 1991; final revision, Dec. 12, 1993. Associate Technical Editor: R. M. Bowen.

Downloaded 03 May 2010 to 171.66.16.20. Redistribution subject to ASME license or copyright; see http://www.asme.org/terms/Terms_Use.cfm

numerical solutions diverge from the exact solutions, regardless of the value of β.

Acknowledgments

The authors wish to acknowledge the financial support of INOUE Foundation for Science, Tokyo, and the National Natural Science Foundation of China, Beijing.

References

Clifton, R. J., 1967, "A Difference Method for Plane Problems in Dynamic Elasticity," *Quarterly of Applied Mathematics*, Vol. 25, No. 1, pp. 97–116.

Fyfe, I. M., 1975, "The Applicability of Elastic/Viscoplastic Theory in Stress Wave Propagation," ASME JOURNAL OF APPLIED MECHANICS, Vol. 42, pp. 141–146.

Perzyna, P., 1963, "The Constitutive Equations for Rate Sensitive Plastic Materials," *Quarterly of Applied Mathematics*, Vol. 20, No. 4, pp. 321–332.

Takeuchi, K., Matsumoto, H., and Nakahara, I., 1967, "Propagation of Torsional Stress Waves in a Circular Cylinder," *Transactions of the Japan Society of Mechanical Engineers*, Vol. 33, No. 251, pp. 1018–1026, (in Japanese).

On a Class of Planar Motions of Flexible Rods

H. Cohen[7] and M. Epstein[8]

Introduction

Bend a metal measuring tape to form a small loop and see the loop propagate undisturbed along the tape. Or wrap a bungee rope around a wooden disk and stretch it; the disk will start rolling. Our curiosity thus having been aroused, we set out to translate these observations into analytical terms. It soon became apparent that the relevant problem is the following: What are the most general shape-steady motions of flexible rods? In such motions, the rod appears to be at rest, but on closer inspection, its particles are actually moving at a constant speed along the rod, thus creating the illusion of rest. The inertia forces should, therefore, be responsible for possible shapes which are in principle different from the so-called "elastica" (for which indeed there is no motion) and for extra axial forces ("hoop" stresses balancing the "centrifugal" force).

It was a pleasant surprise to discover in a recent article by Healey and Papadopoulos (1990) a revived interest in the steady motion of strings, a problem already tackled by Routh in the last century. Our present work meshes nicely with theirs and throws light on the essentially difference between the two problems brought about by the bending stiffness. We mention also the work of Konno et al. (1981) on the existence of soliton loops. It seems, however, that their basic equation contains certain approximations and would not be directly comparable to ours. It is also worth mentioning related work by Ross (1977) and by Fosdick and Villaggio (1986). Finally, after the preliminary acceptance of this Note, an article by Coleman and Dill (1992) dealing with a similar problem was published.

1 Equations of Motion

In the absence of external body forces, the planar motion of an inextensible flexible rod satisfies the dynamic equations

$$(N\mathbf{t}+Q\mathbf{n})'=\rho\ddot{\mathbf{r}}, \tag{1}$$

$$M'+Q=I\ddot{\psi}, \tag{2}$$

where N, Q, and M are axial force, shear force and bending moment, respectively, $\mathbf{t}$ and $\mathbf{n}$ are the unit tangent and unit normal at a point in the present configuration, $\mathbf{r}$ is the present position vector, ψ is the present slope, ρ is the constant mass density per unit length, I is the centroidal mass moment of inertia of the constant cross-section, dots denote time derivatives, and primes denote derivatives with respect to the length coordinate s of the beam axis. A thorough discussion of these equations from either a *derived* or *direct* approach, the former based on three-dimensional elasticity theory and the latter on the concept of an elastic directed curve, can be found in Cohen and Whitman (1977) and Cohen (1978), respectively, and for the case of constraints in Epstein (1979) and Cohen and Epstein (1979). In the following, the simplest form of the equations relevant to the analysis are presented. Since the rod has been assumed to be axially inextensible, there is no need to make a distinction between lengths of the axis before or during the deformation process, thus avoiding considerable algebraic manipulations and additional nonlinearities. From the definition of curvature κ of a plane curve it follows that

$$\mathbf{t}'=\kappa\mathbf{n}, \tag{3}$$

$$\mathbf{n}'=-\kappa\mathbf{t}. \tag{4}$$

Also, noting that

$$\mathbf{t}=\cos\psi\mathbf{e}_1+\sin\psi\mathbf{e}_2, \tag{5}$$

$$\mathbf{n}=-\sin\psi\mathbf{e}_1+\cos\psi\mathbf{e}_2, \tag{6}$$

where $\mathbf{e}_1$ and $\mathbf{e}_2$ are Cartesian unit vectors, we obtain

$$\dot{\mathbf{t}}=\dot{\psi}\mathbf{n}, \tag{7}$$

$$\dot{\mathbf{n}}=\dot{\psi}\mathbf{t}, \tag{8}$$

$$\ddot{\mathbf{t}}=\ddot{\psi}\mathbf{n}-\dot{\psi}^2\mathbf{t}, \tag{9}$$

and

$$\ddot{\psi}=\ddot{\mathbf{t}}\cdot\mathbf{n}. \tag{10}$$

Since s measures length, we have

$$\mathbf{t}=\mathbf{r}', \tag{11}$$

so that from (10) and (3) we finally obtain

$$\ddot{\psi}=\frac{\ddot{\mathbf{r}}'\cdot\mathbf{r}''}{\kappa}. \tag{12}$$

Returning to the dynamic Eqs. (1) and (2), we combine them so as to eliminate N and Q, which being constraint forces (by virtue of inextensibility and normality hypothesis, respectively) are not determined by the motion through constitutive equations. Plugging (2) into (1) yields

$$[N\mathbf{t}+(I\ddot{\psi}-M')\mathbf{n}]'=\rho\ddot{\mathbf{r}}. \tag{13}$$

On the other hand, projecting this equation onto $\mathbf{t}$ and $\mathbf{n}$, we get

$$N'-\kappa(I\ddot{\psi}-M')=\rho\ddot{\mathbf{r}}\cdot\mathbf{r}', \tag{14}$$

$$\kappa N=(I\ddot{\psi}-M')'=\rho\ddot{\mathbf{r}}\cdot\frac{\mathbf{r}''}{\kappa}, \tag{15}$$

and, reading off N from (15), we finally obtain

$$\left(\frac{1}{\kappa}\left(-(I\ddot{\psi}-M')'+\rho\ddot{\mathbf{r}}\cdot\frac{\mathbf{r}''}{\kappa}\right)\right)'-\kappa(I\ddot{\psi}-M')=\rho\ddot{\mathbf{r}}\cdot\mathbf{r}'. \tag{16}$$

Since the curvature is given in terms of the motion explicitly as

$$\kappa=(\mathbf{r}''\cdot\mathbf{r}'')^{1/2}, \tag{17}$$

and ψ is also specified in (12), and since the bending moment is given by a constitutive law of the form

$$M=M(\kappa), \tag{18}$$

[7]Faculty of Science, University of Manitoba, Winnipeg, Manitoba, Canada.

[8]Department of Mechanical Engineering, University of Calgary, Calgary, Alberta, Canada.

Contributed by the Applied Mechanics Division for publication in the ASME JOURNAL OF APPLIED MECHANICS. Manuscript received by the ASME Applied Mechanics Division, Sept. 10, 1991; final revision, Dec. 12, 1993. Associate Technical Editor: R. M. Bowen.

Copyright © 1994 by ASME

Downloaded 03 May 2010 to 171.66.16.20. Redistribution subject to ASME license or copyright; see http://www.asme.org/terms/Terms_Use.cfm

we see that (16) is a legitimate PDE for the motion $r = r(s, t)$, provided, of course, the inextensibility constraint

$$\mathbf{r}' \cdot \mathbf{r}' = 1 \tag{19}$$

is identically enforced.

2 Steady Motions

We now investigate the class of nontrivial steady motions of an infinitely long or a closed-loop rod. These are, by definition, solutions of (16) of the form

$$\mathbf{r} = \mathbf{r}(s - ct), \tag{20}$$

where the constant c represents the speed of each and every particle at all instants. We assume for the moment that the function (1) is analytic everywhere. We note that, for solutions of the type (1), if the constraint is satisfied everywhere at one instant of time, then it will also be satisfied everywhere at all times. Given any function $\mathbf{r}$ of a real variable z, a change of variable of the type

$$\frac{ds}{dz} = \left(\frac{d\mathbf{r}}{dz} \cdot \frac{d\mathbf{r}}{dz}\right)^{1/2} \tag{21}$$

will immediately guarantee the satisfaction of the constraint (19). We will assume henceforth that such a change has always been effected.

For solutions of the type (20) we have

$$\dot{\mathbf{r}} = -c\mathbf{r}', \ \ddot{\mathbf{r}} = c^2\mathbf{r}'', \text{ etc.} \tag{22}$$

Using this fact in (16) yields

$$\left(\frac{1}{\kappa}(M' - Ic^2\kappa')'\right)' + \kappa(M' - Ic^2\kappa') = 0, \tag{23}$$

an O.D.E. for κ.

For a linear material, with

$$M = D\kappa, \tag{24}$$

(23) reduces to

$$\left(\frac{\kappa''}{\kappa}\right)' + \kappa\kappa' = 0, \tag{25}$$

which can be integrated to

$$\kappa'' = B\kappa - \frac{1}{2}\kappa^3, \tag{26}$$

where B is an arbitrary constant.

Returning to the general result (23) and noting that for $c = 0$ this equation must furnish the static solution (i.e. the so-called Elastica), we obtain the following:

Proposition: Every static Elastica shape (with no body forces) is also a dynamic solution of the steady class, and vice versa, provided that the static equation be solved for a fictitious material with the constitutive equation

$$M_{\text{modified}} = M(\kappa) - Ic^2\kappa. \tag{27}$$

Corollary: For a linear material the static and dynamic shapes coincide. This follows by the homogeneity of (23) (and also, alternatively, from the realization that (25) furnishes the linear Elastica equation).

Remark: This proposition can be easily extended to the most general case of a constrained elastic rod (Cohen and Epstein, 1979) deforming in space and including, among others, torsional effects.

It may appear odd that solutions of the type (20) turn out to be possible for all values of the speed c. This apparent paradox is clarified when the constraint forces are evaluated, to obtain

$$Q = -(M - Ic^2\kappa)', \tag{28}$$

$$N = \rho c^2 + \frac{(M - Ic^2\kappa)''}{\kappa} \tag{29}$$

which shows that the "wave" is at least in part driven by the adjustable forces of constraint. Indeed, if we consider for instance, a circular loop of radius R rotating steadily on itself, we obtain

$$Q = 0, \tag{30}$$

$$N = \rho c^2. \tag{31}$$

The last equation is identical with the classical "vibrating string" prescription for the wave speed in terms of the string tension and the density.

The case

$$c_{cr}^2 = \frac{M}{I\kappa} \tag{32}$$

deserves special consideration. When (say, for fixed R) c attains this value, the "equivalent stiffness" implied in Eq. (27) vanishes. A further increase in speed will render it negative. Thus, the loop will lose its stability and perhaps chaotic behavior will ensue. This critical value of the speed should not be surprising. Indeed, for linear elasticity the constant D in Eq. (24) is

$$D = E\frac{I}{\rho}, \tag{33}$$

with

$$c_{cr}^2 = \frac{E}{\rho}, \tag{34}$$

the speed of sound in the material! Again for a linear material, Eqs. (28) and (29) reduce to

$$Q = (c_{cr}^2 - c^2)I\kappa', \tag{35}$$

$$N = \rho c^2 + (c_{cr}^2 - c^2)I\frac{\kappa'}{\kappa}. \tag{36}$$

3 Steady Discontinuities

We turn our attention to the possibility of having solutions of the form (20) with discontinuous second derivatives at one point. The equations of motion must then be supplemented with balance equations at this point

$$[N\mathbf{t} + Q\mathbf{n}] = -\rho c[\dot{\mathbf{r}}], \tag{37}$$

$$[M] = -Ic[\dot{\psi}], \tag{38}$$

where [ ] denotes "jump."

The use of c for the speed of propagation needs no explanation. From the kinematic compatibility condition

$$[\dot{\psi}] = -c[\psi'], \tag{39}$$

it follows from (38) that we must have

$$c^2 = \frac{[M]}{I[\kappa]}. \tag{40}$$

If on one of the sides of the discontinuity the curvature is zero, we see that the speed of the particles in a steady motion consistent with the presence of a discontinuity in the curvature must equal the critical speed (32). As for (37) it obviously implies

$$[N] = 0, \tag{41}$$

$$[Q] = 0, \tag{42}$$

but these do not seem to impose new restrictions on the solution.

This section has been included to emphasize the difference between analytic steady solutions, which can exist at any slow speed, and discontinuous steady solutions, which can only be maintained at the critical speed and are, therefore, unlikely in general to be observed in practice.

4 Loop Propagation

By the principle of relativity, if a uniform motion is super-

Downloaded 03 May 2010 to 171.66.16.20. Redistribution subject to ASME license or copyright; see http://www.asme.org/terms/Terms_Use.cfm

imposed on a given solution of (16), a new solution is obtained. Let us consider, in particular, the motion

$$\mathbf{r}=\mathbf{r}_0(s-ct)+c t\mathbf{e}_1 \tag{43}$$

where $\mathbf{r}_0$ is a steady solution satisfying the asymptotic condition

$$\lim_{|z|\to\infty} \mathbf{r}_0(z)\cdot\mathbf{e}_2=0. \tag{44}$$

This is the case of "loops."

If the shape is analytic it can be sustained at low speeds. If, however, the two "tails" of the loop are actually straight, then only the critical speed is sustainable. As the case may be, the proposed solution (43) will keep the points at "infinity" fixed and the loop will propagate (to the right) at the constant speed c.

Analytic loops are characterized by curvature of constant sign with a transition zone ("boundary layer") from an almost constant plateau to "zero."

With a relatively narrow transition zone, these might have been the slowly propagating loops observed as mentioned in the Introduction.

Acknowledgment

This work was supported in part through Operating Grants of the Natural Science and Engineering Council of Canada.

References

Cohen, H.,. 1978, "Decay of Acceleration Waves in Elastic Rods," *Archive for Rational Mechanics and Analysis*, Vol. 67, pp. 151–163.

Cohen, H., and Epstein, M., 1979, "Acceleration Waves in Constrained Elastic Rods," *Archive for Rational Mechanics and Analysis*, Vol. 72, pp. 141–154.

Cohen, H., and Whitman, A. B., 1977, "Waves in Elastic Rods," *Journal of Sound and Vibration*, Vol. 51, pp. 283–302.

Coleman, B. D., and Dill, E. H., 1992, "Flexure Waves in Elastic Rods," *Journal of the Acoustical Society of America*, Vol. 91, pp. 2663–2673.

Epstein, M., 1979, "Thin-Walled Beams as Directed Curves," *Acta Mechanica*, Vol. 33, pp. 229–242.

Fosdick, R., and Villaggio, P., 1986, "Influence of the Bending Stiffness on the Shape of a Belt in Steady Motion, ASME Journal of Applied Mechanics, Vol. 53, pp. 266–270.

Healey, T. J., and Papadopoulos, J. N., 1990, "Steady Axial Motions of Strings," ASME Journal of Applied Mechanics, Vol. 57, pp. 787–789.

Konno, K., Ichikawa, Y.-H., and Wadati, M., 1981, "A Loop Soliton Propagating Along a Stretched Rope," *Journal of the Physics Society of Japan*, Vol. 50, pp. 1025–1026.

Ross, A. L., 1977, "Cable Kinking Analysis and Prevention," *Journal of Engineering for Industry*, pp. 112–115.

A Note on Oscillatory Couette Flow in a Rotating System

R. Ganapathy[9]

An alternative solution is proposed for the oscillatory Ekman boundary layer flow bounded by two parallel plates in relative motion (Muzumder, 1991). The solution brings out among other things, the phenomenon of resonance which is of importance in rotating systems.

[9]Department of Mathematics, National College, Tiruchirapalli 620 001, India.

Contributed by the Applied Mechanics Division of The American Society of Mechanical Engineers for publication in the ASME Journal of Applied Mechanics. Manuscript received by the ASME Applied Mechanics Division, July 20, 1992; final revision, Oct. 14, 1992. Associate Technical Editor: T. R. Akylas.

1 Mathematical Analysis

Recently, Muzumder (1991) investigated the unsteady couette flow of a viscous incompressible fluid between two parallel plates distant d apart in relative motion, with the lower one stationary and the upper moving and oscillating in its own plane with a velocity $U(t) = U_o(1 + \epsilon \cos \omega t)$. The entire system was rotating about an axis normal to the plates with an angular velocity Ω. Choosing the origin on the lower plate, the x-axis parallel to the direction of motion of the upper plate and the z-axis along the axis of rotation, Muzumder obtained the equation for the conservation of momentum as

$$\frac{\partial q}{\partial t}=\nu\frac{\partial^2 q}{\partial z^2}+\frac{\partial U}{\partial t}-2i\Omega(q-U), \tag{1}$$

where $q = u + iv$ is the fluid velocity in the complex form with u and v representing its components along the directions of the x and y-axes, respectively.

In order to solve (1) subject to the boundary conditions

$$q=0 \text{ at } z=0;\ q=U \text{ at } z=d, \tag{2}$$

a solution was sought in the form

$$q(\eta, t)=U_o\left[q_o(\eta)+\frac{\epsilon}{2}q_1(\eta)\exp(i\omega t)\right], \tag{3}$$

where $\eta = z/d$, $q_o = u_o + iv_o$ and $q_1 = u_1 + iv_1$. However, on the basis of mathematical and physical considerations, we observe that this representation for q is not correct. In fact, owing to the appearance of i in the ensuing differential equations, it is just not sufficient to seek a solution of the form given in Eq. (3) and rather the solution must be a linear combination of $\exp(i\omega t)$ and $\exp(-i\omega t)$. Hence, the correct form is

$$q(\eta, t)=U_o\left[q_o(\eta)+\frac{\epsilon}{2}\{q_1(\eta)\exp(i\omega t)+q_2(\eta)\exp(-i\omega t)\}\right]. \tag{4}$$

Substituting (4) into (1) and (2) and collecting the harmonic and nonharmonic terms, we obtain

$$\begin{aligned}
&q_o''-2iKq_o=-2iK,\\
&q_1''-2i(K+\lambda/2)q_1=-2i(K+\lambda/2),\\
&q_2''-2i(K-\lambda/2)q_2=-2i(K-\lambda/2),\\
&q_o(0)=q_1(0)=q_2(0)=0,\\
&q_o(1)=q_1(1)=q_2(1)=1,
\end{aligned} \tag{5}$$

where $K = \Omega d^2/\nu$ is the rotation parameter and $\lambda = \omega d^2/\nu$ is the frequency parameter. Solving Eqs. (5) we get

$$\begin{aligned}
q_o(\eta)&=1-\sinh[(1+i)\sqrt{K}(1-\eta)]/\sinh(1+i)\sqrt{K},\\
q_1(\eta)&=1-\sinh[(1+i)\sigma_1(1-\eta)]/\sinh(1+i)\sigma_1,\\
q_2(\eta)&=1-\sinh[(1+i)\sigma_2(1-\eta)]/\sinh(1+i)\sigma_2,
\end{aligned} \tag{6}$$

where $\sigma_1 = (K+(\lambda/2))^{1/2}$ and $\sigma_2 = (K-(\lambda/2))^{1/2}$.

In order to exemplify the qualitative difference between the solution we have obtained and the one presented by Muzumder (1991), we first seek an asymptotic expansion of q for large K. In fact, if we write

$$q_1(\eta)\exp(i\omega t)+q_2(\eta)\exp(-i\omega t)=u_1(\eta,t)+iv_1(\eta,t), \tag{7}$$

then for a given frequency of oscillation ω, in the limit of large K, we have

$$u_1(\eta,t)\cong 2\cos\omega t-e^{-\sigma_1\eta}\cos(\sigma_1\eta-\omega t)-e^{-\sigma_2\eta}\cos(\sigma_2\eta+\omega t), \tag{8}$$

which shows the emergence of a boundary layer of thickness of order $(K-(\lambda/2))^{-1/2}$ in addition to the one obtained by

Downloaded 03 May 2010 to 171.66.16.20. Redistribution subject to ASME license or copyright; see http://www.asme.org/terms/Terms_Use.cfm

imposed on a given solution of (16), a new solution is obtained. Let us consider, in particular, the motion

$$\mathbf{r}=\mathbf{r}_0(s-ct)+ct\mathbf{e}_1 \tag{43}$$

where $\mathbf{r}_0$ is a steady solution satisfying the asymptotic condition

$$\lim_{|z|\to\infty} \mathbf{r}_0(z)\cdot\mathbf{e}_2=0. \tag{44}$$

This is the case of "loops."

If the shape is analytic it can be sustained at low speeds. If, however, the two "tails" of the loop are actually straight, then only the critical speed is sustainable. As the case may be, the proposed solution (43) will keep the points at "infinity" fixed and the loop will propagate (to the right) at the constant speed c.

Analytic loops are characterized by curvature of constant sign with a transition zone ("boundary layer") from an almost constant plateau to "zero."

With a relatively narrow transition zone, these might have been the slowly propagating loops observed as mentioned in the Introduction.

Acknowledgment

This work was supported in part through Operating Grants of the Natural Science and Engineering Council of Canada.

References

Cohen, H.,. 1978, "Decay of Acceleration Waves in Elastic Rods," *Archive for Rational Mechanics and Analysis*, Vol. 67, pp. 151–163.

Cohen, H., and Epstein, M., 1979, "Acceleration Waves in Constrained Elastic Rods," *Archive for Rational Mechanics and Analysis*, Vol. 72, pp. 141–154.

Cohen, H., and Whitman, A. B., 1977, "Waves in Elastic Rods," *Journal of Sound and Vibration*, Vol. 51, pp. 283–302.

Coleman, B. D., and Dill, E. H., 1992, "Flexure Waves in Elastic Rods," *Journal of the Acoustical Society of America*, Vol. 91, pp. 2663–2673.

Epstein, M., 1979, "Thin-Walled Beams as Directed Curves," *Acta Mechanica*, Vol. 33, pp. 229–242.

Fosdick, R., and Villaggio, P., 1986, "Influence of the Bending Stiffness on the Shape of a Belt in Steady Motion, ASME Journal of Applied Mechanics, Vol. 53, pp. 266–270.

Healey, T. J., and Papadopoulos, J. N., 1990, "Steady Axial Motions of Strings," ASME Journal of Applied Mechanics, Vol. 57, pp. 787–789.

Konno, K., Ichikawa, Y.-H., and Wadati, M., 1981, "A Loop Soliton Propagating Along a Stretched Rope," *Journal of the Physics Society of Japan*, Vol. 50, pp. 1025–1026.

Ross, A. L., 1977, "Cable Kinking Analysis and Prevention," *Journal of Engineering for Industry*, pp. 112–115.

A Note on Oscillatory Couette Flow in a Rotating System

R. Ganapathy[9]

An alternative solution is proposed for the oscillatory Ekman boundary layer flow bounded by two parallel plates in relative motion (Muzumder, 1991). The solution brings out among other things, the phenomenon of resonance which is of importance in rotating systems.

[9]Department of Mathematics, National College, Tiruchirapalli 620 001, India.

Contributed by the Applied Mechanics Division of The American Society of Mechanical Engineers for publication in the ASME Journal of Applied Mechanics. Manuscript received by the ASME Applied Mechanics Division, July 20, 1992; final revision, Oct. 14, 1992. Associate Technical Editor: T. R. Akylas.

1 Mathematical Analysis

Recently, Muzumder (1991) investigated the unsteady couette flow of a viscous incompressible fluid between two parallel plates distant d apart in relative motion, with the lower one stationary and the upper moving and oscillating in its own plane with a velocity $U(t) = U_o(1 + \epsilon \cos \omega t)$. The entire system was rotating about an axis normal to the plates with an angular velocity Ω. Choosing the origin on the lower plate, the x-axis parallel to the direction of motion of the upper plate and the z-axis along the axis of rotation, Muzumder obtained the equation for the conservation of momentum as

$$\frac{\partial q}{\partial t}=\nu\frac{\partial^2 q}{\partial z^2}+\frac{\partial U}{\partial t}-2i\Omega(q-U), \tag{1}$$

where $q = u + iv$ is the fluid velocity in the complex form with u and v representing its components along the directions of the x and y-axes, respectively.

In order to solve (1) subject to the boundary conditions

$$q=0 \text{ at } z=0;\ q=U \text{ at } z=d, \tag{2}$$

a solution was sought in the form

$$q(\eta, t)=U_o\left[q_o(\eta)+\frac{\epsilon}{2}q_1(\eta)\exp(i\omega t)\right], \tag{3}$$

where $\eta = z/d$, $q_o = u_o + iv_o$ and $q_1 = u_1 + iv_1$. However, on the basis of mathematical and physical considerations, we observe that this representation for q is not correct. In fact, owing to the appearance of i in the ensuing differential equations, it is just not sufficient to seek a solution of the form given in Eq. (3) and rather the solution must be a linear combination of $\exp(i\omega t)$ and $\exp(-i\omega t)$. Hence, the correct form is

$$q(\eta, t)=U_o\left[q_o(\eta)+\frac{\epsilon}{2}\{q_1(\eta)\exp(i\omega t)+q_2(\eta)\exp(-i\omega t)\}\right]. \tag{4}$$

Substituting (4) into (1) and (2) and collecting the harmonic and nonharmonic terms, we obtain

$$\begin{aligned}
&q_o''-2iKq_o=-2iK,\\
&q_1''-2i(K+\lambda/2)q_1=-2i(K+\lambda/2),\\
&q_2''-2i(K-\lambda/2)q_2=-2i(K-\lambda/2),\\
&q_o(0)=q_1(0)=q_2(0)=0,\\
&q_o(1)=q_1(1)=q_2(1)=1,
\end{aligned} \tag{5}$$

where $K = \Omega d^2/\nu$ is the rotation parameter and $\lambda = \omega d^2/\nu$ is the frequency parameter. Solving Eqs. (5) we get

$$\begin{aligned}
q_o(\eta)&=1-\sinh[(1+i)\sqrt{K}(1-\eta)]/\sinh(1+i)\sqrt{K},\\
q_1(\eta)&=1-\sinh[(1+i)\sigma_1(1-\eta)]/\sinh(1+i)\sigma_1,\\
q_2(\eta)&=1-\sinh[(1+i)\sigma_2(1-\eta)]/\sinh(1+i)\sigma_2,
\end{aligned} \tag{6}$$

where $\sigma_1 = (K+(\lambda/2))^{1/2}$ and $\sigma_2 = (K-(\lambda/2))^{1/2}$.

In order to exemplify the qualitative difference between the solution we have obtained and the one presented by Muzumder (1991), we first seek an asymptotic expansion of q for large K. In fact, if we write

$$q_1(\eta)\exp(i\omega t)+q_2(\eta)\exp(-i\omega t)=u_1(\eta,t)+iv_1(\eta,t), \tag{7}$$

then for a given frequency of oscillation ω, in the limit of large K, we have

$$u_1(\eta,t)\cong 2\cos\omega t-e^{-\sigma_1\eta}\cos(\sigma_1\eta-\omega t)-e^{-\sigma_2\eta}\cos(\sigma_2\eta+\omega t), \tag{8}$$

which shows the emergence of a boundary layer of thickness of order $(K-(\lambda/2))^{-1/2}$ in addition to the one obtained by

Copyright © 1994 by ASME

Downloaded 03 May 2010 to 171.66.16.20. Redistribution subject to ASME license or copyright; see http://www.asme.org/terms/Terms_Use.cfm

Muzumder, namely a boundary layer of thickness of order $(K + (\lambda/2))^{-1/2}$. These boundary layers which are a direct consequence of the cyclonic and anticyclonic components of the impressed harmonic oscillations, are essentially due to a combination of a Stokes layer and the usual Ekman layer. Further, these layers propagate zonally and the vorticity which pervades these layers is carried from the lower boundary. Consequently, boundary layers appear close to both the surfaces which is otherwise expected, for, the equation governing the flow is a combination of both the local acceleration and rotation. In the nondimensional form, the thickness of these boundary layers reduces to $[2\nu/|2\Omega \pm \omega|]^{1/2}$. Finally, when the forcing frequency ω is equal to the natural frequency 2Ω of the rotating fluid, there arises the resonance effect in which case the solution reduces to

$$q(\eta,t) = U_o[q_o(\eta) + \frac{\epsilon}{2} q_1(\eta) \exp(i\omega t)], \tag{9}$$

since $q_2(\eta)$ becomes zero. Thus, the solution obtained by Muzumder agrees with the correct solution only in the special case $\omega = 2\Omega$ and consequently, his solution cannot be expected to reveal the essential flow characteristics properly. In fact, the velocity graphs given in Muzumder (1991) are not admissible whenever $\omega \neq 2\Omega$ and for the same reason we claim that the graphs shown in Muzumder (1991) for the shearing stress components are incorrect.

2 Conclusion

Although Muzumder claims to have solved this boundary value problem, yet from the foregoing analysis it is evident that neither the method adopted by him nor his analysis is valid for a rotating system and as such his results fail to predict the flow characteristics properly.

Acknowledgment

The author is thankful to Dr. H. A. Stone of Harvard University for his very useful suggestions which led to a definite improvement of the paper.

Reference

Muzumder, B. S., 1991, "An Exact Solution of Oscillatory Couette Flow in a Rotating System," ASME Journal of Applied Mechanics, Vol. 58, pp. 1104–1107.

Closed-Form Analysis of the Free Edge Effect in Angle-Ply Laminates

W. Becker[10]

Introduction

It is one of the limitations of classical laminated plate theory that it does not include the "free edge effect"—the occurrence of interlaminar stresses in a boundary layer region along the free edges of laminated composites. As a typical composite laminate with free edges, the tensile coupon depicted in Fig. 1 is considered in the following. It has a symmetric angle-ply $[\pm\theta]_s$ lay-up with four layers of equal thickness $h/4$ and a width b and lies within the x-y plane of the shown cartesian x-y-z coordinate system.

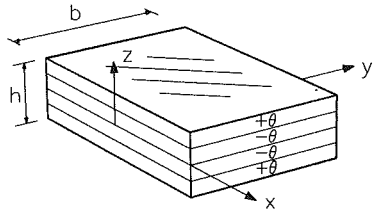


Fig. 1 Finite width angle-ply laminate coupon

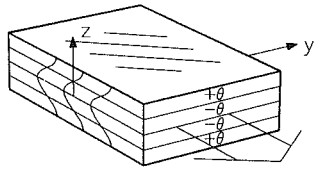


Fig. 2 Free edge deformation

Then, due to the discontinuity of the lay-up angle, uniaxial tensile loading in the x-direction gives rise to interlaminar shear stresses τ_{xz} at the $+\theta/-\theta$ interfaces near the edges, within a distance comparable to the laminate thickness h.

Since the original paper of Pipes and Pagano (1970), the free edge effect in angle-ply laminates has been treated by several numerical investigations (as Wang and Crossman, 1977; Herakovich et al., 1985; Herakovich, 1989). For a deeper mechanical understanding some closed-form analytical approaches have also been attempted (e.g., Puppo and Evensen, 1970; Tang, 1975; Tang and Levy, 1975; Hsu and Herakovich, 1977; Wang and Choi, 1982; Wang, 1983; Kassapoglou and Lagace, 1987). However, exact solutions have turned out to be not easily accessible.

The intent of the present contribution is to give a good approximate solution that does not involve too much numerical effort. To this end a certain higher-order deformation mode is introduced for the near-edge region and is taken into account appropriately. The whole analysis is of a closed-form analytical character, gives good results, and is easy to apply which makes it interesting for engineering purposes.

Basic Setting

The considered laminate coupon is presumed to be wide in comparison to its thickness ($b \gg h$) so that the predictions of classical laminated plate theory are recovered within the plate interior. Then it suffices to restrict the analysis to the edge given by $y = 0$ (see Fig. 1).

According to classical laminated plate theory, uniaxial homogeneous tensile loading in the x-direction gives rise to the following displacements in the x, y, and z direction:

$$\begin{aligned} u &= u(x) = \epsilon_x^0 x, \\ v &= v(y) = -\nu_{xy}^{\text{eff}} \epsilon_x^0 y, \\ w &= w(z) = -\nu_{xz}^{\text{eff}} \epsilon_x^0 z, \end{aligned} \tag{1}$$

where the quantities ν_{xy}^{eff} and ν_{xz}^{eff} denote effective Poisson's ratios of the laminate. In particular, the displacements u and v are independent from the thickness coordinate z. On the other hand, however, experimental findings (e.g., Herakovich et al., 1985) as well as numerical analyses (e.g., Pipes and Pagano, 1970; Herakovich et al., 1985) show a marked z dependence of the displacement u at the free edge. The respective free edge deformation is qualitatively indicated in Fig. 2. The stated z dependence is not linear, but of a higher-order character. For an approximative analytical description of the observed deformation shape a cos-function is chosen, and the representation (1) is improved as follows:

[10]Dornier GmbH, Deutsche Aerospace, Abteilung RST111, Postfach 1420, D-W-7990 Friedrichshafen-1, Fed. Republic of Germany.

Contributed by the Applied Mechanics Division of The American Society of Mechanical Engineers for publication in the ASME Journal of Applied Mechanics. Manuscript received by the ASME Applied Mechanics Division, June 26, 1991; final revision, Jan. 12, 1993. Associate Technical Editor: G. J. Dvorak.

Downloaded 03 May 2010 to 171.66.16.20. Redistribution subject to ASME license or copyright; see http://www.asme.org/terms/Terms_Use.cfm

Muzumder, namely a boundary layer of thickness of order $(K + (\lambda/2))^{-1/2}$. These boundary layers which are a direct consequence of the cyclonic and anticyclonic components of the impressed harmonic oscillations, are essentially due to a combination of a Stokes layer and the usual Ekman layer. Further, these layers propagate zonally and the vorticity which pervades these layers is carried from the lower boundary. Consequently, boundary layers appear close to both the surfaces which is otherwise expected, for, the equation governing the flow is a combination of both the local acceleration and rotation. In the nondimensional form, the thickness of these boundary layers reduces to $[2\nu/|2\Omega \pm \omega|]^{1/2}$. Finally, when the forcing frequency ω is equal to the natural frequency 2Ω of the rotating fluid, there arises the resonance effect in which case the solution reduces to

$$q(\eta,t) = U_o[q_o(\eta) + \frac{\epsilon}{2} q_1(\eta) \exp(i\omega t)], \tag{9}$$

since $q_2(\eta)$ becomes zero. Thus, the solution obtained by Muzumder agrees with the correct solution only in the special case $\omega = 2\Omega$ and consequently, his solution cannot be expected to reveal the essential flow characteristics properly. In fact, the velocity graphs given in Muzumder (1991) are not admissible whenever $\omega \neq 2\Omega$ and for the same reason we claim that the graphs shown in Muzumder (1991) for the shearing stress components are incorrect.

2 Conclusion

Although Muzumder claims to have solved this boundary value problem, yet from the foregoing analysis it is evident that neither the method adopted by him nor his analysis is valid for a rotating system and as such his results fail to predict the flow characteristics properly.

Acknowledgment

The author is thankful to Dr. H. A. Stone of Harvard University for his very useful suggestions which led to a definite improvement of the paper.

Reference

Muzumder, B. S., 1991, "An Exact Solution of Oscillatory Couette Flow in a Rotating System," ASME Journal of Applied Mechanics, Vol. 58, pp. 1104–1107.

Closed-Form Analysis of the Free Edge Effect in Angle-Ply Laminates

W. Becker[10]

Introduction

It is one of the limitations of classical laminated plate theory that it does not include the "free edge effect"—the occurrence of interlaminar stresses in a boundary layer region along the free edges of laminated composites. As a typical composite laminate with free edges, the tensile coupon depicted in Fig. 1 is considered in the following. It has a symmetric angle-ply $[\pm\theta]_s$ lay-up with four layers of equal thickness $h/4$ and a width b and lies within the x-y plane of the shown cartesian x-y-z coordinate system.

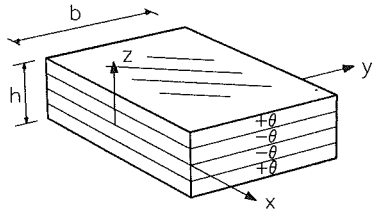


Fig. 1 Finite width angle-ply laminate coupon

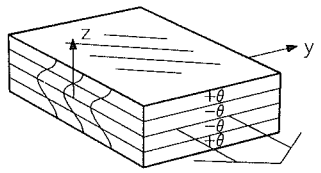


Fig. 2 Free edge deformation

Then, due to the discontinuity of the lay-up angle, uniaxial tensile loading in the x-direction gives rise to interlaminar shear stresses τ_{xz} at the $+\theta/-\theta$ interfaces near the edges, within a distance comparable to the laminate thickness h.

Since the original paper of Pipes and Pagano (1970), the free edge effect in angle-ply laminates has been treated by several numerical investigations (as Wang and Crossman, 1977; Herakovich et al., 1985; Herakovich, 1989). For a deeper mechanical understanding some closed-form analytical approaches have also been attempted (e.g., Puppo and Evensen, 1970; Tang, 1975; Tang and Levy, 1975; Hsu and Herakovich, 1977; Wang and Choi, 1982; Wang, 1983; Kassapoglou and Lagace, 1987). However, exact solutions have turned out to be not easily accessible.

The intent of the present contribution is to give a good approximate solution that does not involve too much numerical effort. To this end a certain higher-order deformation mode is introduced for the near-edge region and is taken into account appropriately. The whole analysis is of a closed-form analytical character, gives good results, and is easy to apply which makes it interesting for engineering purposes.

Basic Setting

The considered laminate coupon is presumed to be wide in comparison to its thickness ($b \gg h$) so that the predictions of classical laminated plate theory are recovered within the plate interior. Then it suffices to restrict the analysis to the edge given by $y = 0$ (see Fig. 1).

According to classical laminated plate theory, uniaxial homogeneous tensile loading in the x-direction gives rise to the following displacements in the x, y, and z direction:

$$\begin{aligned} u &= u(x) = \epsilon_x^0 x, \\ v &= v(y) = -\nu_{xy}^{\text{eff}} \epsilon_x^0 y, \\ w &= w(z) = -\nu_{xz}^{\text{eff}} \epsilon_x^0 z, \end{aligned} \tag{1}$$

where the quantities ν_{xy}^{eff} and ν_{xz}^{eff} denote effective Poisson's ratios of the laminate. In particular, the displacements u and v are independent from the thickness coordinate z. On the other hand, however, experimental findings (e.g., Herakovich et al., 1985) as well as numerical analyses (e.g., Pipes and Pagano, 1970; Herakovich et al., 1985) show a marked z dependence of the displacement u at the free edge. The respective free edge deformation is qualitatively indicated in Fig. 2. The stated z dependence is not linear, but of a higher-order character. For an approximative analytical description of the observed deformation shape a cos-function is chosen, and the representation (1) is improved as follows:

[10]Dornier GmbH, Deutsche Aerospace, Abteilung RST111, Postfach 1420, D-W-7990 Friedrichshafen-1, Fed. Republic of Germany.

Contributed by the Applied Mechanics Division of The American Society of Mechanical Engineers for publication in the ASME Journal of Applied Mechanics. Manuscript received by the ASME Applied Mechanics Division, June 26, 1991; final revision, Jan. 12, 1993. Associate Technical Editor: G. J. Dvorak.

Copyright © 1994 by ASME
Downloaded 03 May 2010 to 171.66.16.20. Redistribution subject to ASME license or copyright; see http://www.asme.org/terms/Terms_Use.cfm

$$u = u(x, y, z) = \epsilon_x^0 x + s(y)\cos\mu z,$$
$$v = \quad v(y) \quad = -\nu_{xy}^{\text{eff}}\epsilon_x^0 y,$$
$$w = \quad w(z) \quad = -\nu_{xz}^{\text{eff}}\epsilon_x^0 z,$$

with

$$\mu = \frac{2\pi}{h}. \tag{2}$$

In doing so, the function $s(y)$ represents the declining behavior of the near-edge deformations away from the edge and will be determined in the sequel.

The displacements (2) give the following strain components:

$$\epsilon_x = \epsilon_x^0, \qquad \epsilon_y = -\nu_{xy}^{\text{eff}}\epsilon_x^0, \qquad \epsilon_z = -\nu_{xz}^{\text{eff}}\epsilon_x^0,$$
$$\gamma_{yz} = 0, \quad \gamma_{xz} = -\mu s(y)\sin\mu z, \quad \gamma_{xy} = \dot{s}(y)\cos\mu z. \tag{3}$$

Herein the dot designates differentiation with respect to y.

The accompanying stress components result from the strains (3) by Hooke's law

$$\begin{bmatrix}\sigma_x\\ \sigma_y\\ \sigma_z\\ \tau_{yz}\\ \tau_{xz}\\ \tau_{xy}\end{bmatrix} = \begin{bmatrix}\overline{C}_{11} & \overline{C}_{12} & \overline{C}_{13} & 0 & 0 & \overline{C}_{16}\\ \overline{C}_{12} & \overline{C}_{22} & \overline{C}_{23} & 0 & 0 & \overline{C}_{26}\\ \overline{C}_{13} & \overline{C}_{23} & \overline{C}_{33} & 0 & 0 & \overline{C}_{36}\\ 0 & 0 & 0 & \overline{C}_{44} & \overline{C}_{45} & 0\\ 0 & 0 & 0 & \overline{C}_{45} & \overline{C}_{55} & 0\\ \overline{C}_{16} & \overline{C}_{26} & \overline{C}_{36} & 0 & 0 & \overline{C}_{66}\end{bmatrix}\begin{bmatrix}\epsilon_x\\ \epsilon_y\\ \epsilon_z\\ \gamma_{yz}\\ \gamma_{xz}\\ \gamma_{xy}\end{bmatrix}, \tag{4}$$

where the elastic stiffnesses $\overline{C_{ij}}$ are layer-wise constant.

The stress components, on their part, have to satisfy the equilibrium conditions from which in the following use will be made only of

$$\tau_{xy,y} + \tau_{xz,z} = 0. \tag{5}$$

Determination of Displacements and Interlaminar Shear Stress

With the displacements (2) the equilibrium condition (5) cannot be exactly fulfilled at every point (x, y, z) of the laminate, but equilibrium can be satisfied in an average sense for respective stress resultants after an integration through the laminate thickness—the usual procedure in classical plate theory. To this end here, condition (5) is integrated directly as well as after multiplication by $\cos\mu z$:

$$\int_{-h/2}^{h/2}[\tau_{xy,y} + \tau_{xz,z}]dz = 0,$$
$$\int_{-h/2}^{h/2}[\tau_{xy,y} + \tau_{xz,z}]\cos\mu z dz = 0. \tag{6}$$

Substituting relations (3) and (4) successively into conditions (6) and performing the integrations, it can be verified that the first condition of (6) is satisfied automatically for symmetric angle-ply laminates, whereas the second condition of (6) gives the following differential equation for the unknown function $s(y)$:

$$c_{66}^{c2}\ddot{s}(y) - \mu^2 c_{55}^{c2} s(y) = 0. \tag{7}$$

Herein the quantities c_{66}^{c2} and c_{55}^{c2} are abbreviating notations for the following "stiffness resultants" of the laminate:

$$c_{66}^{c2} = \int_{-h/2}^{h/2}\overline{C}_{66}\cos^2\mu z dz, \quad c_{55}^{c2} = \int_{-h/2}^{h/2}\overline{C}_{55}\cos^2\mu z dz. \tag{8}$$

The mechanically relevant part of the general solution of differential Eq. (7) (declining behavior) can be given as

$$s(y) = ke^{-\lambda\mu y} \quad \text{with} \quad \lambda = \sqrt{\frac{c_{55}^{c2}}{c_{66}^{c2}}}. \tag{9}$$

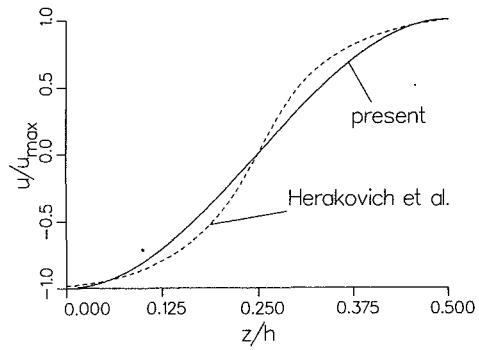


Fig. 3 Free edge displacement u

Herein k is a free constant. It is to be determined from the free-edge stress boundary condition at $y = 0$

$$\tau_{xy}(x, 0, z) = 0. \tag{10}$$

In analogy to the averaged form (6) of the equilibrium condition (5), the free-edge boundary condition (10) is demanded in the following integrated way (for $y = 0$):

$$\int_{-h/2}^{h/2}\tau_{xy}dz = 0, \quad \int_{-h/2}^{h/2}\tau_{xy}\cos\mu z dz = 0. \tag{11}$$

The first of these conditions is satisfied automatically for the underlying symmetric angle-ply laminate, whereas the second condition yields

$$k = \frac{c_{16}^{c1} - \nu_{xy}^{\text{eff}}c_{26}^{c1} - \nu_{xz}^{\text{eff}}c_{36}^{c1}}{c_{66}^{c2}\lambda\mu}\epsilon_x^0. \tag{12}$$

Herein the quantities c_{16}^{c1}, c_{26}^{c1}, and c_{36}^{c1} are abbreviating notations for the following "stiffness resultants" of the laminate:

$$c_{16}^{c1} = \int_{-h/2}^{h/2}\overline{C}_{16}\cos\mu z dz, \quad c_{26}^{c1} = \int_{-h/2}^{h/2}\overline{C}_{26}\cos\mu z dz,$$
$$c_{36}^{c1} = \int_{-h/2}^{h/2}\overline{C}_{36}\cos\mu z dz. \tag{13}$$

Thus with relations (9), (12), and (13), the function $s(y)$ is given and enables the straightforward calculation of the accompanying stresses by means of Eqs. (3) and (4). In particular, the following representation is obtained for the interlaminar shear stress τ_{xz} at the $+\theta/-\theta$-interface $(z = h/4)$:

$$\tau_{xz}(y, h/4) = -\overline{C}_{55}k\mu e^{-\lambda\mu y}. \tag{14}$$

This result means an exponentially declining behavior of τ_{xz} with the characteristic length $1/\lambda\mu$. Whereas this outcome is in acceptable accordance with other results, the strong point of the analysis presented so far is that it does involve only little computational effort. In particular, the closed-form analytical character of the approach makes it easy to study the effect of varying parameters.

Comparison to Numerical Investigations

Finally, the predictions of the presented analysis are to be compared to known numerical investigations. Herakovich et al. (1985) have determined the displacement u at the free edge $y = 0$ by finite element analysis in good agreement with experimental findings. For a $[\pm 30\ \text{deg}]_s$ laminate, their displacement distribution through the thickness is given in Fig. 3 together with the corresponding behavior of the present approach. Obviously, the introduced cos-deformation mode of the present analysis seems to be quite appropriate, although the numerically determined slope $u_{,z}$ is somewhat steeper at the $+30/-30$ deg interface.

In their pioneering work Pipes and Pagano (1970) have determined the behavior of the interlaminar shear stress τ_{xz} at the upper interface of a $[\pm 45\ \text{deg}]_s$ laminate by means of a

Downloaded 03 May 2010 to 171.66.16.20. Redistribution subject to ASME license or copyright; see http://www.asme.org/terms/Terms_Use.cfm

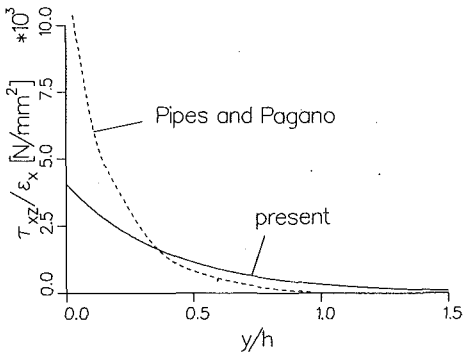


Fig. 4 Interlaminar shear stress τ_{xz} at $+45/-45$ deg interface

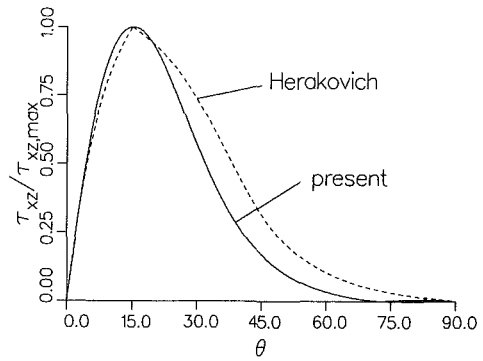


Fig. 5 Maximum interlaminar shear stress τ_{xz} at $+\theta/-\theta$ interface

finite difference technique. In Fig. 4 their result is given together with the behavior of τ_{xz} according to relation (14) for the same laminate and loading. The principal characteristics are reflected in a satisfactory way by the present result (14), although Pipes and Pagano predict a somewhat more pronounced stress localization which lets suppose the occurrence of a stress singularity. On the other hand, in reality the interlaminar stress τ_{xz} actually remains finite as it does according to relation (14). Whatever precise stress values may occur at the edge $y=0$, in any case the closed-form result (14) is very useful for comparative studies.

Such a comparative study has been performed by Herakovich (1989) when he varied the lay-up angle θ within a range of 0 to 90 deg. By finite element analyses he determined the maximum magnitudes of the occurring interlaminar shear stress τ_{xz}. The normalized result is given in Fig. 5 together with the respective predictions of the present approach. Obviously, the agreement is quite good. In particular, the maximum value of interlaminar shear stress occurs for $\theta=15$ deg in both cases.

In all, the observed accordances support the usefulness of the performed closed-form analysis. The presented approach gives a good further insight into the angle-ply edge effect and is easy to apply, which is convenient for engineering purposes.

References

Herakovich, C. T., Post, D., Buczek, M. B., Czarnek, R., 1985, "Free Edge Strain Concentrations in Real Composite Laminates: Experimental-Theoretical Correlation," ASME JOURNAL OF APPLIED MECHANICS, Vol. 52, pp. 787–793.

Herakovich, C. T., 1989, "Free Edge Effects in Laminated Composites," *Handbook of Composites, Vol. 2—Structure and Design*, C. T. Herakovich and Y. M. Tarnopol'skii, eds., Elsevier, Amsterdam, pp. 187–230.

Hsu, P. W., and Herakovich, C. T., 1977, "Edge Effects in Angle-Ply Composite Laminates," *Journal of Composite Materials*, Vol. 11, pp. 422–428.

Kassapoglou, C., and Lagace, P. A., 1987, "Closed Form Solutions for the Interlaminar Stress Field in Angle-Ply and Cross-Ply Laminates," *Journal of Composite Materials*, Vol. 21, pp. 292–308.

Pipes, R. B., and Pagano, N. J., 1970, "Interlaminar Stresses in Composite Laminates Under Uniform Axial Extension," *Journal of Composite Materials*, Vol. 4, pp. 538–548.

Puppo, A. H., and Evensen, H. A., 1970, "Interlaminar Shear in Laminated Composites Under Generalized Plane Stress," *Journal of Composite Materials*, Vol. 4, pp. 204–220.

Tang, S., 1975, "A Boundary Layer Theory—Part I: Laminated Composites in Plane Stress," *Journal of Composite Materials*, Vol. 9, pp. 33–41.

Tang, S., and Levy, A., 1975, "A Boundary Layer Theory—Part II: Extension of Laminated Finite Strip," *Journal of Composite Materials*, Vol. 9, pp. 42–52.

Wang, A. S. D., and Crossman, F. W., 1977, "Some New Results on Edge Effect in Symmetric Composite Laminates," *Journal of Composite Materials*, Vol. 11, pp. 92–106.

Wang, S. S., and Choi, I., 1982, "Boundary Layer Effects in Composite Laminates: Part 1—Free-Edge Stress Singularities," ASME JOURNAL OF APPLIED MECHANICS, Vol. 49, pp. 541–548.

Wang, S. S., and Choi, I., 1982, "Boundary Layer Effects in Composite Laminates: Part 2—Free-Edge Stress Solutions and Basic Characteristics," ASME JOURNAL OF APPLIED MECHANICS, Vol. 49, pp. 549–560.

Wang, S. S., 1983, "Elasticity Solutions for a Class of Composite Laminate Problems with Stress Singularities," *IUTAM Symposium, Mechanics of Composite Materials: Recent Advances*, Hashin and Herakovich, eds., pp. 259–281.

Stochastic Response of Hysteretic Systems to Narrow-Band Excitation

W. Q. Zhu,[11,14] C. D. Huang,[12,14] and T. T. Soong[13,14]

1 Introduction

It is well known that many engineering systems exhibit hysteresis when subjected to severe dynamic loadings. In the last three decades, much work has been done on the analysis of dynamic response of hysteretic systems. The dynamic loadings in all analyses are modeled as either sinusoidal (Caughey, 1960; Jennings, 1964; Iwan, 1966) or wide-band random excitation (Wen, 1989). To the authors' knowledge, no analysis has been made on the response of hysteretic systems to narrow-band excitations, which is also of practical interest.

The purpose of the present Note is to study the behavior of the stationary response of smooth and bilinear hysteretic systems subject to narrow-band excitations. The probability density of the displacement and the joint probability density of the displacement and velocity are obtained by using the quasi-static method (Stratonovich, 1967) and digital simulation. Based on these probability densities, it is shown that response of hysteretic systems to narrow-band excitations can be nonresonant and resonant depending on the values of the ratio of the excitation central frequency to the natural frequency of the system. In the resonant zone, the response is essentially non-Gaussian. For bilinear hysteretic systems with strong yielding, stochastic jumps may occur for certain values of the ratio between nonresonant and resonant zones.

2 The Quasi-Static Method

Consider a single-degree-of-freedom hysteretic system subject to a narrow-band excitation $\xi(\tau)$. The nondimensional equation of motion can be written as

$$x'' + 2\zeta x' + g(x, x') = \xi(\tau) \tag{1}$$

where $x = y/\Delta$, $\tau = \omega_0 t$; y = displacement; Δ = characteristic displacement; ω_0 = natural frequency of pre-yield system; $g(x, x')$ = nondimensional restoring force; a prime represents derivative with respect to τ. For bilinear hysteretic systems,

[11]Visiting Associate Professor.

[12]Research Assistant.

[13]Samuel P. Capen Professor of Engineering Science.

[14]Department of Civil Engineering, State University of New York at Buffalo, Buffalo, NY 14260.

Contributed by the Applied Mechanics Division of THE AMERICAN SOCIETY OF MECHANICAL ENGINEERS for publication in the ASME JOURNAL OF APPLIED MECHANICS. Manuscript received by the ASME Applied Mechanics Division, May 27, 1992; final revision, Nov. 23, 1992. Associate Technical Editor: P. D. Spanos.

Downloaded 03 May 2010 to 171.66.16.20. Redistribution subject to ASME license or copyright; see http://www.asme.org/terms/Terms_Use.cfm

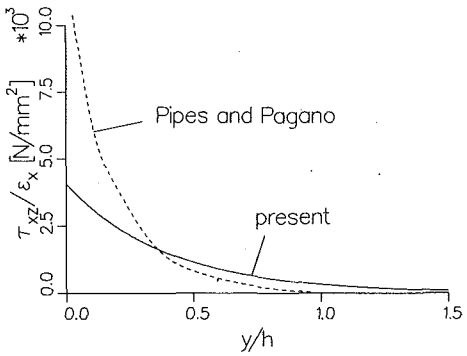


Fig. 4 Interlaminar shear stress τ_{xz} at $+45/-45$ deg interface

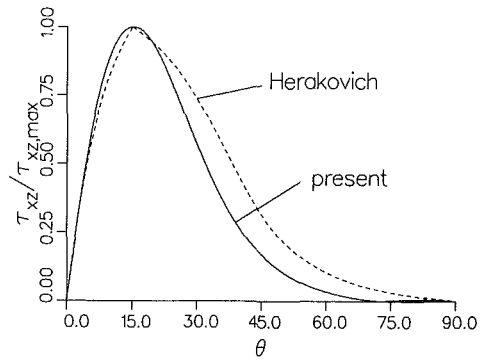


Fig. 5 Maximum interlaminar shear stress τ_{xz} at $+\theta/-\theta$ interface

finite difference technique. In Fig. 4 their result is given together with the behavior of τ_{xz} according to relation (14) for the same laminate and loading. The principal characteristics are reflected in a satisfactory way by the present result (14), although Pipes and Pagano predict a somewhat more pronounced stress localization which lets suppose the occurrence of a stress singularity. On the other hand, in reality the interlaminar stress τ_{xz} actually remains finite as it does according to relation (14). Whatever precise stress values may occur at the edge $y=0$, in any case the closed-form result (14) is very useful for comparative studies.

Such a comparative study has been performed by Herakovich (1989) when he varied the lay-up angle θ within a range of 0 to 90 deg. By finite element analyses he determined the maximum magnitudes of the occurring interlaminar shear stress τ_{xz}. The normalized result is given in Fig. 5 together with the respective predictions of the present approach. Obviously, the agreement is quite good. In particular, the maximum value of interlaminar shear stress occurs for $\theta=15$ deg in both cases.

In all, the observed accordances support the usefulness of the performed closed-form analysis. The presented approach gives a good further insight into the angle-ply edge effect and is easy to apply, which is convenient for engineering purposes.

References

Herakovich, C. T., Post, D., Buczek, M. B., Czarnek, R., 1985, "Free Edge Strain Concentrations in Real Composite Laminates: Experimental-Theoretical Correlation," ASME JOURNAL OF APPLIED MECHANICS, Vol. 52, pp. 787–793.

Herakovich, C. T., 1989, "Free Edge Effects in Laminated Composites," *Handbook of Composites, Vol. 2—Structure and Design*, C. T. Herakovich and Y. M. Tarnopol'skii, eds., Elsevier, Amsterdam, pp. 187–230.

Hsu, P. W., and Herakovich, C. T., 1977, "Edge Effects in Angle-Ply Composite Laminates," *Journal of Composite Materials*, Vol. 11, pp. 422–428.

Kassapoglou, C., and Lagace, P. A., 1987, "Closed Form Solutions for the Interlaminar Stress Field in Angle-Ply and Cross-Ply Laminates," *Journal of Composite Materials*, Vol. 21, pp. 292–308.

Pipes, R. B., and Pagano, N. J., 1970, "Interlaminar Stresses in Composite Laminates Under Uniform Axial Extension," *Journal of Composite Materials*, Vol. 4, pp. 538–548.

Puppo, A. H., and Evensen, H. A., 1970, "Interlaminar Shear in Laminated Composites Under Generalized Plane Stress," *Journal of Composite Materials*, Vol. 4, pp. 204–220.

Tang, S., 1975, "A Boundary Layer Theory—Part I: Laminated Composites in Plane Stress," *Journal of Composite Materials*, Vol. 9, pp. 33–41.

Tang, S., and Levy, A., 1975, "A Boundary Layer Theory—Part II: Extension of Laminated Finite Strip," *Journal of Composite Materials*, Vol. 9, pp. 42–52.

Wang, A. S. D., and Crossman, F. W., 1977, "Some New Results on Edge Effect in Symmetric Composite Laminates," *Journal of Composite Materials*, Vol. 11, pp. 92–106.

Wang, S. S., and Choi, I., 1982, "Boundary Layer Effects in Composite Laminates: Part 1—Free-Edge Stress Singularities," ASME JOURNAL OF APPLIED MECHANICS, Vol. 49, pp. 541–548.

Wang, S. S., and Choi, I., 1982, "Boundary Layer Effects in Composite Laminates: Part 2—Free-Edge Stress Solutions and Basic Characteristics," ASME JOURNAL OF APPLIED MECHANICS, Vol. 49, pp. 549–560.

Wang, S. S., 1983, "Elasticity Solutions for a Class of Composite Laminate Problems with Stress Singularities," *IUTAM Symposium, Mechanics of Composite Materials: Recent Advances*, Hashin and Herakovich, eds., pp. 259–281.

Stochastic Response of Hysteretic Systems to Narrow-Band Excitation

W. Q. Zhu,[11,14] C. D. Huang,[12,14] and T. T. Soong[13,14]

1 Introduction

It is well known that many engineering systems exhibit hysteresis when subjected to severe dynamic loadings. In the last three decades, much work has been done on the analysis of dynamic response of hysteretic systems. The dynamic loadings in all analyses are modeled as either sinusoidal (Caughey, 1960; Jennings, 1964; Iwan, 1966) or wide-band random excitation (Wen, 1989). To the authors' knowledge, no analysis has been made on the response of hysteretic systems to narrow-band excitations, which is also of practical interest.

The purpose of the present Note is to study the behavior of the stationary response of smooth and bilinear hysteretic systems subject to narrow-band excitations. The probability density of the displacement and the joint probability density of the displacement and velocity are obtained by using the quasi-static method (Stratonovich, 1967) and digital simulation. Based on these probability densities, it is shown that response of hysteretic systems to narrow-band excitations can be nonresonant and resonant depending on the values of the ratio of the excitation central frequency to the natural frequency of the system. In the resonant zone, the response is essentially non-Gaussian. For bilinear hysteretic systems with strong yielding, stochastic jumps may occur for certain values of the ratio between nonresonant and resonant zones.

2 The Quasi-Static Method

Consider a single-degree-of-freedom hysteretic system subject to a narrow-band excitation $\xi(\tau)$. The nondimensional equation of motion can be written as

$$x'' + 2\zeta x' + g(x, x') = \xi(\tau) \tag{1}$$

where $x = y/\Delta$, $\tau = \omega_0 t$; y = displacement; Δ = characteristic displacement; ω_0 = natural frequency of pre-yield system; $g(x, x')$ = nondimensional restoring force; a prime represents derivative with respect to τ. For bilinear hysteretic systems,

[11]Visiting Associate Professor.

[12]Research Assistant.

[13]Samuel P. Capen Professor of Engineering Science.

[14]Department of Civil Engineering, State University of New York at Buffalo, Buffalo, NY 14260.

Contributed by the Applied Mechanics Division of THE AMERICAN SOCIETY OF MECHANICAL ENGINEERS for publication in the ASME JOURNAL OF APPLIED MECHANICS. Manuscript received by the ASME Applied Mechanics Division, May 27, 1992; final revision, Nov. 23, 1992. Associate Technical Editor: P. D. Spanos.

Copyright © 1994 by ASME

Downloaded 03 May 2010 to 171.66.16.20. Redistribution subject to ASME license or copyright; see http://www.asme.org/terms/Terms_Use.cfm

$$g(x, x') = \begin{cases} x, & a \le 1, \\ x + (1-\alpha)(\alpha - 1), & a > 1, \quad -a \le x \le 2-a \\ \alpha x + (1-\alpha), & a > 1, \quad 2-a \le x \le a \end{cases} \tag{2}$$

where α is the ratio of post-yield to pre-yield stiffness and a is the nondimensional amplitude of displacement. For smooth hysteretic systems (Bouc-Wen model),

$$g(x, x') = \alpha x + (1-\alpha)z \tag{3}$$

$$z' = -\gamma |x'| z |z|^{n-1} - \beta x' |z|^n + A x', \tag{4}$$

where $(1-\alpha)z$ is the nondimensional hysteretic restoring force and β, γ, A, and n are parameters which control the shape of the hysteresis. Equation (4) can be integrated to yield a functional relationship between z and x (Cai and Lin, 1990). For the special case of $A = n = 1$ and $\beta \neq \pm\gamma$,

$$z(x) = \begin{cases} \dfrac{1}{\gamma - \beta}[1 - e^{-(\gamma-\beta)(x+x_o)}], & -a \le x \le -x_o \\ \dfrac{1}{\gamma + \beta}[1 - e^{-(\gamma+\beta)(x+x_o)}], & x_o \le x \le a \end{cases} \tag{5}$$

where x_o is uniquely determined for a given amplitude a by solving $z(-x_o) = 0$. Equations (2) and (5) hold for $x' \ge 0$. The values of $g(x, x')$ and $z(x)$ for $x' \le 0$ can be obtained using symmetry properties of these functions about $x = x' = 0$.

Suppose that $\xi(\tau)$ is a narrow-band Gaussian stationary random process. It can be expressed as

$$\xi(\tau) = \rho \cos(\nu\tau + \theta) \tag{6}$$

where $\rho = \rho(\tau)$ and $\theta = \theta(\tau)$ are slowly varying amplitude and phase, respectively, of the excitation and $\nu\omega_o$ is central frequency of the excitation. It has been shown (Lin, 1976) that ρ and θ are independent, ρ has Rayleigh distribution, and θ is uniformly distributed over $[0, 2\pi)$, i.e.,

$$p_s(\rho) = \frac{\rho}{\sigma_\xi^2} \exp\left(-\frac{\rho^2}{2\sigma_\xi^2}\right), \quad \rho \ge 0 \tag{7}$$

$$p_s(\theta) = \frac{1}{2\pi}, \quad 0 \le \theta < 2\pi. \tag{8}$$

Assume that the stationary response of the system described by Eq. (1) exists and it is narrow band. It can be expressed as

$$x = a \cos \Phi, \quad x' = -\nu a \sin \Phi \tag{9}$$

where $\Phi = \nu\tau + \varphi$ and $a = a(\tau)$ and $\varphi = \varphi(\tau)$ are slowly varying amplitude and phase, respectively, of the system. Using the quasi-static method, we obtain

$$\rho = \sqrt{[F(a) - 2\zeta a\nu]^2 + [H(a) - a\nu^2]^2} \tag{10}$$

and

$$\theta = \varphi - \tan^{-1}\frac{F(a) - 2\zeta a\nu}{H(a) - a\nu^2}. \tag{11}$$

For bilinear systems,

$$F(a) = \begin{cases} 0, & a \le 1 \\ -\dfrac{4}{\pi a}(1-\alpha)(a-1), & a > 1 \end{cases} \tag{12}$$

$$H(a) = \begin{cases} a, & a \le 1 \\ \dfrac{a}{\pi}[(1-\alpha)\Phi^* + \alpha\pi - \dfrac{1}{2}(1-\alpha)\sin 2\Phi^*], & a > 1 \end{cases} \tag{13}$$

where $\Phi^* = \cos^{-1}[(a-2)/a]$, $0 \le \Phi^* \le \pi$. For the Bouc-Wen model,

$$F(a) = (1-\alpha)\frac{2}{\pi}\left\{\frac{2(\beta x_o/a - \gamma)}{\gamma^2 - \beta^2} - \frac{1}{(\gamma-\beta)^2 a}[1 - e^{(\gamma-\beta)(a-x_o)}] - \frac{1}{(\gamma+\beta)^2 a}[e^{-(\gamma+\beta)(a+x_o)} - 1]\right. \tag{14}$$

$$H(a) = \alpha a + (1-\alpha)\frac{2}{\pi}\left\{\frac{1}{\gamma-\beta} \times \int_\pi^{\Phi^{**}} [1 - e^{-(\gamma-\beta)(a\cos\Phi + x_o)}]\cos\Phi d\Phi + \frac{1}{\gamma+\beta}\int_{\Phi^{**}}^{2\pi} [1 - e^{-(\gamma+\beta)(a\cos\Phi + x_o)}]\cos\Phi d\Phi\right. \tag{15}$$

where $\Phi^{**} = \cos^{-1}(-x_o/a)$ and $\pi \le \Phi^{**} \le 2\pi$.

The stationary joint probability density of a and φ can be obtained as follows:

$$p_s(a, \varphi) = p_s(\rho, \theta)\left|\frac{\partial(\rho, \theta)}{\partial(a, \varphi)}\right| \tag{16}$$

where $\partial(\rho, \theta)/\partial(a, \varphi)$ is the Jacobi determinant. It can be easily shown that

$$p_s(a) = p_s(\rho)\left|\frac{\partial\rho}{\partial a}\right|, \quad a \ge 0 \tag{17}$$

$$p_s(\varphi) = \frac{1}{2\pi}, \quad 0 \le \varphi < 2\pi. \tag{18}$$

The stationary joint probability density of the displacement x and velocity x' can be obtained from Eqs. (17) and (18) as follows:

$$p_s(x, x') = p_s(a, \varphi)\left|\frac{\partial(a, \varphi)}{\partial(x, x')}\right| = \frac{1}{2\pi a\nu} p_s(a)\Big|_{a=\sqrt{s^2 + x'^2/\nu^2}}. \tag{19}$$

It can be shown that the solutions of a and φ in Eqs. (10) and (11) are always stable and take "quasi-stable" values.

3 Digital Simulation

In digital simulation, the sample functions of excitation $\xi(\tau)$ are generated by using a linear filter with central frequency ν and bandwidth $\pi\delta/2$ subject to a Gaussian white noise excitation with intensity D. For smooth hysteretic systems, the sample functions of the responses x and x' are computed from Eqs. (1), (3), and (4) by using Runge-Kutta method of the fourth order. For bilinear hysteretic systems, instead of Eq. (2), we use Eq. (3) for the restoring force $g(x, x')$, where z satisfies the following differential equation (Suzuki and Minai, 1987):

$$z' = x'[1 - u(x')u(z-1) - u(-x')u(-z-1)] \tag{20}$$

where $u(\ )$ is a unit step function. Then the responses x and x' are computed from Eqs. (1), (3), and (20).

4 Results and Discussion

The behavior of the stationary response of a hysteretic system to narrow-band random excitations depends mainly on ν, the ratio of the central frequency of the excitation to the natural frequency of pre-yielded hysteretic system. Similar to the case of sinusoidal excitations, the value of ν can be divided into nonresonant and resonant zones. The range of ν-values for resonant zone depends upon the intensity of the excitation, α, and the model of the system.

In the nonresonant zone, the response of both bilinear and smooth hysteretic systems is relatively simple and similar to that due to wide-band random excitations (Zhu and Lei, 1987; Cai and Lin, 1990). The probability densities of the displacement, velocity, and amplitude are all unimodal. However, the displacement and velocity are usually non-Gaussian.

Downloaded 03 May 2010 to 171.66.16.20. Redistribution subject to ASME license or copyright; see http://www.asme.org/terms/Terms_Use.cfm

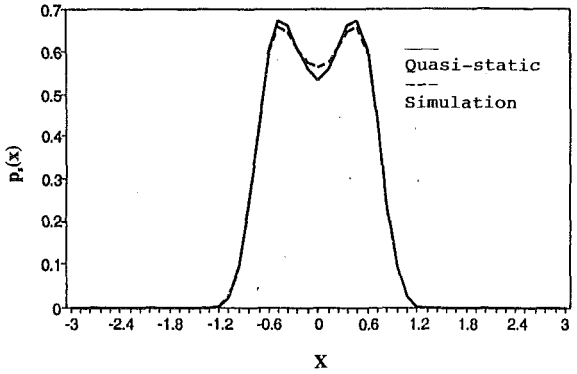


Fig. 1(*a*)

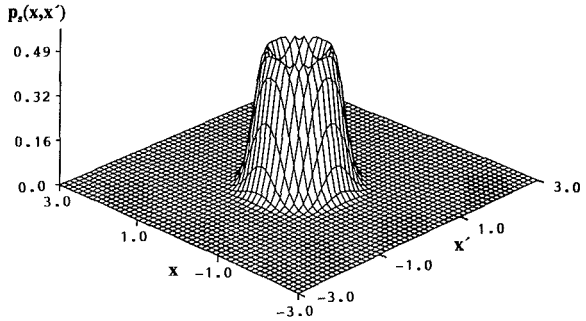


Fig. 1(*b*)

Fig. 1 Stationary probability densities of (*a*) displacement; (*b*) displacement and velocity (from the quasi-static method) of smooth hysteretic system to narrow-band excitation. $\alpha = 0.05$, $\beta = 0.05$, $\gamma = 0.95$, $\delta = 0.01$, $\zeta = 0.01$, $\nu = 1.0$, $D = 0.05$.

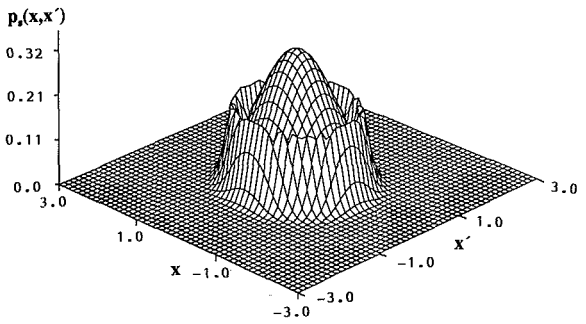


Fig. 2 Stationary probability density of displacement and velocity of bilinear hysteretic system to narrow-band excitation (from the quasi-static method); $\alpha = 0.05$, $\delta = 0.01$, $\zeta = 0.01$, $\nu = 0.89$, $D = 0.05$

In the resonant zone, the stationary displacement and velocity responses of both smooth and bilinear hysteretic systems are essentially non-Gaussian. The probability densities of the displacement and velocity are bi-modal while the joint probability density of the displacement and velocity has a ring of peaks (see Figs. 1(*a*) and 1(*b*)). It implies that the stationary response behaves like a diffused limit cycle. It is noted that although the probability density of the displacement is bi-modal, no jump occurs in this case.

An interesting observation is that, for a range of γ values between nonresonant and resonant zones, the joint probability density of the displacement and velocity of bilinear hysteretic systems with strong yielding (small α) has both a central peak and a ring of peaks with a ring of valley between them (see Fig. 2). In this case, the response contains two types of more probable motions: one is random vibration with smaller amplitudes similar to nonresonant vibration and another with larger amplitudes similar to resonant vibration.

It implies that jumps may occur between the two types of more probable motion and this phenomenon of stochastic jump has been observed in the sample functions of the displacement generated from digital simulation. It is noted that the jump occurs simultaneously in displacement and velocity and that even in this case the stationary variances of the displacement and velocity are unique. For a bilinear hysteretic system under sinusoidal excitation, it was shown rigorously by Caughey (1960) that no jump can occur. The solution of a in Eq. (10) is simple valued. However, for certain combinations of the parameters, the function $\partial\rho/\partial a$ can be such that $p_s(a)$ in Eq. (17) is bimodal.

References

Cai, G. Q., and Lin, Y. K., 1990, "On Randomly Excited Hysteretic Structures," ASME JOURNAL OF APPLIED MECHANICS, Vol. 57, pp. 442–448.

Caughey, T. K., 1960, "Sinusoidal Excitation of a System with Bilinear Hysteresis," ASME JOURNAL OF APPLIED MECHANICS, Vol. 27, pp. 640–644.

Iwan, W. D., 1966, "A Distributed-Element Model for Hysteresis and its Steady-State Dynamic Responses," ASME JOURNAL OF APPLIED MECHANICS, Vol. 33, pp. 893–900.

Jennings, P. C., 1964, "Periodic Response of General Yielding Structure," *Journal of Engineering Mechanics Division*, ASCE, Vol. 90, pp. 131–165.

Lin, Y. K., 1976, *Probabilistic Theory of Structural Dynamics*, Robert E. Krieger, Melbourne, FL.

Stratonovich, R.L., 1967, *Topics in the Theory of Random Noise*, Vol. 2, Gordon and Breach, New York.

Suzuki, Y., and Minai, R., 1987, "Application of Stochastic Differential Equation to Seismic Reliability Analysis of Hysteretic Structure," *Proc. U.S. Japan Joint Seminar on Stochastic Approaches in Earthquake Engineering*, Boca Raton, FL, pp. 334–356.

Wen, Y. K., 1989, "Methods of Random Vibration for Inelastic Stucture," ASME *Applied Mechanics Reviews*, Vol. 42, No. 2, pp. 39–52.

Zhu, W. Q., and Lei, Y., 1988, "Stochastic Averaging of Energy Envelope of Bilinear Hysteretic Systems," *Nonlinear Stochastic Dynamic Engineering Systems*, Proc. IUTAM Symposium, F. Ziegler and G. I. Schuëller, eds., Springer-Verlag, Berlin.

Stresses Around a Circular Hole in a Uniform Bar in Torsion

J. A. Greenwood[15]

Introduction

It is well known that in problems in plane stress or plane strain, the presence of a circular hole leads to a stress concentration factor (for uniaxial tension) equal to 3. Recently, Kienzler and Duan (1987) and Greenwood (1989) have shown that a more powerful result holds: the hoop stress σ_θ round the hole is related to the stresses at the same points without a hole (σ_r^i and σ_θ^i) according to

$$\sigma_\theta = 2(\sigma_\theta^i - \sigma_r^i + \sigma_o^i) \tag{1}$$

where σ_o^i is the mean value of σ_θ^i (or σ_r^i) round the circle.

The corresponding classical result for a hole in a uniform shaft subject to torsion is that the stress is doubled. We show here that a similar more powerful result holds.

Analysis

Consider first the values of the torsional stress function, in the absence of the hole, around the circle which will later become the hole. If the mean value of the stress function on this circle is ϕ_o then we can write

[15]Department of Engineering, Cambridge University, Trumpington Street, Cambridge, CB2 1PZ, U.K.

Contributed by the Applied Mechanics Division of THE AMERICAN SOCIETY OF MECHANICAL ENGINEERS for publication in the ASME JOURNAL OF APPLIED MECHANICS. Manuscript received by the ASME Applied Mechanics Division, Sept. 13, 1990; final revision, Feb. 3, 1993. Associate Technical Editor: L. M. Keer.

Downloaded 03 May 2010 to 171.66.16.20. Redistribution subject to ASME license or copyright; see http://www.asme.org/terms/Terms_Use.cfm

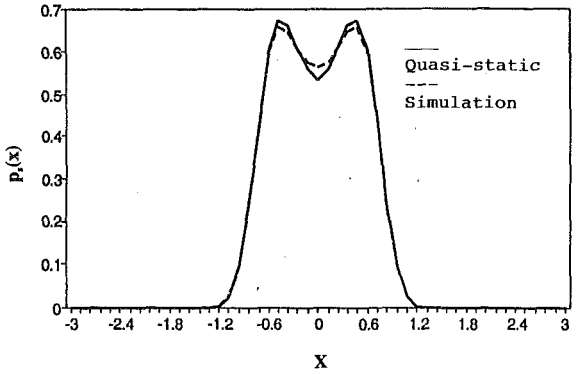


Fig. 1(*a*)

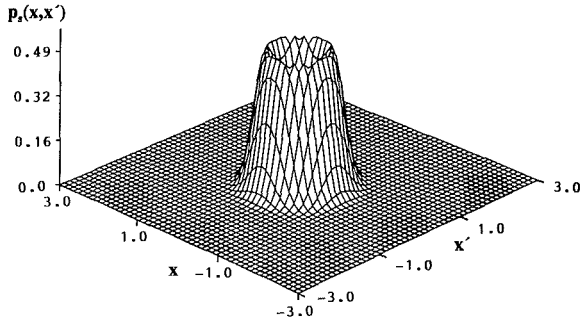


Fig. 1(*b*)

Fig. 1 Stationary probability densities of (*a*) displacement; (*b*) displacement and velocity (from the quasi-static method) of smooth hysteretic system to narrow-band excitation. $\alpha = 0.05$, $\beta = 0.05$, $\gamma = 0.95$, $\delta = 0.01$, $\zeta = 0.01$, $\nu = 1.0$, $D = 0.05$.

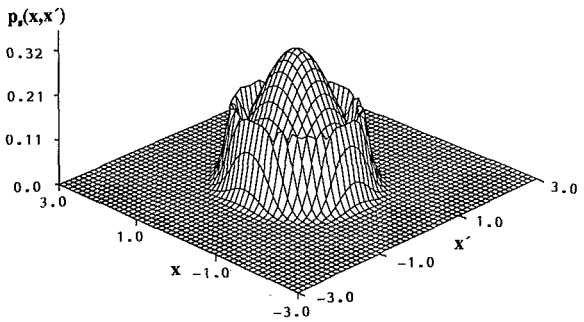


Fig. 2 Stationary probability density of displacement and velocity of bilinear hysteretic system to narrow-band excitation (from the quasi-static method); $\alpha = 0.05$, $\delta = 0.01$, $\zeta = 0.01$, $\nu = 0.89$, $D = 0.05$

In the resonant zone, the stationary displacement and velocity responses of both smooth and bilinear hysteretic systems are essentially non-Gaussian. The probability densities of the displacement and velocity are bi-modal while the joint probability density of the displacement and velocity has a ring of peaks (see Figs. 1(*a*) and 1(*b*)). It implies that the stationary response behaves like a diffused limit cycle. It is noted that although the probability density of the displacement is bimodal, no jump occurs in this case.

An interesting observation is that, for a range of γ values between nonresonant and resonant zones, the joint probability density of the displacement and velocity of bilinear hysteretic systems with strong yielding (small α) has both a central peak and a ring of peaks with a ring of valley between them (see Fig. 2). In this case, the response contains two types of more probable motions: one is random vibration with smaller amplitudes similar to nonresonant vibration and another with larger amplitudes similar to resonant vibration.

It implies that jumps may occur between the two types of more probable motion and this phenomenon of stochastic jump has been observed in the sample functions of the displacement generated from digital simulation. It is noted that the jump occurs simultaneously in displacement and velocity and that even in this case the stationary variances of the displacement and velocity are unique. For a bilinear hysteretic system under sinusoidal excitation, it was shown rigorously by Caughey (1960) that no jump can occur. The solution of a in Eq. (10) is simple valued. However, for certain combinations of the parameters, the function $\partial\rho/\partial a$ can be such that $p_s(a)$ in Eq. (17) is bimodal.

References

Cai, G. Q., and Lin, Y. K., 1990, "On Randomly Excited Hysteretic Structures," ASME JOURNAL OF APPLIED MECHANICS, Vol. 57, pp. 442–448.

Caughey, T. K., 1960, "Sinusoidal Excitation of a System with Bilinear Hysteresis," ASME JOURNAL OF APPLIED MECHANICS, Vol. 27, pp. 640–644.

Iwan, W. D., 1966, "A Distributed-Element Model for Hysteresis and its Steady-State Dynamic Responses," ASME JOURNAL OF APPLIED MECHANICS, Vol. 33, pp. 893–900.

Jennings, P. C., 1964, "Periodic Response of General Yielding Structure," *Journal of Engineering Mechanics Division*, ASCE, Vol. 90, pp. 131–165.

Lin, Y. K., 1976, *Probabilistic Theory of Structural Dynamics*, Robert E. Krieger, Melbourne, FL.

Stratonovich, R.L., 1967, *Topics in the Theory of Random Noise*, Vol. 2, Gordon and Breach, New York.

Suzuki, Y., and Minai, R., 1987, "Application of Stochastic Differential Equation to Seismic Reliability Analysis of Hysteretic Structure," *Proc. U.S. Japan Joint Seminar on Stochastic Approaches in Earthquake Engineering*, Boca Raton, FL, pp. 334–356.

Wen, Y. K., 1989, "Methods of Random Vibration for Inelastic Stucture," ASME *Applied Mechanics Reviews*, Vol. 42, No. 2, pp. 39–52.

Zhu, W. Q., and Lei, Y., 1988, "Stochastic Averaging of Energy Envelope of Bilinear Hysteretic Systems," *Nonlinear Stochastic Dynamic Engineering Systems*, Proc. IUTAM Symposium, F. Ziegler and G. I. Schuëller, eds., Springer-Verlag, Berlin.

Stresses Around a Circular Hole in a Uniform Bar in Torsion

J. A. Greenwood[15]

Introduction

It is well known that in problems in plane stress or plane strain, the presence of a circular hole leads to a stress concentration factor (for uniaxial tension) equal to 3. Recently, Kienzler and Duan (1987) and Greenwood (1989) have shown that a more powerful result holds: the hoop stress σ_θ round the hole is related to the stresses at the same points without a hole (σ_r^i and σ_θ^i) according to

$$\sigma_\theta = 2(\sigma_\theta^i - \sigma_r^i + \sigma_o^i) \tag{1}$$

where σ_o^i is the mean value of σ_θ^i (or σ_r^i) round the circle.

The corresponding classical result for a hole in a uniform shaft subject to torsion is that the stress is doubled. We show here that a similar more powerful result holds.

Analysis

Consider first the values of the torsional stress function, in the absence of the hole, around the circle which will later become the hole. If the mean value of the stress function on this circle is ϕ_o then we can write

[15]Department of Engineering, Cambridge University, Trumpington Street, Cambridge, CB2 1PZ, U.K.

Contributed by the Applied Mechanics Division of THE AMERICAN SOCIETY OF MECHANICAL ENGINEERS for publication in the ASME JOURNAL OF APPLIED MECHANICS. Manuscript received by the ASME Applied Mechanics Division, Sept. 13, 1990; final revision, Feb. 3, 1993. Associate Technical Editor: L. M. Keer.

Copyright © 1994 by ASME

Downloaded 03 May 2010 to 171.66.16.20. Redistribution subject to ASME license or copyright; see http://www.asme.org/terms/Terms_Use.cfm

$$\phi(\theta) = \phi_o + \Sigma A_n \cos n\theta + \Sigma B_n \sin n\theta.$$

The solution of the torsion equation $\nabla^2\phi = -2G\Omega$ (where Ω is the angle of twist per unit length) can conveniently be taken as a particular integral plus a (harmonic) complementary function so that we can write for $r \le a$

$$\phi = \phi_o - \frac{1}{2} G\Omega(r^2 - a^2) + \Sigma\left(\frac{r}{a}\right)^n \{A_n \cos n\theta + B_n \sin n\theta\}.$$

Then since $\tau_{z\theta} = -(\partial\phi/\partial r)$; $\tau_{zr} = +(1/r)(\partial\phi/\partial\theta)$ the initial stresses round the hole are

$$\tau_t^i = \tau_{z\theta}^i|_{r=a} = G\Omega a - \Sigma \frac{nA_n}{a} \cos n\theta - \Sigma \frac{nB_n}{a} \sin n\theta$$

$$\tau_n^i = \tau_{zr}^i|_{r=a} = -\Sigma \frac{nA_n}{a} \sin n\theta + \Sigma \frac{nB_n}{a} \cos n\theta$$

that is, around any circle the tangential and normal components of the shear stress are related as a Fourier series and its allied series.

We now wish to add a second function ϕ_2 such that $\nabla^2(\phi + \phi_2) = -2G\Omega$ with $(\phi + \phi_2)$ constant around $r = a$—the usual condition on the stress function to give $\tau_n = 0$. Thus ϕ_2 must be a harmonic function, valid for $r \ge a$, such that on $r = a$, $\phi = -\phi_2$. The condition for the displacements to be single valued is (Timoshenko and Goodier, 1951, p. 296)

$$\oint_C \frac{\partial\phi}{\partial n}\, ds = -2G\Omega A$$

where A is the area enclosed by a contour C: if C is a circle of radius a, the condition becomes $\bar{\tau}_t = G\Omega a$. Since it is already satisfied by the initial stresses, then ϕ_2 must satisfy

$$\oint_C \frac{\partial\phi_2}{\partial n}\, ds = 0$$

(i.e., the mean value of $\tau_{z\theta}$ round the circle does not change). Clearly

$$\phi_2 = -\Sigma A_n \left(\frac{a}{r}\right)^n \cos n\theta - \Sigma B_n \left(\frac{a}{r}\right)^n \sin n\theta. \tag{2}$$

Then the perturbing stresses will be

$$\tau_{z\theta}^{(2)} = -\Sigma \frac{nA_n}{a} \left(\frac{a}{r}\right)^{n+1} \cos n\theta - \Sigma \frac{nB_n}{a} \left(\frac{a}{r}\right)^{n+1} \sin n\theta$$

$$\tau_{zr}^{(2)} = +\Sigma \frac{nA_n}{a} \left(\frac{a}{r}\right)^{n+1} \sin n\theta - \Sigma \frac{nB_n}{a} \left(\frac{a}{r}\right)^{n+1} \cos n\theta \tag{3}$$

so that on $r = a$, $\tau_n^i + \tau_n^{(2)} = o$ as desired; while

$$\tau_t^{(2)} = \tau_t^i - G\Omega a = \tau_t^i - \bar{\tau}_t^i$$

or

$$\tau_t = 2\tau_t^i - \bar{\tau}_t^i = 2\tau_t^i - G\Omega a \tag{4}$$

with an obvious similarity to (1).

We note that a circular hole at the center of the circular shaft has no effect since $\tau_t^i = \bar{\tau}_t^i$; but that well away from the center the initial stresses will be relatively constant, $\bar{\tau}_t^i$ small, and the stresses almost doubled.

The general doubling of the stress at a small hole in torsion has long been known (Larmor, 1892). But it now appears that it is true in detail, point by point. The rule is *not*, of course, that the largest shear stress is twice the largest value of $|\tau|$ round the circle; only the variable part of the tangential component of τ is doubled; but it seems likely there will usually be little difference in the cases of most interest.

Hermann and his collaborators (e.g., Honein and Herrman, 1988) have shown that in plane elastostatics there are simple relations between the solutions inside and outside a circle from which the complete stress field in the presence of a hole can be obtained from that with no hole. Their methods are based on Milne-Thompson's "Circle Theorem" (Milne-Thompson, 1960), which in the present context asserts directly that if the original stress function is
then our second function will be

$$\phi_2 = -\phi_1(a^2/r, \theta) \quad (r \ge a) \tag{5}$$

which is indeed Eq. (2). Our equation $\tau_t = 2\tau_t^i - G\Omega a$ follows immediately. However, using Eq. (5) we can go further and, like Herrman, obtain the complete stress. We find

$$\tau_{z\theta}(r, \theta) = \tau_{z\theta}^i(r, \theta) + \frac{a^2}{r^2} \tau_{z\theta}^i\left(\frac{a^2}{r}, \theta\right) - G\Omega \frac{a^4}{r^3}$$

$$\tau_{zr}(r, \theta) = \tau_{zr}^i(r, \theta) - \frac{a^2}{r^2} \tau_{zr}^i\left(\frac{a^2}{r}, \theta\right) \tag{6}$$

reducing to Eq. (4) at the hole $r = a$.

Like Kienzler's formula (1), Eq. (4) is valid only when the nearest free surface is sufficiently far away. In plane stress (and strain), the perturbing stresses normally decay as r^{-2}, suggesting that the boundary should be at least three radii away from the center of the hole. From Eq. (3) we see that in torsion also the perturbing stresses decay as r^{-2}, and the same rule applies. However, unlike plane stress, it seems clear from the property that the shear flow is constant that the presence of the boundary will always increase the perturbing stresses and that our doubling is only a lower (unsafe) bound. In any case, because large torsion stresses inevitably occur near the shaft boundary, where our results cannot be used, it is clear that the method must be of academic interest only.

References

Greenwood, J. A., 1989, "Stresses Around Circular Holes and Inclusions," *I. J. Mech. Sci.*, Vol. 31, pp. 219–227.

Honein, T., and Herrman, G., 1988, "The Involution Correspondence in Plane Elastostatics for Regions Bounded by a Circle," ASME JOURNAL OF APPLIED MECHANICS, Vol. 55, pp. 566–573.

Kienzler, R., and Duan, Z. P., 1987, "On the Distribution of Hoop Stress Around Circular Holes in Elastic Sheets," ASME JOURNAL OF APPLIED MECHANICS, Vol. 54, pp. 110–114.

Larmor, J., 1892, "Influence of Flaws and Air Cavities on the Strength of Materials," *Philosophical Magazine*, Vol. 33, pp. 70–78.

Milne-Thompson, L. M., 1960, *Theoretical Hydrodynamics*, Macmillan, London.

Timoshenko, S., and Goodier, J. N., 1951, *Theory of Elasticity*, 2nd ed., McGraw-Hill, New York.

A Note on Axisymmetric *J*-Integrals

H. F. Nied[16]

1 Introduction

The purpose of this Note is to provide an explicit *J*-integral expression for conical cracks in axisymmetric stress fields. In two-dimensional crack configurations, the *J*-integral provides a convenient method for computing the energy release rate (energy/area) associated with the extension of cracks in linear or nonlinear elastic materials. In this Note an equivalent energy release rate quantity, usable as a failure criterion for axisymmetric conical cracks, is derived from the three-dimensional J_k-integrals originally established by Eshelby (1956, 1970). Since the three-dimensional J_k-integrals represent the energy released by the translation (not extension) of a whole crack (Budiansky and Rice, 1973), it will be shown that the general axisymmetric

[16]Coated Abrasive Division, Norton Company, Troy, NY 12181-0808. Mem. ASME.

Contributed by the Applied Mechanics Division of THE AMERICAN SOCIETY OF MECHANICAL ENGINEERS for publication in the ASME JOURNAL OF APPLIED MECHANICS. Manuscript received by the ASME Applied Mechanics Division, Feb. 20, 1992; final revision, Feb. 3, 1993. Associate Technical Editor: A. K. Noor.

Downloaded 03 May 2010 to 171.66.16.20. Redistribution subject to ASME license or copyright; see http://www.asme.org/terms/Terms_Use.cfm

$$\phi(\theta) = \phi_o + \Sigma A_n \cos n\theta + \Sigma B_n \sin n\theta.$$

The solution of the torsion equation $\nabla^2\phi = -2G\Omega$ (where Ω is the angle of twist per unit length) can conveniently be taken as a particular integral plus a (harmonic) complementary function so that we can write for $r \le a$

$$\phi = \phi_o - \frac{1}{2} G\Omega(r^2 - a^2) + \Sigma\left(\frac{r}{a}\right)^n \{A_n \cos n\theta + B_n \sin n\theta\}.$$

Then since $\tau_{z\theta} = -(\partial\phi/\partial r)$; $\tau_{zr} = +(1/r)(\partial\phi/\partial\theta)$ the initial stresses round the hole are

$$\tau_t^i = \tau_{z\theta}^i|_{r=a} = G\Omega a - \Sigma \frac{nA_n}{a} \cos n\theta - \Sigma \frac{nB_n}{a} \sin n\theta$$

$$\tau_n^i = \tau_{zr}^i|_{r=a} = -\Sigma \frac{nA_n}{a} \sin n\theta + \Sigma \frac{nB_n}{a} \cos n\theta$$

that is, around any circle the tangential and normal components of the shear stress are related as a Fourier series and its allied series.

We now wish to add a second function ϕ_2 such that $\nabla^2(\phi + \phi_2) = -2G\Omega$ with $(\phi + \phi_2)$ constant around $r = a$—the usual condition on the stress function to give $\tau_n = 0$. Thus ϕ_2 must be a harmonic function, valid for $r \ge a$, such that on $r = a$, $\phi = -\phi_2$. The condition for the displacements to be single valued is (Timoshenko and Goodier, 1951, p. 296)

$$\oint_C \frac{\partial\phi}{\partial n}\, ds = -2G\Omega A$$

where A is the area enclosed by a contour C: if C is a circle of radius a, the condition becomes $\bar{\tau}_t = G\Omega a$. Since it is already satisfied by the initial stresses, then ϕ_2 must satisfy

$$\oint_C \frac{\partial\phi_2}{\partial n}\, ds = 0$$

(i.e., the mean value of $\tau_{z\theta}$ round the circle does not change). Clearly

$$\phi_2 = -\Sigma A_n \left(\frac{a}{r}\right)^n \cos n\theta - \Sigma B_n \left(\frac{a}{r}\right)^n \sin n\theta. \tag{2}$$

Then the perturbing stresses will be

$$\tau_{z\theta}^{(2)} = -\Sigma \frac{nA_n}{a} \left(\frac{a}{r}\right)^{n+1} \cos n\theta - \Sigma \frac{nB_n}{a} \left(\frac{a}{r}\right)^{n+1} \sin n\theta$$

$$\tau_{zr}^{(2)} = +\Sigma \frac{nA_n}{a} \left(\frac{a}{r}\right)^{n+1} \sin n\theta - \Sigma \frac{nB_n}{a} \left(\frac{a}{r}\right)^{n+1} \cos n\theta \tag{3}$$

so that on $r = a$, $\tau_n^i + \tau_n^{(2)} = o$ as desired; while

$$\tau_t^{(2)} = \tau_t^i - G\Omega a = \tau_t^i - \bar{\tau}_t^i$$

or

$$\tau_t = 2\tau_t^i - \bar{\tau}_t^i = 2\tau_t^i - G\Omega a \tag{4}$$

with an obvious similarity to (1).

We note that a circular hole at the center of the circular shaft has no effect since $\tau_t^i = \bar{\tau}_t^i$; but that well away from the center the initial stresses will be relatively constant, $\bar{\tau}_t^i$ small, and the stresses almost doubled.

The general doubling of the stress at a small hole in torsion has long been known (Larmor, 1892). But it now appears that it is true in detail, point by point. The rule is *not*, of course, that the largest shear stress is twice the largest value of $|\tau|$ round the circle; only the variable part of the tangential component of τ is doubled; but it seems likely there will usually be little difference in the cases of most interest.

Hermann and his collaborators (e.g., Honein and Herrman, 1988) have shown that in plane elastostatics there are simple relations between the solutions inside and outside a circle from which the complete stress field in the presence of a hole can be obtained from that with no hole. Their methods are based on Milne-Thompson's "Circle Theorem" (Milne-Thompson, 1960), which in the present context asserts directly that if the original stress function is
then our second function will be

$$\phi_2 = -\phi_1(a^2/r, \theta) \quad (r \ge a) \tag{5}$$

which is indeed Eq. (2). Our equation $\tau_t = 2\tau_t^i - G\Omega a$ follows immediately. However, using Eq. (5) we can go further and, like Herrman, obtain the complete stress. We find

$$\tau_{z\theta}(r, \theta) = \tau_{z\theta}^i(r, \theta) + \frac{a^2}{r^2} \tau_{z\theta}^i\left(\frac{a^2}{r}, \theta\right) - G\Omega \frac{a^4}{r^3}$$

$$\tau_{zr}(r, \theta) = \tau_{zr}^i(r, \theta) - \frac{a^2}{r^2} \tau_{zr}^i\left(\frac{a^2}{r}, \theta\right) \tag{6}$$

reducing to Eq. (4) at the hole $r = a$.

Like Kienzler's formula (1), Eq. (4) is valid only when the nearest free surface is sufficiently far away. In plane stress (and strain), the perturbing stresses normally decay as r^{-2}, suggesting that the boundary should be at least three radii away from the center of the hole. From Eq. (3) we see that in torsion also the perturbing stresses decay as r^{-2}, and the same rule applies. However, unlike plane stress, it seems clear from the property that the shear flow is constant that the presence of the boundary will always increase the perturbing stresses and that our doubling is only a lower (unsafe) bound. In any case, because large torsion stresses inevitably occur near the shaft boundary, where our results cannot be used, it is clear that the method must be of academic interest only.

References

Greenwood, J. A., 1989, "Stresses Around Circular Holes and Inclusions," *I. J. Mech. Sci.*, Vol. 31, pp. 219–227.

Honein, T., and Herrman, G., 1988, "The Involution Correspondence in Plane Elastostatics for Regions Bounded by a Circle," ASME JOURNAL OF APPLIED MECHANICS, Vol. 55, pp. 566–573.

Kienzler, R., and Duan, Z. P., 1987, "On the Distribution of Hoop Stress Around Circular Holes in Elastic Sheets," ASME JOURNAL OF APPLIED MECHANICS, Vol. 54, pp. 110–114.

Larmor, J., 1892, "Influence of Flaws and Air Cavities on the Strength of Materials," *Philosophical Magazine*, Vol. 33, pp. 70–78.

Milne-Thompson, L. M., 1960, *Theoretical Hydrodynamics*, Macmillan, London.

Timoshenko, S., and Goodier, J. N., 1951, *Theory of Elasticity*, 2nd ed., McGraw-Hill, New York.

A Note on Axisymmetric *J*-Integrals

H. F. Nied[16]

1 Introduction

The purpose of this Note is to provide an explicit *J*-integral expression for conical cracks in axisymmetric stress fields. In two-dimensional crack configurations, the *J*-integral provides a convenient method for computing the energy release rate (energy/area) associated with the extension of cracks in linear or nonlinear elastic materials. In this Note an equivalent energy release rate quantity, usable as a failure criterion for axisymmetric conical cracks, is derived from the three-dimensional J_k-integrals originally established by Eshelby (1956, 1970). Since the three-dimensional J_k-integrals represent the energy released by the translation (not extension) of a whole crack (Budiansky and Rice, 1973), it will be shown that the general axisymmetric

[16]Coated Abrasive Division, Norton Company, Troy, NY 12181-0808. Mem. ASME.

Contributed by the Applied Mechanics Division of THE AMERICAN SOCIETY OF MECHANICAL ENGINEERS for publication in the ASME JOURNAL OF APPLIED MECHANICS. Manuscript received by the ASME Applied Mechanics Division, Feb. 20, 1992; final revision, Feb. 3, 1993. Associate Technical Editor: A. K. Noor.

Copyright © 1994 by ASME

Downloaded 03 May 2010 to 171.66.16.20. Redistribution subject to ASME license or copyright; see http://www.asme.org/terms/Terms_Use.cfm

crack extension problem, i.e., local displacement in the direction of the crack, can be solved by evaluating three-dimensional J_k for two translations. The resulting integral expressions reduce to a contour and an area integral in the meridianal plane.

J-integrals for axisymmetric crack configurations, subjected to axisymmetric loading, have been derived by Astiz et al. (1977) and Bergkvist and Lan Huong (1977). Amestoy et al. (1981) derived a J-integral expression for three-dimensional cracks expressed in terms of a contour and an area integral in the plane normal to the crack front. In addition, deLorenzi (1985) obtained an equivalent axisymmetric expression using the virtual crack extension method and Kuo (1987) has derived an axisymmetric energy release rate integral expression valid for nonaxisymmetric loading. With the exception of deLorenzi's (1985) virtual crack extension formula, the axisymmetric J-integrals explicitly reported in these papers assume that the crack plane is perpendicular to the axis of revolution. While this geometric configuration is of great significance, there are a number of important axisymmetric fracture problems where the crack surface is not confined to a flat plane, e.g., "cone"-shaped surface cracks formed under spherical indenters.

In two dimensions the J-integral can be simply represented by a line integral if no body forces are present. Axisymmetric J-integrals derived from three-dimensional J_k involve the evaluation of a line integral plus an area integral (Astiz et al., 1977; Bergkvist and Lan Huong, 1977; Amestoy et al., 1981). However, as will be shown, when the crack surface takes the shape of a circular cylinder aligned with the axis of revolution, the area integral vanishes and the axisymmetric J-integral reduces to a line integral similar in form to the two-dimensional case.

2 Three-Dimensional and Two-Dimensional J-Integrals

In three dimensions the energy release rate can be obtained from components of path-independent surface integrals introduced by Eshelby (1956, 1970), cf. Knowles and Sternberg (1972), and Budiansky and Rice (1973). The three-dimensional J-integral is a vector quantity with Cartesian components given by

$$J_k = \int \int_S (Wn_k - T_i u_{i,k})\, ds \tag{1}$$

where S is a closed surface surrounding the whole crack, n_i are the components of the outward unit normal with respect to the surface S, T_i are the components of the stress vector acting on this surface, and u_i are the components of displacement. The strain energy density W, in Eq. (1), is determined from

$$W = \int_0^{\epsilon_{ij}} \sigma_{ij}\, d\epsilon_{ij}. \tag{2}$$

The three-dimensional J-integral in Eq. (1) yields the energy released by the translation of the whole crack and has units of energy/length. The local energy release rate per unit area is the differential element of three-dimensional J_k on the curve that describes the three-dimensional crack front. In two-dimensional and axisymmetric problems, this rate is not a function of the crack front curvilinear coordinates. For plane fracture problems, the component of the J-integral vector directed parallel to the crack represents the energy release rate per unit of crack translation in the k-direction. In this special case, when the crack surfaces are not loaded, S can be reduced to toroidal surfaces surrounding the crack fronts defined by the contour Γ. Thus J_1 represents the usual scalar quantity for the two-dimensional J-integral expressed by

$$J_1 = J = \int_\Gamma \left(Wn_1 - T_i \frac{\partial u_i}{\partial x_1} \right) ds \tag{3}$$

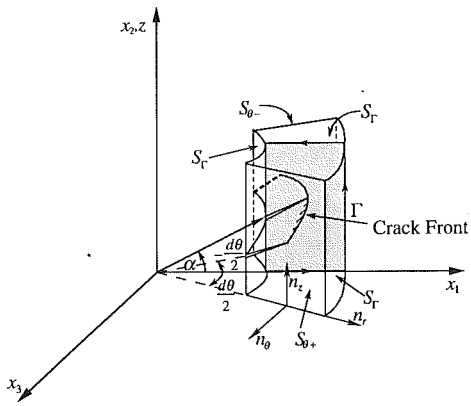


Fig. 1 Cylindrical volume surrounding crack-tip

where the crack is assumed to be along the local x_1-axis and the path Γ of the line integral in Eq. (3) is defined by a counterclockwise contour from one crack face to the other and enclosing the crack tip. If the two-dimensional crack is oriented at an angle α with respect to the x_1-axis, then there are two relevant global Cartesian components from Eq. (1) that contribute to J. The component of the J vector parallel to the crack in this case is given by

$$\bar{J} = \cos\alpha J_1 + \sin\alpha J_2. \tag{4}$$

This follows directly from Eq. (1), since in this case the crack displacement is given by $\delta 1 = \cos\alpha\, \delta 1_1 + \sin\alpha\, \delta 1_2$. Thus the two-dimensional crack extension problem, i.e., local displacement in the direction of the crack, is equivalent to two separate crack translations. By substituting the definition of the stress vector $T_r = \sigma_{rs} n_s$ into Eq. (4), substituting the definitions for the Cartesian components of strain, and noting that $n_1 ds = dx_2$, $n_2 ds = -dx_1$, the two-dimensional J-integral for a crack oriented at an angle α with respect to the x_1-axis is given by

$$\bar{J} = \int_\Gamma \left[\left(\sigma_{12} \frac{\partial u_1}{\partial x_2} + \sigma_{22}\epsilon_{22} - W \right) \sin\alpha + \left(\sigma_{12}\epsilon_{11} + \sigma_{22} \frac{\partial u_2}{\partial x_1} \right) \cos\alpha \right] dx_1 + \left[\left(W - \sigma_{11}\epsilon_{11} - \sigma_{21} \frac{\partial u_2}{\partial x_1} \right) \cos\alpha - \left(\sigma_{11} \frac{\partial u_1}{\partial x_2} + \sigma_{21}\epsilon_{22} \right) \sin\alpha \right] dx_2. \tag{5}$$

3 Axisymmetric J-Integrals

Figure 1 represents a cylindrical volume generated by rotating about the z-axis of the contour Γ from $-d\theta/2$ to $+d\theta/2$. The contour Γ can be of arbitrary shape, but for simplicity is depicted in Fig. 1 as a rectangle. The total surface of this volume surrounds a planar sector of the axisymmetric crack-tip of interest, which is oriented at an angle α with respect to the global $x_1 - x_3$ plane. The surface S of this volume can be broken into the three distinct surfaces shown in the figure, i.e., $S = S_\Gamma + S_{\theta+} + S_{\theta-}$.

The component of the three-dimensional J-integral vector directed parallel to the crack surface will be designated J_R and can be obtained by transforming the Cartesian components in Eq. (1) to spherical coordinates, i.e.,

$$J_R = \cos\alpha \cos\theta J_1 + \sin\alpha J_2 + \cos\alpha \sin\theta J_3. \tag{6}$$

Since we are only interested in the particular case where loading and crack shape are axisymmetric, J_R will not be a function of θ and we will therefore evaluate J_R at $\theta = 0$, i.e.,

$$J_R = \cos\alpha J_1 + \sin\alpha J_2. \tag{7}$$

Downloaded 03 May 2010 to 171.66.16.20. Redistribution subject to ASME license or copyright; see http://www.asme.org/terms/Terms_Use.cfm

Transformation of the Cartesian components of the three-dimensional J-integral vector (1) to cylindrical coordinates and evaluation for small angle θ ($\cos\theta \approx 1$, $\sin\theta \approx \theta$) yields

$$J_1 = \int \int_S \left[Wn_r - W\theta n_\theta - T_r \frac{\partial u_r}{\partial r} - T_z \frac{\partial u_z}{\partial r} + T_\theta \left(\theta \frac{u_r}{r} \right) \right] ds \quad (8)$$

$$J_2 = \int \int_S \left[Wn_z - T_r \frac{\partial u_r}{\partial z} - T_z \frac{\partial u_z}{\partial z} \right] ds \quad (9)$$

$$J_3 = \int \int_S \left[Wn_\theta + W\theta n_r - T_r\theta \frac{\partial u_r}{\partial r} - T_z\theta \frac{\partial u_z}{\partial r} - T_\theta \frac{u_r}{r} \right] ds. \quad (10)$$

The surface integrals in (8)-(10) can be broken into two separate integrals over the surfaces S_Γ and $(S_{\theta+} + S_{\theta-})$ respectively. For these surfaces, elements of infinitesimal surface area become $dS_\Gamma = rd\Gamma\, d\theta$ and $dS_{\theta+} = dS_{\theta-} = drdz = dA$.

Evaluating the integrals (8)-(10) on the surface S_Γ, neglecting terms of $O(\theta^2)$ and recognizing that $n_\theta = 0$, the contributions to the first surface integration are

$$J_1^{S_\Gamma} = \int_{-d\theta/2}^{d\theta/2} d\theta \int_\Gamma \left[Wn_r - T_r \frac{\partial u_r}{\partial r} - T_z \frac{\partial u_z}{\partial r} \right] rd\Gamma \quad (11)$$

$$J_2^{S_\Gamma} = \int_{-d\theta/2}^{d\theta/2} d\theta \int_\Gamma \left[Wn_z - T_r \frac{\partial u_r}{\partial z} - T_z \frac{\partial u_z}{\partial z} \right] rd\Gamma \quad (12)$$

$$J_3^{S_\Gamma} = 0. \quad (13)$$

Substitution of Eqs. (11)-(13) into Eq. (7), replacement of appropriate displacement derivatives and tractions with cylindrical strain and stress components, and recognizing $n_r d\Gamma = dz$ and $n_z d\Gamma = -dr$, results in the following expression for the J-integral evaluated over the surface S_Γ:

$$J_R^{S_\Gamma} = d\theta \int_\Gamma \left[\left(\sigma_{rz} \frac{\partial u_r}{\partial z} + \sigma_{zz}\epsilon_{zz} - W \right) \sin\alpha + \left(\sigma_{rz}\epsilon_{rr} + \sigma_{zz} \frac{\partial u_z}{\partial r} \right) \cos\alpha \right] rdr + \left[\left(W - \sigma_{rr}\epsilon_{rr} - \sigma_{zr} \frac{\partial u_z}{\partial r} \right) \cos\alpha - \left(\sigma_{rr} \frac{\partial u_r}{\partial z} + \sigma_{zr}\epsilon_{zz} \right) \sin\alpha \right] rdz. \quad (14)$$

In a similar manner the J-integral components are evaluated on the surfaces $S_{\theta-}$ and $S_{\theta+}$. On these surfaces (see Fig. 1) $n_r = n_z = 0$, $n_\theta = -1$ on $S_{\theta-}$ ($\theta = -d\theta/2$) and $n_\theta = +1$ on $S_{\theta+}$ ($\theta = d\theta/2$). The only contribution to the surface integral in this case comes from J_1 (Eq. (8)) and is given by

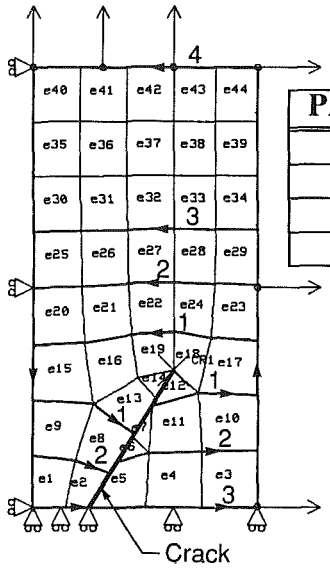
$$J_1 = \int \int_{S_{\theta-}+S_{\theta+}} \left(-Wn_\theta\theta + T_\theta \frac{u_r}{r}\theta \right) dA = -d\theta \int \int_A (W - \sigma_{\theta\theta}\epsilon_{\theta\theta}) dA. \quad (15)$$

Since J_2 vanishes on the surfaces $S_{\theta-}$ and $S_{\theta+}$, substitution of (15) into (7) results in the sole contribution to the expression for J_R from these surfaces, i.e.,

$$J_R^{(S_{\theta-}+S_{\theta+})} = -\cos\alpha d\theta \int \int_A (W - \sigma_{\theta\theta}\epsilon_{\theta\theta}) dA. \quad (16)$$

Combining Eq. (14) and (16) we obtain the complete expression for J_R

$$J_R = d\theta \int_\Gamma \left(W\bar{n}_1 - \bar{T}_1 \frac{\partial \bar{u}_1}{\partial \bar{x}_1} - \bar{T}_2 \frac{\partial \bar{u}_2}{\partial \bar{x}_1} \right) x_1 d\Gamma - d\theta \cos\alpha \int \int_A (W - \sigma_{\theta\theta}\epsilon_{\theta\theta}) dA \quad (17)$$



PATH	J^*
1	0.77045
2	0.77136
3	0.76785
4	0.77688

Fig. 2 J-integral paths for crack at an angle

where the first integral in (17) symbolically represents, in Cartesian form, the transformed terms given by Eq. (14). Note that J_R has units energy/length.

Finally, the energy release rate for a unit area of crack extension is

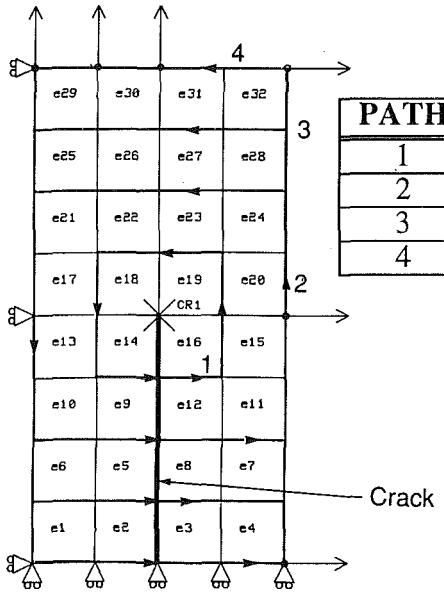
$$\frac{J_R}{r_c d\theta} = \frac{1}{r_c} \int_\Gamma \left(W\bar{n}_1 - \bar{T}_1 \frac{\partial \bar{u}_1}{\partial \bar{x}_1} - \bar{T}_2 \frac{\partial \bar{u}_2}{\partial \bar{x}_1} \right) x_1 d\Gamma - \frac{1}{r_c} \cos\alpha \int \int_A (W - \sigma_{\theta\theta}\epsilon_{\theta\theta}) dA \quad (18)$$

where r_c is the radial distance from the axis of revolution to the crack-tip. The expression for the energy release rate given by (18) consists of both a line integral and an area integral. Equation (18) is a more general form of the axisymmetric J-integrals given by Astiz et al. (1977) and Bergkvist and Lan Huong (1977). It is interesting to note that the area integral term in (18) vanishes for $\alpha = \pm 90$ deg, i.e., crack configurations where the crack surface takes the shape of a circular cylinder. In such a situation, the axisymmetric J-integral reduces to the integral given in (14) and except for the term r, is identical to the two-dimensional J-integral in Eq. (5).

4 Numerical Examples

A finite element numerical example for a conical axisymmetric crack configuration, that demonstrates the path independence of the axisymmetric J-integral given by (18), is depicted in Fig. 2. The crack is oriented at an angle with respect to the axis of revolution. The rod has a radius of two units and a length of four units. The mouth of the crack is located at $z = 0$ and at a radius of 0.5 units from the z-axis. The crack-tip has coordinates of $r = 1.25$ units, $z = 1.25$ units ($\alpha = 59.036$ deg). The applied stresses σ_0 are acting on the cylinder's entire outer radius and are also applied to a portion of the end of the rod from $0 < r < 1.25$ units. The finite element model consisted of 44 cubic elements with "enriched" elements at the crack-tip, of the type introduced by Benzley (1974), which are used to directly calculate the stress intensity factors. Four separate paths where chosen for evaluation of the axisymmetric J-integral. The normalized energy release rates, for crack length a, computed from (18) along the four paths is tabulated in Fig. 2. The normalized energy release rate is essentially path independent with the average value for J^* equal to 0.7716. Poisson's ratio $\nu = 0.3$ and elastic modulus $E = 30 \times 10^6$ were used in the calculation and J^* is given by

Downloaded 03 May 2010 to 171.66.16.20. Redistribution subject to ASME license or copyright; see http://www.asme.org/terms/Terms_Use.cfm



PATH	J^*
1	0.66730
2	0.67228
3	0.66847
4	0.67917

Fig. 3 *J*-integral paths for cylindrical crack

$$J^* = \frac{J}{\sigma_0^2 a\left(\frac{1-\nu^2}{E}\right)}. \tag{19}$$

The stress intensity factors computed independently using the enriched elements, yielded values of $K_I^* = 0.8634$ and $K_{II}^* = -0.0960$ ($K^* = K/\sigma_0 a^{1/2}$). Computing a total energy release rate from these two stress intensity factors, using the relationship

$$J = \frac{(1-\nu^2)}{E}(K_I^2 + K_{II}^2) \tag{20}$$

gives a value of $J^* = 0.7547$. Comparing this with the average J^* value of 0.7716 from the four paths yields a two percent difference.

A second numerical example is shown in Fig. 3. The dimensions of the rod and the applied loading are identical to those in the previous example. In this case the crack has a length $a = 2$ units and is oriented at 90 deg to the x-axis. Thus the crack surface forms a cylinder about the z-axis. Since $\alpha = 90$ deg, according to Eq. (18) there should be no contribution from the area integration in the J-integral calculation. The four paths shown in Fig. 3 were used to compute the J^* values tabulated in Fig. 3. The J^* values are again path independent. The stress intensity factors computed using the "enriched" crack-tip elements were $K_I^* = 0.7512$ and $K_{II}^* = 0.2843$. Computing a total energy release rate from the stress intensity factors yields $J^* = 0.6451$. Comparison with the average J^* value from the four paths in Fig. 3, $J_{av}^* = 0.6718$, indicates that in this example the axisymmetric J-integral calculation differs by four percent from the energy release rates obtained from independently calculated values of K_I and K_{II}.

5 Conclusion

In this Note, an axisymmetric J-integral, a special case of the three-dimensional J-integral, was derived for cracks oriented at an angle to the axis of revolution. The axisymmetric J-integral was shown to have a simple form involving both a line integral and an area integral. It is interesting to note that when the crack surface takes the shape of a cylinder about the axis of revolution, the contribution to the J-integral from the area integration vanishes and the axisymmetric J-integral, except for a factor of r, becomes identical to the two-dimensional J-integral.

References

Amestoy, M., Bui, H. D., Labbens, R., 1981, "On the Definition of Local Path Independent Integrals in Three-Dimensional Crack Problems," *Mechanical Research Communications*, Vol. 8, No. 4, pp. 231–236.

Astiz, M. A., Elices, M., and Galvez, V. S., 1977, "On Energy Release Rates in Axisymmetrical Problems," *Fracture 1977*, Vol. 3, ICF4, Waterloo, Canada, June 19–24, pp. 395–399.

Benzley, S. E., 1974, "Representation of Singularities with Isoparametric Finite Elements," *Int. Journal for Numerical Methods in Engineering*, Vol. 8, pp. 537–545.

Bergkvist, H., and Lan Huong, G., 1977, "J-Integral Related Quantities in Axisymmetric Cases," *Int. Journ. of Fracture*, Vol. 13, pp. 556–558.

Bergkvist, H., and Lan Huong, G., 1977, "Energy Release Rates in Cases of Axial Symmetry," *Proceedings of Fracture Mechanics and Technology*, Hong Kong, Mar. 21–25, Sijthoff and Noordhoff, pp. 1053–1066.

Budiansky, B., and Rice, J. R., 1973, "Conservation Laws and Energy-Release Rates," ASME JOURNAL OF APPLIED MECHANICS, Vol. 40, pp. 201–203.

deLorenzi, H. G., 1985, "Energy Release Rate Calculations by the Finite Element Method," *Eng. Fracture Mech.*, Vol. 21, No. 1, pp. 129–143.

Eshelby, J. D., 1956, "The Continuum Theory of Lattice Defects," *Solid State Physics*, Vol. 3, F. Seitz and D. Turnbull, eds., Academic Press, New York, pp. 79–141.

Eshelby, J. D., 1970, "The Energy Momentum Tensor in Continuum Mechanics," *Inelastic Behavior of Solids*, M. F. Kanninen et al., eds., McGraw-Hill, New York.

Knowles, J. K., and Sternberg, E., 1972, "On a Class of Conservation Laws in Linearized and Finite Elastostatics," *Archive for Rational Mechanics and Analysis*, Vol. 7, pp. 55–129.

Kuo, A., 1987, "On the Use of a Path-Independent Line Integral for Axisymmetric Cracks with Nonaxisymmetric Loading," ASME JOURNAL OF APPLIED MECHANICS, Vol. 54, pp. 833–837.

Potential Functions of an Edge Dislocation Associated With a Circular Inclusion

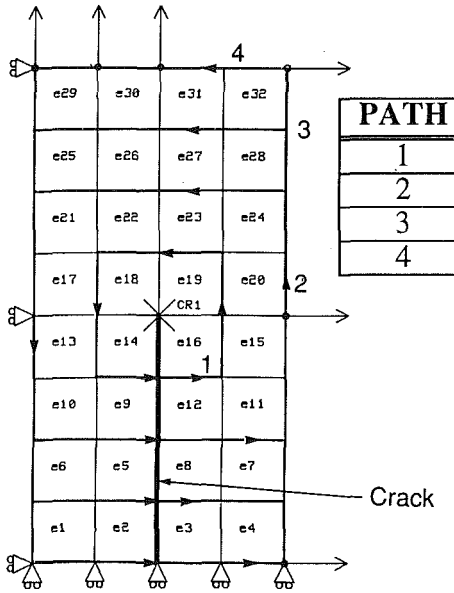
Ru-Min Chao[17]

There is an increasing interest in the interfacial debonding problem of a ceramic-fiber/ceramic-matrix composite system. England (1966), Perlman and Sih (1967), Toya (1974), and Piva (1982) discussed the interfacial crack problem of an infinite elastic solid and a dissimilar fiber. Their analyses have the common feature that there is overlapping of the crack faces near the tips, which is unrealistic. The reason for this is that during the course of the solution, the crack faces were assumed to open, but Dundurs and Comninou (1979) proved that, excluding certain material combinations, an interfacial crack between dissimilar elastic media will have an intervening contact zone ahead of the crack tips. In order to make these solutions still usable, we can adopt either the idea of small-scale contact, which was proposed by Rice (1988), or the idea of Suo and Hutchinson (1989), and redefine the complex stress intensity factor of the classical type (see Chao and Laws, 1990). However, an arc shape crack can have an extensive contact region under certain loading orientations (Chao and Laws, 1992). Therefore, Rice's, Suo's, and Hutchinson's ideas are not suitable for all the loading conditions and the closure problem of a fiber-matrix interfacial debonding crack must be reconsidered.

[17]Department of Naval Architecture and Marine Engineering, National Cheng Kung University, Tainan, Taiwan 70101, Republic of China. Assoc. Mem. ASME.

Contributed by the Applied Mechanics Division of THE AMERICAN SOCIETY OF MECHANICAL ENGINEERS for publication in the ASME JOURNAL OF APPLIED MECHANICS. Manuscript received by the ASME Applied Mechanics Division, Feb. 21, 1992; final revision, Feb. 3, 1993. Associate Technical Editor: X. Markenscoff.

Downloaded 03 May 2010 to 171.66.16.20. Redistribution subject to ASME license or copyright; see http://www.asme.org/terms/Terms_Use.cfm



PATH	J^*
1	0.66730
2	0.67228
3	0.66847
4	0.67917

Fig. 3 *J*-integral paths for cylindrical crack

$$J^* = \frac{J}{\sigma_0^2 a\left(\frac{1-\nu^2}{E}\right)}. \tag{19}$$

The stress intensity factors computed independently using the enriched elements, yielded values of $K_I^* = 0.8634$ and $K_{II}^* = -0.0960$ ($K^* = K/\sigma_0 a^{1/2}$). Computing a total energy release rate from these two stress intensity factors, using the relationship

$$J = \frac{(1-\nu^2)}{E}(K_I^2 + K_{II}^2) \tag{20}$$

gives a value of $J^* = 0.7547$. Comparing this with the average J^* value of 0.7716 from the four paths yields a two percent difference.

A second numerical example is shown in Fig. 3. The dimensions of the rod and the applied loading are identical to those in the previous example. In this case the crack has a length $a = 2$ units and is oriented at 90 deg to the x-axis. Thus the crack surface forms a cylinder about the z-axis. Since $\alpha = 90$ deg, according to Eq. (18) there should be no contribution from the area integration in the J-integral calculation. The four paths shown in Fig. 3 were used to compute the J^* values tabulated in Fig. 3. The J^* values are again path independent. The stress intensity factors computed using the "enriched" crack-tip elements were $K_I^* = 0.7512$ and $K_{II}^* = 0.2843$. Computing a total energy release rate from the stress intensity factors yields $J^* = 0.6451$. Comparison with the average J^* value from the four paths in Fig. 3, $J_{av}^* = 0.6718$, indicates that in this example the axisymmetric J-integral calculation differs by four percent from the energy release rates obtained from independently calculated values of K_I and K_{II}.

5 Conclusion

In this Note, an axisymmetric J-integral, a special case of the three-dimensional J-integral, was derived for cracks oriented at an angle to the axis of revolution. The axisymmetric J-integral was shown to have a simple form involving both a line integral and an area integral. It is interesting to note that when the crack surface takes the shape of a cylinder about the axis of revolution, the contribution to the J-integral from the area integration vanishes and the axisymmetric J-integral, except for a factor of r, becomes identical to the two-dimensional J-integral.

References

Amestoy, M., Bui, H. D., Labbens, R., 1981, "On the Definition of Local Path Independent Integrals in Three-Dimensional Crack Problems," *Mechanical Research Communications*, Vol. 8, No. 4, pp. 231–236.

Astiz, M. A., Elices, M., and Galvez, V. S., 1977, "On Energy Release Rates in Axisymmetrical Problems," *Fracture 1977*, Vol. 3, ICF4, Waterloo, Canada, June 19–24, pp. 395–399.

Benzley, S. E., 1974, "Representation of Singularities with Isoparametric Finite Elements," *Int. Journal for Numerical Methods in Engineering*, Vol. 8, pp. 537–545.

Bergkvist, H., and Lan Huong, G., 1977, "J-Integral Related Quantities in Axisymmetric Cases," *Int. Journ. of Fracture*, Vol. 13, pp. 556–558.

Bergkvist, H., and Lan Huong, G., 1977, "Energy Release Rates in Cases of Axial Symmetry," *Proceedings of Fracture Mechanics and Technology*, Hong Kong, Mar. 21–25, Sijthoff and Noordhoff, pp. 1053–1066.

Budiansky, B., and Rice, J. R., 1973, "Conservation Laws and Energy-Release Rates," ASME JOURNAL OF APPLIED MECHANICS, Vol. 40, pp. 201–203.

deLorenzi, H. G., 1985, "Energy Release Rate Calculations by the Finite Element Method," *Eng. Fracture Mech.*, Vol. 21, No. 1, pp. 129–143.

Eshelby, J. D., 1956, "The Continuum Theory of Lattice Defects," *Solid State Physics*, Vol. 3, F. Seitz and D. Turnbull, eds., Academic Press, New York, pp. 79–141.

Eshelby, J. D., 1970, "The Energy Momentum Tensor in Continuum Mechanics," *Inelastic Behavior of Solids*, M. F. Kanninen et al., eds., McGraw-Hill, New York.

Knowles, J. K., and Sternberg, E., 1972, "On a Class of Conservation Laws in Linearized and Finite Elastostatics," *Archive for Rational Mechanics and Analysis*, Vol. 7, pp. 55–129.

Kuo, A., 1987, "On the Use of a Path-Independent Line Integral for Axisymmetric Cracks with Nonaxisymmetric Loading," ASME JOURNAL OF APPLIED MECHANICS, Vol. 54, pp. 833–837.

Potential Functions of an Edge Dislocation Associated With a Circular Inclusion

Ru-Min Chao[17]

There is an increasing interest in the interfacial debonding problem of a ceramic-fiber/ceramic-matrix composite system. England (1966), Perlman and Sih (1967), Toya (1974), and Piva (1982) discussed the interfacial crack problem of an infinite elastic solid and a dissimilar fiber. Their analyses have the common feature that there is overlapping of the crack faces near the tips, which is unrealistic. The reason for this is that during the course of the solution, the crack faces were assumed to open, but Dundurs and Comninou (1979) proved that, excluding certain material combinations, an interfacial crack between dissimilar elastic media will have an intervening contact zone ahead of the crack tips. In order to make these solutions still usable, we can adopt either the idea of small-scale contact, which was proposed by Rice (1988), or the idea of Suo and Hutchinson (1989), and redefine the complex stress intensity factor of the classical type (see Chao and Laws, 1990). However, an arc shape crack can have an extensive contact region under certain loading orientations (Chao and Laws, 1992). Therefore, Rice's, Suo's, and Hutchinson's ideas are not suitable for all the loading conditions and the closure problem of a fiber-matrix interfacial debonding crack must be reconsidered.

[17]Department of Naval Architecture and Marine Engineering, National Cheng Kung University, Tainan, Taiwan 70101, Republic of China. Assoc. Mem. ASME.

Contributed by the Applied Mechanics Division of THE AMERICAN SOCIETY OF MECHANICAL ENGINEERS for publication in the ASME JOURNAL OF APPLIED MECHANICS. Manuscript received by the ASME Applied Mechanics Division, Feb. 21, 1992; final revision, Feb. 3, 1993. Associate Technical Editor: X. Markenscoff.

Copyright © 1994 by ASME

Downloaded 03 May 2010 to 171.66.16.20. Redistribution subject to ASME license or copyright; see http://www.asme.org/terms/Terms_Use.cfm

A similar problem occurred in a slit interfacial crack. Comninou (1977) and others considered the interfacial crack as a continuous distribution of edge dislocations along the interface. Her method requires the knowledge of the stress field of a single edge dislocation located at the interface. To apply Comninou's method to the fiber-matrix interfacial crack problem, one also needs to know the stress fields of an edge dislocation located at the interface. Dundurs and Mura (1964), and Dunurs and Sendeckyj (1965) gave the Airy stress functions of an edge dislocation associated with a circular inclusion. In terms of Muskhelishvili (1953) complex potentials, one can refer to List (1966), Stagni (1982), Warren (1983), and Gharpuray et al. (1990). When the edge dislocation with Burgers vector $b_x + ib_y$ goes into the fiber-matrix interface, i.e., $z_o = r_o e^{i\theta_o}$ and $r_o = a$ where a is the radius of the fiber, cf. Fig. 1, the stresses in the fiber are

$$\sigma_{rr}=\frac{1-\alpha}{1-\beta}\left\{\frac{2}{r_1}(b_2\cos\theta_1-b_1\sin\theta_1)+\frac{r}{r_1^2}(b_2\cos(2\theta_1-\theta)-b_1\sin(2\theta_1-\theta))\right.$$
$$-\frac{r_o}{r_1^2}(b_2\cos(2\theta_1-2\theta+\theta_o)-b_1\sin(2\theta_1-2\theta+\theta_o))$$
$$\left.+\frac{\alpha-\beta}{1+\alpha-2\beta}\frac{2}{r_o}(b_2\cos\theta_o-b_1\sin\theta_o)\right\}$$
$$-\frac{1}{r_1}\frac{1-\alpha}{1+\beta}(b_2\cos(2\theta-\theta_1)-b_1\sin(2\theta-\theta_1)), \quad (1)$$

$$\sigma_{r\theta}=\frac{1-\alpha}{1-\beta}\left\{\frac{r}{r_1^2}(b_1\cos(2\theta_1-\theta)+b_2\sin(2\theta_1-\theta))\right.$$
$$\left.-\frac{r_o}{r_1^2}(b_1\cos(2\theta_1-2\theta+\theta_o)+b_2\sin(2\theta_1-2\theta+\theta_o))\right\}$$
$$+\frac{1}{r_1}\frac{1-\alpha}{1+\beta}(b_1\cos(2\theta-\theta_1)+b_2\sin(2\theta-\theta_1)), \quad (2)$$

$$\sigma_{\theta\theta}=\frac{1-\alpha}{1-\beta}\left\{\frac{2}{r_1}(b_2\cos\theta_1-b_1\sin\theta_1)\right.$$
$$+\frac{r}{r_1^2}(b_2\cos(2\theta_1-\theta)-b_1\sin(2\theta_1-\theta))$$
$$+\frac{r_o}{r_1^2}(b_2\cos(2\theta_1-2\theta+\theta_o)-b_1\sin(2\theta_1-2\theta+\theta_o))$$
$$\left.+\frac{\alpha-\beta}{1+\alpha-2\beta}\frac{2}{r_o}(b_2\cos\theta_o-b_1\sin\theta_o)\right\}$$
$$+\frac{1}{r_1}\frac{1-\alpha}{1+\beta}(b_2\cos(2\theta-\theta_1)-b_1\sin(2\theta-\theta_1)), \quad (3)$$

and the displacements of the fiber are

$$2\mu_F u_r^{(F)}=\left(\kappa_F\frac{1-\alpha}{1-\beta}-\frac{1-\alpha}{1+\beta}\right)(b_2\cos\theta-b_1\sin\theta)\ln r_1$$
$$+\left(\kappa_F\frac{1-\alpha}{1-\beta}+\frac{1-\alpha}{1+\beta}\right)(b_1\cos\theta+b_2\sin\theta)\theta_1$$
$$+\frac{1-\alpha}{1-\beta}\left\{\frac{\alpha-\beta}{1+\alpha-2\beta}(\kappa_F-1)\frac{r}{r_o}(b_2\cos\theta_o-b_1\sin\theta_o)\right.$$
$$+\left(\frac{r_o}{r_1}(b_2\cos(\theta_o+\theta_1-\theta)-b_1\sin(\theta_o+\theta_1-\theta))\right)$$
$$\left.-\frac{r}{r_1}(b_2\cos\theta_1-b_1\sin\theta_1)\right\}, \quad (4)$$

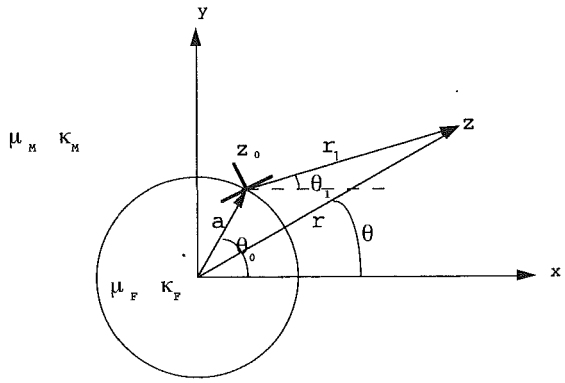


Fig. 1 Edge dislocation in the fiber-matrix interface

$$2\mu_F u_\theta^{(F)}=\left(\kappa_F\frac{1-\alpha}{1-\beta}+\frac{1-\alpha}{1+\beta}\right)(b_2\cos\theta-b_1\sin\theta)\theta_1$$
$$-\left(\kappa_F\frac{1-\alpha}{1-\beta}-\frac{1-\alpha}{1+\beta}\right)(b_1\cos\theta+b_2\sin\theta)\ln r_1$$
$$+\frac{\alpha-\beta}{1-\beta}(\kappa_F+1)\frac{r}{r_o}(b_2\cos\theta_o-b_1\sin\theta_o)$$
$$+\frac{1-\alpha}{1-\beta}\left\{\frac{r_o}{r_1}(b_2\sin(\theta_o+\theta_1-\theta)+b_1\cos(\theta_o+\theta_1-\theta))\right.$$
$$\left.-\frac{r}{r_1}(b_2\cos\theta_1-b_1\sin\theta_1)\right\} \quad (5)$$

where $z = re^{i\theta}$, $z - z_o = r_1 e^{i\theta_1}$, $b_1 + ib_2 = (\mu_M(b_x+ib_y)/\pi(\kappa_M+1))$ and α and β are the Dundurs parameters which are defined as

$$\alpha=\frac{\mu_F(\kappa_M+1)-\mu_M(\kappa_F+1)}{\mu_F(\kappa_M+1)+\mu_M(\kappa_F+1)};\quad \beta=\frac{\mu_F(\kappa_M-1)-\mu_M(\kappa_F-1)}{\mu_F(\kappa_M+1)+\mu_M(\kappa_F+1)}.$$

When $z_o = x_o$, i.e., the dislocation is located at the real axis, these formulas reduce to the special case of Warren (1983). Notice that μ_i and ν_i represent the shear modulus and Poisson's ratio of the fiber or matrix; and $\kappa_i = 3-4\,\nu_i$ for plane strain $\kappa_i = (3-\nu_i/1+\nu_i)$ for plane stress. One then can use the above expressions to formulate the fiber-matrix interfacial crack problem. Finally, we remark that the problem of a fiber-matrix interfacial crack with the crack surfaces partially in contact had been solved by using the Mushkhelishvili complex potentials with the help of a complex, variable and it will be reported at a later date.

Acknowledgments

The author would like to thank the reviewers for many useful comments.

References

Chao, R., and Laws, N., 1992, "Closure of An Arc Crack in an Isotropic Homogeneous Material due to Uni-axial Loading," *Quarterly Journal of Mech. and Applied Math.*, Vol. 45, Pt. 4, pp. 629–640.

Chao, R., and Laws, N., 1990, "Loss of Stiffness due to Microcracking in Uni-directional Ceramic Matrix Composites," *Damage Mechanics in Engineering Materials*, Ju, Krajcinovic, and Schreyer, eds., ASME, pp. 55–62.

Comninou, M., 1977, "The Interface Crack," ASME JOURNAL OF APPLIED MECHANICS, Vol. 44, pp. 631–636.

Dundurs, J., and Mura, T., 1964, "Interaction Between an Edge Dislocation and a Circular Inclusion," *J. Mech. Phys. Solids*, Vol. 12, pp. 177–189.

Dundurs, J., and Sendeckyj, G. P., 1965, "Edge Dislocation Inside a Circular Inclusion," *J. Mech. Phys. Solids*, Vol. 13, pp. 141–147.

England, A. H., 1966, "An Arc Crack Around a Circular Elastic Inclusion," ASME JOURNAL OF APPLIED MECHANICS, Vol. 33, pp. 637–640.

Gharpuray, V. M., Keer, L. M., and Lewis, J. L., 1990, "Crack Emanating From Circular Voids or Elastic Inclusions in PMMA near a Bone-Implant Interface," *Journal of Biomech. Eng.*, Vol. 112, pp. 22–28.

Downloaded 03 May 2010 to 171.66.16.20. Redistribution subject to ASME license or copyright; see http://www.asme.org/terms/Terms_Use.cfm

Muskhelishvili, N. I., 1953, *Some Basic Problems in the Mathematical Theory of Elasticity*, Noordhoff, Groningen, Holland.
Perlman, A. B., and Sih, G. C., 1967, "Elastostatic Problems of Curvilinear Cracks in Bonded Dissimilar Materials," *Int. J. Engrg. Sci.*, Vol. 5, pp. 856-867.
Piva, A., 1882, "A Crack Along a Circular Interface Between Dissimilar Media," *Meccanica*, Vol. 17, pp. 85-90.
Rice, J. R., 1988, "Elastic Fracture Mechanics Concepts for Interfacial Cracks," ASME JOURNAL OF APPLIED MECHANICS, Vol. 55, pp. 98-103.
Suo, Z., and Hutchinson, J. W., 1989, "Sandwich Test Specimens for Measuring Interface Crack Toughness," *Material Science and Engineering*, Vol. A107, pp. 135-143.
Toya, M., 1974, "A Crack Along the Interface of a Circular Inclusion Embedded in an Infinite Solid," *J. Mech. Phys. Solid*, Vol. 22, pp. 325-348.
Warren, W. E., 1983, "The Edge Dislocation Inside an Elliptical Inclusion," *Mechanics of Materials*, Vol. 2, pp. 319-330.

Green Functions for Cylindrical Elastic Waves in Aluminum: Comparison Between Theory and Experiments

A. Mourad[18], B. Castagnède[19], and E. Mottay[20]

A comparison between experimental and theoretical displacement fields for the tangential force problem (which is a model of the thermoelastic regime for laser generated ultrasound) at an aluminum interface is reported. The numerical predictions are based on a standard formulation of the transient generation of elastic waves along a line source. In the configuration of a purely elastic thin plate, the cylindrical elastic waves are then detected on the other side by a point-like receiver. The experimental works is carried out with a pulsed Nd:YAG laser for the generation and a laser interferometric probe for the detection of ultrasonic waves.

Introduction

The solution of Lamb's normal force problem for the generation of transient elastic waves in an isotropic half-space received wide attention in the past, e.g., Johnson (1974) and references therein, Gakenheimer (1971), and Miklowitz (1978). The problem of a moving source was also investigated by Gakenheimer and Miklowitz (1969), and Gakenheimer (1970) produced some numerical predictions of the displacement fields (Green functions) in an isotropiuc half-space. At the same time, many attempts were done to extend solutions of the Lamb's problem to an anisotropic half-space by using the Cagniard/De Hoop method. For instance, Kraut (1963) first provided the Cagniard contours in the complex plane for a transversely isotropic solid. This work was treated further in a book by van der Hijden (1987). In the last decade, De Hoop and van der Hijden considered various configurations dealing with a fluid/isotropic solid plane interface, for the case of an impulsive point source (1984, 1985) as well as for a line source (1983). The last problem is very appealing due to the simplification of the calculations and is readily simulated experimentally by using a laser source with cylindrical optics. In a seminal paper, Rose (1984) discussed in great detail the theoretical Green functions for such thermoelastic laser source and various authors (see, e.g., Dewhurst et al., 1982 or Telshow and Conant (1990) did achieve experimental work (primarily in the case of point sources) for the comparison between theoretical Green functions and experimental displacement fields. The present contribution is such an example when dealing with focusing cylindrical optics including results for the off-epicenter configuration.

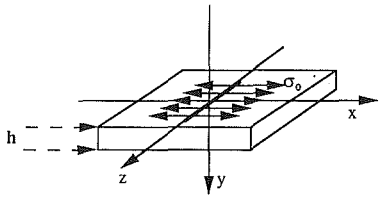


Fig. 1 Geometry of the problem

Theoretical Background

Let us consider a plane problem, where the dynamic displacement field has no component along direction Y, and does not depend on this coordinate (Fig. 1). The wave equation for the longitudinal wave (having velocity C_L), and the transverse wave (with velocity C_T) can be written as a function of the potentials φ and ψ:

$$\Delta\varphi(x, z, t) = \frac{1}{C_L^2}\ddot{\varphi}; \quad \Delta\psi(x, z, t) = \frac{1}{C_T^2}\ddot{\psi},$$

$$\text{with } -\infty < x < +\infty,\ z > 0,\ t > 0,$$

where Δ denotes the Laplacian, and with the following initial conditions

$$\varphi(x, z, 0) = \dot{\varphi}(x, z, 0) = \psi(x, z, 0) = \dot{\psi}(x, z, 0) = 0.$$

The boundary conditions for a thermoelastic source are given by

$\sigma_Z(x, o, t) = 0$; $\sigma_{ZX} = \sigma_0\, d\delta(x)/dr\, H(t)$ for $-\infty < x < +\infty$; $\sigma_Z(x, h, t) = 0$; $\sigma_{ZX}(x, h, t) = 0$, where σ_Z and σ_{ZX} are the normal and tangential stresses, $\delta(x)$ is the Dirac function, and $H(t)$ is the Heaviside function.

The displacement field is computed on the surface, i.e., $z = h$, by using the Cagniard/de Hoop inversion method, by solely taking into account the direct longitudinal mode and its first multiple reflection (labeled, respectively, L and $3L$ on Fig. 2), the direct transverse wave (T) and the head wave (HW). Thus the computed waveforms are rigorously exact unless there is a crossing between the first subsequent multiple reflection mode ($2LT$) and the T mode (poing I on Fig. 2, showing that $\theta_{\min} \approx \tan^{-1}[2.2] = 65$ deg). In such a case, the waveform remains valid up to the arrival of the T mode.

Experimental Results

The pulsed Nd:YAG laser used in this work provided 10 ns duration pulses at wavelength 532 nm. It was operated at approximately 60 mJ per pulse output energy. The line source (obtained using a Newport Corp. cylindrical lens) extended over a 25-30 mm length. With such a source (which is significantly longer than the sample thickness, here 12.5 mm), one

[18]Graduate Student, Laboratoire de Mecanique Physique, URA CNRS 867, Université de Bordeaux I, 33405 Talence, France.
[19]Professor, Laboratoire d'Acoustique, URA CNRS 1101, Université du Maine, 72017 Le Mans, France.
[20]Research Engineer, B. M. Industries, 7, rue du bois Chaland Lisses, 91029 Evry, France.
Contributed by the Applied Mechanics Division of THE AMERICAN SOCIETY OF MECHANICAL ENGINEERS for publication in the ASME JOURNAL OF APPLIED MECHANICS. Manuscript received by the ASME Applied Mechanics Division, Apr. 21, 1992; final revision, Sept. 14, 1992. Associate Technical Editor: W. N. Sharpe, Jr.

Downloaded 03 May 2010 to 171.66.16.20. Redistribution subject to ASME license or copyright; see http://www.asme.org/terms/Terms_Use.cfm

Muskhelishvili, N. I., 1953, *Some Basic Problems in the Mathematical Theory of Elasticity*, Noordhoff, Groningen, Holland.
Perlman, A. B., and Sih, G. C., 1967, "Elastostatic Problems of Curvilinear Cracks in Bonded Dissimilar Materials," *Int. J. Engrg. Sci.*, Vol. 5, pp. 856-867.
Piva, A., 1882, "A Crack Along a Circular Interface Between Dissimilar Media," *Meccanica*, Vol. 17, pp. 85-90.
Rice, J. R., 1988, "Elastic Fracture Mechanics Concepts for Interfacial Cracks," ASME JOURNAL OF APPLIED MECHANICS, Vol. 55, pp. 98-103.
Suo, Z., and Hutchinson, J. W., 1989, "Sandwich Test Specimens for Measuring Interface Crack Toughness," *Material Science and Engineering*, Vol. A107, pp. 135-143.
Toya, M., 1974, "A Crack Along the Interface of a Circular Inclusion Embedded in an Infinite Solid," *J. Mech. Phys. Solid*, Vol. 22, pp. 325-348.
Warren, W. E., 1983, "The Edge Dislocation Inside an Elliptical Inclusion," *Mechanics of Materials*, Vol. 2, pp. 319-330.

Green Functions for Cylindrical Elastic Waves in Aluminum: Comparison Between Theory and Experiments

A. Mourad[18], B. Castagnède[19], and E. Mottay[20]

A comparison between experimental and theoretical displacement fields for the tangential force problem (which is a model of the thermoelastic regime for laser generated ultrasound) at an aluminum interface is reported. The numerical predictions are based on a standard formulation of the transient generation of elastic waves along a line source. In the configuration of a purely elastic thin plate, the cylindrical elastic waves are then detected on the other side by a point-like receiver. The experimental works is carried out with a pulsed Nd:YAG laser for the generation and a laser interferometric probe for the detection of ultrasonic waves.

Introduction

The solution of Lamb's normal force problem for the generation of transient elastic waves in an isotropic half-space received wide attention in the past, e.g., Johnson (1974) and references therein, Gakenheimer (1971), and Miklowitz (1978). The problem of a moving source was also investigated by Gakenheimer and Miklowitz (1969), and Gakenheimer (1970) produced some numerical predictions of the displacement fields (Green functions) in an isotropiuc half-space. At the same time, many attempts were done to extend solutions of the Lamb's problem to an anisotropic half-space by using the Cagniard/De Hoop method. For instance, Kraut (1963) first provided the Cagniard contours in the complex plane for a transversely isotropic solid. This work was treated further in a book by van der Hijden (1987). In the last decade, De Hoop and van der Hijden considered various configurations dealing with a fluid/isotropic solid plane interface, for the case of an impulsive point source (1984, 1985) as well as for a line source (1983). The last problem is very appealing due to the simplification of the calculations and is readily simulated experimentally by using a laser source with cylindrical optics. In a seminal paper, Rose (1984) discussed in great detail the theoretical Green functions for such thermoelastic laser source and various authors (see, e.g., Dewhurst et al., 1982 or Telshow and Conant (1990) did achieve experimental work (primarily in the case of point sources) for the comparison between theoretical Green functions and experimental displacement fields. The present contribution is such an example when dealing with focusing cylindrical optics including results for the off-epicenter configuration.

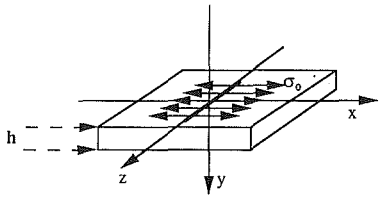


Fig. 1 Geometry of the problem

Theoretical Background

Let us consider a plane problem, where the dynamic displacement field has no component along direction Y, and does not depend on this coordinate (Fig. 1). The wave equation for the longitudinal wave (having velocity C_L), and the transverse wave (with velocity C_T) can be written as a function of the potentials φ and ψ:

$$\Delta\varphi(x, z, t) = \frac{1}{C_L^2}\ddot{\varphi}; \quad \Delta\psi(x, z, t) = \frac{1}{C_T^2}\ddot{\psi},$$

$$\text{with } -\infty < x < +\infty,\ z > 0,\ t > 0,$$

where Δ denotes the Laplacian, and with the following initial conditions

$$\varphi(x, z, 0) = \dot{\varphi}(x, z, 0) = \psi(x, z, 0) = \dot{\psi}(x, z, 0) = 0.$$

The boundary conditions for a thermoelastic source are given by

$\sigma_Z(x, o, t) = 0$; $\sigma_{ZX} = \sigma_0\, d\delta(x)/dr\, H(t)$ for $-\infty < x < +\infty$; $\sigma_Z(x, h, t) = 0$; $\sigma_{ZX}(x, h, t) = 0$, where σ_Z and σ_{ZX} are the normal and tangential stresses, $\delta(x)$ is the Dirac function, and $H(t)$ is the Heaviside function.

The displacement field is computed on the surface, i.e., $z = h$, by using the Cagniard/de Hoop inversion method, by solely taking into account the direct longitudinal mode and its first multiple reflection (labeled, respectively, L and $3L$ on Fig. 2), the direct transverse wave (T) and the head wave (HW). Thus the computed waveforms are rigorously exact unless there is a crossing between the first subsequent multiple reflection mode ($2LT$) and the T mode (poing I on Fig. 2, showing that $\theta_{\min} \approx \tan^{-1}[2.2] = 65$ deg). In such a case, the waveform remains valid up to the arrival of the T mode.

Experimental Results

The pulsed Nd:YAG laser used in this work provided 10 ns duration pulses at wavelength 532 nm. It was operated at approximately 60 mJ per pulse output energy. The line source (obtained using a Newport Corp. cylindrical lens) extended over a 25-30 mm length. With such a source (which is significantly longer than the sample thickness, here 12.5 mm), one

[18]Graduate Student, Laboratoire de Mecanique Physique, URA CNRS 867, Université de Bordeaux I, 33405 Talence, France.
[19]Professor, Laboratoire d'Acoustique, URA CNRS 1101, Université du Maine, 72017 Le Mans, France.
[20]Research Engineer, B. M. Industries, 7, rue du bois Chaland Lisses, 91029 Evry, France.
Contributed by the Applied Mechanics Division of THE AMERICAN SOCIETY OF MECHANICAL ENGINEERS for publication in the ASME JOURNAL OF APPLIED MECHANICS. Manuscript received by the ASME Applied Mechanics Division, Apr. 21, 1992; final revision, Sept. 14, 1992. Associate Technical Editor: W. N. Sharpe, Jr.

Copyright © 1994 by ASME
Downloaded 03 May 2010 to 171.66.16.20. Redistribution subject to ASME license or copyright; see http://www.asme.org/terms/Terms_Use.cfm

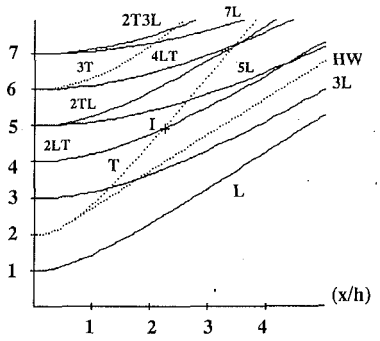


Fig. 2 Wavefronts arrivals in an aluminum plate of thickness h when the source is scanned along axis x. The vertical axis is the time normalized to the arrival of the direct longitudinal mode.

generates mainly elastic waves having symmetry of revolution along the source line axis (i.e., cylindrical waves). In this configuration the source is in the thermoelastic regime, and no damage is experienced by the solid. The detection of the elastic waves impinging on the other surface is done by using a Mac-Zehnder laser interferometer, specially designed for the purpose of characterizing solid materials, built by the French manufacturer B. M.industries. It has a 200 KHz-4MHz bandwidth and a sensitivity of 100 mV/nm. Such an interferometric probe enables very precise measurement of the normal displacements with respect to the sample surface.

Figures 3 and 4 present some characteristic results obtained in a 12.5-mm thick aluminum plate, at the epicenter location (i.e., the observation angle $\theta = 0$), and at an off-epicenter location where $\theta = 50$ deg. The first sharp peak represents the triggering of the digitizing oscilloscope and consequently shows the absolute timing origin of the experiment. The recording of the experimental waveforms was obtained after 100 averages. The level of noise is visible before the triggering of the scope and does not exceed 0.02 nm. The arrival of the various bulk modes is unmistakable on these waveforms. The agreement between these experimental waveforms and the theoretical normal displacement fields is good. The various features of interest are thus observed with the right temporal delays and with the correct amplitude displacement shape. However, the $3L$ mode which can theoretically be shown to be absent for the epicenter configuration is not generally clearly identified for other observation angles, with exception, for instance here, at 50 deg.

It should be emphasized that the experimental results are not trivial to achieve, because there is less signal when dealing with cylindrical waves compared to the case of spherical waves. This is related to the fact that with convergent standard optics, the source can be focussed down to a small spot, although with cylindrical optics the same energy is distributed along the source line. Also, as the beam is collimated in the second case, one uses a combination of a divergent lens followed by a convergent collimating lens illuminating the cylindrical lens, resulting in optical losses at the various glass/air interfaces. Thus the available energy is decreased by a non-negligible factor. The authors made an estimate of a 20 dB difference in terms of the detected signal amplitude in the generation of cylindrical waves relative to the generation of spherical waves.

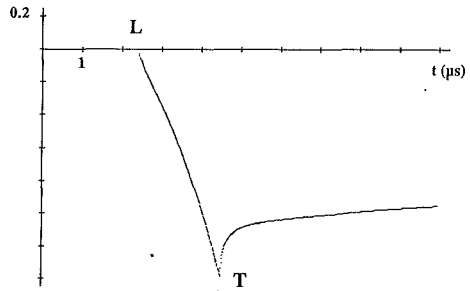


Fig. 3(*a*)

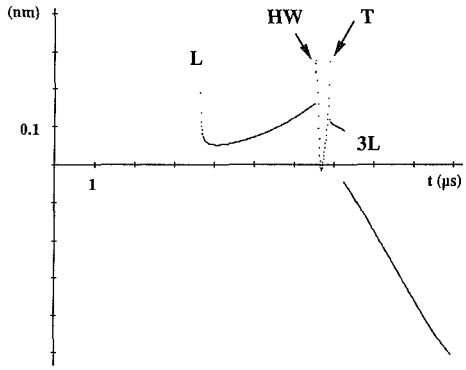


Fig. 3(*b*)

Fig. 3 Theoretical waveforms in a 12.5-mm thick aluminum plate for two observation angles θ. (*a*) $\theta = 0$ deg (Epicenter); (*b*) $\theta = 50$ deg. The displacement scale is obtained by normalization to the experimental results.

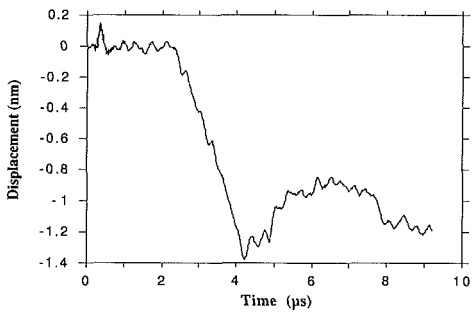


Fig. 4(*a*)

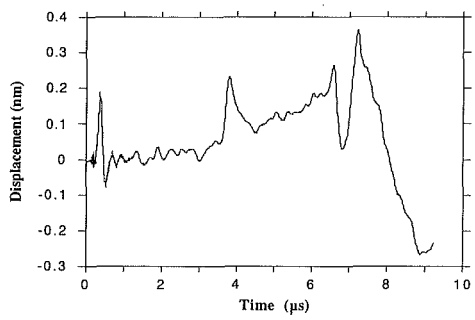


Fig. 4(*b*)

Fig. 4 Experimental waveforms in a 12.5-mm thick aluminum plate for two observation angles θ. (*a*) $\theta = 0$ deg (Epicenter); (*b*) $\theta = 50$ deg.

References

De Hoop, A. T., and van der Hijden, J. H. M. T., 1983, "Generation of Acoustic Waves by an Impulsive Line Source in a Fluid/Solid Configuration with a Plane Boundary," *J. Acoust. Soc. Am.*, Vol. 74, pp. 333–342.

De Hoop, A. T., and van der Hijden, J. H. M. T., 1984, "Generation of Acoustic Waves by an Impulsive Point Source in a Fluid/Solid Configuration with a Plane Boundary," *J. Acous. Soc. Am.*, Vol. 75, pp. 1709–1715.

De Hoop, A. T., and van der Hijden, J. H. M. T., 1985, "Seismic Waves Generated by an Impulsive Point Source in a Fluid/Solid Configuration with a Plane Boundary," *Geophysics*, Vol. 50, pp. 1083–1090.

Dewhurst, R. J., Hutchins, D. A., and Palmer, S. B., 1982, "Quantitative Measurements of Laser-Generated Acoustic Waveforms," *J. Appl. Phys.*, Vol. 53, pp. 4064–4071.

Downloaded 03 May 2010 to 171.66.16.20. Redistribution subject to ASME license or copyright; see http://www.asme.org/terms/Terms_Use.cfm

Gakenheimer, D. C., 1971, "Response of an Elastic Half-Space to Expanding Surface Loads," ASME JOURNAL OF APPLIED MECHANICS, Vol. 38, pp. 99–110.
Gakenheimer, D. C., 1970, "Numerical Results for Lamb's Point Load Problem," ASME JOURNAL OF APPLIED MECHANICS, Vol. 37, pp. 522–524.
Gakenheimer, D. C., and Miklowitz, J., 1969, "Transient Excitation of an Elastic Half-Space by a Point Load Traveling on the Surface," ASME JOURNAL OF APPLIED MECHANICS, Vol. 36, pp. 505–515.
Johnson, L. R. 1974, "Green's Function for Lamb's Problem," *Geophys. J. R. astr. Soc.*, Vol. 37, pp. 99–131.
Kraut, E. A., 1963, "Advances in the Theory of Anisotropic Elastic Waves Propagation," *Reviews of Geophysics*, Vol. 1, pp. 401–448.
Miklowitz, J., 1978, *The Theory of Elastic Waves and Waveguides*, North-Holland, Amsterdam, pp. 231–366.
Rose, L. R. F., 1984, "Point-Source Representation for Laser-Generated Ultrasound," *J. Acous. Soc. Am.*, Vol. 88, pp. 1494–1502.
Telshow, K. L., and Conant, R. J., 1990, "Optical and Thermal Parameter Effects on Laser-Generated Ultrasound," *J. Acoust. Soc. Am.*, Vol. 75, pp. 723–732.
van der Hijden, J. H. M. T., 1987, *Propagation of Transient Elastic Waves in Stratified Anisotropic Media*, (Applied Mathematics and Mechanics, Vol. 32), North-Holland, Amsterdam.

Criteria of Dynamic Crack Initiation

Masaaki Watanabe[21]

A criteria of dynamic crack initiation is proposed as $K_{Ic}^{dyn} = K_{Ic} \frac{\sigma_c^{dyn.}}{\sigma_c} \left(\frac{t_{q.s.}}{t}\right)^{\alpha_S/2}$ *for* $t \le t_{q.s.}$, *where* $K_{Ic}^{dyn.}$ *is the dynamic critical stress intensity factor for initiation and* K_{Ic}, the static fracture toughness. σ_c *and* $\sigma_c^{dyn.}$ *are critical stresses for a growth of microcracks generated at the tip of a crack, in quasi-static and dynamic loading conditions, respectively.* $t_{q.s.}$ *is the characteristic time of quasi-static growth of a crack and* t *is a loading time.* α_s *is a positive number. This criteria is compared with various different experiments and found to be in qualitative agreement with them.*

Ravi-Chandar and Knauss (1984) performed the elaborate experiment of dynamic fracture. The specimen material used in their experiment is Homalite-100 of such size that reflected waves do not interact with the crack tip for duration of the experiment. Thus a literally unbounded (plate) medium is simulated. Stress wave loading on the crack surfaces is achieved by using an electromagnetic loading device and the crack-tip stress field is monitored by the method of caustics. Among numerous interesting results of their experiment (1984, 1985), we only consider an effect of the rate of loading on crack initiation. They found that a loading rate effect on the initiation stress intensity factor is negligible when time to rupture is on the order of 50 μs. With higher loading rates, the stress intensity factor at initiation increases markedly as shown in Fig. 1. Ravi-Chandar and Knauss found that the dynamic critical stress intensity factor at initiation, $K_{Ic}^{dyn.}$, shows the following loading time dependence $K_{Ic}^{dyn.} - K_{Ic} = b_1 t^{-2}$, where b_1 is a proportionality constant. They explained this time dependence in terms of viscous response of the materials. Birch and Williams (1978) performed a conventional energy measuring impact test using two tough polymers, MDPE and PTFE. They measured a rate effect of "fracture toughness," $G_{Ic}^{dyn.}$, and found $G_{Ic}^{dyn.} = b_2 t^{-0.42}$, where t is a loading time defined as $t = \Delta/V$; V is an impact striker speed and Δ, the displacement. b_2 is a proportionality constant. This time dependence is discussed in terms of loss process in the craze region at the crack tip. Williams and Hodgkinson (1981) performed impact tests for three polymers HDPE, PTFE, and PMMA by changing a strain rate (20-620 s^{-1}) and temperatures. They obtained a similar rate effect of the "fracture toughness," as shown in Fig. 2,

$$G_{Ic}^{dyn.} = b_3 t^{-0.5} \quad (1)$$

to the previous work of Birch and Williams, where b_3 is a constant. They explained this effect in terms of notch tip blunting induced by adiabatic heating at the crack tip.

These experiments discussed can be explained by the criteria of dynamic crack initiation, which is proposed in this paper.

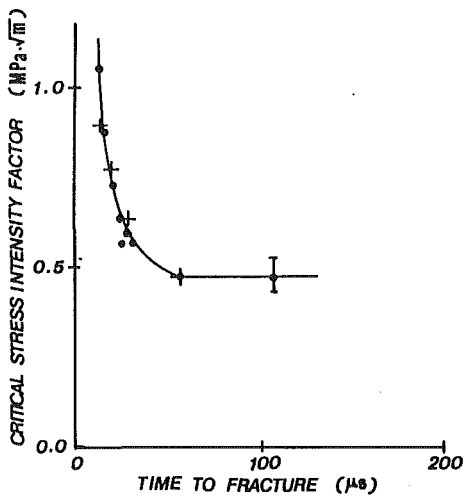


Fig. 1 Variation of the stress intensity factor for initiation. The marked point + is obtained by the criteria $K_{Ic}^{dyn} = K_{Ic}(t_{q.s.}/t)^{\alpha_s/2}$ for $t \le t_{q.s.}$ where K_{Ic} = 0.47 MPa$\sqrt{m}$, $t_{q.s.}$ = 57 μs and α_s = 0.9 are used. The criteria for this case, $\sigma_c^{dyn.} = \sigma_{cr}$ is derived by Watanabe (1991). This figure is taken from Ravi-Chandar and Knauss (1984).

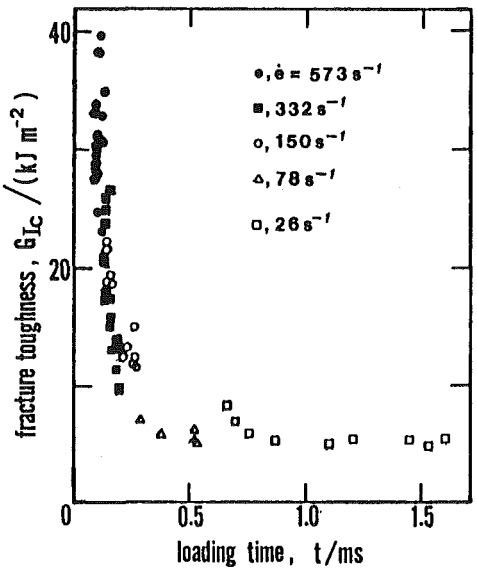


Fig. 2 The "fracture toughness" $G_{Ic}^{dyn.}$ as a function of loading time t for HDPE at 0°C. This figure is taken from Williams and Hodgkinson (1981).

[21]Faculty of Engineering, Kinki University, Takaya, Higashi-Hiroshima, Hiroshima 729-17, Japan.

Contributed by the Applied Mechanics Division of THE AMERICAN SOCIETY OF MECHANICAL ENGINEERS for publication in the ASME JOURNAL OF APPLIED MECHANICS. Manuscript received by the ASME Applied Mechanics Division, Oct. 17, 1991; final revision, Dec. 5, 1992. Associate Technical Editor: M. E. Fourney.

Downloaded 03 May 2010 to 171.66.16.20. Redistribution subject to ASME license or copyright; see http://www.asme.org/terms/Terms_Use.cfm

Gakenheimer, D. C., 1971, "Response of an Elastic Half-Space to Expanding Surface Loads," ASME JOURNAL OF APPLIED MECHANICS, Vol. 38, pp. 99–110.
Gakenheimer, D. C., 1970, "Numerical Results for Lamb's Point Load Problem," ASME JOURNAL OF APPLIED MECHANICS, Vol. 37, pp. 522–524.
Gakenheimer, D. C., and Miklowitz, J., 1969, "Transient Excitation of an Elastic Half-Space by a Point Load Traveling on the Surface," ASME JOURNAL OF APPLIED MECHANICS, Vol. 36, pp. 505–515.
Johnson, L. R. 1974, "Green's Function for Lamb's Problem," *Geophys. J. R. astr. Soc.*, Vol. 37, pp. 99–131.
Kraut, E. A., 1963, "Advances in the Theory of Anisotropic Elastic Waves Propagation," *Reviews of Geophysics*, Vol. 1, pp. 401–448.
Miklowitz, J., 1978, *The Theory of Elastic Waves and Waveguides*, North-Holland, Amsterdam, pp. 231–366.
Rose, L. R. F., 1984, "Point-Source Representation for Laser-Generated Ultrasound," *J. Acous. Soc. Am.*, Vol. 88, pp. 1494–1502.
Telshow, K. L., and Conant, R. J., 1990, "Optical and Thermal Parameter Effects on Laser-Generated Ultrasound," *J. Acoust. Soc. Am.*, Vol. 75, pp. 723–732.
van der Hijden, J. H. M. T., 1987, *Propagation of Transient Elastic Waves in Stratified Anisotropic Media*, (Applied Mathematics and Mechanics, Vol. 32), North-Holland, Amsterdam.

Criteria of Dynamic Crack Initiation

Masaaki Watanabe[21]

A criteria of dynamic crack initiation is proposed as $K_{Ic}^{dyn} = K_{Ic}\dfrac{\sigma_c^{dyn.}}{\sigma_c}\left(\dfrac{t_{q.s.}}{t}\right)^{\alpha_S/2}$ *for* $t \le t_{q.s.}$, *where* $K_{Ic}^{dyn.}$ *is the dynamic critical stress intensity factor for initiation and* K_{Ic}, the static fracture toughness. σ_c *and* $\sigma_c^{dyn.}$ *are critical stresses for a growth of microcracks generated at the tip of a crack, in quasi-static and dynamic loading conditions, respectively.* $t_{q.s.}$ *is the characteristic time of quasi-static growth of a crack and* t *is a loading time.* α_s *is a positive number. This criteria is compared with various different experiments and found to be in qualitative agreement with them.*

Ravi-Chandar and Knauss (1984) performed the elaborate experiment of dynamic fracture. The specimen material used in their experiment is Homalite-100 of such size that reflected waves do not interact with the crack tip for duration of the experiment. Thus a literally unbounded (plate) medium is simulated. Stress wave loading on the crack surfaces is achieved by using an electromagnetic loading device and the crack-tip stress field is monitored by the method of caustics. Among numerous interesting results of their experiment (1984, 1985), we only consider an effect of the rate of loading on crack initiation. They found that a loading rate effect on the initiation stress intensity factor is negligible when time to rupture is on the order of 50 μs. With higher loading rates, the stress intensity factor at initiation increases markedly as shown in Fig. 1. Ravi-Chandar and Knauss found that the dynamic critical stress intensity factor at initiation, $K_{Ic}^{dyn.}$, shows the following loading time dependence $K_{Ic}^{dyn.} - K_{Ic} = b_1 t^{-2}$, where b_1 is a proportionality constant. They explained this time dependence in terms of viscous response of the materials. Birch and Williams (1978) performed a conventional energy measuring impact test using two tough polymers, MDPE and PTFE. They measured a rate effect of "fracture toughness," $G_{Ic}^{dyn.}$, and found $G_{Ic}^{dyn.} = b_2 t^{-0.42}$, where t is a loading time defined as $t = \Delta/V$; V is an impact striker speed and Δ, the displacement. b_2 is a proportionality constant. This time dependence is discussed in terms of loss process in the craze region at the crack tip. Williams and Hodgkinson (1981) performed impact tests for three polymers HDPE, PTFE, and PMMA by changing a strain rate (20-620 s^{-1}) and temperatures. They obtained a similar rate effect of the "fracture toughness," as shown in Fig. 2,

$$G_{Ic}^{dyn.} = b_3 t^{-0.5} \quad (1)$$

to the previous work of Birch and Williams, where b_3 is a constant. They explained this effect in terms of notch tip blunting induced by adiabatic heating at the crack tip.

These experiments discussed can be explained by the criteria of dynamic crack initiation, which is proposed in this paper.

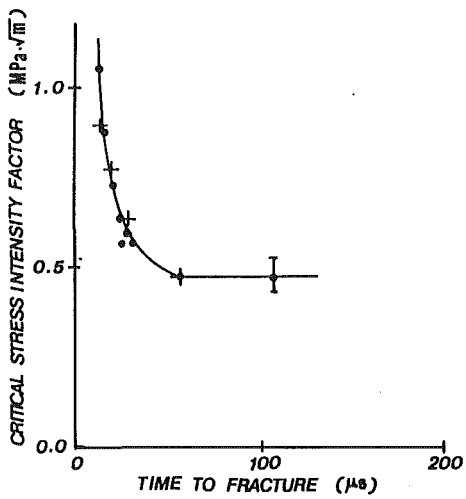


Fig. 1 Variation of the stress intensity factor for initiation. The marked point + is obtained by the criteria $K_{Ic}^{dyn} = K_{Ic}(t_{q.s.}/t)^{\alpha_s/2}$ for $t \le t_{q.s.}$ where K_{Ic} = 0.47 MPa$\sqrt{m}$, $t_{q.s.}$ = 57 μs and α_s = 0.9 are used. The criteria for this case, $\sigma_c^{dyn.} = \sigma_{cr}$ is derived by Watanabe (1991). This figure is taken from Ravi-Chandar and Knauss (1984).

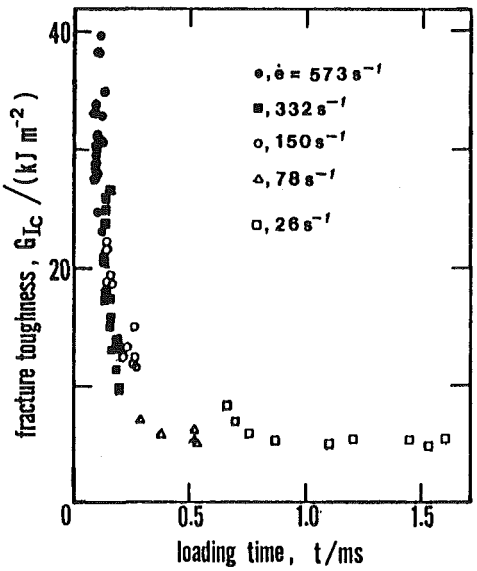


Fig. 2 The "fracture toughness" $G_{Ic}^{dyn.}$ as a function of loading time t for HDPE at 0°C. This figure is taken from Williams and Hodgkinson (1981).

[21]Faculty of Engineering, Kinki University, Takaya, Higashi-Hiroshima, Hiroshima 729-17, Japan.

Contributed by the Applied Mechanics Division of THE AMERICAN SOCIETY OF MECHANICAL ENGINEERS for publication in the ASME JOURNAL OF APPLIED MECHANICS. Manuscript received by the ASME Applied Mechanics Division, Oct. 17, 1991; final revision, Dec. 5, 1992. Associate Technical Editor: M. E. Fourney.

Copyright © 1994 by ASME
Downloaded 03 May 2010 to 171.66.16.20. Redistribution subject to ASME license or copyright; see http://www.asme.org/terms/Terms_Use.cfm

This criteria is written as

$$K_{Ic}^{\text{dyn.}}/K_{Ic}=(\sigma_c^{\text{dyn.}}/\sigma_c)\,(t_{q.s.}/t)^{\alpha_s/2} \text{ for } t\le t_{q.s.}. \quad (2)$$

A simplified form of this criteria is proposed previously by Watanabe (1991).

A Criteria of Dynamic Crack Initiation

Ravi-Chandar and Knauss (1984, 1985) found that microcracks generated at the tip of a crack plays an important role for dynamic behavior of a crack. Following this observation, Watanabe (1991) have developed a general theory of dynamic crack propagation. We assume that microcracks with an average radius, r_0, and a characteristic time, t_0, exist initially. When the external stress is applied, microcracks are assumed to grow in a self-similar manner, statistically. The radius, $r(t)$, of microcracks grow in time according to

$$r(t)=r_0(t/t_0)^{\alpha} \quad \text{for } t\ge t_0 \quad (3)$$

where α is a positive number.

The density, $n(r)$, of microcracks with radius, r, is assumed to be

$$n(r)=n_0(r_0/r)^{\beta} \quad \text{for } r\ge r_0, \quad (4)$$

with the condition, $n_0r_0^2\ll 1$. β is a positive number and n_0, the density of initial microcracks.

The microcrack, located within a length R_{Ic} from the crack tip in the static loading condition, becomes unstable with the critical stress σ_c. The length, $R_{Ic}^{\text{dyn.}}$, and the critical stress, $\sigma_c^{\text{dyn.}}$, in dynamically loaded case is also defined correspondingly. The critical stresses σ_c and $\sigma_c^{\text{dyn.}}$ for a growth of microcracks generated at the tip of a crack, in quasi-static and dynamic loading conditions, are defined as

$$\sigma_c=\frac{K_{Ic}}{\sqrt{2\pi R_{Ic}}},\quad \sigma_c^{\text{dyn.}}=\frac{K_{Ic}^{\text{dyn.}}}{\sqrt{2\pi R_{Ic}^{\text{dyn.}}}}. \quad (5)$$

$\sigma_c^{\text{dyn.}}$, $K_{Ic}^{\text{dyn.}}$, and $R_{Ic}^{\text{dyn.}}$ are supposed to be time dependent unlike those for quasi-static loading conditions. σ_c and $\sigma_c^{\text{dyn.}}$ are primarily determined by microscopic properties of the medium. Equation (5) is used to give an order of magnitude of R_{Ic} and $R_{Ic}^{\text{dyn.}}$.

The microcracks located in an area $wR_{Ic}^{\text{dyn.}}$ grow in time according to Eq. (3), where w is a width of the specimen. Since the critical stress for a growth of microcracks varies depending on local properties around them, they do not always start to grow at the instant of loading. Thus the length, $r(t)$, can be regarded as the maximum radius of microcracks, where t is a loading time. The average number of microcracks with $r(t)\ge r_0$ in the area $wR_{Ic}^{\text{dyn.}}$ can be given as $<n>\, wR_{Ic}^{\text{dyn.}}$, where $<n>$ and $<f(r)>$ are defined as

$$<n>=\int_{r_0}^{r} n(r)dr/\int_{r_0}^{r} dr,$$

$$<f(r)>=\int_{r_0}^{r} f(r)\,n(r)\,dr/\int_{r_0}^{r} n\,(r)\,dr. \quad (6)$$

In Eq. (6) we have shown the averaged quantity, $<f(r)>$, of $f(r)$ for later references.

Since the fracture surface at crack initiation is found to be smooth according to the experiment of Ravi-Chandar and Knauss, we assume that numerous microcracks in the shape of a disk are generated in the plane of a crack. The total area $S_2^{\text{dyn.}}$ of the disk-shaped microcracks in the area $wR_{Ic}^{\text{dyn.}}$ of the crack plane can be written as

$$S_2^{\text{dyn.}}=<n>w\,R_{Ic}^{\text{dyn.}}\,<\pi r^2>. \quad (7)$$

The suffix 2 in $S_2^{\text{dyn.}}$ has a meaning that the spacial dimension of microcracks is two dimensional, i.e., in the shape of a disk.

We postulate that a crack starts to grow when the condition

$$S_2^{\text{dyn.}}=S_c \quad (8)$$

is satisfied, where $S_c=w\,R_{Ic}$. The physical meaning of this postulate can be revealed when Eq. (8) is written in terms of dynamic critical stress intensity factor. Making use of Eqs. (5) and (7), we find

$$K_{Ic}^{\text{dyn.}}=\frac{\sigma_c^{\text{dyn.}}}{\sigma_c}\sqrt{\frac{1}{<n><\pi r^2>}}K_{Ic}. \quad (9)$$

R.H.S. of Eq. (9) is the fracture toughness which is determined by the material properties and microcracks generated at the crack tip.

Since the relation $K_{Ic}^{\text{dyn.}}=K_{Ic}$ holds in a quasi-static condition, a quasi-static microcrack growth occurs when the condition

$$<n>^{-1/2}<r^2>^{-1/2}\approx\sqrt{\pi}\,\frac{\sigma_c}{\sigma_c^{\text{dyn.}}} \quad (10)$$

is satisfied. $<n>^{-1/2}$ represents the average distance between the disk-shaped microcracks in the plane of a crack. Since $\sigma_c^{\text{dyn.}}/\sigma_c\approx 1$ is supposed to hold in a quasi-static case, a crack starts to grow when the radius of disk-shaped microcracks nearly equals to the average distance between microcracks in the plane of a crack. In other words, a crack starts to propagate quasi-statically when microcracks literally link up with each other.

We now calculate $<n><\pi r^2>$ from Eqs. (6), (4), and (3)

$$<n><\pi^2>=\int_{r_0}^{r}\pi r^2 n(r)\,dr/\int_{r_0}^{r}dr=\frac{n_0\pi\,r_0^2}{3-\beta}\left(\frac{t}{t_0}\right)^{\alpha(2-\beta)}$$

$$=\left(\frac{t}{t_{q.s.}}\right)^{\alpha(2-\beta)} \quad \text{for } t\le t_{q.s.} \quad (11)$$

where $t_{q.s.}$ is defined by

$$\frac{t_{q.s.}}{t_0}=\left(\frac{3-\beta}{n_0\,\pi\,r_0^2}\right)^{1/\alpha(2-\beta)}. \quad (12)$$

The condition $r/r_0\gg$ is assumed in calculating Eq. (11). We note here the condition $t_{q.s.}/t_0\gg 1$ holds, since $n_0r_0^2\ll 1$ is assumed. $t_{q.s.}$ represents a characteristic time of quasi-static crack initiation. Substituting Eq. (11) into Eq. (9) we obtain dynamic crack initiation condition in terms of dynamic critical stress intensity factor as follows:

$$K_{Ic}^{\text{dyn.}}=K_{Ic}\,\frac{\sigma_c^{\text{dyn.}}}{\sigma_c}\left(\frac{t_{q.s.}}{t}\right)^{\alpha_s/2} \quad \text{for } t\le t_{q.s.} \quad (2)$$

where α_s is defined as $\alpha_s=\alpha(2-\beta)$. We note here that all terms in R.H.S. of Eq. (2) except for the static fracture toughness, K_{Ic}, are associated with microcracks generated at the tip of a crack.

An energy release rate, which is equivalent to Eq. (2), is

$$G_{Ic}^{\text{dyn.}}=G_{Ic}\left(\frac{\sigma_c^{\text{dyn.}}}{\sigma_c}\right)^2\left(\frac{t_{q.s.}}{t}\right)^{\alpha_s} \quad \text{for } t\le t_{q.s.} \quad (13)$$

where $G_{Ic}^{\text{dyn.}}$ and G_{Ic} are defined by $G_{Ic}^{\text{dyn.}}=(K_{Ic}^{\text{dyn.}})^2/E$ and $G_{Ic}=(K_{Ic})^2/E$ for a case of the plane stress. E is the Young's modulus.

Comparison Between the Criteria and the Experiments

Numerous criterion for crack instability under stress wave loads have been proposed. Shockey, Kalthoff, and Erlich (1983) have reviewed and critically examined these criterion by comparing them with the experiments. They performed plate impact experiments on epoxy specimens embedded with thin circular disks that acted as internal penny-shaped cracks. In this experiment an essentially rectangular tensile load pulse is produced by impacting two plates. Time dependence of the

Downloaded 03 May 2010 to 171.66.16.20. Redistribution subject to ASME license or copyright; see http://www.asme.org/terms/Terms_Use.cfm

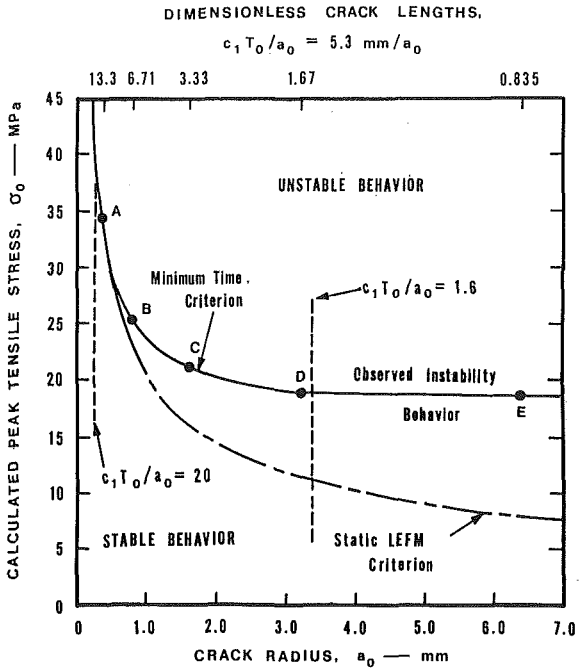


Fig. 3 Comparison of the experimentally determined dynamic crack instability behavior with curves predicted by the "minimum time instability criterion." This figure is taken from Shockey, Kalthoff, and Erlich (1983).

stress intensity factor changes as a function of $c_1 T_0/a_0$, where T_0 is duration of the applied stress σ_0, and a_0, a radius of the disk. c_1 is a velocity of longitudinal waves. Kalthoff and Shockey (1977) defined three domains of instability behavior, which is known as "the minimum time instability criterion." If the condition $c_1 T_0/a_0 > 20$ is satisfied, the circular disk experience a nominally rectangular stress intensity history, the amplitude of which is equal to the static stress intensity and it's duration is practically equal to duration of the applied stress. In this case the crack becomes unstable when the dynamic stress intensity factor exceeds the static fracture toughness, K_{Ic}. This criterion is shown as a static LEFM criterion in Fig. 3. The disk-shaped cracks experience a more triangular stress intensity history when the condition $c_1 T_0/a_0 < 1.6$ is satisfied. In this case the maximum value of the stress intensity curve does not continue to increase with crack length but is constant at $0.59\,\alpha_0\sqrt{\pi T_0 c_1}$ and the instability should occur at a constant stress as is shown by the solid line (region D-E) in Fig. 3. For intermediate crack length, stress duration ratios and the instability conditions change gradually from that postulated for long pulses to that for short ones (region BCD of Fig. 3). In this region instability should occur when the stress intensity factor exceeds the fracture toughness for certain minimum time. "The minimum time instability criterion" is essentially the extension of classical static fracture mechanics to the crack instability under short pulse loads by taking account of the stress intensity history at the crack tip.

In this paper we have proposed a criteria of dynamic crack initiation based on behavior of microcracks generated at the tip of a crack. We only considered loading time as an important parameter and did not take detailed account of the transient stress at the crack tip unlike "the minimum time instability criterion." However, we can identify the existence of three different regimes, the quasi-static ($t \approx t_{q.s.}$), strongly time dependent ($t << t_{q.s.}$) and the intermediate regime, which is in accord with "the minimum time instability criterion." The direct comparison between the criteria and the experiments performed by Kalthoff and Shockey (1977), Shockey, Kalthoff, and Erlich (1983), and Homma, Shockey, and Murayama (1983) is not possible since the loading time is not measured.

We can compare the criteria, Eq. (2), with the experiments of Ravi-Chandar and Knauss (1984) and Williams and Hodgkinson (1981) since the experimental results are expressed in terms of a loading time. In the former experiment, we find $\alpha_s = 0.9$ for the case $\sigma_c^{dyn.}/\sigma_c = 1$. In the latter, they have experimentally found $\alpha_s = 0.5$. It is desirable to give the reason why numerical values of the number α_s changes for different materials. The material dependence of such parameters as $\sigma_c^{dyn.}/\sigma_c$, α_s and $t_{q.s.}$ in R.H.S. of Eq. (2) could be given if dynamic behavior of microcracks generated at the crack tip is clarified theoretically. For example, the growth law and the density distribution function of microcracks shown in Eqs. (3) and (4) have to be derived theoretically. We are unable to give such a theory at this stage. It is interesting, however, that a criteria proposed in this paper is in agreement with the observation of Ravi-Chandar and Knauss (1985) in that a crack propagates by linking up microcracks generated at the tip of a crack. Besides the criteria, Eq. (2) is in accord with the "minimum time instability criterion" and various different experimental results as discussed.

References

Birch, M. W., and Williams, J. G., 1978, "The Effect of Rate on the Impact Fracture Toughness of Polymers," *Int. J. of Fracture*, Vol. 14, pp. 69–84.

Homma, H., Shockey, D. A., and Murayama, Y., 1983, "Response of Cracks in Structural Materials to Short Pulse Loads," *J. of Mech. Phys. of Solids*, Vol. 31, pp. 261–279.

Kalthoff, J. F., and Shockey, D. A., 1977, "Instability of Cracks under Impulse Loads," *J. of Appl. Phys.*, Vol. 48, pp. 986–993.

Ravi-Chandar, K., and Knauss, W. G., 1984, "An Experimental Investigation into Dynamic Fracture," *Int. J. of Fracture*, Part I, Vol. 25, pp. 247–262.

Ravi-Chandar, K., and Knauss, W. G., 1985, "An Experimental Investigation into Dynamic Fracture," *Int. J. of Fracture*, Part II, Vol. 26, pp. 65–80; Part III, pp. 141–154; Part IV, pp. 189–200.

Shockey, D. A., Kalthoff, J. F., and Erlich, D. C., 1983, "Evaluation of Dynamic Crack Instability Criterion," *Int. J. of Fracture*, Vol. 22, pp. 217–229.

Watanabe, M., 1991, "Qualitative Analysis of the Dynamic Crack Initiation and Propagation," *Colloque C3, Suppl. au J. de Physique III*, C3-pp. 713–718.

Williams, J. G., and Hodgkinson, J. M., 1981, "Crack-Blunting Mechanisms in Impact Tests on Polymers," *Proc. Roy. Soc. London.*, Vol. A375, pp. 231–248.

Downloaded 03 May 2010 to 171.66.16.20. Redistribution subject to ASME license or copyright; see http://www.asme.org/terms/Terms_Use.cfm

Journal of Applied Mechanics

Discussions

Random Vibrations of Externally Damped Viscoelastic Timoshenko Beams With General Boundary Conditions[1]

I. Elishakoff[2]. It appears that the clarification should be provided to the statement contained in the paper under discussion. The authors mention that "... Elishakoff and Livshits (1989) have obtained the *closed-form* solution, but for an incomplete differential equation of a simply supported beam with external damping ... They neglected ... three ... forcing function terms ... They claimed ... that this incorrect equation was more consistent than the original Timoshenko equation". Discussion about the forcing function terms is contained in the paper by Samuels and Eringen (1958). They show that the governing equation reduces to $Lw_b = P$; see Eq. (11) in their paper. As far as other terms are concerned, the central one is the fourth-order derivative of the transverse displacement with respect to time, in the equation describing the so-called "Timoshenko beam theory." Sayir (1986, 1987) uncovered by the asymptotic solution of the three-dimensional elastodynamic equation, for the beam of the circular cross-section, that this term is of secondary importance in comparison with other terms in the Timoshenko beam equation. Moreover, he found that if one includes this term, then several other terms, of the same order, should be included too. A physical argument, to substantiate these findings, is quite clear: the above term represents a *correction*, due to the shear deformation, of the *corrective* term due to the rotary inertia, and therefore has a smaller-order contribution than of the terms responsible for genuine contributions of either the rotary inertia or shear deformation. Interestingly, Timoshenko himself did not overestimate the significance of this term. In his paper (1921) as well as in his now classic book (the reader may consult the latest edition, by Weaver, Timoshenko, Young, 1990, p. 436), when calculating the natural frequencies of the simply-supported beam arrives at the conclusion that "... it can be shown that this term is a small quantity of the second order compared with the quantity $\pi^2 r_g^2 A_i^2$ ..." Motivated by this observation, Elishakoff and Lubliner (1984) and later Elishakoff and Livshits (1989) neglected this term and then performed the random vibration analysis resulting in the closed-form solutions. They neglected this term in the differential equation itself, rather than doing so in the characteristic equation, as was done by Timoshenko. The equation thus obtained is simpler than original Timoshenko equation, and more consistent, since it takes into account first-order correction terms due to both rotary inertia and shear deformation and does not include the secondary effect stemming by correcting the corrective term. Such a simplification was adopted also by Tseitlin (1961), Egle (1969) in his energy based derivations of the natural frequencies, and much earlier by Love (1927). Therefore, the "incomplete Timoshenko equation" could be referred to as "Love's equation" as was done in the paper by Abramovich and Elishakoff (1990b). It should be noted that this simpler and more consistent equation yields results in close vicinity to those obtained by the analysis through "complete Timoshenko equations." Indeed, Samuels and Eringen (1958) have found that for a simply-supported beam subjected to the timewise white noise excitation, the difference between the results obtained by the classical Bernoulli-Euler equations and original Timoshenko equations constitutes less than five percent. With simple and consistent "incomplete" equations the results of the classical and nonclassical treatments coincide, as was shown by Elishakoff and Livshits (1989). Thus the results are in agreement as they should be, both for free vibrations (Elishakoff and Lubliner, 1984, see Fig. 1; Abramovich and Elishakoff, 1990a, see Fig. 1), dynamic instability (Lottati and Elishakoff, 1987), and random vibrations (Elishakoff and Livshits, 1989).

To sum up, it appears that for response problems, if the excitation covers the range of moderately high frequencies, the use of the "incomplete Timoshenko equation" (or Love's equation) is quite justifiable, since it eliminates unnecessary numerical difficulties accompanying the original Timoshenko equations which are more complicated but not more consistent than the former one.

References

Abramovich, H., and Elishakoff, I., 1990a, "Bolotin's Dynamic Edge Effect Method Incorporating Shear Deformation and Rotary Inertia," *Journal of Sound and Vibration*, Vol. 136, pp. 355–359.

Abramovich, H., and Elishakoff, I., 1990b, "Influence of Shear Deformation and Rotary Inertia on Vibration Frequencies via Love's Equations," *Journal of Sound and Vibration*, Vol. 137, pp. 516–522.

Egle, D. M., 1969, "An Approximate Theory for Transverse Shear Deformation and Rotary Inertia Effects in Vibrating Beams," NASA CR-1317.

Elishakoff, I., and Livshits, D., 1989, "Some Closed-Form Solutions in Random Vibration of Timoshenko Beams," *Probabilistic Engineering Mechanics*, Vol. 4, pp. 49–54.

Elishakoff, I., and Lubliner, E., 1984, "Random Vibration of a Structure via Classical and Nonclassical Theories," *Probabilistic Methods in the Mechanics of Solids and Structures*, S. Eggwertz and N. C. Lind, eds., Springer, Berlin, pp. 455–468.

Lottati, I., and Elishakoff, I., 1987, "Influence of Shear Deformation and Rotary Inertia on Flutter of a Cantilevered Beam-Exact and Symbolic Computerized Solutions," *Refined Theories in Beams, Plates and Shells and Their Applications*, I. Elishakoff, and H. Irretier, eds., Springer, Berlin, pp. 261–273.

Love, M. A., 1927, *A Treatise on the Mathematical Theory of Elasticity*, 4th ed., Dover, New York, pp. 430–431.

Sayir, M., 1987, "Theoretical and Experimental Results on the Dynamic Behavior of Composite Beams, Plates and Shells," *Refined Dynamical Theories of Beams, Plates and Shells, and Their Applications*, I. Elishakoff and H. Irretier, eds., Springer, Berlin, pp. 72–90.

Sayir, M., 1986–1993, personal communications (extended version to be published).

Timoshenko, S. P., 1921, "On the Correction for Shear of the Differential Equation for Transverse Vibrations of Prismatic Bars," *Philosophical Magazine*, Series 6, Vol. 41, pp. 744–746.

Tseitlin, A. I., 1961, "On the Effect of Shear Deformation and Rotary Inertia

[1]By M. P. Singh and A. S. Abdelnaser, and published in the Mar. 1993 issue of the ASME JOURNAL OF APPLIED MECHANICS, Vol. 60, pp. 149–156.

[2]Professor of Mechanical Engineering and Associate Director, Center for Applied Stochastics Research, Florida Atlantic University, Boca Raton, FL 33431-0991. Mem. ASME.

Copyright © 1994 by ASME
Downloaded 03 May 2010 to 171.66.16.20. Redistribution subject to ASME license or copyright; see http://www.asme.org/terms/Terms_Use.cfm

in Vibrations of Beams on Elastic Foundation," *PMM-Journal of Applied Mathematics and Mechanics*, Vol. 25, pp. 531–535.
Weaver, W. Jr., Timoshenko, S. P., and Young, D. M., 1990, *Vibration Problems in Engineering*, John Wiley and Sons, New York.

Buckling of Thick Orthotropic Cylindrical Shells Under External Pressure[3] and Stability Loss in Thick Transversely Isotropic Cylindrical Shells Under Axial Compression[4]

S. B. Dong[5]. The author has carefully formulated the governing equations for stability analysis of homogeneous, circular cylinders based on three-dimensional elasticity. Such an approach is needed for currently popular composite materials due to their inherently low transverse shear and normal stiffnesses. Also, a three-dimensional formulation is needed when the geometry can be characterized as a thick cylinder.

The author's derivation begins with nonlinear strain-displacement relations and stress equilibrium equations referred to deformed geometry. Upon linearization about the prebuckled equilibrium configuration, a set of governing equations suitable for linear bifurcation buckling is obtained. Buckling due (1) to external pressure under plane strain conditions was considered in the first paper for homogeneous, cylindrically orthotropic materials, and (2) to axial compression for homogeneous, transversely isotropic materials in the second paper. It is this writer's opinion that both of these analyses were executed correctly and well.

In connection to this topic, attention is called to Biot's incremental deformation theory (1965), the theoretical and analytical essences of which are essentially the same as that of the author's. The respective approaches in the derivation may differ somewhat, however, the governing equations for linear bifurcation analysis are virtually equivalent for all practical purposes.

Also, this writer wishes to call attention to a paper by Bradford and Dong (1978), which has escaped the author's literature review. In this paper, the main focus was on natural vibrations of laminated orthotropic cylinders under initial stress based on Biot's theory. The analysis was carried out using semi-analytical finite elements, where the modeling occurs in the thickness direction. Therefore, arbitrary laminate profiles composed any stacking sequence of distinct orthotropic layers may be treated. In a small section of the paper, the case of elastic buckling was discussed, on the basis that the natural frequency goes to zero under the initial stress state. Only one example was given, that being for the long isotropic column of circular cross-section. It is noted that this finite element approach can serve equally well in calculating bifurcation buckling loads.

The same two examples of the author in his second paper were considered. Results based on the finite element method of Bradford and Dong (1978) were computed and compared in Table 1. The finite element model consisted of 41 nodes through the thickness, which translates to an algebraic eigensystem size of 123 degrees-of-freedom. The comparison shows relatively good agreement between the two methods for both examples. Except for the isotropic cylinder with $R_2/R_1 = 1.30$, the finite element results were lower.

Table 1 Comparison of Normalized Critical Loads $\sigma_0 R_2/(E_3 h)$ for $l/R_2 = 5$

	Isotropic Cylinder $\sigma_o R_2/(E_3 h)$			Transversely Isotropic Cylinder $\sigma_o R_2/(E_3 h)$		
R_2/R_1	n, m	Kardomateas	Bradford and Dong	n, m	Kardomateas	Bradford and Dong
1.10	2, 1		0.381	2, 1	0.167	0.164
1.15	2, 1	0.454	0.422	2, 1	0.162	0.152
1.20	2, 2	0.437	0.428	2, 2	0.164	0.157
1.25	2, 2	0.443	0.425	2, 2	0.163	0.155
1.30	1, 1	0.449	0.484	2, 2	0.167	0.156

n, m—circumferential and axial wave numbers in solution form $\mathbf{u} = \exp\{i(m\pi x/l + n\theta)\}$

References

Biot, M. A., 1965, *Mechanics of Incremental Deformation*, John Wiley and Sons, New York.
Bradford, L. G., and Dong, S. B., 1978, "Natural Vibrations of Orthotropic Cylinders Under Initial Stress," *Journal of Sound and Vibration*, Vol. 60, pp. 157–175.

Author's Closure[6]

The author would like to thank Professor Dong for his gracious comments regarding the author's solution to the buckling of thick shells, based on three-dimensional elasticity, and for calling his attention to the paper by Bradford and Dong (1978). The latter is undoubtedly a very well formulated finite element study with very interesting results. The comparison of the results from this work and the author's is definitely a contribution that enhances both papers. Again, the author is grateful to Professor Dong for his effort and time to produce these results and provide a comparison.

[3]By G. A. Kardomateas and published in the Mar. 1993 issue of the ASME JOURNAL OF APPLIED MECHANICS, Vol. 60, pp. 195–202.
[4]By G. A. Kardomateas and published in the June 1993 issue of the ASME JOURNAL OF APPLIED MECHANICS, Vol. 60, pp. 506–513.
[5]Professor, Civil and Environmental Engineering Department, University of California, Los Angeles, CA 90024.
[6]George A. Kardomateas, Associate Professor, School of Aerospace Engineering, Georgia Institute of Technology, Atlanta, GA 30332-0150.

Downloaded 03 May 2010 to 171.66.16.20. Redistribution subject to ASME license or copyright; see http://www.asme.org/terms/Terms_Use.cfm

in Vibrations of Beams on Elastic Foundation," *PMM-Journal of Applied Mathematics and Mechanics*, Vol. 25, pp. 531–535.
Weaver, W. Jr., Timoshenko, S. P., and Young, D. M., 1990, *Vibration Problems in Engineering*, John Wiley and Sons, New York.

Buckling of Thick Orthotropic Cylindrical Shells Under External Pressure[3] and Stability Loss in Thick Transversely Isotropic Cylindrical Shells Under Axial Compression[4]

S. B. Dong[5]. The author has carefully formulated the governing equations for stability analysis of homogeneous, circular cylinders based on three-dimensional elasticity. Such an approach is needed for currently popular composite materials due to their inherently low transverse shear and normal stiffnesses. Also, a three-dimensional formulation is needed when the geometry can be characterized as a thick cylinder.

The author's derivation begins with nonlinear strain-displacement relations and stress equilibrium equations referred to deformed geometry. Upon linearization about the prebuckled equilibrium configuration, a set of governing equations suitable for linear bifurcation buckling is obtained. Buckling due (1) to external pressure under plane strain conditions was considered in the first paper for homogeneous, cylindrically orthotropic materials, and (2) to axial compression for homogeneous, transversely isotropic materials in the second paper. It is this writer's opinion that both of these analyses were executed correctly and well.

In connection to this topic, attention is called to Biot's incremental deformation theory (1965), the theoretical and analytical essences of which are essentially the same as that of the author's. The respective approaches in the derivation may differ somewhat, however, the governing equations for linear bifurcation analysis are virtually equivalent for all practical purposes.

Also, this writer wishes to call attention to a paper by Bradford and Dong (1978), which has escaped the author's literature review. In this paper, the main focus was on natural vibrations of laminated orthotropic cylinders under initial stress based on Biot's theory. The analysis was carried out using semi-analytical finite elements, where the modeling occurs in the thickness direction. Therefore, arbitrary laminate profiles composed any stacking sequence of distinct orthotropic layers may be treated. In a small section of the paper, the case of elastic buckling was discussed, on the basis that the natural frequency goes to zero under the initial stress state. Only one example was given, that being for the long isotropic column of circular cross-section. It is noted that this finite element approach can serve equally well in calculating bifurcation buckling loads.

The same two examples of the author in his second paper were considered. Results based on the finite element method of Bradford and Dong (1978) were computed and compared in Table 1. The finite element model consisted of 41 nodes through the thickness, which translates to an algebraic eigensystem size of 123 degrees-of-freedom. The comparison shows relatively good agreement between the two methods for both examples. Except for the isotropic cylinder with $R_2/R_1 = 1.30$, the finite element results were lower.

Table 1 Comparison of Normalized Critical Loads $\sigma_0 R_2/(E_3 h)$ for $l/R_2 = 5$

	Isotropic Cylinder $\sigma_o R_2/(E_3 h)$			Transversely Isotropic Cylinder $\sigma_o R_2/(E_3 h)$		
R_2/R_1	n, m	Kardomateas	Bradford and Dong	n, m	Kardomateas	Bradford and Dong
1.10	2, 1		0.381	2, 1	0.167	0.164
1.15	2, 1	0.454	0.422	2, 1	0.162	0.152
1.20	2, 2	0.437	0.428	2, 2	0.164	0.157
1.25	2, 2	0.443	0.425	2, 2	0.163	0.155
1.30	1, 1	0.449	0.484	2, 2	0.167	0.156

n, m—circumferential and axial wave numbers in solution form $\mathbf{u} = \exp\{i(m\pi x/l + n\theta)\}$

References

Biot, M. A., 1965, *Mechanics of Incremental Deformation*, John Wiley and Sons, New York.
Bradford, L. G., and Dong, S. B., 1978, "Natural Vibrations of Orthotropic Cylinders Under Initial Stress," *Journal of Sound and Vibration*, Vol. 60, pp. 157–175.

Author's Closure[6]

The author would like to thank Professor Dong for his gracious comments regarding the author's solution to the buckling of thick shells, based on three-dimensional elasticity, and for calling his attention to the paper by Bradford and Dong (1978). The latter is undoubtedly a very well formulated finite element study with very interesting results. The comparison of the results from this work and the author's is definitely a contribution that enhances both papers. Again, the author is grateful to Professor Dong for his effort and time to produce these results and provide a comparison.

[3]By G. A. Kardomateas and published in the Mar. 1993 issue of the ASME JOURNAL OF APPLIED MECHANICS, Vol. 60, pp. 195–202.
[4]By G. A. Kardomateas and published in the June 1993 issue of the ASME JOURNAL OF APPLIED MECHANICS, Vol. 60, pp. 506–513.
[5]Professor, Civil and Environmental Engineering Department, University of California, Los Angeles, CA 90024.
[6]George A. Kardomateas, Associate Professor, School of Aerospace Engineering, Georgia Institute of Technology, Atlanta, GA 30332-0150.

Copyright © 1994 by ASME
Downloaded 03 May 2010 to 171.66.16.20. Redistribution subject to ASME license or copyright; see http://www.asme.org/terms/Terms_Use.cfm

Journal of Applied Mechanics

Book Reviews

Fundamentals of Friction: Macroscopic and Microscopic Processes (NATO Advanced Science Institute Series, Series E: Applied Sciences, Vol. 220), edited by I. L. Singer and H. M. Pollack. Kluwer Academic Publishers, Dordrecht, The Netherlands, 1993. 621 pages. Price: $199.00.

REVIEWED BY O. VINGSBO[1]

The book consists of 28 papers, presented at the NATO Advanced Study Institute on the Fundamentals of Friction, held in July 1991 in the German Harz mountains. The objective of the Institute was to bring together experts from the two fields of "classical" macroscopic surface mechanics, and "modern" surface science, including molecular dynamics and point contact microscopy of atomic resolution. Thus, friction phenomena are approached by macroscopic models and experiments, as well as by what is being learned at the microscopic level (in current jargon referred to as nano tribology).

The papers are divided into seven chapters. Five deal with the classical macro aspects, while, not unexpectedly, only one is devoted to the atomic scale approach. One final chapter brings together three papers on self-induced stick-slip vibrations and instabilities in friction systems.

The five macromechanical papers are mainly based on K. L. Johnson's continuum mechanical formulation of surface mechanics. (Johnson contributes an Appendix, summarizing the concepts of his well-known book "Contact Mechanics.") After an initial chapter with broader perspectives on energy dissipation (by D. Tabor) and fluctuations in friction (by E. Rabinowicz), a second chapter is focused on adhesion contributions to frictional forces, both between smooth and rough surfaces and between particles in granular materials. Chapter 3 deals with fracture, deformation, and shear of the sliding interfaces, while Chapters 4 and 5 treat lubricated contacts from the tribochemical point of view and with respect to molecularly thin surface films.

The sixth chapter represents the atomic scale approach to friction. An introductory paper by McClelland and Glosli presents two atomistic models for friction as well as frictionless and wearless sliding contacts. The models are applied in molecular dynamics calculations of frictional force and energy and are compared to the results of atomic force microscope (AFM) measurements. In a second paper a team of researchers from the Institute of Physics at the University of Basel gives an update on Friction Force Microscopy (FFM). The authors also report experiments on dry mica and magneto optical disks, and of 2 and 4-molecular-layer soap films. A final group of three papers deal with computational and simulation techniques for atomic scale surface contacts. Ferrante and Bozzolo from NASA Lewis Research Center in Cleveland discuss the use of different potential functions (first principles compared to pair, many body, and semi-empirical potentials) for modeling surface energy and friction forces. Uzi Landman's pioneering group from Georgia Institute of Technology in Atlanta give a detailed report of their computer simulations of the contact between an atomically sharp tip and a surface. Based on large-scale molecular dynamics calculations they demonstrate the atomic interaction processes of jump-to-contact, elastic and plastic yield, necking, wetting, stick-slip and materials transfer, in metalic, ionic and covalent crystal structures as well as in alkane films. A final paper by Belak and Stowers from Lawrence Livermore National Laboratory describes a similar molecular dynamics method for two and three-dimensional simulations of indentation and scraping. The method is also applied to two-dimensional orthogonal metal cutting.

To a professional tribologist, this book is extremely interesting. It gives a broad overview of the current front line in friction research, and at the same time provides examples of spearhead projects and techniques. The chapter on new approaches on the nano and atomic scale is particularly fascinating.

The General Problem of the Stability of Motion, by A. M. Lyapunov. Taylor and Francis, Bristol, PA, 1993. 270 pages. Price: $65.00.

REVIEWED BY J. A. WALKER[2]

In 1892 there appeared a remarkable Russian memoir entitled "The General Problem of The Stability of Motion." This work served as a doctoral dissertation for the great Russion mathematician Alekandr Mikhailovich Lyapunov (1857–1918). In it the question of stability or instability of motions (and equilibria) of mechanical systems was considered with unprecedented depth and clarity. The stability theory of today is based upon this seminal work.

Only a few pages of this lengthy memoir (250 pages) were devoted to a brilliantly simple idea, which Lyapunov called a "second method" of stability analysis. Consider the real n-dimensional evolution equation

$$\dot{x}(t) = f(x(t)), \quad t \geq 0$$

with initial data $x(0) = x_o$. Let $V(x)$ be any known real-valued function of x such that the function

$$\dot{V}(x) \equiv (\nabla V(x))^T (f(x))$$

is non-negative on some set S. This implies that $V(x(t))$ is nonincreasing during any time interval over which $x(t)$ remains in S. Using this "obvious" result, Lyapunov obtained surprisingly simple sufficient conditions for both the stability

[1]Department of Mechanical Engineering, University of Houston, Houston, TX 77204-4792 and Uppsala University, Uppsala, Sweden.

[2]Department of Mechanical Engineering, Northwestern University, Evanston, IL 60208.

Copyright © 1994 by ASME
Downloaded 03 May 2010 to 171.66.16.20. Redistribution subject to ASME license or copyright; see http://www.asme.org/terms/Terms_Use.cfm